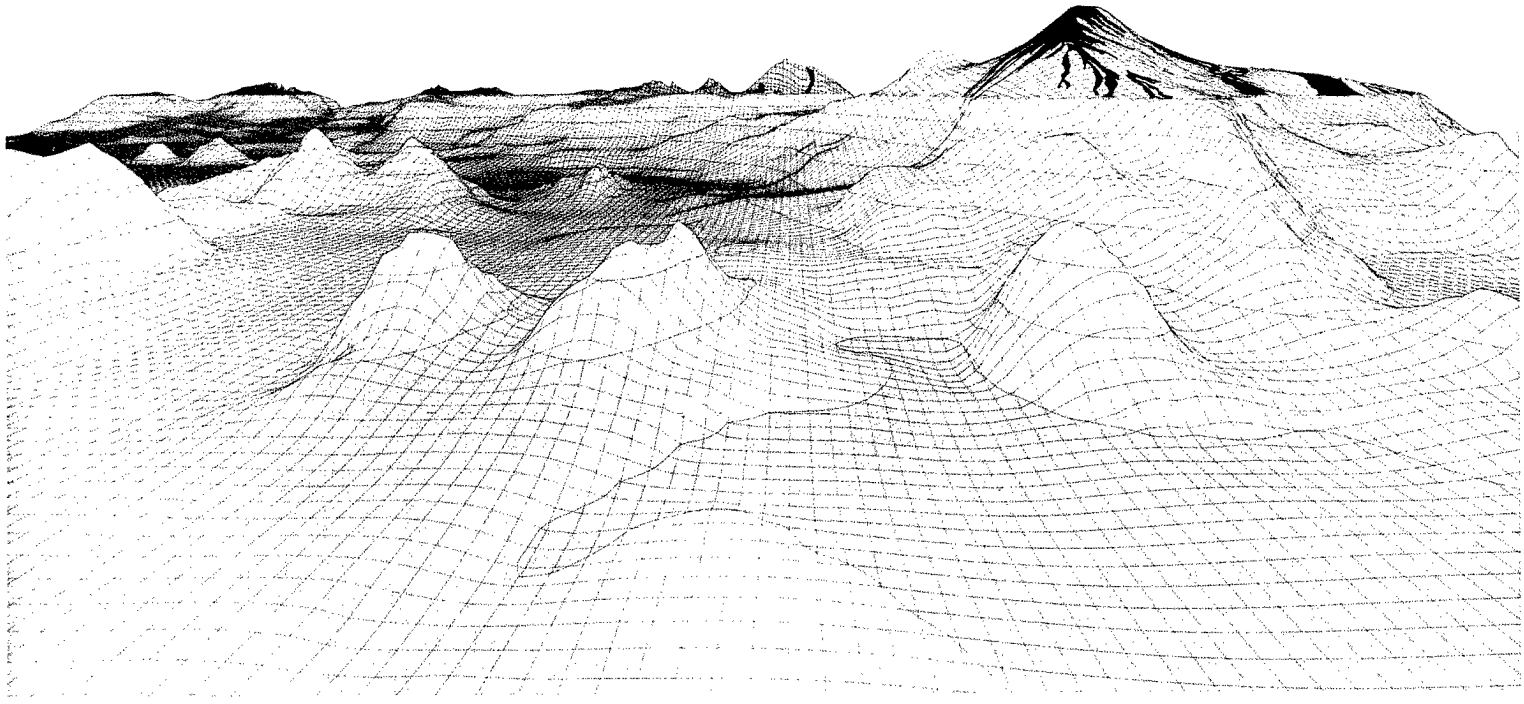
'Aha Huliko'a



TOPOGRAPHIC EFFECTS IN THE OCEAN

DISTRIBUTION STATEMENT A
Approved for public release
Distribution Unlimited

19970717 121

Proceedings
Hawaiian Winter Workshop
University of Hawaii at Manoa
January 17–20, 1995

DEPARTMENT OF THE NAVY
OFFICE OF NAVAL RESEARCH
SEATTLE REGIONAL OFFICE
1107 NE 45TH STREET, SUITE 350
SEATTLE WA 98105-4631

IN REPLY REFER TO:

4330
ONR 247
11 Jul 97

From: Director, Office of Naval Research, Seattle Regional Office, 1107 NE 45th St., Suite 350, Seattle, WA 98105
To: Defense Technical Center, Attn: P. Mawby, 8725 John J. Kingman Rd., Suite 0944, Ft. Belvoir, VA 22060-6218

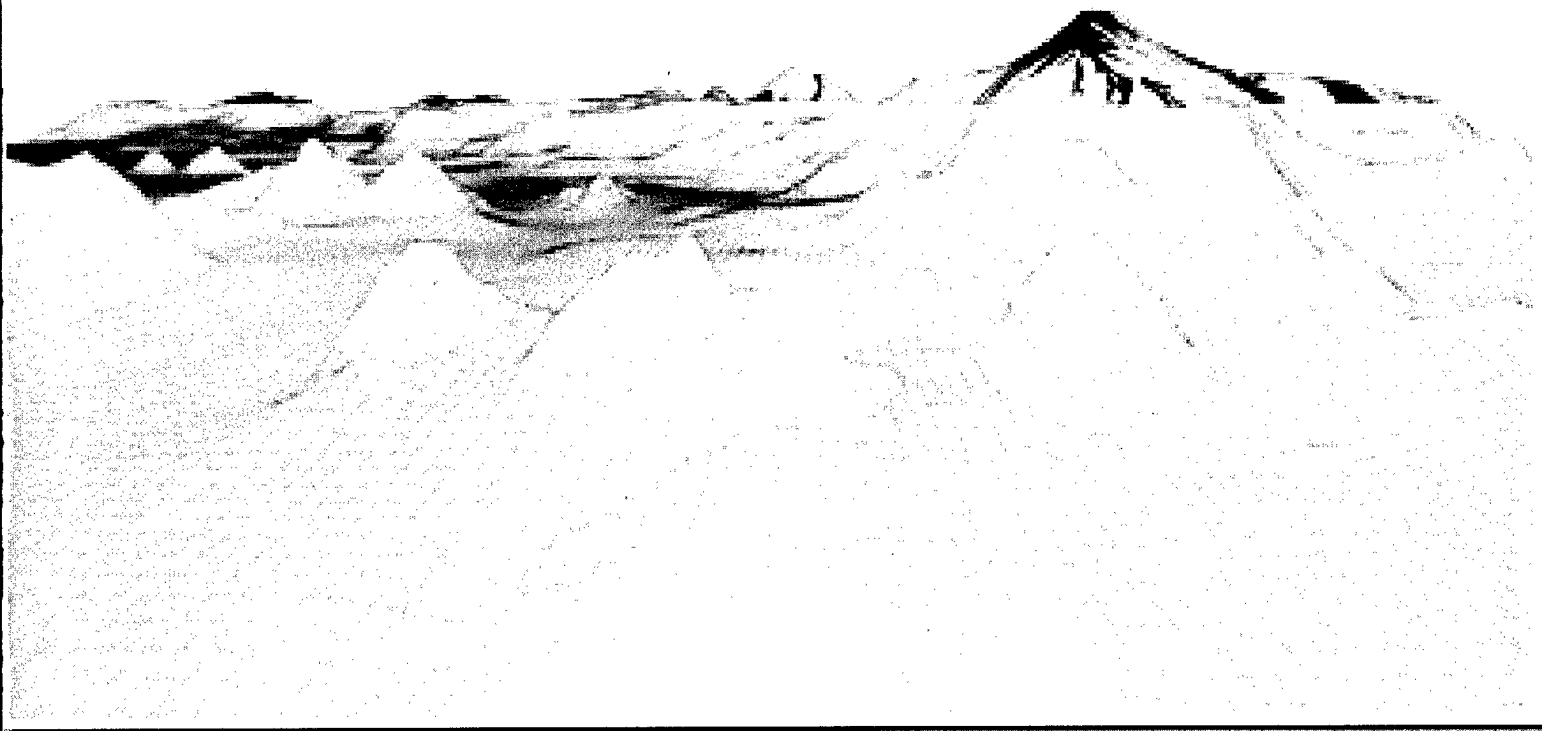
Subj: RETURNED GRANTEE/CONTRACTOR TECHNICAL REPORTS

1. This confirms our conversations of 27 Feb 97 and 11 Jul 97. Enclosed are a number of technical reports which were returned to our agency for lack of clear distribution availability statement. This confirms that all reports are unclassified and are "APPROVED FOR PUBLIC RELEASE" with no restrictions.

2. Please contact me if you require additional information. My e-mail is *silverr@onr.navy.mil* and my phone is (206) 625-3196.

ROBERT J. SILVERMAN

'Aha Huliko'a



TOPOGRAPHIC EFFECTS IN THE OCEAN

PROCEEDINGS
'Aha Huliko'a
Hawaiian Winter Workshop
University of Hawaii at Manoa
January 17–20, 1995

PETER MÜLLER
DIANE HENDERSON
editors

DISTRIBUTION STATEMENT A
Approved for public release;
Distribution Unlimited

Sponsored by the U.S. Office of Naval Research,
the School of Ocean and Earth Science and Technology,
and the Department of Oceanography, University of Hawaii
(Cover image from Dynamic Graphics)

DTIC QUALITY INSPECTED 5

SOEST Special Publication • 1995

Cover, title page design by Nancy Hulbirt and Brooks Bays,
production assistance by May Izumi and Barbara Jones, Publication Services, SOEST.

FOREWORD

The eighth ʻAha Hulikoʻa[†] Hawaiian Winter Workshop was held January 17-20, 1995, at the East-West Center in Honolulu, Hawaii. The topic was Flow-Topography Interactions.

Topography affects ocean circulation in many ways. Topography guides and blocks ocean currents; it supports special wave modes and traps others; it rectifies time-dependent flows and breaks up depth-independent flows; it exerts a stress on mean flows and causes mixing. Many of these topographic effects have recently been studied by intense observational programs and by high resolution numerical simulations. These studies were the object of the workshop's lecture and discussions. Overall, they showed that the influence of seafloor topography on ocean circulation is greater than previously assumed.

The lectures of the workshop are published in these proceedings. The order of the papers follows loosely the agenda of the workshop and covers seamounts, abyssal circulations, ocean-shelf exchanges, and the rectification process. Also included is a summary of the meeting.

The workshop, made possible by a grant from the U.S. Office of Naval Research, was hosted by the Department of Oceanography of the School of Ocean and Earth Science and Technology, University of Hawaii. Support by the SOEST Enrichment Fund and the Joint Institute for Marine and Atmospheric Research is gratefully acknowledged. The excellent facilities and capable staff of the East-West Center contributed greatly to the success of the meeting. This proceedings volume came into existence through the creative and dedicated research of the scientists who gathered and Hawaii and provided the articles that follow.

Peter Müller
Diane Henderson

Department of Oceanography
School of Ocean and Earth Science and Technology
1000 Pope Road
University of Hawaii
Honolulu, HI 96822

[†] ʻAha Hulikoʻa is a Hawaiian phrase meaning an assembly that seeks into the depth of a matter.

This work is related to Department of the Navy Grant N-00014-94-I-0600 issued by the Office of Naval Research. The U.S. Government has a royalty-free license throughout the world in all copyrightable material herein.



PARTICIPANTS

R. Kloosterziel
G. Mitchum, E. Kunze, D. Luther, D. Moore
G. Carnevale, C. Garrett, C. Frankignoul, C. Eriksen, G. Ivey, N. Hogg, M. Hendershott, S. Thorpe
P. Müller, D. Haidvogel, J. Huthnance, R. Ford, B. Hickey, S. Allen, J. Becker, A. Shchepetkin, L. Maas, J. Verron, A. Beckmann, G. Holloway
L. Goodman, J. Whitehead, R. Salmon, R. Holman, E. Chassignet, P. Haines

Table of Contents

Waves, Mean Flows, and Mixing at a Seamount
Charles C. Eriksen 1

Fine- and Microstructure Observations of Trapped Diurnal Oscillations Atop Fieberling Seamount
Eric Kunze and John M. Toole 15

Waves Trapped to Discrete Topography: Existence and Implications
D.S. Luther 43

Numerical Modeling of Time-Mean Flow at Isolated Seamounts
A. Beckmann 57

Rossby Waves over a Lattice of Different Seamounts
M. C. Hendershott 67

Focusing of Internal Waves and the Absence of Eigenmodes
Leo R.M. Maas 73

Topographic Filtering and Reflectionless Transmission of Long Waves
Leo R.M. Maas 79

Circulation, Exchange and Mixing at the Ocean-Shelf Boundary
J.M. Huthnance 85

Coastal Submarine Canyons
B.M. Hickey 95

Shelf Break Momentum Transport by Internal Waves Generated by Along-Slope Currents over Topography
S.A. Thorpe, D. Jiang, and J.M. Keen 111

Flow Separation in the Ocean
Chris Garrett 119

An Inertial Model of the General Circulation in an Ocean with Bottom Topography
Janet M. Becker 125

Altimetric Observations of Rossby Wave Variability near Topography
Gary T. Mitchum 131

Some Examples of Topographic Influence on the Abyssal Circulation
Nelson G. Hogg 137

Critical Control by Topography—Deep Passages, Straits, and Shelf Fronts
J.A. Whitehead 141

A Simple Model of Abyssal Flow
Rick Salmon 157

Realistic-Bathymetry, Small-Dissipation Solutions for the North Atlantic/Caribbean
R. Ford 163

Quasi-Geostrophic Flow over Anisotropic Topography
G.F. Carnevale, R. Purini, P. Orlandi, and P. Cavazza 169

The Frequency Dependence of Bottom Trapping and its Implications for Gravity Current Interaction with Topography
Susan E. Allen 191

Internal Waves, Bottom Slopes and Boundary Mixing
G.N. Ivey, P. De Silva, and J. Imberger 199

Rectified Flows over a Finite Length Shelf Break: a Bank and a Canyon Case
J. Verron, D. Renouard, and D.L. Boyer 207

Wind-Driven Residual Currents over a Coastal Canyon
D.B. Haidvogel and A. Beckmann 219

Interaction of Turbulent Barotropic Shallow-Water Flow with Topography
Alexander F. Shchepetkin 225

Topographic Stress Parameterization in a Primitive Equation Ocean Model:
Impact on Mid-latitude Jet Separation
Andreas J. Roubicek, Eric P. Chassignet, and Annalisa Griffa 239

Measuring the Skill of an Ocean Model under Eddy-Topographic Effects,
Based on a Global Inventory of Long-Term Current Meters
Greg Holloway and Tessa Sou 253

The Interaction of Waves, Currents and Nearshore Bathymetry
R.A. Holman 257

Meeting Report: Topographic Effects in the Ocean
P. Müller and G. Holloway 263

Waves, Mean Flows, and Mixing at a Seamount

Charles C. Eriksen

School of Oceanography, University of Washington, Box 357940, Seattle WA 98195-7940

Abstract. Moored array measurements of current and temperature at Fieberling Guyot (32° 25'N, 127° 47'W) are dominated by internal wave and tidal band fluctuations. Internal wave band variance on the flanks of the seamount is dominated by amplification of waves by reflection at and near the local critical frequency of the sloping bottom. Diurnal, slightly superinertial, and semidiurnal band fluctuations exhibit coherent downward phase propagation. These have the character of a forced evanescent response as opposed to free vertically-radially standing seamount trapped wave modes. At depths near the summit rim, mean horizontal flows have a component toward deeper water, while on the flanks mean flows are much weaker but have a component toward shallower water. In both cases, the mean Eulerian flows appear driven by fluctuations.

Introduction

Until recently, very little was known about the character of oceanic flow near seamounts, particularly seamounts that occupy a substantial fraction of the water column. Most observations and theories were concerned with distortions of mean flows by isolated topographic features rather than with wavelike fluctuations found near them. Theories have addressed the possibility that Taylor caps may isolate water above a seamount from surrounding water masses. Chapman and Haidvogel, 1992, considered formation of Taylor caps over large seamounts, in contrast to much previous work restricted to considering topography that occupied only a small fraction of the total depth. By contrast, observations at Fieberling Guyot, a large seamount in the eastern North Pacific (32° 25'N, 127° 47'W) show that flows are dominated by fluctuations rather than the mean. These fluctuations are predominately tidal (Eriksen, 1991, Brink, 1995) in the depth range bracketing the summit and centered at the critical frequency for internal wave reflection off a slope deep on the seamount flanks (Eriksen, 1995). Mean flows are generally parallel to depth contours near the bottom in an anticyclonic sense but do have slight cross-isobath components. Near the summit, horizontal flows are in the off-slope sense, consistent with local downwelling (Eriksen, 1991, Brink, 1995), yet on the steep flanks of the seamount, flows near the bottom have an onslope (radially inward) sense. This paper discusses the possibility that these radial mean flows are associated with the fluctuating flows in tidal and internal wave bands.

The paper begins with a brief summary of the structure of internal wave band motions on the steep flank of Fieberling Guyot and their connection to mixing events. The description and analysis of Eriksen, 1995, is extended to include buoyancy and momentum flux estimates and their spatial structures. The following section presents a description of motions in diurnal and semidiurnal frequencies and the band between them, which includes the inertial frequency. Brink, 1995, confined his description to motions in tidal bands near the seamount summit, while motions over a continuum across the inertial frequency all exhibit a similar structure, including continuous downward phase propagation to the bottom on the sloping flanks. As with internal waves, these motions generate eddy fluxes of buoyancy and momentum. Kunze, 1995, recognized the phase structure of flow atop Fieberling in velocity profile surveys and showed the consistency in several respects of a vortex trapped internal wave model with these observations, in contrast to Brink's seamount trapped wave model. Here, we offer another possible explanation: that the motions observed are an evanescent wave response to forcing across a wide range of frequencies, both subinertial and superinertial. Finally, the paper examines the mean flows observed both near the summit and on the flank of the seamount, emphasizing the radial component of flow near the bottom from which vertical motion is inferred. In the last section, the possibility that internal wave breaking and evanescent wave rectification generates mean flows is discussed.

The Field Study

The observations used here were collected as part of a multi-disciplinary project called TOPO, sponsored by the U.S. Office of Naval Research. The field program at Fieberling Guyot included a thirteen-month moored array of current and temperature sensors at various locations on and near the seamount. Details of the records are presented in Wichman *et al*, 1993. Records considered here are from moorings were set near the summit (C), at

the rim of the summit plain (R2 and R3), and on the seamount flanks (F2, F3, F4, and F5) (Figure 1). These moorings were located over one quadrant rather than on all sides of the guyot for reasons of economy. Seamount bathymetry was surveyed with a multi-beam depth sounder prior to the deployment cruise and again, in more detail near the mooring sites, on the recovery cruise. The cluster consisting of three moorings F3, F4, and F5, each separated by roughly 300 m on the southwest flank of the seamount, formed an internal wave array while the summit, rim, and flank moorings together formed an array to detect bottom-trapped motions that propagate azimuthally around the seamount.

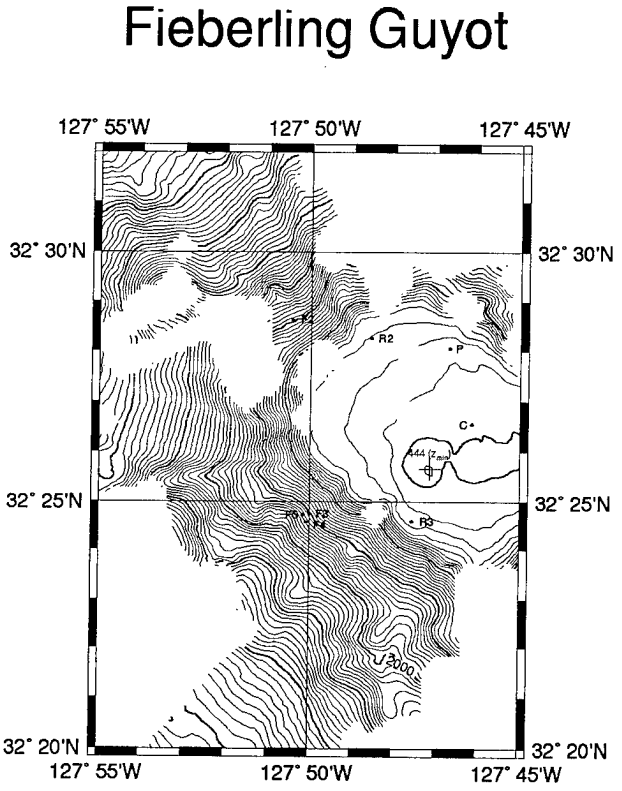


Figure 1. Bathymetry and locations of moorings on the western summit region of Fieberling Guyot. The moorings designated C, R, and F were placed near the center, on the rim of the summit plain, and on the flanks of the seamount. The triangle of moorings F3, F4, and F5 formed an internal wave array. The mooring P was from a pilot study one year before the rest of the array was set (see Eriksen, 1991). Depth contours are from a partial Hydrosweep survey of the seamount on the mooring recovery cruise on *R/V Thompson*. Depth contours are drawn every 50 m with every tenth contour drawn with heavy curve. The summit, a rocky spur is at 444 m depth. The seamount rises from a surrounding region of 4500 m depth.

Roden, 1991, 1994, allowed use of his conductivity-temperature-depth (CTD) surveys near Fieberling Guyot in August, 1989 and May, 1991 to calculate average temperature and salinity profiles, temperature-salinity relationships, and buoyancy frequency profiles. These are used to interpret temperature fluctuations variously as buoyancy or vertical velocity fluctuations through assuming that temperature fluctuations are reflect vertical advection of the mean gradient field.

Standard techniques of spectral analysis were applied to a common 364-day period subset of the records starting October 1, 1990. Independent spectral estimates were formed by averaging over 13 adjacent frequency bands for periods 12 h and longer and doubling the amount of averaging for each successive octave above the semidiurnal band. Complex empirical orthogonal functions (CEOFs) are used to describe the coherent structures of variability in each frequency band. This technique uses the eigenvalues and eigenvectors of a cross-spectral matrix (or coherence matrix) to describe variability in terms of the independent coherent structures ranked by their contribution to the total variance (Wallace and Dickinson, 1972, Eriksen, 1985). Consideration is limited to frequency bands in which a single empirical mode dominates. This has the effect of eliminating incoherent fluctuations from calculations of eddy fluxes and their gradients.

Internal Wave Structure

Internal wave band fluctuations on the flank of Fieberling Guyot are dominated by the process of wave reflection from a sloping boundary. While linear theory for the ideal case of reflection off an infinite sloping plane is consistent with several aspects of this process, nonlinearities are clearly apparent as well (Eriksen, 1995). Internal waves incident on a sloping boundary are obliged to change their wavenumber magnitude upon reflection. For downward rays incident from deeper water, reflection magnifies the vertical and onslope components of wavenumber. This magnification is forced by the requirement to match the projection parallel to the slope of incident and reflected wavenumbers. Waves incident at arbitrary orientations to the sloping boundary are turned more normal to isobaths by reflection. The energy density of reflected waves is amplified over that of incident waves by the ratio of the vertical wavenumber amplification squared because both ray tube widths and group speeds are inversely proportional to the vertical wavenumber amplification. Reflected waves dominate the wave field due to energy density enhancement and the enhancement is greater nearer the internal wave critical frequency σ_c where incident rays match the bottom slope.

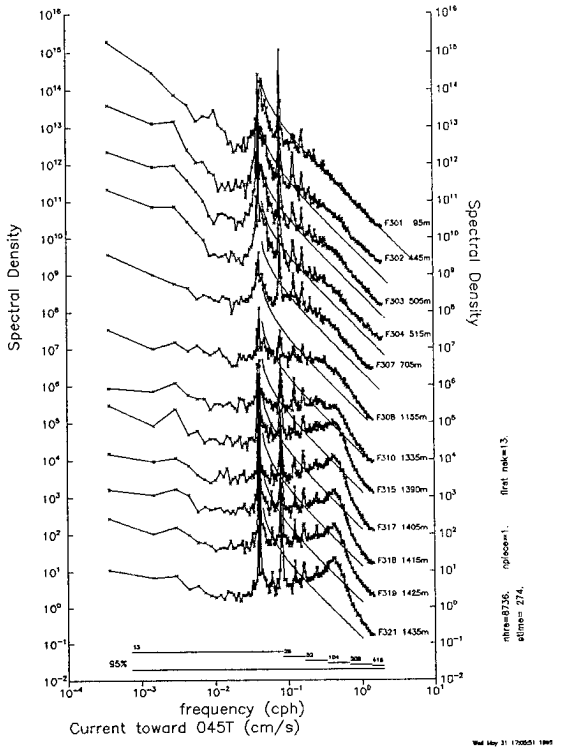


Figure 2. Spectra of the onslope (northeast) component of current on mooring F3 on Fieberling Guyot. Spectra are labeled by instrument number and depth and are arranged in order of depth from 95 m to 1435 m (where the anchor depth of the mooring was 1455 m). Scales are correct for the deepest spectral estimate (F321) and are successively offset by one decade for spectra at shallower depths. Smooth curves superimposed are the Garrett-Munk model estimates for the open deep ocean and serve as references fro the observed spectra. Their endpoints are at the inertial frequency f and the local buoyancy frequency N. Spectra are enhanced about the internal wave critical frequency σ_c = 0.42 cph. Intervals of 95% confidence are based on frequency averaging of a multiple of 13 independent spectral estimates.

The spectra of current in the onslope direction (i.e. normal to local isobaths) calculated from the records on F3, the heavily instrumented mooring in the internal wave cluster on the southwest flank of the seamount, indicate substantial departure from the Garrett-Munk model spectra that characterize deep open ocean spectra (Figure 2). The departure is strongest near the bottom and takes the form an enhancement at the local critical frequency σ_c = 0.42 cph. The enhancement around the critical frequency is evident even several hundred m above the bottom, while the spectrum from 95 m depth closely matches the Garrett-Munk prediction. A single CEOF describes half or more of the variance in each frequency band in the bottom 300m, from an octave below to an octave above the critical frequency (Eriksen, 1995). When records from all depths on mooring F3 are decomposed into CEOFs, two frequency ranges stand out as being dominated by a single mode: a band from 24 through 16 h and a band from about 4 to 1.5 h (Figure 3). Discussion of the longer period band motions is deferred until below. The shorter period band is centered on the local internal wave critical frequency.

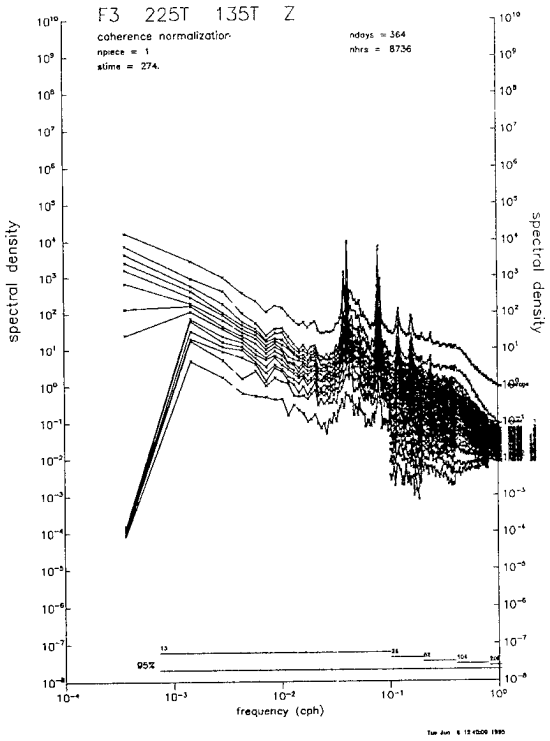


Figure 3. Spectra of complex empirical orthogonal functions calculated from the eigenvalues and eigenfunctions of the coherence matrix of current and temperature records on mooring F3. The top curve gives the average spectrum and each curve below it depicts the energy density accounted for by successively higher empirical mode. A single CEOF dominates structure over a band from the diurnal peak to a period of roughly 16 h and also over a band from about 4 to 1.5 h period, as is evident in the distinct separation of the second curve from the top from all other curves below it over these ranges.

Both spectra and the complex eigenfunctions that dominate variance near the critical frequency indicate that linear theory accounts for much of the behavior of motions in the internal wave band. Linear features include the transition between prominent upward and

offslope phase propagation at subcritical frequencies to downward and onslope propagation at supercritical frequencies. Waves are aligned across isobaths near the critical frequency, as expected by the linear theory of internal wave reflection off a sloping bottom. Linear theory is also consistent with the observed ratio of vertical to horizontal wavenumber for these eigenfunctions.

Linear theory fails to account for the finite enhancement of spectra at the critical frequency itself, for the decay of spectral enhancement with height off the bottom, and the vanishing of wavenumber at the critical frequency rather than the presence of only very fine scales. Statically unstable conditions are frequently found in the bottom few hundred m on the seamount flank. More than 11% of Richardson number estimates over a 10 m separation are found to be negative while altogether more than 25% are less than 0.25. Shear and density gradient fluctuations near the critical frequency dominate variance in the internal wave band as well as overall variance. Internal wave reflection is responsible for wave breaking, hence loss from the wave field to dissipation and to production of potential energy (buoyancy mixing). The rate of potential energy production diminishes with distance from the bottom, suggesting a convergence of turbulent fluxes.

Records from the internal wave array can be used to compute eddy fluxes of heat and momentum. Since the temperature-salinity relationship is well defined in the depth range of instruments on moorings F4 and F5 and those nearby on F3, temperature can reliably be converted to density to form fluctuation buoyancy b' where $b' \equiv -g\,(\rho - \bar{\rho})\,\rho_0^{-1}$ is the departure from the mean with ρ signifying density, g density, mean quantities have an overbar, and reference values have a subscript zero. Since vertical velocity is not measured directly, a vertical advection assumption $b'_t + N^2 w' = 0$ is used, where N is the average buoyancy frequency. The possibility of estimating vertical eddy transport of buoyancy is, of course, precluded.

The structure of eddy fluxes calculated from the dominant complex eigenfunction structure integrated across the internal wave band shows an offslope buoyancy transport that diminishes with distance from the sloping bottom (Figure 4, top left panel). Accompanying this flux are onslope and upward fluxes of momentum. These two results can be traced to the rotation in time of current vectors in the vertical plane normal to isobaths: their sense is to turn clockwise when viewed with shallow water on the right (Eriksen, 1995). The convergence of these fluxes suggests mean Eulerian flows, as discussed below.

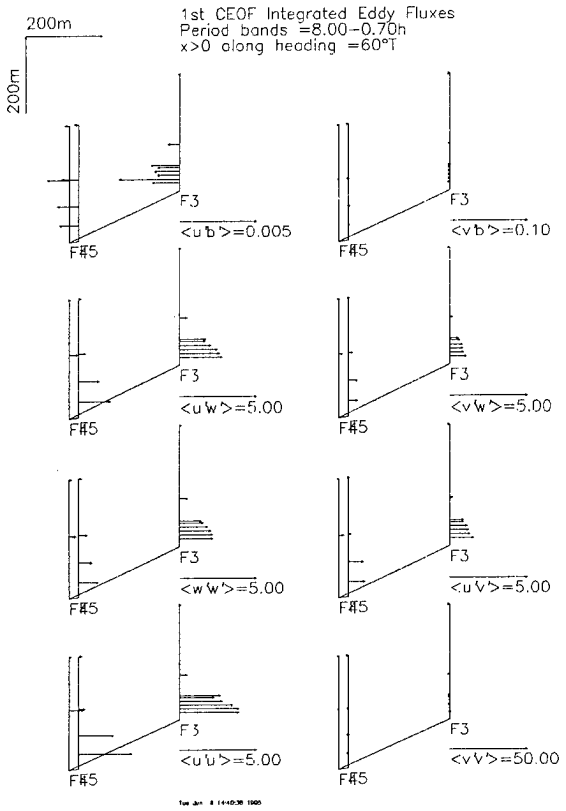


Figure 4. Internal wave band eddy fluxes of momentum (lower six panels) and buoyancy (top two panels) calculated from the first CEOF describing variability within 300 m of the bottom at moorings F3, F4, and F5. Fluxes are drawn as vectors in the vertical plane along 60°T heading (the local onslope direction). Perturbation current components are taken as a right-handed triad with u in the onslope direction. Units given in the scale are cm^2/s^2 for momentum and cm^2/s^3 for buoyancy fluxes.

Diurnal through Semidiurnal Structure

A single empirical mode dominates flow structure in the diurnal and semidiurnal tidal frequency bands, but also over a broad range of periods from diurnal (subinertial) to about 16 h (superinertial). The dominant mode has similar, but not identical, structure throughout this range. CEOF spectra illustrate the dominance of a single empirical mode at the tidal peaks O_1, P_1-K_1 (the latter are indistinguishable in a one year record), M_2, and S_2 (Figure 3). They also illustrate the less pronounced, but still evident, dominance of a single mode from slightly subinertial (0.94f) to somewhat superinertial (1.46*f*) frequencies (where f = 1/22.385 cph is the inertial

frequency. The inertial frequency divides this range dynamically, since free internal gravity waves are possible only at superinertial frequencies. Despite this division, coherent bottom-trapped flow patterns of similar structure are found over a broad range of frequencies spanning it.

The existence of a roughly cylindrically symmetric first azimuthal mode diurnal oscillation trapped near the summit at Fieberling Guyot has recently been documented. Brink, 1995, gives an interpretation in terms of radially and vertically standing free modes whereas Kunze, 1995, noted the predominance of downward propagating phase in the clockwise component of current, consistent with the pilot mooring results (Eriksen, 1991). Similar flow structures appear over a broad range of frequencies, not simply at the diurnal tidal lines. Moreover, downward propagating phase is a consistent feature of these oscillations.

Above the seamount summit and near the summit rim, currents are nearly circularly polarized in the clockwise sense both at the diurnal tidal frequencies and across the continuum from diurnal to a frequency 50% above diurnal. The higher the frequency in this band, the more eccentric the current ellipse. By contrast, currents near the bottom on the flank of the seamount are nearly rectilinearly polarized with flow nearly parallel to the local isobaths. Current component and vertical displacement amplitudes tend to be highest at depths between those of the summit and the summit plain rim (Figure 5), even when scaled in a WKBJ sense by the local stratification, with the exception that amplitudes tend to rise sharply at the bottom. (Following the stretching convention of Kunze, 1995, the reference buoyancy frequency is 3 cph and depths are stretched from the ocean surface; the seamount summit (444 m) is at 570 stretched m and the summit plain rim (700 m) is at 750 stretched m.) The total range of amplitudes is rather small, only a factor of two or so.

The CEOF decomposition describes the temporal relationship between measured quantities through their relative phases. Current component and displacement phases all tend to increase with depth (Figure 6) indicating downward phase propagation. The rates of change of phase are different for the different flow components because their relative phases differ with position. For example, offslope (southwestward) current lags alongslope (southeastward) current by roughly 90° near the summit but is nearly in phase with it at depth, hence phase change rates with depth are different for the two components. The rate of phase increase with depth for the azimuthal component of flow gives a stretched vertical wavenumber of about 1 cycle per stretched vertical km downward at 24 h period. At 16 h period, the

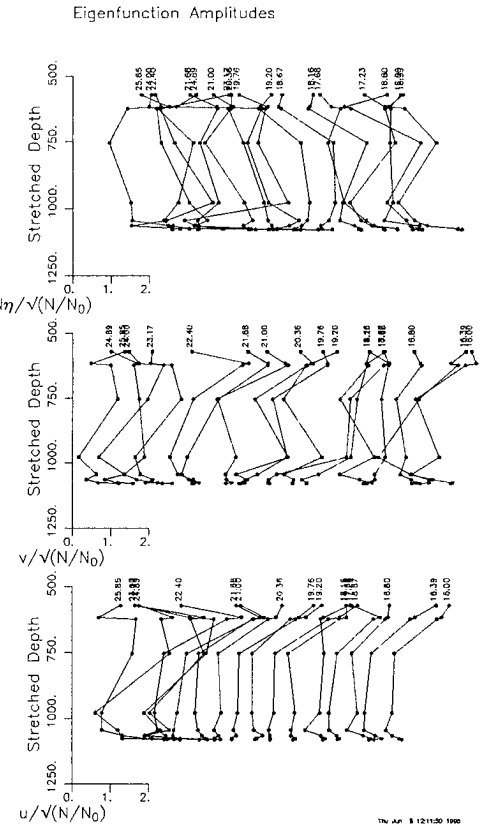


Figure 5. WKBJ scaled current and vertical displacement eigenfunction amplitudes for the first CEOF mode on mooring F3. The three panels give scaled amplitudes for the offslope component u (bottom panel), the alongslope component in the anticlockwise direction around the seamount v (middle panel), and upward displacement times buoyancy frequency $N\eta$ (top panel). Depth is stretched by the local buoyancy frequency with a reference N_0 = 3 cph. The upper three estimates are from depths near the summit, the fourth is from just below the summit rim, and the five deepest estimates are from near the bottom along the seamount flank. Independent frequency estimates, labelled by period in h, are successively offset by 0.5 in amplitude.

wavenumber magnitude is reduced to about 2/3 cycle per stretched vertical km.

The amplitudes and relative phase between offslope (equivalent to radial in cylindrical geometry) current and vertical displacement determine the contribution to eddy buoyancy flux from each frequency band. Kunze, 1995, notes that eddy buoyancy flux from diurnal period oscillations is in the offslope direction. The CEOF formalism allows eddy fluxes to be calculated from the coherent fluctuations of current and temperature across the moored array. We use records from the three moorings C, R3, and F3 to describe the onslope-vertical

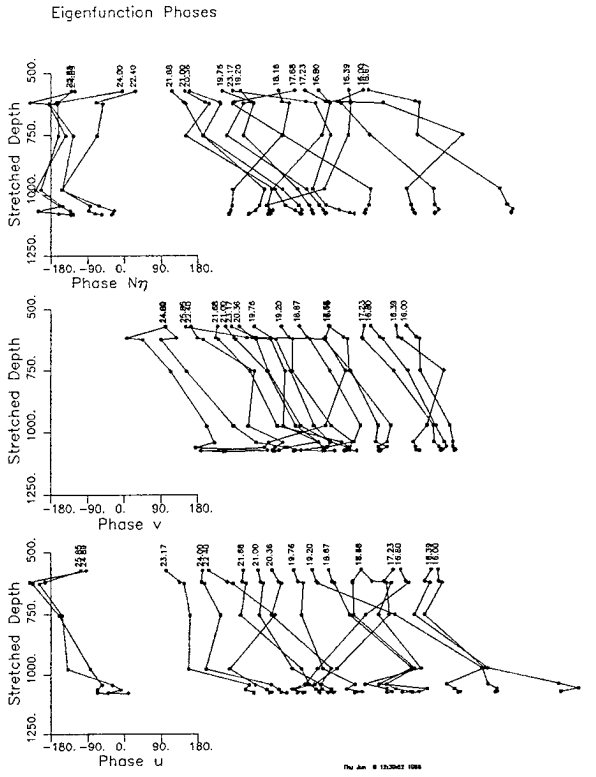


Figure 6. First CEOF mode current and vertical displacement eigenfunction phases on mooring F3 plotted against WKBJ stretched depth as in Figure 5. The three panels give relative phases for the offslope component u (bottom panel), the alongslope component in the anticlockwise direction around the seamount v (middle panel), and upward displacement times buoyancy frequency $N\eta$ (top panel). Phases have been adjusted by integral cycles to minimize implied wavenumber magnitude. Independent frequency estimates, labelled by period in h, are successively offset by 45° in phase. The phase convention is that more positive phases lag.

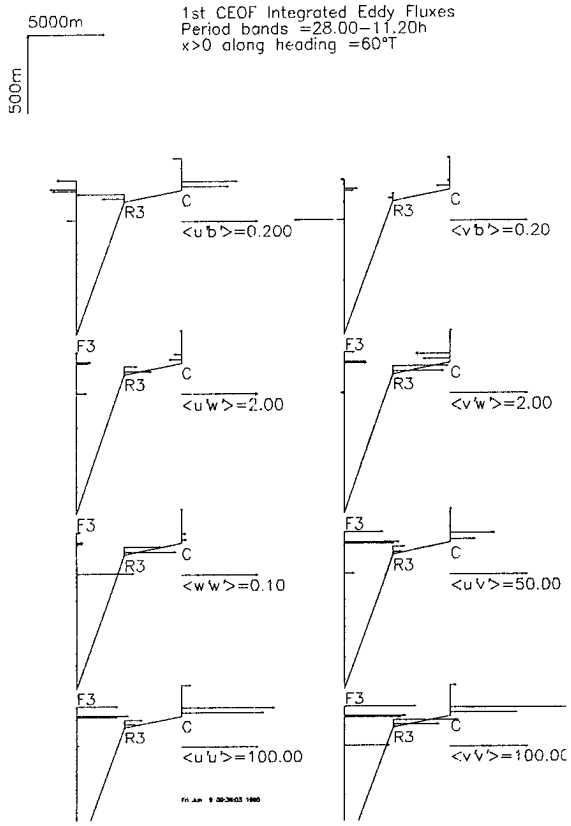


Figure 7. Diurnal through semidiurnal band eddy fluxes of momentum (lower six panels) and buoyancy (top two panels) calculated from the first CEOF describing variability at depths in a range about the summit depth at Fieberling Guyot using moorings C, R3, and F3. Fluxes are drawn as vectors in the vertical plane along 60°T heading (the local onslope direction). Perturbation current components are taken as a right-handed triad with u' in the onslope direction. Units given in the scale are cm^2/s^2 for momentum and cm^2/s^3 for buoyancy fluxes.

structure of eddy fluxes (Figure 7). The onslope gradient of onslope buoyancy flux contributed by tidal and intertidal frequency oscillations (an integration from 28 to 11.2 h periods, top left panel, Figure 7) changes sign from offslope in the region over the summit plain to onslope in the region over the seamount flank (over a depth range encompassing the summit). Likewise, there is a sign change in the onslope gradient of onslope eddy transport of azimuthal momentum $\langle u'v' \rangle$ between the summit plain and the seamount flank as well. The vertical eddy flux of azimuthal momentum $\langle v'w' \rangle$ has the same vertical gradient above both the summit plain and the flank. The gradients of these eddy fluxes can be related to mean Eulerian flows through the equations for azimuthally and temporally averaged flow, expressed in cylindrical coordinates:

$$UU_r + WU_z - \frac{V^2}{r} - fV - P_r = -\frac{1}{r}\langle ru'^2 \rangle_r - \langle u'w' \rangle_z + \frac{\langle v'^2 \rangle}{r} \quad (1)$$

$$UV_r + WV_z + \frac{UV}{r} + fU = -\langle u'v' \rangle_r - \langle w'v' \rangle_z \quad (2)$$

$$UW_r + WW_z - P_z = -\frac{1}{r}\langle ru'w' \rangle_r + \langle w'^2 \rangle_z \quad (3)$$

$$WN^2 = -\frac{1}{r}\langle ru'b'\rangle_r - \langle w'b'\rangle_z \qquad (4)$$

where (r,θ,z) and (u,v,w) are the offslope, alongslope, and vertical coordinates and velocity components, upper case quantities designate means, primed quantities indicate fluctuations, brackets denote averages, subscripts denote derivatives, N is buoyancy frequency, f the Coriolis parameter, and P is pressure. In the limit of weak mean flows, the nonlinear terms on the left sides of (1) through (3) can be neglected in favor of the balances $U = f^{-1}(-\langle u'v'\rangle_r - \langle w'v'\rangle_z)$ (from (2)) and (4) to give a mean onslope-vertical circulation. Noninteraction theorems (McIntyre,1980) caution that such an Eulerian circulation is exactly compensated by an opposite Stokes drift in the case that the fluctuations take the form of steady, inviscid, unforced waves. Nevertheless, current meters sense Eulerian flow, hence the spatial structures of coherent buoyancy and momentum fluxes indicated in Figures 4 and 7 may be expected to produce flow in the offslope-vertical plane. Estimates of these wave-induced flows are compared with measured mean flows in the following section.

Mean Flows

One year mean flows measured by current meters near the bottom on Fieberling Guyot tend to have an offslope component over the summit plain (at sites C, R2, and R3; see Brink, 1995) and onslope component over the flanks (at sites F2 and F3). Mean currents farther from the bottom tend to be more parallel to isobaths, although the orientation of bottom contours is depth dependent due to departures of the topography from perfect radial symmetry.

Currents at site R2 on the northwest side of the seamount (Figure 8) show the mean anticyclonic circulation above the summit region as a flow most intense about 105 m above the bottom (535 m depth). The current spiral turns leftward with depth at this site and current within the strongest part of the anticyclone appears to be parallel to the bottom contours. Flow closer to the bottom is offslope at roughly 1 cm/s while flow above the anticyclone maximum appears onslope at about the same rate. Mean current at site R3, also on the summit plain rim, is similarly sheared, with an offslope component near the bottom of about 1 cm/s as a departure from otherwise alongslope flow in the anticyclonic sense around the seamount (Figure 9). The mean flow 50 m off the bottom (535 m depth) is 10.3 cm/s in contrast to 12.4 cm/s found at the same depth, but a greater distance from the geometric center of the seamount, at site R2.

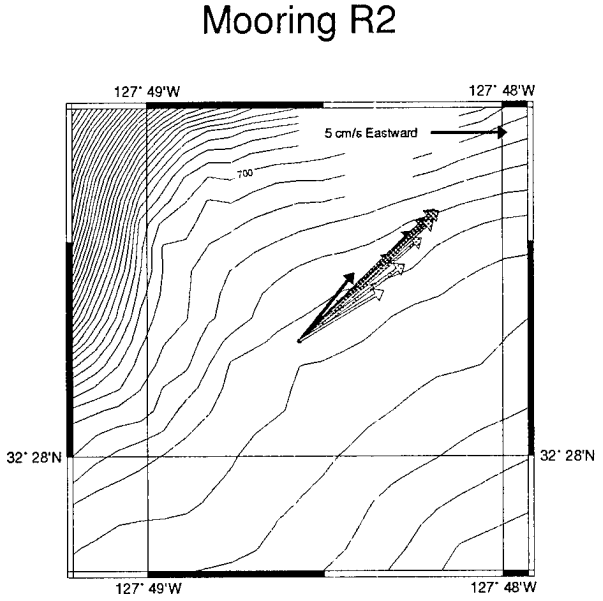


Figure 8. Mean flow over one year starting October 1, 1990, at 15, 35, 55, 75, 95, 115, 135, 155, 175, and 195 m above the bottom at the ADCP mooring site R2. Vectors are shaded in order of depth (the closest to bottom is solid). Depth contours at 10 m intervals are based on a Hydrosweep survey and the mooring position is based on acoustic and undithered GPS navigation. (Surveyed depth exceeds that inferred from the moored pressure record by 6 m at this site.)

Mean current on the flanks of the seamount is weaker and is directed slightly in the onslope direction, in contrast to the flow near the summit plain rim (Figure 10). Records from various locations within the internal wave array on the southwest flank have onslope flow components of up to about 0.2 cm/s. None of the currents measured within 160 m of the bottom over one year indicates an offslope component of flow. Moreover, the observed current vectors suggest an onslope component of flow even when compared to nearby isobaths of corresponding depth. Progressive vector diagrams (not shown) indicate that onslope flow exists even when the alongslope current is in the opposite sense for a few days or more.

Alongslope currents near the bottom tend to be modulated with a fortnightly signal in phase with the diurnal tidal current amplitude, although they vary also with low frequency flow impinging on the seamount (Eriksen, 1991, Brink, 1995, Kunze, 1995). That is, when diurnal fluctuations are strong, the anticyclone atop Fieberling is strong and conversely. This suggests that circulation near the seamount is, at least in part, due to rectification of tidal fluctuations. The onslope component may also be influenced by fluctuations, diurnal and

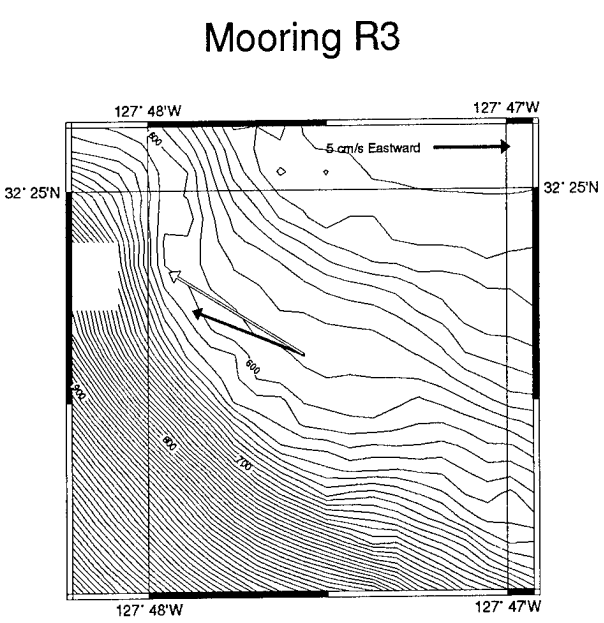


Figure 9. Mean flow over one year starting October 1, 1990, at 20 and 50 m above the bottom at the mooring site R2. The deeper vector is solid. Depth contours at 10 m intervals are based on a Hydrosweep survey and the mooring position is based on acoustic and undithered GPS navigation. Surveyed depth exceeds that inferred from moored pressure records by 3 m at this site.

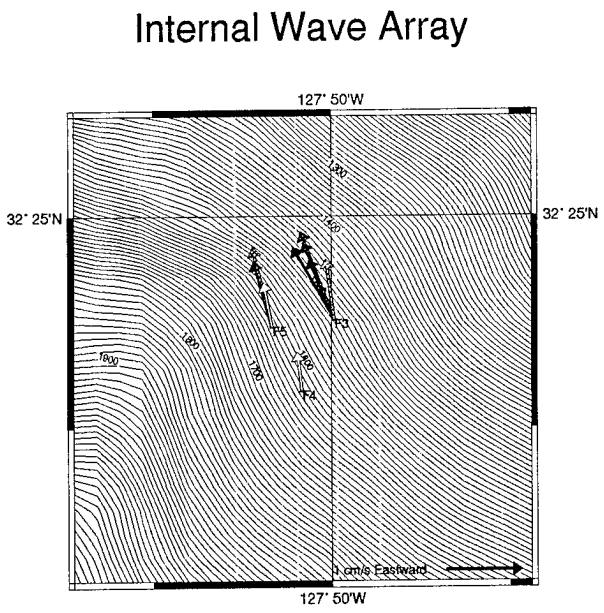


Figure 10. Mean flow over one year starting October 1, 1990, at 20 to 160 m above the bottom at the internal wave array sites. Currents 20 m from the bottom are drawn with a solid vector with currents farther off the bottom shaded more lightly to a height of 160 m, where vectors are unshaded. Instrument heights from the bottom are 20, 30, 40, 60, and 120 m off the bottom on F3, 160 m off the bottom on F4, and 40, 90, and 160 m off the bottom on F5. Depth contours at 10 m intervals are based on a Hydrosweep survey and the mooring position is based on acoustic and undithered GPS navigation. Surveyed depth exceeds that inferred from moored pressure records by 40-45 m at this site.

otherwise. Codiga, 1993, found subinertial oscillations to rectify into producing a low frequency anticyclonic swirl in a laboratory simulation.

The eddy fluxes in the vicinity of the summit plain rim are dominated by tidal, especially diurnal, fluctuations. The gradients in offslope buoyancy flux above the summit plain and the flank imply mean Eulerian downwelling of about 50 m/day and upwelling of 5 m/day, respectively, in the two regions according to the balance in (4), neglecting vertical mixing. Given the slope on the summit plain of about 0.05, about 1.2 cm/s of offslope flow is implied by mass conservation in the radial vertical plane, rather close to the flow observed (solid arrows, Figures 8 and 9) The linearized version of (2) relies on the vertical gradient of vertical eddy transport and radial gradient of radial transport of alongslope momentum to balance Coriolis acceleration. Referring to the two middle panels of Figure 7, both gradients appear of different sign at different locations. Since it is the sum of two terms, each of uncertain sign, that determines mean flow, no reliable estimate of radial flow can be made from this balance. The buoyancy flux structure, however, appears of the correct sign and magnitude to explain the offslope flow found near the bottom at the rim.

The eddy flux structure near the bottom on the flank also suggests an Eulerian mean flow of the sign observed, but due to internal wave rather than tidal processes. Radial buoyancy flux is in the offslope sense due to internal wave fluctuations (top left panel, Figure 4) and diminishes with distance from the bottom, whether offslope or vertical. The magnitude of vertical eddy buoyancy flux by wave breaking and the scale over which it changes implies that it can be neglected as a source of induced upwelling in the balance (4). The convergent pattern of radial buoyancy flux implies an upwelling of roughly 13 m/day. This, together with the bottom slope within the internal wave array of 0.45 implies an onslope flow of about 0.03 cm/s. This estimate is at least a factor of 3 weaker than what is observed directly. The linear version of the azimuthal momentum balance (2) on the flank is clearer than it is near the summit rim. The two flux gradient terms partially offset one another, but vertical gradients of vertical transport are somewhat larger than offslope

gradients of offslope transport of alongslope momentum. The difference implies an onslope mean flow of about 0.3 cm/s, a factor of 3 or so larger than what is measured directly. The mass and azimuthal momentum balances predict onslope flows that bracket that is observed directly, while neither balance agrees well with the current meter observations.

Trapped Waves over a Sloping Plane

The fluctuations observed at Fieberling Guyot span a relatively broad frequency range that includes the inertial frequency. While Brink, 1989, has found free resonant solutions trapped to a seamount, these are restricted to subinertial frequencies. Kunze, 1995, has suggested that the diurnal frequency fluctuations at Fieberling are dynamically superinertial waves confined to the anticyclonic vortex near the seamount summit. Although vortex trapped waves support a radial buoyancy flux and vertical phase propagation, both observed features, the observed waves extend to the bottom on the seamount flanks well beyond where the vortex is found and exist at superinertial frequencies where they could not be trapped by a vortex with only anticyclonic vorticity. Radial-vertical seamount trapped modes support neither radial buoyancy flux nor vertical phase propagation, but they do extend to the bottom. Brink, 1990, considered a forced problem, where the seamount response is a superposition of standing modes each excited off resonance, but the forcing was only at the diurnal (subinertial) frequency.

The purpose of this section is to point out that bottom-trapped waves can exist at both subinertial and superinertial frequencies that exhibit vertical phase propagation and support onslope heat flux, at least in infinite sloping plane geometry. Rhines, 1970, found the special case of these waves that satisfies no normal flow at the bottom and propagates freely both along and across isobaths, but always with shallow water to the right. Since motion is everywhere parallel to the bottom and rectilinear, these waves cannot support an onslope buoyancy flux. Propagating rays of this type at the same frequency can be combined to form vertical-onslope standing modes. Whether propagating or standing, these wave modes can be though of as a Kelvin wave generalized to continuous stratification over a sloping plane bottom. The more general form of these waves does not satisfy the simple slip boundary condition, hence these must be forced by normal flow at the boundary. They are evanescent waves. They do support onslope buoyancy flux, appear to propagate along the boundary, and can exist over a range of superinertial and at all subinertial frequencies. They are the response to periodic normal flow forced at the boundary.

The linear inviscid equations of motion in a uniformly stratified fluid over an infinite planar bottom can be written as:

$$u_t - fv = -p_x \tag{5a}$$

$$v_t + fu = -p_y \tag{5b}$$

$$N^2 w + w_{tt} = -p_{zt} \tag{5c}$$

$$u_x + v_y + w_z = 0 \tag{5d}$$

where (u,v,w) specifies the onslope, alongslope, and upward current components of flow in a right-handed coordinate system, p is reduced pressure, and N and f are the buoyancy frequency and Coriolis parameter. Propagating plane wave solutions that are trapped to a planar bottom with slope s specified by $z=sx$ exist when u,v,w and p all vary as $e^{i(kx+ly+mz-\sigma t)}e^{K(sx-z)}$ where (k,l,m) specify (real) wavenumber components and Ks and K are the (real) offslope and upward decay rates. (The decay scale normal to the boundary is $\left(K\sqrt{1+s^2}\right)^{-1}$ or $\frac{\cos\alpha}{K}$ where $s \equiv \tan\alpha$.) The system of equations (5) reduces to:

$$Q(p_{xx} + p_{yy}) = p_{zz} \tag{6}$$

where $Q \equiv \frac{N^2 - \sigma^2}{\sigma^2 - f^2}$. Evanescent solutions to (6) are possible because two wavenumber components (onslope and vertical) are complex, while the third (alongslope) is real. Such solutions describe waves trapped to the boundary when the dispersion relations

$$\left(\frac{Ks}{\kappa}\right)^2 = -Qs^2\left(\cos^2\varphi + \frac{\sin^2\varphi}{\left(1 - Qs^2\right)}\right) \tag{7a}$$

and

$$\frac{m}{k} = -Qs \tag{7b}$$

are satisfied, where $\kappa \equiv \sqrt{k^2 + l^2}$ is the horizontal wavenumber magnitude and the angle $\varphi \equiv Cos^{-1}\left(\frac{k}{\kappa}\right) = Sin^{-1}\left(\frac{l}{\kappa}\right) = Tan^{-1}\left(\frac{l}{k}\right)$ specifies the real wavenumber direction in the horizontal plane ($\varphi = 0$ is an onslope wave, $\varphi = \frac{\pi}{2}$ is an alongslope wave with shallow water on the right). For a given pressure signal p, the current components are:

$$u = \frac{\kappa p}{\sigma^2 - f^2}\left(\sigma\cos\varphi + i\left(f\sin\varphi - \frac{\sigma Ks}{\kappa}\right)\right) \tag{8a}$$

$$v = \frac{\kappa p}{\sigma^2 - f^2}\left(\sigma \sin\varphi - \frac{fKs}{\kappa} - if\cos\varphi\right) \quad (8b)$$

$$w = \frac{\kappa p}{\sigma^2 - f^2}\left(\sigma s\cos\varphi - \frac{i\sigma K}{Q\kappa}\right). \quad (8c)$$

Solutions are valid for all direction angles φ for subinertial frequencies $\sigma < f$ but for only the restricted range of angles for which K remains real and positive in the range $f < \sigma < \sigma_c$, that is, at superinertial frequencies less than the internal wave critical frequency σ_c where $\sigma_c \equiv \sqrt{N^2 \sin^2\alpha + f^2 \cos^2\alpha}$. While these waves decay normal to the sloping bottom, phase lines are tilted upward and offslope at subinertial frequencies and upward and onslope at superinertial frequencies. They are level in the onslope-vertical plane at the inertial frequency. In the limit of vanishing frequency, phase lines attain an offslope-upward tilt of $\frac{f^2}{N^2 s}$. In the limit of the critical frequency, phase lines are parallel to the sloping bottom in the onslope-vertical plane.

The special case of these waves for which flow is everywhere parallel to the boundary, i.e., $w = su$, requires that:

$$\frac{Ks}{\kappa} = \frac{Qs^2 \frac{f}{\sigma}\sin\varphi}{Qs^2 - 1} \quad (9)$$

This restriction recovers the Rhines,1970, solution for edge waves. These are restricted to positive alongslope wavenumbers $l>0$ and to frequencies $\sigma < N\sin\alpha$, a more restrictive range than for evanescent waves.

The quantity $\frac{Ks}{\kappa}$ appearing in (7a) and (9) is the ratio of the horizontal length scale of the wave to its offslope decay scale. Large values of this ratio indicate that waves decay in only a fraction of a horizontal wave scale, thus are tightly bottom trapped. Contours of $\frac{Ks}{\kappa}$ calculated for parameters relevant to the summit region of Fieberling Guyot indicate that trapping is relatively gentle (i.e. $\frac{Ks}{\kappa} \sim 1$) for most wave orientations at superinertial frequencies and for orientations close to the alongslope direction at subinertial frequencies (Figure 11). While evanescent waves of any direction are possible at subinertial frequencies, the range of directions is tightly confined to alongslope at slightly superinertial frequencies, but broadens to nearly any direction close to the internal wave reflection critical frequency. Note that directions with an onslope component ($-\frac{\pi}{2} < \phi < \frac{\pi}{2}$) correspond to upward propagation at subinertial frequencies and downward propagation at superinertial frequencies and conversely for directions with an offslope component ($\frac{\pi}{2} < \varphi < \frac{3\pi}{2}$) by (7b) since Q changes sign (from -∞ to +∞) across the inertial frequency. Figure 11 is drawn only for the first two quadrants in direction because of these symmetries.

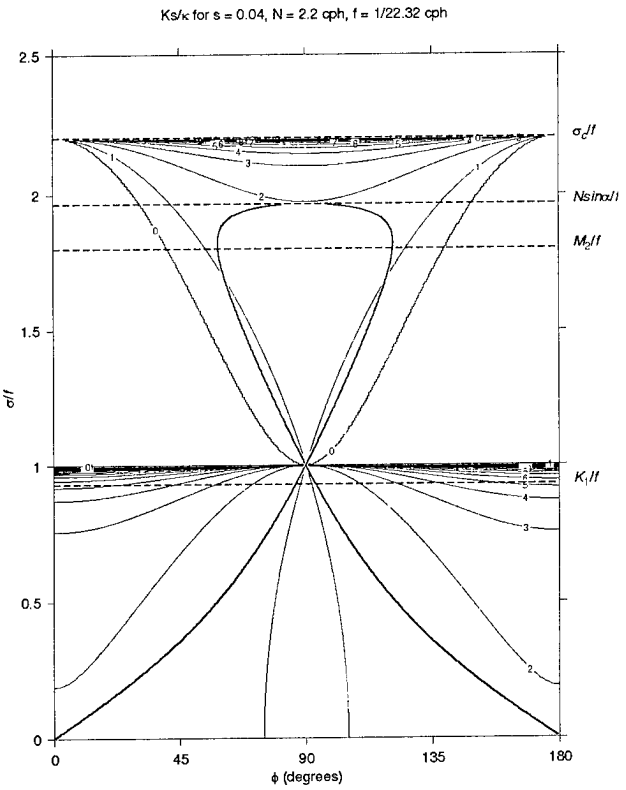


Figure 11. Ratio of horizontal length scale to offslope decay scale for evanescent waves as a function of frequency σ horizontal wavenumber vector orientation φ. Dispersion curves for edge waves are superimposed as heavy curves. Parameters are relevant to the summit region of Fieberling Guyot. Dashed lines mark the internal wave critical frequency (the maximum evanescent wave frequency), the maximum edge wave frequency, and the lunar semidiurnal and the lunisolar diurnal tidal frequencies. The ratio is not contoured where evanescent waves are not possible. Small ratios correspond to weak trapping. The orientations φ=0° and 90° correspond to pure onslope and alongslope (with shallow water to the right) propagation, respectively. Superinertial-onslope and subinertial-offslope waves propagate downward, and conversely.

Edge waves, however, are restricted to the range of directions plotted (all alongslope with shallow water to the right for $f>0$). These dispersion curves are drawn on the same set of axes as heavy curves in Figure 11. For the slope, stratification, and rotation parameters relevant to the summit region of Fieberling Guyot (s=0.04, N=2.2 cph, f=1/22.32 cph), edge waves are moderately trapped over their complete frequency range.

Both diurnal and semidiurnal tidal frequencies fall within the range of possible evanescent and edge wave frequencies (Figure 11). Diurnal frequency motions are only slightly subinertial and, as such, will be strongly trapped for all orientations except those nearly alongslope. Diurnal edge waves are aligned 3.6° onslope and offslope from the alongslope direction. At superinertial frequencies, the range of possible orientations broadens with increasing frequency. Semidiurnal edge waves attain nearly the most cross-isobath orientation possible over the possible range of superinertial frequencies. These and evanescent waves are weakly to at most moderately trapped to the bottom at superinertial frequencies (Note $0<\frac{Ks}{\kappa}<2$ for superinertial frequencies in this case).

Evanescent and edge wave amplitudes in pressure p can be expressed in terms of the energy density of the waves. The average energy per unit frequency per unit surface area normal to the slope E is

$$E = \frac{\rho_0 \kappa^2 \langle PP^* \rangle}{8K\left(\sigma^2 - f^2\right)^2}\left\{\left(\sigma^2 + f^2\right)\left(1 + \frac{K^2 s^2}{\kappa^2}\right)\right. \qquad (10)$$

$$\left. - 4\sigma f \frac{Ks}{\kappa}\sin\varphi + \left(\sigma^2 + N^2\right)\left(s^2\cos^2\varphi + \frac{K^2}{Q^2\kappa^2}\right)\right\}$$

where $\langle PP^* \rangle$ is the variance in reduced pressure per unit frequency at the bottom $z = sx$. The energy density E is a sum of potential and horizontal and vertical kinetic energies averaged over a wave period. Given the energy density E, the component amplitudes (u,v,w) appearing in (8) can be found by interpreting the amplitude of p as the standard deviation of pressure found in a specified frequency band from the spectrum $\langle PP^* \rangle$ since $\langle pp^* \rangle = \langle PP^* \rangle e^{2K(sx-z)}$. Normalization by energy density E allows currents associated with waves of different frequency or wavenumber to be compared, as with the current ellipses discussed next.

The current ellipse signature of evanescent waves varies considerably with wave orientation and frequency. The current ellipses in the horizontal and vertical-onslope planes for diurnal evanescent waves over a small range of wavenumber vector orientations ($79.2°<\varphi<90°$) that includes the edge wave orientation are given in Figure 12. Horizontal ellipses and horizontal projections of wavenumber vectors are given in the top row of this figure for waves directed onslope. Vertical-onslope current ellipses (with a vertical exaggeration of 10) are given in the second row. The lower two rows display the corresponding ellipses for waves with offslope senses. The sense of rotation of the current vectors changes in both the horizontal and onslope-vertical planes depending on whether waves are directed more or less onslope or offslope than the edge wave. In general, current ellipses in the vertical-onslope plane intersect the bottom, demonstrating the need for motions to be forced normal to the bottom in order to excite evanescent waves. Edge waves have flow everywhere parallel to the bottom, so can exist as free waves. The ellipses of Figure 12 indicate how minor departures from no normal flow at the bottom can induce substantial horizontal current fluctuations.

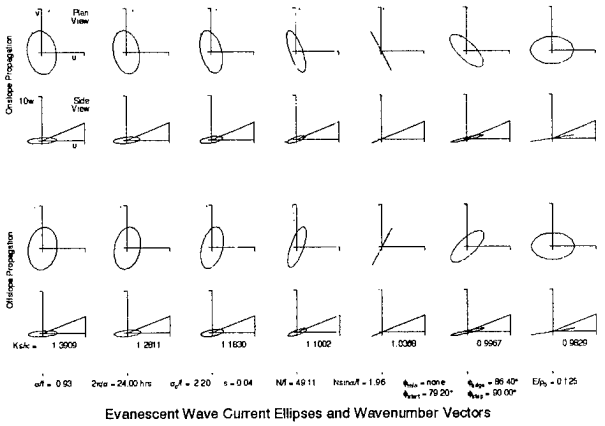


Figure 12. Current ellipses for evanescent waves of various orientation relative to isobaths at a fixed (diurnal) frequency. The top row shows current ellipses in the horizontal plane along with the horizontal projection of the wavenumber vector. The Second row shows corresponding current ellipses and the bottom slope in the onslope-vertical plane, exaggerated tenfold vertically. From right to left in each row, waves are directed more onslope and upward in the top two rows. The bottom two rows are the corresponding ellipses for waves directed increasingly offslope and downward from right to left. Waves are normalized to have equal energy.

Current ellipses for evanescent waves generally are not aligned with the wavenumber vector orientation. Waves travelling parallel to isobaths have current ellipses oriented normal to them, but in general horizontal ellipses and wavenumber vectors are not normal to one another. Edge waves not only have flow everywhere parallel to the bottom, but also have rectilinear flow

(ellipses collapse to straight lines). Pairs of rays with horizontal wavenumber vectors symmetric about the alongslope direction (i.e. $\varphi = \pm\frac{\pi}{2} \pm \theta$) can be summed to form standing modes in the vertical-onslope plane. In the case of standing modes, horizontal and vertical ellipses are oriented either parallel or normal to isobaths and the horizontal plane, respectively. Whereas individual rays can carry onslope or offslope momentum and buoyancy fluxes, standing modes cannot.

The horizontal buoyancy flux $F^b \equiv \langle u'b' \rangle$ of a propagating evanescent wave component is

$$F^b = -\frac{N^2 \langle pp^* \rangle \sigma K \kappa \cos\varphi}{2\left(\sigma^2 - f^2\right)^2} \left\{\frac{f\kappa s}{\sigma K}\sin\varphi - s^2 + \frac{1}{Q}\right\} \quad (11)$$

The expression in curly brackets vanishes for edge waves, by (9). If the mean buoyancy balance is given by $WN^2 = -\frac{\partial}{\partial x}F^b$, (the rectilinear version of (4), but without vertical mixing), then the mean Eulerian upwelling induced by the waves is $W = -KsF^bN^{-2}$. By continuity, $U=W/s$. This Eulerian flow parallel to the bottom and decreasing exponentially from it with a scale $\cos\alpha\,(2K)^{-1}$, is exactly offset by the Stokes drift components $\left(U^S, W^S\right)$ which are equal and opposite to (U,W), in accordance with the predictions of nonacceleration theorems. So, while a mean Eulerian onslope or offslope flow can be induced by linear inviscid evanescent waves, there is no net Lagrangian circulation so induced. If mixing is introduced, the resulting non-zero Lagrangian mean circulation can be expected to have scales comparable to the domain in which the evanescent oscillations are found.

Discussion

The flow found near Fieberling Guyot is dominated by relatively narrow-band signals, and in this it is probably not unusual for a seamount. It is in strong contrast to open deep ocean flows, where mesoscale eddy motions tend to dominate current variance. The three strong characteristics of currents at Fieberling are 1) the mean anticyclone near the summit, 2) the diurnal-inertial-semidiurnal band of structurally similar flows, and 3) the near-critical reflection internal wave band. That fluctuations in the summit anticyclone modulate with the spring-neap cycle suggests that wave processes are important to its existence. Estimates of mean circulation in the vertical-radial plane based on eddy flux gradients, albeit crude, are in rough agreement with the horizontal currents measured directly. These suggest a pattern of downwelling above the summit plain and upwelling on the seamount flanks. There is no strong evidence that these flows are other than Eulerian means induced by the presence of bottom intensified wave motions. The level of mixing found by Eriksen, 1995, and the vertical scale over which it varies together are too small to produce mean flows even as big as the Eulerian flows observed.

Both internal wave band and diurnal motions effect measurable offslope buoyancy fluxes. Internal waves reflect off the steeply sloped flanks of the seamount in such a way as to generate rotary motions of current vectors in the vertical-onslope plane to generate offslope buoyancy flux near the bottom that decays with distance from it. Since these motions are strongest near the bottom, their decay implies a convergence of buoyancy flux, hence an induced (at least Eulerian) upwelling to compensate for it. The vertical gradients vertical buoyancy flux implied by the observed rate of density overturns are substantially weaker than observed horizontal gradients of offslope buoyancy flux.

Diurnal motions in the vertical onslope plane reach a maximum a hundred or more m above the seamount summit plain and at a finite radial distance from the seamount center, however roughly it can be defined. The offslope buoyancy flux these motions carry has gradients of both signs, implying downwelling at small radii (over the summit plain to about the rim) and upwelling outside this region, with the upwelling region more concentrated than that of downwelling. While there is considerable turbulent mixing reported above the summit plain, the magnitude of its gradients are weak compared to those of offslope buoyancy flux.

Neither the free seamount trapped wave whose resonant frequency is closest to the diurnal frequency (29 h period, according to Brink, 1995), nor the vortical trapped wave of Kunze, 1995, completely explains the nature of the diurnal and up-to-slightly-superinertial motions observed at Fieberling Guyot. The principal shortcomings of the seamount trapped wave model of Brink, 1990, are the failure to account for the observed phase propagation, offslope buoyancy flux, and frequency bandwidth (superinertial as well as subinertial) of the motions at Fieberling. The vortex-trapped wave model of Kunze, 1995, accounts for downward phase propagation and offslope buoyancy flux, but cannot account for these features at superinertial frequencies nor at depths and radii well removed from the near-summit intensified anticyclone.

An examination of uniformly stratified rotating flow over a planar sloping boundary demonstrates that, at least locally, evanescent and edge waves are possible at both subinertial and superinertial frequencies. These waves are bottom trapped with scales that can be comparable to

the degree of trapping observed at Fieberling. They can propagate vertically and horizontally with scales that are also comparable to those observed at Fieberling. The possibility of trapped wave motions at superinertial frequencies occurs because even though the governing equation (6) is hyperbolic for $\sigma > f$ ($Q > 0$), two complex wavenumber components can be offset by a real third component, hence waves can be trapped in two dimensions, and propagate in the third. These waves are possible in addition to free internal gravity waves (which propagate in all three dimensions). The possible generalization of this solution to arbitrary stratification and bottom boundary shape is not clear. Nevertheless, evanescent waves can be expected to be supported where stratification and bottom slope are locally uniform.

The response of a seamount to externally imposed flow is equivalent to forcing flow normal to the bottom at the bottom. The prominent responses found at Fieberling are at the diurnal and semidiurnal tides. The forced response of a linear, inviscid system can be calculated by the projection of forcing onto the normal modes of the system. This approach was followed by Brink, 1990, where the response away from resonance was calculated as the sum of phase-locked free modes. Seamount trapped waves form a complete discrete basis set and the projection of forcing at arbitrary frequencies defines the contribution of each mode to the total response. While individual modes are standing in the vertical-offslope plane, the phase-locked sum of such modes should lead to apparent vertical-radial phase propagation at arbitrary locations. Curiously, the Brink, 1995, solutions do not indicate sufficiently robust phase differences to match observed phase changes. Brink's normal modes are subinertial only so that if superinertial trapped free modes are possible, they may contribute to forced response as well.

The ray solutions of evanescent waves at a particular frequency can be summed over a variety of wavenumber orientations to produce a response that not only exhibits phase propagation, but varies the shape of current ellipses with distance from the bottom. Such a response could be formed by forcing with an arbitrary waveform at a particular frequency.

Acknowledgments

I thank Robert Reid, John Dahlen, and their colleagues at the C. S. Draper Laboratory, the captains and crews of R/V Washington and R/V Thompson, and Neil Bogue for help in carrying out the moored measurements. The analysis benefitted from discussions with Chris Garrett, Dan Codiga, Eric Kunze, and Ken Brink. This study was part of the U. S. Office of Naval Research Accelerated Research Initiative on Flow over Abrupt Topography and was supported under ONR grant numbers N00014-89-J-1621 and N00014-94-I-0081.

References

Brink, K. H., 1989: The effect of stratification on seamount-trapped waves, *Deep-Sea Res.*, 36, 825-844.

Brink, K. H., 1990: On the generation of seamount-trapped waves, *Deep-Sea Res.*, 37, 1569-1582.

Brink, K. H., 1995: Tidal and lower frequency currents above Fieberling Guyot, *J. Geophys. Res.*, 100, 10817-10832.

Chapman, D. C. and D. B. Haidvogel, 1992: Formation of Taylor caps over a tall isolated seamount in a stratified ocean, *Geophys. Astrophys. Fluid Dyn.*, 64, 31-65.

Codiga, D. L., 1993: Laboratory realizations of stratified seamount-trapped waves. *J. Phys. Oceanogr.*, 23, 2053-2071.

Eriksen, C. C., 1985: Moored observations of deep low-frequency motions in the central Pacific Ocean: Vertical structure and interpretation as equatorial waves, *J. Phys. Oceanogr.*, 15, 1085-1113.

Eriksen, C. C., 1991: Observations of amplified flows atop a large seamount, *J. Geophys. Res.*, 96, 15227-15236.

Eriksen, C. C., 1995: Internal wave reflection and mixing at Fieberling Guyot, *J. Geophys. Res.*, in press.

Kunze, E., and J. M. Toole, 1995: Fine- and microstructure observations of trapped diurnal oscillations atop Fieberling seamount, *Proceedings of the 1995 'Aha Huliko'a Hawaiian Winter Workshop*, this volume.

McIntyre, M. E., 1980: An introduction to the generalized Lagrangian-mean description of wave, mean-flow interaction, *Pure and Applied Geophys.*, 118, 152-176.

Rhines, P., 1970: Edge-, bottom-, and Rossby waves in a rotating stratified fluid, *Geophys. Fluid Dyn.*, 1, 273-302.

Roden, G. I., 1991: Mesoscale flow and thermohaline structure around Fieberling seamount, *J. Geophys. Res.*, 96, 16653-16672.

Roden, G. I., 1994: Effects of the Fieberling seamount group upon flow and thermohaline structure in the spring of 1991, *J. Geophys. Res.*, 99, 9941-9961.

Wallace, J. M., and R. F. Dickinson, 1972: Empirical orthogonal representation of time series in the frequency domain. Part I: Theoretical considerations, J. Appl. Meteor., 11, 887-892.

Wichman, C. A., C. C. Eriksen, N. M. Bogue, K. H. Brink, D. E. Frey, R. D. Pillsbury, G. M. Pittock, and S. A. Tarbell, 1993: Fieberling Guyot moored array data, *School of Oceanography Technical Report A93-1*, Univ. of Washington, Seattle, 373 pp.

Fine- and Microstructure Observations of Trapped Diurnal Oscillations Atop Fieberling Seamount

Eric Kunze
School of Oceanography, University of Washington, Seattle, Washington

John M. Toole
Woods Hole Oceanographic Institution, Woods Hole, Massachusetts

Abstract. Fine- and microstructure profiles collected over Fieberling Seamount at 32°26'N in the eastern North Pacific reveal (i) an anticyclonic vortex cap of relative vorticity $-0.50f \pm 0.15f$, (ii) intensified diurnal oscillations of 15 cm s^{-1}, and (iii) elevated turbulence levels of eddy diffusivity $K_\rho \simeq 10 \times 10^{-4}$ m^2 s^{-1} co-existing in a 200-m thick layer atop the summit plain. The vortex is *not* a Taylor cap because a strong negative potential vorticity anomaly is associated with it. It is at least partially maintained against Ekman downwelling by rectification of the diurnal oscillation as evidenced by its fortnightly cycle. The diurnal oscillation is slightly subinertial and driven by the barotropic K_1 and O_1 diurnal tides. It closely resembles a seamount-trapped topographic wave, but (i) its energy maximum is 50 m above the bottom, (ii) its horizontal velocity vector turns counterclockwise with depth, and (iii) there is a 180° phase difference between its radial velocity u_r' and the vertical displacement $\xi' = -T'/\overline{T}_z$, producing a net positive radial heat-flux $\langle u_r'T' \rangle$. These features are more consistent with an upward-propagating vortex-trapped near-inertial internal wave with a slightly subinertial frequency allowed by the strong negative vorticity of the vortex cap. This wave would be encountering a vertical critical layer at the top of the cap where its energy would be lost to turbulence. Observed turbulence levels imply decay times for the wave of ~3 days, emphasizing the strongly forced nature of this system.

1. Introduction

The peaks of seamounts have been found to be sites of enhanced near-bottom semidiurnal, diurnal, and inertial currents with moored current-meters (Noble *et al.*, 1988; Noble and Mullineaux, 1989; Genin *et al.*, 1989; Padman *et al.*, 1992; Eriksen, 1991) and profilers (Kunze and Sanford, 1986; Kunze *et al.*, 1992). These elevated velocities support abundant populations of benthic filterfeeders (Genin *et al.*, 1986, 1992). However, little is known about how topography intensifies these currents. Kunze and Sanford (1986) interpreted their signal as a critically-reflected upward-propagating near-inertial wave based on the counterclockwise turning of the signal's horizontal velocity with depth. On the other hand, Genin *et al.* (1989), Eriksen (1991), Noble *et al.* (1994), and Brink (1995) report slightly subinertial diurnal tidal frequencies associated with the dominant motions above Fieberling Guyot, so they advance that the fluctuations are seamount-trapped topographic waves.

Sloping bottom topography will cause internal waves with characteristic slopes $Cg_z/Cg_H = k_H/k_z$ identical to the bottom slope α to be critically reflected to high wavenumbers (Wunsch, 1969; Phillips, 1977; Eriksen, 1982; 1985) and scattered (Baines, 1971; Bell, 1975; Gilbert and Garrett, 1989; Müller and Xu, 1992), dramatically amplifying internal-wave shear and strain, and turbulence production.

Sloping topography also allows bottom-trapped topographic waves with frequencies $\omega \leq N\sin\alpha$ (Rhines, 1970) although nonplanar bathymetry will not trap superinertial frequencies $\omega > f$ (Huthnance, 1978). Brink (1989, 1990) and Chapman (1989) formulated a model for stratified seamount-trapped topographic waves. They showed that the gravest mode for Fieberling Guyot's geometry and stratification is slightly subinertial and nearly resonant with the diurnal tide.

A vortex cap is also expected over a seamount. Both potential vorticity-conserving Taylor cap dynamics (Hogg, 1973; Swaters and Mysak, 1985; Roden, 1987) and wave rectification over topography (Loder, 1980; Maas and Zimmerman, 1989a, 1989b; Haidvogel *et al.*, 1993) imply formation of an anticyclonic vortex over the seamount's summit. A Taylor cap would require an impinging geostrophic flow and, in the absence of damping, would have the same potential vorticity as the surrounding ocean. Stratification will limit the vertical extent of the vortex above the seamount (Zyryanov, 1981; Chapman and Haidvogel, 1992) to $H = fL/N \sim 100$ m for $f = 7.8 \times 10^{-5}$ s^{-1}, the buoyancy frequency $N = 4.3 \times 10^{-3}$ s^{-1}, and the radius of the seamount summit $L = 7$ km.

To better understand the impact of seamounts on internal waves, tides, and turbulent mixing, fine- and microstructure profiles were collected over Fieberling Guyot during March 1991 (Montgomery and Toole, 1993). Here we use the profile time-series and surveys to characterize the temporal and spatial structure of the co-existing vortex cap, diurnal oscillations, and turbulence atop Fieberling Guyot's summit plain.

The vortex cap is ~200-m thick and has core vorticities $\zeta = -0.50f \pm 0.15f$. The presence of the anticyclonic vortex cap raises the possibility that the observed diurnal oscillation is not a seamount-trapped topographic wave but a vortex-trapped near-inertial internal wave (Kunze, 1986; Kunze *et al.*, 1995; Appendix A).

The coinciding diurnal shear layer is also 200-m thick. Maximum velocities of 15 cm s^{-1} are found 50–100 m above the bottom over the summit plain, unlike the bottom-intensified seamount-trapped wave (Brink, 1995). This signal decays rapidly as one moves radially off the summit. At any instant and depth, the horizontal velocity of the diurnal wave forms a unidirectional jet over the summit plain. This horizontal structure is consistent with either a gravest seamount-trapped mode (Brink, 1990) or a gravest vortex-trapped internal wave mode (Kunze *et al.*, 1995). The velocity vector turns counterclockwise with depth over the entire 200-m thick layer of intensified motion. This turning corresponds to a vertical wavelength $\lambda_z = 250$ m. If interpreted as a vortex-trapped near-inertial wave, it implies upward energy propagation. It contradicts Brink's predicted turning of only ~90° confined to within 50 m of the bottom due to a time-dependent bottom Ekman layer.

Elevated turbulence levels of $\varepsilon \simeq 10^{-7}$ W kg^{-1} are found coincident with the vortex cap and the diurnal oscillation, corresponding to eddy diffusivities of 10×10^{-4} m^2 s^{-1}. This is sufficient to drain the wave in ~3 days if it is the energy source for the turbulence. The eddy diffusivity over the summit plain is not sufficiently enhanced for seamounts to play a dominant role in global mixing of the pycnocline.

2. Trapped Wave Models

Two extant models may describe the diurnal shear layer observed above the summit plain of Fieberling Guyot —seamount-trapped topographic waves (Brink, 1989, 1990) and vortex-trapped near-inertial internal waves (Kunze *et al.*, 1995; Appendix A). These two types of waves share many properties in common and their observable differences are subtle.

2.1 Seamount-Trapped Topographic Waves

Brink (1989, 1990) and Chapman (1989) formulated a model for seamount-trapped waves on tall seamounts in a stratified, rotating fluid, extending the barotropic models of Rhines (1969), Huthnance (1974), Hunkins (1986), and Kowalik (1994). These waves are bottom-trapped topographic waves (Rhines, 1970) wrapped around a seamount so that their along-isobath wavenumber is quantized. Laboratory experiments (Codiga, 1993; Boyer and Zhang, 1990; Zhang and Boyer, 1993) and numerical simulations (Haidvogel *et al.*, 1993) have verified generation of seamount-trapped oscillations by barotropic subinertial forcing in stratified, rotating fluids.

For the stratification profile and geometry of Fieberling Guyot, Brink showed that the gravest-mode (highest frequency) seamount-trapped wave had a slightly subinertial frequency that was nearly resonant with the diurnal tide. This mode evanesces rapidly away from the bottom with a vertical decay scale of ~50 m and a radial decay scale of a few kilometers (radial mode 0). It propagates clockwise around the seamount with azimuthal mode $n = -1$. The first azimuthal mode is most likely to be excited by largescale forcing because it has flow in the same direction on opposite sides of the seamount (Brink, 1990). The resulting jet rotates clockwise in time. Observationally, Brink's predictions are consistent with the diurnal frequency and horizontal structure of the dominant velocity fluctuations above the summit plain of Fieberling Seamount (Eriksen, 1991; Noble *et al.*, 1994; Brink, 1995).

Of particular importance for distinguishing gravest seamount-trapped waves from vortex-trapped waves is that their radial velocity u_r' and vertical displacement ξ' signals are 90° out of phase (section 2.2). This implies that inviscid seamount-trapped waves have zero radial heat-flux $< u_r' T' >$. Also, the horizontal velocity vector undergoes 180° reversals, but no turning, with depth. The addition of bottom friction might produce a counterclockwise-turning-with-depth, time-dependent benthic Ekman layer of thickness and turning scale

$$k_z^{-1} \sim \sqrt{\frac{\nu_e}{|\omega_i - f_{eff}|}} \qquad (1)$$

(Maas and van Haren, 1987), where the intrinsic frequency $\omega_i = \omega_E - nV_\theta/r \simeq \omega_E - n\zeta/2 = K_1 + \zeta/2\,\omega_E$ is the Eulerian frequency, V_θ is the horizontal velocity of the vortex, and $f_{eff} = f + \zeta$. However, (1) depends on the profiles of turbulence and stratification. Eddy viscosity will also alter the phase relations but only by a few degrees (Appendix C).

2.2 Vortex-Trapped Near-Inertial Internal Waves

The anticyclonic vortex above the summit plain with core vorticity $-0.50f$ is sufficient to reduce the lower bound of the internal waveband from the planetary Coriolis frequency f to an effective Coriolis frequency $f_{eff} = f + \zeta$ (Weller, 1982; Kunze, 1985; Kunze, 1986), well below the diurnal frequencies $K_1 = 0.933f = 1.87f_{eff}$ and $O_1 = 0.865f = 1.73f_{eff}$. This allows diurnal frequencies to propagate as near-inertial internal waves within the confines to the negative vorticity core. Kunze *et al.* (1995) formulated a model for a vortex-trapped near-inertial radial mode while investigating near-inertial wave critical layers in a warm-core ring. The superposition of plane waves reflecting off the lateral sides of the vortex sets up a radial mode that closely resembles a seamount-

trapped wave in its horizontal structure. Like the seamount-trapped wave, the most likely azimuthal mode for largescale forcing is $n = -1$, corresponding to clockwise azimuthal propagation around the vortex. The intrinsic, or Lagrangian, frequency then is $\omega_i = \omega_E - nV_\theta/r \simeq K_1 + \zeta/2 = 0.933f - 0.25f = 0.683f > f_{eff} = f + \zeta = 0.50f$. Like the gravest seamount-trapped wave, this mode has maximum velocity amplitudes near vortex center and, at any given instant, forms a nearly unidirectional jet in the vortex core that rotates clockwise in time. Decay is rapid moving radially out of the vortex.

Unlike the seamount-trapped topographic wave, a vortex-trapped wave is an internal wave and is therefore free to carry energy and momentum upward into the overlying water column. For a near-inertial wave of upward energy propagation, the horizontal velocity vector turns counterclockwise with depth. The associated vertical wavelength is

$$\lambda_z = \lambda_r \sqrt{\frac{\omega_i^2 - f_{eff}^2}{N}}\ , \qquad (2)$$

where λ_r is the radial wavelength (Appendix A, Kunze *et al.*, 1995). Since the wave can propagate freely only inside the vortex, its energy will accumulate in a vertical critical layer at the top of the core until instabilities transfer it to turbulence production and mixing (Kunze *et al.*, 1995). Thus, for a vortex-trapped wave, energy, shear. and turbulent dissipation maxima above the bottom are expected. For upward and clockwise azimuthal propagation, the radial velocity u_r' is 180° out of phase with the vertical displacement $\xi' = -T'/\overline{T}_z$, for a net outward radial heat-flux $<u_r'T'>$.

Including an eddy viscosity of 10×10^{-4} m^2 s^{-1}, consistent with the microstructure measurements, does not significantly alter the dispersion relation between frequency, vertical wavenumber, and horizontal wavenumber (2), or the consistency relations between horizontal velocity components u_r' and v_θ', and thus will not alter the turning with depth. The phase relation between a viscous wave's vertical displacement ξ' and the horizontal velocities is modified by at most 6° for the vertical wavelengths of interest (Appendix B).

2.3 Summary of Commonalities and Differences

In the context of Fieberling Seamount, seamount- and vortex-trapped waves share the following properties:

- Both are forced by the barotropic diurnal tide, so their Eulerian frequencies $\omega_E = \omega_i + nV_\theta/r \simeq \omega_i - \zeta/2 = K_1, O_1$.
- The horizontal velocity vectors of both rotate in time with the radial and azimuthal velocities 90° out of phase above the summit plain.
- Both propagate clockwise azimuthally around the seamount (azimuthal mode $n = -1$).
- Both decay radially away from the seamount.

The differences are more subtle:

- The vortex-trapped wave requires a vortex of sufficient strength to permit a diurnal Eulerian frequency. The seamount-trapped wave does not and will not exist if the frequency is effectively superinertial.
- The vortex-trapped wave will carry energy and momentum into the stratified water column and thus can have an energy maximum above the bottom (upward energy propagation implies counterclockwise turning of the horizontal velocity vector with depth). The seamount-trapped wave is a bottom-trapped topographic wave so it should have its maximum signal at the bottom and little turning of the velocity vector with depth. (Bottom friction might induce a time-dependent benthic Ekman layer having counterclockwise turning with depth.)
- The radial velocity u_r' and temperature T' fluctuations for vortex-trapped waves propagating upward and clockwise around the vortex are in phase so produce a net outward radial heat-flux $<u_r'T'>$. (In the absence of dissipative processes, the divergences of this heat-flux and a nonzero vertical momentum-flux $<v_\theta'w'>$ drive a wave-induced mean circulation $\tilde{u}_r$ and $\tilde{w}$ which exactly counterbalance the wave fluxes and there is no net change to the background mean fields; see Appendix A.) For inviscid seamount-trapped waves, the radial heat-flux is zero. These phase relations are only slightly modified by inclusion of eddy viscous effects (Appendices B and C).

3. Measurements and Analysis

3.1 Data

Profiles were collected over the summit and flanks of Fieberling Guyot (32°26'N, 127°45'W) with the High-Resolution Profiler (HRP; Schmitt *et al.*, 1988), Sippican expendable current profilers (XCPs; Sanford *et al.*, 1982; Sanford *et al.*, 1993), and Sippican T-5 (1600-m) expendable bathythermographs (XBTs) in March 1991 as part of the ONR-sponsored Abrupt Topography Program to investigate the impact of seamounts on physical and biological oceanography. At the seamount's latitude, the Coriolis frequency is 7.8×10^{-5} s^{-1} (22.4 h), so both the K_1 (24.0 h, $0.933f$) and O_1 (25.9 h, $0.865f$) diurnal tides are subinertial. Barotropic diurnal tides propagate northwest here (Schwiderski, 1981a, b).

Fieberling Guyot rises from an abyssal plain of 4000–4500-m depth to a summit plain at 500–700-m depth (Fig. 1). A narrow pinnacle southwest of the geometric center of the summit plain attains 440-m depth. By definition, a guyot has a flat top (apart from the pinnacle). Radial bottom slopes on the summit plain are ~0.05 compared to flank slopes exceeding 0.2. The abrupt change in

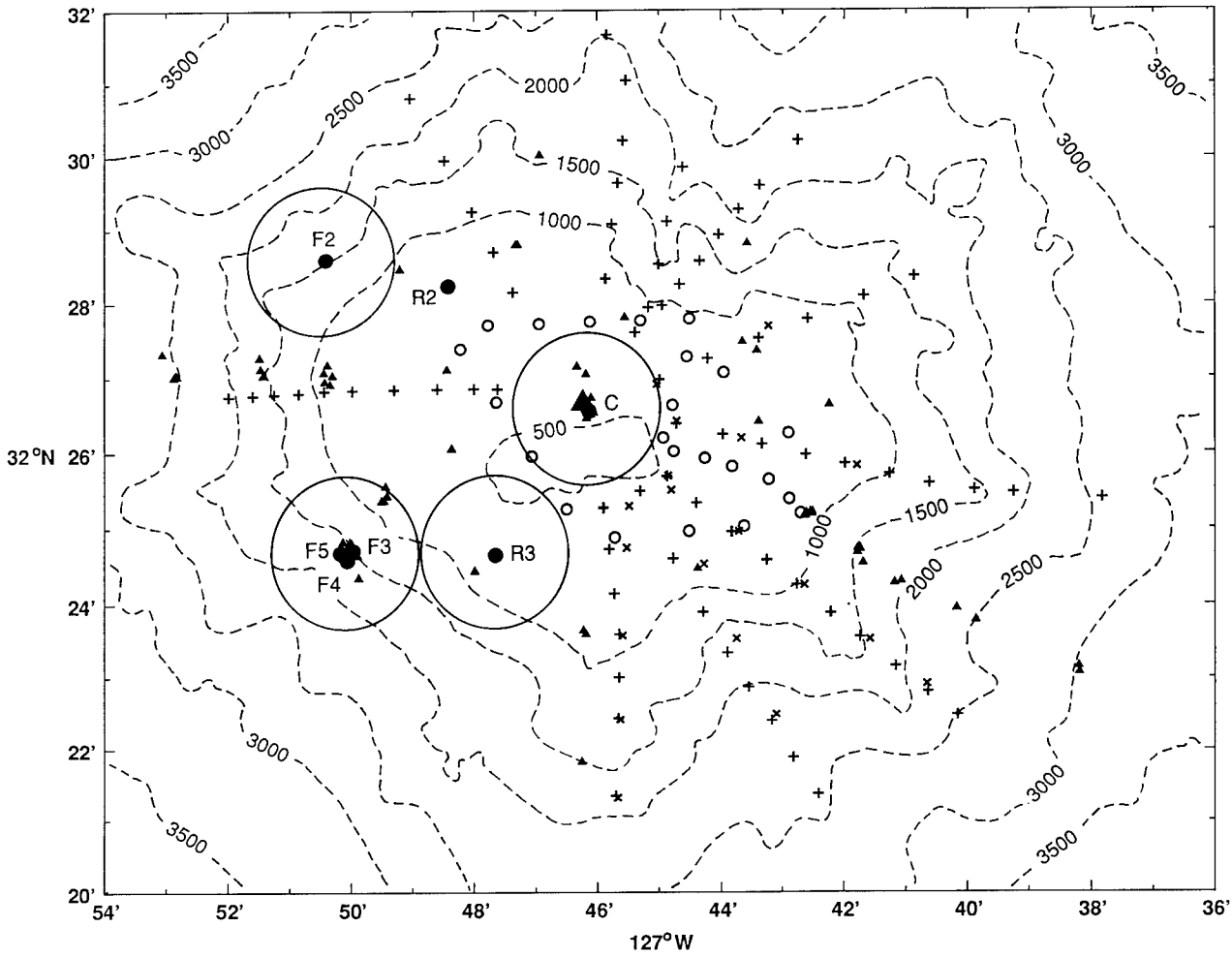


Figure 1. Velocity profiler stations (XCP, +, x, o; HRP, ▲) and current-meter mooring sites (⊙) over the summit plain and flanks of Fieberling Guyot. Bathymetry is in meters. HRP measurements consist of day-long profile time-series at C and F3, spoke time-series to the west and southeast, and a survey around the rim. Radial XCP spokes were made from seamount center to the 2500-m isobath. Surveys to the south and east were collected on 7 March 1991 (+, x), to the north and west on 8 March (+), and on the summit plain on 18 March (o).

slope near the 700-m isobath will be referred to as the summit rim and has an average radius of 5 km. The summit plain is elongated so that the rim radius is about 6.5 km zonally and half that meridionally (Fig. 1). Beyond the rim, Fieberling Guyot can be described as a Gaussian of radial scale r = 12 km (Codiga, 1991). It is the northwesternmost of the Fieberling seamount chain. For the motions on the summit plain discussed here, Fieberling appears to be dynamically isolated from its nearest neighbor, Fieberling II, which lies 40 km to the southeast. This is consistent with the conclusion of Roden (1991) that only in the abyss did the seamount chain affect background impinging currents as a group.

Other relevant measurements are two mesoscale CTD surveys conducted in August 1989 (Roden, 1991) and in April–May 1991 (Roden, 1994) and year-long current-meter mooring deployments from September 1990 to September 1991 at seven sites on Fieberling Guyot and the abyssal plain to the west (Wichman *et al.*, 1993; Noble *et al.*, 1994; Brink, 1995; Eriksen, 1995). The moorings were sited at the center of the summit plain (C in Fig. 1), to the northwest and southwest on the rim (R2 and R3), to the northwest and southwest in 1500-m water on the flanks (F2 and F3–5), and 40 km to the northwest and southwest on the abyssal plain.

The HRP measurements include day-long time-series sampled every 3 h at the central (C) and southwest flank (F3) mooring sites, repeated radial sections to the 3000-m isobath over the western and southeastern flanks, and a survey around the rim (Fig. 1). Profiles 20–40 km from the peak on the neighboring abyssal plain are described by Toole *et al.* (1994). The stratified turbulent benthic boundary layer overlying the flanks is discussed by Toole *et al.* (1995).

The HRP is a freefall profiler (Schmitt *et al.*, 1988). Its sensor suite includes a CTD and a two-axis acoustic current-meter which provide finescale vertical profiles of temperature, salinity, pressure, and horizontal velocity relative to an unknown but depth-independent constant. Also included are a high-speed thermistor, a dual-needle conductivity probe, and airfoil velocity shear probes to estimate microscale temperature and velocity dissipation rates. Schmitt *et al.* (1988) and Polzin (1992) detail the reduction of the microstructure data which follows the methodology developed by Neil Oakey at the Bedford Institute of Oceanography—half-meter segments of microstructure data are windowed, Fourier-transformed, and corrected for sensor and electronic interface responses. Gradient variances are then estimated by integrating the gradient spectra out to a spectral minimum (beyond which instrument noise dominates). Dissipation rate estimates assume three-dimensional isotropy. The production/dissipation balances of Osborn and Cox (1972) and Osborn (1980) are used to obtain diapycnal eddy diffusivity estimates, employing a mixing efficiency of 0.25 (Oakey, 1982).

For the seamount cruise, HRP was equipped with a Sea-Data Inc. acoustic altimeter to trigger release of the descent weight when the profiler got within 10 m of the bottom. The weight-release criterion was effective over the summit plain but less reliable over the steep flanks (presumably because of poor acoustic backscatter). HRP dives frequently terminated up to 100 m above the bottom, and one made contact with the bottom.

Most of the XCPs were deployed along radial spokes from near the center of the summit plain to the 2500-m isobath on the flanks of the guyot (Fig. 1). XCP profiles in water depths less than 1600 m measured into the bottom. A survey of 43 profiles was conducted to the south and east between 0800 and 1300 hours on 7 March (+), with 19 of the stations being reoccupied between 1330 and 1730 hours (**x**). A survey of 34 profiles was conducted to the north and west between 0500 and 0900 hours on 8 March (+). Finally, a survey of 24 profiles was conducted over the summit plain a week and a half later between 0500 and 0830 hours on 18 March (o). Most of the XCP data were collected within a few hours of the same phase of the diurnal tide. No expendable probes were dropped within 1 nmi of the moorings to prevent fouling of the current-meter rotors with expendable wire. As a result, the southwest quadrant was undersampled.

The expendable current profiler (XCP) measures the horizontal velocity to within an unknown but depth-independent constant using the voltage drop induced by seawater's motion through Earth's magnetic field and measures temperature with an XBT thermistor to 1600-m depth. Preanalysis processing averages the data in 3-m bins, with typical rms errors of ±0.4 cm s^{-1} and ±0.06°C for velocity and temperature, respectively.

3.2 Analysis

Two features predicted to occur atop a seamount are (i) a vortex cap, which should be axisymmetric and dominantly in the azimuthal velocity v_θ, and (ii) an azimuthal-mode-one seamount- or vortex-trapped wave forced by the barotropic diurnal tide, which should consist of a unidirectional, slightly subinertial jet over the summit which turns clockwise in time (see Fig. 15).

The vortex and wave signals will be separated in the profile surveys by azimuthal averaging $\langle\cdot\rangle_\theta$. Averaging the east and north velocities filters out axisymmetric flow, isolating the expected diurnal wave signal. Averaging azimuthal and radial velocities filters out all azimuthal modes except mode zero, isolating the axisymmetric vortex. We caution that numerical simulations do not always find the vortex to be axisymmetric (Haidvogel *et al.*, 1993). While it might be preferable to fit the data to azimuthal modes as done by Codiga (1995), the present scheme captures the dominant signals above the summit plain and produces results indistinguishable from those of modal fitting. The coordinate system is centered on the seamount centroid (32°26.2'N, 127°45.5'W) as determined by Codiga (1991). The unknown barotropic offset is handled by arbitrarily removing the depth-average between 150 and 300 m before azimuthal averaging. This emphasizes perturbations at the summit depth and below. To compensate for the nonuniform azimuthal sampling (Fig. 1), the azimuthal averages are weighted by the sampling in the N, W, S, and E quadrants. This works for the velocity signals but may not handle the dipolar temperature (displacement) signal around the seamount adequately. Toole *et al.* (1995) explore the effects of averaging relative to local bathymetry orientation.

4. The Vortex Cap

4.1 Spatial Structure

Radial sections of azimuthally-averaged radial velocity $\langle u_r \rangle_\theta$ and azimuthal velocity $\langle v_\theta \rangle_\theta$ are displayed in Fig. 2. The profiles have been WKB-stretched to

$$N_0 = 5.2\times10^{-3}\ \mathrm{s}^{-1}\left[z \rightarrow \int_z^0 (N(z)/N_0)\,dz \right]$$

to remove variations in the vertical scale and amplitude due solely to changes in the buoyancy frequency N. True depths are indicated along the right axes.

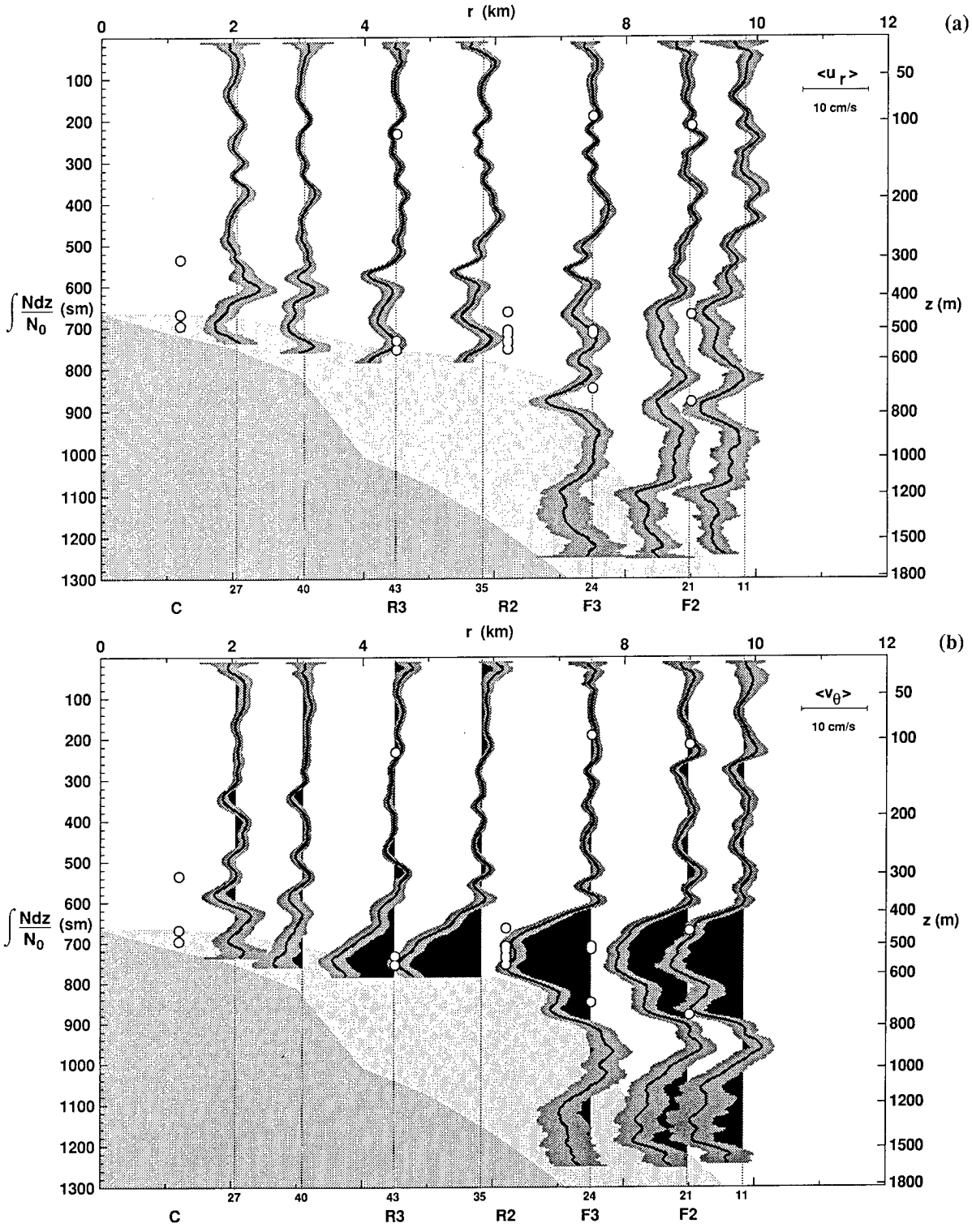


Figure 2. Radial profile sections of azimuthally-averaged (a) radial velocity $\langle u_r \rangle_\theta$ and (b) azimuthal velocity $\langle v_\theta \rangle_\theta$ with one standard error indicated by dark shading. Uneven azimuthal sampling (Fig. 1) is compensated for before averaging. The depth coordinate (left axis) has been WKB-stretched with respect to $N_0 = 5.2 \times 10^{-3}$ s^{-1}; true depths are shown along the right axis. Numbers along the bottom axis correspond to the number of drops going into each average, darker and lighter silhouettes to extremes in the WKB-normalized bathymetry, and open circles to current-meter sites. The radial velocity $\langle u_r \rangle_\theta$ (a) is everywhere less than 2 cm s^{-1}. The azimuthal velocity $\langle v_\theta \rangle_\theta$ (b) exhibits anticyclonic flow of up to 10 cm s^{-1} over the summit rim at 6–8 km radius between 600 and 900 sm (400- and 800-m depth).

Radial velocities (Fig. 2a) are everywhere less than 2 cm s^{-1}. The uniformly weak radial flows suggest that our azimuthal averaging scheme is not biased. At some depths, e.g., 580 sm (stretched meters), there is a suggestion of persistent in- or outflow. These instances are of such small vertical scale that we hesitate to equate them with the 1–2 cm s^{-1} radial outflow reported near the bottom by Eriksen (1991) and Brink (1995) because of possible problems with azimuthal nonuniformity, because of the short duration of our sampling, and because the profile surveys were collected during a time of relatively weak radial flow as inferred from the R2 ADCP velocities (see Fig. 6).

The average azimuthal velocity (Fig. 2b) displays a much more clearly defined signal. A 200-sm thick layer of anticyclonic flow resides atop the summit plain. Maximum speeds of ~ –10 cm s^{-1} are found at the rim (radius r = 7 km). The vortex is bounded above by a 100-m thick $\partial < v_\theta >_\theta / \partial z = 1.5 \times 10^{-3}$ $s^{-1} = 0.3\overline{N}$ vertical shear layer and below by a 200-m thick 10^{-3} s^{-1} = $0.25\,\overline{N}$ shear layer. Corresponding relative vorticities $\zeta = \partial <v_\theta>_\theta / \partial r + <v_\theta>_\theta / r$ (Fig. 3) are noisier because they involve derivatives. The vorticity has values of $-0.50f \pm 0.15f$ over the summit plain and vanishes over the seamount flanks so, in the vortex core, the effective Coriolis frequency f_{eff} = $0.5f$ = $2\pi/(44.8$ h) < K_1, O_1. Freeland (1994) observed a 40-m thick vortex cap of similar strength in ADCP surveys atop Cobb Seamount that was steady on 6–7 day timescales. However, during a different cruise, Codiga (1995) found vorticities weaker than $-0.1f$ atop Cobb. There is a hint that the vorticity vanishes inside a 2-km radius (Fig. 3), but vortex center position uncertainties are large enough that this cannot be stated conclusively. The absence of a positive vorticity annulus outside the azimuthal velocity maximum indicates that the azimuthal velocity $<v_\theta>_\theta$ falls off as r^{-1} for radii $r > 7$ km.

4.2 Comparison with Current-Meter Observations

Figures 4 and 5 compare the XCP vorticities and azimuthal velocities with 2-day averages of the current-meter records (Wichman *et al.*, 1993) about the time of the 7–8 March XCP surveys. The current-meter relative vorticity is inferred assuming solid-body rotation, $\zeta = 2V_\theta / r$. The current-meter data verify anticyclonic swirling between 400- and 600-m depth (Fig. 4), albeit slightly stronger. The current-meters and profilers also both reveal nearly solid-body rotation inside 7-km radius (Fig. 5). Azimuthal currents fall off more slowly in the current-meter data than in the profile data at larger radii. Mean flows shallower than 400 m are weak and show no reluctance to cross isobaths.

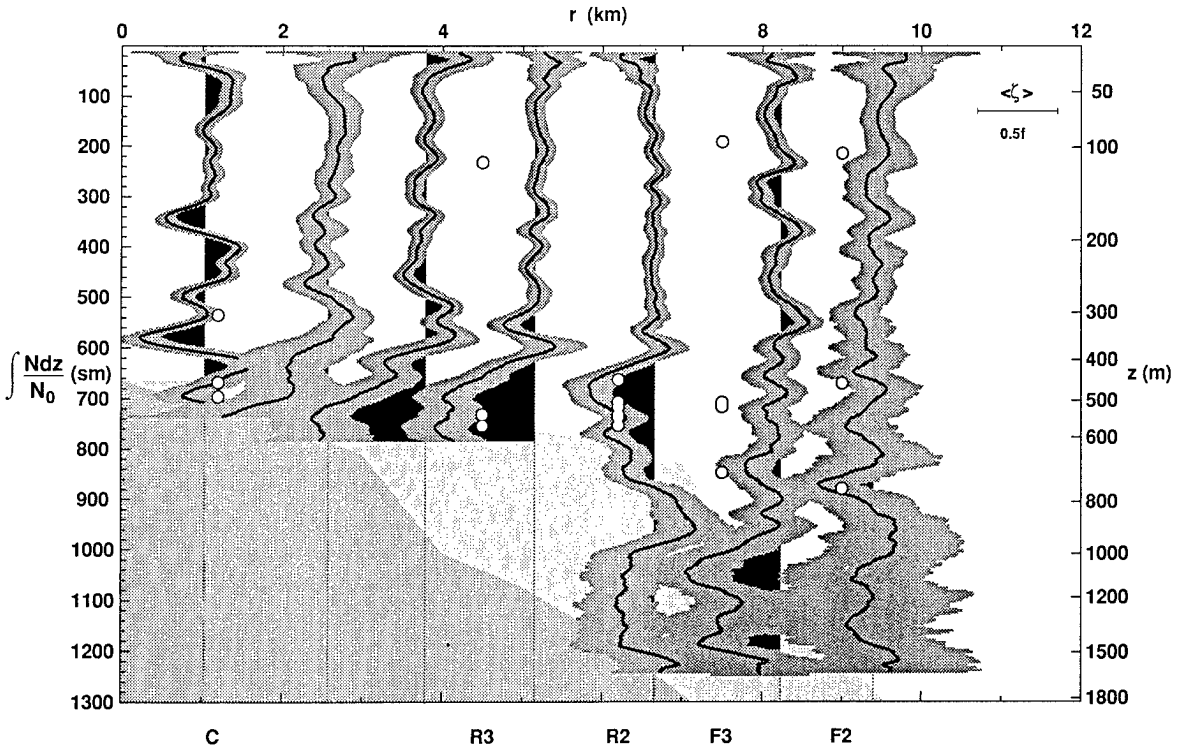


Figure 3. Radial profile sections of azimuthally-averaged relative vorticity $<\zeta>_\theta = \partial <v_\theta>_\theta / \partial r + <v_\theta>_\theta / r$ with one standard error indicated by dark shading. Relative vorticities of $\sim -0.50f \pm 0.15f$ are found in a 200-m thick layer over the summit plain. Vorticities vanish at radii $r > 8$ km, indicating that $<v_\theta>_\theta \propto r^{-1}$. Weak vorticities inside 2-km radius may reflect measurement uncertainty in the position of the vortex center.

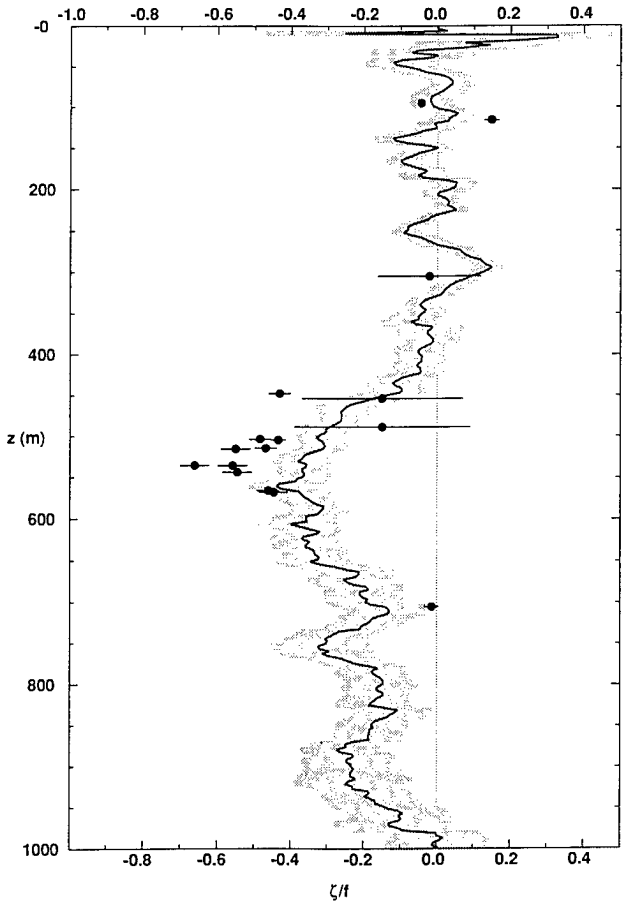


Figure 4. Comparison of the vertical structure of the relative vorticity at r = 6.7 km from the XCP surveys (solid curve) with 4-day smoothed current-meter vorticities $\zeta \simeq 2\langle v_\theta \rangle_t / r$ (•) from inside 7-km radius at the time of the XCP surveys assuming solid-body rotation. XCP vorticities are $-0.35f$ to $-0.40f$ between 500- and 650-m depth, vanishing abruptly shallower than 400 m and more gradually deeper than 900 m. Current-meter vorticities are slightly stronger at $-0.5f$ to $-0.6f$.

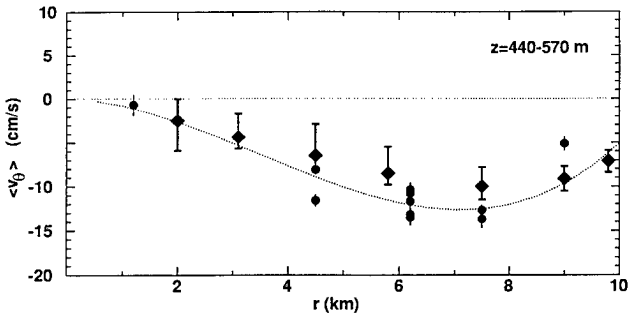


Figure 5. Comparison of the radial dependence of 4-day smoothed current-meter and azimuthally-averaged XCP azimuthal velocities, $\langle v_\theta \rangle_t$ (•) and $\langle v_\theta \rangle_\theta$ (♦), in the depth range 440–570 m. The dotted line is a cubic least-squares fit setting $\langle v_\theta \rangle = 0$ at $r = 0$ and $r = 11$ km. The current-meters indicate extreme azimuthal velocities of -14 cm s^{-1} at r = 6–7.5 km with near solid-body rotation at smaller radii. XCPs indicate a similar structure but slightly weaker velocities of ~ -10 cm s^{-1}.

Differences between profiler and current-meter velocities likely arise because the two measurements do not sample the same part of the flow. If the vortex is not perfectly circular, is off center, or is otherwise not axisymmetric as found in numerical simulations (Haidvogel *et al.*, 1993), differences in the profiler and current-meter estimates would result.

4.3 Temporal Behavior

Fortnightly modulation of the vortex strength is apparent in 2-day smoothed azimuthal velocities from the rim moorings (e.g., at R2, Fig. 6). This implies that the vortex cap, with its dome of cold water over the seamount peak, is at least partially sustained against benthic Ekman pumping and turbulent decay by rectification of the K_1 and O_1 tidal fluctuations. In particular, Eriksen (1991) and Brink (1995) argue that diurnal-wave radial heat-fluxes balance downward Ekman pumping over the summit plain. Freeland (1994) suggested that the vortex observed atop Cobb Seamount was forced by wave rectification also. This raises the question of whether the vortex cap on Fieberling's summit is a Taylor cap or maintained entirely by rectified tidal flux-divergences, and raises doubts about past oceanographic interpretations of isopycnal doming over seamounts in terms of Taylor cap dynamics. Wave rectification induced by intense dissipative processes appears to be at least as important a driving mechanism here but is poorly understood.

The R2 current-meter time-series show that the vortex abruptly turns on and off every few months (Fig. 6). The same behavior is seen at R3. Brink (1995) argues that this is a function of the impinging zonal flow direction. His Fig. 13 shows a tendency for a vortex cap to be present during eastward flow in the far field and suppressed during westward flow. This is contrary to β-plane dynamics predictions. McCartney (1975) and Verron and LeProvost (1985) find that westward flow produces trapped vortices while eastward flow generates a Rossby wave wake in barotropic β-plane simulations of flow past a small-amplitude seamount. The HRP and XCP measurements were taken at a time of transition from weak eastward to weak westward impinging flow ($\overline{u} \simeq \pm 1$ cm s^{-1}). Since the vortex flow exceeds the impinging flow, the fluid it contains is isolated.

4.4 Potential Vorticity Anomaly

Even though the HRP profiles reveal a 200-m thick positive density anomaly ($\langle \delta\sigma_\theta \rangle = 0.02$ m, Fig. 7a) associated with the vortex cap atop the summit plain (site C, $r \sim 1$ km) compared to the flank (F3, $r = 7.5$ km), corresponding to an upward vertical displacement of 4 m, it is too weak to produce a discernible buoyancy frequency

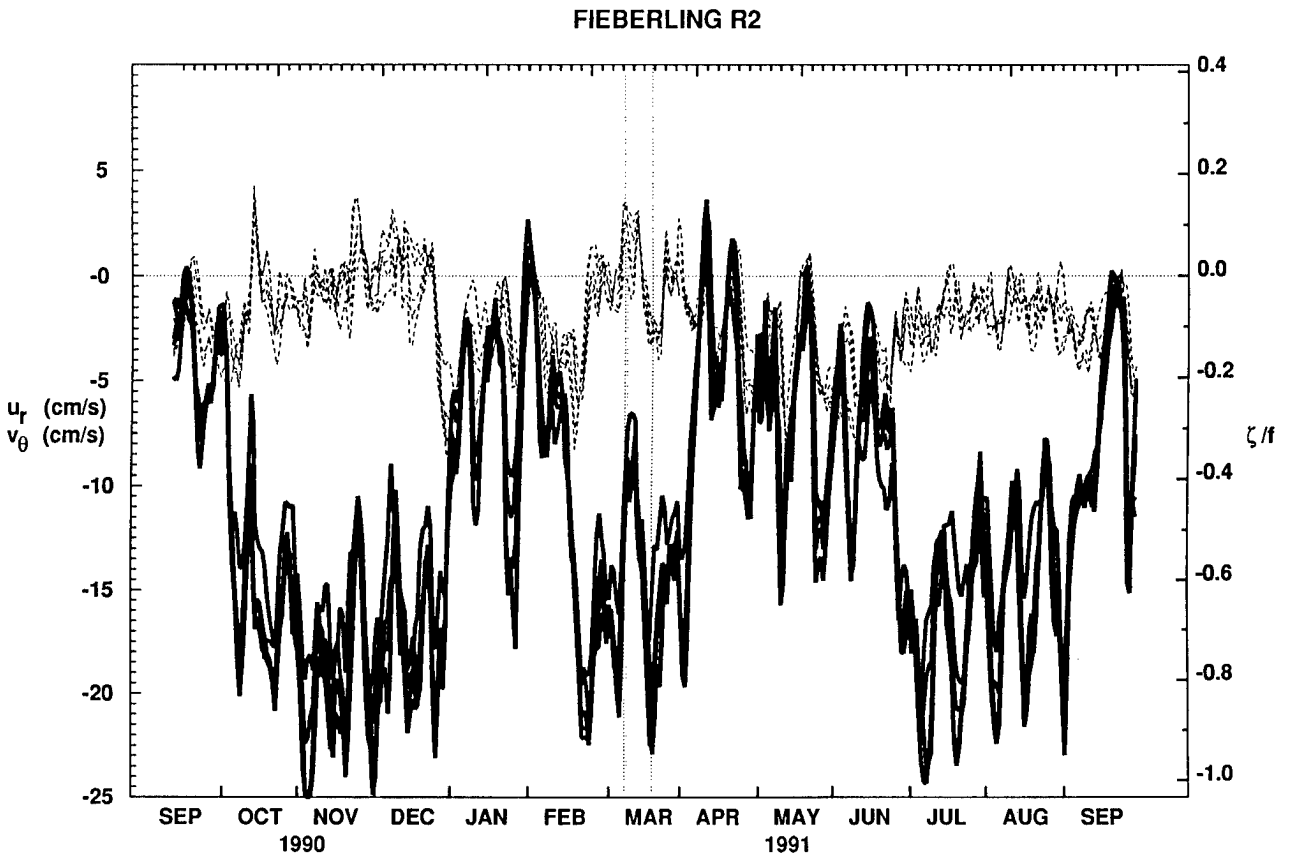


Figure 6. Time-series of 4-day smoothed azimuthal velocity $\langle v_\theta \rangle_t$ (solid) and radial velocity $\langle u_r \rangle_t$ (dotted) from the upward-looking ADCP at R2 on the summit plain's rim (Fig. 1) in the depth range 500–570 m (700–750 sm). The azimuthal velocity is also expressed as a relative vorticity (right axis) assuming solid-body rotation, $\zeta = 2\langle v_\theta \rangle_t / r$. XCP survey periods are indicated by dotted vertical lines. The radial velocity tends to be less than ±5 cm s^{-1} while the azimuthal velocity is consistently negative. Fortnightly fluctuations in $\langle v_\theta \rangle_t$ are of insufficient strength to shut off or reverse its direction. Every 2–3 months, the azimuthal velocity abruptly shifts between ~15–20 cm s^{-1} and ~5 cm s^{-1} accompanied by less dramatic changes in the radial velocity.

anomaly. As a result, the relative vorticity of the vortex cap induces a negative potential vorticity anomaly of $-0.25\, f\overline{N}^2$ (Fig. 7b) only slightly diminished by the weak positive buoyancy frequency anomaly. The presence of a potential vorticity anomaly is *not* consistent with pure Taylor cap dynamics, which preserves potential vorticity. Irreversible dissipative processes, such as those associated with wave rectification, must play a role in creating a potential vorticity anomaly (Ertel, 1942; Haynes and McIntyre, 1987). Viscous damping and bottom friction by themselves would produce a positive anomaly and thus cannot be responsible for the observed anomaly. If features like this potential vorticity anomaly are occasionally shed off seamounts, they might explain the submesoscale potential vorticity anomalies found beside Ampere Seamount by Kunze and Sanford (1993).

4.5 Cyclogeostrophic Balance

The subinertial azimuthally-averaged radial momentum equation can be expressed

$$\boxed{\frac{V_\theta^2}{r} + fV_\theta = \frac{\partial P}{\partial r}} + \frac{\partial \langle u_r'^2 \rangle}{\partial r} + \frac{\langle u_r'^2 \rangle - \langle v_\theta'^2 \rangle}{r} + \frac{\partial \langle u_r' w' \rangle}{\partial z}, \tag{3}$$

where the reduced, or kinematic, pressure $P = \boldsymbol{P}/\rho_o$ and $\boldsymbol{P}$ is the dynamic pressure. The boxed terms are the cyclogeostrophic (gradient-wind) balance expected for steady inviscid flow with curvature in the absence of strong forcing, e.g., rings and Meddies. We will refer to the lefthand side of (3) as the effective Coriolis acceleration. Figure 8 compares the right- and lefthand sides of a radially-integrated cyclogeostrophic balance

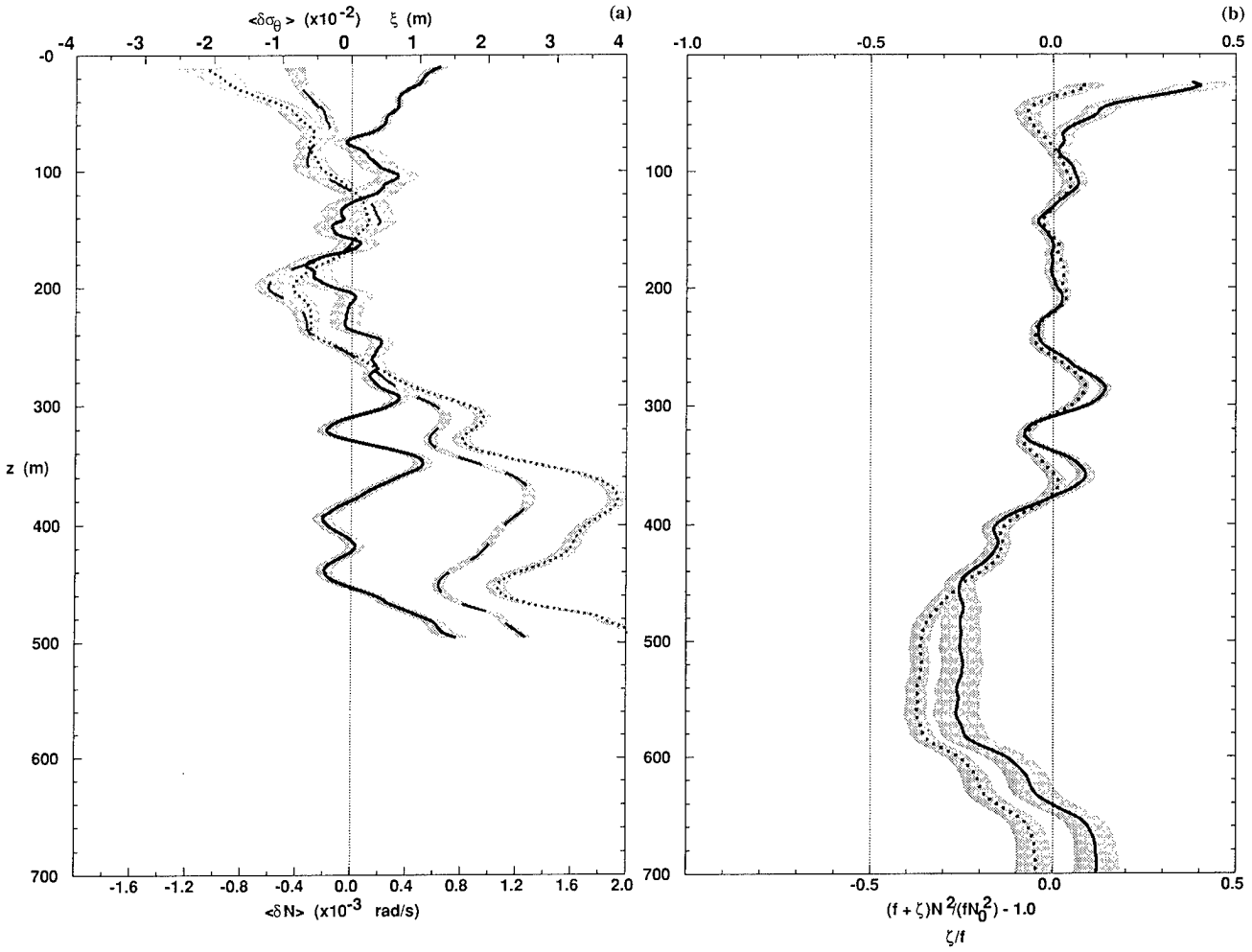


Figure 7. (a) Average HRP density anomaly $<\delta\sigma_\theta>$ (dashed), buoyancy frequency anomaly $<\delta N>$ (solid), and vertical displacement $<\xi>$ (dotted) profiles at site C ($r \sim 1$ km) on the summit plain compared to site F3 ($r = 7.5$ km) on the flanks. The 200-m thick $<\delta\sigma_\theta> = 0.02$ density anomaly above the summit plain is too weak to produce a significant buoyancy frequency anomaly. (b) Average profiles of relative vorticity ζ/f (dotted) and potential vorticity anomaly $[(f+\zeta)N_C^2 - fN_{F_3}^2]/fN_{F_3}^2$ atop the summit plain ($r < 7$ km). The vortex cap has a negative potential vorticity anomaly of $-0.25fN_{F_3}^2$.

$$\int_r^{r_o}\left[\frac{V_\theta^2}{r}+fV_\theta\right]\cdot dr = \delta P = \int_z^{200\,\mathrm{m}} \delta B\cdot dz \simeq g\frac{\partial\sigma_\theta}{\partial T}\int_z^{200\,\mathrm{m}}\delta T\cdot dz\,, \tag{4}$$

making use of the hydrostatic balance, $\partial P/\partial z = B$, and the local T, σ_θ-relation, $\partial\sigma_\theta/\partial T$, in the XCP data to infer pressure anomalies δP from the temperature anomalies δT relative to the outermost radial bin at $r \sim 10$ km. The vertical integral is taken from the center of our 150–300 m level of no motion. The effective Coriolis acceleration is evident in the negative anomaly between 400- and 600-m depth (dotted curve in Fig. 8). For radii $r < 4$ km, the pressure anomaly δP in this depth range (solid curve) is of the same sign and comparable magnitude, so the vortex cap is in cyclogeostrophic balance. At larger radii, the magnitudes of the two sides of (4) remain comparable but the vertical structure differs. The discrepancy becomes even greater below 600-m depth, where a growing negative pressure anomaly has no balancing signal from the effective Coriolis acceleration. This discrepancy is seen independently in both the XCP and HRP data. The horizontal momentum-flux divergences on the righthand side of (3) cannot account for it, making at most a 10% contribution. The vertical momentum-flux divergence contribution might be estimated from $<u_r'^2>$ and the bottom slope

$$\int_r^{r_o}\frac{\partial <u_r'w'>}{\partial z}dr = \int_r^{r_o}\frac{\partial(\alpha <u_r'>)}{\partial z}dr.$$

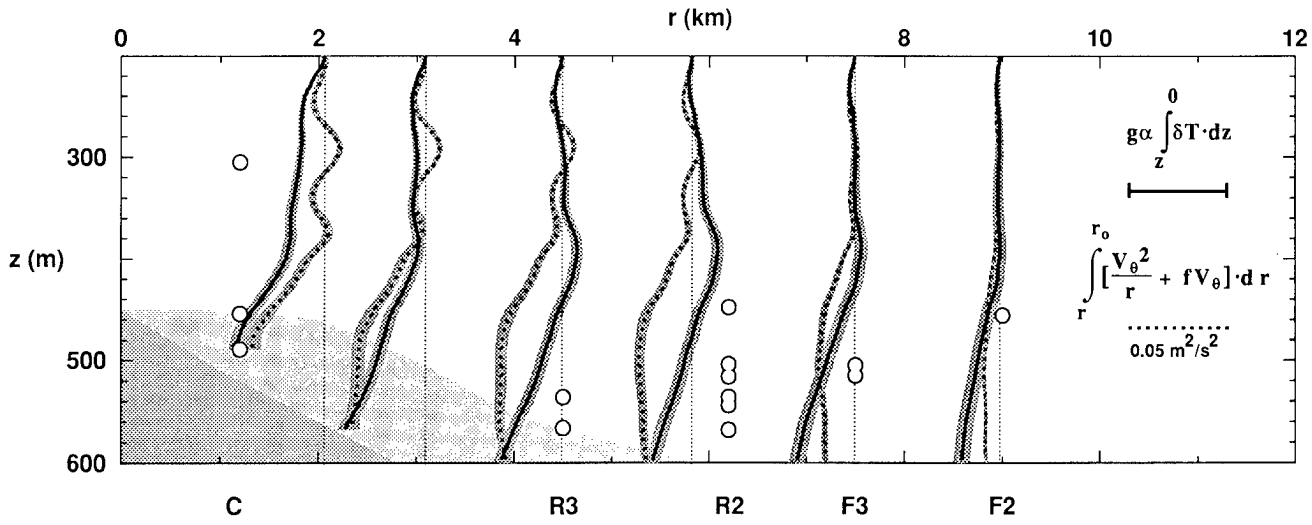


Figure 8. Comparison of the radially-integrated mean effective Coriolis acceleration $\int_r^{r_0}\left[\frac{<v_\theta>_\theta^2}{r} + f<v_\theta>_\theta\right]\cdot dr$ (dotted) with the vertically-integrated buoyancy anomaly $g\frac{\partial\sigma_\theta}{\partial T}\int_{z_o}^{z}<\delta T>_\theta \cdot dz$ (solid) as a test of the cyclogeostrophic (gradient-wind) balance (3). The quantities are comparable immediately above the summit plain for radii $r < 4$ km; a dome of cold water exists over the summit plain. But the vertically-integrated buoyancy anomaly has a different vertical structure for $r > 4$ km.

Assuming that $\alpha = \alpha_o \exp[(z - z_b)/(z_b - z_0)]$, where α_o is the bottom slope on the flanks, z_b the bottom depth, and z_0 the depth of the summit plain, so that α decays toward zero when moving off the bottom on a depth scale comparable to that from the bottom to the summit plain, the vertical momentum-flux divergence is unable to explain the observed discrepancy at $r > 4$ km. Reasonable alternative relations for α yield similar results.

The sole remaining plausible explanation for the discrepancy is that the azimuthal sampling is inadequate to filter out the dipolar horizontal temperature structure of the diurnal wave, $n\theta - \omega t$. At depths below the summit rim over the flanks, there is usually one azimuthal bin with no data points in it. We conclude that the unbalanced pressure anomaly δP at radii $r > 4$ km and depths $z > 500$ m is due to sampling bias.

4.6 Radial Heat Fluxes and Wave Rectification

Brink (1995) also reported a dome of cold water over the summit associated with anticyclonic flow. He argued that an outward radial heat-flux $<u_r'T'> = 0.4$°C cm/s was maintaining the vortex cap against benthic Ekman downwelling $\overline{w}\overline{T}_z$ ($\overline{w} = -0.03$ to -0.13 cm s^{-1} and $\overline{T}_z = (0.7\text{–}1.5) \times 10^{-2}$ °C m^{-1}) inferred from the near-bottom radial outflow found by Eriksen (1991) and himself. His Ekman term was an order of magnitude larger than his radial heat-flux divergence, which is an order of magnitude larger still than our estimate (Figs. 17 and 18). A possible reason for this discrepancy is that Brink's parameterization overestimated the bottom stress. A factor of ten smaller value arises using an eddy viscosity of 10×10^{-4} m^2 s^{-1} as inferred from the turbulent measurements. Over a sloping bottom, MacCready and Rhines (1993) have shown that downslope Ekman transport will set up horizontal pressure gradients which suppress the bottom flow geostrophically, isolating the mean flow and eliminating the bottom stress. In this case, the vortex would become semidetached. There are indications that the azimuthal velocity $<v_\theta>_\theta$ and relative vorticity $<\zeta>_\theta$ weaken toward the bottom near the summit rim (Figs. 2 and 3). Variable bathymetry is another means by which the bottom stress might be overestimated if the vortex is in contact with the bottom over only a small fraction of its azimuth. But the above arguments do not explain the persistent outward radial velocities observed near the bottom (Eriksen, 1991; Brink, 1995; Freeland, 1994).

Here, we wish to point out some subtleties in the wave rectification problem that hinder inferring balances with incomplete data. Consider steady ($\partial/\partial t = 0$), azimuthally-averaged ($\partial/\partial\theta = 0$) conservation of azimuthal momentum and buoyancy in a tall (or equivalently a vertically-integrated) vortex ($\partial/\partial z \simeq 0$)

$$(f + \zeta)\tilde{u}_r = -\frac{\partial <v_\theta' w'>}{\partial z} \tag{5}$$

$$N^2\tilde{w} = -\frac{1}{r}\frac{\partial[r<u_r' b'>]}{\partial r} \tag{6}$$

$$\frac{1}{r}\frac{\partial(r\tilde{u}_r)}{\partial r}+\frac{\partial \tilde{w}}{\partial z}=0\,. \qquad (7)$$

where $\zeta = V_\theta/r + \partial V_\theta/\partial r$ is the background mean vorticity, b', u_r', v_θ', and w' are the wave buoyancy, radial, azimuthal, and vertical velocities, and $\tilde{u}_r$ and $\tilde{w}$ are *wave-induced mean* flows forming a cross-stream circulation. The $<u_r'v_\theta'>$ horizontal momentum-flux vanishes (see Fig. 17), and Brink (1995) showed that $\tilde{u}_r\partial\overline{B}/\partial r$ is negligible. The vertical buoyancy-flux $<w'b'>$ due to turbulent mixing, $K_\rho N^2 \lesssim 2\times10^{-8}\,\mathrm{m^2\,s^{-3}}$, could contribute as much as the Ekman downwelling only if confined to vertical scales of 3–10 m, so it will be ignored here. Substituting (5) and (6) into continuity (7), we find that

$$\frac{<v_\theta'w'>}{f+\zeta}=-\frac{<u_r'b'>}{N^2}, \qquad (8)$$

recognizing that the constants of integration are zero for a wave field. As shown in Appendix A, this relation holds exactly for inviscid vortex-trapped waves. Thus, in (5) and (6), wave fluxes can exactly balance wave-induced mean advective fluxes to maintain a steadystate independent of the Ekman flow; the background field remains unchanged by the waves' radial heat-flux and vertical momentum-flux unless dissipative processes act to alter their interrelationship. This is a general result for waves propagating in a background mean shear known as the *nonacceleration theorem* (Andrews and McIntyre, 1976; Dunkerton, 1980). If the radial heat-flux arises from a vortex-trapped wave as interpreted here, its role in maintaining the background vortex cannot be evaluated without measurements of the vertical momentum-flux $<v_\theta'w'>$. How forced/damped waves affect the mean depends sensitively on the strength and nature of the dissipative processes. For example, in cases where such damping can be parameterized as eddy diffusivities and viscosities, the background diffuses in the vertical or horizontal depending on the eddy Prandtl number (see, e.g., Flierl and Mied, 1985). Our main point here is that, without knowing the detailed nature of the dissipative processes or measuring all the flux-divergences, determination of the rate of change of background quantities is subject to misinterpretation. In the present case, the data do not allow reliable estimation of the vertical momentum-flux $<v_\theta'w'>$.

5. The Diurnal Shear Layer

5.1 Temporal Behavior

Current-meter time-series (Genin *et al.*, 1989; Eriksen, 1991; Noble *et al.*, 1994; Brink, 1995) have established that there is a ±15 cm s^{-1} diurnal oscillation atop the summit plain of Fieberling Guyot with large contributions from both K_1 (0.933*f*) and O_1 (0.865*f*) tidal frequencies. Both are 100 times as energetic as the barotropic tides in the far field, with K_1 being about four times larger than O_1. Beating of these two tidal constituents produces a subharmonic fortnightly cycle and a harmonic at M_2 (δT = 0.28°C). The diurnal frequency is confirmed by the HRP profile time-series at C though the tidal constituents cannot be separated. Grayscale HRP time-series at site C (Fig. 9) reveal clockwise rotation of the velocity vector with time and counterclockwise rotation with depth (downward phase propagation) below 300-m depth. Dropped lag coherences for vertical wavelengths λ_z = 32–128 sm imply a period of 23.6 h (0.95*f*), consistent with the current-meter measurements. Similar vertical and temporal phase behavior is observed in the 300- to 600-m depth range of the flank profile time-series, well-isolated from the bottom.

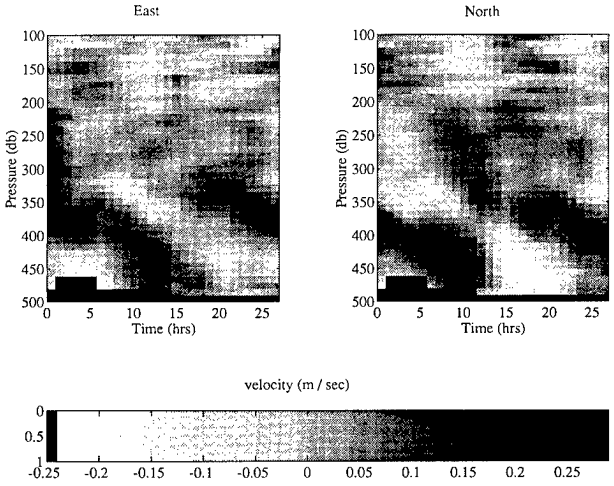


Figure 9. Grayscale plots of east and north velocity from a 27-h long HRP profile time-series at site C on the summit plain. HRP profiles were collected every 3 h. The depth average has been set equal to zero. Larger amplitudes and downward phase propagation are evident below 300-m depth.

Vertical isopycnal excursions of ±20 m are observed in the center and flank HRP time-series with similar vertical and temporal scales as found in velocity. Their downward phase propagation over the flank leads us to conclude that the steplike structures in the temperature and salinity profiles are produced by the diurnal strain field and not turbulent mixing. At site C on the summit plain, the vertical displacement field is dominated by semidiurnal harmonics.

5.2 Spatial Structure

Azimuthally averaging the east and north velocities in the XCP snapshots filters out axisymmetric flow associated with the vortex and isolates azimuthal-mode-one structure associated with the diurnal oscillations.

Diurnally backrotating the profiles to a common time before averaging did not capture significantly more variance because the XCP profiles were all collected within a few hours of the same phase of the diurnal tidal forcing.

Radial profile sections of azimuthally-averaged, WKB-normalized east and north velocity, $\langle u \rangle_\theta$ and $\langle v \rangle_\theta$, are displayed in Fig. 10. WKB-stretching produces higher vertical resolution where N is small, accounting for the smaller vertical scales at depth than in shallow water. A 150-sm thick layer of intensified shear is evident immediately above the summit plain (550–700 sm, 350–500 m). The signal decays on 3–4 km radial scales away from the summit but is still visible at 10-km radius.

The efficacy of the averaging scheme in isolating the bulk of the variance above the summit plain is demonstrated in Fig. 11. Between 550- and 650-sm depth, the variance in the average (a) greatly exceeds that in the residual (b). At other depths, the residual contains more variance than the average, indicating that azimuthal-mode-one structure dominates only immediately above the summit plain. Maximum velocities exceeding 15 cm s^{-1} lie between 600 and 650 sm (400 and 450 m), ~ 50 m above the bottom. Velocity maxima 50 m above the bottom at ~ 450-m depth are also seen at the rim in the ADCP data (Brink, 1995). This is not consistent with the evanescence away from the bottom expected for seamount-trapped waves.

The relatively low variance in both the average and residual between 150- and 500-sm depth is a consequence of assuming a level of no motion in that depth range. This may also result in excess variance below the summit depth, particularly in the residual (Fig. 11b), so this signal cannot unambiguously be interpreted as due to critical reflection from the flank slopes. Conservatively, the difference between the WKB-normalized residual kinetic energies at 300–550 sm and 700–1200 sm can be thought of as a measure of the uncertainty in the barotropic velocity.

The diurnal shear layer (Fig. 10) is present in both east and north velocities but is out of phase in the vertical in the sense that the velocity vector turns counterclockwise with depth. This can be seen most clearly in Fig. 12, which displays a radial slice of the orientation of the horizontal velocity vector, $\theta = \text{Arctan}(\langle v \rangle_\theta / \langle u \rangle_\theta)$, in the depth range where the signal is most energetic; the orientation θ is a measure of the phase for near-inertial internal gravity waves. It increases monotonically with depth by 240° in 150 sm. This uniform phase gradient $\partial\theta/\partial z$ ($\equiv k_z$) is consistent with the upward-looking ADCP measurements in the bottom 50 m at R2 (Fig. 1). Brink (1995) reports that the ADCP-measured phase gradient above 550 m (750 sm) is four times greater than in his (1989) seamount-trapped wave model including a time-dependent benthic Ekman layer. The XCP profiles show that this gradient also extends over a depth range four times larger than predicted by his model (Fig. 13). The gradient corresponds to a vertical wavelength $\lambda_z \simeq$ 250 sm. If interpreted as a near-inertial internal wave, the counterclockwise turning with depth implies downward phase and upward energy propagation. The orientation also increases by 30° in 5–7 km radius (Fig. 12). For an internal wave, energy propagates along lines of constant phase in the vertical plane, so this implies outward as well as upward energy propagation.

Vertical wavenumber spectra (Fig. 14) reiterate the rotary character of the signal with depth. The shear layer over the summit plain appears as a peak at vertical wavelength λ_z = 256 sm in the counterclockwise-with-depth (CCW) spectrum over the summit. The peak is most pronounced in the variance-preserving spectrum. There is no corresponding enhancement in the clockwise-with-depth (CW) spectrum at this wavelength. The CW spectrum is redder ($k_z^{-5/2}$) than the GM model (Garrett and Munk, 1975; Cairns and Williams, 1976) but has comparable levels at lower wavenumbers ($\lambda_z >$ 50 sm). At radii greater than 10 km, there are no significant peaks in either the CCW or CW spectra. Both have the same spectral slope but slightly lower (0.7) levels than the GM model. Spectral slopes are steeper (k_z^{-3}) for vertical wavelengths $\lambda_z <$ 50 sm. Clockwise rotation dominates above 500-sm depth (300 m) as is typical of the ocean pycnocline (Leaman and Sanford, 1975).

Figure 15 compares the horizontal structure of the amplitude and phase of the λ_z = 256 sm CCW component with that of the gravest-mode seamount- and vortex-trapped waves. The observed structure resembles the gravest mode in that the largest amplitudes are found above the summit plain and it exhibits nearly uniform orientation. Moving off the summit plain, the observed vectors become weaker and of more random orientation. Comparing just the radial decay of amplitude, Fig. 16 displays an envelope of solutions for the vortex-trapped near-inertial wave model constrained by the observed buoyancy frequency N, vortex radius r_o, vorticity ζ, and vertical wavelength λ_z (gray stippling). Further constraining the Eulerian frequency to be equal to the K_1 diurnal frequency produces the black envelope of solutions. The seamount-trapped wave model behavior (Δ) better matches the vortex-trapped model behavior than the XCP data (•), but all three show the largest amplitude inside the vortex and decay on scales of a few kilometers outside the vortex. Since the gravest-mode horizontal structure for the two wave models is nearly identical, it cannot be used to identify the dynamics of the diurnal shear layer.

5.3 Radial Heat-Flux

A striking feature in the summit plain current-meter records is the radial heat-flux $\langle u_r'T' \rangle$ associated with the diurnal oscillations (Brink, 1995). Johnson and Sanford

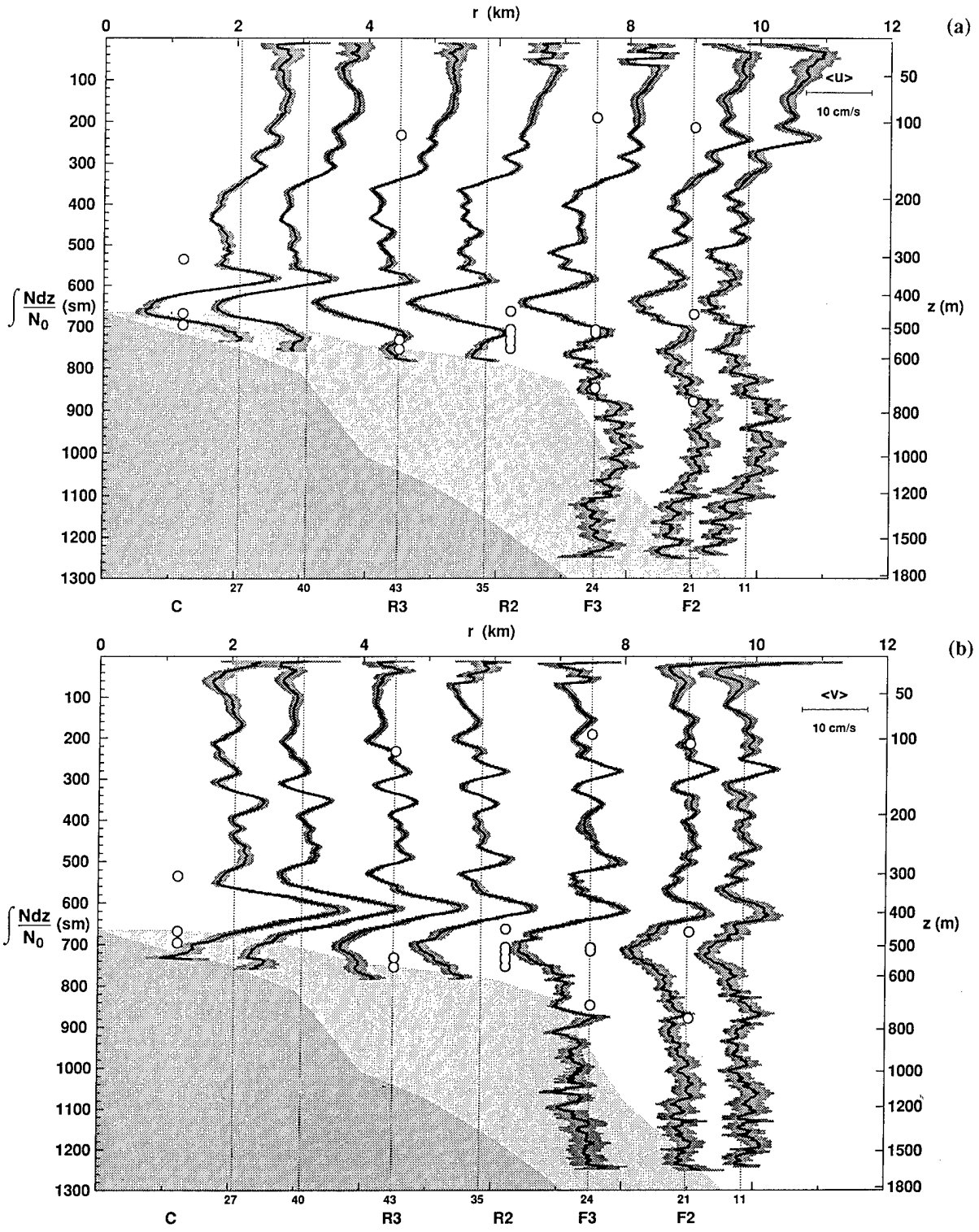


Figure 10. Radial sections of azimuthally-averaged, WKB-normalized east velocity $\langle u \rangle_\theta$ (a) and north velocity $\langle v \rangle_\theta$ (b) over the summit plain and flanks. Shading about the profiles indicates one standard error. WKB-stretched depths are indicated along the left axis and true depths along the right axis. Light and dark silhouettes indicate extremes of bathymetry, open circles the locations of current-meters (Wichman *et al.*, 1993), and numbers at the bottom the number of drops going into each average. A 150-sm thick layer of 10–15 cm s^{-1} shear lies 50–100 sm above the summit plain and rim, evanescing radially away from the seamount. Extrema in $\langle u \rangle_\theta$ and $\langle v \rangle_\theta$ are not at the same depths but offset in the sense that the velocity vector turns counter-clockwise with depth (see Figs. 12 and 13). There is also a horizontally-coherent wave of $\lambda_z = 50$ sm in $\langle v \rangle_\theta$ but not $\langle u \rangle_\theta$ between 200- and 400-sm depth.

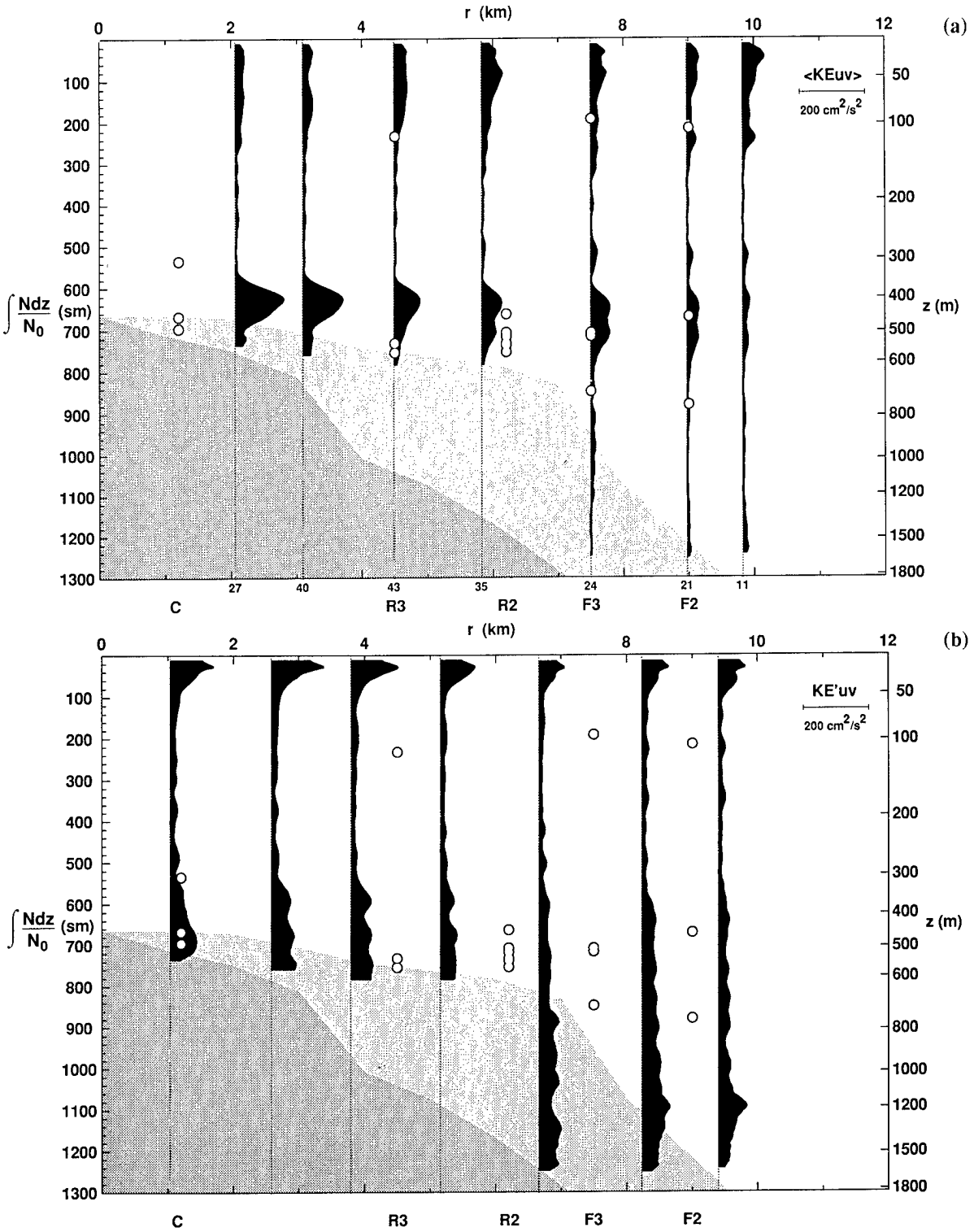


Figure 11. Radial sections of WKB-normalized (a) average Cartesian kinetic energy $\langle KE_{uv}\rangle_\theta = (\langle u\rangle_\theta^2 + \langle v\rangle_\theta^2)/2$ and (b) the residual energy $KE_{uv} = \langle u'^2 + v'^2\rangle_\theta/2$. The average kinetic energy (a) has a peak exceeding 100 cm^2 s^{-2} between 600 and 700 sm (400–500 m depth), 50–100 sm above the summit plain. This peak corresponds to the 150-m thick shear layer in Fig. 10. The residual kinetic energy (b) has more uniform overall energies with no well-pronounced peak above the summit, demonstrating the efficacy of the averaging scheme in isolating the feature over the summit plain. The larger residual energy below 500-sm depth is due to removal of 150–500 sm velocities from the profiles before averaging.

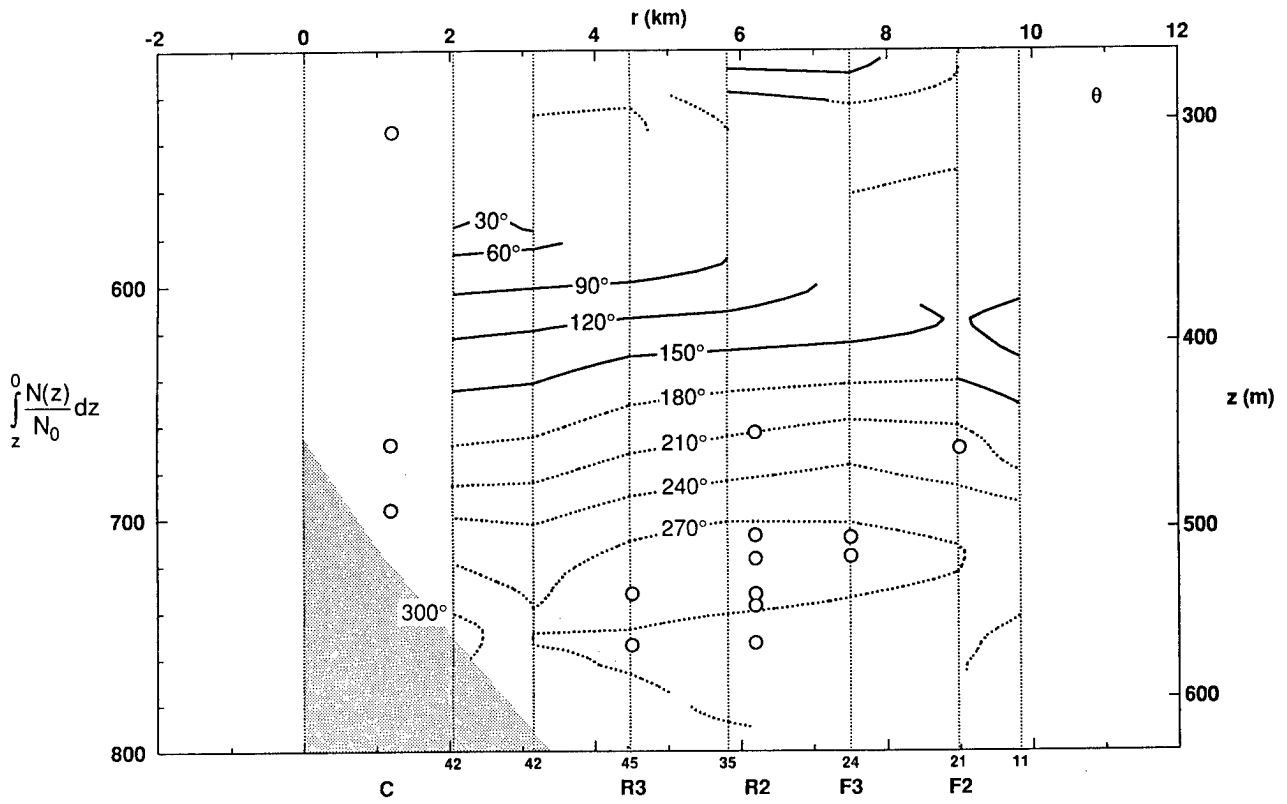


Figure 12. Radial section of the orientation of the azimuthally-averaged Cartesian horizontal velocity, θ = Arctan($\langle v \rangle_\theta / \langle u \rangle_\theta$), in the shear layer (Fig. 10). The orientation θ is only contoured where the horizontal kinetic energy exceeds 15 cm^2 s^{-2}. The increase of the orientation θ by 240° from 580- to 720-sm depth reveals that the velocity vector turns counterclockwise with depth. The corresponding vertical wavelength is ~210 sm. The sense of the turning is consistent with (i) near-inertial waves of upward energy propagation or (ii) subinertial time-dependent bottom Ekman spirals. The orientation θ also increases by 25–30° in 6-km radius, consistent with a radial wavelength of ~80 km. In a vertical plane, internal-wave energy propagates along lines of constant phase, so this interpretation would imply upward and outward energy propagation.

(1980) reported similar correlations between vertical displacements and outward velocities on the flanks of Bermuda; they interpreted their result as evidence of an anisotropic internal wave field. Radial velocity/vertical displacement correlations are also seen on the Fieberling summit plain in the profiler data. Vertical wavenumber coherences $\langle u_r' v_\theta' \rangle$, $\langle u_r' \xi' \rangle$ and $\langle v_\theta' \xi' \rangle$ are significant in vertical wavelengths λ_z = 100–300 sm for r = 6–10 km (Fig. 17). On these scales, u_r' and v_θ' are 90° out of phase, consistent with the counterclockwise turning with depth of the horizontal velocity vector (Fig. 12); radial velocity u_r' and vertical displacement $\xi' = -T' / \overline{T}_z$ are 180° out of phase, implying an outward radial heat-flux, and azimuthal velocity v_θ' and vertical displacement ξ' are 90° out of phase. These properties are more consistent with a vortex-trapped near-inertial internal wave than with a seamount-trapped topographic wave. Adding viscous damping $\nu_e k_z^2$ with $\nu_e = 10 \times 10^{-4}$ m^2 s^{-1}, consistent with the observed turbulence levels, causes the theoretical phase relations to diverge from their inviscid values, but not by enough to explain the data (see Appendices B and C).

The radial structure of the radial displacement-flux $\langle u_r' \xi' \rangle$ (solid line) resembles that of a vortex-trapped wave, having a zero crossing near 3-km radius with positive values inside that radius and negative values outside (Fig. 18). We caution, however, that Haidvogel *et al.* (1993) found a radial heat-flux in numerical simulations where the forcing frequency and Coriolis frequency f were too far apart for a vortex-trapped wave to exist.

6. Turbulence and Mixing

The kinetic energy dissipation rate ε and temperature-variance turbulent dissipation rate χ_T exceed $\varepsilon = 10^{-6}$ W kg^{-1} and $\chi_T = 10^{-7}$ °C^2 s^{-1}, respectively, in the 200-m thick diurnal shear layer above Fieberling's summit plain. Dissipations of comparable magnitude are found in shallower, more stratified water in association with the upper-ocean internal wave field and surface mixed-layer during periods of strong wind-stress. But above 300-m depth, the dissipation rates exhibit no spatial pattern. Below 300 m, the average kinetic energy turbulent dissipation is 100 times larger in the diurnal shear layer over the summit

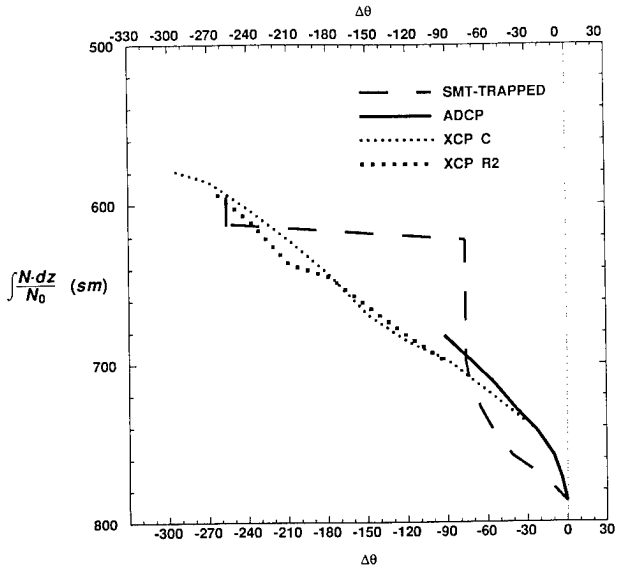


Figure 13. Comparison of the velocity orientation Δθ as a function of WKB-stretched depth from Brink's (1990) seamount-trapped wave model (dashed), the rim R2 ADCP mooring (solid), and XCPs near the center and on the rim of the summit plain (dotted). XCP and ADCP gradients are roughly consistent in the overlapping depth range 680–780 sm. The model's time-dependent bottom Ekman spiral is also roughly consistent with the turning in this depth range. However, the XCP profiles indicate that the phase gradient $\theta_z$extends to 580-sm depth while the seamount-trapped wave model indicates uniform phases above 700 sm until 620-sm depth, then a 180° phase shift (velocity reversal) at shallower depths.

plain than at similar depths 10 km away (Fig. 19). Patches of high energy turbulent dissipation are well-correlated with the sites of Froude number (not shown). Error bars are 97% confidence limits computed using the bootstrap technique (Efron and Gong, 1983) and do not differ significantly from those computed assuming a log-normal distribution (Baker and Gibson, 1987).

The average kinetic energy dissipation rate ε above the summit plain is $(3.3 \pm 0.1) \times 10^{-8}$ W kg^{-1}, sufficient to drain the total energy in the diurnal oscillation (~5.0×10^{-3} m^2 s^{-2}) and vortex cap (~2.5×10^{-3} m^2 s^{-2}) in 3 days. For comparison, the amount of time it would take open-ocean turbulence to deplete a Garrett-and-Munk internal wave field is 100 days. The short depletion time over Fieberling Seamount implies that barotropic diurnal tides are continuously supplying energy to these motions on a similar timescale to maintain the observed signals. The issue of intensified near-bottom turbulence contributing little mixing because it acts in an unstratified benthic boundary layer (Garrett, 1990) is not germane above either the summit plain or the flanks (Toole *et al.*, 1995) where strong turbulence is found in the stratified waters.

The diapycnal eddy diffusivities inferred from the microstructure data ($K_T = \chi_T/(2\overline{T}_z^2)$, Osborn and Cox, 1972; $K_\rho \le 0.25\varepsilon/\overline{N}^2$, Osborn, 1980) have a typical open-ocean value of 0.1×10^{-4} m^2 s^{-1} above 300-m depth (Fig. 20). In the 200-m thick layer atop the summit plain, they approach 50×10^{-4} m^2 s^{-1} (excluding diffusivities within 10 m of the bottom that could be in a bottom boundary layer). The steady Ekman scale height for an effective eddy viscosity of 50×10^{-4} m^2 s^{-1} is 8 m. Similar eddy diffusivities (100×10^{-4} m^2 s^{-1}) were found by Mudge (1994) at Cobb Seamount. In his case, the largest values were near the rim depth and extended outward several seamount radii. Nabatov and Ozmidov (1988) found numerous 10-m thick patches above and in detached layers in the vicinity of Josephine and Ampere seamounts with turbulent dissipation rates of $(6.0–400.0) \times 10^{-7}$ W kg^{-1}. Osborn (1978) reported average dissipation rates of 10^{-8} W kg^{-1} within 5–80 km of an island, corresponding to eddy diffusivities of 10^{-4} m^2 s^{-1}, but these measurements were not proximal to the topography and the turbulence may have been due to a recent storm passage. Toole *et al.* (1995) and Eriksen (1995) find eddy diffusivities of $(2.0–6.0) \times 10^{-4}$ m^2 s^{-1} in the stratified boundary layer above the flanks of Fieberling.

Averaged over the ocean basin, these diffusivities are at most equivalent to the 0.1×10^{-4} m^2 s^{-1} observed in the main pycnocline (Moum and Osborn, 1986; Gregg, 1989; Ledwell *et al.*, 1993; Toole *et al.*, 1994; Polzin *et al.*, 1995), so seamount mixing cannot raise basin-average mixing levels to a vertical advection-diffusion balance (Munk, 1966) value of 10^{-4} m^2 s^{-1}.

7. Summary and Discussion

Fine- and microstructure profiles collected over Fieberling Seamount reveal a 200-m thick layer of intense activity overlying the summit plain. In this layer there coexists (i) an anticyclonic vortex cap of relative vorticity $-0.5f$ (Fig. 2b), (ii) a slightly subinertial diurnal shear layer (Figs. 9 and 10), and (iii) intensified turbulence with average dissipation rates $\varepsilon = 3.3 \times 10^{-8}$ W kg^{-1} (Fig. 19) and eddy diffusivities $K_\rho = 10 \times 10^{-4}$ m^2 s^{-1} (Fig. 20). All these motions appear to be ultimately driven by the barotropic K_1 and O_1 diurnal tides. The turbulence levels imply decay times of ~3 days, so it is clear that the barotropic tides are continually pumping energy into the summit motions.

The vortex was in cyclogeostrophic balance, at least inside $r = 4$ km (Fig. 8). At larger radii and depths greater than 600 m, the radial pressure gradient and effective Coriolis acceleration do not balance. This imbalance could not be explained by a contribution from momentum-flux divergences. It appears to be the result of inadequate azimuthal sampling. The strength of the vortex exhibited a fortnightly cycle with peak-to-peak variations of $-0.4f$ to $-0.5f$ (Fig. 6), evidence that it was at least partially driven by the diurnal tides. Other evidence that the

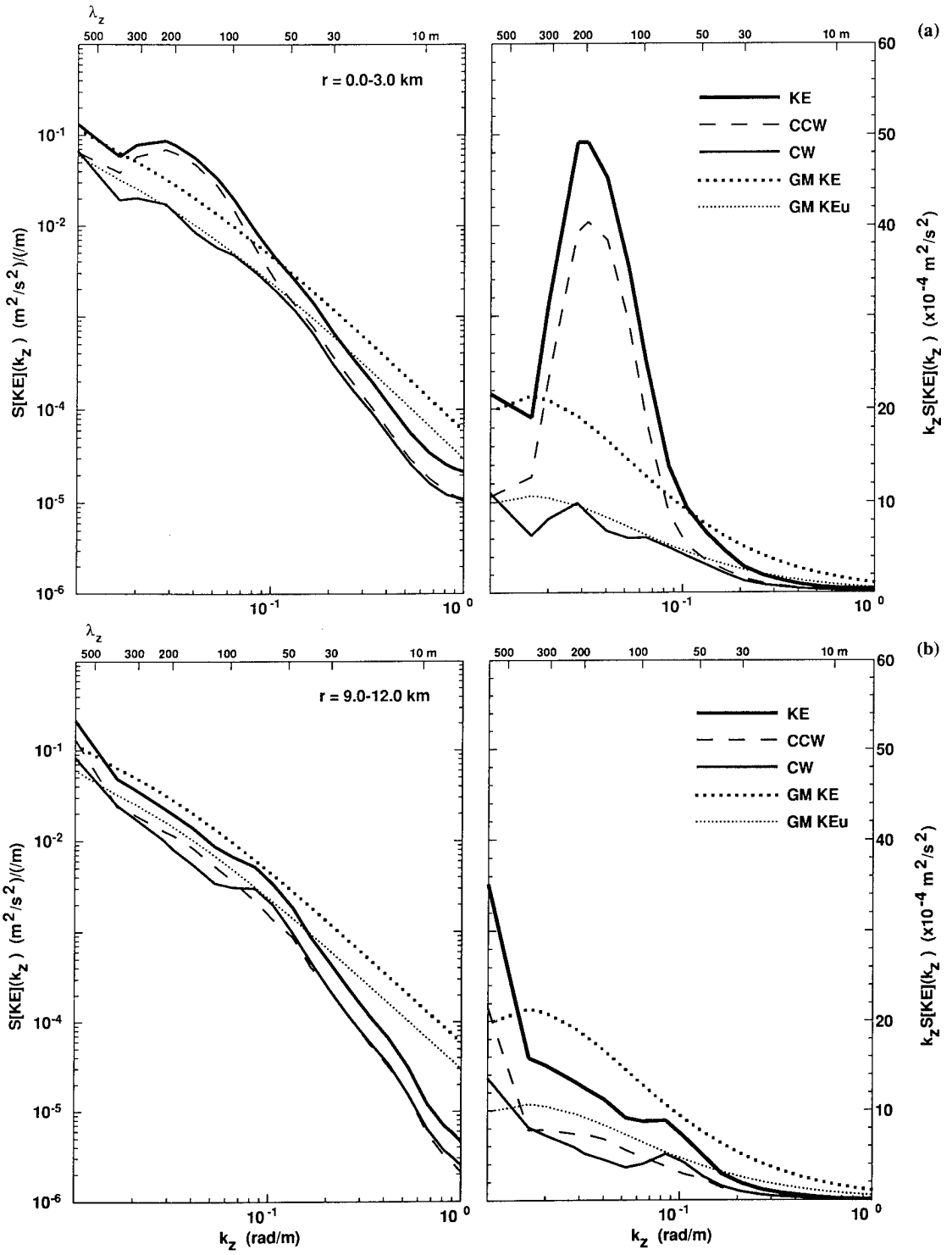


Figure 14. Rotary vertical wavenumber spectra of kinetic energy for drops at 0–3 km (upper two panels) and 9–12 km radius (lower two panels). Spectra are presented in both log-log (left panels) and variance-preserving (right panels) formats. The 0–3 km spectra emphasize the depth-rotary nature of the shear-layer signal above the summit plain. They are dominated by a counterclockwise-with-depth (CCW) peak at λ_z = 256 sm. There is no corresponding enhancement of CW energy. Away from the seamount, clockwise and counterclockwise spectra are similar and slightly below GM model levels.

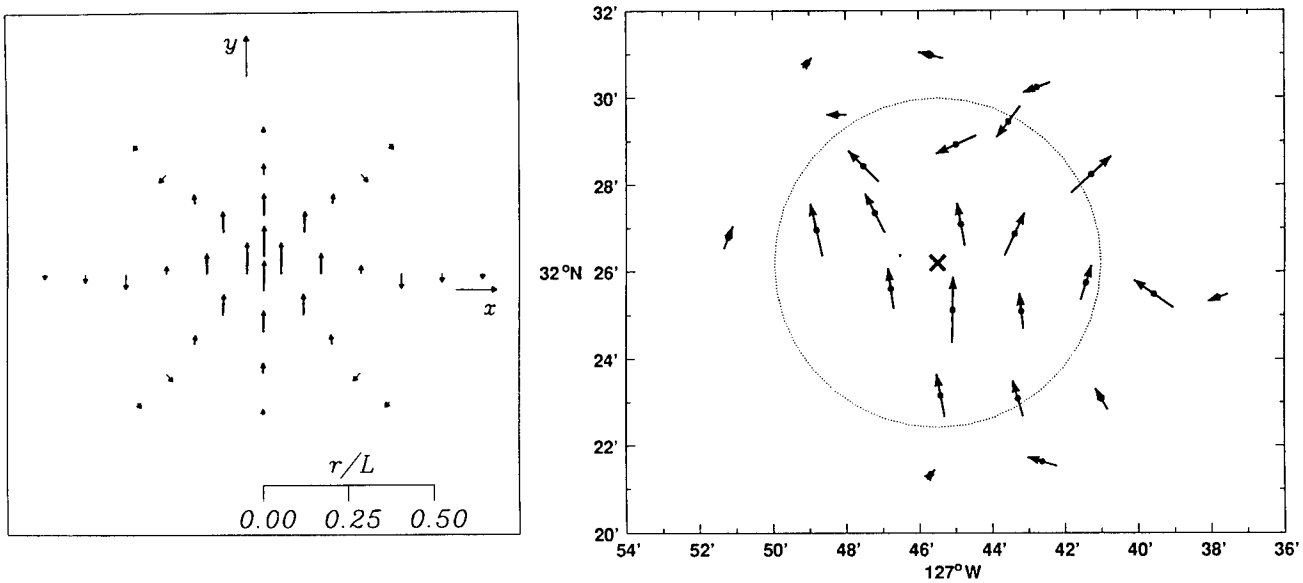


Figure 15. Horizontal structure for lowest-mode seamount- or vortex-trapped wave (left panel; after Brink, 1989), and the amplitude and phase of the observed λ_z = 256 m counterclockwise-with-depth signal (right panel). The seamount- and vortex-trapped wave have identical horizontal structure. The observations have been averaged in 2' × 2' bins. Over the summit plain, the signal is strongest and has nearly uniform orientation. Off the summit, amplitudes are weaker and orientation more random.

vortex cap could not be explained with inviscid Taylor cap dynamics is that its core contained a negative potential vorticity anomaly (Fig. 7) while Taylor cap dynamics conserve potential vorticity. Wave rectification of the diurnal tides is the most likely mechanism for maintaining the cold dome of the vortex against benthic Ekman decay. An outward radial heat-flux $\langle u_r'T' \rangle$ is associated with the diurnal shear layer but, without measurements of the vertical momentum-flux $\langle v_\theta' w' \rangle$, the role that the diurnal oscillation plays in driving the vortex cannot be evaluated rigorously. The vortex strength also changed dramatically every few months for reasons that were unclear but may be related to changes in the direction of the impinging background flow (Brink, 1995).

The diurnal shear layer also displays a fortnightly modulation of the K_1 beating against the O_1 tide. Its jet-like azimuthal-mode-one horizontal structure rotates clockwise with time and counterclockwise with depth (λ_z = 250 sm). Its slightly subinertial frequency (Fig. 9) and horizontal structure (Figs. 15 and 16) closely resemble those of a seamount-trapped topographic wave (Brink, 1989, 1990). However, a vortex-trapped near-inertial internal wave has similar properties (Kunze *et al.*, 1995). Moreover, the maximum variance being 50 m above the bottom, the continuous counterclockwise turning of the velocity vector with depth (Figs. 12 and 13), and the radial heat-flux (Figs. 17 and 18) more closely resemble a vortex-trapped than a seamount-trapped wave.

We conclude that the diurnal shear layer observed in the HRP and XCP measurements is a vortex-trapped internal wave forced by the barotropic tide impinging on the seamount summit, its subinertial frequency being allowed

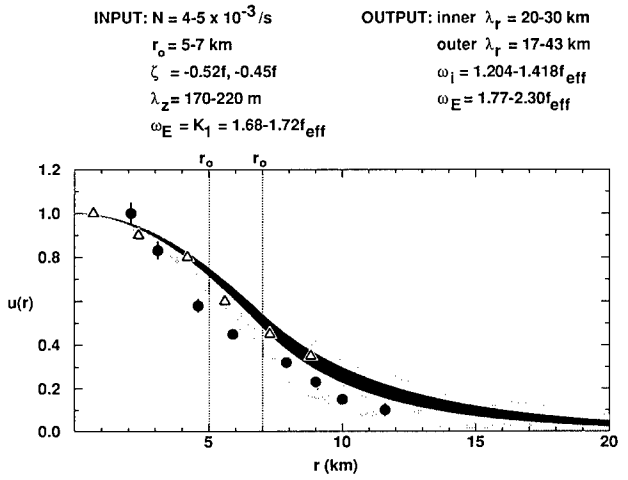


Figure 16. Radial structure of horizontal velocity for a vortex-trapped mode (stippled envelope) constrained by the observed range of buoyancy frequency N, core vorticity ζ, core radius r_o and vertical wavelength λ_z. If further constrained to have the observed K_1 diurnal Eulerian frequency, only the solid envelope results, corresponding to an inner radial wavelength of 27 km and an outer (decay) radial wavelength λ_{r_0} = 25 km. A seamount-trapped wave has identical radial structure (Δ). XCP observations (ϕ) lie near the model curves.

by the strong negative vorticity of the vortex cap. If this interpretation is correct, then, for deep seamounts where the only significant slightly subinertial forcing is the barotropic tides, this phenomenology will be found only just poleward of 30°. Equatorward of 30°, diurnal frequencies can propagate as free internal waves and thus will not be trapped. Much poleward of 30°, a vortex cap

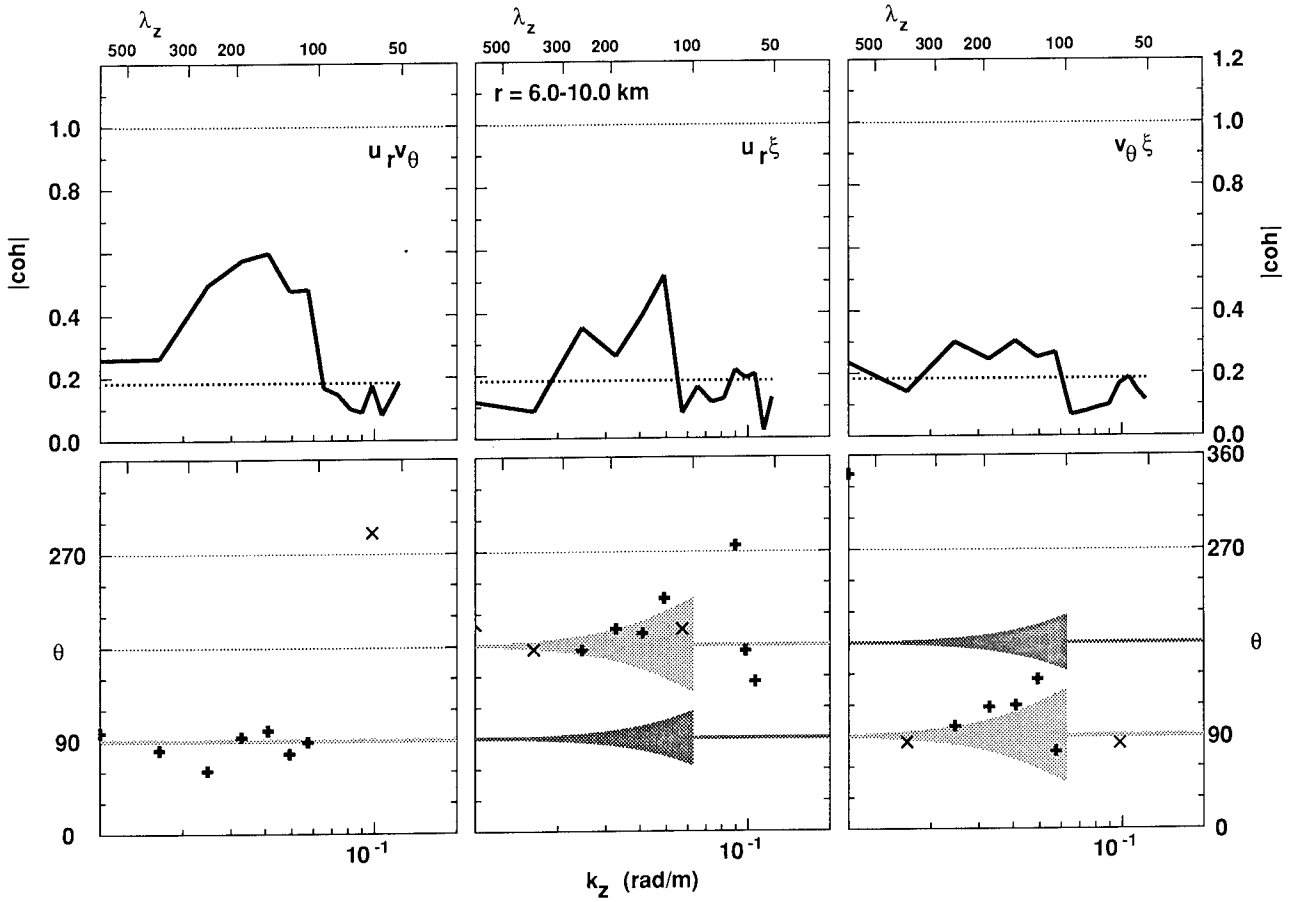


Figure 17. Coherence magnitude (upper panels) and phase (lower panels) as a function of vertical wavenumber for XCP and HRP profiles at radius r = 6–10 km. Phase relations for vortex- and seamount-trapped waves are shown by the light and dark stippling, respectively. The spreading of the phase relations by an eddy viscosity $\nu_e \leq 100 \times 10^{-4}$ m^2 s^{-1} (Appendices B and C) is shown for $\lambda_z > 100$ m. Coherence is significant for vertical wavelengths λ_z = 100–300 m. In this band, radial and azimuthal velocities are 90° out of phase (consistent with the CCW turning with depth), radial velocity u_r' and vertical displacement ξ' 180° out of phase (corresponding to an outward radial heat-flux), and azimuthal velocity v_θ' and vertical displacement ξ' 90° out of phase. These last two phase relations are consistent with vortex-trapped waves propagating upward and clockwise around the seamount, but not with seamount-trapped waves.

will not be strong enough to allow a free diurnal wave in its confines or, equivalently, the vertical wavelength of an allowed vortex-trapped wave (2) would be so small that its amplitude would be undetectable. These restrictions may not apply to shallow seamounts, where broadband atmospheric forcing includes slightly subinertial frequencies that will be resonant with vortex-trapped waves. Given the intermittency of atmospheric forcing and the short decay times of the observed wave, vortex-trapped waves may appear only during forcing. The above is consistent with Codiga's (1995) finding of a diurnal seamount-trapped wave atop shallow Cobb Seamount at 46°45'N.

Elevated turbulence levels of $\varepsilon \simeq 10^{-7}$ W kg^{-1} are found coincident with the vortex cap and the diurnal oscillation, corresponding to eddy diffusivities of 10×10^{-4} m^2 s^{-1}. This is not sufficiently enhanced for seamounts to play a dominant role in global mixing of the pycnocline, in particular, for them to account for an average eddy diffusivity of 10^{-4} m^2 s^{-1} inferred from a diapycnal advection-diffusion balance (Munk, 1966). With the mixing not occurring in the ocean interior or at lateral boundaries, the surface seems the most likely site of diapycnal mixing for the ocean.

Acknowledgments. We thank Charlie Eriksen and Ken Brink for making their moored current-meter data available to other Fieberling Seamount investigators. Valuable insights into seamount-trapped waves were provided by Ken Brink and Dan Codiga. The HRP data were collected and analyzed under ONR contract N00014-89-J-1073. The XCP data were collected under ONR contract N00014-90-J-1535 and analyzed under contracts N00014-90-J-1535 and N00014-94-I-0038.

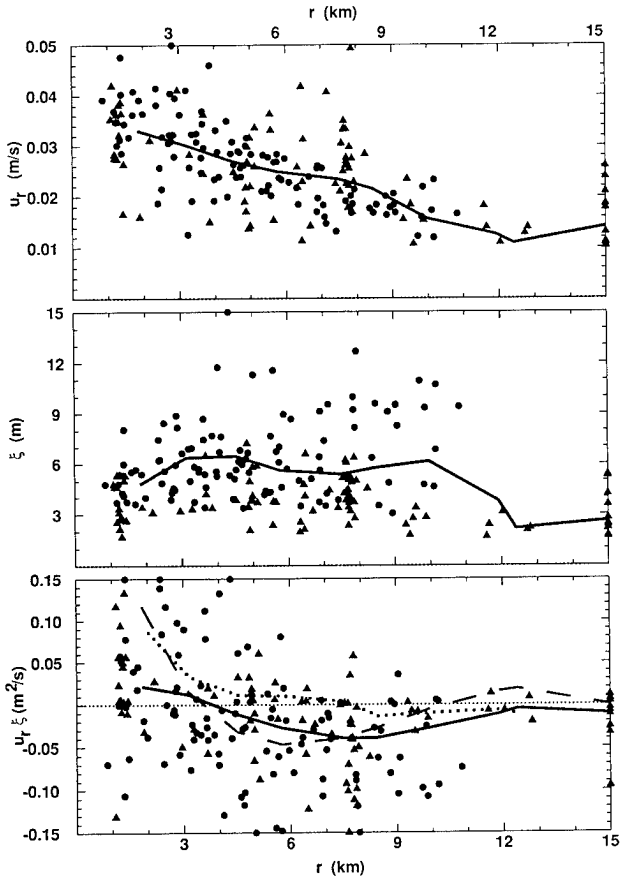


Figure 18. Radial structure of rms radial velocity u_r' (a), rms vertical displacement ξ' (b) and the real (co-spectral) part of the radial displacement flux $u_r'\xi'$ (c) in the λ_z= 100–300 m band. Dots and triangles correspond to values from individual XCPs and HRPs, respectively. Solid curves are radially-smoothed values. The dotted curve in the $u_r'\xi'$ panel depicts a vortex-trapped wave model prediction given the rms u_r' radial structure, the dashed line uses the rms u_r' inside 1-km radius and the vortex-trapped wave model structure.

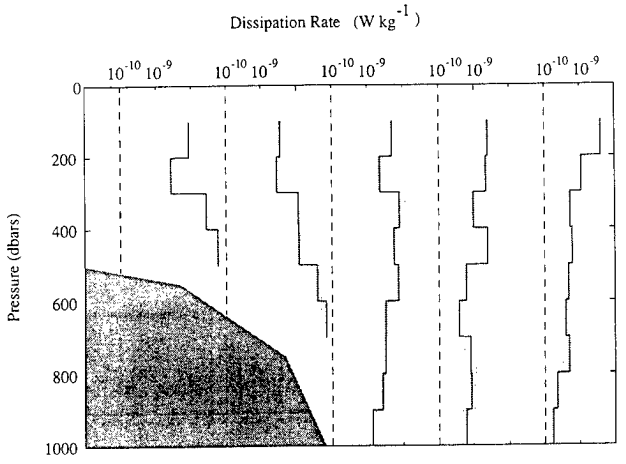


Figure 19. Average kinetic energy dissipation rate ε (W kg^{-1}) as a function of depth and radial distance from seamount center with 97% bootstrap confidence limits. Averages are in 100-m thick depth bins, and radial bins over the summit plain, about the rim, the 1500-m isobath, the 2500-m isobath and > 10 km from the seamount center.

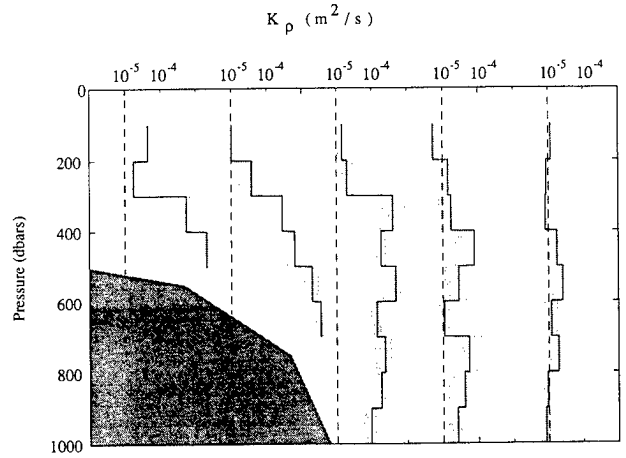


Figure 20. Average turbulent eddy diffusivity K_ρ (m^2 s^{-1}) inferred from the kinetic energy dissipation rate ε (Fig. 19) as a function of depth and radius. Error bars are 97% confidence limits determined with bootstrap methods. A mixing efficiency of 0.25 is assumed (Oakey, 1982).

References

Andrews, D.G., and M.E. McIntyre, 1976: Planetary waves in horizontal and vertical shear: The generalized Eliassen-Palm relation and the mean zonal acceleration, *J. Atmos. Sci.*, 33, 2049–2053.

Baines, P., 1971: The reflection of internal/inertial waves from bumpy surfaces, Part 1, *J. Fluid Mech.*, 46, 273–291.

Baker, M.A., and C.H. Gibson, 1987: Sampling turbulence in the stratified ocean: Statistical consequences of strong intermittency, *J. Phys. Oceanogr.*, 17, 1817–1836.

Bell, T.H., 1975: Topographically generated internal waves in the open ocean, *J. Geophys. Res.*, 80, 320–327.

Boyer, D.L., and X. Zhang, 1990: Motion of oscillatory currents past isolated topography, *J. Phys. Oceanogr.*, 20, 1425–1448.

Brink, K.H., 1989: The effect of stratification on seamount-trapped waves, *Deep-Sea Res.*, 36, 825–844.

Brink, K.H., 1990: On the generation of seamount-trapped waves, *Deep-Sea Res.*, 37, 1569–1582.

Brink, K.H., 1995: Tidal and lower frequency currents above Fieberling Guyot, *J. Geophys. Res.*, submitted.

Cairns, J.L., and G.O. Williams, 1976: Internal wave observations from a midwater float, 2, *J. Geophys. Res.*, 81, 1943–1950.

Chapman, D.C., 1989: Enhanced subinertial diurnal tides over isolated topographic features, *Deep-Sea Res.*, 36, 815–824.

Chapman, D.C., and D.B. Haidvogel, 1992: Formation of Taylor caps over a tall isolated seamount in a stratified ocean, *Geophys. Astrophys. Fluid Dyn.*, 64, 31–65.

Codiga, D.L., 1991: Fitting Fieberling Guyot, *TopoNews*, Newsletter of ONR Accelerated Research Initiative Flow Over Abrupt Topography, 4, 14–15.

Codiga, D.L., 1993: Laboratory realizations of stratified seamount-trapped waves, *J. Phys. Oceanogr.*, 23, 2053–2071.

Codiga, D.L., 1995: ADCP and CTD observations at Cobb Seamount: Low-frequency circulation and amplified subinertial tidal currents, Ph.D. thesis, University of Washington, 92 pp.

Dunkerton, T.J., 1980: A Lagrangian-mean theory of wave/mean flow interaction with applications to nonacceleration and its breakdown, *Rev. Geophys. Space Phys.*, 18, 387–400.

Efron, B., and G. Gong, 1983: A leisurely look at the bootstrap, the jackknife and cross-validation, *Amer. Stat.*, 37, 36–48.

Eriksen, C.C., 1982: Observations of internal wave reflection off sloping bottoms. *J. Geophys. Res.*, 87, 525–538.

Eriksen, C.C., 1985: Implications of ocean bottom reflection for internal wave spectra and mixing, *J. Phys. Oceanogr.*, 15, 1145–1156.

Eriksen, C.C., 1991: Observations of amplified flows atop a large seamount, *J. Geophys. Res.*, 96, 15,227–15,236.

Eriksen, C.C., 1995: Internal wave reflection and mixing at Fieberling Guyot, *J. Geophys. Res.*, submitted.

Ertel, H., 1942: Ein neuer hydrodynamischer Wirbelsatz, *Meteorol. Z.*, 59, 277–281.

Flierl, G.R., and R.P. Mied, 1985: Frictionally induced circulations and spindown of a warm-core ring, *J. Geophys. Res.*, 90, 8917–8927.

Freeland, H., 1994: Ocean circulation at and near Cobb Seamount, *Deep-Sea Res.*, 41, 1715–1732.

Garrett, C., 1990: The role of secondary circulation in boundary mixing., *J. Geophys. Res.*, 95, 989–993.

Garrett, C.J.R., and W.H. Munk, 1975: Space-time scales of internal waves: A progress report, *J. Geophys. Res.*, 80, 291–297.

Genin, A., P.K. Dayton, P.F. Lonsdale and F.N. Spiess, 1986: Corals on seamount peaks provide evidence of current acceleration over deep-sea topography, *Nature*, 322, 59–61.

Genin, A., M. Noble and P.F. Lonsdale, 1989: Tidal currents and anticyclonic motions on two North Pacific seamounts, *Deep-Sea Res.*, 36, 1803–1815.

Genin, A., C.K. Paull and W.P. Dillon, 1992: Anomalous abundances of deep-sea fauna on a rocky bottom exposed to strong currents, *Deep-Sea Res.*, 39, 293–302.

Gilbert, D., and C. Garrett, 1989: Implications for ocean mixing of internal wave scattering off irregular topography, *J. Phys. Oceanogr.*, 19, 1716–1729.

Gregg, M.C., 1989: Scaling turbulent dissipation in the thermocline, *J. Geophys. Res.*, 94, 9686–9698.

Haidvogel, D.B., A. Beckmann, D.C. Chapman and R.-Q. Lin, 1993: Numerical simulation of flow around a tall isolated seamount, Part II: Resonant generation of trapped waves, *J. Phys. Oceanogr.*, 23, 2373–2391.

Haynes, P.H., and M.E. McIntyre, 1987: On the evolution of vorticity and potential vorticity in the presence of diabatic heating and frictional or other forces, *J. Atmos. Sci.*, 44, 828–841.

Hogg, N.G., 1973: On the stratified Taylor column, *J. Fluid Mech.*, 58, 517–537.

Hunkins, K., 1986: Anomalous diurnal tidal currents on the Yermak Plateau., *J. Mar. Res.*, 44, 51–69.

Huthnance, J.M., 1974: On the diurnal tidal currents over Rockall Bank, *Deep-Sea Res.*, 21, 23–35.

Huthnance, J.M., 1978: On coastal-trapped waves: Analysis and numerical calculation by inverse iteration, *J. Phys. Oceanogr.*, 8, 74–92.

Johnson, C.L., and T.B. Sanford, 1980: Anomalous behavior of internal gravity waves near Bermuda, *J. Phys. Oceanogr.*, 10, 2021–2034.

Kowalik, Z., 1994: Modeling of topographically amplified diurnal tides in the Nordic seas, *J. Phys. Oceanogr.*, 24, 1717–1731.

Kunze, E., 1985: Near-inertial wave propagation in geostrophic shear, *J. Phys. Oceangr.*, 15, 544–565.

Kunze, E., 1986: The mean and near-inertial velocity fields in a warm-core ring. *J. Phys. Oceanogr.*, 16, 1444–1461.

Kunze, E., and T.B. Sanford, 1986: Near-inertial wave interactions with mean flow and bottom topography near Caryn Seamount, *J. Phys. Oceanogr.*, 16, 109–120.

Kunze, E., M.A. Kennelly and T.B. Sanford, 1992: The depth dependence of shear finestructure off Point Arena and near Pioneer Seamount, *J. Phys. Oceanogr.*, 22, 29–41.

Kunze, E., and T.B. Sanford, 1993: Submesoscale dynamics near a seamount. Part I: Measurements of Ertel vorticity, *J. Phys. Oceanogr.*, 23, 2567–2588.

Kunze, E., R.W. Schmitt and J.M. Toole, 1995: The energy balance in a warm-core ring's near-inertial critical layer, *J. Phys. Oceanogr.*, 25, 942–957.

Leaman, K.D., and T.B. Sanford, 1975: Vertical energy propagation of inertial waves: A vector spectral analysis of velocity profiles, *J. Geophys. Res.*, 80, 1975–1978.

Ledwell, J.R., A.J. Watson and C.S. Law, 1993: Evidence of slow mixing across the pycnocline from an open-ocean tracer-release experiment, *Nature*, 364, 701–703.

LeBlond, P.H., 1966: On the damping of internal gravity waves in a continuously stratified ocean, *J. Fluid Mech.*, 25, 121–142.

Loder, J.H., 1980: Topographic rectification on the sides of Georges Bank, *J. Phys. Oceanogr.*, 10, 1399–1416.

Maas, L.R.M., and J.J.M. van Haren, 1987: Observations on the vertical structure of tidal and inertial currents in the central North Sea, *J. Mar. Res.*, 45, 293–318.

Maas, L.R.M., and J.T.F. Zimmerman, 1989a: Tide-topography interactions in a stratified shelf sea. I. Basic equations for quasi-nonlinear internal tides, *Geophys. Astrophys. Fluid Dyn.*, 45, 1–35.

Maas, L.R.M., and J.T.F. Zimmerman, 1989b: Tide-topography interactions in a stratified shelf sea, II. Bottom-trapped internal tides and baroclinic residual currents, *Geophys. Astrophys. Fluid Dyn.*, 45, 37–69.

MacCready, P., and P.B. Rhines, 1993: Slippery bottom boundary layers on a slope, *J. Phys. Oceanogr.*, 23, 5–22.

McCartney, M., 1975: Inertial Taylor columns on a beta-plane, *J. Fluid Mech.*, 68, 71–95.

Montgomery, E.T., and J.M. Toole, 1993: Fine- and microstructure observations at Fieberling Guyot: R/V New Horizon Cruise Report, Woods Hole Oceanogr. Inst. Tech. Rpt. WHOI-93-15, 27 pp.

Moum, J.N., and T.R. Osborn, 1986: Mixing in the main thermocline, *J. Phys. Oceanogr.*, 16, 1250–1259.

Mudge, T.D., 1994: Mixing around a shallow seamount, Masters thesis, University of Victoria, Victoria, B.C., Canada, 126 pp.

Müller, P., and N. Xu, 1992: Scattering of oceanic internal gravity waves off random bottom topography, *J. Phys. Oceanogr.*, 22, 474–488.

Munk, W., 1966: Abyssal recipes, *Deep-Sea Res.*, 13, 707–730.

Nabatov, V.N., and R.V. Ozmidov, 1988: Study of turbulence above seamounts in the Atlantic Ocean, *Oceanology*, 28, 161–166.

Noble, M., D.A. Cacchione and W.C. Schwab, 1988: Observations of strong mid-Pacific internal tides above Horizon Guyot, *J. Phys. Oceanogr.*, 18, 1300–1306.

Noble, M., and L.S. Mullineaux, 1989: Internal tidal currents over the summit of Cross Seamount, *Deep-Sea Res.*, 36, 1791–1802.

Noble, M.A., K.H. Brink and C.C. Eriksen, 1994: Diurnal-period currents trapped above Fieberling Guyot: Observed characteristics and model comparisons, *Deep-Sea Res.*, 41, 643–658.

Oakey, N.S., 1982: Determination of the rate of dissipation of turbulent energy from simultaneous temperature and velocity shear microstructure measurements, *J. Phys. Oceanogr.*, 12, 256–271.

Osborn, T.R., 1978: Measurements of energy dissipation adjacent to an island, *J. Geophys. Res.*, 83, 2939-2957.

Osborn, T.R., 1980: Estimates of the local rate of vertical diffusion from dissipation measurements, *J. Phys. Oceanogr.*, 10, 83–89.

Osborn, T.R., and C.S. Cox, 1972: Oceanic finestructure, *Geophys. Fluid Dyn.*, 3, 321–345.

Padman, L., A.J. Plueddemann, R.D. Muench and R. Pinkel, 1992: Diurnal tides near the Yermak Plateau, *J. Geophys. Res.*, 97, 12,639–12,652.

Phillips, O.M., 1977: *The Dynamics of the Upper Ocean,* Cambridge University Press, Cambridge, 336 pp.

Polzin, K.L., 1992: Observations of turbulence, internal waves and background flows: An inquiry into the relationshiops between scales of motion, Ph.D. thesis, WHOI Tech. Rpt. 93-39, 244 pp.

Polzin, K.L., J.M. Toole and R.W. Schmitt, 1995: Finescale parameterizations of turbulent dissipation, *J. Phys. Oceanogr.*, 25, 306–328.

Rhines, P., 1969: Slow oscillations in an ocean of varying depth, Part I. Abrupt topography, *J. Fluid Mech.*, 37, 161–189.

Rhines, P., 1970: Edge-, bottom- and Rossby waves in a rotating stratified fluid, *Geophys. Fluid Dyn.*, 1, 273–302.

Roden, G.I., 1987: Effect of seamount and seamount chains on ocean circulation and thermohaline structure, *Seamounts, Islands and Atolls*, B.H. Keating, P. Fryer, R. Batiza, and G.W. Boehlert, (eds.), AGU, Washington, DC, pp. 335–354.

Roden, G.I., 1991: Mesoscale flow and thermohaline structure around Fieberling Seamount, *J. Geophys. Res.*, 96, 16,653–16,672.

Roden, G.I., 1994: Effects of the Fieberling seamount group upon flow and thermohaline structure in the spring of 1991, *J. Geophys. Res.*, 99, 9941–9961.

Sanford, T.B., R.G. Drever, J.H. Dunlap and E.A. D'Asaro, 1982: Design, operation and performance of an expendable temperature and velocity profiler (XTVP), Tech. Rpt. 8110, Appl. Phys. Lab, Univ. of Wash., Seattle, WA 83 pp.

Sanford, T.B., E.A. D'Asaro, E. Kunze, J.H. Dunlap, R.G. Drever, M.A. Kennelly, M.D. Prater and M.S. Horgan, 1993: An XCP user's guide and reference manual, Tech. Rpt. APL-UW TR 9309, Appl. Phys. Lab, Univ. of Washington, Seattle, WA, 59 pp.

Schmitt, R.W., J.M. Toole, R.L. Koehler, E.C. Mellinger, and K.W. Doherty, 1988: The development of a fine- and microstructure profiler, *J. Ocean Atmos. Techno.*, 5, 484–500.

Schwiderski, E.W., 1981a: Global ocean tides, Part IV: The diurnal luni-solar declination tide (K_1). Atlas of tidal charts and maps, TR81-142, Naval Surface Weapons Center, Dahlgren, VA.

Schwiderski, E.W., 1981b: Global ocean tides, Part V: The diurnal principal lunar tide (O_1). Atlas of tidal charts and maps, TR81-142, Naval Surface Weapons Center, Dahlgren, VA.

Swaters, G.E., and L.A. Mysak, 1985: Topographically induced baroclinic eddies near a coastline with application to the Northeast Pacific, *J. Phys. Oceanogr.*, 15, 1470–1485.

Toole, J.M., K.L. Polzin and R.W. Schmitt, 1994: Estimates of diapycnal mixing in the abyssal ocean, *Science*, 264, 1120–1123.

Toole, J.M., R.W. Schmitt, K.L. Polzin, and E. Kunze, 1995: Fine- and microstructure observations of boundary mixing on the flanks of Fieberling Guyot, in preparation.

Verron, J., and C. LeProvost, 1985: A numerical study of quasi-geostrophic flow over isolated topography, *J. Fluid Mech.*, 154, 231–252.

Weller, R.A., 1982: The relation of near-inertial motions observed in the mixed-layer during the JASIN (1978) experiment to the local wind stress and to the quasigeostrophic flow field, *J. Phys. Oceanogr.*, 12, 1122–1136.

Wichman, C.A., C.C. Eriksen, N.M. Bogue, K.H. Brink, D.E. Frye, R.D. Pillsbury, G.M. Pittock, and S.A. Tarbell, 1993: Fieberling Guyot moored array data, Tech. Rpt. A93-1, School of Oceanography, University of Washington, Seattle, WA, 373 pp.

Wunsch, C., 1969: Progressive internal waves on slopes, *J. Fluid Mech.*, 35, 131–144.

Zhang, X., and D.L. Boyer, 1993: Laboratory study of rotating, stratified, oscillatory flow over a seamount, *J. Phys. Oceanogr.*, 23, 1122–1141.

Zyryanov, V.N., 1981: A contribution to the theory of Taylor columns in a stratified ocean, *Izvestiya, Atmos. Ocean Phys.*, 17, 793–800.

Appendix A: Vortex-Trapped Near-Inertial Waves

Following Kunze *et al.* 1995), consider the equations of motion for a hydrostatic ($\omega_i << N$) internal wave of the form $\psi = \psi_0(r)\cdot\exp[i(n\theta + k_z z - \omega_E t)]$, where n is the azimuthal mode number, k_z the vertical wavenumber, and ω_E the invariant Eulerian frequency, inside an axisymmetric vortex $V_\theta(r)$

$$-i\left[\omega_E - \frac{nV_\theta}{r}\right]u_r - \left[f + \frac{2V_\theta}{r}\right]v_\theta = -\frac{\partial p}{\partial r}$$

$$-i\left[\omega_E - \frac{nV_\theta}{r}\right]v_\theta + \left[f + \frac{V_\theta}{r} + \frac{\partial V_\theta}{\partial r}\right]u_r = -\frac{inp}{r}$$

$$0 = -ik_z p + b \qquad \Rightarrow \qquad \boxed{p = \frac{-N^2 w}{\omega_i k_z}} \qquad \text{(A1)}$$

$$-i\left[\omega_E - \frac{nV_\theta}{r}\right]b + N^2 w = 0 \quad \Rightarrow \quad \boxed{b = \frac{-iN^2 w}{\omega_i}}$$

$$\frac{1}{r}\frac{\partial (ru_r)}{\partial r} + \frac{inv_\theta}{r} + ik_z w = 0\,,$$

where (u_r, v_θ, w) are the radial, azimuthal and vertical wave velocities, V_θ the mean azimuthal velocity, $b = -N^2\xi$ the wave-induced buoyancy anomaly, p the wave-induced pressure, and the intrinsic frequency $\omega_i = \omega_E - nV_\theta/r$. Assuming that the buoyancy frequency depends only weakly on radius, the radial derivatives of ω_i and p are

$$\frac{\partial \omega_i}{\partial r} = \frac{n}{r}\left[\frac{V_\theta}{r} - \frac{\partial V_\theta}{\partial r}\right] \qquad \text{(A2)}$$

$$\frac{\partial p}{\partial r} = -\frac{N^2}{\omega_i k_z}\frac{\partial w}{\partial r} + \frac{nN^2}{\omega_i^2 k_z r}\left(\frac{V_\theta}{r} - \frac{\partial V_\theta}{\partial r}\right) w\,. \qquad \text{(A3)}$$

Thus, the two horizontal momentum equations in (A1) can be expressed

$$-i\omega_i u_r - \left[f + \frac{2V_\theta}{r}\right]v_\theta = \frac{N^2}{\omega_i k_z}\frac{\partial w}{\partial r} - \frac{nN^2}{\omega_i^2 k_z r}\left(\frac{V_\theta}{r} - \frac{\partial V_\theta}{\partial r}\right) w$$

$$-i\omega_i v_\theta + \left[f + \frac{V_\theta}{r} + \frac{\partial V_\theta}{\partial r}\right]u_r = i\frac{nN^2}{\omega_i k_z r} w\,. \qquad \text{(A4)}$$

The azimuthal momentum equation implies

$$\boxed{v_\theta = -i\left[\frac{f + V_\theta/r + \partial V_\theta/\partial r}{\omega_i}\right]u_r - \frac{nN^2}{\omega_i^2 k_z r} w} \qquad \text{(A5)}$$

which, when substituted into the radial momentum equation and continuity, yields

$$-i\omega_i k_z r\left[\omega_i^2 - (f + 2V_\theta/r)(f + V_\theta/r + \partial V_\theta/\partial r)\right]u_r$$

$$= N^2\omega_i r\frac{\partial w}{\partial r} - nN^2(f + 3V_\theta/r - \partial V_\theta/\partial r)w \qquad \text{(A6)}$$

$$w = -i\left[\frac{\omega_i^2 k_z r}{n^2N^2 - \omega_i^2 k_z^2 r^2}\right]\frac{\partial (ru_r)}{\partial r}$$

$$- i\left[\frac{n\omega_i k_z r(f + V_\theta/r + \partial V_\theta/\partial r)}{n^2N^2 - \omega_i^2 k_z^2 r^2}\right]u_r\,.$$

For an azimuthal mode $n = -1$, $n^2N^2 << \omega_i^2 k_z^2 r^2$ provided $r >> N\lambda_z/(2\pi\omega_i) \simeq 3$ km for $N = 5 \times 10^{-3}$ s^z, $\lambda_z = 210$ m and $\omega_i = K_1 + \zeta/2 = 5.7 \times 10^{-5}$ s–1. Except in the inner core, the vertical velocity w can be simplified to

$$\boxed{w = \frac{i}{k_z}\frac{\partial u_r}{\partial r} + \mathrm{i}\left[\frac{\omega_i + n(f + V_\theta/r + \partial V_\theta/\partial r)}{\omega_i k_z r}\right]u_r} \qquad \text{(A7)}$$

with radial derivative

$$\frac{\partial w}{\partial r} = \frac{i}{k_z}\frac{\partial^2 u_r}{\partial r^2} + i\left[\frac{\omega_i + n(f + V_\theta/r + \partial V_\theta/\partial r)}{\omega_i k_z r}\right]\frac{\partial u_r}{\partial r}$$

$$+ i\left[\frac{n}{\omega_i k_z r}\frac{\partial^2 V_\theta}{\partial r^2}\right. \qquad \text{(A8)}$$

$$\left. - \left(\frac{\left[\omega_i + n\left(f + \frac{V_\theta}{r} + \frac{\partial V_\theta}{\partial r}\right)\right]\left[\omega_i + n\left(\frac{V_\theta}{r} - \frac{\partial V_\theta}{\partial r}\right)\right]}{\omega_i^2 k_z r^2}\right)\right] u_r\,.$$

Substituting w (A7) and $\partial w/\partial r$ (A8) into (A6),

$$\frac{\partial^2 u_r}{\partial r^2} + \left[\frac{\omega_i - 2n(V_\theta/r - \partial V_\theta/\partial r)}{\omega_i r}\right]\frac{\partial u_r}{\partial r} +$$

$$\left\{\frac{n}{\omega_i r}\frac{\partial^2 V_\theta}{\partial r^2} + \frac{[\omega_i^2 - (f + 2V_\theta/r)(f + V_\theta/r + \partial V_\theta/\partial r)]k_z^2}{N^2} - \right. \quad \text{(A9)}$$

$$\left.\frac{[\omega_i + n(f + V_\theta/r + \partial V_\theta/\partial r)][\omega_i + n(f + 4V_\theta/r - 2\partial V_\theta/\partial r)]}{\omega_i^2 r^2}\right\}$$

$$\times u_r = 0 .$$

A.1 Application

Consider a vortex containing a core in solid-body rotation ζ inside radius $r = r_o$ and azimuthal velocities falling off as r^{-1} outside the velocity maximum ($\zeta = 0$). Also recall that the observed wave has azimuthal mode $n = -1$ corresponding to clockwise propagation around the vortex.

A.2 Inside the Core

For $r < r_o$, $V_\theta = \zeta r/2$, $V_\theta/r = \partial V_\theta/\partial r = \zeta/2$, and $\partial^2 V_\theta/\partial r 2^2 = 0$ so that (A9) can be simplified to

$$\frac{\partial^2 u_r}{\partial r^2} + \frac{1}{r}\frac{\partial u_r}{\partial r}$$

$$+ \left[\frac{(\omega_i^2 - f_{eff}^2)k_z^2}{N^2} - \frac{(\omega_i - f_{eff})^2}{\omega_i^2 r^2}\right]u_r = 0$$

which, in the context of our previous assumption that $r >> N/(\omega_i k_z)$ or recognizing that $\omega_i - f_{eff} << \omega_i$ for the near-inertial waves of interest here, simplifies further to

$$\boxed{\frac{\partial^2 u_r}{\partial r^2} + \frac{1}{r}\frac{\partial u_r}{\partial r} + \frac{(\omega_i^2 - f_{eff}^2)k_z^2}{N^2}u_r = 0} \quad \text{(A10)}$$

where $f_{eff} = f + \zeta$ as found by Kunze *et al.* (1995). This has $J_0(k_r r)$ Bessel function solutions for $\omega_i > f_{eff}$ where the radial cylindrical "wavenumber"

$$k_r = \frac{k_z\sqrt{\omega_i^2 - f_{eff}^2}}{N} .$$

A.3 Outside the Core

For $r > r_o$, $V_\theta = \zeta r_o^2/(2r)$, $V_\theta/r = \zeta r_o^2/(2r^2)$, $\partial V_\theta/\partial r = -\zeta r_o^2/(2r^2)$, $\partial V_\theta/\partial r^2 = \zeta r_o^2/r^3$ where ζ is the core vorticity, and (A9) can be simplified to

$$0 = \frac{\partial^2 u_r}{\partial r^2} + \left[\frac{1}{r} + \frac{2\zeta r_o^2}{\omega_i r^3}\right]\frac{\partial u_r}{\partial r}$$

$$+ \left[\frac{(\omega_i^2 - f(f + \zeta r_o^2/r^2))k_z^2}{N^2}\right.$$

$$\left. - \frac{\omega_i^2 - 2\omega_i(f + \zeta r_o^2/r^2) + f(f + 3\zeta r_o^2/r^2)}{\omega_i^2 r^2}\right]u_r .$$

For $r >> N/(\omega_i k_z)$, this can be approximated as

$$\boxed{\frac{\partial^2 u_r}{\partial r^2} + \left[\frac{1}{r} + \frac{2\zeta r_o^2}{\omega_i r^2}\right]\frac{\partial u_r}{\partial r} + \left[\frac{(\omega_i^2 - f(f + \zeta r_o^2/r^2))k_z^2}{N^2}\right]u_r = 0} \quad \text{(A11)}$$

which becomes a modified Bessel equation

$$\frac{\partial^2 u_r}{\partial r^2} + \frac{1}{r}\frac{\partial u_r}{\partial r} + \left[\frac{(\omega_i^2 - f^2)k_z^2}{N^2}\right]u_r = 0$$

with trapped solutions $K_0(k_o r)$ where $k_o = k_z\sqrt{f^2 - \omega_i^2}/N$ as $r \to \infty$ for $\omega_i < f$.

A vortex-trapped near-inertial wave will have Bessel function solutions inside the core ($r < r_o$, $\omega_i > f_{eff}$) (A10) and distorted modified Bessel function solutions outside the core ($r > r_o$, $\omega_i < f$) (A11). Finding trapped radial modes involves matching the Eulerian frequency $\omega_E = K_1$, the vertical wavelength λ_z, the azimuthal mode number n, the radial velocity u_r, and the radial divergence $\partial(ru_r)/\partial r$ at $r = r_o$. Kunze *et al.* (1995) neglected terms involving $\zeta r_o^2/r^2$ in (A11) so that analytic solutions $J_0(k_r r)$ and $K_0(k_o r)$ could be matched. This was also done for the envelope of solutions displayed in Fig. 16 which correspond to the observed range of buoyancy frequency $N = (4–5) \times 10^{-3}$ s^{-1}, core radius r_o = 5–7 km, core vorticity $-0.52f$ to $-0.45f$, vertical wavelength λ_z = 170–220 m and Eulerian frequency $\omega_E = K_1$. Neglecting the straining terms $\zeta r_o^2/r^2$ in (A11) will have a slight effect on the inner radial wavelengths $2\pi/k_r$ and the outer radial decay lengths $2\pi/k_o$ but this has not yet been quantified.

Appendix B: Viscous Near-Inertial Waves

Consider the equations of motion for hydrostatic rectilinear internal waves of the form $\psi = \psi_0(r)\cdot\exp[i(k_x x + k_z z - \omega_i t)]$, where $\boldsymbol{k} = (k_x, 0, k_z)$ is the wavevector chosen so the horizontal direction of propagation lies along the x-axis ($k_y = 0$) and ω_i the intrinsic frequency damped by eddy viscosity ν_e and eddy diffusivity κ_e,

$$-i\omega_i u - fv = -ik_x p + \nu_e k_z^2 u$$

$$-i\omega_i v + fu = \nu_e k_z^2 v$$

$$0 = -ik_z p + b \qquad \Rightarrow \qquad \boxed{p = \frac{-ib}{k_z}} \quad \text{(B1)}$$

$$-i\omega_i b + N^2 w = \kappa_e k_z^2 b \quad \Rightarrow \quad \boxed{b = \frac{-iN^2 w}{(\omega_i - i\kappa_e k_z^2)}}$$

$$k_x u + k_z w = 0 \quad \Rightarrow \quad \boxed{w = \frac{-k_x u}{k_z}}$$

so that

$$[\omega_i - i\nu_e k_z^2]\cdot u - fv = \frac{N^2 k_x^2 \cdot u}{(\omega_i - i\kappa_e k_z^2)k_z^2}$$

$$-[i\omega_i + \nu_e k_z^2]\cdot v + fu = 0 \quad \Rightarrow \quad \boxed{v = \frac{-ifu}{(\omega_i - i\nu_e k_z^2)}} \tag{B2}$$

and the buoyancy is

$$\boxed{b = \frac{iN^2 k_x u}{(\omega_i - i\kappa_e k_z^2)k_z}} \; . \tag{B3}$$

Substituting the boxed expression for v in (B2) into the first expression in (B2) and assuming weakly-damped ($\nu_e k_z^2$, $\kappa_e k_z^2 << f$) near-inertial ($N^2 k_x^2 << f^2 k_z^2$) waves, the dispersion relation can be approximated by

$$\boxed{\omega_i = f + \frac{N^2 k_x^2}{2f k_z^2} + i\nu_e k_z^2} \; . \tag{B4}$$

The effect of viscosity appears as a weak evanescence in time (or in the direction of energy propagation $\boldsymbol{C_g}$). Within the context of this approximation, the eddy diffusivity has no impact on the dispersion relation because near-inertial waves have relatively weak buoyancy signals. More general viscous internal wave behavior can be found in LeBlond (1966). For $\nu_e = 10 \times 10^{-4}$ m^2 s^{-1} and λ_z = 100–300 m, $\nu_e k_z^2 = (0.4\text{–}4.0) \times 10^{-6}$ s^{-1} so is much smaller than the Coriolis frequency $f = 7.8 \times 10^{-5}$ s^{-1}. Substituting the dispersion relation (B4) into (B3) and (B2), we obtain the following consistency relations between the buoyancy b, north velocity v, and east velocity u:

$$b = \frac{N^2 k_x}{f k_z}\left[i - i\frac{N^2 k_x^2}{2f^2 k_z^2} + \frac{(\nu_e - \kappa_e)k_z^2}{f} \right]\cdot u$$

$$v = -i\left[1 - \frac{N^2 k_x^2}{2f^2 k_z^2}\right]\cdot u. \tag{B5}$$

The phase relations between uv, ub and vb are then

$$\phi_{uv} = \frac{\pi}{2}$$

$$\phi_{ub} = \text{Arctan}\left[\frac{2f^2 k_z^2 - N^2 k_x^2}{2f k_z^2 (\nu_e - \kappa_e)k_z^2}\right]$$

$$\simeq \text{Arctan}\left[\frac{f}{(\nu_e - \kappa_e)k_z^2}\right] \tag{B6}$$

$$\phi_{vb} = \text{Arctan}\left[\frac{-(\nu_e - \kappa_e)k_z^2}{f}\right],$$

so that the two horizontal velocity components remain 90° out of phase but the velocity and buoyancy perturbations have slightly modified phase relations if the eddy viscosity and diffusivity differ from zero and each other (eddy Prandtl number $\nu_e/\kappa_e \neq 1.0$). For an eddy viscosity $\nu_e = 10 \times 10^{-4}$ m^2 s^{-1} and λ_z = 100 m, the phase relations differ by at most 3° from their inviscid values. These are shown in Fig. 17 for Prandtl numbers ranging from zero to infinity.

Appendix C: Viscous Stratified Topographic Waves

Following Rhines (1970) and Appendices A and B, the equations of motion for stratified bottom-trapped topographic waves with eddy viscous ν_e and diffusive κ_e forcing on gentle slopes ($\alpha << 1$) are

$$-i(\omega - i\nu_e k_\perp^2)u_\parallel - fv = -ik_\parallel \, p + b\alpha$$

$$-i(\omega - i\nu_e k_\perp^2)v + fu_\parallel = -ik_y p$$

$$f\alpha v = -ik_\perp p + b \tag{C1}$$

$$-i(\omega - i\kappa_e k_\perp^2)b = -N^2 \alpha u_\parallel \quad \Rightarrow \quad \boxed{b = \frac{-iN^2 \alpha \cdot u_\parallel}{(\omega - i\kappa_e k_\perp^2)}}$$

$$k_\parallel u_\parallel + k_y v = 0 \quad \Rightarrow \quad \boxed{v = \frac{-k_\parallel u_\parallel}{k_y}} \; ,$$

where ($u_\parallel$, v) are the across- and along-isobath velocities parallel to the bottom, the flow normal to the bottom $w_\perp$ is assumed to vanish identically, and ($k_\parallel$, k_y, $k_\perp$) are the across-isobath, along-isobath and normal wavenumbers in a coordinate system lying in the plane of the bathymetry. It has been assumed that $k_\perp >> k_\parallel$, k_y in the viscous terms consistent with the observations. Substituting the boxed expressions for buoyancy b and along-isobath velocity v into the first three expressions of (C1),

$$\left[\frac{-i(\omega - i\nu_e k_\perp^2)}{k_\parallel} + \frac{f}{k_y} + \frac{iN^2\alpha^2}{(\omega - i\kappa_e k_\perp^2)k_\parallel}\right]u_\parallel = -ip$$

$$\left[\frac{i(\omega - i\nu_e k_\perp^2)k_\parallel}{k_y^2} + \frac{f}{k_y}\right]u_\parallel = -ip \tag{C2}$$

$$\left[\frac{-f\alpha k_\parallel}{k_y k_\perp} + \frac{iN^2\alpha}{(\omega - i\kappa_e k_\perp^2)k_\perp}\right]u_\parallel = -ip$$

or, equating the lefthand sides,

$$(\omega - i\nu_e k_\perp^2)(\omega - i\kappa_e k_\perp^2) = \frac{N^2\alpha^2 k_y^2}{k_H^2}$$

$$(\omega - i\nu_e k_\perp^2)(\omega - i\kappa_e k_\perp^2)k_\parallel k_\perp \qquad \text{(C3)}$$

$$- ifk_y k_\perp(\omega - i\kappa_e k_\perp^2) - N^2\alpha k_y^2 = 0,$$

which can be solved for ω and $k_\perp$ in terms of N, f, α, ν_e, κ_e, k_y and $k_\parallel$. Assuming that the frequency ω is changed only slightly so that it can be expressed in terms of the inviscid solution $\omega = N\alpha k_y/k_H + \delta\omega$, where $\delta\omega << N\alpha k_y/k_H$, the first equation in (C3) implies

$$\omega \simeq \frac{N\alpha k_y}{k_H} + \frac{i(\nu_e + \kappa_e)k_\perp^2}{2} \qquad \text{(C4)}$$

where $N\alpha k_y/k_H \simeq f >> \nu_e k_\perp^2$, $\kappa_e k_\perp^2$ from before. Substituting (C4) into the second equation in (C3) gives

$$\frac{N^2\alpha^2 k_y k_\parallel k_\perp}{k_H^2} - ifk_\perp\left(\frac{N\alpha k_y}{k_H} + \frac{i(\nu_e - \kappa_e)k_\perp^2}{2}\right) \qquad \text{(C5)}$$

$$- N^2\alpha k_y = 0$$

and, assuming a solution for $k_\perp$ perturbed about the inviscid solution

$$k_\perp = \frac{Nk_H^2}{N\alpha k_\parallel - ifk_H} = Nk_H^2\frac{N\alpha k_\parallel + ifk_H}{N^2\alpha^2 k_\parallel^2 + f^2 k_H^2}, \qquad \text{(C6)}$$

leads to a viscous perturbation

$$\delta k_\perp = \frac{N^2 f(\nu_e - \kappa_e)k_H^8}{2\alpha k_y(N\alpha k_\parallel - ifk_H)^4}. \qquad \text{(C7)}$$

This could blow up if $k_y = 0$, invalidating the small perturbation approximation. Based on the observational results of a diurnal Eulerian frequency $\omega_E = K_1$ and an imaginary vertical wavenumber at most comparable to the real vertical wavenumber, $k_z \simeq Re\{k_\perp\}$, we can quantify the relationship between buoyancy b and $u_\parallel$ in (C1)

$$b \simeq \frac{-iN^2\alpha u_\parallel}{f + \frac{i(\nu_e - \kappa_e)k_\perp^2}{2}} \simeq \frac{-N^2\alpha}{f}\left[\frac{(\nu_e - \kappa_e)k_z^2}{2f} + i\right]u_\parallel \qquad \text{(C8)}$$

so the phase relation between $u_\parallel$ and b becomes

$$\phi_{ub} = \text{Arctan}\left(\frac{2f}{(\nu_e - \kappa_e)k_z^2}\right) \qquad \text{(C9)}$$

perturbed from the inviscid solution by half the amount that viscous near-inertial waves are perturbed from their inviscid solution. We apply viscous phase relation offsets (B6) and (C9) to seamount- and vortex-trapped waves under the assumption that the geometry is not a major consideration.

Waves Trapped To Discrete Topography: Existence and Implications

D.S. Luther

School of Ocean and Earth Science and Technology, University of Hawaii, Honolulu, Hawaii

Abstract. The characteristics of observed energetic waves trapped to discrete topographic features, especially islands and mid-ocean ridge segments, are discussed. Resonant oscillations may occur due to closed propagation paths or zero group velocity along isobaths. The waves are forced directly by fluctuating winds, and may also be forced indirectly through the atmosphere's excitation of open ocean waves that subsequently impinge upon the topography. Evidence of energy leakage from one resonant island trapped wave to a resonant wave trapped to a neighboring island is reviewed. The potential importance of the poorly understood island and ridge trapped waves to teleconnections, mixing at the water-earth boundary, effluent dispersal, and general circulation simulations is noted.

Introduction

Perhaps the most important characteristic of the ocean's many types of free waves is their ability to propagate information about a disturbance from the region of forcing to an otherwise quiescent distant location. Waveguides, produced for example by topography at a coast (e.g., yielding refractive trapping to the coast), or by the reversal of sign of the vertical Coriolis parameter at the equator (equatorially-trapped waves), etc., enhance this characteristic by reducing the energy loss that would otherwise occur if the wave were to propagate in all directions indiscriminately. The wave is focused in a particular direction so that its energy density is not diminished by dispersal in multiple directions. For example, long period waves (periods greater than a day) trapped to continental coastlines are now well respected for their impact on currents and temperature fields far from the point of origin (e.g., *Brink*, 1991). Long period waves trapped to the equator play a variety of roles in the onset and maturation of climatically significant phenomena by propagating information about atmospheric changes across ocean basins (e.g., the El Niño phenomenon; *Philander*, 1990).

This note reviews some wave types whose existence has received minimal attention in the literature, and whose impact has been noted only briefly but could be substantial in both the teleconnection sense outlined above and the local sense of how strong the ocean's response will be to imposed forcing. The waves in question are those trapped to discrete topography, by which is meant topography of limited extent, though this concept will not be made precise for this review. Such topographic features as islands, seamounts, ridge segments and plateaus enable many kinds of free waves to exist that are trapped to the topography in a stratified ocean and therefore are guided to freely propagate in (usually) only one direction, i.e., along isobaths.

The reason the scale of the 'discrete' topography will not be defined rigorously is that some of the more interesting observations that have arisen lately are of waves trapped to a mid-ocean ridge segment, e.g., the Juan de Fuca Ridge. These waves raise the question of existence and propagation for long distances along the mid-ocean ridges. If a ridge-trapped wave were generated by a storm in the South Pacific Ocean could it propagate up to the equator along the East Pacific Rise? This paper will concentrate on discussing those observations of waves trapped to more discrete features, especially the Hawaiian Islands and the Juan de Fuca ridge segment. Waves trapped to seamounts, which have been found to reach amplitudes up to 40 cm/s (*Eriksen*, 1991), are treated by other authors in this volume.

There are now quite a few observations of narrowband (in frequency) wave motions that appear to be resonances of the oceanic fluid system in the presence of discrete topographic features. These resonant waves are the most easily identifiable members of the whole class of oscillations which can exist at discrete topography, but are just a small portion of this class. The resonance can occur because the wavelength of a particular wave neatly circumscribes the discrete topography in an integral number of wavelengths, or because the characteristic dispersion of the trapped oscillations admits a zero group velocity point in the (single) direction of propagation thus allowing energy to accumulate. Perhaps what is most remarkable about these resonances is their existence at all, and especially their existence as underdamped oscillations in the presence of highly irregular topography that intuitively would be expected to cause strong damping. As will be seen, the irregular topography of such features as mid-ocean ridges does not seem to inhibit the existence of resonances which necessarily have been studied with only the smoothest of ideal geometries.

The resonant oscillations are easy to study, and have been studied with datasets not specifically intended for that purpose, because their amplification at discrete fre-

quencies makes them identifiable in autospectra of oceanic variables taken at widely separated locations, and, because being narrow-band in frequency usually implies small wavenumber bandwidth, leading to relatively high horizontal coherence. Thus it is easier to describe these phenomena from a sparse array of instruments than it is to describe broad-band phenomena.

An important practical consequence of narrow-band resonance among trapped waves is that the resonant waves are reservoirs of energy well above what would be present at the topographic boundary due to ambient open ocean variability. Such reservoirs must have an impact on mixing at the boundaries, or on dispersal of the products of such mixing, especially since the trapped waves tend to have their largest amplitudes right at the boundary. If you subscribe to the idea that sub-thermocline mixing occurs at water-earth boundaries (*Gilbert and Garrett*, 1989), then at mid-depth levels (2000m - 3000 m) in the ocean you have to be concerned about what motions exist along the ~50,000 km of mid-ocean ridge crests. Irrespective of a role in global mixing, the resonant oscillations definitely play a role in the redistribution of anthropogenic and hydrothermal effluents (e.g., *Cannon et al.*, 1991), as will be clear from the following examples. It is also clear that non-linear advection can result in strong residual currents, as already demonstrated by observations (*Eriksen*, 1991) and numerical simulations (*Haidvogel et al.*, 1993) of resonant waves at seamounts.

Killworth (1989a) has emphasized the importance of topographic waves in extracting energy from coastal Kelvin waves (when the ridge intersects a coast). A logical extension of this idea is that ridge waves may be important sinks for open ocean Rossby wave energy. The implications for general circulation models which either don't have the horizontal resolution to resolve the various topographic wave modes or incorporate general Laplacian damping is that the shorter-scale topographic waves will be under-represented resulting in underdamping of the Kelvin or Rossby type motions.

On the following pages I will present examples of what appear to be resonant oscillations trapped to specific topographic features, including especially the Hawaiian Islands and the Juan de Fuca Ridge. The material presented is from both a review of the literature and ongoing research.

Considering that many topographic waves are physically distant from the sea surface and hence apparently isolated from the action of surface winds, investigation of how the waves are forced has led to some especially intriguing observations and speculations of new energy pathways or energy transfer mechanisms. Waves trapped to seamounts and ridges, for instance, that are evanescent upward still may be forced by atmospheric winds, either directly via the wind's establishment of forced oscillations that are evanescent downward from the surface but still intersect the topography (producing a "tunnelling" of energy from the surface to the topography),

Table 1. Examples of waves trapped to discrete topography

	Period	Characteristics	References
Ridge Segments			
Juan de Fuca Ridge (~46°N, 129°W)	4 days	baroclinic; trapped to ridge crest horizontally and vertically	*Thomson* (1989) *Chave et al.* (1989) *Cannon et al.* (1991) *Allen and Thomson* (1993)
Faroe-Iceland Ridge (~63°N, 10°W)	1.8 days	barotropic; trapped horizontally	*Miller et al.* (1995)
Banks, Plateaus, Seamounts			
Rockall Bank (~57°N, 14°W)	1 day	barotropic; trapped horizontally	*Huthnance* (1974)
Yermak Plateau (~82°N, 10°E)	1 day	barotropic; trapped horizontally	*Hunkins* (1986)
Fieberling Guyot (~32°N, 128°W)	1 day	baroclinic; bottom trapped; rectification observed	*Eriksen* (1991) *Noble et al.* (1994)
Islands			
Bermuda Is. (~32°N, 65°W)	10 hrs to 17 dys	baroclinic; Kelvin Wave analogue	*Wunsch* (1972a) *Hogg* (1980) *Eriksen* (1982)
Hawaiian Is. (~21°N, 157°W)	17 hrs to 5 dys	baroclinic; Kelvin Wave analogue	*Luther* (1985) *Lumpkin* (1995)
Kerguelen Is. (~49°S, 70°E)	1.5 dys	barotropic; shelf wave analogue	*Saint-Guily and Lamy* (1988)

or indirectly through generation of free barotropic waves which subsequently propagate into the region of a ridge. That the surface atmospheric fields do generate both evanescent and free barotropic waves at sub-inertial frequencies has been theoretically investigated (e.g., *Frankignoul and Müller*, 1979; *Müller and Frankignoul*, 1981) and observationally confirmed (e.g., *Luther et al.*, 1990; *Chave et al.*, 1992). The intermediary oscillation could transmit the atmosphere's effects over long distances before exciting the topographic waves, as may occur with surface gravity wave excitation of trapped waves around the Hawaiian Islands. Finally, resonances on neighboring topographic features may co-oscillate after one or the other resonance has been excited, as the trapped waves around the Hawaiian Islands demonstrate. Examples of some of these phenomena will be presented in the following pages.

Some Examples of Waves Trapped to Discrete Topography

Table 1 summarizes characteristics of some oscillations that have been observed at discrete topographic features. This is not an exhaustive list, but it will give a flavor of the growing number of observations of such waves, and will provide some information on their salient features. Note that seamount trapped waves are treated in detail by other authors in this volume, and so will not be discussed further here. In this section, observations of waves trapped to the Juan de Fuca Ridge and to the Hawaiian Islands will be explored.

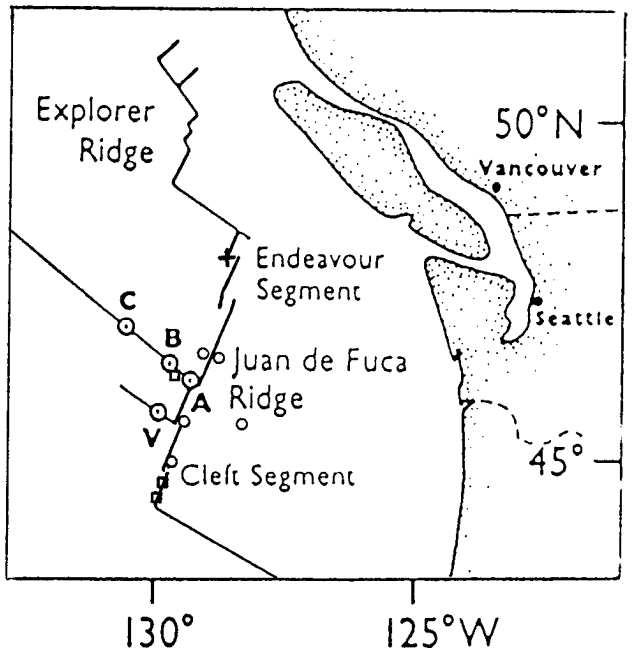


Figure 1. Line drawing of the Juan de Fuca Ridge and its segments. Three open squares show approximate locations of some of *Cannon et al.'s* (1991) moorings, including one between Axial and Brown Bear seamounts; the open circles indicate locations of five of *Chave et al.'s* instruments; and, the cross at the end of the Endeavor Segment locates the *Thomson* (1989) array. Circles with dots are seamounts: (A) Axial; (B) Brown Bear; (C) Cobb; and, (V) Vance. Figure modified from *Cannon et al.* (1991).

Ridge Waves

Cannon et al. (1991) describe several years of current and temperature observations from instruments moored at the southern end of the Juan de Fuca Ridge (JDFR) and at Axial Seamount in the middle of the ridge (Figures 1 & 2). Instruments near the ridge crest are dominated by a ~4-day oscillation that rotates predominantly clockwise (Figures 3 & 4). The oscillation is ubiquitous in all records in all years (Figure 4). The oscillation has maximum currents near the bottom in the rift valley. Near-bottom amplitudes are not uncommonly 10-15 cm/s (Figure 3). The currents decay upward and away (perpendicularly) from the ridge axis. Near the bottom the 4-day oscillation is more energetic than the

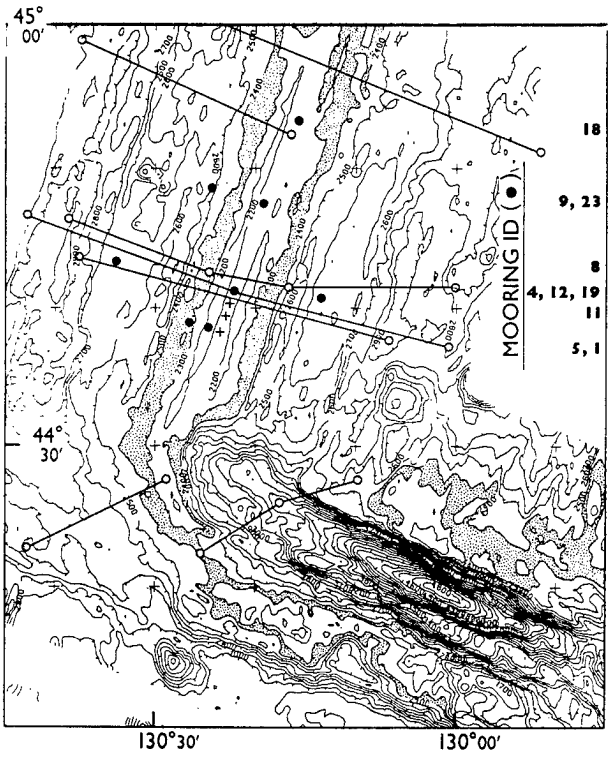


Figure 2. Chart of the southern end (the Cleft Segment) of the Juan de Fuca Ridge showing detailed locations of some of *Cannon et al.'s* (1991) moorings. Moorings are shown by solid circles with identification (ID) numbers on the right (4, 12, and 19 are at the same central location; 8 is on the west side; 11 is on the east side). Solid lines between open circles are conductivity-temperature-depth (CTD) sections. The contour interval is 100 m, and 2300-2400 m are stippled to better outline the ridge. Figure modified from *Cannon et al.* (1991).

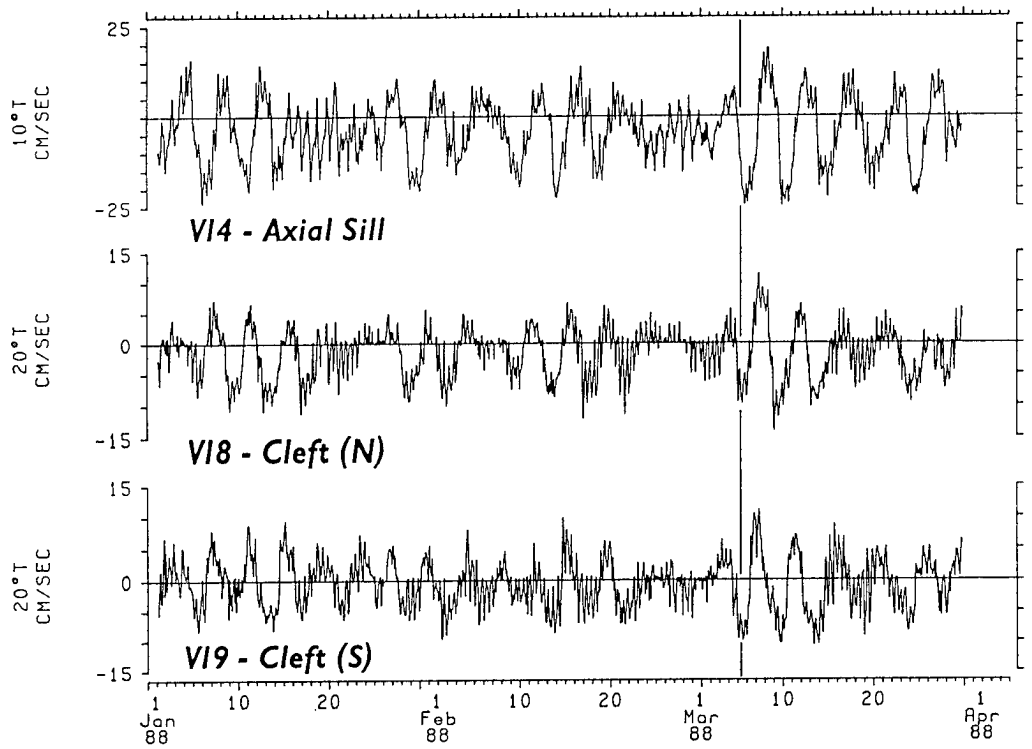


Figure 3. Currents (2.8-hour filtered) along 20° true in the rift valley of the Juan de Fuca Ridge (mooring 19, south; 18, north; see Figure 2) and across (10° true) the Axial-Brown Bear sill (Figure 1) for winter 1988, showing the 4-day signal dominating the tidal flows. Vertical line shows northward propagation of the 4-day oscillation. Figure taken from *Cannon et al.* (1991).

tides and inertial oscillations (Figure 4), but a few hundred meters off the bottom it is not. The oscillation is most energetic in winter suggesting direct atmospheric forcing, which is borne out by coherence between local wind stress and currents at mooring 19.

The oscillation is highly correlated along and across the ridge. *Cannon et al.'s* (1991) experiment extended about halfway along the JDFR (Figure 1) for a distance of approximately 150 km. Coherence phases among all the *Cannon et al.* (1991) moorings, irrespective of location across the ridge, indicate a northward phase propagation of 1-1.5 m/s. This phase speed range corresponds to a wavelength range of ~350-500 km that brackets the ~450 km length of the JDFR.

At the northern end of the JDFR, on the Endeavor Segment approximately 200 km north (Figure 1) of *Cannon et al's* (1991) most northerly instruments, *Thomson* (1989) and *Allen and Thomson* (1993) report observations of a 4-day oscillation with the same characteristics (such as clockwise polarization, amplification near the ridge crest, and vertical trapping) as reported by *Cannon et al.* (1991).

Chave et al. (1989) report observations of the 4-day oscillation in measurements of the horizontal electric field made on and near the JDFR. At periods greater than 1 day, the horizontal electric field is proportional to the vertically-averaged horizontal water velocity, an effect due to motional induction caused by the seawater moving through the earth's stationary magnetic field. The array of electrometers was able to detect clearly a decay of the oscillation away from the ridge axis, as well as the clockwise rotary character of the motion at the ridge. They also find a factor of 3 decay of energy along the ridge, from south to north, over ~150 km distance. This last observation is consistent with the energy levels reported by *Cannon et al.* (1991) compared with those shown by Allen and Thomson (1993). The *Chave et al.* (1989) results deviate from *Cannon et al's* (1991) in their estimation of a southward propagation speed for the wave on the eastern flank of the JDFR, whereas *Cannon et al.* (1991) report northward propagation on both sides of the crest.

The 4-day oscillation is certainly a type of stratified, topographic oscillation. *Allen and Thomson* (1993) have simulated many of the characteristics (e.g., clockwise polarization, bottom and ridge crest trapping) of the oscillation with a forced model under the assumption of no along-ridge variability. *Killworth* (1989a, 1989b) has performed the most complete analysis to date of the potential suite of free oscillations trapped to a ridge, but necessarily restricted his model to no more than two fluid layers to retain a certain amount of analytical trac-

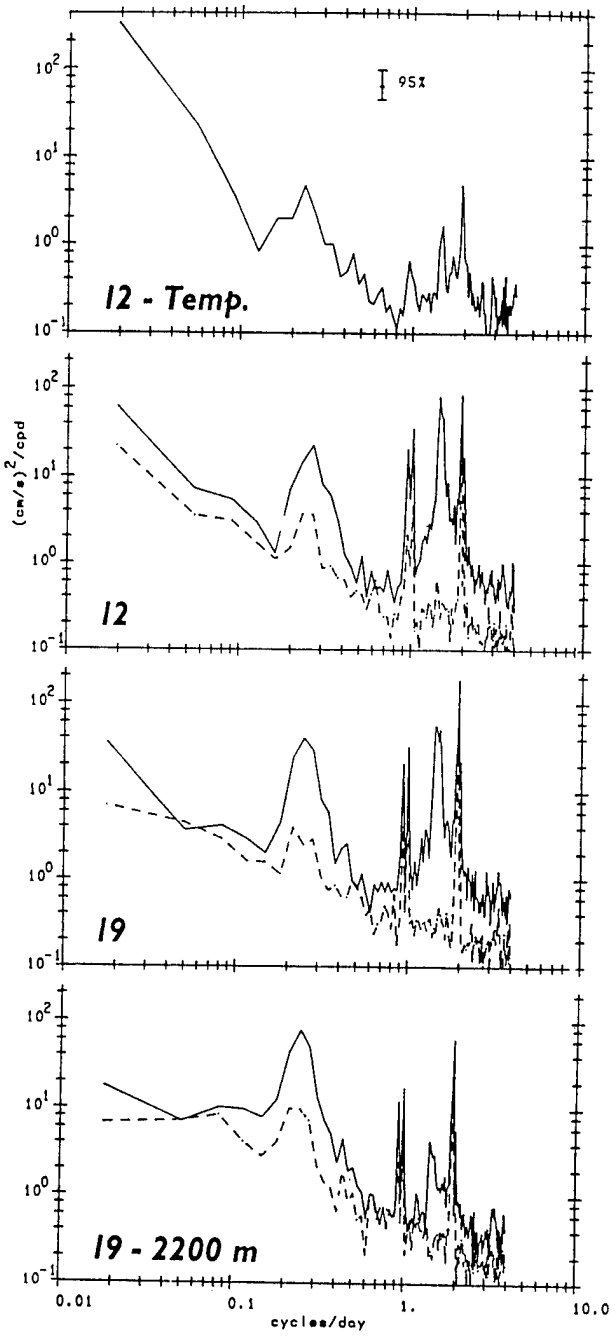


Figure 4. From top to bottom, auto-spectral densities for temperature at 2000 m at mooring 12, currents at 2000 m at mooring 12, currents at 2000 m at mooring 19, and near-bottom currents at 2200 m at mooring 19. Mooring 12 was deployed in 1986-1987, while mooring 19 was deployed in 1987-1988. For the currents, the solid curve is clockwise. Confidence limits of 95% are shown for 24 degrees of freedom. Figure taken from *Cannon et al.* (1991).

tability. Even so, *Killworth's* models provide enough information on wave structure and dispersion to speculate as to why the JDFR 4-day oscillation is resonant, and why there might be different phase propagation directions at different distances from the ridge.

Many of the solutions presented by Killworth have very asymmetric structures. That is, they have very large amplitudes only at the crest and on one side of the ridge, i.e., the side where the ridge crest is to the right of the direction of propagation (northern hemisphere case). One can then readily imagine that oscillations could propagate north along the west side of the JDFR and south along the east side. Reinforcement, that is resonance, occurs when the distance of a transit around the ridge equals an integral number of along-isobath wavelengths of the oscillation. The gravest mode (mode 1) would have a wavelength equal to twice the length of the JDFR. The second gravest resonant mode (mode 2) would have a wavelength equal to the length of the JDFR, and so on. *Cannon et al's* (1991) phase speed measurements could correspond to a mode 2 wave, while *Chave et al.'s* (1989) measurements suggest mode 1. (N.b., *Chave et al.* (1989) point out that their phase speed estimate is uncertain to about a factor of 2, so that their 3 m/s speed is not significantly different from *Cannon et al.'s* (1991) 1.5 m/s speed; *Chave et al.* (1989) definitely observe southward propagation.)

It is remarkable that such a resonance should occur along the JDFR in the presence of that ridge's highly irregular topography. Figures 1 & 2 only give a scant indication of the true complexity of the topography. Notice that the JDFR is not even a single continuous ridge, but has several discontinuities (offsets) along its length. As will be shown below, resonant waves exist trapped to, and propagating around, highly irregular island topo-geometries, as well.

An appealing way to reconcile the existence of a resonance with the complicated structure of the JDFR is to argue that, for a specific frequency and along-ridge wavenumber, zero group velocity along the ridge permits an accumulation of energy. In this case, one imagines the resonant character of the wave as being determined not by whether a complete circuit of the topography can be circumnavigated by the wave, but by the existence of a group velocity zero point on the frequency-wavenumber dispersion curves that permits local accumulation of energy at a particular frequency. Then every small segment of the JDFR can have its own zero group velocity point, and, since the cross-ridge profile of these segments is nearly the same, they could all have resonances at approximately the same frequency, and hence excitation of a resonance at one location could spread down the ridge.

The dispersion characteristics of the waves explored by *Killworth* (1989a, 1989b) have particular frequencies

and along-ridge wavenumbers where the along-ridge group velocities are zero, which would then permit the accumulation of energy, as for instance is the case for equatorially-trapped internal gravity waves (*Wunsch and Gill*, 1976). There would still be phase propagation, and given the structures calculated by *Killworth*, there could easily be two oscillations at the same ridge segment with exactly the same frequency and exactly the same along-ridge wavelength, but which have phase propagation in opposite directions and are therefore relatively isolated from each other because their amplitudes are strongest on opposite sides of the ridge. This scenario, then, could also explain the observations of northward propagation on the west side of the JDFR and southward propagation on the east side.

What is not explained by either scenario above is the apparent dominance of northward propagation at the top of the ridge in *Cannon et al.'s* (1991) observations. Of course, for the zero group velocity resonance, one could argue that the wave with northward phase propagation is stronger for some reason than the southward propagating wave.

The difference between the two scenarios of resonance above is more than an esoteric thought experiment. Whether energy propagates readily along the ridge directly relates to the major introductory point about whether the effects of forcing at one location on a mid-ocean ridge can travel far from the source. If the resonance on the JDFR is due to a wave propagating energy along the JDFR, then we can conclude that the substantial topographic irregularities do not impede propagation of these mesoscale waves along the ridge, hence we could expect to see disturbances propagate reasonably rapidly for thousands of kilometers along ridge crests. If, however, the resonance on the JDFR is due to zero group velocity, then the question of whether any ridge waves can propagate very far along a ridge is left unanswered, although diffusion of the energy of the resonance along the ridge is still possible through leakage to resonant waves on neighboring ridge segments.

Irrespective of this issue of whether or not the waves propagate energy along the ridges, the JDFR resonance demonstrates the existence of non-trivial ridge-trapped oscillations, which has a number of important local implications as outlined in the introduction.

Island-Trapped Waves (ITW)

Using sea level data, *Luther* (1985) showed that both sub-inertial and super-inertial waves are trapped to individual islands of the Hawaiian group. A few of the modes identified by *Luther* (1985) are indicated in sea level power spectra in Figure 5. That these oscillations can be associated with substantial current amplitudes is demonstrated in Figure 7. *Luther* (1985) established that the sub-inertial trapped oscillations were baroclinic,

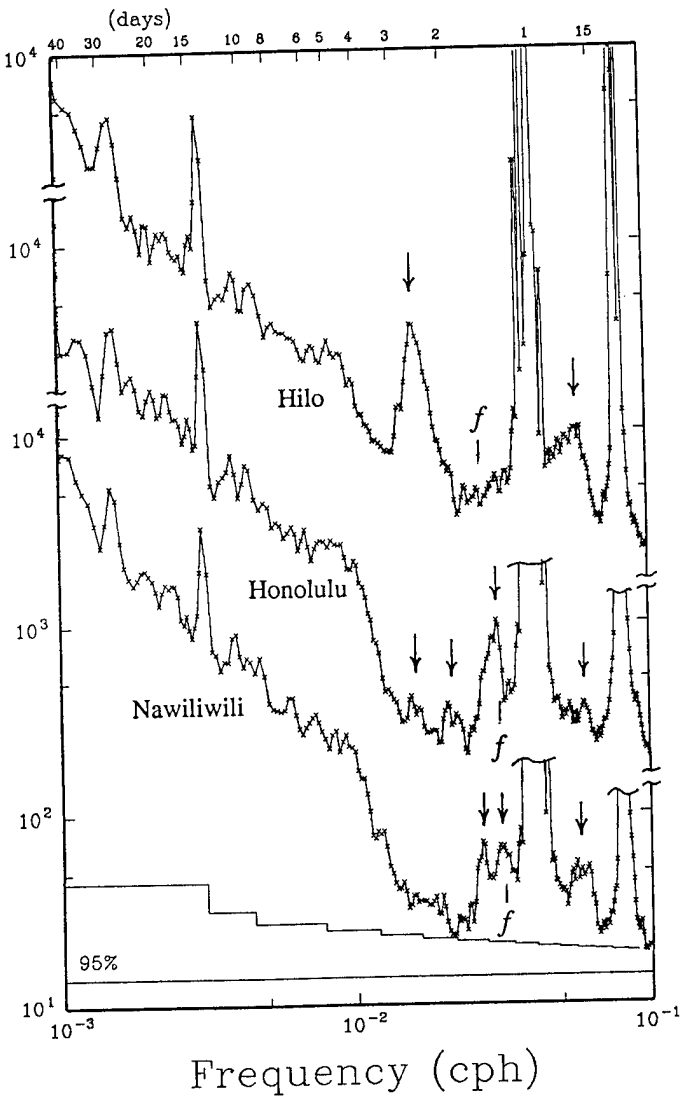


Figure 5. Energy density spectra of adjusted sea level (the isostatic effect of air pressure has been removed) from Hilo, Honolulu and Nawiliwili (see Figure 6 for locations), employing 24, 18 and 13 years of data, respectively. Suspected ITW are indicated with arrows. The inertial frequency for the mean latitude of each island is indicated with *f*. For ease of comparison, each spectrum is displaced from its neighbors by one decade along the ordinate. The diurnal and semi-diurnal tidal peaks in the Honolulu and Nawiliwili spectra have been clipped to simplify the figure. The fortnightly and monthly tides are clearly evident. The 95% confidence intervals at the bottom of the figure are exact for Nawiliwili but are slightly large for the other spectra. An increasing averaging bandwidth results in a decreasing confidence interval as frequency increases. The confidence intervals apply to each independent point. Every other point plotted is independent. The ordinate is in units of $(cm)^2/cph$.

Kelvin-like trapped waves as first described by *Wunsch* (1972a) at Bermuda. The dynamics of the super-inertial modes are still unknown.

The potential impact of ITW on horizontal dispersion near Hawaii is suggested by Figure 8; band-passed currents (integrated over time) are shown in four frequency bands, including the sub-inertial band encompassing the gravest ITW mode around the island of Hawaii. Assuming the integrated currents emulate the Lagrangian drift of fluid particles, trapped waves were responsible for advection over 6 km compared to 2 km for inertial, diurnal and semi-diurnal motions.

Since baroclinic modes other than the first have little sea level deflection (unless the higher modes are substantially more energetic than the first), *Luther* (1985) necessarily only found clear evidence for first baroclinic modes, with a hint of a couple of second baroclinic modes. At Oahu, for instance, power spectral peaks at 1.5 days and 2 days (Figure 5) correspond to peaks in coherence amplitude between sea level stations on opposite sides of the island (Figure 9). The coherence phase at these periods is not significantly different (at the 95% level) from what would be expected (~105°) for an azimuthal mode 1 wave propagating clockwise around the island as appropriate for Kelvin waves. *Luther* (1985) concluded that the 1.5 day oscillation was the 1st baroclinic, 1st azimuthal ITW mode for Oahu and that the 2 day oscillation was the 2nd baroclinic, 1st azimuthal mode.

At Bermuda, where sea level deflections of the modes are not at all robust (compare *Wunsch's*, 1972b, Figure 2 with Figure 5 here), *Hogg* (1980) observed modes as high as the 4th baroclinic in current meter data. For the island of Hawaii, the 4th baroclinic, 1st azimuthal mode would have a period of approximately 8 days, assuming the validity of the cylindrical model for computing the resonant periods. *Hogg* (1980) also speculated that strong coherence among current meter records at ~17 days may be due to an island or topographically trapped oscillation. This information is presented simply to indicate the potential range of periods for which trapped waves may provide a significant amount of the nearshore variability.

Figure 10 shows power spectra of azimuthal velocity taken from a mooring (C10 in Figure 6) near the island of Hawaii. A clear peak at 2.7 days period is seen at 54 m and 363 m. This is probably the 1st baroclinic, 1st azimuthal mode identified by *Luther* (1985) and seen in Figure 5 (top). At the deepest depth available (771 m), the 2.7-day peak is no longer evident, but a peak at 4.5 days is seen. Whether this longer period peak represents a higher baroclinic trapped mode(s) is the subject of current research. At the moment, the cause of the 4-5 day peak at 771 m in Figure 10 is suspected to be that, at this depth, the graver baroclinic/radial modes with smaller periods are relatively weaker than the higher baroclinic/radial modes with longer periods. Our intuition on this point comes from the results of *Brink*

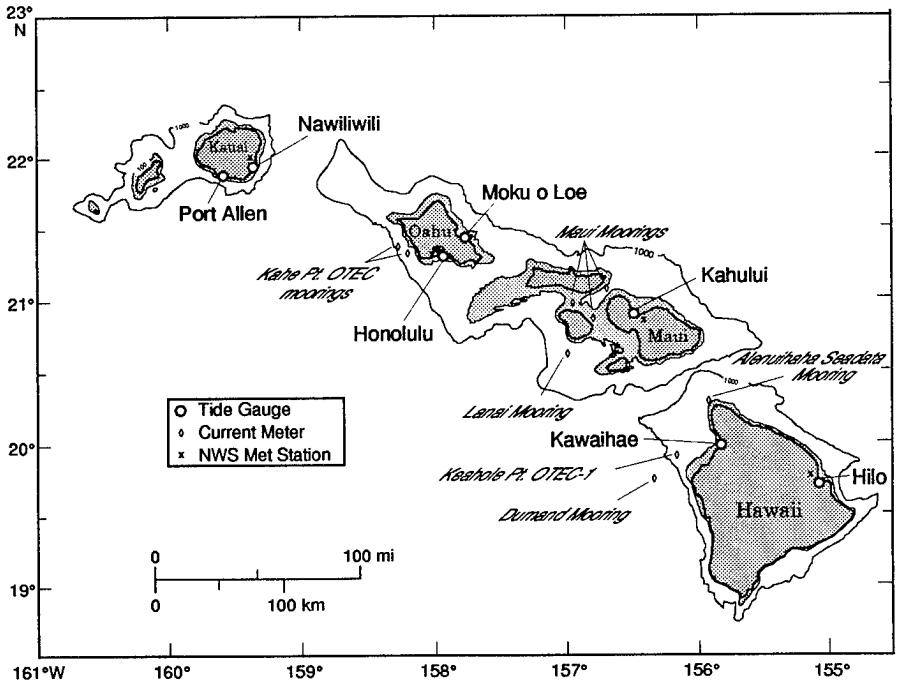


Figure 6. Map of the Hawaiian Islands showing locations of sea level and meteorological stations and current meter mooring sites, not all of which are mentioned in the text. Dark shading is land; light shading defines the 100 m isobath. The 1000 m isobath is also shown. Figure taken from *Lumpkin* (1995).

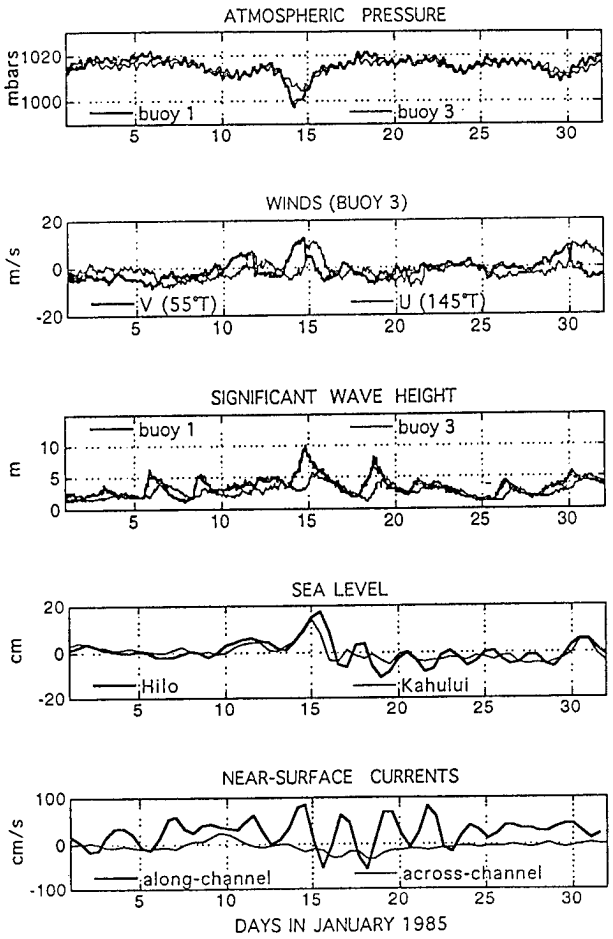


Figure 7. Sea level from Hilo and Kahului (neither adjusted for the isostatic effect of air pressure), and currents from the Alenuihaha Channel mooring (Figure 6), for a time period when the ITW mode around the island of Hawaii (~2.5 day period) was particularly strong. These data have been low-pass filtered to remove energetic tidal fluctuations. Also shown are atmospheric pressure, winds and significant wave height from two NOAA buoys to the west of the islands (~23°N, 162°W, and ~19°N, 161°W). Figure courtesy of M. Merrifield.

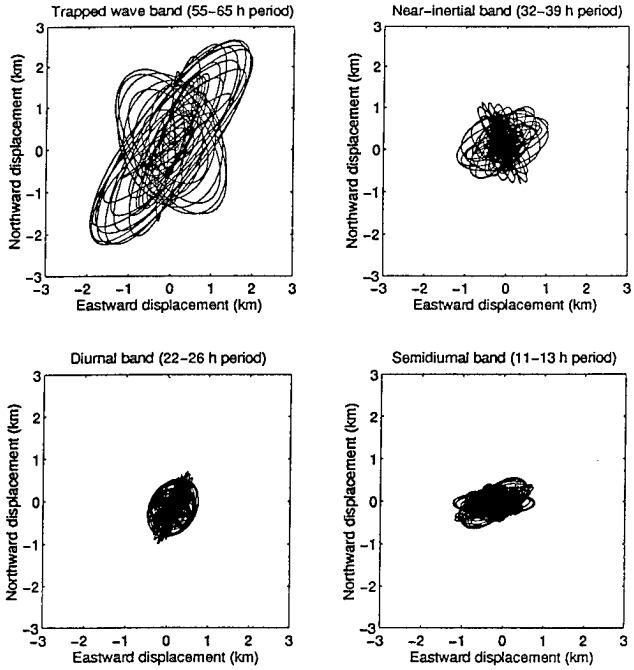


Figure 8. Progressive vector plots of the currents at 54 m at the Keahole Pt. OTEC-1 site, off the leeward coast of the island of Hawaii (Figure 6). Band-passing has isolated the motion at 55-65 h period (top left), 32-39 h period (top right), 22-26 h period (bottom left) and 11-13 h period (bottom right). The 55-65 h band encompasses the gravest ITW mode around the island of Hawaii. Figure taken from *Lumpkin* (1995).

(1989), whose calculations show that the higher baroclinic/radial, seamount-trapped modes occur at longer periods than the gravest modes and are more bottom trapped. [The term "baroclinic/radial" modes is now used to emphasize that with significant topography the classic definition of baroclinic modes is usually not valid. Higher modes have more nodes offshore than graver modes, but the nodes tend to be neither vertically nor horizontally oriented.]

Identification of as many normal modes as possible is an important tool for discriminating the dynamical appropriateness of models of variability around the islands, akin to the discrimination of earth structure models by the enumeration of normal modes of the earth (e.g., *Gilbert and Dziewonski*, 1975). For instance, *Hogg* (1980) showed how an ad hoc incorporation of a sloping bottom will significantly alter the expected equivalent depths for each baroclinic mode and thus alter the expected resonant mode periods.

One of the important results from *Luther* (1985) was the realization that good agreement between the observed periods of the first baroclinic sub-inertial ITWs and the theoretical periods of simple baroclinic Kelvin-like modes trapped to a cylindrical island (*Wunsch*, 1972a) could be achieved by matching the circumference of the real island (at the 20m isobath) to the circumference of the hypothetical cylindrical island. Previously (*Wunsch*, 1972a; *Hogg*, 1980), arbitrary idealized geometric figures (i.e., ellipses) were fit to the real island geometry and employed to estimate an effective cylindrical island radius. But, the cylindrical island is not expected to yield very useful predictions of higher baroclinic mode sub-inertial ITW frequencies (e.g., *Hogg*, 1980), which can also be deduced from the fact that the Burger number (the ratio of the internal Rossby radius of deformation to the radial scale of the topography) for the higher modes is relatively small. In other words, based on *Hogg's* (1980) work and *Brink's* (1989) study of seamount-trapped waves, it is certain that the dynamics of the ITW is non-trivially dependent upon topography, especially for the higher

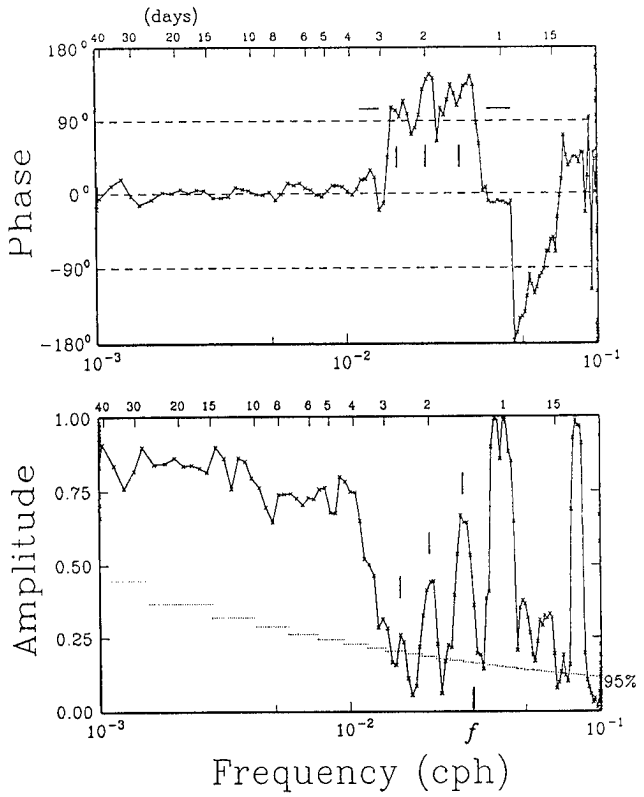


Figure 9. Coherence amplitude and phase between 8 years of adjusted sea level (isostatic effect of air pressure has been removed from the sea level) from Honolulu and Moku o Loe on the island of Oahu (Figure 6). High coherence amplitude is seen at the diurnal and semi-diurnal tidal frequencies. The high coherence amplitude with zero phase at periods greater than 3 days is due to open ocean barotropic oscillations. High coherence amplitude at 1.5 and 2 days is due to the 1st and 2nd baroclinic ITW modes around Oahu, respectively, both of which have auto-spectral peaks in Figure 5. The coherence phase at these periods is not significantly different from the −105° expected for an azimuthal mode 1 clockwise-propagating wave. A possible third baroclinic mode at about 2.7 days is also highlighted in this figure and Figure 5. The inertial frequency for the mean latitude of Oahu is indicated with *f*. The 95% level of no significance is indicated with a dotted line.

baroclinic/radial modes. However, given the success of mapping a real island to a cylindrical one, it is likely that a simple improvement of the model can yield reasonably good agreement with observations. That simple improvement is to include a radially-dependent, but azimuthally-invariant topography. The modal structures and frequencies can be obtained by resonance iteration, in a straight-forward adaptation of *Brink's* (1989) calculation of stratified-topographic, seamount-trapped waves. Brink has recently modified his code for this purpose.

The power spectra in Figure 5 clearly suggest the existence of narrow-band, super-inertial oscillations at frequencies between the diurnal and semi-diurnal tides at each of the islands. *Luther* (1985) concluded, on the basis of coherence between sea level stations (Honolulu and Moku o Loe) on opposite sides of Oahu, that the inter-tidal peaks at the Oahu stations were due to oscillations propagating around the island that were probably trapped. He suggested that *Wunsch's* (1972a) theory of pseudo-resonant trapped waves might explain the peaks, as it did for super-inertial peaks at Bermuda. *Wunsch* (1972a) studied the reflection of an internal plane wave from a cylindrical island and found that at certain frequencies nearshore amplification occurred; he called this amplification a pseudo-resonance since there is not a true trapping of the wave around the island, i.e., free internal gravity waves exist at all frequencies to carry the energy away from the island. *Lumpkin* (1995) has evaluated the full *Wunsch* (1972a) solution with parameters appropriate for the Hawaiian Islands and has found that, for any reasonable choice of baroclinic and azimuthal mode numbers (i.e., less than 25 for each), the pseudo-resonances always occur closer to the inertial frequency *f* than 1.25*f*, whereas the inter-tidal peaks in Figure 5 occur at approximately twice the inertial frequency (at about 17 hours period). [N.b., the phase lags found by *Luther*, 1985, suggest by Occam's razor an azimuthal mode number less than 4.]

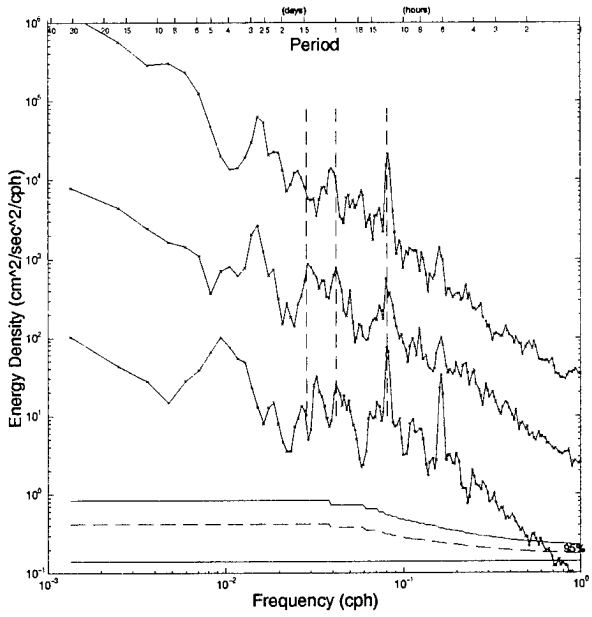


Figure 10. Azimuthal velocity spectra for 109-day long current records from the Keahole Pt. OTEC-1 site: 54 m (top), 363 m (middle) and 771 m (bottom). The 54 m (771 m) spectrum has been displaced up (down) one decade for viewing convenience. The sub-inertial peaks in the 54 m spectrum are at 2.8, 2.2 and 1.6 days period. Peaks in the 363 m spectrum are at 4.0, 2.8, 2.2 and 1.9 days period. The 771 m spectrum peaks at 4.4, 2.2 and 1.6 days period. The vertical dashed lines mark the inertial, diurnal and semi-diurnal periods. Figure taken from *Lu kin* (1995).

Furthermore, if it is assumed that the inter-tidal waves that are showing up in the sea level observations at each island have the same horizontal phase speed, it is hard to imagine how they could produce nearly the same resonant frequency at islands like Kauai and Hawaii whose circumferences differ by a factor of three. (The resonant frequencies of the sub-inertial trapped waves after all - *Wunsch*, 1972a - are directly related to island size.) With similar periods of the super-inertial modes at each island, the differing island sizes also seem to rule out a refractively-trapped explanation, as might occur due to the sloping topography around the islands. However, if the oscillation is baroclinic it is hard to imagine that the topography doesn't play a role.

A relationship has been sought between the frequencies of the inter-tidal oscillations and sum or difference frequencies of the prominent tidal and inertial frequencies. The inter-tidal oscillations have a strong seasonal dependence (e.g., Figure 11 and *Luther*, 1985) and so a connection with the tides is unlikely. Despite the seasonal dependence, no coherence with atmospheric variables has been detected. Interannual dependence of the wave's amplitude rules out a connection to the sub-inertial trapped waves, since the super-inertial waves are found to be stronger in years when the sub-inertial waves are weakest and vice versa (Figure 11).

For now, there are a couple of pieces of information suggesting a connection between the inter-tidal oscillations and near-inertial oscillations. First, the most prominent inter-tidal spectral peaks (at Hilo, Hawaii, and Nawiliwili, Kauai; Figure 5) are at approximately half the inertial period. Second, a comparison by Lumpkin (1995) of cotemporal sea level data from Hilo and Kawaihae on opposite sides of the island of Hawaii yields the startling result (Figure 12) that Kawaihae displays a strong near-inertial peak (and Hilo doesn't) while Hilo shows a strong $2f$ peak (and Kawaihae doesn't). Inter-tidal coherence between the two stations is high only at periods slightly longer than the Hilo peak. At Oahu at least, *Luther* (1985) showed that the inter-tidal auto-spectral peaks for stations on opposite sides of the island coincided with coherence amplitude

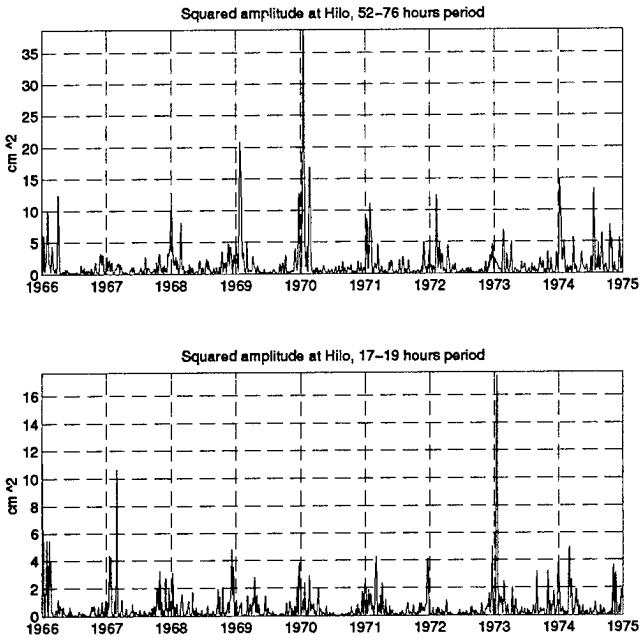


Figure 11. Variance of adjusted sea level from Hilo, 1966-1974, obtained from a complex demodulation using a 5-point Butterworth IIR filter with a cutoff frequency yielding the equivalent bandpasses of 52-76 h (top) & 17-19 h. Note the seasonal dependence (highest variance in winter) for both the sub-inertial and super-inertial motions, but note that they do not have the same interannual dependence of variance, and are therefore not likely to be dynamically linked to each other. Figure taken from *Lumpkin* (1995).

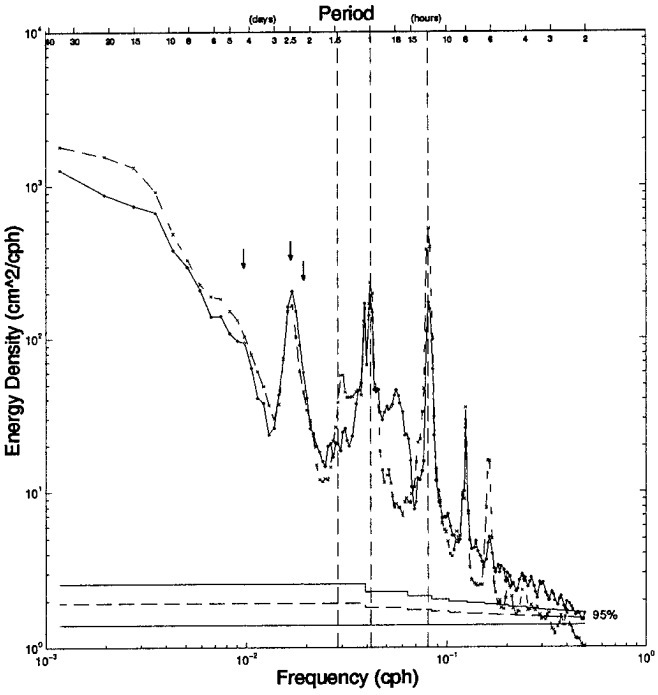


Figure 12. Adjusted sea level spectra for Hilo (solid) and Kawaihae, both on the island of Hawaii, for the same 3.5 year time period. The major tidal constituents have been analyzed and subtracted. Arrows indicate the theoretical periods of the first baroclinic, first azimuthal (center) and second baroclinic, first azimuthal (left) and second azimuthal (right) ITW modes. The vertical dashed lines mark the inertial, diurnal and semi-diurnal periods. Both spectra have an impressive sub-inertial peak centered at 2.5 days period, corresponding to the gravest ITW mode. The Kawaihae record has a near-inertial (super-inertial) peak at 1.4 days period which is not present at Hilo; an inter-tidal peak in the Hilo spectrum reaches its maximum at ~17.9 hours, but is not seen at Kawaihae. Figure from *Lumpkin* (1995).

peaks with significantly non-zero phase lags that indicated propagation around the island.

The present state of our knowledge of the dynamics of the narrow-band, super-inertial oscillations observed at the Hawaiian Islands is quite unsatisfactory. Furthermore, unlike the sub-inertial ITW which have been shown to be associated with significant currents, no such correspondence has yet been found for the super-inertial waves. They remain a curiosity, but whether they are more than that is not known.

Forcing Mechanisms

Ridge Waves

The generation of bottom trapped oscillations, such as the seamount trapped waves and the ridge waves discussed earlier, has been considered in some sense to be independent of the winds. For instance, regarding the forcing of seamount trapped waves, *Brink* (1990) has stated that it seems unlikely that such bottom-trapped features could be forced by surface wind stress effects. Rather, he suggests resonant excitation by ambient oceanic currents. Of course, this sidesteps the issue of what causes the "ambient oceanic currents." In fact, at periods from the inertial to 10 days in which the JDFR wave resonance occurs, the atmosphere readily forces oceanic currents (e.g., *Frankignoul and Müller*, 1979; Müller and Frankignoul, 1981) that are evanescent from the sea surface (at the shorter periods in this band) or barotropic free waves (at the longer periods). The evanescent oscillations tend to have large vertical decay scales so that they have non-negligible velocities at the seafloor. Therefore, the "ambient oceanic currents" needed to force waves trapped over bottom topographic features could be directly forced by the fluctuating winds (as opposed to being the result of mean current instability, for instance).

A potential flaw in this sequence of events is that the (barotropic or evanescent) currents forced by the fluctuating winds are not very energetic. *Luther et al.* (1991) and *Chave et al.* (1992) observed amplitudes of only O(1 cm/s) for barotropic currents directly forced by the atmosphere in the mid-latitude North Pacific. But this simply emphasizes one of our points, that is, the existence of free waves trapped to topography, especially if the dynamics impose a resonance, permits local near-topography enhancement of the initial forcing amplitude. *Chapman* (1989) and *Haidvogel et al.* (1993) find amplification factors up to O(100) times the strength of the incident barotropic current in analytical and numerical models of forcing of waves trapped to isolated topographic features.

Cannon et al. (1991) detected significant coherence between local wind stress and the 4-day oscillating currents over the southern JDFR. In conjunction with the winter-time enhancement of the energy in this band that they and *Allen and Thomson* (1993) report, direct atmospheric forcing of the JDFR waves appears certain.

Island-Trapped Waves

Direct forcing by the wind is clearly capable of exciting at least the gravest sub-inertial ITW. Figure 11 exhibits a seasonal cycle in the energy of the gravest ITW mode around the island of Hawaii, which characteristic is generally interpreted as resulting from direct forcing by the atmosphere (*Wunsch*, 1972a; *Hogg*, 1980). Furthermore, Figure 13 shows significant coherence amplitude between adjusted sea level and north wind stress at the period of the gravest ITW around the island of Hawaii. The phase associated with this high coherence rapidly changes nearly 180° at the ITW period as expected for a forced resonance. This type of evidence of excitation of resonant ITW modes was also found by *Hogg* (1980) at Bermuda.

The simplest model of the wind forcing is to consider a flat-topped, cylindrical island with an imposed

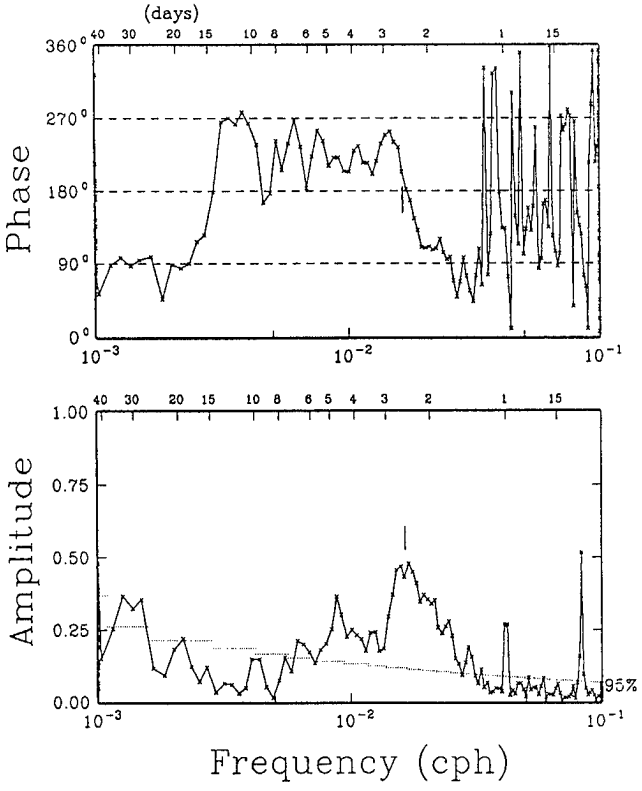


Figure 13. Coherence amplitude and phase between 24 years of adjusted sea level and north wind stress from Hilo. The period of the gravest sub-inertial ITW mode around the island of Hawaii is indicated by the short vertical lines in the amplitude and phase plots. Due to the highly significant coherence amplitude and the nearly 180° phase shift, the gravest ITW around Hawaii can be considered to be resonantly forced by the local wind field.

homogeneous, uni-directional, oscillating wind stress. Under these conditions it is easy to imagine that an azimuthal mode one ITW could be excited by the divergence of the wind-produced Ekman flux as it encounters the island. On one side of the island the horizontal flux divergence causes a set-down of the thermocline, and on the other side a set-up. Half a period later the set-down/set-up pattern is reversed, thus potentially reinforcing an azimuthal mode 1 wave that has propagated halfway round the island. The dynamics of this scenario has been qualitatively confirmed by *Lumpkin* (1995) with a simple analytical model that examines the model response as the forcing frequency varies. The normalized energy spectrum from this model is presented in Figure 14. The figure clearly displays the lower frequencies and shorter offshore decay scales of successively higher baroclinic modes. All the modes have an azimuthal wavenumber of 1, since the choice of forcing projects only onto that mode. Model parameters were chosen so that the maximum sea level energy density and frequency bandwidth of the gravest ITW mode matches the sea level spectrum at Hilo in Figure 5. With this choice of parameters, the second mode (at $\omega / f_0 = .35$) is a factor of 2 too energetic, while the energy of the mode 1 currents is actually underpredicted by a factor of 2 compared with the available moored current meter observations.

Insofar as the model is unable to match observed spectral energy levels or explain other significant characteristics of the observations, such as the sea level vs. wind stress coherence functions at specific locations around the islands, successively more sophisticated models need to be investigated, first incorporating radial topographic variations following *Brink's* (1990) analysis of forced seamount-trapped waves, then modelling the near-island amplification of the winds due to island orography, and so on. It is also probable that at times a temporally-confined model of the wind-forcing (see the wind data in Figure 5) is the appropriate paradigm for the forcing function. Azimuthal variations in the topography (Figure 6) are also likely to contribute to the specific character of the ITW modes around each island.

Despite the clear relationship between the gravest ITW mode around Hawaii Is. and the wind in Figure 13, *Luther* (1985) has already noted that it is easy to find time periods, including whole years, when the sea level signatures of the ITW around many of the islands are not significantly coherent with the local winds. *Luther* (1985) has postulated two additional mechanisms of ITW forcing to account for this. First, due to the narrowness of the inter-island channels, it is possible that significant energy in an ITW mode around one island will leak (scatter, if you prefer) to a neighboring island, exciting a co-oscillation of that island's ITW modes. *Lumpkin* (1995) found, using time-dependent coherence functions (Figure 15), a number of time periods which

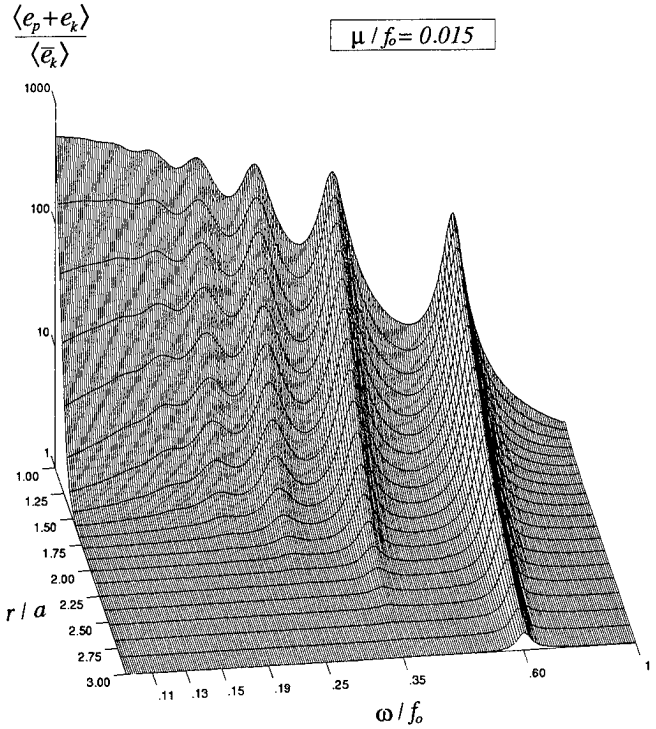


Figure 14. Total mean specific energy divided by mean background specific kinetic energy for the forced island-trapped wave model of Lumpkin (1995), with a dissipation time scale $\mu^{-1} = f_0 / 0.015$ (≈15.8 days). Frequencies from $\omega / f_0 = 0.1$ to $\omega / f_0 = 1$ (inertial) are shown; tick marks are at the inertial frequency and at the baroclinic eigenfrequencies. The energy ratio is given for radial distance r ranging from the island radius a to $3a$. Note that the trapping scale decreases for increasing baroclinic mode (decreasing frequency). Figure taken from *Lumpkin* (1995).

appear to clearly show such co-excitation of the Maui group's gravest ITW by Hawaii's gravest ITW, while also showing time periods when the gravest Hawaii Island ITW was strong and the Maui Island ITW was weak (e.g., winter of 1974), and vice versa (summer-fall of 1971). In both the latter cases, there is no coherence between the islands indicating that the individual islands do have separate resonances, although just why the leakage should not always occur is not immediately apparent. A multiple regression analysis of the Hilo and Kahului sea levels and local winds has confirmed that leakage from the island of Hawaii to Maui is more important than local wind forcing at Maui, although the latter does occur.

This is perhaps the first time such a co-oscillation phenomenon has been identified in the ocean. Quantification of this process, and the extent to which it occurs between other islands in the group is the subject of current research. This process may explain the existence of the 4-day oscillation all along the JDFR, despite the discontinuous nature of that ridge (Figure 1). That is, if the JDFR resonance is due to the excitation of waves that have zero along-ridge group velocity, the

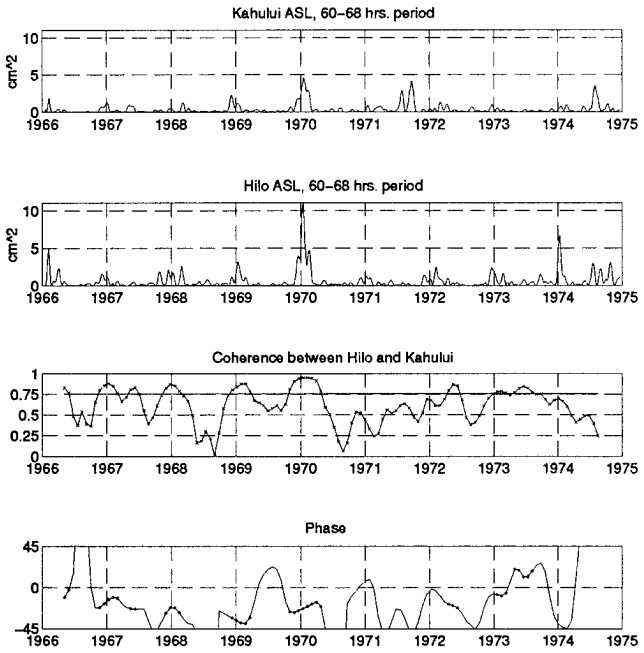


Figure 15. Bottom two frames, running coherence amplitude and phase between band-passed adjusted sea level records from Kahului and Hilo for the 2.5 to 2.83 days period band. The complex demodulated variance in this band for each station is presented in the top two frames. The coherence was calculated from the phase-bearing band-passed signals and not from the variance envelopes. The horizontal line at coherence amplitude 0.75 indicates the 95% confidence level. Figure from *Lumpkin* (1995).

similarity of the cross-ridge topographies for each small segment ensures that the resonant modes will all have the same frequencies. Then excitation of a resonant mode on one small ridge segment could result in co-oscillation of neighboring segments' resonant modes, and so on down the length of the JDFR. If one postulates a small amount of energy loss as this process occurs, the observation of south to north decay of energy in the 4-day oscillation discussed earlier could be explained.

Continuing in a speculative vane, as appropriate for this workshop presentation, note that *Luther* (1985) found a reasonable correspondence between the incidence of large tsunamis and ITW excitation at Hawaii. He postulated that the divergence of the radiation stress associated with a tsunami as it shoals would be sufficient to produce a substantial set-up/set-down profile of the thermocline (as well as of the sea surface), since the thermocline is relatively shallow and is relatively close to shore due to the steepness of the island topography. After the passage of the tsunami, when the stress divergence which maintained the thermocline set-up/set-down is gone, the thermocline profile will try to relax to its former position and this relaxation process should generate ITW. Such a sequence of events could also occur when large ocean swells hit the islands to produce the huge surf for which Hawaii is famous (note the significant wave height in Figure 7).

It is only in the last ten years that adequate time series of surface gravity wave energy have become available to permit a better testing of the gravity wave excitation mechanism. And there is certainly sufficient wind data now to be able to isolate those time periods when local wind forcing could not be responsible for the ITW generation. Investigations with these data are in progress. If the surface gravity wave forcing of ITW is found to actually occur it will represent a new addition to the suite of mechanisms by which the atmosphere generates internal motions in the ocean.

In summary, it is easy to imagine that at times a broad-scale oscillating wind (possibly rotating anticyclonically) is responsible for significant sub-inertial ITW excitation, while at other times short-lived storm events, or surface gravity wave set-up/set-down, contribute significantly to the wave excitation. And then at other times wave energy at one island may be due to leakage from ITW modes around a neighboring island.

Final Remarks

There is sufficient observational evidence to conclude that energetic, resonant, baroclinic oscillations exist trapped to islands and mid-ocean ridges. The lowest order dynamics of these waves is known, but significant details remain un-determined, such as the specific role of topography for the ITW and the cause of the resonance of the JDFR waves. For the super-inertial oscillations at the Hawaiian Islands, even the lowest order dynamics is not known.

Direct atmospheric forcing of both ITW and ridge waves has been demonstrated. The former is most likely via divergence of the Ekman transport as it impinges on the island, and the latter may involve a "tunnelling" of energy from the surface to the topography if the frequency-wavenumber characteristics of the forcing do not permit the generation of free open-ocean Rossby waves. Indirect atmospheric forcing is postulated for ridge waves through the intermediary of Rossby or Kelvin waves, and for ITW through the intermediary of surface gravity waves.

The existence of resonant ridge waves engenders the notion of a whole class of waves capable of propagating information long distances along the mid-ocean's ridges. Their extraction of energy from non-topographic Rossby or Kelvin waves may be a significant sink of energy that, for instance, is poorly modeled in GCM's.

Both the ITW and ridge waves imply the existence of enhanced current amplitudes in the immediate vicinity of the topography. This variability may be important to oceanic mixing by intensifying boundary layer shears or improving the efficiency of removal of boundary-mixed water. The waves must certainly enhance the dispersal

of anthropogenic effluents at islands and hydrothermal effluents at mid-ocean ridges. In addition, both wave types may result in substantial rectified flows.

The concept of energy leakage, or forcing of one resonant trapped oscillation by a resonant oscillation trapped to a neighboring topographic feature, has good support from the observations of ITW at the Hawaiian Islands, and may be responsible for the diffusion of energy down the JDFR. However, this problem has many non-intuitive aspects (e.g., *Jansons and Johnson*, 1988; Hendershott, this volume). Most importantly, energy propagation through, for instance, an array of seamounts may not necessarily proceed in the straightforward manner that previous discussions would suggest; that is, even if the seamounts have identical resonant frequencies, a resonance excited at one seamount need not spread equally to all the others, even if they are in close proximity.

Acknowledgments. This work benefited from discussions with R. Lumpkin, M. Merrifield and S. Allen. I am grateful to G. Cannon and R. Lumpkin for permitting the use of many of their figures.

References

Allen, S.E., and R.E. Thomson, 1993: Bottom-trapped subinertial motions over midocean ridges in a stratified rotating fluid, *J. Phys. Ocean.*, 23, 566-581.

Brink, K.H., 1989: The effect of stratification on seamount-trapped waves, *Deep-Sea Res.*, 36, 825-844

Brink, K.H., 1990: On the generation of seamount-trapped waves, *Deep-Sea Res.*, 37, 1569-1582.

Brink, K. H., 1991: Coastal-trapped waves and wind-driven currents over the continental shelf, *Ann. Rev. Fluid Mech.*, 23, 389-412

Cannon, G.A., D.J. Pashinski, and M.R. Lemon, 1991: Mid-depth flow near hydrothermal venting sites on the southern Juan de Fuca Ridge, *J. Geophys. Res.*, 96, 12,815-12,831.

Chapman, D.C., 1989: Enhanced subinertial diurnal tides over isolated topographic features, *Deep-Sea Res.*, 36, 815-824.

Chave, A.D., J.H. Filloux, D.S. Luther, L.K. Law, and A. White, 1989: Observations of motional electromagnetic fields during EMSLAB, *J. Geophys. Res.*, 94, 14,153-14,166.

Chave, A.D., D.S. Luther, and J.H. Filloux, 1992: The Barotropic Electromagnetic and Pressure Experiment, 1. Atmospherically-forced barotropic currents, *J. Geophys. Res.*, 97, 9565-9593.

Eriksen, C.C., 1982: An upper ocean moored current and density profiler applied to winter conditions near Bermuda, *J. Geophys. Res.*, 87, 7879-7902.

Eriksen, C.C., 1991: Observations of amplified flows atop a large seamount, *J. Geophys. Res.*, 96, 15,227-15,236.

Frankignoul, C., and P. Müller, 1979: Quasi-geostrophic responseof an infinite β-plane ocean to stochastic forcing by theatmosphere, *J. Phys. Ocean.*, 9, 105-127.

Gilbert, D. and C. Garrett, 1989: Implications for mixing of internal wave scattering off irregular topography. *J. Phys. Ocean.*, **19**, 1716-1729.

Gilbert, F and A.M. Dziewonski, 1975: An Application of normal mode theory to the retrieval of structural parameters and source mechanisms from seismic spectra, *Phil. Trans. Roy. Soc. Lond.*, A278, 187-269.

Haidvogel, D.B., A. Beckmann, D.C. Chapman, and R.-Q. Lin, 1993: Numerical simulation of flow around a tall isolated seamount. Part II: Resonant generation of trapped waves, *J. Phys. Ocean.*, 23, 2373-2391.

Hogg, N., 1980: Observations of internal Kelvin waves trapped round Bermnuda, *J. Phys. Ocean.*, 20, 1353-1376

Hunkins, K., 1986: Anomalous diurnal tidal currents on the Yermak Plateau, *J. Mar. Res.*, 44, 51-69.

Huthnance, J.M., 1974: On the diurnal tidal currents over Rockall Bank, *Deep-Sea Res.*, 21, 23-35.

Jansons, K.M., and E.R. Johnson, 1988: Topographic Rossby waves above a random array of seamountains, *J. Fluid Mech.*, 191, 373-388.

Killworth, P.D., 1989a: How much of a baroclinic coastal Kelvin wave gets over a ridge?, *J. Phys. Ocean.*, 19, 321-341.

Killworth, P.D., 1989b: Transmission of a two-layer coastal Kelvin wave over a ridge, *J. Phys. Ocean.*, 19, 1131-1148.

Lumpkin, R., 1995: Resonant coastal waves and superinertial oscillations, M.S. Thesis, U. Hawaii, Honolulu, HI, 106 pp.

Luther, D.S., 1985: Trapped waves around the Hawaiian Islands, Proceedings of the 3rd Hawaiian Winter Workshop, L. Magaard (ed.), U. of Hawaii, Honolulu, HI, pp. 261-301.

Luther, D.S., Chave, A.D., J.H. Filloux, and P.F. Spain, 1990: Evidence for local and nonlocal barotropic responses to atmospheric forcing during BEMPEX, *Geophys. Res. Lett.*, 17, 949-952.

Luther, D.S., Filloux, J.H., and A.D. Chave, 1991: Low-frequency, motionally induced electromagnetic fields in the ocean: 2, Electric field and Eulerian current comparison, *J. Geophys. Res.*, 96, 12,797-12,814.

Miller, A.J., P.F.J.G. Lermusiaux, and P.-M. Poulain, 1995: A 1.8-day topographic Rossby mode resonance trapped to the Iceland-Faroe Ridge, *Proc. 10th Conf. Atmos. Oc. Waves and Stability*, Big Sky, Montana, 5-9 June, 1995.

Müller, P., and C. Frankignoul, 1981: Direct atmospheric forcing of geostrophic eddies, *J. Phys. Ocean.*, 11, 287-308.

Noble, M.A., K.H. Brink, and C.C. Eriksen, 1994: Diurnal-period currents trapped above Fieberling Guyot: observed characteristics and model comparisons, *Deep-Sea Res.*, 41, 643-658.

Philander, S.G., 1990: *El Niño, La Niña, and the Southern Oscillation*, Academic Press, New York, 289 pp.

Saint-Guily, B., and A. Lamy, 1988: Waves trapped by the Kerguelen Island escarpement, *C. R. Acad. Sci. Paris*, 307, II, 573-578.

Thomson, R., 1989: Effects of topography and buoyant plumes on near-bottom currents over a mid-ocean ridge, *IEEE Oceans '89: The Global Ocean*, 1, 73-76.

Wunsch, C., 1972a: The spectrum from two years to two minutes of temperature fluctuations in the main thermocline at Bermuda, *Deep-Sea Res.*, 19, 577-593.

Wunsch, C., 1972b: Bermuda sea level in relation to tides, weather and baroclinic fluctuations, *Rev. Geophys. Sp. Phys.*, 10, 1-49.

Wunsch, C., and A.E. Gill, 1976: Observations of equatorially trapped waves in Pacific sea level variations, *Deep-Sea Res.*, 23, 371-390.

Numerical Modeling of Time-Mean Flow at Isolated Seamounts

A. Beckmann

Alfred-Wegener-Institute for Polar and Marine Research, Bremerhaven, F.R.Germany

Abstract. A numerical σ-coordinate ocean circulation model is used to investigate the strength and spatial structure of rectified flow at the flanks of a tall and steep isolated seamount. This study is closely related to and motivated by the studies of flow around Fieberling Guyot in the northeast Pacific; however, an idealized form of the topography, both smooth and with irregularities, is prescribed. A series of experiments with varying resolution and geometrical/environmental parameters is analyzed for mean flow generation. A regime is found where the presence of the rectified flow influences the wave amplification. The efficiency of the rectification mechanism is quantified for a wide range in parameter space. The along-isobath flow is generally bottom intensified, with its maximum very close to the seamount's summit. Finally, the model results are briefly compared to simple theoretical concepts for parametrization of flow-topography interaction effects.

Introduction

Isolated submarine topography is known to be the source of mesoscale variability in the ocean and therefore of great importance for the local and regional environment. Time-dependent forcing will generate transient density perturbations and flow intensifications at the seamount which propagate in form of "seamount trapped waves" clockwise (on the northern hemisphere) along closed depth contours. In particular, periodic forcing is capable of producing a strong wave response by resonant amplification. In addition to these time-variable phenomena, steady solutions of flow around isolated seamounts exist: both are due to the steady part of the forcing (uniform far field "climatological" flow) and to the nonlinear rectification processes at the seamount itself.

There is a large body of literature on the influence of such isolated topography on the circulation in the ocean and atmosphere. Hogg (1980) gives a comprehensive overview of early theoretical studies. Recent observations (Eriksen, 1991; Brink, 1995), advanced analytical treatment of quasigeostrophic flow past obstacles (Fennel and Schmidt, 1991), and laboratory realizations of stratified seamount trapped waves (Codiga, 1993) are evidence for continued and even increased interest.

The purpose of numerical modeling is to extend these prior studies to more realistic (fully non-linear) regimes. Progress with primitive equation modeling of steep and tall topography was made only very recently (Chapman and Haidvogel, 1992, 1993; Haidvogel et al., 1993). In idealized configurations smooth, symmetric seamounts in a fluid with linear or exponential stratification and forced by steady or diurnally varying barotropic ambient flow are studied.

In an attempt to prepare us for models featuring real bathymetry, some of the following questions will be addressed:

- — the role of resolution;
- — the role of individual processes (nonlinearity, stratification); and
- — the role of topographic scale changes and irregularities.

Finally, the implications for parametrization of the mean flow rectification will be considered briefly.

The Spatial Structure of Trapped Flow at Seamounts

Seamount Trapped Waves

Theoretically, an infinite set of trapped waves exists at isolated seamounts, at discrete sub-inertial frequencies and azimuthal wavenumbers (Brink, 1989). In practice, only the gravest modes have been observed in reality and found in numerical models. The linear waves have one up- and one down-welling lobe; most of the flow crosses the seamount's summit and returns at the flanks (see Brink, 1989). These waves were found to occur broadly in parameter space, both as a function of stratification and forcing frequency (Haidvogel et al., 1993). Trapped waves of near-diurnal frequency are of particular interest, because the forcing at the tidal periods K_1 and O_1 are dominant in many parts of the open ocean.

In previous studies on the influence of stratification, the Burger number

$$S^* = \frac{NH}{fR} \tag{1a}$$

has been used as a combined measure of stratification and rotation, where N is a vertical average Brunt-Väisälä frequency, H the maximum water depth, f the Coriolis parameter and R the horizontal scale of the seamount.

Acknowledging that seamount trapped waves are in most cases limited to the upper flanks of the topography, the choice of N and H as representative of the whole water column seems inappropriate. Consequently, for this study the Burger number was defined as the first internal Rossby radius of deformation r_D at the seamount's summit relative to the seamount radius R,

$$S = \frac{r_D}{R}, \qquad (1b)$$

thus representing an integral measure of the stratification at the location of the maximum of the seamount trapped wave. We will look at values of S of order 1. For comparison, the Burger number range in the Haidvogel et al. (1993) study is $S = 0$ to 0.2.

Time-Mean Flow

The time-mean flow at isolated seamounts can reach O(10 cm s^{-1}) (e.g., Brink, 1995 at Fieberling Guyot), about 50% of the observed wave amplitude. This mean flow is thought to be the result of non-linear momentum and density advection of the seamount trapped wave. The strength of the mean circulation depends first and foremost on the amplitude of the generating wave, which in turn is a function of the environmental parameters (like stratification, rotation, forcing). The rectification efficiency (defined as mean flow amplitude relative to wave amplitude) found in numerical models (see Haidvogel et al., 1993) is a few tens of %, even at maximum resonance.

The dynamical balance for the dominant azimuthal component of the mean flow consists of radially inward (upslope) directed horizontal eddy fluxes of momentum, compensated by radially outward (downslope) mean advection. Correspondingly, the net inward mean transport of heat is balanced by outward eddy heat fluxes. This leads to a cap of dense water on top of the seamounts.

The time-mean secondary circulation is directed clockwise around the mean flow, featuring downwelling in the center of the vortex.

Although substantial mean flows were found in previous idealized models of flow around seamounts, effects of the presence of the mean flow on the wave propagation and/or resonance were not observed: the rectified flow seemed to be linearly superimposed on the propagating wave.

A Model of Flow at Fieberling Guyot

Preliminary results are available from a high resolution simulation of the response to tidal forcing of the stratified, non-linear ocean at Fieberling Guyot (Beckmann and Haidvogel, 1994). Their numerical model is a variant of the semi-spectral primitive equation model SPEM (Haidvogel et al., 1991) with a terrain-following vertical ("sigma") coordinate and a spectral approach in the vertical.

The experimental configuration is very similar to the idealized studies of Haidvogel et al. (1993): the computational domain is a periodic f-plane channel. The horizontal grid is "stretched," focussing on the seamount; the grid spacing is less than 1000 m in the seamount vicinity. The topography was derived from a high resolution data set and linearly interpolated to the numerical grid. No further smoothing of the bottom relief was applied.

The model is initialized with an exponential background stratification (fitted to measurements in the vicinity of Fieberling Guyot) and driven by a diurnal period barotropic current. The 1 cm s^{-1} amplitude and north-south orientation of the forcing are idealizations made from observations (Brink, 1995). A weak biharmonic lateral viscosity/diffusivity of 10^7 m^4 s^{-1}, linear bottom friction of $3 \cdot 10^{-4}$ m s^{-1} and a bottom-intensified vertical viscosity are used.

The model is spun up for 25 days before the model fields are averaged over one wave period. Both the instantaneous and the time-mean flow fields show several of the observed characteristics: A trapped wave of 12.6 cm s^{-1} amplitude is generated, setting up an anticyclonic time-mean flow at the upper flanks of the seamount of 6.2 cm s^{-1} (rectification efficiency of about 50%). The depth dependent vertical viscosity was found to improve the vertical structure of the simulated mean flow. Other characteristic properties of the model results compare less favorably with the observations. The vertical phase gradients and the secondary circulation of the mean flow are not yet reproduced realistically. More detailed analyses of these and future model results will be published in a forthcoming paper.

A comparison run with a smooth Gaussian fit to the topography give slightly smaller values of wave and mean flow. This is a first indication that topographic irregularities can alter the wave and mean flow response; it is unclear, though, whether this happens for purely geometric reasons (large scale asymmetries; locally steeper slopes) or by the presence of an additional rectification mechanism (form stress, see Haidvogel and Brink, 1986; Holloway et al., 1989) on these smaller scales.

This simulation with realistic topography represents a major step beyond previous idealized studies and it is far from straightforward to interpret the results. The runs differ in various respects: The forcing amplitude is larger by a factor of 5, and we expect both larger absolute values of wave-related currents and a more intense mean flow. At the same time, the higher horizontal resolution (by a factor of 8) and the correspondingly smaller values of diffusivity/viscosity (by a factor of 2/100) might also increase the response of the waves. The more realistic (i.e., generally stronger) stratification will have an

influence on the vertical decay scale of the trapped response.

The real geometry is characterized by a smaller radius and steeper flanks than used in previous studies; their effects on wave amplification and mean flow generation has not been investigated. The geometric and environmental situation yields a Burger number regime that has never before been explored and simple extrapolations into this parameter range are not very well justified. Finally, the asymmetries of the real seamount and the background bottom roughness on various scales may contribute in various ways: Both a net damping effect on the waves and an enhancement of the mean flow via the form stress mechanism seem plausible.

Parameter Studies

In this section we try to answer the question "Which factors contribute in what way to the generation of mean flow at real seamounts?" In order to investigate these issues, a series of some 60 experiments were carried out, exploring the sensitivity to various environmental and geometrical seamount properties.

The Model Configuration

The model used here is the latest version of the terrain-following sigma coordinate model SPEM (Haidvogel et al. 1991), which is formulated with finite differences on a staggered vertical grid. The model employs a fourth order algorithm (McCalpin, 1994) to reduce the spurious flow generated by the truncation errors of the pressure gradient terms. Models of this type have now been repeatedly and successfully applied in configurations with large variations in depth (Chapman and Haidvogel, 1992, 1993; Haidvogel et al., 1993; Beckmann and Haidvogel, 1994).

The basic shape of the seamount was chosen to accommodate several features of real seamounts, which are found to be tall and steep, and relatively flat on top. In particular, the seamount was not assumed Gaussian, but rather of a tanh-shape. As a consequence, the diameter and the slope can be prescribed separately. The functional form is

$$H = H_o + \Delta H \tanh((r - R_o)/R) \qquad (2)$$

with

$H_o = 2500$ m
$\Delta H = 2000$ m
$R_o = 20000$ m
$R = 8000$ m

The resulting maximum slope $(\nabla H)|_{max} = 25$ % is close to observed gradients.

This seamount was placed in the center of the periodic channel domain of 256 × 256 km. To account for the expected bottom trapped nature of both the seamount trapped wave and the mean flow, the vertical grid is stretched quadratically towards the bottom, as depicted in Figure 1. In comparison to an equidistant discretization this improves the resolution at the lower boundary of the model dramatically: the minimum grid spacing is 3.5 m at the top of the seamount and 35 m in the deep ocean; the maximum grid spacing just below the surface varies between 80 and 800 m. The horizontal resolution was chosen to be 2 km uniformly across the model domain; the Coriolis parameter of $f_o = 1.03 \cdot 10^{-4}$ s^{-1} corresponds to 45°N.

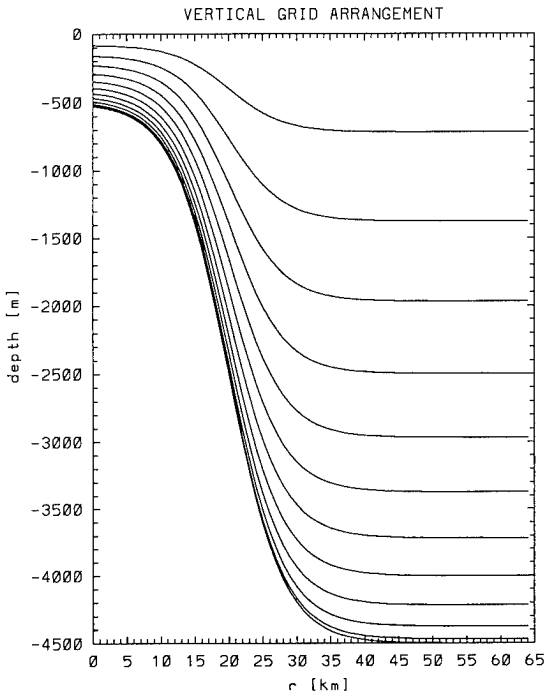


Figure 1. Coordinate lines form the quadratically stretched vertical grid as a function of radial distance from the seamount's center.

An exponential initial stratification of realistic strength was prescribed as

$$\rho = 28.0 - 2.5 \cdot e^{-(z/1000\,\mathrm{m})} \qquad (3)$$

with a corresponding Rossby radius of 9 km over the seamount's summit and 36 km in deep water, typical for mid-latitudes in the North Pacific. The Burger number for this experiment is

$$S = \frac{r_D}{R} = 0.5 \qquad (4)$$

(for comparison, $S^* = 11$).

Similar to previous idealized studies, the model is forced with diurnal barotropic tidal forcing of the form

$$u_f = U_o \tanh(t/3T)\sin(2\pi t/T) \quad (5)$$

with $U_o = 1$ cm s^{-1} and $T = 1$ day.

The viscous and diffusive terms are of particular importance for the amplification and rectification process. A standard linear bottom friction of $r_b = 3\cdot10^{-4}$ m s^{-1} was chosen in addition to a weak background biharmonic lateral viscosity/diffusivity $\nu_{uv} = \nu_\rho = 10$ ˘ m ˜s ‘. The experiments were run for 20 days with a time step of 43.2 s; the last day was averaged to obtain the time-mean fields.

The Central Experiment

The central experiment serves as the standard solution and is used to illustrate the spatial structure of the wave and the mean flow. Table 1 lists the maximum point-wise velocities for the central experiment and, for comparison, identical experiments with linearized dynamics or homogeneous fluid.

Table 1. Maximum point-wise velocities for the central experiment and two additional runs with different physics.

	central reference	linearized dynamics	homogeneous fluid
total			
$\bar{v}_{WAVE}$	55.61	28.87	-
$\bar{v}_{MEAN}$	31.37	0.35	-
ratio	56%	1.2%	-
barotropic			
$\bar{v}_{WAVE}$	4.73	4.67	14.61
$\bar{v}_{MEAN}$	1.68	0.06	0.90
ratio	36%	1.2%	6%

The wave and mean flow amplitudes are quite large, and although wave amplifications of O(50) have been reported before, a mean flow of this strength has not been found in previous numerical models. It is interesting to note that the barotropic part is only a small fraction (9 and 6 %) of the wave and mean flow fields, respectively.

Figure 2 shows a snapshot of the density perturbation at various depths. At the upper flanks of the seamount (600 and 700 m) the first azimuthal mode seamount trapped wave is clearly visible. Right above the seamount's summit the additional cap of denser water dominates the density perturbation. The highly bottom trapped nature of both the wave and the mean flow becomes clear at the 400 m level, where only a weak indication of the wave is visible.

The mean flow in Figure 3 shows a similar structure as found in Haidvogel et al. (1993), but with much more pronounced bottom trapping. The mean flow is along isobaths for the most part, but even the secondary circulation in the radial-vertical plane is quite substantial: a radially outward current of up to 7 cm s^{-1} at the bottom returns in a thin layer of fluid above. The circulation is closed by downwelling in the center of the seamount of up to 100 m/day and a somewhat weaker upwelling motion above the upper flanks.

Unlike in the studies by Haidvogel et al. (1993), where the wave amplitude differed only insignificantly between linearized and non-linear dynamics (cf. their experiments 1B and 3B), the rectification process is strong enough to have a significant feed-back on the wave. This can be deduced from the wave amplitude of the linearized experiment, which is smaller by a factor of 2. There is a significant amount of vorticity ς in the time-mean Taylor cap, exceeding $-f$ at the top. We are in a regime where the existing mean flow reduces the ambient vorticity $f + \varsigma$ for the wave in a shallow layer above the seamount and thereby leads to an increased wave response.

The weak residual time-mean flow for the linearized dynamics can be attributed to the weak remaining trend in the forcing and the remnants of transients from the initialization process.

Finally, it should be noted that removing the stratification results in much weaker point-wise velocities; the barotropic response, however, is enhanced.

Resolution Dependence

The issue of horizontal resolution and its influence on the modeling of seamount trapped waves was previously investigated in a more technical paper by Beckmann and Haidvogel (1993). It is obvious that the spatial scales set by the seamount need to be resolved properly, but how stringent are these constraints?

The combination of the terrain-following model concept and the stretched vertical coordinate gives an exceptionally good vertical resolution of the wave and mean flow fields. It is unknown, however, how much horizontal resolution is needed for convergence of the solution and whether there is significant degradation of the result for less resolution. For this reason, a first series of experiments varies the horizontal resolution without changing any other model parameter: identical dissipation and time step are used for all five experiments.

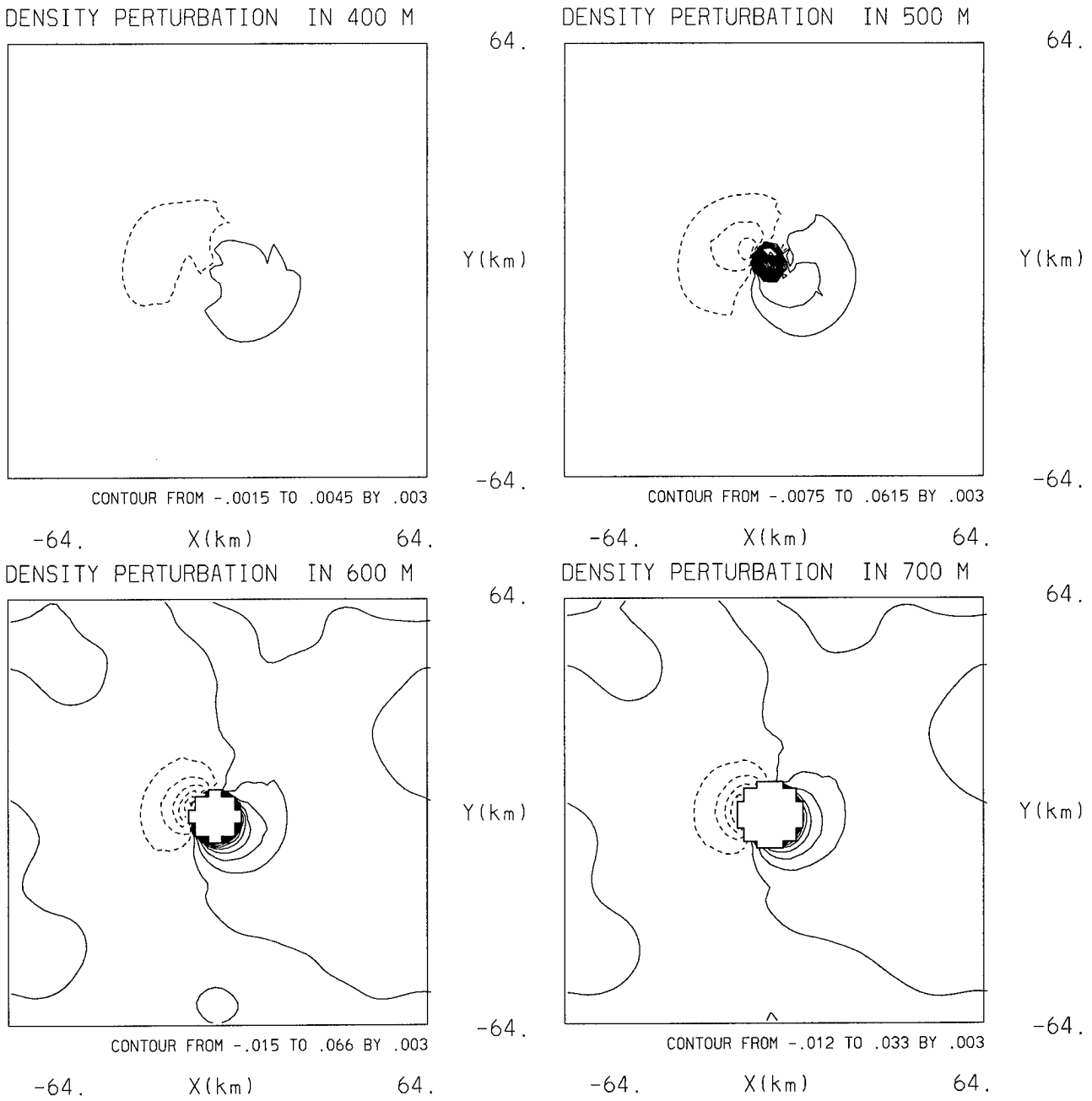


Figure 2. Snapshot of the horizontal structure of the density perturbation for seamount trapped wave in the central experiment: (a) 400 m; (b) 500 m; (c) 600 m; and (d) 700 m. Only the inner quarter of the domain is shown.

Figure 4 summarizes the results: while the wave response and mean flow generation increase with increasing resolution down to about 2 km grid spacing, further increase results in slightly reduced wave amplitudes; the rectified flow seems to have reached convergence.

An explanation involves the fact that the rectification process requires a finite amount of friction to break the symmetry of the seamount trapped wave. Too much friction, however, will damp the wave and reduce the rectified flow. The non-uniform convergence is an indication that the implicit diffusion/viscosity in the numerical model still dominates over the explicitly prescribed values for 4, 3 and 2 km resolution but is below that level for 1.5 and 1 km resolutions.

It should be noted that the results for the least resolving case differ from all others by the apparent existence of a higher vertical mode, a circulation pattern which might be used as evidence for insufficient numerical resolution.

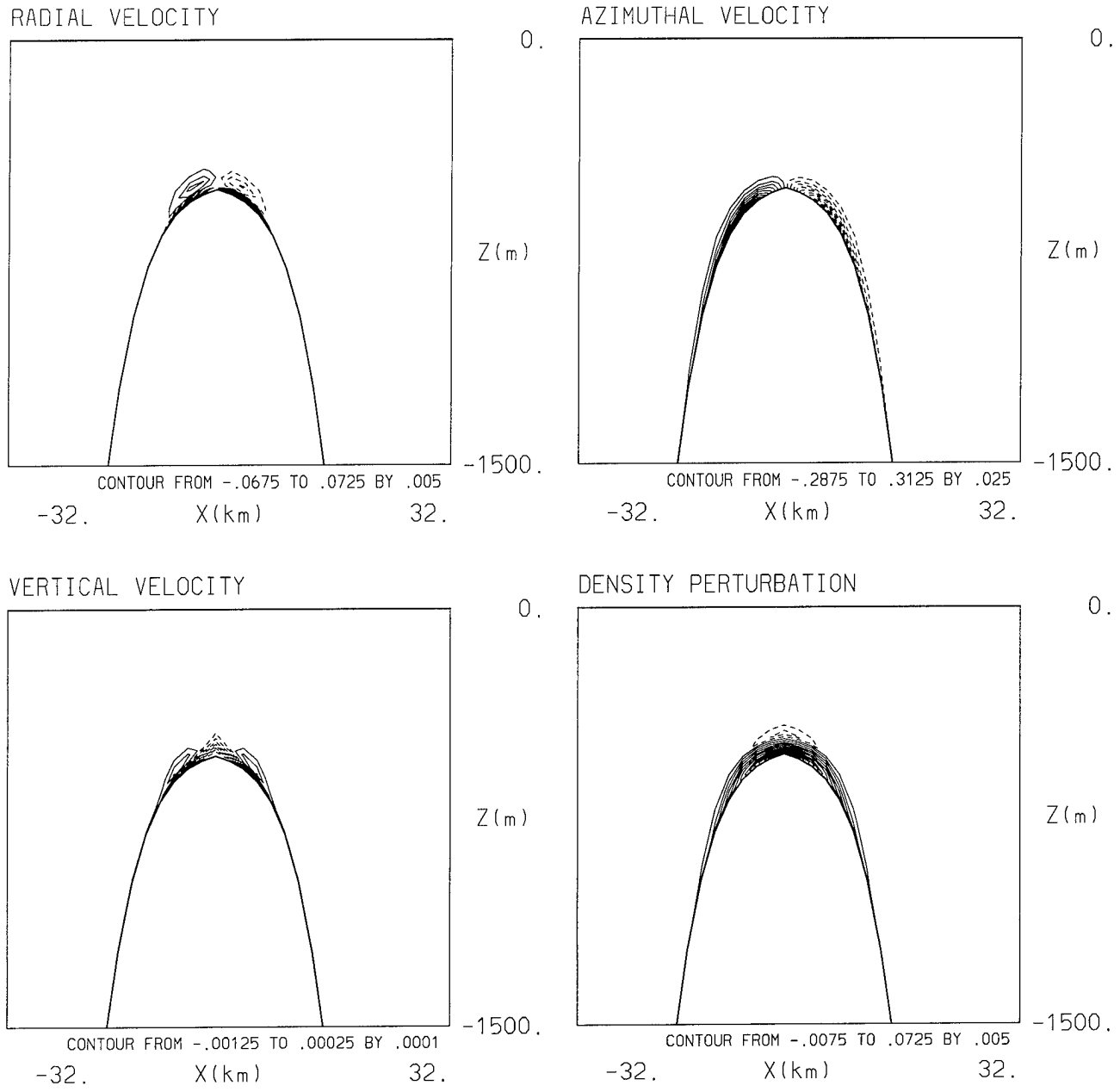


Figure 3. Spatial structure of the time-mean flow in the central experiment: (a) radial velocity; (b) azimuthal velocity; (c) vertical velocity; and (d) density perturbation. Shown is the radial-vertical plane focussing on the upper 1500 m of the inner quarter of the model domain.

Variations of Shape and Topographic Irregularities

While changes of the fractional seamount height and functional form had been considered in previous studies (e.g., Chapman and Haidvogel, 1992), there is no systematic investigation of seamount radius and slope, azimuthal asymmetries and small-scale bottom roughness.

Examples from these three categories of topographic variations are considered in this study. The basic form of the topographic obstacle (2) was modified in the following way:

$$R_o = R_1 + R_2 \sin(n \cdot \theta + \theta_o) \qquad (6)$$

Radial Shape of the Seamount

In this class of variations, the influence of seamount diameter and slope is investigated. The radius of the seamount (R_1) was varied between 15 and 25 km (Fig. 5). The maximum resonance was found for a radius of 20 km, this is for a Burger number of $S = r_D / R_o = 0.5$, which coincides with the central case reported in the previous section.

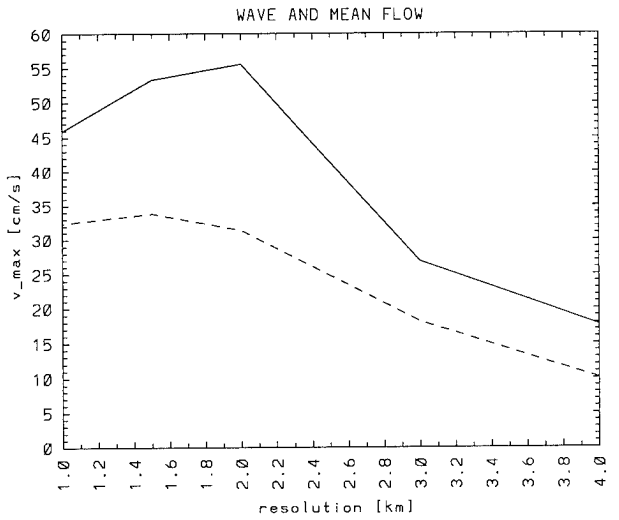


Figure 4. Wave amplification (solid line) and mean flow rectification (dashed line) as a function of horizontal resolution: the maximum point-wise velocity.

The rectified mean flow is directly proportional to the wave amplitude for most of the parameter space, except for very wide seamounts, where the lobes of the seamount trapped wave are separated and cannot interact effectively. Very thin seamounts, on the other hand, seem to have a smaller perturbing effect on the barotropic tidal flow, thus resulting in generally weaker resonance.

In a next step, the slope of the seamount (R_2) was varied between 6 and 12 km (Fig. 6). This represents a change in maximum slope from 16.7 to 33.3%. Again, there is a maximum, in this case at around 9 km, where maximum resonance occurs. Steeper slopes suppress the wave amplitude and essentially eliminate the mean flow generation.

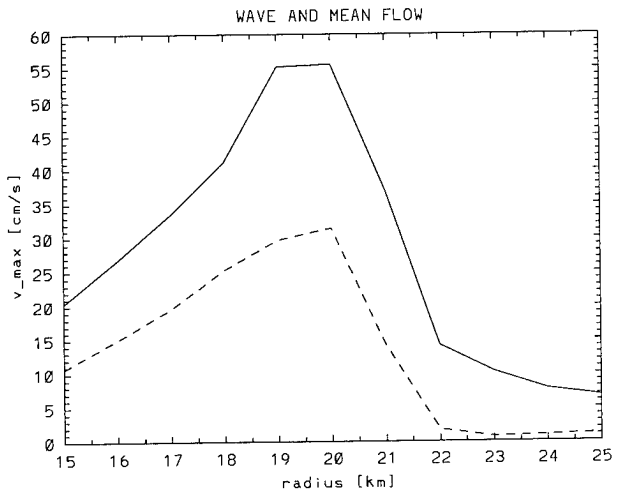


Figure 5. As Fig. 4, but as a function of seamount radius R_1.

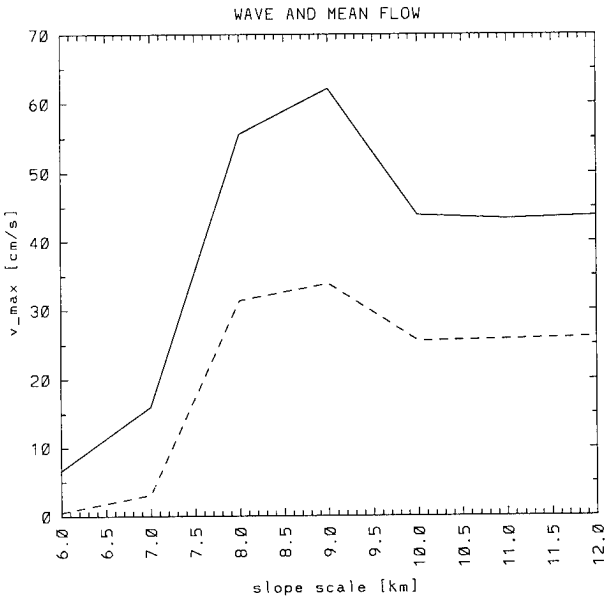


Figure 6. As Fig. 4, but as a function of seamount slope R_2.

Azimuthal Asymmetries

Variations in the azimuthal direction were added in the form of sinusoidal changes in radius of varying mode number. A first series of experiments investigates the effect of amplitude changes for mode 2 asymmetries; subsequently, higher order perturbations were investigated and possible effects of the angle of attack for an asymmetric seamount were tested.

The introduction of an azimuthal asymmetry with $n = 2$ generally reduces the wave and mean flow response (Fig. 7). Obviously, a symmetric seamount has to be regarded

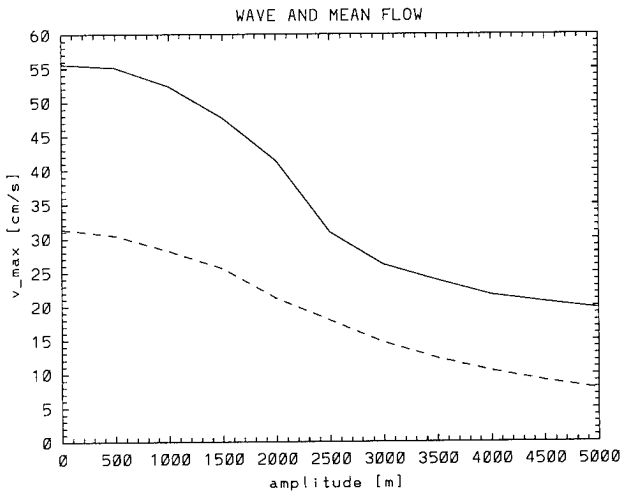


Figure 7. As Fig. 4, but as a function of the amplitude of the mode 2 asymmetry.

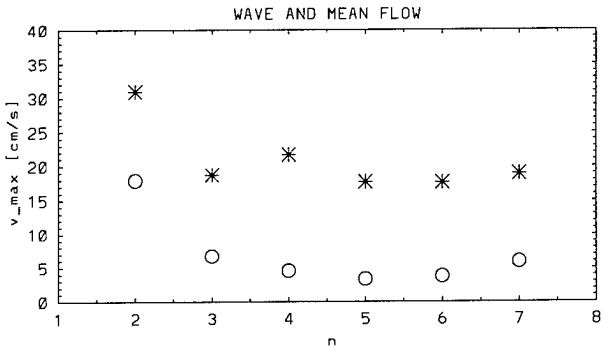


Figure 8. As Fig. 4, but as a function of azimuthal mode number n. Solutions exist only at discrete points: asterisks denote the wave amplification, circles the mean flow rectification.

as the optimal geometry for resonant amplification and rectification. Azimuthal pressure variations of the wave correlated with the topographic asymmetries do not contribute enough to compensate the reduction of wave amplification due to the geometrical changes.

Higher order azimuthal variations (Fig. 8) tend to decorrelate the non-linear interaction between the wave lobes even more. The rectification efficiency drops from 50% to less than 25%.

The orientation of the asymmetric seamount with respect to the main axis of the forcing was varied between θ_o = 0° and 180° (Fig. 9). This "angle of attack" was found to be of only minor importance for the trapped flow response: 10% difference in the wave amplitude is found, with a maximum at θ_o = 0° , when the mean flow hits the obstacle on the larger flanks in prograde direction.

Bottom Roughness

Lastly, the smooth seamount topography was modified by adding a random bottom roughness of varying rms-value. The random perturbations are weighted by the

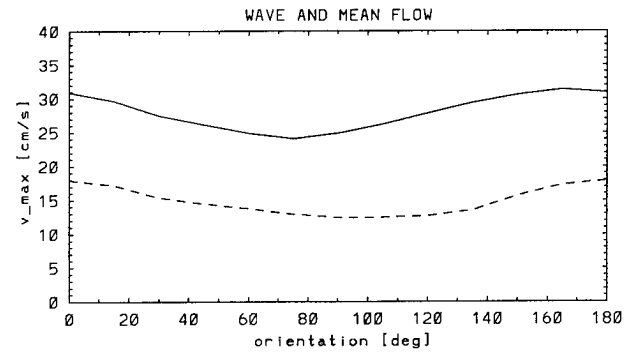


Figure 9. As Fig. 4, but as a function of seamount orientation θ_o relative to the forcing flow.

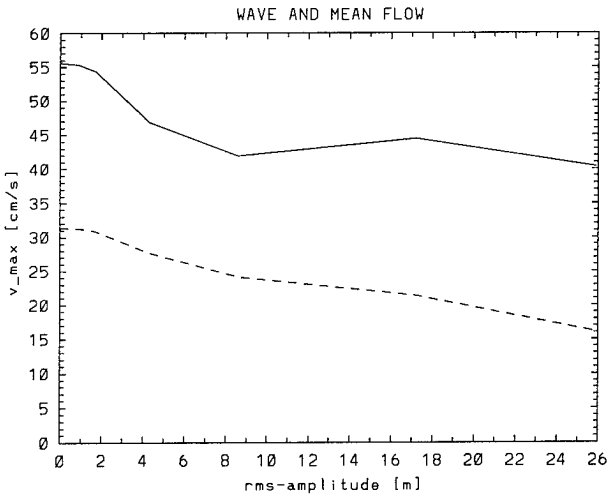


Figure 10. As Fig. 4, but as a function of rms-amplitude of the random bottom roughness.

deviation from maximum water depth, thus being largest on top of the seamount and essentially zero in the deep ocean away from the obstacle. This way, even relatively small rms-values should have an influence on the resonant and rectified flow. The general tendency of added bottom roughness is to act as a sink of wave energy (Fig. 10). Similar to the azimuthal asymmetries, bottom roughness destroys the systematic non-linear interaction of the wave and thus reduces both the amplification and rectification.

Latitudinal Dependence

In addition to the changes in seamount geometry the Coriolis parameter f was varied between 30°N and 65°N to obtain an idea of the sensitivity to environmental parameters.

The dependence on latitude was found to be immense: Figure 11 covers the latitudinal range between 30°N, the critical latitude for trapped diurnal waves, and 65°N and shows large differences in the maximum point-wise velocities across the parameter range. As expected from the studies of Haidvogel et al. (1993), a larger Coriolis parameter (reducing the Burger number) gives much larger response at high latitudes. It is noteworthy, though, that a variation of f by a factor smaller than 2 can account for a change in amplification by a factor of 6.

Implications for Parametrizations

Arguments from statistical mechanics can be used to derive a simplified form of the systematic flow along topographic depth contours caused by interaction between fluctuating flow and topographic variations. A parametrization of this "fifth force" for coarse resolution models was proposed by Holloway (1992): the lateral viscous terms should be modified to drive the barotropic part of the horizontal flow field towards a state of cyclonic

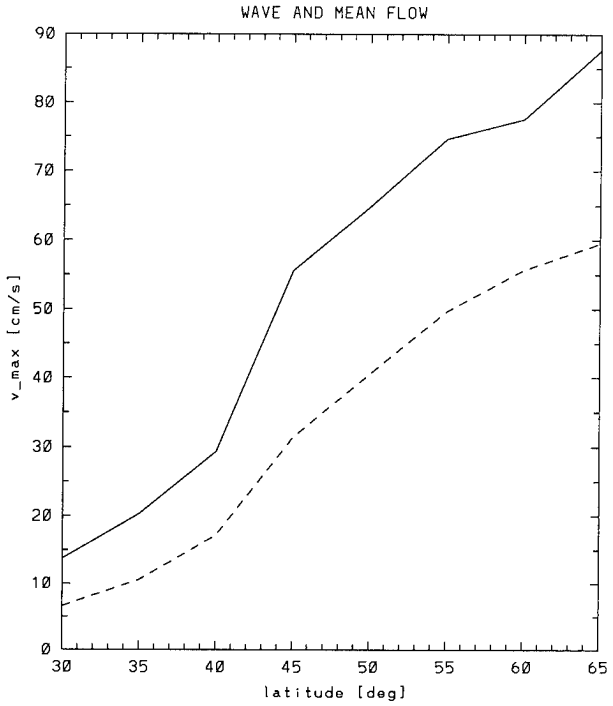


Figure 11. As Fig. 4, but as a function of latitude.

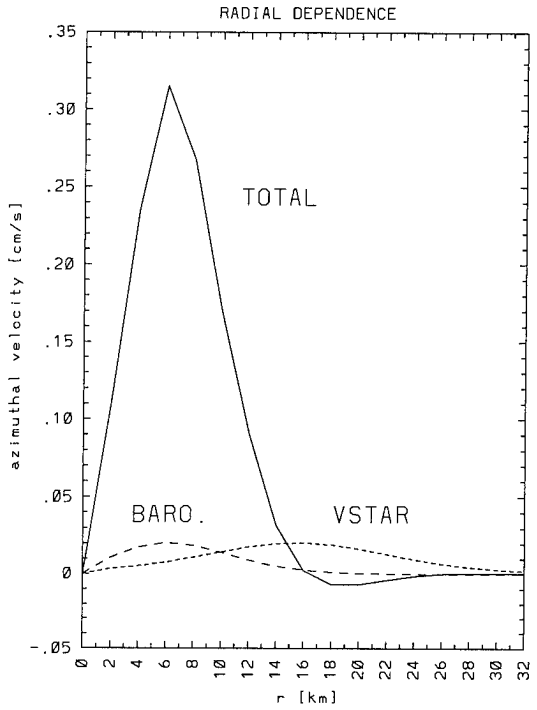


Figure 12. Azimuthal time-mean velocities as a function of radial distance from the seamount center: total bottom flow, barotropic part, and the climatological velocity from eq. (8) with $L = 1200$ m.

circulation around ocean basins. It was shown that this approach can give results closer to observations (Eby and Holloway, 1994).

In principle, the time-mean flow around a seamount is based on the same physical process. It is therefore obvious to ask whether we can learn from these experiments about the structure of mean flows and how to parameterize them?

According to Holloway (1992) the barotropic time-mean "climatological" velocities can be derived from a streamfunction of the form

$$\psi^* = -L^2 fH \tag{7}$$

As a result, the azimuthal component of the mean flow would be approximated by

$$V^* = \frac{1}{H}\psi_r^* = -fL^2\frac{H_r}{H} \tag{8}$$

Figure 12 compares the azimuthal time-mean flow at the bottom and its barotropic part from the central experiment with the V^* from theory.

First of all it is obvious that the barotropic part represents only a small portion of the flow field; the rectified response is mainly baroclinic. But even a look at the barotropic component shows significant differences: while V^* has its maximum at the location of the maximum H_r / H, the model concentrates its time-mean momentum at a smaller radius. As a consequence, maximum velocities and transports do not match. If L = 1200 m is chosen (as for Fig. 12), the velocities are comparable, but the transport is too large by a factor of 4. If this is compensated by the choice of a smaller L, the resulting velocities are too small.

It is not clear whether or not we should expect the mean flow structure at seamounts to be fundamentally different from the form stress rectified flow at straight continental slopes, due to the geometric peculiarity of the radially symmetric topography. Further detailed studies are needed.

Similarly, attempts to introduce vertical structure in the parametrization need more attention; they would have to take into account a corresponding density perturbation

$$fv_z^* = -g\rho_r^* \tag{9}$$

but this extension is not straightforward.

Summary and Conclusions

Geometrical and environmental parameters are varied in a series of numerical experiments featuring a tall, steep and isolated seamount forced by diurnal barotropic flow. Several classes of topographic changes and irregularities are investigated for their influence on wave amplification and mean flow generation. Changes of the radial shape of the seamount are found to be the most crucial in determining the actual amplitude of the trapped flow. All azimuthal irregularities tend to reduce the wave response and the amount of rectification.

The results of Haidvogel et al. (1993) are found to be robust through the parameter space. The instantaneous near seamount response is dominated by the first azimuthal mode seamount trapped wave; higher modes could not be detected. However, a regime was found in which the vorticity of the mean flow modified the local environment of the wave enough to cause an enhancement of the wave amplitude through non-linear feed-back.

Returning to the comparison of the real Fieberling Guyot topography and its smooth Gaussian fit we have to conclude that the slightly increased flow amplitudes for the real Fieberling Guyot bathymetry are likely to be the joint effect of steeper slopes that increase and asymmetries combined with bottom roughness that decrease the response.

References

Beckmann, A. and D.B. Haidvogel, 1993: Numerical simulation of flow around a tall isolated seamount. Part I: Problem formulation and model accuracy. *J. Phys. Oceanog.* 23 , 1736–1753.

Beckmann, A. and D.B. Haidvogel, 1994: Resonant Generation of Waves and Mean Currents at Fieberling Guyot. Ocean Sciences Meeting 1994, San Diego, CA.

Brink, K.H., 1989: The effect of stratification on seamount-trapped waves, *Deep-Sea Res.* 36 , 825–844.

Brink, K.H., 1995: Tidal and Lower Frequency Currents Above Fieberling Guyot, *J. Geophys. Res.*, 100, 10,817–10,832.

Chapman, D.C. and D.B. Haidvogel, 1992: Formation of Taylor Caps over a tall, isolated seamount in a stratified ocean. *Geophys. Astrophys. Fluid Dyn.* 64 , 31–65.

Chapman, D.C. and D.B. Haidvogel, 1993: Generation of internal lee waves trapped over a tall isolated seamount. *Geophys. Astrophys. Fluid Dyn.* 69 , 31–65.

Codiga, D.L., 1993: Laboratory realizations of stratified seamount-trapped waves. *J. Phys. Oceanog.* 23 , 2053–2071.

Eby, M. and G. Holloway, 1994: Sensitivity of a large-scale ocean model to a parameterization of topographic stress. *J. Phys. Oceanog.* 24 , 2577–2588.

Eriksen, C.C., 1991: Observations of amplified flows atop a large seamount. *J. Geophys. Res.* 96 , 15227–15236.

Fennel, W., and M. Schmidt, 1991: Responses to topographical forcing. *J. Fluid Mech.* 223 , 209–240.

Haidvogel, D.B., J.L. Wilkin and R.E. Young, 1991: A semi-spectral primitive equation ocean circulation model using vertical sigma and orthogonal curvilinear horizontal coordinates. *J. Comp. Phys.* 94 , 151–185.

Haidvogel, D.B., A. Beckmann, D.C. Chapman and R.-Q. Lin, 1993: Numerical Simulation of Flow Around a Tall Isolated Seamount: Part II: Resonant Generation of Trapped Waves. *J. Phys. Oceanog.* 23 , 2373–2391.

Haidvogel, D.B. and K.H. Brink, 1986: Mean currents driven by topographic drag over the continental shelf and slope. *J. Phys. Oceanog.* 16 , 2159–2171.

Hogg, N.G., 1980: Effects of bottom topography on ocean currents. In: Orographic Effects in Planetary Flows, *GARP Publication Series*, 23, 167–205.

Holloway, G., 1992: Representing topographic stress for large-scale ocean models. *J. Phys. Oceanog.* 22, 1033–1046.

Holloway, G., K. Brink and D. Haidvogel, 1989: Topographic stress in coastal circulation dynamics. In: Neshyba, S., et al. (eds.), *Poleward Flows along Eastern Ocean Boundaries.* Coastal and Estuarine Studies, 34, Springer-Verlag, New York, 374 pp.

McCalpin, J.D., 1994: A comparison of second-order and fourth-order pressure gradient algorithms in a σ-ordinate ocean model. *Int. J. Num. Meth. Fl.*, 18, 361–383.

Rossby Waves over a Lattice of Different Seamounts

M. C. Hendershott

Scripps Institution of Oceanography 0209, La Jolla CA 92093

Abstract. Topographic (β=0) Rossby waves over an infinite rectangular lattice of identical seamounts have the form of plane waves propagating in frequency bands close to the natural frequencies of the topographic Rossby waves trapped around one seamount in isolation (Rhines). When the height of the seamounts varies randomly and the seamounts are separated by more than a few seamount radii, then the topographic Rossby wave field is described by a model first introduced by Anderson in another context. In this model, randomness in seamount height converts the extended plane waves into localized modes whose horizontal scale of energy trapping decreases with increasing disorder in seamount height. The numerical results of Mackinnon and Kramer are used to quantify this relationship.

1. Introduction

The ability of Rossby waves to transmit low frequency energy over long distances in the ocean is important directly or implicitly in most quasianalytical theories of the large scale circulation as well as in the interpretation of results obtained from numerical models of ocean circulation. Our qualitative ideas about such waves have grown largely out of analytical or quasianalytical solutions of the linearized shallow water equations or of the quasigeostrophic equations over ocean bottom relief that is either flat or has some very simple form which makes analysis feasible. But basin scale modes and much smaller scale topographic modes can easily have very similar frequencies (Miller, 1986). This observation raises the question of whether and/or when Rossby modes computed over smoothed relief would have recognizable counterparts over realistic relief.

An important aspect of this question has been addressed for surface gravity waves by Devillard et al. (1989), who found that for bottom relief and waves varying in only one direction, any amount of random variation in the underlying bottom relief changed the travelling waves into standing modes spatially localized over a horizontal scale that became ever larger as the random variation of the relief was decreased. The present calculation establishes a similar result for two dimensional topographic Rossby waves.

Even when β=0, Rhines (1970) has shown that energy transmission over unlimited distances via traveling topographic Rossby waves can occur if the bottom relief is periodic in space. It is shown below that if a collection of identical seamounts arrayed on a periodic lattice and separated by more than a few seamount radii is randomly perturbed in seamount height, then these traveling topographic Rossby waves extending over the entire horizontal plane are changed into spatially standing modes localized over a horizontal scale that becomes ever smaller as the random variation of the relief is increased. This is accomplished by transforming the Rossby wave problem into a form previously investigated by Anderson (1958) in another context, and then making use of quantitative numerical studies of the horizontal scale of localization for this model (MacKinnon and Kramer, 1983). The salient results are summarized in Figure (1).

2. Topographic Rossby waves over a Lattice of Seamounts

Over a single isolated seamount of radius $\hat{a}_l$ that is centered at $r_l = (x_l, y_l)$ and whose relief $D(x,y) = \partial D\,(1-h(x,y))$ varies only for $|r-r_l| < \hat{a}_l$ so that

$$h(x,y) = \begin{cases} P_l(|r-r_l|) & |r-r_l| < \hat{a}_l \\ 0 & |r-r_l| > \hat{a}_l \end{cases} \qquad (2.1)$$

the streamfunction ψ_{lK} describing purely topographic (β=0) seamount oscillations with natural frequency σ_{lK} satisfies

$$-i\sigma_{lK}\nabla^2\psi_{lK} + J(\psi_{lK}, f_0 P_l) = 0 \qquad (2.2)$$

The subscript l indexes the seamount (in preparation for the case of many seamounts) while the subscript K orders modes over the seamount. From (2.2) the sign of σ_{lK} changes with the sign of the relief; $\sigma_{lK} < 0$ for hills.

In cylindrical coordinates r,θ centered at r_l, the eigenfunctions over circularly symmetric relief have the separated form

$$\psi = \begin{cases} e^{in\Theta}\,\varphi_{lK}(r) & r<\hat{a}_l \\ e^{in\Theta}\,\varphi_{lK}(\hat{a}_l)(\hat{a}_l/r)^n & r>\hat{a}_l \end{cases} \tag{2.3}$$

n=1,2,3 ... . The index K is usually a pair of integers indexing variation of ψ_{lK} in the θ,r directions. Thus over the particular relief

$$h(x,y) = \begin{cases} h_0(1-(r/\hat{a}_l)^2) & r<\hat{a}_l \\ 0 & r>\hat{a}_l \end{cases} \tag{2.4}$$

the eigenfunctions ψ_{lK} are of the form

$$\psi = \begin{cases} A\,e^{in\Theta}\,J_n(\alpha_{nm}r) & r<\hat{a}_l \\ A\,e^{in\Theta}\,J_n(\alpha_{nm}\hat{a}_l)(\hat{a}_l/r)^n & r>\hat{a}_l \end{cases} \tag{2.5}$$

in which A is a constant and the eigenfrequencies σ_{lK} are given by

$$\sigma_{l,nm} = -2nh_l f_0/(\alpha_{nm}\hat{a}_l)^2$$
$$J_{n-1}(\alpha_{nm}\hat{a}_l) = 0 \qquad n,m = 1,2,3 \tag{2.6}$$

The index K in (2.3) is the pair n,m in (2.6). Seamount oscillations over the tophat relief

$$h(x,y) = \begin{cases} h_l & r<\hat{a}_l \\ 0 & r>\hat{a}_l \end{cases} \tag{2.7}$$

are of the form

$$\psi = \begin{cases} e^{in\Theta}(r/\hat{a}_l)^n & r<\hat{a}_l, \quad A=(4n\pi)^{-1/2} \\ e^{in\Theta}(\hat{a}_l/r)^n & r>\hat{a}_l, \quad n=1,2,3... \end{cases} \tag{2.8}$$

and are degenerate in that all modes of angular wavenumber n have the same radial variation, and the eigenfrequency

$$\sigma_{lK} = -f_0 h_l/2 \tag{2.9}$$

is the same for all the modes. Nonetheless the tophat modes will be found useful because their simplicity facilitates estimation of the coupling between seamounts; away from the seamount their dependance on r,θ is the same as in the general case (2.3).

Over isolated seamount l, of arbitrary shape, eigenfunctions ψ_{lK} satisfy the orthogonality relationships

$$\overline{\psi^*_{lL}J(\psi_{lK},f_0P_l)} = -i\sigma_{lK}\,\overline{\nabla\psi^*_{lL}\cdot\nabla\psi_{lK}} = -i\sigma_{lK}\delta_{KL}$$
$$\overline{\psi_{lL}J(\psi_{lK},f_0P_l)} = -i\sigma_{lK}\,\overline{\nabla\psi_{lL}\cdot\nabla\psi_{lK}} = 0 \tag{2.10}$$

in which the overbar here and everafter indicates integration over the entire horizontal plane. The constant A in (2.8) has been chosen in accord with (2.10).

For every eigenfunction ψ_{lK} with frequency σ_{lK} there is another eigenfunction ψ_{lK}* with eigenfrequency $-\sigma_{lK}$. A given eigensolution and its complex conjugate are indistinguishable when free but respond differently to forcing. This is most obvious in the case where clockwise rotation of phases about a hill necessarily forces counterclockwise rotation of phases about any neighboring hill, a sense of rotation of phases opposite to that associated with free seamount oscillations at the neighboring hill.

Now let the relief be an ensemble of distinct seamounts:

$$h(x,y) = \sum_s P_s(|r-r_s|) \tag{2.11}$$

Expand the total streamfunction $\psi(x,y,t)$ over this relief in individual seamount eigenfunctions:

$$\psi(x,y,t) = \sum_{lK}\left[a_{lK}(t)\psi_{lK}(x,y) + b_{lK}(t)\psi^*_{lK}(x,y)\right] \tag{2.12}$$

The total energy E is

$$2E = \rho\overline{\nabla\psi\cdot\nabla\psi^*} = \rho\sum_{lK,nM} a^*_{nM}a_{lK}\,\overline{\nabla\psi^*_{nM}\cdot\nabla\psi_{lK}} + \ldots \tag{2.13}$$

in which ρ is the mass per unit surface area of the fluid layer. With the normalization of (2.10), $|a_{lK}|^2$ and $|b_{lK}{}^2|$ are the energies associated with ψ_{lK} and ψ_{lK}* in isolation. Insert the expansion (2.12) into the governing equation

$$\partial\nabla^2\psi/\partial t + J(\psi, f_0h) = 0 \tag{2.14}$$

for linearized nondivergent quasigeostrophic flow over relief h given by (2.11) to obtain

$$\sum_{lK} [\![\dot{a}_{lK} \nabla^2 \psi_{lK} + \dot{b}_{lK} \nabla^2 \psi^*_{lK} + a_{lK} \sum_s J(\psi_{lK}, f_0 P_s) + b_{lK} \sum_s J(\psi^*_{lK}, f_0 P_s)]\!] = 0 \tag{2.15}$$

Multiplying (2.15) by ψ_{0M} and ψ_{0M} * separately and then integrating the resulting equations over the horizontal plane yields the following coupled ode's for the amplitudes a_{lK} and b_{lK}:

$$\begin{aligned}
&\overline{\nabla\psi^*_{0M}\cdot\nabla\psi_{0M}}\,\dot{a}_{0M} + \sum_K\sum_{l\neq 0}[\overline{\nabla\psi^*_{0M}\cdot\nabla\psi_{lK}}]\,\dot{a}_{lK} \\
&+ \overline{\nabla\psi^*_{0M}\cdot\nabla\psi^*_{0M}}\,\dot{b}_{0M} + \sum_K\sum_{l\neq 0}[\overline{\nabla\psi^*_{0M}\cdot\nabla\psi^*_{lK}}]\,\dot{b}_{lK} = \\
&(D^{M*M}_{000} + \sum_{s\neq 0} D^{M*M}_{00s})\,a_{0M} + \sum_K\sum_{l\neq 0}[D^{M*K}_{0l0} + D^{M*K}_{0ll}]a_{lK} \\
&+ \sum_K\sum_{l\neq 0}\sum_{s\neq 0}(D^{M*K}_{0ls})a_{lK} + [D^{M*M*}_{000} + \sum_{s\neq 0} D^{M*M*}_{00s}]b_{0M} \\
&+ \sum_K\sum_{l\neq 0}(D^{M*K*}_{0l0} + D^{M*K*}_{0ll})b_{lK} + \sum_K\sum_{l\neq 0}\sum_{s\neq 0,l}[D^{M*K*}_{0ls}]b_{lK}
\end{aligned} \tag{2.16}$$

$$\begin{aligned}
&[\overline{\nabla\psi_{0M}\cdot\nabla\psi_{0M}}]\,\dot{a}_{0M} + \sum_K\sum_{l\neq 0}\overline{\nabla\psi_{0M}\cdot\nabla\psi_{lK}}\,\dot{a}_{lK} \\
&+\overline{\nabla\psi_{0M}\cdot\nabla\psi^*_{0M}}\,\dot{b}_{0M} + \sum_K\sum_{l\neq 0}[\overline{\nabla\psi_{0M}\cdot\nabla\psi^*_{lK}}]\,\dot{b}_{lK} = \\
&[D^{MM}_{000} + \sum_{s\neq 0} D^{MM}_{00s}]a_{0M} + \sum_K\sum_{l\neq 0}(D^{MK}_{0l0} + D^{MK}_{0ll})a_{lK} \\
&+\sum_K\sum_{l\neq 0}\sum_{s\neq 0,l}[D^{MK}_{0ls}]a_{lK} + (D^{MM*}_{000} + \sum_{s\neq 0} D^{MM*}_{00s})b_{0M} \\
&+\sum_K\sum_{l\neq 0}[D^{MK*}_{0l0} + D^{MK*}_{0ll}]b_{lK} + \sum_K\sum_{l\neq 0}\sum_{s\neq 0,l}(D^{MK*}_{0ls})b_{lK}
\end{aligned} \tag{2.17}$$

In (2.16) and (2.17) terms refering to the seamount labeled 0 have been isolated, and the notation

$$D^{M*K}_{0ls} = \overline{\psi^*_{0M}\, J(\psi_{lK}, f_0 P_s)} \tag{2.18}$$

has been introduced. In (2.16) and (2.17) only, the square brackets [] enclose terms which are found upon detailed calculation to vanish. The remaining nonzero terms may be grouped as follows:

$$S_{0M} = \sum_{s=0} i D^{M*M}_{00s} \tag{2.19}$$

$$\phi^{MK}_{0l} = \sum_{s\neq 0,l} i\, D^{M*K}_{0ls} \tag{2.20}$$

$$\Delta^{MK}_{0l} = \overline{\nabla\psi_{0M}\cdot\nabla\psi_{lK}} \tag{2.21}$$

and we have the particular values

$$\begin{aligned}
&\overline{\nabla\psi^*_{0M}\cdot\nabla\psi_{0M}} = 1 \\
&D^{M*M}_{000} = -i\sigma_{0M}\overline{\nabla\psi^*_{0M}\cdot\nabla\psi_{0M}} = 1, \\
&D^{M*K*}_{0ll} + D^{M*K*}_{0l0} = -i(\sigma_{0M}-\sigma_{lK})(\Delta^{MK}_{0l})^* \\
&\Delta^{MK}_{00} = 0, \qquad D^{M*M}_{000} = -i\sigma_{0M}
\end{aligned} \tag{2.22}$$

S_{0M} in (2.19) is a small correction to the eigenfrequency σ_{0M} of seamount oscillation ψ_{0M} over seamount 0 due to the presence of all the other seamounts. ϕ^{MK}_{0l} in (2.20) is the interaction between eigensolution pairs at sites 0 and l because of their overlap with all other seamounts. Δ^{MK}_{0l} in (2.21) is the direct interaction between complex conjugate eigensolution pairs at sites 0 and l.

With the introduction of (2.19) - (2.22), (2.16) - (2.17) become

$$\begin{aligned}
&i\dot{a}_{0M} + i\sum_K\sum_{l\neq 0}(\Delta^{MK}_{0l})^*\,\dot{b}_{lK} = (\sigma_{0M} + S_{0M})\,a_{0M} \\
&+\sum_K\sum_{l\neq 0}(\phi^{MK}_{0l})\,a_{lK} + \sum_K\sum_{l\neq 0}(\sigma_{0M}-\sigma_{lK})(\Delta^{MK}_{0l})^*\,b_{lK}
\end{aligned} \tag{2.23}$$

and

$$\begin{aligned}
&i\dot{b}_{0M} + i\sum_K\sum_{l\neq 0}(\Delta^{MK}_{0l})\,\dot{a}_{lK} = -(\sigma_{0M} + S_{0M})\,b_{0M} \\
&-\sum_K\sum_{l\neq 0}(\phi^{MK}_{0l})^*\,b_{lK} - \sum_K\sum_{l\neq 0}(\sigma_{0M}-\sigma_{lK})(\Delta^{MK}_{0l})a_{lK}
\end{aligned} \tag{2.24}$$

3. Topographic Rossby waves over a Lattice of Randomly Differing Seamounts

Rhines (1970) has shown that if all the seamounts are identical and they are arrayed in a rectangular lattice, then even in the absence of β, energy initially in topographic Rossby waves can propagate indefinitely. If the distance R between seamounts somewhat exceeds the seamount radius â, then detailed calculations (some of which are shown subsequently) show that the correction and coupling terms (2.19)-(2.21) decay as positive powers of a/R. If we label lattice positions by x,y (in units of R), then the solutions

found by Rhines (1970) have the form

$$a_{xy,M} = e^{i(\mu x + \nu y - \sigma(\mu,\nu))}$$
$$\sigma(\mu,\nu) \approx \sigma_{0M}[\,1 + O(a/R)^{2n+2}(\cos(\mu x)+\cos(\nu y))\,] \tag{3.1}$$

where n is the angular order of an individual seamount oscillation with frequency σ_{0M}. Plane waves thus propagate within frequency bands that are centered about the frequencies σ_{0M} of isolated seamount oscillations and have widths the order of $\sigma_{0M}(a/R)^{2n+1}$.

The question now to be addressed is 'what happens to these propagating topographic modes when the seamounts are of slightly differing heights h_l?' We thus consider a periodic lattice of seamounts whose individual seamount oscillation frequencies are randomly distributed about a central value σ_*. The width of this distribution will be supposed to be small relative to the size of σ_*. For motions at a fixed frequency ω, (2.23)-(2.24) may be compactly written as

$$\left[\begin{bmatrix}\sigma & 0\\ 0 & -\sigma\end{bmatrix}+\begin{bmatrix}S & 0\\ 0 & -S\end{bmatrix}+\begin{bmatrix}\phi & 0\\ 0 & -\phi^*\end{bmatrix}\right]\begin{bmatrix}a\\ b\end{bmatrix} =$$
$$+\begin{bmatrix}0 & \sigma\Delta^*-\Delta^*\sigma\\ \Delta\sigma-\sigma\Delta & 0\end{bmatrix}\begin{bmatrix}a\\ b\end{bmatrix} = \omega\begin{bmatrix}I & \Delta^*\\ \Delta & I\end{bmatrix}\begin{bmatrix}a\\ b\end{bmatrix} \tag{3.2}$$

in which σ is the diagonal matrix of individual site eigenfrequencies σ_{0M}, and S, ϕ, and Δ are matrices whose elements are given by (2.19)-(2.21).

As long as the disorder in seamount height is sufficiently small that individual seamount oscillation frequencies associated with different angular or radial orders do not overlap, we may retain but one mode per site (typically the mode having the smallest angular wavenumber n=1 and consequently the greatest frequency). The elements of S, ϕ, and Δ may be shown to decay as positive powers of (a/R), so that (3.2) may be simplified by left multiplication by the factor

$$\begin{bmatrix}I & \Delta^*\\ \Delta & I\end{bmatrix}^{-1} = \begin{bmatrix}(1-\Delta^*\Delta)^{-1} & -(1-\Delta^*\Delta)^{-1}\Delta^*\\ -(1-\Delta^*\Delta)^{-1}\Delta & (1-\Delta^*\Delta)^{-1}\end{bmatrix}$$
$$\simeq \begin{bmatrix}(1+\Delta^*\Delta) & -\Delta^*\\ -\Delta & (1+\Delta^*\Delta)\end{bmatrix} \tag{3.3}$$

The result is

$$\begin{bmatrix}(\sigma+S+\phi+\Delta^*\sigma\Delta) & \sigma\Delta^*\\ -\sigma\Delta & -(\sigma+S+\phi^*+\Delta\sigma\Delta^*)\end{bmatrix}\begin{bmatrix}a\\ b\end{bmatrix} = \omega\begin{bmatrix}a\\ b\end{bmatrix} \tag{3.4}$$

Here, terms such as $\Delta\Delta^*\Delta$ have been neglected relative to terms such as $\Delta\Delta^*$, and terms such as Δ^*S and $\Delta^*\phi$ have been neglected relative to terms such as $\Delta^*\sigma$.

Now we consider motions at a frequency ω that is close to the natural frequencies σ_o of individual seamounts in the ensemble (the single subscript now indexes seamounts). The dominant terms of the diagonal elements of (3.3) are thus the diagonal matrix σ, so that the linear equations for a may be close to resonance but those for b are far from resonance. Consequently we may take

$$b \simeq -(\omega I+\sigma)^{-1}\sigma\Delta a \tag{3.5}$$

Hence (3.3) finally becomes

$$\omega I a = (\sigma+S)a + Va$$
$$V = (\phi+\Delta^*\sigma\Delta-\sigma\Delta^*(\omega I+\sigma)^{-1}\sigma\Delta) \simeq (\phi+\sigma_*\Delta^*\Delta/2) \tag{3.6}$$

in which σ_* denotes the average of the individual free seamount oscillation frequencies σ_0. The terms neglected in (3.5) would contribute minor modifications to V and S in (3.6).

We now evaluate the elements of ϕ and of $\Delta^*\Delta$ appearing in (3.6). We have

$$\phi_{0l} = \sum_{s\neq 0,l} i\overline{\psi_0^* J(\psi_l^*, f_0 h_s)} = \sum_{s\neq 0,l} -i\overline{f_0 h_s J(\psi_l^*,\psi_0^*)}$$
$$\simeq \sum_{s\neq 0,l}(-\sigma_s\hat{a}_s^2\hat{a}_0\hat{a}_l)\frac{1}{(x_s-x_l-i(y_s-y_l))^2}\frac{1}{(x_s-x_0+i(y_s-y_0))^2} \tag{3.7}$$

and

$$\Delta_{0l}^* = \overline{\nabla\psi_0^*\nabla\psi_l^*} = -(i/\sigma_l)\overline{\psi_0^* J(\psi_l^*, f_0 h_l)}$$
$$= (i/\sigma_l)\overline{f_0 h_l J(\psi_l^*,\psi_0^*)} = -\hat{a}_0\hat{a}_l\frac{1}{(x_0-x_l+i(y_0-y_l))} \tag{3.8}$$

The evaluation of V in (3.6) thus requires evaluation of the sum

$$S_{0l}(x,y) = \sum_{x,y\neq x_0,x_l}\frac{1}{(x-x_0-i(y-y_0))^2}\frac{1}{(x-x_l-i(y-y_l))^2} \tag{3.9}$$

This will be illustrated for the particular case $y_0=y_l=0$. It is convenient to write (3.9) as

$$S_{0l}=R^{-4}S_{\mu\nu}=R^{-4}\sum_{n,m\neq\nu,0;\mu,0}\frac{1}{(n-\nu-im)^2}\frac{1}{(n-\mu+im)^2} \qquad (3.10)$$

Note that

$$S_{\nu\mu}=\frac{d}{d\nu}\frac{d}{d\nu}\sum\frac{1}{(n-\nu-im)}\frac{1}{n-\mu+im)}$$
$$=\frac{d}{d\nu}\frac{d}{d\nu}\sum\left[\left(\frac{n-\nu}{(n-\nu)^2+m^2}-\frac{n-\mu}{(n-\mu)^2+m^2}\right)\left(\frac{\nu-\mu-2im}{(\nu-\mu)^2+4m^2}\right)\right. \qquad (3.11)$$
$$\left.+\left(\frac{1}{(n-\nu)^2+m^2}-\frac{1}{(n-\mu)^2+m^2}\right)\left(\frac{2im}{\nu-\mu+2im}\right)\right]$$

Since the summation indices exclude n,m = υ,0; μ,0, the very last sum in (3.11) may be written as

$$\sum_m\left(\frac{2im}{\nu-\mu+2im}\right)\left(\sum_{all\,n}\frac{1}{(n-\mu)^2+m^2}-\frac{1}{m^2}-\frac{1}{(\nu-\mu)^2+m^2}\right) \qquad (3.12)$$

In this form it is clear that this sum exactly equals the next to last sum in (3.11) so that the last two terms of (3.11) cancel. The imaginary part of the summand in first two sums in (3.11) is odd in m and hence the corresponding sum vanishes. The remaining summands are odd in n-ν and n-μ. Since the corresponding sums exclude n,m = ν,0; μ,0, (3.11) may finally be written as

$$\frac{d}{d\nu}\frac{d}{d\mu}\frac{2}{(\mu-\nu)^2}=\frac{12}{(\mu-\nu)^4} \qquad (3.13)$$

so that the sum (3.10) is

$$S_{0l}=\frac{12}{R^4(\mu-\nu)^4}=\frac{12}{(x_0-x_l)^4} \qquad (3.14)$$

On account of the rapid decrease of S_{0l} with site separation, we truncate the sum over all seamounts that is implicit in the matrix equation (3.6) to a sum over nearest geographical neighboring sites, and so finally obtain an approximate version of (3.6);

$$\omega a_0=(\sigma_0+S_0)a_0+V(a_e+a_w+a_n+a_s) \qquad (3.15)$$
$$V=6\sigma_*(a/R)^4$$

now notated in an obvious geographical manner in which site e is east of site o ... .

4. The Anderson Model

(3.15) has the form of model employed by Anderson (1958) to discuss the nature of single electron wavefunctions in a spatially random potential. In the numerical study of MacKinnon and Kramer (1983) that model is studied in the form

$$(\omega-\sigma_*)a_0=(\sigma_0+S_0-\sigma_*)a_0+V(a_e+a_w+a_n+a_s) \qquad (4.1)$$

The effective individual site frequencies σ_0+S_0 are supposed randomly distributed over the range $\sigma_*\pm\Delta\sigma$. The interaction potential V is taken constant. It is convenient to discuss the results in terms of a disorder parameter W defined by

$$W=\Delta\sigma/V=\frac{\Delta\sigma}{\sigma_*}\frac{1}{6(a/R)^4} \qquad (4.2)$$

Over a given relief, the topographic Rossby normal modes and their natural frequencies could in principle be found by solving the eigenvalue problem (3.6) or its approximate form (4.1). But we wish to study the properties of normal modes over an ensemble of reliefs characterized by Δσ or, equivalently, W. What can be done is most simply illustrated for the case of a one dimensional chain of seamounts labeled i=1,2, ... , for which (4.1) becomes

$$(\omega-\sigma_*)a_i=(\sigma_i+S_i-\sigma_*)a_i+V(a_{i+1}+a_{i-1}) \qquad (4.3)$$

Rather than considering the eigenvalue problem, as part of whose solution the natural frequencies ω are determined, we fix the frequency ω near σ_*, specify a_1 and a_2, and solve for a_i, i=3,4,5 ... . If the individual site frequencies σ_i+S_i were all the same, then the solution would be a plane wave whose amplitude would neither grow or decay along the chain. But if the normal modes of the chain are all evansescent, then solutions of this 'Cauchy' problem with σ_i+S_i specified randomly within $\sigma_*\pm\Delta\sigma$ will ultimately grow exponentially along the chain for almost any initial values a_1 and a_2. Such exponential growth characterizes not only solutions of the one dimensional problem, but also solutions of the two dimensional problem of a long 'bar' of lattice sites. Numerical estimates of the growth rate must necessarily be made by solving such a Cauchy problem for bars of finite width; MacKinnon and Kramer (1983) carry out such studies and explain how the results are to be extrapolated to a bar of infinite width.

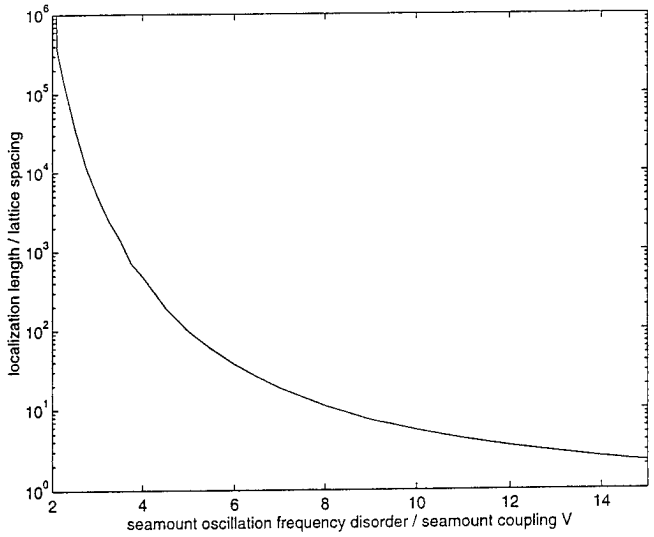


Figure 1. Localization length ξ/R (units of lattice spacing R) vs disorder $W = (\Delta\sigma/\sigma_*)/[6(a/R)^{-1}]$.

They find that the exponential growth scale or 'localization length' ξ (units of lattice spacing R) increases as W is decreased. Their numerical results are summarized in Figure (1). Thus if, for example, the ratio â/R of seamount radius to lattice spacing is 1/4, then a disorder $\Delta\sigma/\sigma_*$ of about 25% leads to a localization length of about five lattice spacings. If the lattice spacing is increased so that â/R is 1/6, then a disorder of about 4% results in a similar localization length. Identification of this exponential growth rate with the localization scale of the modes over the full lattice is discussed in the one dimensional case by Crisanti et al. (1993; the numerical results of MacKinnon and Kramer (1983) in two dimensions correspond to the largest possible horizontal localization scale of the modes over the full lattice.

5. Discussion

The Anderson model (4.1) was the result of supposing that the topographic Rossby modes over the entire seamount lattice are primarily composed only of individual seamount oscillations of angular order n=1. If the seamounts are not too dissimilar, then there will also be topograhic Rossby modes over the full lattice that are primarily composed only of individual seamount oscillations of angular order n=2, 3 ... as well. But for sufficiently high angular order or sufficiently great seamount disorder, indivdual seamount oscillations of different angular orders at different seamounts may have very similar frequencies, so that coupling between different angular orders can no longer be neglected. Thus, although the foregoing analysis shows that the highest frequency lattice modes are localized by disorder in seamount height, the assumption of small seamount height disorder made in going from (3.2) to (4.1) is violated at sufficiently small frequencies. The ultimate consequences of this are not presently understood.

The observation that the degree of localization induced by a given disorder in seamount frequency increases as the coupling V becomes smaller indicates that the inclusion of stratification or a free surface would have increased the degree of localization because individual seamount oscillations would then decay exponentially away from lattice sites.

The foregoing results suppose that $\beta=0$. If all the seamounts are identical save one and if the natural frequency of seamount oscillations of, say, angular order n=1 about that seamount in isolation falls outside the bands within which plane topographic Rossby waves propagate over the lattice of identical seamounts, then a disturbance initially localized at that seamount will not ultimately propagate entirely away. It may be shown that this continues to be true for sufficiently small but nonzero β. This suggests, but does not prove, a similar result for more general relief.

Acknowledgements. A. Miller and R. Salmon provided helpful discussions. C. D. Winant helped me with the preparation of the manuscript. This work was supported by the National Science Foundation, grant OCE88-00080.

REFERENCES

Anderson, P. W., 1958: Absence of Diffusion in Certain random Lattices. *Phys. Rev.*, **109**, 1492-1505.

Crisanti, A., G. Paladin and A. Vulpiani, 1993. Products of Random Matrices. Springer-Verlag, 161 pp.

Devillard, P, F. Dunlop and B. Souillard, 1988. *J. Fluid Mech.*, **186**, 521-538.

MacKinnon, A. and B. Kramer, 1983: The Scaling Theory of Electrons in Disordered Solids: Additional Numerical Results. *Zeit. für Physik*, **53**, 1-13.

Miller, A. M. , 1986. Nov-divergent planetary oscillations in mid-latitude ocean basins with continental shelves. *J. Phys. Oceanogr.*, **16**, 1914-1928.

Rhines, P. B., 1970: Wave Propagation in a Periodic Medium with Application to the Ocean. *Rev. Geophys. Space Phy.*, **8**, 303-319.

Focusing of Internal Waves and the Absence of Eigenmodes

Leo R.M. Maas
Netherlands Institute for Sea Research, P.O. Box 59, 1790 AB Texel, The Netherlands

Abstract The spatial structure of inviscid, monochromatic, internal waves in a uniformly stratified fluid is governed by the wave equation in spatial coordinates. Following *Magaard* (1962), solutions for this equation can be constructed by means of a recursive mapping. Solutions for a closed domain with supercritical side walls suggest that internal waves get focused to a fixed limiting trajectory, irrespective of the location where energy is introduced. As the focusing is accompanied by amplitude growth, this thus offers a mechanism by which 'mixing at a distance', along certain very special ray paths, may be accomplished. The location of the attracting trajectory is a fractal function of the frequency of the monochromatic wave. Solutions exist for *any* frequency of the wave field and thus no specific spatial patterns, 'eigenmodes', prevail.

Introduction

It is a well-known feature of plane internal waves, propagating through a uniformly-stratified fluid, that they retain their angle with respect to the horizontal upon reflection from a sloping bottom (*Phillips,* 1977). For a wave entering a subcritically sloping wedge (having a slope which is less than that of the energy flux vector) the reflecting wave, bouncing back and forth between bottom and surface, propagates into the wedge, see Figure 1. Upon each reflection from the bottom the amplitude and wavenumber increase and will eventually become so large that they will give rise to nonlinear and / or viscous effects. This implies that the energy, which the incoming wave field carries, will be deposited there and will locally contribute to mixing (*Wunsch,* 1968, 1969). If the basin, however, has a supercritical side-wall, incoming internal waves will be reflected back into the deep-sea region. It seems legitimate to wonder what happens if the (2D) basin consists of two opposing supercritical side-walls. Because, in that case, neither of the two corner regions will 'attract' the incoming internal wave, one might anticipate that the internal wave will be engaged in some complex process of criss-crossing of the basin. What exactly its ray path will be, however, is not immediately obvious.

When one looks for a stationary internal wave pattern of a particular frequency in an enclosed basin its streamfunction is determined by a hyperbolic equation in spatial coordinates that vanishes at the boundary. *Cushman-Roisin et al.* (1989) and *Münnich* (1993) each developed numerical algorithms that compute the structure of these patterns. The results seem to be partly at variance with analytical results that are discussed here and, more extensively, in *Maas and Lam* (1995; ML hereafter), due to the discretization of the bottom *Magaard* (1962, 1968) showed that the partial differential equation can, remarkably, also be solved by an implicit map, which relates the new position at which a wave ray reflects from the surface to its previous position. By supplying a streamfunction-related 'field variable' (carried invariantly along the ray) in a unique interval the streamfunction field is determined completely. Magaard applied this heuristically to a subcritical domain. It turns out that the map can be obtained explicitly for some simple bottom shapes, of which only the parabola will be considered here. With some modification this map can also be used for a basin with supercritical sidewalls, which enables us to address the question, raised above, quantitatively.

Bi-modal map

Consider a uniformly-stratified fluid in a parabolic basin with depth

$$H(x) = \tau(1 - x^2), \quad x \in [-1, 1] \tag{1}$$

and rigid lid at $z = 0$. The spatial structure of the streamfunction of a monochromatic wave of frequency ω is determined, in dimensionless form, by the canonical hyperbolic equation (see *e.g.* ML)

$$\frac{\partial^2 \psi}{\partial x^2} - \frac{\partial^2 \psi}{\partial z^2} = 0, \tag{2a}$$

where

$$\psi = 0 \quad \text{at} \quad z = 0, -H(x). \tag{2b,c}$$

The only non-dimensional quantity still appearing in this problem, Eq. (1), is the 'virtual' depth,

$$\tau = \frac{N D}{\omega L}, \tag{3}$$

which is the product of the aspect ratio (where D and L are the depth and half-width of the basin respectively) and the ratio of the buoyancy N and wave

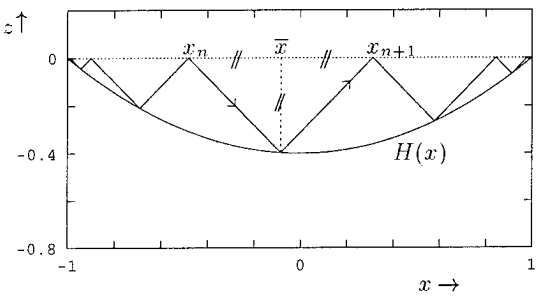


Figure 1. Sketch of a wave ray, propagating to the right in a parabolic basin given by (1) with $\tau = 0.4$.

frequency ω. This can, alternatively, be interpreted as a scaled period of the wave. *Magaard* (1962, 1968) shows that a solution of (2a), that also vanishes at the surface, is given by

$$\psi(x,z) = f(x-z) - f(x+z), \qquad (4)$$

for arbitrary function $f(x)$. Physically $f(x)$ is (except for a phase factor) related to the surface pressure, and its derivative to the horizontal velocity at the surface. Note that by adopting this kind of scaling the wave rays (along the directions of the characteristics $z = \pm\, x + const.$) always make an angle of 45^o with respect to the horizontal, regardless of frequency. This scaling has as its disadvantage that rays can be plotted for just one frequency at a time, but makes it easier to assess the ray diagrams. In particular, from Figure 1, it is obvious that successive surface reflections of a wave ray (denoted by x_n, $n = .., -1, 0, 1, 2, ..$) are related by

$$\frac{x_{n+1} - x_n}{2} = sH(\bar{x}), \qquad (5)$$

where $\bar{x} = (x_n + x_{n+1})/2$ and sign $s = +1, -1$ determines the two modes of the map for rightward and leftward moving characteristics respectively. The boundary condition at the bottom, $z = -H(x)$, then implies

$$f(x + H(x)) = f(x - H(x)). \qquad (6)$$

Applied at $\bar{x}$, Eq.6 and Figure 1 show that this implies that f is carried invariantly along the characteristic: $f(x_{n+1}) = f(x_n)$. From this Figure it is obvious that once we specify $f(x)$ for x-values in between two successive surface reflections of any arbitrary ray, then this function is determined over the whole interval $x \in (-1, 1)$. The parabolic bottom in (1) has maximum slope at its corners where it is $\pm 2\tau$. In the example of Figure 1 the topography is everywhere subcritical ($2\tau < 1$) and successive x_n approach the right ($s = +1$) or left ($s = -1$) corner respectively.

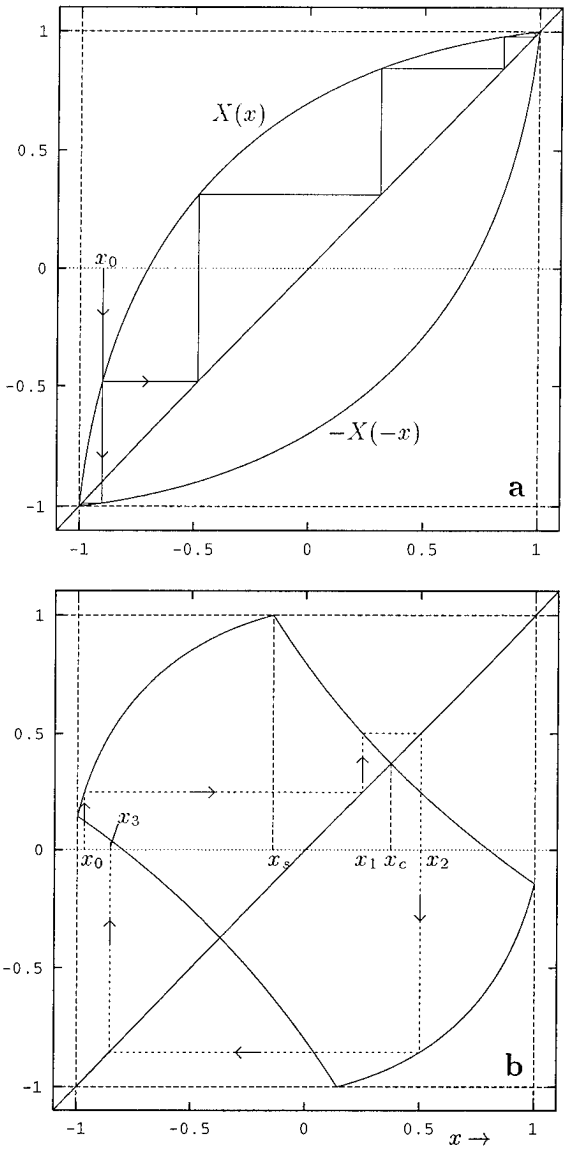


Figure 2. The bi-modal map for a) subcritical ($\tau = 0.4$) and b) supercritical ($\tau = 0.7$) values of the map parameter. Successive surface intersections are given by x_n, $n = 0, 1, 2, ...$ Special points are indicated as x_s and x_c, see Figure 3.

The corners act as *attractors*. This is also evident in a graph of the map that we obtain explicitly from (5) for $H(x)$ given by (1) as

$$X(x) = -x - \frac{1}{\tau} + \sqrt{\frac{4x}{\tau} + 4 + \frac{1}{\tau^2}}. \qquad (7)$$

Here the 'rightward map' ($s = +1$) is considered and the successor of x is denoted by $X(x)$. The successor of x with a leftward map leads to $-X(-x)$.

For subcritical topographies $\tau \leq 1/2$ the rightward and leftward map are decoupled (Figure 2a), when

$\tau > 1/2$, however, the corners are no longer attracting and the rightward and leftward map get coupled (Figure2b). Also, once $x > x_s$ — where x_s is the point whose rightward map brings it directly into the right-hand corner — the ray reflects downwards and its image is given by ML as

$$Y(x) = \frac{2}{\tau} - x - 2X(x). \tag{8}$$

At the same time, once this happens, the horizontal direction in which the ray propagates should be reversed and one should shift to the leftward map (lower curves in Figures 2a,b). A similar thing happens when the ray reflects from the leftward side of the basin, and again $s \to -s$. Figure 3 gives a geometrical construction of $Y(x)$ once the direct image of x, *i.e.* X, lies outside the physical domain. Also given in this diagram are

$$x_s = \frac{2}{\tau} - 3 \tag{9a}$$

and the point where the critical characteristic reflects from the surface

$$x_c = \frac{3}{4\tau} - \tau. \tag{9b}$$

These two 'points' play a special role in the subsequent part of this paper.

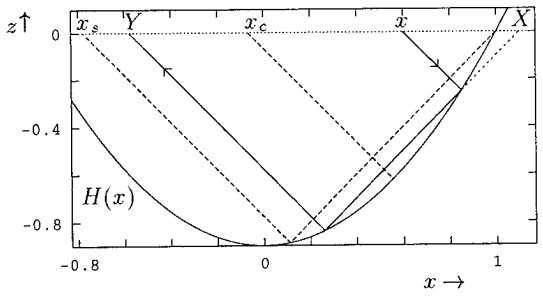


Figure 3. Construction of successive surface intersections of characteristics for a super-critically reflecting bottom. The critical characteristic (surface intersection x_c) and characteristic going through the right-hand corner (intersecting at x_s) are given by dashed lines. Note that X and Y are always each other's images for the rightward map.

Focusing of internal waves

With the bi-modal map given, the ultimate fate of a wave-ray can be obtained by iterating it both 'forward' (initially to the right) and 'backward' (initially to the left). In this way it can be observed

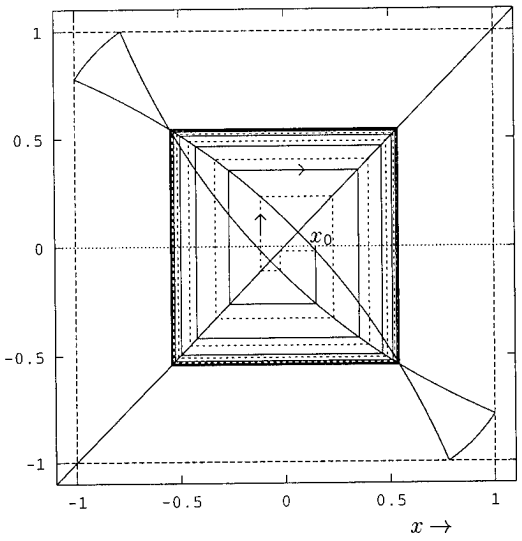


Figure 4. Bi-modal map (curved lines) and trajectories of a ray (rectangular lines) starting at x_0 for $\tau = 0.9$. Solid (dashed) lines indicate the ray that initially 'moves' to the right (left).

that the rays approach a limit cycle regardless of the direction which they start out with. In the example of Figure 4 this is a limit cycle characterized by *two* reflections from the surface (a period-2 attractor). For even-period attractors this attractor is always unique, for odd-period attractors each attractor also has a mirror-image, but the particular attractor favored asymptotically, *i.e.* for n large, depends both on the initial location and direction which the wave ray follows (see ML; this explains why in Figure 6 below, the odd-period attractors are asymmetric: the mirrored attractor also exists, but is not reached with the initial conditions used). The approach of the attractor can, of course, also be viewed in the physical domain, which is shown, for this value of τ, in Figure 5. Independent of the direction in which the rays leave x_0 initially, the attractor is asymptotically traversed in the same sense.

The shape of the attractor is a function of the dimensionless parameter τ, the scaled period of the internal wave. A nice way of presenting this is by plotting just the surface reflections of the attractor, that is of the asymptotic state of a wave ray (n large). In Figure 6 this has been presented for values of $\tau \in (1/2, 1)$. The lower boundary of this interval is determined by the requirement that the bottom be supercritical. The upper bound is arbitrarily chosen so as to guarantee that there is always at least one ray that is reflected simply forward (this is the corner point, $x = -1$, for $\tau = 1$). A similar pattern exists, however, in the next band $\tau \in (1, 3/2)$ (ML). It is observed that there exist regions where the 'qualitative charac-

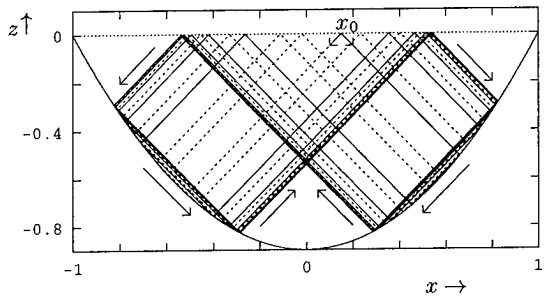


Figure 5. Construction of ray pattern for $\tau = 0.9$ and $x_0 = 0.15$ by iterated mapping. Right and leftward 'moving' characteristics are drawn as solid and dashed lines respectively. The final sense in which the limit cycle is traversed has been indicated by arrows.

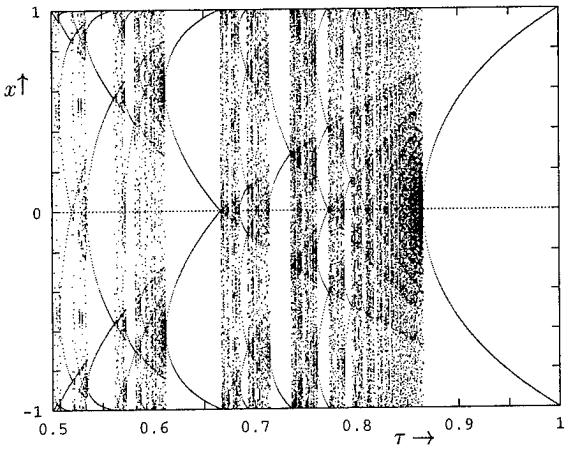


Figure 6. Plot of $x_{900} - x_{1100}$ for $x_0 = 0.123456789$ and $s = +1$ in the interval $1/2 \leq \tau \leq 1$, where τ is incremented with 1/1600 of this interval.

ter' of the attractor (the period, say) is invariant for small variations of τ, like the period-2 attractor discussed in Figures 4 and 5 in $1/2\sqrt{3} < \tau \leq 1$. These smooth bands are interrupted, however, by high period bands. Expansion of such bands shows that they qualitatively repeat these same features over and over again at ever reduced scales. As a function of τ the attractor, therefore, is fractal. Note that the wave rays are never diverging (chaotic), as has been verified by calculating Lyapunov exponents which are always less than or equal to zero (ML).

Specification of the wave field

It has been argued in the discussion on the subcritical parabolic bottom, Figure 1, that once $f(x)$ is specified in between any two successive reflections of an arbitrary wave ray then both $f(x)$ and, as a consequence, the streamfunction pattern are determined in the complete domain. This statement is modified in the case the bottom is (partly) supercritical and no complete classification is available yet. For the cases that the frequency (τ) is in the period-2 (or 4) band, *two* regions ('fundamental intervals') exist in which $f(x)$ can be arbitrarily specified, such that by its specification the solution is determined completely. In Figure 7 an example has been given for the period-2 region: $\tau = 0.9$. The intervals on which $f(x)$ can be freely specified are found by inspection and are given (Figure 7a) by $(-x_c, x_c)$ and $(-1, x_s)$. The latter range may also be replaced by the mirror interval $(-x_s, 1)$. It is observed that once we follow a beam of rays, originating in each of these fundamental intervals, in both the right and leftward direction (indicated by solid and dashed lines respectively), two regions are traced out in the physical $x-z$ plane, that are complementary to each other and that each ray is ultimately approaching the attractor. This indicates that once $f(x)$ is specified in the regions indicated at the top of Figures 7b and 7c, this field variable is determined over the whole region $x \in (-1, 1)$. This has been demonstrated for a particular choice of $f(x)$ in Figure 8a, being a sine, displaced differently in the two fundamental intervals. With this function $f(x)$ the streamfunction pattern $\psi(x, z)$ of the oscillatory streamfunction $Re[\psi(x, z)e^{i\omega t}]$, where t is time, can be determined as

$$\psi = \begin{cases} f(x-z) - f(x+z) & \text{in I} \\ f(a(z-x) - x + z) - f(x+z) & \text{in II} \\ f(x-z) - f(-a(x+z) - x - z) & \text{in III,} \end{cases} \tag{10a}$$

where regions I, II and III are defined as

$$\begin{aligned} \text{I} &: \{x, z\ ;\ |x| - 1 \leq z \leq 0\} \\ \text{II} &: \{x, z\ ;\ -H(x) \leq z < x - 1\} \\ \text{III} &: \{x, z\ ;\ -H(x) \leq z < -x - 1\}, \end{aligned} \tag{10b}$$

and

$$a(y) \equiv \frac{1 + \sqrt{1 + 4\tau(\tau + y)}}{\tau}. \tag{10c}$$

For $f(x)$ real, the resulting pattern is, formally, a spatially standing internal wave pattern. As in the study of internal waves approaching a wedge (*Wunsch*, 1968, 1969) it is unlikely, however, that the waves approaching the attractor ever get back (in order to form a standing wave) as other physical processes (like nonlinear and viscous effects), neglected sofar, will become active and drain the incoming energy flux, implying mixing along the attractor within the basin. A more correct solution would equally have to show an internal wave pattern just propagating *towards* the

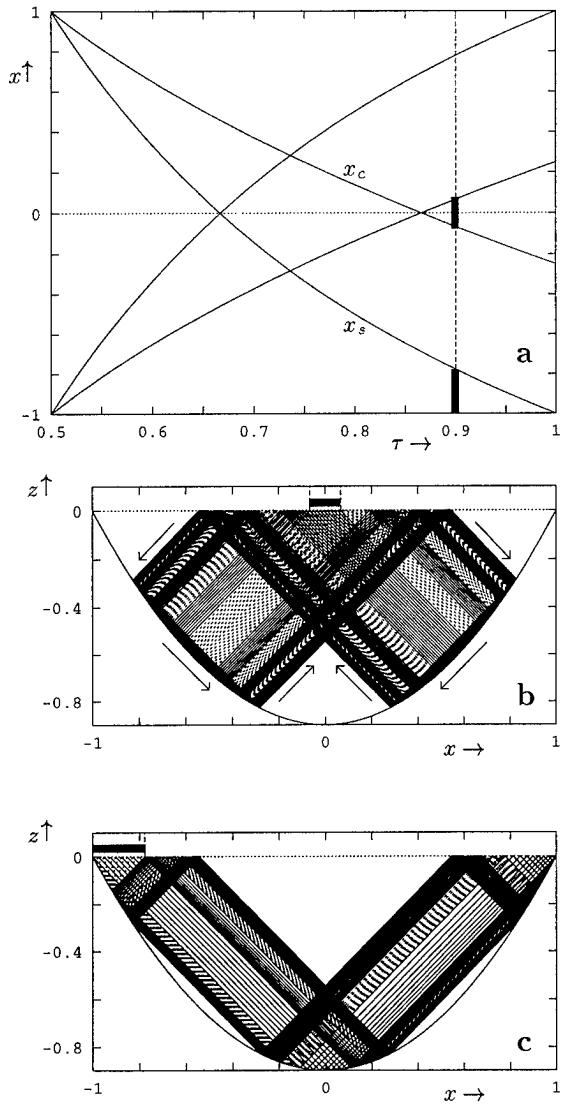


Figure 7. (a) Lines $\pm x_c(\tau)$ and $\pm x_s(\tau)$ as a function of τ. For $\tau = 0.9$ the fundamental intervals have been indicated. b) Rays coming from the inner and c) outer fundamental intervals in the specific 2-cycle case.

attractor. The technical implementation of this and the evaluation of a proper initial value problem are currently being studied.

Absence of eigenmodes

It has been expected that internal waves in enclosed stratified basins will be characterized by the existence of eigenmodes. This is suggested by the presence of such modes for the corresponding surface gravity wave problem and similar modes for interfacial waves in a two-layer fluid, referred to as internal seiches (*Defant*, 1941). Consider, for instance, the long wave modes that appear at the surface of a ho-

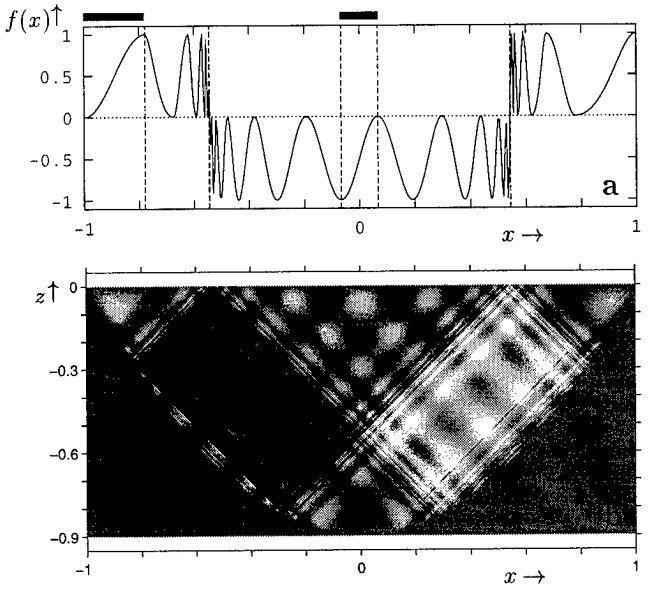


Figure 8. a) Function $f(x)$, specified in the two fundamental intervals (parts of x-axis indicated at the top, corresponding to those indicated on the dashed line of Figure 7a), and subsequently calculated values of $f(x)$ in remaining parts of domain for $\tau = 0.9$. b) Spatial structure of streamfunction field, $\psi(x, z)$, obtained from $f(x)$ with Eq. (10).

mogeneous fluid in a one-dimensional basin $x \in (0, 1)$ of constant depth. The horizontal velocity field is determined by the wave equation

$$\frac{\partial^2 u}{\partial t^2} - \frac{c^2}{L^2}\frac{\partial^2 u}{\partial x^2} = 0. \qquad (11)$$

Here L denotes the basin length and c is the long wave speed. For monochromatic waves, $u(x) \propto e^{i\omega t}$, solutions, $u_n(x) = \sin n\pi x$, vanishing at the sides of the basin, determine a discrete set of frequencies

$$\omega'_n = n\pi,$$

where frequency has been nondimensionalized with L/c: $\omega' = \omega L/c$. The existence of eigenmodes is useful because, when they form a complete set, the forcing — which in the above example should appear at the right-hand of (11) with a spatial part $F(x)$, say — can be projected on the eigenmodes and the solution of the forced problem can subsequently be written down as the sum over the eigenmodes

$$u = \sum_{n=1}^{\infty} \frac{F_n}{\omega'^2 - \omega'^2_n} \sin n\pi x,$$

weighted with amplitudes, F_n, that are determined by the projections of the forcing

$$F_n = \int_0^1 F(x) \sin n\pi x dx.$$

Münnich (1993, 1994) noted that this correspondence breaks down once the fluid is continuously stratified. This phenomenon is foreshadowed by the degeneracy of the 'eigenmodes' that appear in a rectangular, stratified basin. For a streamfuncion field describing linear internal gravity waves, $\psi(x,z)e^{i\omega t}$, the spatial pattern is determined by

$$\frac{\partial^2 \psi}{\partial x^2} - \omega'^2 \frac{\partial^2 \psi}{\partial z^2} = 0,$$

where the wave frequency has here been normalized with the buoyancy frequency and the aspect ratio, and the rectangle is given by $x, z \in [0,1] \times [0,1]$. With vanishing streamfunction at the boundary solutions are obtained as

$$\psi(x,z) = \sin n\pi x \sin m\pi z, \qquad (12a)$$

provided

$$\omega'_{n,m} = \pm \frac{n}{m}, \qquad (12b)$$

for natural numbers n, m. As *Münnich* (1993, 1994) remarks, it is clear from (12) that, first of all, the 'eigenfrequencies' $\omega'_{n,m}$, being rational, are no longer well-seperated — they are *dense* within the real numbers — and, second, that the 'eigenmodes' are no longer unique, as any common multiple, $j \in \mathbf{N}$, of n and m leads, by (12b), to the same eigenfrequency but has a mode structure (12a) that is the j-tuple of the original mode. As is observed in ML this implies that for this geometry, in the case of forcing, we can circumvent the forward and backward discrete Fourier transform and are able to construct the solution directly from the specified forcing by means of the ray method.

These results apply also to nonrectangular basins, except that the degeneracy, as Figure 6 shows, is even worse, because 'eigenmodes' exist for frequencies within *compact* domains and are, within the fundamental intervals, completely arbitrary. Instead, for the parabola discussed here, there is just a discrete set of wave frequencies for which *no* stationary internal wave pattern exists. It is clear that by this time the 'eigenmode' has lost all its specificness and this terminology is no longer useful. The 'failure of the eigen value approach' has previously been noted by *Cushman-Roisin et al.* (1989), but the way the bottom is discretized in their numerical approach (by a set of horizontal and vertical line segments) precludes the identification of the focusing phenomenon.

Acknowledgements

The author is grateful to Peter Müller for organizing a stimulating conference. TeXnical assistence by Frans-Peter Lam during the preparation of the manuscript is equally appreciated.

References

Cushman-Roisin, B., V. Tverberg and E.G. Pavia, 1989: Resonance of internal waves in fjords: a finite-difference model. *J. Mar. Res. 47*, 547-567.

Defant, A., 1941: *Physical Oceanography, Vol. II*, Pergamon Press.

Maas, L.R.M. and F.-P.A. Lam, 1995: Geometric focusing of internal waves, *submitted to J. Fluid Mech.*

Magaard, L., 1962: Zur Berechnung interner Wellen in Meeresräumen mit nicht-ebenen Böden bei einer speziellen Dichteverteilung. *Kieler Meeresforschungen 18*, 161-183.

Magaard, L., 1968: Ein Beitrag zur Theorie der internen Wellen als Störungen geostrophischer Strömungen. *Deutsche Hydrogr. Zeitschr. 21*, 241-278.

Münnich, M., 1993: On the influence of bottom topography on the vertical structure of internal seiches. Dissertation ETH Zürich, 97 pp.

Münnich, M., 1994: The influence of bottom topography on internal seiches in continuously stratified media. In:*Hopfinger, E. B. Voisin and G. Chavand; Preprints of the Fourth International Symposium on Stratified Flows, Vol. 2*, 8pp.

Phillips, O.M., 1977: *The dynamics of the upper ocean, 2nd ed.*, Cambridge University Press.

Wunsch, C., 1968: On the propagation of internal waves up a slope. *Deep-Sea Res. 15*, 251-258.

Wunsch, C., 1969: Progressive internal waves on slopes. *J. Fluid Mech. 35*, 131-144.

Topographic Filtering and Reflectionless Transmission of Long Waves

Leo R.M. Maas
Netherlands Institute for Sea Research, P.O. Box 59, 1790 AB Texel, The Netherlands

Abstract The equation governing the passage of monochromatic, long waves over variable topography can be transformed into a Schrödinger equation. There are several transformations accomplishing this. A 'naive' transformation (in which only the horizontal coordinate is stretched) has a 'potential' that is non-vanishing, even if the slope in topography vanishes. A transformation, in which also the surface elevation field is stretched, has a 'potential' vanishing outside the sloping region. This transformation has the property that it displays scattering against a background of adiabatic variations. That is, the plane waves that result if the potential is approximated to vanish identically, display amplitude and wave length variations, in the original frame, as in WKB-theory. For smooth bottom profiles, typical for the continental slope, the potential has a positive lobe, the top of which acts as a 'topographic cut-off frequency'. This lobe is missed by piecewise-linear topographies. The trapped modes of the adjacent negative side lobe are the topographic Rossby wave modes. For a particular smooth bottom-profile, long waves, coming from a specific direction, can be shown to pass reflectionless.

Schrödinger equation

It is often instructive to consider scattering problems in terms of a Schrödinger equation, because it allows one to qualitatively assess the local nature of the wave field under consideration. The relevance of this equation for the long-wave equations is discussed in the next section. The Schrödinger equation,

$$\frac{d^2\Psi}{dx^2} + [E - V(x)]\Psi = 0, \qquad (1)$$

describes the shape of the state variable $\Psi(x)$, related to the wave field, $\psi(x,t) = \Psi(x)e^{-i\sigma t}$, (with t denoting time and σ the frequency), due to inhomogeneities of the 'medium' through which the wave propagates as a function of the coordinate x. The variations of the medium are here represented by the 'potential' $V(x)$. For localized variations of the medium it is natural to expect the potential to vanish outside the x-region for which these variations occur. For values of the 'energy' E greater than the maximum value of the potential, V_{max}, (like E_1 in Figure 1) the quantity in square brackets in (1) is everywhere positive and hence the solution is locally sinusoidal. It is therefore expected that the wave will not be greatly attenuated by the scattering potential. If E drops below this maximum, but is otherwise positive (E_2 in Figure 1), this quantity is negative over some x-interval and hence the wave field will be exponentially decaying over this range leading to great attenuation of an incoming wave field: waves can pass only through 'tunneling'. For negative values of the 'energy', $V_{min} < E < 0$, like E_3 in Figure 1, trapped waves can exist. Finally, for still lower values, like E_4, wave solutions no longer exist. Here we will concentrate on positive values of the 'energy' parameter, E. Actually, this quantity is usually not related to the true energy of the wave field, but rather is to be regarded a metaphor for the frequency of the wave involved. Therefore, for an incoming spectrum of waves, the existence of a maximum in the potential, V_{max}, can directly be interpreted as a (soft) cut-off frequency: for waves with energy (frequency) well above it, waves can pass unimpeded, for waves with energy (frequency) below V_{max}, waves are strongly attenuated. The cut-off frequency is *soft*, however, since no rigorous cut-off (zero transmission) of the incoming wave field below this frequency is implied. A potential like the one shown in Figure 1 thus acts as a high-pass filter.

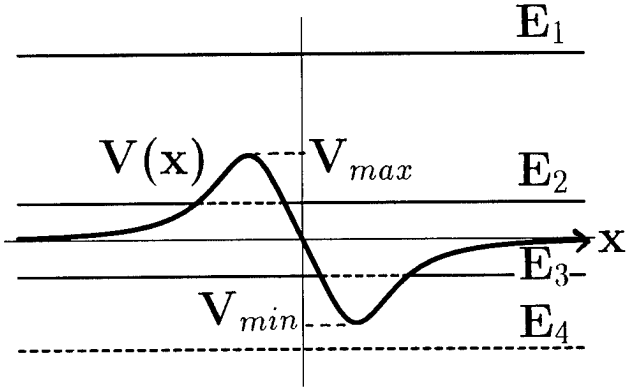


Figure 1. Sketch of a 'typical' potential $V(x)$ and four levels of the energy, E_1 to E_4. Solid (dashed) parts of the energy levels refer to sinusoidal (exponential) behaviour of the wave field.

Topographic filtering

Consider a long, plane wave propagating on an f-plane at the surface of a homogeneous fluid incident on a smoothly and monotonically varying topography $H(x)$. Let the surface elevation take the form $\zeta(x)\exp(ily - i\sigma t)$. Here l indicates the wavenumber in the along-slope direction y. We non-dimensionalize with length (L) and depth (H_0) scales appropriate to the shelf edge and with the inertial frequency, f:

$$\mathbf{x} \to L\mathbf{x},\ l \to l/L,\ H \to H_0 h(x),\ \sigma \to f\sigma,$$

where $h(x)$ is a nondimensional shape-function, modeling the shelf edge. The cross-isobath structure of the elevation field, $\zeta(x)$, is then determined by

$$\frac{d}{dx}\left(h\frac{d\zeta}{dx}\right) + \left[\epsilon^2(\sigma^2-1) - l^2 h - \frac{l}{\sigma}\frac{dh}{dx}\right]\zeta = 0. \quad (2)$$

Here $\epsilon = L/R$ is the ratio of the external scale L and the Rossby deformation scale, $R = \sqrt{gH_0}/f$. The square of ϵ is known as the divergence parameter. In general this is a small quantity. For instance, taking $H_0 = 1$ km, $L = 100$ km, $g = 10m^2s^{-1}$, $f = 10^{-4}s^{-1}$ one obtains $\epsilon = 10^{-1}$. However, since the theory may equally be applied to interfacial waves this quantity may be order one. In this case depth is replaced by equivalent depth, $h_e(x) = h_1 h_2(x)/(h_1 + h_2(x))$ and gravity, g, by reduced gravity g', being equal to g multiplied by the relative density difference of thetwo layers. Typical values of these lead to a phase speed of about one-hundredth of its value in the barotropic case.

Equation (2) can be 'naively' transformed to a Schrödinger equation by multiplying it with h and identifying hd/dx with $d/d\xi$, which amounts to a stretching of the horizontal coordinate,

$$\xi = \int_0^x \frac{1}{h(x')}dx', \quad (3)$$

in inverse proportion to water depth. The equation then takes the form

$$\frac{d^2\zeta}{d\xi^2} + \left[\epsilon^2(\sigma^2-1)h(\xi) - l^2h^2(\xi) - \frac{l}{\sigma}\frac{dh}{d\xi}\right]\zeta = 0, \quad (4)$$

where $h(\xi) = h(x(\xi))$. This equation was employed by *Saint-Guily* (1976), who, for the depth profile

$$h(\xi) = 1 + \lambda\tanh\xi, \quad (5)$$

with $\lambda \in (-1, 1)$, was able to calculate the *trapped* modes — the topographic Rossby waves — exactly. For the case of *free, propagating* waves, however, the potential is not 'physically realistic' as one may observe by concentrating for example on waves of normal incidence ($l = 0$). In this case (4) simplifies to

$$\frac{d^2\zeta}{d\xi^2} + \epsilon^2(\sigma^2-1)h(\xi)\zeta = 0,$$

which, for the tanh-shaped topography considered, leads to a potential that is non-vanishing at infinity and therefore does not satisfy the requirement that the scattering be localized.

For this reason a transformation is employed that stretches not only the horizontal but also the vertical coordinate (the elevation). Discussion is for the sake of simplicity here limited to waves of normal incidence ($l = 0$), for which case (2) takes the form

$$\frac{d}{dx}\left(h\frac{d\zeta}{dx}\right) + \epsilon^2(\sigma^2-1)\zeta = 0. \quad (6)$$

The general case of obliquely incident waves can be treated likewise. If we now adopt the following stretching (*Morse and Feshbach,* 1953, p.730)

$$\xi = \int_0^x \frac{1}{\sqrt{h(x')}}dx',\ \zeta = \frac{Z}{h^{1/4}}, \quad (7)$$

then (6) takes the form

$$\frac{d^2Z}{d\xi^2} + \left[\epsilon^2(\sigma^2-1) - \frac{1}{h^{1/4}}\frac{d^2h^{1/4}}{d\xi^2}\right]Z = 0,$$

which is a Schrödinger equation once we identify energy and potential as $E = \epsilon^2(\sigma^2-1)$ and $V(\xi) = h^{-1/4}d^2h^{1/4}/d\xi^2$ respectively. This shows that 'energy' E is indeed related to frequency σ. Since the second ξ-derivative of $h^{1/4}$ is related to first and second x-derivatives of the topography $h(x)$ (see below), which vanish away from the sloping region, it is evident that this form of the potential does also vanish outside that region and hence is of the localised form we expect it to have as a scattering potential. Also, the expression for E nicely identifies its positive values with freely propagating, superinertial ($\sigma > 1$) waves and its negative values with trapped, subinertial ($\sigma < 1$) waves.

Without actually solving the resulting equation a number of inferences can be drawn from the form it has.

First, assume that we are dealing with energy-values (frequencies) which are much greater than the maximum value of the potential $E >> V_{max}$. Then, we can approximate the potential by assuming that it vanishes identically, $V(\xi) = 0$. In this case, the solutions in the transformed plane consist, of course, of plane waves of the form $Z = Z_0\exp(\pm i\sqrt{E}\xi)$. In the original frame this solution reads

$$\zeta = \frac{Z_0}{h^{1/4}} \exp(\pm i\sqrt{E} \int_0^x \frac{1}{\sqrt{h(x')}} dx' - i\sigma t),$$

which contains wave number variations (the x-derivative of the phase factor) inversely proportional to $\sqrt{h}$ and amplitude variations inversely proportional to $h^{1/4}$. The latter is known as Green's law (*Mei*, 1989). These are consistent with adiabatic variations such as occur in WKB approximation, which would have group velocity c_g and phase velocity proportional and hence wave number variations inversely proportional to $\sqrt{h}$, and which would require conservation of energy flux, proportional to $|\zeta|^2 c_g$. Since amplitude (and wave number) variations associated with adiabatic changes do not form part of the scattering process the physically appropriate frame of reference in which to consider scattering is that based on (7). Any amplitude and wave number variations obtained in that frame are truely associated with scattering.

Second, consider a typical monotonic shelf edge, like $h^{1/4} = 1 + \lambda \tanh \xi$, which is similar to the topography employed by *Saint-Guily* (1976) except that it now applies to the quarter power of the topography. Then, the potential takes the form

$$V(\xi) = -2\lambda \frac{T(1-T^2)}{1+\lambda T},$$

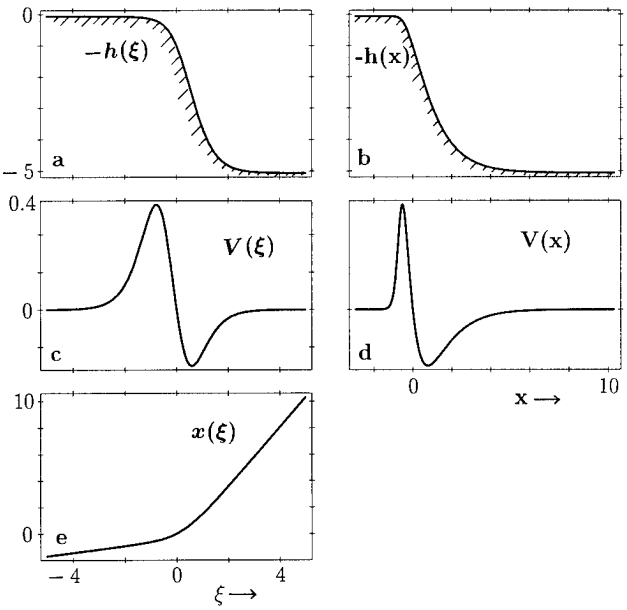


Figure 2. Sketches of the topography $h(\xi) = (1 + \lambda \tanh \xi)^4$ for $\lambda = 1/2$ as a function of ξ (a) and, parametrically, of x (b). The potential $V(\xi) = h^{-1/4} d^2 h^{1/4}/d\xi^2$ can be obtained from these, both in the transformed (c), as well as, again parametrically, in the original frame (d). Here the x-dependence on ξ is given by $x = \int_0^\xi \sqrt{h(\xi)} d\xi = \xi(1+\lambda^2) + 2\lambda \ln[\cosh \xi] - \lambda^2 \tanh \xi$, see (e).

where $T \equiv \tanh \xi$, see Figures 2 and 3a. The potential is observed to have the typical two-lobed shape adopted in the discussion of Figure 1, the positive lobe extending over the top of the shelf edge. The position of the maximum value of the potential, T_{max}, as well as its value at this position, V_{max}, can be determined analytically as a function of the 'depth-contrast parameter' λ. Their expressions are rather cumbersome and are therefore just shown graphically (Figure 3b). Now, since the topology of the problem would not change when we vary the shape of the monotonically sloping topography, we may expect the occurence of a positive lobe ($V(\xi) > 0$ for some range of ξ) to be a generic feature of this scattering problem. Therefore, following the discussion in the introduction, one may infer that there exists a topographic cut-off frequency $\sigma_T \equiv (1 + \epsilon^{-2} V_{max}(\lambda))^{1/2}$, for *any* monotonically-sloping topography, which is a function of the geometrical parameters (the divergence parameter ϵ^2 and the depth-contrast parameter λ). For the parameters considered previously $\epsilon = 10^{-1}$, and for $\lambda = 1/2$, which has $V_{max} \approx 1/2$, we obtain $\sigma_T \approx 7$. For interfacial waves, with $\epsilon \approx 1$, σ_T approaches the inertial frequency even closer ($\sigma_T \downarrow 1$). It is likely that this quantity σ_T must be observable as a dividing frequency when comparing adjacent directional deep-sea and shelf spectra, such that for $\sigma > \sigma_T$, waves can pass the sloping region fairly easy (and vice versa).

Third, expanding the expression of the potential we find

$$V = \frac{1}{4h}\frac{d^2h}{d\xi^2} - \frac{3}{16}\left(\frac{1}{h}\frac{dh}{d\xi}\right)^2 = \frac{1}{4}\frac{d^2h}{dx^2} - \frac{1}{16h}\left(\frac{dh}{dx}\right)^2.$$

Since $h > 0$ for all x, the second term in the last expression at the right is always negative. Hence the potential is positive only because of the existence of the first term in that expression, which is related to the (convex) curvature of the topography at the top of the shelf slope (*Meyer*, 1979). It is clear that

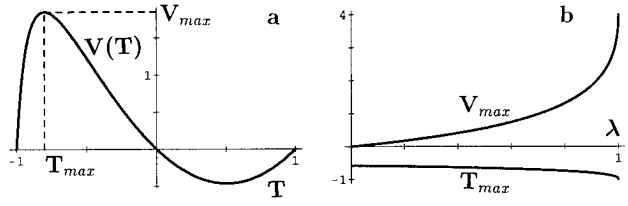


Figure 3. (a) Potential V as a function of T for $\lambda = 0.9$. Since $T \equiv \tanh \xi$ is a monotonic function of ξ this is a compact way of representing the ξ-dependence of the potential. In this figure the position, T_{max}, and value of the peak of the potential, V_{max}, have been indicated, which are shown as a function of λ in (b) and (c).

this term would be absent in piecewise linear topographies, which would therefore exclude the phenomenon of tunneling and, to some extent, topographic filtering.

Reflectionless transmission

Another artifact would actually be introduced when approximating a smooth, monotonic topography by a piecewise-linear topography. This is the spurious phenomenon of reflectionless transmission at certain discrete wave frequencies (which have wave lengths that are multiples of twice the size of the linearly sloping region). It is generally regarded that the occurence of these reflectionless frequencies is not realistic (*Kajiura,* 1963; *Meyer,* 1979; *Mei,* 1989). Indeed, for a *smooth* monotonic profile, *Kajiura* (1963) showed that the transmission coefficient is a steadily decreasing function of frequency. Reflectionless transmission of normally-incident long waves over smooth topographies is found only for (symmetric) ridges. *Fitz-Gerald* (1976) obtained this result semi-analytically without restriction on wave length by an iterative scheme (see also *Rouseau,* 1952).

Surprisingly, as will be shown below, reflectionless transmission may also occur for a smooth, monotonically-increasing depth profile. This occurs for a particular angle of incidence of the long waves. Ironically, this can be demonstrated most easily by employing the naive transformation (3) and using the *Saint-Guily* (1976) topography (5). Eq. (4) then reads

$$\frac{d^2\zeta}{d\xi^2} + \left[E - l^2(1+\lambda^2) + \lambda(E-2l^2)\tanh\xi \right.$$

$$\left. -l\lambda(\frac{1}{\sigma} - l\lambda)\mathrm{sech}^2\xi\right]\zeta = 0.$$

This is of the form

$$\frac{d^2\zeta}{d\xi^2} + \left[E' + n(n+1)\mathrm{sech}^2\xi\right]\zeta = 0,$$

with $n \in \mathbb{N}$, for which *Kay and Moses* (1956) showed that the potential is reflectionless for any positive value of the energy E' (see also, *Lamb,* 1980). Identifying coefficients between these equations we find that long waves are able to pass the tanh-shaped shelf edge reflectionless provided

$$E = 2l^2, \tag{8}$$

and

$$l\lambda(\frac{1}{\sigma} - l\lambda) = -n(n+1). \tag{9}$$

Because $E' = E - l^2(1+\lambda^2)$ we verify from (8) that E' satisfies the positivity constraint: $E' = l^2(1-\lambda^2)$. Since

$$E = \epsilon^2(\sigma^2 - 1), \tag{10}$$

which, from the dispersion relation applied in the far field, equals $h(l^2+k^2)$, we find, assuming the waves to enter from the deep region, where $h = 1+\lambda$,

$$E = (1+\lambda)\frac{l^2}{\sin^2\alpha}.$$

Here the absolute value κ of the wavenumber vector $\mathbf{k} = (k,l) = \kappa(\cos\alpha, \sin\alpha)$ that makes an angle α with the x-direction, has been replaced in terms of l and α. Hence, inserting this expression for E in (8) and eliminating l^2, we find that waves coming from directions α_* determined by

$$\sin^2\alpha_* = \frac{1+\lambda}{2} \tag{11}$$

are able to pass this shelf edge reflectionless, provided they satisfy also the second constraint (9). From (10) and (8) we obtain σ as a function of $b \equiv l\lambda$:

$$\sigma = \sqrt{1+a^2b^2}, \tag{12}$$

where $a^2 = 2/\lambda^2\epsilon^2$. Inserting this into (9) and plotting both the left and right-hand sides of this equation as a function of b (Figure 4), we find at their intersections the wave numbers for which waves coming from directions determined by (11) are able to pass the shelf edge reflectionless. From (12) their frequencies can be obtained. For $a > 1$, these are approximately determined by the two asymptotic (dashed) curves of Figure 4 which lead to

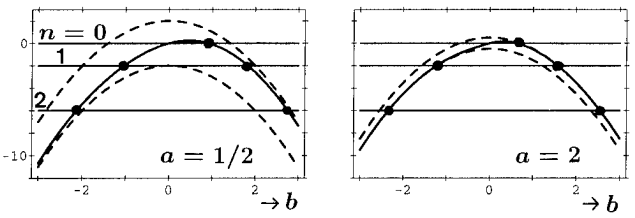


Figure 4. Plot of $b/\sqrt{1+a^2b^2} - b^2$ and $-n(n+1)$ (solid lines) as a function of b for two values of a and integer $n \in \{0,1,2\}$. Heavy dots indicate values of b (*i.e.* scaled along-isobath wavenumber l) for which waves, coming from a direction α_* given by (11), are able to pass the tanh-shaped shelf edge reflectionless. Dashed lines indicate the two asymptotes $\pm 1/a - b^2$.

$$\sigma_n^2 = 1 + \frac{l}{|l|}a + a^2 n(n+1), \quad n \in \mathbb{N}.$$

For $n = 0$ only one physically realistic solution is obtained, having the coast at its left (in the Northern Hemisphere), seen from the along-shelf propagation direction ($l > 0$). The expression of the frequency for general values of a is slightly more involved.

Conclusions

It is shown qualitatively that a monotonically-sloping shelf edge generally acts as a topographic filter for incoming long super-inertial waves. This filter can be characterized by a (soft) cut-off frequency above (below) which waves can pass the topography without (with) much attenuation. This frequency is solely dependent on parameters characterizing the geometry of the problem (topographic scales, latitude and earth rotation rate). The filtering properties are crucially dependent on the existence of a convex part of the bottom shape at the top of the shelf edge. It provides the positive lobe of the localized potential in the Schrödinger equation to which the scattering problem can be transformed. It is attractive to view this positive lobe of the potential of a shelf edge as providing a natural shield by which the shelf region is 'protected' against incoming waves. Each shelf edge, however, also has an Achilles' heel. It is transparent for waves of particular discrete frequencies, coming from two directions determined by the 'depth-contrast parameter', that are able to pass the shelf edge without any reflection. These are the two directions for which the shelf edge under consideration is particularly 'vulnerable'. Although no parameter-sensitivity analysis of these results has been made yet it is conjectured that a true shelf edge should show its 'vulnerability' over some range of angles and frequencies around those calculated. It would be useful, therefore, to make a catalogue for shelf edges around the world identifying these reflectionless angles and frequencies at each location.

References

Fitz-Gerald, G.F., 1976: The Reflexion of plane gravity waves traveling in water of variable depth, *Phil. Trans. Roy. Soc. London A, 284,* 49-89.

Kajiura, K., 1963: On the partial reflection of water waves passing over a bottom of variable depth, *Proc. Tsunami Meetings 10th Pacific Science Congress. IUGG Monograph, 24,* 206-234.

Kay, I., and H.E. Moses, 1956: Reflectionless transmission through dielectrics and scattering potentials, *J. Appl. Phys., 27,* 1503-1508.

Lamb, G.L., jr., 1980: *Elements of soliton theory,* Wiley-Interscience, New-York.

Mei, C.C., 1989: *The applied dynamics of ocean surface waves,* World Scientific, Singapore.

Meyer, R.E., 1979: Surface-wave reflection by underwater ridges, *J. Phys. Ocean., 9,* 150-157.

Morse, P.M., and H. Feshbach, 1953: *Methods of Theoretical Physics I,* McGraw-Hill, New York.

Rouseau, M., 1952: Contribution a la théorie des ondes liquides de gravité en profondeur variable *Publ. Sci. et Techniq. du Min. de l'air, 71,* 275.

Saint-Guily, B., 1976: Sur la propagation des ondes de seconde classe le long d'un talus continental, *C.R. Acad. Sci. Paris, 282,* 141-144.

Circulation, Exchange and Mixing at the Ocean-Shelf Boundary

J.M. Huthnance

Proudman Oceanographic Laboratory, Bidston Observatory, Birkenhead, Merseyside L43 7RA, UK

Abstract. The coastal ocean meets the deep sea at the continental shelf edge. Steep bathymetry may inhibit ocean-shelf exchange, but in combination with stratification gives rise to special processes and modelling challenges. A preliminary assessment is made of potentially influential processes in ocean-shelf exchange, water-mass structure and general circulation, according to their scales and context: internal tides and waves; upwelling, fronts and filaments; downwelling, cascading; along-slope currents, instability and meanders; eddies; tides, surges and coastal-trapped waves. Present and planned measurements to improve this assessment are discussed; also implications and prospects for modelling.

Introduction

Interest in the continental shelf edge has increased in recent years. For example, exchanges and the possibility of an active ocean-shelf boundary, with particular shelf-edge contributions to fluxes, are of topical interest for global fluxes, budgets and their response to climate change and human activities (e.g., Wollast, 1993). Physical processes underlie shelf-water characteristics and many such fluxes.

The need for improved process understanding is illustrated by contrasting satellite remote-sensed images west of Scotland. A sharp shelf-edge boundary to a coccolithophore bloom on 17 May 1980 (CZCS; Pingree and Mardell, 1981) suggests a strong bathymetric constraint, whereas the water mass boundary (to the Scottish Coastal Current) showing on 13 April 1981 (IR; Booth and Ellett, 1983) is on the shelf, suggesting freer exchange across the shelf edge. Moreover, the spatial and temporal measurement scales required for flux estimates remain unknown in general.

Currents varying on time-scales of days or longer tend to be constrained by geostrophy to flow along depth contours, inhibiting ocean-shelf exchange. Other factors may facilitate exchange:

- processes enhanced or special to the shelf edge (e.g., Huthnance, 1981)
- proximity to the equator (weaker geostrophic constraint)
- friction relaxes the geostrophic constraint, notably in Ekman layers
- shorter-scale excursions combined with non-conservative processes, for net <uC>.

Unfortunately, coherent estimates of <uC> checked by budget closure are rare.

This lack of naive estimates of flux suggests a more informed approach through process understanding, and model development and testing for representation of processes. Then extrapolation and integration over processes, space (context) and time can be carried out by extending the models.

Initial Assessment of Processes

The following have been considered as potentially influential processes in ocean-shelf exchange, water-mass structure and general circulation, according to their scales and context:

- coastal trapped waves
- along-slope currents
  - western boundary currents
  - relation to ocean circulation
    - boundary current separation
    - secondary circulation
  - instability, meanders, eddies
- Ekman transport and upwelling
  - jets, squirts and filaments
  - downwelling and cascading
- tides, storm surges, inertial currents
- fronts
- internal tides and waves
- surface waves
- capes and canyons
  - cross-contour flow
  - local upwelling
  - wave reflections

For this purpose, literature has been reviewed, and theory and previous measurements interpreted. More details are in Huthnance (1995).

Interim Conclusions by Process

Coastal trapped waves underlie and control phenomena important to ocean-margin circulation, exchange and mixing, rather than making an independent contribution. Their magnitude is generally determined by the forcing of a "primary" phenomenon. They propagate effects of forcing from one location to another along the shelf, and may make a distinctive contribution to the magnitude of circulation and exchange, via a near-resonant response or

propagation to a shelf/slope sector of.different character (e.g., narrower). We still lack a complete description of super-inertial waves.

Along-slope currents may be driven with speeds O(0.1 m/s) by a variety of forcing mechanisms: fresh-water runoff: the oceanic density and associated pressure field; winds - either steady or unsteady with biased form drag; upwelling; non-linear waves, tides or eddies; geostrophic adjustment following mixing. Transfer and deposition of momentum by internal lee waves may redistribute the current. Different cross-slope distributions and ageostrophic cross-slope "secondary" circulation correspond to the different types of forcing, which still need to be resolved in many contexts. Along-slope continuity (distinguishing dynamics, transport, and water mass) remains an issue. The relation to oceanic circulation needs further clarification, with scope for investigation using simple ocean models and a cross-slope section (Fig. 1). Existing model solutions appear to be partial, e.g., Huthnance (1984) omits the effect of stratification on the sloping boundary layers; boundary solutions reviewed by Garrett *et al.* (1993) typically omit alongslope pressure gradients representing sustained forcing, alongshore flow divergence and time-dependence, any of which may assist cross-slope flow and matching to oceanic flow. *Western boundary currents* appear to be distinct as part of the ocean circulation, and show (relative to their greater strength of order 1 m/s) limited exchange with the shelf; *eddies* and streamers in Gulf Stream Warm Core Rings (for example) do show some exchange.

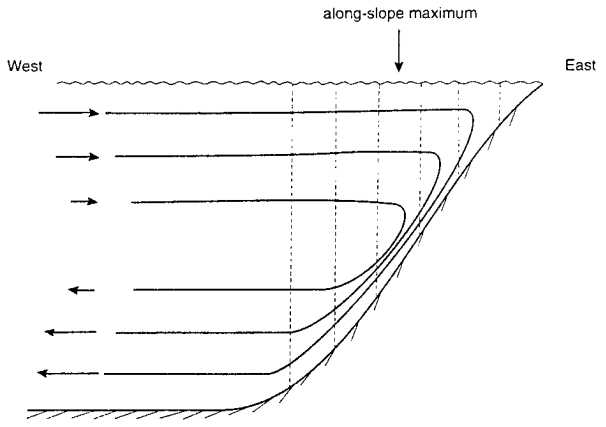


Figure 1. Schematic cross-slope section. Streamlines of cross-slope exchange (—) match the baroclinic shear (→) associated with the oceanic density field and form the Ekman transport under an along-slope current (velocity contours ---). However, solutions allowing for buoyancy forces in this section are the subject of continuing research.

Upwelling and *downwelling* juxtapose ocean and shelf waters in structures depending on the context and duration of forcing. Hence they enable mixing to change water masses and bring about ocean-shelf exchange, especially locally in jets and filaments. *Cascading* (e.g., Fig. 2) also tends to be local, the result of dense water (e.g., from winter cooling or salinated by evaporation or ice formation) finding a route off the shelf below the less dense adjacent slope water. Initially, cascading may be caused by instability of the flow in geostrophic balance with the cross-slope gradient of density, or it may be in the bottom Ekman layer under this flow; then any depression in the shelf edge is liable to facilitate and concentrate the process; hydraulic control may then operate. There is a need for measurements over long periods to improve statistics and estimates of the magnitude, space- and time-scales of these often intermittent and seasonal events.

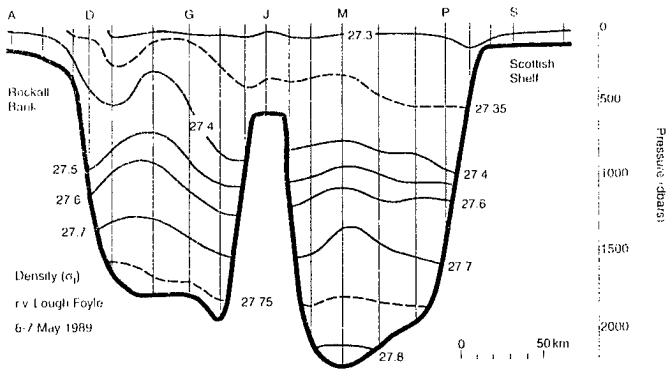


Figure 2. Evidence of late-winter cascading, 1989, off the eastern side of Rockall Bank near 57½°N, 13½°W (D.J. Ellett, personal communication).

Tidal and *wind-driven* currents are important in many shelf and slope seas, notably the north-west European shelf where they commonly exceed 0.5 m/s and are generally the largest contributor to turbulence, friction and mixing. Inertial currents may be particularly important to vertical mixing in the interior via their associated shear. Although transports are large (and long-period winds may drive substantial along-shelf displacements) the cross-slope flow is oscillatory, tending to limit exchange to the results of shear dispersion. Tides and wind-driven currents in homogeneous waters are quite well predicted, but measurements of mid-water turbulence would aid confident model predictions of inertial motions and associated mixing.

Fronts are associated with differential tidal mixing, fresher waters nearshore (Fig. 3) and well-developed upwelling. Cross-frontal transport and exchange depend critically on frontal instability and (e.g., frictional)

relaxation of geostrophic constraints to allow cross-frontal flow. There remains scope for a general formulation predicting the occurrence of fronts, taking account of both buoyancy factors (surface heating, lateral freshwater input) and both surface stirring (wind, waves) and bottom stirring by tides.

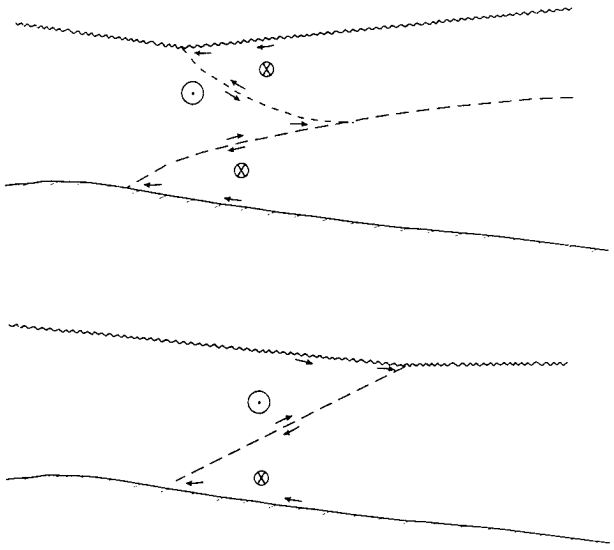


Figure 3. Schematic cross-front sections. (i) Tidal mixing fronts, between vertically mixed and summer-stratified seas, often have a strong density contrast across the lower interface. (ii) Fresher water on the shelf will tend to flow off-shelf above a shelf-break front. The sketch shows possible surface slopes (exaggerated) and gravitational cross-slope circulation (→, ←) associated with any (friction-induced) deficit in otherwise geostrophic along-slope flow (⊗ - into paper; ⊙ - out of paper, northern hemisphere).

Internal tides and *waves* are ubiquitous in the ocean, but of widely-varied magnitude according to location near the shelf edge, which is a principal generator of internal tides and consequent solitons contributing to the internal wave field. These motions are important to internal mixing, and to bottom currents and mixing where they are locally intense, notably in canyons. There remains a need for closely-spaced measurements of currents and temperature time-series, to test developing 3-D models of internal tides and waves.

Surface waves are often large enough to be important for near-surface mixing, but there is no special effect of the shelf edge in comparison with elsewhere in the ocean. Near-bed currents are small for typical shelf-edge depths, for all but the longest waves and shallowest shelves.

Along-shelf curvature of depth contours or changes of depth, associated with *capes* and *canyons*, may affect ocean-margin circulation, exchange and mixing processes in several ways: relaxation *via* small length scales of the constraint for geostrophic flow along depth contours; a "conduit" for the return of flow forced by winds (for example, Fig. 4) as the balance between wind stress and the pressure field varies according to depth; local intensification of upwelling or internal waves. In addition, the extra length of an irregular ocean-shelf boundary increases the scope for ocean-shelf exchange.

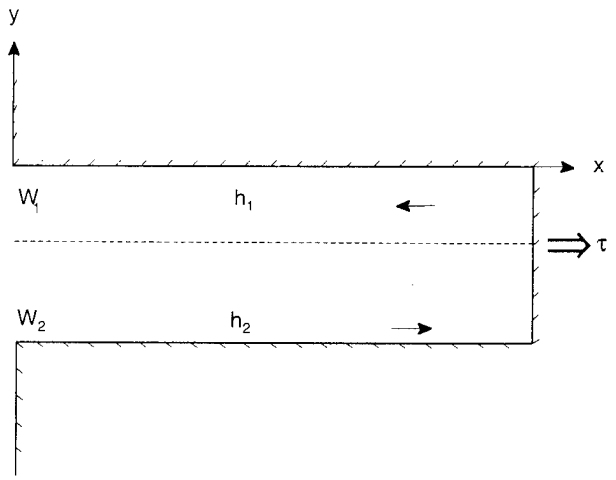


Figure 4. Deep embayment with wind stress τ inducing raised surface elevation at the head (right). The resulting exchange is *via* inflow in the shallower water "2" driven by the wind, and return flow in the deeper water "1" where the surface-slope-induced pressure gradient is more effective.

Comparison of Processes

This is synthesised in the following tables. These estimates are not uniformly applicable: they only apply where the process or phenomenon occurs; the magnitude scales according to the controlling variables via the formula given under "Scale." The numerical values derive from the given scale using "typical" values for the context, as given below (along with other notation).

Overall, many processes contribute O(1 m^2s^{-1}) exchange, albeit distributed in different ways through the water column (which will be significant according to the constituent transported). On this basis, internal tides (for example) are important only where exceptionally large, but upwelling should be important wherever it occurs. Larger exchanges potentially accompany boundary current divergence (although there is no evidence of values as large as tabulated), tides (but the return flow half a cycle later tends to reduce any longer-term transport), and canyons locally. Perhaps surprisingly, the Gulf Stream does not in practice seem to be the cause of larger exchanges than (for example) the relatively weak slope current around Scotland.

Table 1. Notation

Symbol	Meaning	Value	Unit
a	surface wave amplitude	1	m
A/hb	marginal sea area / entrance strait cross-section	10^5	—
C	constituent concentration		
c_p	specific heat	4.2	J/(g^{o}C)
C_D	quadratic bottom friction coefficient	0.003	—
d	deep ocean depth	4000	m
div	divergence in western boundary current	10^{-3}	km^{-1}
f	Coriolis parameter	10^{-4}	s^{-1}
g	gravitational acceleration	10	m s^{-2}
g′	reduced gravity: g × density change across thermocline / ρ	0.01	m s^{-2}
h	water depth (shelf and slope)	100	m
h_X	depth gradient across slope		
h_O	depth of principal oceanic circulation or thermocline	1000	m
$h_O/\Delta h$	ocean current depth / (ocean current depth - shelf-sea depth)	1	—
$h_O\lvert\rho^{-1}\nabla\rho\rvert$	steric slope	10^{-7}	—
h′	depth of seasonal thermocline	25	m
H	surface heat flux (winter cooling)	100	W m^{-2}
k	linear bottom friction coefficient	1	mm s^{-1}
k_I	linear friction coefficient below oceanic circulation	½	mm s^{-1}
L_T	topographic length scale h/h_X (over steep slope)	10	km
L_X/L_Y	ratio of zonal to meridional scales, oceanic gyre	5	—
N^2	squared Brunt-Väisälä frequency = $-g\rho^{-1}\partial\rho/\partial z$		
R_I	internal Rossby deformation radius = $(g'h')^{1/2}/f$ or Nh/f		
Sv	1 Sverdrup volume transport	10^6	m^{3}s^{-1}
t	duration of wind forcing	10^5	s
t_D	time constant for tidal shear dispersion	10^3	s
u	cross-slope velocity	0.1	m/s
u	vector velocity		
v	along-slope velocity	0.1	m s^{-1}
V_W	western boundary current speed	1	m s^{-1}
w	wind speed	10	m s^{-1}
W_S	shelf width	100	km
α	thermal expansion coefficient	10^{-4}	(^{o}C)$^{-1}$
α′	frontal exchange coefficient	0.0055	—
β	northward gradient of Coriolis parameter	10^{-11}	s^{-1}m^{-1}
Δh_I	small random topographic irregularities	10	m
$2\Delta h/h_O$	where Δh is height of ridge with associated upwelling	1	—
∂_x	cross-stream gradient in western boundary current	0.01	km^{-1}
ζ	surface tide amplitude in shelf sea	1	m
	in marginal sea connected by narrow strait	0.1	m
$<\zeta>$	internal tide soliton amplitude	50	m
λ	combined length of internal solitons per tide	1	km
ρ	sea-water density	10^3	kg m^{-3}
σ	forcing frequency (e.g., tide, wind)	10^{-4}	s^{-1}
σ_W	surface-wave frequency	1	s^{-1}
τ	wind stress on sea surface (↔ wind speed ~ 10 m/s)	0.1	N m^{-2}
©	eddy circulation	10^5	m^{2}s^{-1}
<.>	ensemble average (usually effected as a space- or time-average)		

Table 2. Exchange

Process		Scale	e.g., m^2/s
slope current		kv/f	1
	e.g., Atlantic inflow Malin-Lewis		(0.2 Sv / 300 km)
	total Scottish slope		1
topographic irregularities		$v\,\Delta h_I$	1
eddy		$©h_O(h_O/\Delta h)/f$	(1 Sv × 12 d)
warm-core ring streamer		?	(1 Sv)
	aggregate (Middle Atlantic Bight)		0.3
impulsive wind		$\tau/\rho f$	1
upwelling	- wind	$\tau/\rho f$	1
	- div. W boundary current	$2h_O2V_W\partial_X(V_W/\partial\, _Xh_O)div/f$	20
jets (narrow-shelf upwelling areas)		?	(2 Sv)
	aggregate		2
front		$\alpha' h(g'h')^{1/2}$	0.3
	e.g., along isopycnals, Middle Atlantic Bight		0.2
cascading(1)		$(0.6)^{-1}(g\alpha/\rho c_p)^{2/3}\, h(H^2/W_S)^{1/3}/f$	0.25
tides(2)		$\sigma\zeta W_S$	10
	strait to marginal sea	$\sigma\zeta A$	(>1 Sv)
	shear dispersion ($hu = \sigma\zeta W_S$)	$t_D uh\,\lvert\mathbf{u}\rvert/L_T$	0.1
internal tide solitons(3)		$<\zeta>\lambda$/tide	1
waves' Stokes drift		$0.01w^2$	1
W boundary current and bend		$(h/h_O)^2(L_X/L_Y)\,\tau/\rho\beta$	(½ Sv)
slope current and bend θ		$v\theta kL_T/f$	(0.01 θ Sv)
cape eddy		hvL_T	(0.1 Sv)
canyon return flow(4)		$h\tau/\rho k$	10
ridge-associated upwelling		$(2\Delta h/h_O)\,\tau/\rho f$	1

Notes

Estimates in parentheses indicate exchange per "event" as distinct from a value per unit length of shelf.

(1) An along-shelf average is estimated, but cascading is liable to be localised down shelf-edge depressions.

(2) Tidal flows return only 6 hours later; the exchange may be only temporary.

(3) No value is typical; that given is large but may occur locally.

(4) Such values are localised to broad shelves such as the North Sea with an on-offshore canyon axis across the shelf width. However, canyons also facilitate many of the other processes and increase the length of shelf-edge boundary for exchange associated with slope currents and fronts.

Table 3. Circulation

Process	Scale	e.g., m s^{-1}
slope current forced by:		
JEBAR	$h_O^2 \lvert \rho^{-1}\nabla\rho \rvert g/8k$	0.1
steady wind	$\tau/\rho k$	0.1
unsteady wind(1)	$t\tau/\rho h$	0.1
biased form drag	$(\tau/2\pi\rho)$ min(1/k, t/h)	0.01
wave rectification(2)	$u^2 f/L_T\sigma^2$	0.01
eddy momentum	$uvh/L_T k$	0.1
western boundary current	$(L_X/L_Y)\tau/\rho k_I$	1
eddies, warm-core rings, jets	?	0.5
tides	ζ max$\{(g/h)^{1/2}, \sigma W_S/h\}$	0.3
in strait to marginal sea	$\sigma\zeta A/hb$	>1

Notes

(1) In the presence of seasonal stratification, the effective depth h will be that of the upper layer down to the thermocline, ie. less, so that the upper-layer current (only) is greater.

(2) Internal motion, notably the internal tide, may reduce the effective length scale L_T to $(g'h')^{1/2}/\sigma$ so that the rectified flow is locally greater.

Overall, there are several agents of currents ~ 0.1 m/s, but in particular contexts western boundary currents, instabilities manifested as eddies, warm-core rings and jets, and tidal currents may be very much stronger.

Table 4. Energy potentially available for mixing

Process	Scale	W/m^2
surface waves	$1.5 \times 10^{-5}\ \rho g\sigma W a^2$	150
or	$5 \times 10^{-7}\ \rho w^3$	500
wind	τv	10
internal tides(1)	$\rho g' \langle\zeta^2\rangle \lambda/L_T$ per tide	50
internal waves	0.1×1 kW/m / L_T	10
bottom-reflected internal waves	fn(h_X, f/N) $\times$ 30 mW m^{-2} flux $\downarrow$	1
bottom friction	$\rho C_D v^3$	3
tidal(2) (currents 0.3 or 0.7 m/s)		100 or 1000
canyon-intensified internal waves(3)	$\langle\rho C_d u^3\rangle$	150

Notes

(1) No value is typical; that given is large but may occur locally.

(2) These dissipation estimates correspond respectively to an average and to locally greater values for the northwest European shelf.

(3) This estimate is local to the canyon floor where an empirical value 0.5 m s^{-1} is supposed for the intensified internal wave current.

These values highlight the importance of waves for surface mixing, of internal motions for mixing in the interior, and the highly variable importance of tidal currents and internal waves near the bottom, according to context.

Relation to Context

The estimates in these tables depend on the context (e.g., shelf width W_S, depth h, slope h_x, latitude through f, seasonality/N, winds through τ, waves, etc.). This

dependence varies (e.g., some increase with W_S and others do not). Therefore the relative importance of different processes differs according to context. There is no one ranking of processes in order of importance. Paradoxically, the common estimate ~ 1 m^2s^{-1} for exchange may assist ranking in a particular context where there is a departure from typical values. Wind-driven exchanges vary as τ/f, for example, and are therefore larger in equatorial regions (for a given wind stress and appropriate direction) whilst tidal exchanges are even larger for a wider shelf.

Discussion

Flux estimated naively from measurements as <uC> is uncertain, owing to the need for a comprehensive yet intensive array in space and time. This derives from the geostrophic constraint on overall cross-slope flow, and hence a tendency for cross-slope flow to be relatively small in magnitude, with small time and space scales for structure and coherence. It is also necessary for the array to detect small correlations of u and C.

An approach through process understanding is therefore suggested. Present knowledge of processes' contributions to fluxes has been reviewed. On this basis, a classification of shelves might be attempted, firstly on local physical grounds according to shelf width, depth etc. An assessment of processes' global contribution should then take into account the length of shelf where a process is important.

Processes interact, and the ocean margin topography is complex. Therefore, it seems that numerical models must eventually be invoked to provide the sought-after synthesis over processes, time and space.

Measurements are essential to test models. The sequence of hypothesis (embodied in a model) suggesting experimental arrays, and measurements in turn causing model revision, is the essence of the scientific method. In the shelf-edge context, the choice of the model area and the need to initialise the model place a critical demand on measurements around the boundary of the experiment. Other competing demands on the experimental array are the need for duration to provide statistics of intermittent processes, versus detail to define their form; a compromise may be detailed measurements for a shorter duration to add value to measurements from a sparser long-term array.

Water-mass analysis provides a valuable complement to process studies in the form of an integrated (but uncontrolled) measure of cross-slope transport. Drogued buoys may provide an intermediate Lagrangian view, less integral but more controlled through the choice of deployment times and locations.

Measurements may be wanted in a variety of locations so that individual processes are well-developed to test their representation by models; yet there is a case for locations to be representative of significant lengths of ocean margin.

The developing interest in processes of shelf-ocean exchange, and the relationship between the nature of ageostrophy and the cross-slope structure of quasi-geostrophic flow, are reducing model resolution and the accompanying scale of required measurements to the internal deformation radius R_I, and in the vertical to an emphasis near the sloping sea-floor.

Model requirements on shelf-wide scales were discussed by Huthnance (1992). They include the representation of stratification, 3-D flow, friction, non-linear effects (notable for correct total friction and currents affecting slow waves) and forcing (wind, buoyancy) as appropriate, all with sufficient resolution in time and space. For finer-scale models, there are additional concerns. The model coordinates and advection scheme need to address simultaneously (i) the distribution of stratification and bathymetry such that the maximum of Nh_x over the sea bed can be described, (ii) advection over the sloping bed, and (iii) dynamical balance of the JEBAR term and of initialising data.

Although fine resolution is needed, shelf-edge models need to take account of phenomena in a large area; the extent of influence from 'upstream' may be 1000 km. This may be through open boundary conditions or embedding in a wider-area model. Either there are technical problems to be addressed in making the wider-area and nested models (two-way) interactive, or there is an intellectual challenge to finding 'off-line' open-boundary or matching conditions that are not interactive yet satisfy the needs of both the wider-area and fine shelf-edge models. One factor which may assist is that the distance 1000 km relates to the decay distance for a first mode coastal-trapped wave; if the large-area model has a good approximation to this (a relatively easy requirement on gross stratification and/or shelf/ocean depth ratio and shelf-slope widths) then the effect of poor boundary conditions in the fine model may relate only to higher modes and penetrate a much shorter distance before decay.

Hence there remains full scope for application of the scientific method through models and experiments - the latter at sea, in the laboratory and with simpler models. The emphasis is on fine scales R_I and near the sea bed, on the model grid in relation to stratification, bathymetry and advection, and on accounting for external influences in both experiment and model. In view of the prospective application of models, we have not attempted to be fully quantitative in estimating circulation, exchange transports and mixing rates. Rather, the aim has been to provide a basis for deciding what may be the important features and physics to include in a model of a chosen region, and the processes to be resolved in measurements to test models.

Table 5. Previous and planned studies

Previous experiment	Context contrast	Conclusions
Scotian Shelf	shelf-edge front strong T, S variations (cold air outbreaks)	long-period fluctuating transports
SEEP-I SEEP-II	no slope current eddies from Gulf Stream	stratification helps exchange
Southern Atlantic Bight	shallow shelf Gulf Stream alongside	dominance of GS changes associated upwelling
CODE (N California) Coastal Transition Zone Program	narrow shelf strong wind-stress curl strong summer upwelling jets, filaments weak tides	large exchange (?) via upwelling & filaments affects production features tied to capes and ridges
Concurrently	Characteristics	
SES (Hebrides, 1995-6)	slope current strong wind forcing	separate coastal current some upwelling, cascading
OMEX (Celtic Sea, 1993-6)	bends and canyon weak slope current	very wide shelf strong tides "upstream"
MORENA (Portugal, 1993-6)	narrow shelf	summer upwelling, etc.

OMEX (Ocean Margin Exchange) involves more than 40 European partners spanning interests in physics, chemistry, biology, sediments and air-sea exchange. It includes the review of processes oulined here, and the following moorings and other deployments:

- current meter moorings from June or December 1993; six over the southern Portugal slope and offshelf, four over the Goban Spur, and (from April 1994) three north-west of Ireland in 660 m water depth;
- eleven drogued buoys over the slope off Portugal, deployed in December 1993, and possibly some more to be deployed over the Goban Spur;
- CTD sections contributing to the EC *Shelf Edge Fisheries and Oceanography Study*, which is altogether collating 15-20 repeated cross-slope sections off Western Europe.

OMEX also comprises remote sensing, and several modelling studies: internal waves, waves over the shelf and slope, ocean circulation and the eastern boundary, 3-D prognostic hydrodynamic modelling of the OMEX study areas. There are also many studies in the other disciplines.

SES (Shelf Edge Study, west of Scotland and part of the UK Land-Ocean Interaction Study) has the following measurement components:

- initial extensive survey (March 1995) of bathymetry and the sea bed along the slope (side-scan sonar, coring)
- six seasonal cruises (~ 3-monthly starting May 1995) with intensive surveys (ADCP, SeaSoar, CTD) and sampling (for chlorophyll, nutrients, tracers)
- mooring array (some maintained for 18 months): one main cross-slope section near 56.4°N and a reduced array ~ 25 km along-slope to the north
- tracking of instrumented drogued buoys
- satellite remote sensing.

SES is also funding studies of internal tides and waves; the along-slope current and its continuity; interpretation of the drogued buoy tracks for eddies, dispersion and exchange; ocean-shelf exchange by tracers/water mass; laboratory models (internal and long waves); 3-D prognostic numerical models; several studies in other disciplines.

Acknowledgments. This work was supported by the EU through the MAST programme, contract MAS2-CT93-0069 (Ocean Margin Exchange - OMEX).

References

Booth, D.A., and D.J. Ellett (1983) The Scottish continental slope current. *Cont. Shelf Res.*, **2**, 127-146.

Garrett, C., P. MacCready, and P. Rhines (1993) Boundary mixing and arrested Ekman layers: rotating stratified flow near a sloping boundary. *Ann. Rev. Fluid Mech.*, **25**, 291-323.

Huthnance, J.M. (1981) Waves and currents near the continental shelf edge. *Prog. Oceanogr.*, **10**, 193-226.

Huthnance, J.M. (1984) Slope currents and "JEBAR". *J. Phys. Oceanogr.*, **14**, 795-810.

Huthnance, J.M. (1992) Extensive slope currents and the ocean-shelf boundary. *Prog. Oceanogr.*, **29**, 161-196.

Huthnance, J.M. (1995) Circulation, exchange and water masses at the ocean margin: the role of physical processes at the shelf edge. *Prog. Oceanogr.*, in press

Pingree, R.D., and G.T. Mardell (1981) Slope turbulence, internal waves and phytoplankton growth at the Celtic Sea shelf break. *Phil. Trans. R. Soc. London*, A**302**, 663-682.

Wollast, R. (1993) Interactions of carbon and nitrogen cycles in the coastal zone. pp.195-210 in *Interactions of C, N, P and S biogeochemical cycles and global change* (ed. R. Wollast, R.T. Mackenzie, and L. Chou), NATO ASI Series, I **4**. Berlin: Springer-Verlag.

Coastal Submarine Canyons

B.M. Hickey

School of Oceanography, Box 357940, University of Washington, Seattle, WA 98195-7940
e-mail: bhickey@u.washington.edu

Abstract. Roughly 20% of the shelf edge between Alaska and the Equator is interrupted by steep, narrow and abrupt submarine canyons. Such canyons have long been of interest to geological and biological oceanographers. Physical oceanographers have suggested that mixing, internal wave activity, upwelling and cross-shelf/slope transport are enhanced within submarine canyons and that waves may be generated or modified by the canyon topography. These processes may significantly affect mass balances on regional and even larger scales. For example, the existence of submarine canyons along the Pacific shelf edge provides up to 30% more coastline over which upwelling and/or mixing can occur. The state of our knowledge with respect to such processes is described in this paper and critical research areas are identified.

Measurements in submarine canyons are among the most difficult in the ocean to make and, until recently, models of submarine canyon circulation and their effects on regional circulation have been few and highly idealized. Thus, understanding both the circulation within submarine canyons and the effect of canyons on the large-scale coastal circulation is yet a relatively immature field. Considerable progress has been made recently towards understanding the interaction of the steep topography of coastal canyons with time-dependent, stratified coastal circulation. This progress is due to the availability of measurements over canyon flanks (as opposed to simply along the axis) and to the development of models that include both realistically steep and abrupt topography as well as a canyon shape (as opposed to, e.g., a channel). Results indicate that for incident flow with the coastline on the left (upwelling-favorable), downwelling of shelf water occurs over the upstream wall of the canyon and upwelling typically occurs over the canyon axis and over the downstream wall. Upwelling water flows shoreward within the canyon and exits at the head and along its downstream wall. In the upper water column, with realistic stratification and inflow conditions, the flow is directed essentially straight over the canyon. Cyclonic relative vorticity occurs on the upstream side of the canyon near the rim and anticyclonic, over the canyon axis and on the downstream side. The cyclonic vorticity is associated with shelf water that has fallen into the canyon. Nonlinear effects tend to sweep spatial patterns downstream. The deeper circulation is cyclonic for upwelling-favorable incident flow (in the northern hemisphere), a result of layer stretching during upwelling. In the one canyon for which the data adequately resolve the spatial structure of the velocity field over the canyon, results suggest that a Taylor-cap-like circulation pattern occurs for Rossby numbers below about 0.25. Closed streamlines have not been observed in model results for the cases examined to date. Although models suggest that enhanced mixing due to internal wave focusing within canyons and wave generation and modification by canyons should be important, evidence for such processes is either extremely limited or nonexistent.

Numerous questions remain. For example, under what circumstances is the circulation within a canyon closed? How does an incident flow with an undercurrent interact with a canyon? How does the specific shape of a canyon affect its interaction with the regional flow field? Are particles preferentially retained within canyons? How does the presence of a canyon impact the local and regional marine ecosystem? What is the effect of a canyon on regional mass and momentum balances?

Background

The shelf edge of many continental margins is interrupted at irregular intervals by submarine canyons. A typical coastal submarine canyon has scales similar to that of the Grand Canyon: ~10-30 km wide and ~2 km deep. Canyons may cut across the shelf all the way to shore, or they may barely indent the outer shelf. Coastal canyons have long been of interest to geological and biological oceanographers.

Measurements in submarine canyons are among the most difficult in the ocean to make. This is because most coastal canyons have extremely steep slopes, making it challenging to safely obtain CTD profiles and to accurately deploy moored arrays over the slopes. Fishing activities often are intense over these same slopes so that it is difficult to maintain moored arrays in the water for extended periods. Last, the lateral coherence scales are very small—typically 10 km or less even along the canyon axis for both the monthly mean and the subtidal flow—so that arrays must be very heavily instrumented in order to delineate spatially coherent signals. Until recently, models of submarine canyon circulation and of the effect of canyons on the regional circulation have been few and highly idealized. For these reasons, the understanding of both the circulation within submarine canyons and the effect of canyons on the regional scale coastal circulation is a relatively immature field.

Fear of the complicating effects of submarine canyons has induced most researchers to make measurements outside their suspected range of influence. This was the case in the early 1970s and 1980s on the U.S. west coast when wind-driven dynamics were the focus of attention. In spite of purposeful selection against three-dimensional features, researchers usually failed to find two-dimensional mass balance. Consequently, during the 1980s, even straighter shelf-edge topography was selected for most field studies. A few field studies of canyons took place during the late 1970s and early 1980s. However, these studies were performed either by or with geological oceanographers, with a mind-set towards axial processes in canyons; for example, turbidity flows (e.g., Shepard et al., 1979; Hickey et al., 1986; Noble and Butman, 1989). Therefore, instrumentation was placed primarily along canyon axes and below canyon rims. Recent studies indicate that much of the interesting canyon dynamics occurs over the flanks of a canyon and just above its rim (Hickey, 1995).

Realistically shaped canyons have been given little attention by modelers. This omission may be due in part to the widely held idea that theories developed for a hill (which are comparatively numerous) can be applied directly to a depression. This is not the case, however, because boundary layers are free to communicate at all depths within a depression; for a hill or a seamount, communication can occur only over the top of the obstacle. Whereas the height of a hill is of fundamental importance to the effect of the hill on the regional flow field, the depth of a coastal canyon (beyond a minimum depth that depends on incident flow conditions) has only a small effect on the disturbance to the regional flow field. Moreover, the presence of the coastal wave guide introduces north-south asymmetries into the canyon-flow interactions. The additional complexities of having one open boundary, steep slopes, and abrupt changes in isobath orientation, as well as the existence of the strong and time-variable forcing that generally occurs in coastal regions where canyons are most common, make the problem particularly difficult. Early analytical models that included canyon topography typically made the assumption that the canyon could be considered as a perturbation to the regional topography; i.e., the canyon was extremely wide (Allen, 1976). Regional numerical models to date have provided insufficient spatial resolution to address details of the interaction processes. However, such models have demonstrated that canyons affect the spatial patterns of regional upwelling; in particular, they suggest that upwelling is enhanced on the downstream side of a canyon (e.g., Hurlburt, 1974; Peffley and O'Brien, 1976).

In the first attempts at modeling canyon circulation and its interaction with shelf flow on more realistic scales, the canyon was simulated as a vertical-walled channel (i.e., without a closed end) (Klinck, 1988, 1989). In spite of the absence of a canyon headwall, the latter models provided the first useful insight into canyon/flow interaction. Two- and three-layer linear models were used to describe the steady state response of the canyon flow and density field for channel widths narrower, wider, and on the order of the Rossby radius. The incident forcing had a sinusoidal cross-shelf structure. With this model configuration, maximum upwelling occurred over the two walls and no north-south asymmetries were predicted. Cyclonic vorticity was observed within the canyon in the region where the incident flow was upwelling favorable.

Two recent models with realistically steep and abrupt topography have provided a major step forward in understanding the interaction of shelf flow with coastal canyons (Allen, 1995; Klinck, 1995). Results from these models are qualitatively consistent with the one set of spatially comprehensive observations that is available. These models as well as the spatially comprehensive dataset will be discussed further in the section on the current state of our knowledge in submarine canyons.

Why are Canyons of Interest?

In some coastal areas, submarine canyons occupy nearly 50% of the shelf edge. An example of such a coastline is shown in Figure 1. The interaction of fluctuating flows over the shelf and slope with abrupt topographies such as these, i.e., the nature of the circulation and mass balance within and in the immediate vicinity of a canyon, presents a fundamental and challenging problem for physical oceanographers. Moreover, canyons play an important role in regional ecosystems. A plethora of anecdotal information suggests that canyons are regions of enhanced species diversity and biological productivity. This productivity enhancement apparently extends all the way up the food chain to include birds and mammals. For example, The Gully, a 1200-m-deep, 12-km-wide submarine canyon off the Scotian shelf, is home to a non-migratory population of 200-300 endangered bottlenose whales (Faucher and Whitehead, 1992). Elevated chlorophyll and zooplankton density, as well as doming of temperature and salinity isopleths, have been observed over this canyon (Bohrer, 1995). The basic hypothesis invoked in most anecdotal accounts is that upwelling is enhanced near canyons and that this upwelling provides a nutrient source that increases phytoplankton and, hence, zooplankton density. Fish, birds, and mammals congregate in the area for the predictable and enhanced source of food. Most reports linking canyons to enhanced productivity have not been presented in the reviewed literature. The studies have not to date included specific efforts to link physical mechanisms and biological effects.

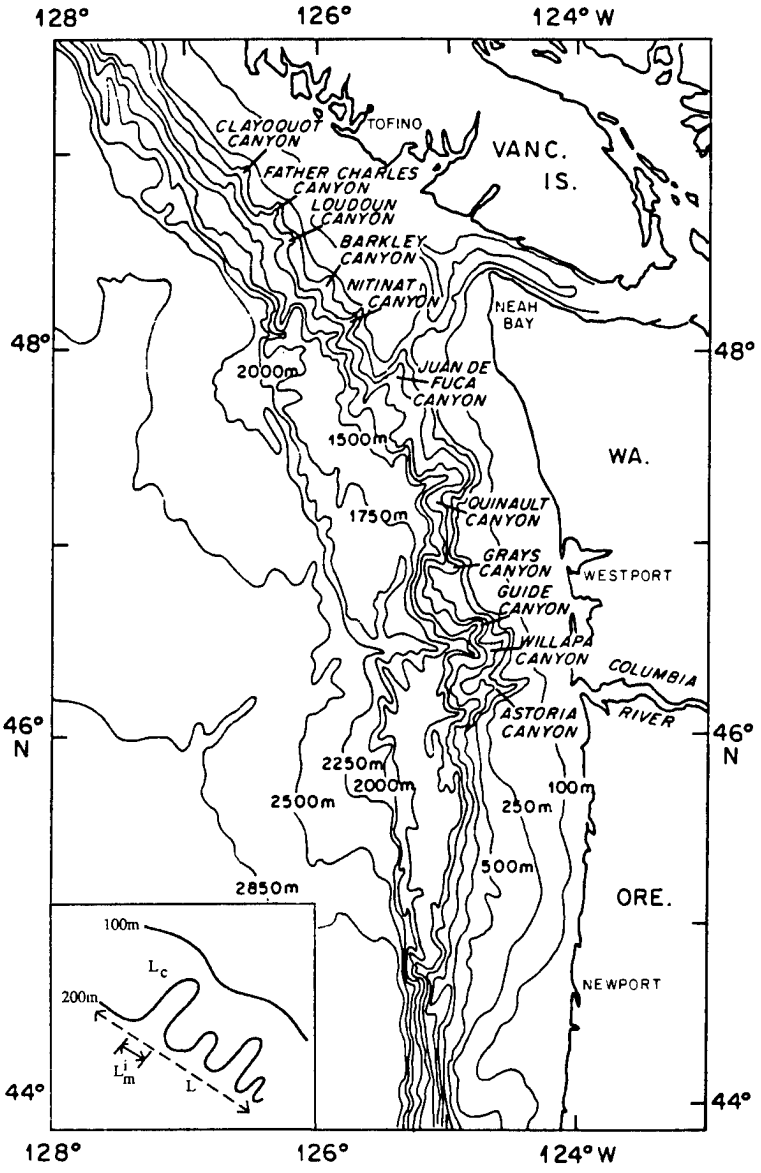


Figure 1. Bathymetric map of the Washington-Oregon coast illustrating the number and frequency of submarine canyons. The inset figure shows the method used for estimating the canyon shelf-edge enhancement factor.

Submarine canyons incising the continental shelf also play an important role in the ultimate fate of sediment in suspension or resuspended over the continental shelf. Many canyons incise the shelf sufficiently far to cut across and thereby interrupt the movement of river-supplied sediment along the shelf in the bottom boundary layer. For example, on the Washington shelf, sediments trend northward and offshore from their source, the Columbia River, intersecting several canyons along the outer shelf from Astoria to Juan de Fuca (see Figure 1) (Nittrouer, 1978). Baker and Hickey (1986) used sediment traps to demonstrate that particles are preferentially concentrated in a canyon following resuspension on the adjacent shelf. Water flowing *over* the canyon, as opposed to *around* the canyon, provides an opportunity for suspended sediment in the water column to settle out at depths deeper than would be otherwise possible. Gardner (1989) shows that focusing of internal waves by canyon walls can elevate bottom currents and hence shear stress sufficiently to resuspend sediment along the canyon floor, after which it can move farther seaward in detached nepheloid layers.

On a regional scale, the presence of coastal submarine canyons can modify and/or enhance the effects of other physical processes. A number of possibilities are listed below. These effects have some basis in model studies. However, only a few have been studied in the field. The state of our knowledge in each of these areas will be reviewed briefly in the next section.

1. Internal Wave Generation and Modification. The topography of a canyon, with sloping bottoms on three sides, is likely to significantly modify the ambient internal wave field. In addition, bottom slopes within the canyon generally differ from those over the continental slope outside the canyon, and offer several angles, any one of

which might be favorable to generation of the internal tide.

2. Enhanced Mixing. Modification of the internal wave field, in particular, amplification and breaking, could lead to enhanced mixing within and around canyons. Enhanced mixing might also result from an increase in bottom shear stress as the flow is steered around the topography.

3. Wave Generation. The interaction of fluctuating shelf flow with the abrupt topography of canyons is likely to result in the generation of a spectrum of trapped and propagating waves.

4. Modification of Coastal-Trapped Waves. The energy of low mode coastal-trapped waves commonly found on continental shelves may be scattered into higher modes by the abrupt change in bottom topography.

5. Shelf/Slope Mass Exchange. Upwelling and downwelling rates and/or the total volume exchanged via these processes may be altered or enhanced by the presence of a canyon.

6. Modification of Regional Currents and Water Properties. For realistic ambient conditions, shelf flow does not simply follow isobaths around a canyon indenting the shelf break. Rather, flow crosses the isobaths into the canyon. The departure of streamlines from the isobaths is a function of many parameters (notably stratification and Rossby number of the incident flow) which vary in space and time. Also, water masses produced and/or modified by canyon processes are not constrained to remain in the vicinity of the canyon. Advection and mixing can move the canyon water downstream and inshore or offshore of the canyon from which it originated, thereby affecting regional salt, heat and mass balances in a fundamental way.

How important are any of the expected canyon transformations and enhancements in regional and global contexts? On the west coast of the U.S., the shelf break occurs generally in the vicinity of the 200-m isobath. To estimate cumulative canyon effects over one specific shelf region, we measured the overall length of the 200-m isobath (L), the length of the 200-m isobath indented by the mouths of canyons ($L_m = \Sigma L^i_m$) and the length of the 200-m isobath including canyons (L_c) for the Pacific coast from Alaska to the Equator (Figure 1). Distances were measured with a ruler whose least division is about 2 km. Results indicate that in this region, almost 20% of the shelf edge is interrupted by canyons; i.e., the mouths of canyons occupy 20% of the shelf edge (100 L_m /L). In addition, the presence of canyons increases the length of the shelf edge by roughly 30% (100 L_c /L). Thus, if canyons do indeed facilitate exchange between the shelf and the slope or enhance vertical mixing, this example suggests that presence of canyons is likely of first order importance to larger scale mass balances.

In the discussion below, the state of our knowledge with respect to mean flow and fluctuating flow in and around canyons will be presented. This will be followed by a discussion of each of the potential canyon effects that were listed above.

The State of Current Knowledge

Mean Flow Within Submarine Canyons

Observations suggest that the mean flow along canyon axes within a few hundred meters of the canyon floor is predominantly up- or down-canyon. This axial canyon flow is of great interest to geological oceanographers, who view it as a mechanism for transporting sediment from the upper slope to the deep sea. Long term (several month) mean currents along canyon axes do not appear to correspond to any simple spatial pattern: they are sometimes up-canyon, and sometimes down-canyon, often within the same canyon. For example, Hunkins (1988) found mean down-canyon flow in Baltimore Canyon in the canyon head, but up-canyon flow farther seaward. Hickey (1989) found up-canyon flow in the head of Quinault Canyon. Shepard et al. (1979) conclude that of 69 measurements of axial flow, 43 were down-canyon and 26 were up-canyon. They also make the observation that canyons on the east coast of the U.S. (i.e., in a western boundary system) tend to have more up-canyon mean flow than West coast canyons (i.e., in an eastern boundary system). However, presently available data now suggest the opposite: Quinault (Hickey, 1989) and Juan de Fuca (Freeland and Denman, 1982, hydrographic data) suggest up-canyon flow at least at the head; whereas, Baltimore, Lydonia (Noble and Butman, 1989), and Wilmington (Church et al., 1984, from hydrographic data) all suggest down-canyon flow at the head. The observations have been made over different time periods and in different seasons, at different heights above the bottom and in different parts of canyons. Not surprisingly, therefore, no firm understanding of driving mechanisms for mean flow near the canyon floor has emerged. It is safe to say that at this point in time, the direction of the mean flow above the floor of a specific canyon cannot be predicted with any reasonable certainty. To what extent are the mean flows obtained repeatable from year to year? In the one case for which data exist (Quinault), the spatial pattern of the mean flow direction along the canyon axis was the same during two successive years (Hickey et al., 1986).

Few direct current measurements have been made over the canyon flanks: to my knowledge such data exist only for Astoria, Lydonia, and Baltimore. In all cases for which such data have been obtained, a cyclonic flow pattern is observed within the canyon over its edges. For example, data from the head of Lydonia Canyon provide evidence that the mean flow of that canyon is in opposite directions on the two sides and cyclonic (Noble and Butman, 1989). In Baltimore Canyon, the only available data are deep, but they too indicate cyclonic mean flow with flow in opposite directions on the two canyon walls (Hunkins, 1988). Data

in Juan de Fuca Canyon are consistent with a mean cyclonic circulation pattern (Cannon and Lagerloef, 1983). With the exception of the Juan de Fuca data, all examples were obtained for incident flow with the coastline on the right (i.e., downwelling-favorable). The data sets generally included at most one mooring near the shelf break upstream and downstream of the canyon and one in the canyon. With such sparse data it is not possible to determine whether the flow is conserving vorticity and simply following the isobaths around the canyon, or whether the water column has crossed isobaths into deeper water, thereby generating cyclonic relative vorticity as it is forced to stretch. This determination is easier in the case of flow incident with the coast on the left (i.e., upwelling-favorable). In such cases, if the flow is sufficiently slow to be able to follow the isobaths, the data that would result from two moorings on either side of the canyon would suggest an anticyclonic rather than a cyclonic flow pattern.

In the one data set that resolves flow over both the canyon axis and its slopes (Astoria) the flow crosses directly over the isobaths on the upstream side of the canyon to form a mean cyclonic eddy, with maximum velocities over the canyon walls (Hickey, 1995). Under strong incident flow conditions (Rossby number >0.25), the cyclonic eddy disappears from the canyon. This Taylor-cap-like feature decays vertically both above and below the canyon lip, with a scale roughly given by the vertical length scale appropriate for geostrophic flow, fL/N, where f is the Coriolis parameter, L is the canyon width and N is the Väisälä-Brunt frequency. Since the width of Astoria Canyon is less than half that of the local internal Rossby radius, the observed flow is unlikely to be completely geostrophic. In some locations where Astoria data were obtained, the canyon walls were only 3 km apart. For the cases for which appropriate data are available (Astoria, Quinault, Baltimore, Lydonia, and Carson), mean flow at some distance (~50-100 m) *above* the canyon over its walls was not measurably perturbed by the canyon: it was directed straight over the canyon following the curvature of the regional isobaths.

The only observations available on canyon floors have been made along canyon axes. Such flows are generally weak (<5 cm s^{-1}). Whether the flow over the canyon floors is unidirectional to some height off the bottom or whether the flow is in opposite directions over the canyon flanks right down to the canyon floor is presently unknown. Most canyons narrow continuously towards the bottom rather than being flat over a broad region (i.e., over several kilometers), so that at some distance from the sea surface the flow might be unable to follow isobaths around the edges. Although the depth at which the flow would transition to such a regime might be thought to depend on the local internal Rossby radius, flow has been observed to follow the isobaths around at least one canyon at distances much less than the internal Rossby radius (Hickey, 1995). Model results also suggest that, in the absence of friction, flow can be oppositely directed on the two sides of a canyon for canyons much narrower than the Rossby radius (Klinck, 1988). It seems likely that bottom friction might play an important role in determining near-bottom canyon flow. The physics of the near bottom flow in deep canyons, and, in particular, the transition from around-canyon flow to axial flow (if such indeed occurs), has not been addressed to date with either models or observations.

Fluctuations in Canyon Currents and Water Properties

Statistics and forcing mechanisms of subtidal currents in deep submarine canyons (arbitrarily defined as those for which bottom depths exceed 200 m) have only been examined in four studies. In each case, horizontal coherence scales, both along and across the canyon axis, are remarkably small (less than 10-20 km) (Hickey, 1989; Noble and Butman, 1989). Typically, only a small fraction (<25%) of the variance has been explained by conventional statistical analysis (Hickey, 1989; Noble and Butman, 1989). The cross-shelf/slope pressure gradient associated with the along-shelf/slope regional flow incident on or over the canyon is most frequently invoked in discussions of driving mechanisms, with an offshore increase in pressure being related to up-canyon flow, and vice versa for an onshore increase in pressure. For example, Cannon and Lagerloef (1983) illustrate out-canyon flow in the Juan de Fuca Canyon for downwelling-favorable flow conditions. Hickey (1989) demonstrates a statistical relationship between along-axis flow in Quinault Canyon at depths of about 1200 m from the surface (5-50 m above the bottom) and the along-shelf flow over the canyon (near the shelf edge). Noble and Butman (1989) illustrate that for these dynamics to apply to Lydonia Canyon, dissipation must be extremely high, consistent with estimates deduced from the large tidal currents that are present. For both Quinault and Lydonia Canyons, maximum coherence with the shelf forcing occurs at periods of about 3-5 days. In the shallow heads of some canyons or in shelf valleys such as the Hudson, wind set-up (and thus a cross-shelf pressure gradient force) has been related directly to down-canyon flow (e.g., Nelson et al., 1978; Hsueh, 1980). Coherence scales for such depressions might be expected to be larger than those for deep ("real") canyons, which lie below the depth of directly wind-driven shelf currents.

With adequate resolution on the canyon edges, results show that the fluctuating flow on the two sides of the canyon is often in opposite directions (Hickey, 1995; Kinsella et al., 1987). Consequently, the flow cannot be driven by a spatially uniform regional pressure gradient, as deduced from the several data sets which emphasize axial measurement sites. A sequential time series illustrating the changes in the velocity field during an upwelling event in Astoria Canyon is presented in Figure

2. Detailed analysis of the Astoria dataset demonstrates that during an upwelling event, up-canyon flow initially occurs below the canyon lip on both walls and over the axis. This flow is likely to be driven directly by the barotropic cross-shelf/slope pressure gradient associated with the overlying incident shelf flow, as reported in the other canyons (Hickey, 1995). Over the canyon walls, the up- (or down-) canyon flow that occurs at the onset of upwelling (or downwelling) is followed by an increase in cyclonic circulation (with flow in opposite directions on the two walls). This cyclonic circulation is consistent with stretching (or compression) of upwelled (downwelled) layers as these layers drop into the canyon. An example of layer stretching is illustrated in Figure 3. In this figure, recently upwelled layers of shelf water can be traced as a turbid layer across the canyon. The maximum in turbidity coincides with the maximum in stretching vorticity.

Deeper in the canyon, layer stretching due to the upwelling itself causes an additional increase in cyclonic vorticity (Figure 3). Note that the region of large positive vorticity near the rim of the canyon is sandwiched between two layers of strong anticyclonic vorticity, a result of layer compression by the regional upwelling. Current meter data in Carson Canyon off the coast of Newfoundland suggest a response to an upwelling event not unlike that in Astoria Canyon: a strong cyclonic circulation pattern is observed 2-3 days after the onset of upwelling. In this case, the direction of the flow at the shelf break on the two sides of the canyon is the reverse of that normally observed for mean conditions on this western boundary.

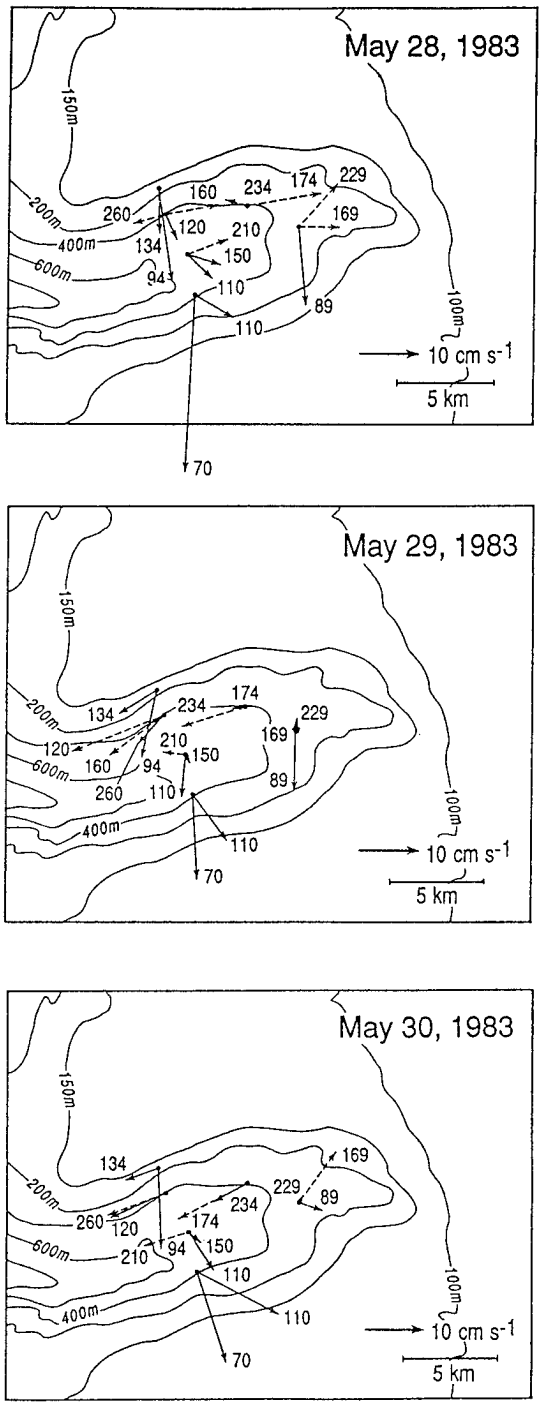


Figure 2. Sequential maps of subtidal vector velocities in Astoria Canyon during an upwelling event. Measurement depth in meters is indicated near the tip of each vector. Locations above (below) the depth of the canyon rim are shown as solid (dashed) arrows. From Hickey (1995).

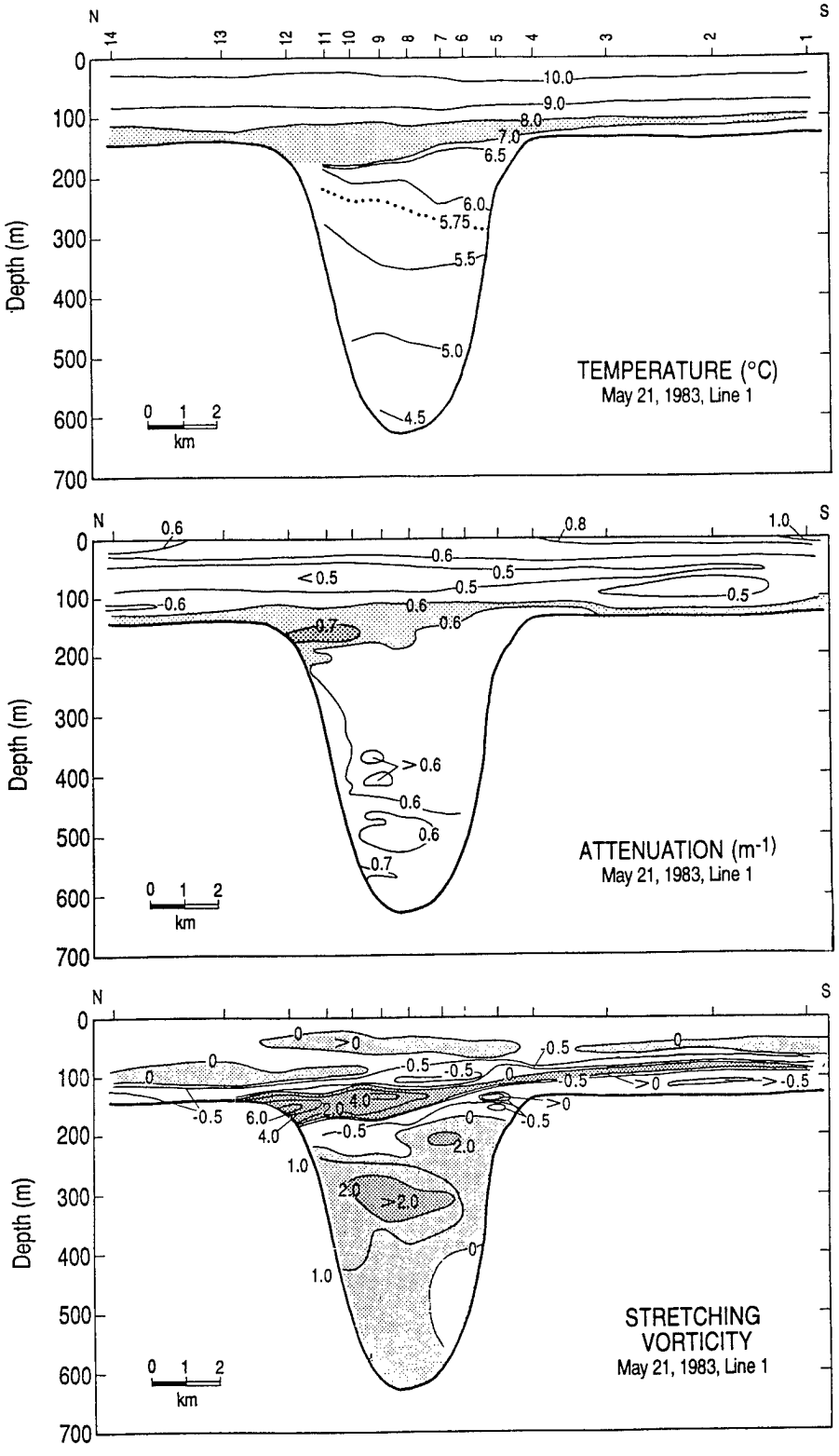


Figure 3. Contoured sections of temperature, attenuation and stretching vorticity on a section across Astoria Canyon during an upwelling event. The shaded region near the canyon lip traces the pathway of water that originated from the bottom boundary layer on the shelf or upper slope as it flows over and up the canyon. The deeper region of shaded vorticity is consistent with layer stretching during the upwelling event. Adapted from Hickey (1995).

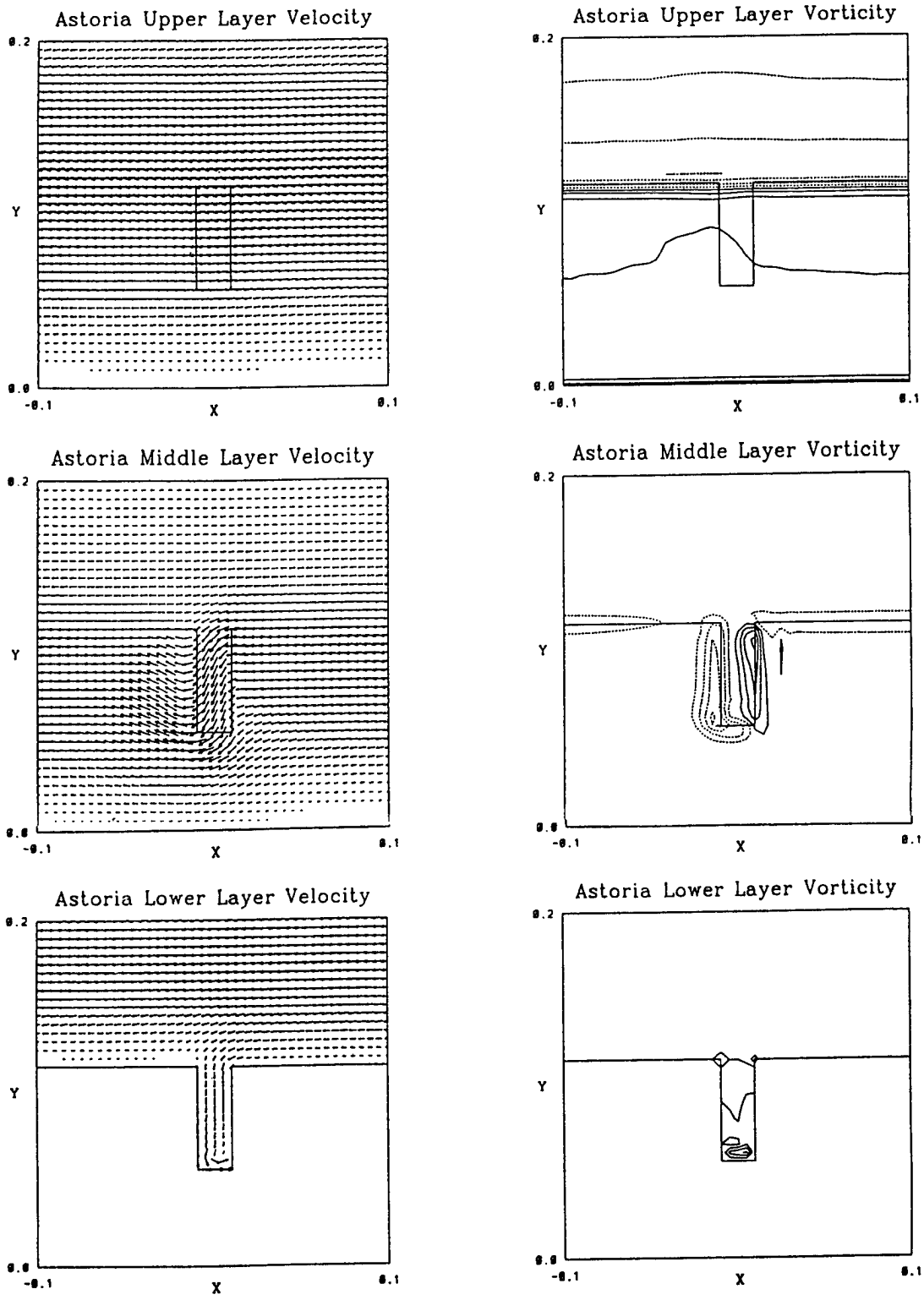


Figure 4. Modeled velocity and vorticity fields for upper, middle, and lower layers after one day of spin-up with a nonlinear numerical model. The model is forced with steady, upwelling-favorable, spatially uniform wind stress. Maximum velocities in the three layers are 47 cm s^{-1} (upper layer), 37 cm s^{-1} (middle layer) and 14 cm s^{-1} (lower layer). Vorticity is contoured from -0.11 *f* to 0.062 *f* by 0.025 f (upper layer), -0.43 *f* to 0.43 *f* by 0.12 *f* (middle layer) and 0 *f* to 0.19 *f* by 0.062 *f* (lower layer). From Allen (1995).

A recent study of submarine canyon dynamics includes both spin-up and steady state, linear and nonlinear models of a shelf/slope system in which a vertical-walled canyon incises the continental slope (Allen, 1995). One nonlinear, three layer model run was designed for the topography and stratification of Astoria Canyon. The relatively large incident velocity (~50 cm s^{-1}) approximates the high Rossby number flow observed in the Astoria field study during upwelling events. In the upper water column the flow is essentially straight over the canyon. In the middle layer, the flow turns shoreward over the canyon. Cyclonic vorticity occurs on the upstream side of the canyon near the rim and anticyclonic on the downstream side (Figure 4). The cyclonic vorticity is associated with shelf water which has fallen into the canyon, consistent with the field observations of Astoria Canyon (Figure 3). Cyclonic vorticity occurs over about 2/3 of the canyon due to the relatively large inflow velocity and the relatively important nonlinear effects, which tend to sweep spatial patterns downstream. The deeper circulation is cyclonic near the canyon head in the model results, consistent with the observations, a result of layer stretching during upwelling. However, modeled vorticity is generally weaker than that observed in the field study of Astoria Canyon (compare Figures 3 and 4). The model-observation discrepancy may be due to the fact that the model results are presented after only one day of spin-up, whereas the observations suggest that maximum cyclonic circulation is observed during spin-down.

Klinck (1995) uses a semi-spectral, primitive equation model (the "SPEM" or "Haidvogel" model) to model the steady state response of a Gaussian canyon (400 m deep and with a half-width of 5 km) to both upwelling and downwelling-favorable overflow events. Klinck uses stratifications corresponding to an internal Rossby radius on the order of the canyon width and three times the canyon width. The Rossby number of his incident flow is 0.1-0.2. The major result of his study is the demonstration that the direction of incident flow (i.e., whether upwelling-favorable or downwelling-favorable) has a stronger effect on the flow disturbance due to the canyon than does stratification. In particular, during upwelling events, downwelling of shelf water occurs over the northern flank of the canyon and upwelling occurs over the canyon axis and over the southern flank (Figure 5). Upwelling water is pumped from the canyon, exiting at the head and along its southern flank. These results are qualitatively similar to observations in Astoria Canyon, as discussed above (see Figure 3). For strong stratification, the canyon effects (including the downwelling) are observed well up over the adjacent shelves. Flow is directed over the canyon at the sea surface, but turns into the canyon at depths close to the canyon rim. Cyclonic vorticity occurs at depth within the canyon due to layer stretching. For downwellingfavorable overflow, downwelling (on the upstream side) and upwelling (on the downstream side) are symmetric with the canyon topography and little water is lost from the shelf to the canyon (Figure 5).

Internal Wave Modification and Generation by a Submarine Canyon

Both models and laboratory experiments suggest that internal waves are focused and therefore amplified within canyons (Hotchkiss and Wunsch, 1982; Baines, 1983; Grimshaw et al., 1985). This result has been confirmed in several canyons, notably Hudson (Hotchkiss and Wunsch, 1982), Quinault (Hickey, 1989) and Monterey (Petruncio et al., 1994). Hotchkiss and Wunsch use statistical analysis of current meter data to illustrate the enhancement of the internal wave field toward the canyon head and toward its floor (Figure 6). The potential energy density averaged over the internal wave band increases roughly 100-fold toward the canyon head and 10-fold toward the bottom at most sites. The energy in the internal wave band is higher everywhere in the canyon where measurements were made than that predicted by the Garrett and Munk (1975) model (see values on Figure 6).

Petruncio et al. (1994) use a time series of shipboard ADCP data to demonstrate bottom enhancement of the semi-diurnal tide within Monterey Canyon. In this canyon, the slope of the canyon axis is near the critical slope for the semi-diurnal tide. This enhancement would not be expected on the much steeper adjacent continental slope. Their data also suggest that the internal tide undergoes significant alteration near the lip of the canyon. In general, the slopes of the canyon walls and the canyon floor can all differ from each other and from those on the adjacent continental slope, and so offer multiple opportunities to achieve the critical angle required for effective generation of internal tides.

Enhancement of Vertical Mixing by Submarine Canyons

Lueck and Osborn (1985) use turbulent velocity profiles to demonstrate that Monterey Submarine Canyon has an extremely turbulent bottom boundary layer. This turbulent layer was up to 170 m thick during their field study. The production of turbulent kinetic energy within a canyon could be related either to internal wave breaking or to bottom friction (or both). Hotchkiss and Wunsch (1982) use their energy analysis of the internal wave band to show that in Hudson Canyon, dissipation due to bottom friction is a factor of ten too small in the internal wave band to account for the influx of internal wave energy into the canyon. They suggest that internal

wave breaking and mixing likely occur near the canyon head. An example of mixing due to bores or wave breaking at internal tidal frequencies is presented by Gardner (1989). Time series of currents, temperature and beam attenuation within Baltimore Canyon are consistent with the hypothesis that bore-like features (breaking internal waves) resuspend sediment along the canyon bottom at tidal frequencies. The ratio of bottom slope to the slope of the internal tide characteristics is less than one, as required for internal wave breaking or bores, in the season in which the observed resuspension was most intense. Sediment-laden water moves up-canyon and then down-canyon, ultimately detaching from the bottom boundary layer and moving offshore as intermediate nepheloid layers. Maps of light transmission taken inside and outside Baltimore Canyon illustrate the resulting enhancement of suspended particle concentrations within the canyon in comparison with the open slope (Figure 7).

A recent study has shown that the thickness of the bottom mixed layer over the shelf off northern California is a function of stratification, current speed, and, most importantly, current direction (Lentz and Trowbridge, 1991). To the extent that this is generally the case, the height and structure of the bottom mixed layer in the vicinity of a canyon are likely to be strongly modified by canyon-related processes. For example, if the flow can follow the topography, conservation of mass would require an increase in velocity as the flow is channeled into the narrower shelf region inshore of the canyon. This would increase the bottom shear stress and, consequently, the structure of the bottom boundary layer and the height of the bottom mixed layer. The local density field, itself modified by the canyon effects on upwelling/downwelling and other regional processes, would also affect the structure of the bottom boundary layer and, hence, the bottom mixed layer. To my knowledge, there have been no field studies focused on boundary layer modification and mixing enhancement due to the presence of a submarine canyon for any frequency band.

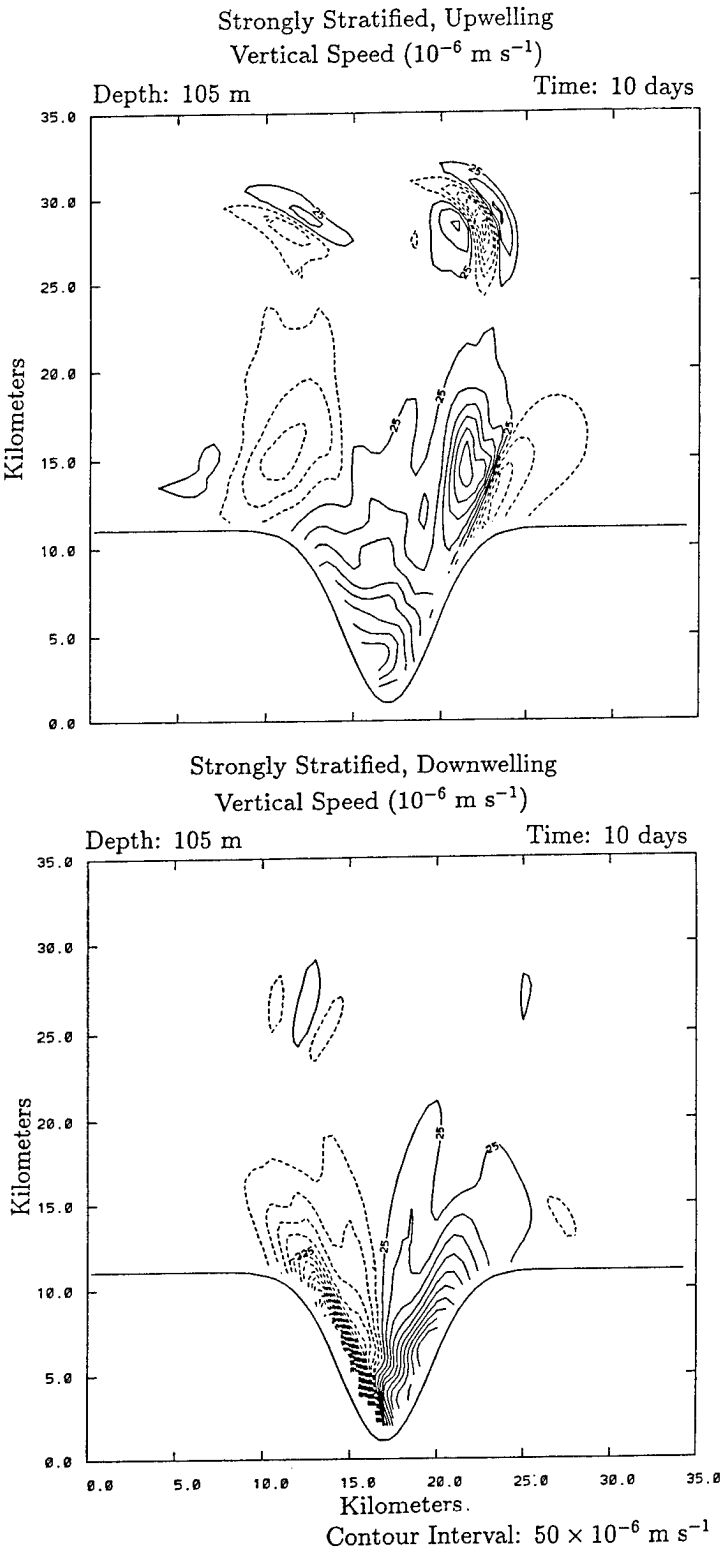


Figure 5. Modeled velocity for strongly stratified upwelling (upper panel) and downwelling (lower panel). The solid line indicates the top of the canyon and the shelf break. The vertical velocity is shown at a depth just below the shelf break (105 m). Solid contours indicate upward flow and dashed controus, downward flow. From Klinck (1995).

Canyons as Wave Makers and Wave Modifiers

The theoretical problem of variable shelf-slope topography was first addressed by Allen (1976). Along-shelf variations in topography were assumed to be greater than the shelf-slope width so that the motion could be treated in the long wave, non-dispersive limit. The resulting perturbation equations are those for barotropic, inviscid shelf waves. For a delta function applied wind stress (meant to model short time scale changes in stress), the flow adjusts through propagation of free shelf waves. For a Heaviside wind stress (meant to simulate steady stress, impulsively applied), Allen found a reduction of onshore flow over the canyon. This result is exactly the opposite of that found in recent models in which canyons are treated as abrupt topographic features (see below). Allen also showed that the energy in a shelf wave incident on a canyon is scattered into other modes.

Wang (1980) extended the study of the effects of a canyon on shelf waves by including finite amplitude topography and allowing waves to be dispersive. He presents numerical solutions for the case of a v-shaped canyon that indents the shelf all the way to the coastline, with a flat bottom seaward of the shelf. He concludes that wave diffraction leads to a reduction of long wave energy transmission (up to 70%), amplitude amplification near the canyon, and generation of strong localized disturbances in the vicinity of the canyon. Interestingly, the phase propagation upstream and downstream of the canyon is not significantly affected by the presence of the canyon. The scattering process transforms the large-scale alongshore motion into smaller-scale cross-shore motion associated with higher wave modes. Thus, Wang concludes that canyons effectively block much of the long wave transmission. We note that this would not likely be the case for submarine canyons that only partially indent the shelf. Perhaps more important, numerical studies of coastal-trapped wave modification by abrupt changes in shelf topography (Wilkin and Chapman, 1990) suggest that Wang's results would be altered dramatically by the inclusion of stratification. In the latter study, inclusion of realistic stratification eliminated all reflected waves and amplified the scattering process. Some upstream influences were produced by evanescent wave modes. No further numerical studies of wave modification by finite amplitude canyons have been presented since Wang (1980).

Generation of standing and radiating waves over and near a canyon at supertidal frequencies and at the inertial period has been examined for a homogeneous water column with a canyon treated as a channel (Klinck, 1988). Waves are generated during geostrophic adjustment to an impulsively imposed cross-shelf barotropic pressure gradient. The frequency of the resulting waves is a function of canyon depth and the width of the incident flow. Strong localized disturbances at these higher frequencies would be expected in the vicinity of a canyon.

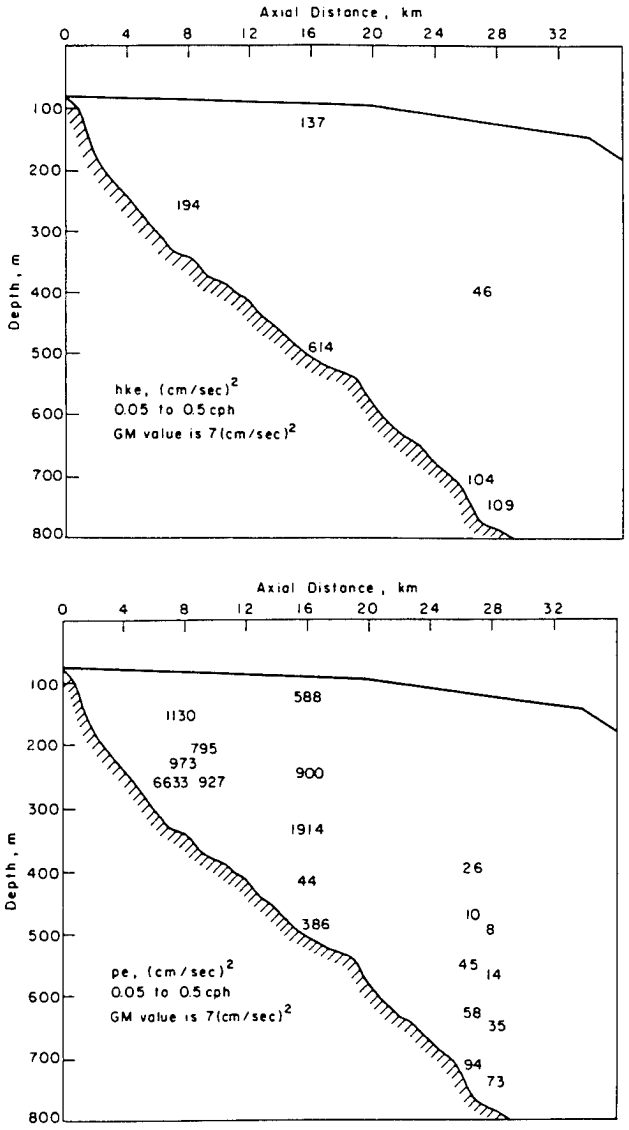


Figure 6. Horizontal kinetic energy density (upper panel) and potential energy density (lower panel) integrated over the internal wave band, shown as a function of location within the canyon. From Hotchkiss and Wunsch (1982).

To my knowledge, no experiment has been designed to search for wave-like disturbances over a canyon and no experiments have been undertaken to study the modification of coastal-trapped waves by canyon topography. Although regional effects on coastal-trapped waves by small scale canyons may be negligible, the effect of broader canyons, which may cause an abrupt narrowing of the shelf for a distance of 20-100 km is unclear.

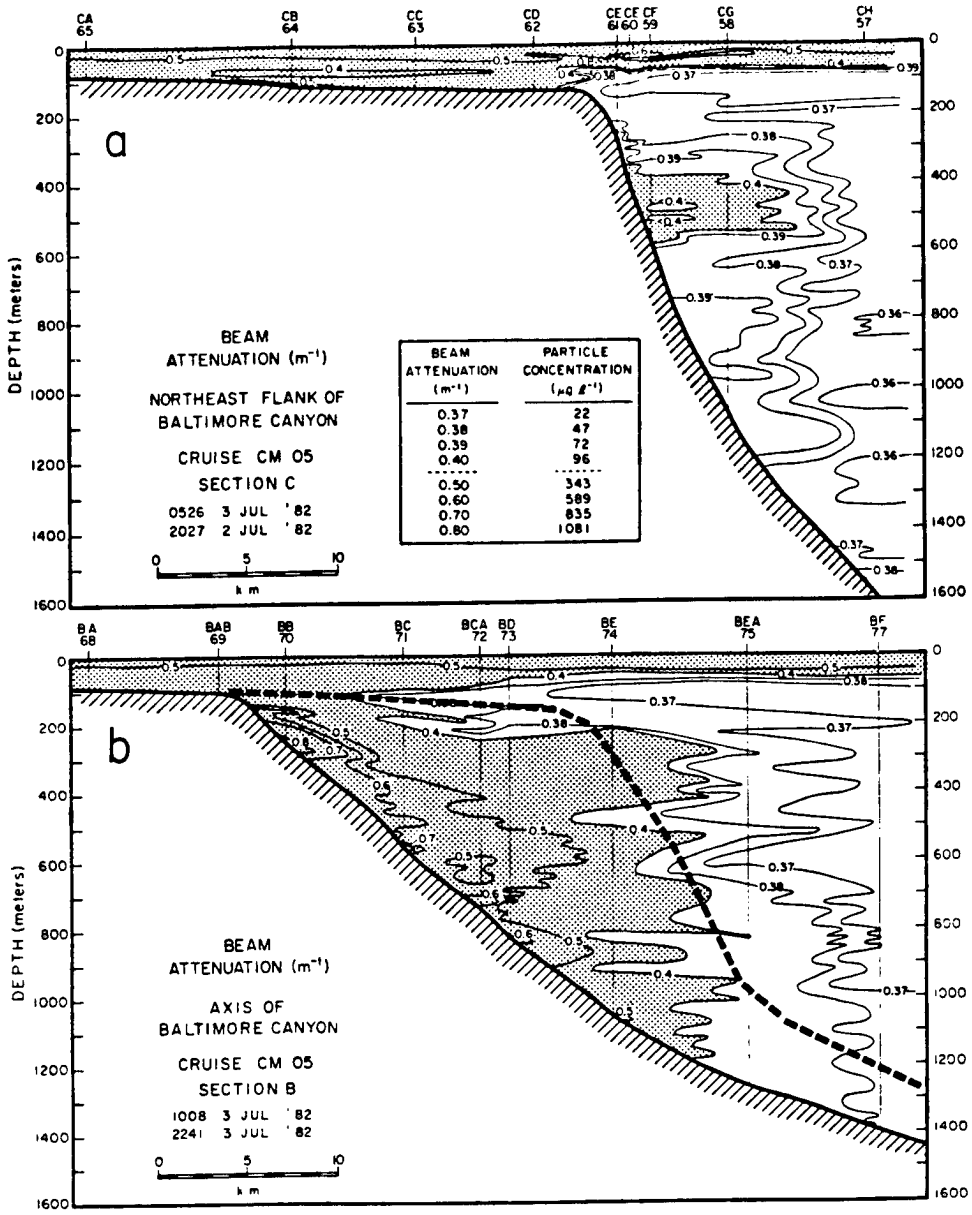


Figure 7. Contoured beam attenuation (m^{-1}) along sections northeast of Baltimore Canyon and along the canyon axis. Contour intervals are 0.1 m^{-1} for values greater than 0.4 m^{-1} (stippled area) and 0.01 m^{-1} for values less than 0.4 m^{-1}. The heavy dotted line indicates the outline of the canyon walls. From Gardner (1989).

The Effect of Canyons on Shelf/Slope Mass Exchange

Church et al. (1984) conclude that shelf-slope exchange is modified by a canyon on the east coast of the U.S. Their data include hydrographic/nutrient/oxygen measurements obtained on a shipboard survey of the shelf and slope in a region including Wilmington Canyon. Their results suggest that the cyclonic circulation pattern observed at that time in the vicinity of the canyon promoted nutrient exchange and biological production. The authors suggest that more direct and time-dependent measurements would be necessary to fully understand the nature of such interactions.

Regional models suggest that upwelling is enhanced on the downstream side of canyons (Peffley and O'Brien, 1976; Cushman-Roisin and O'Brien, 1983). The finer resolution models of realistic canyons described in the preceding section also suggest that upwelling is enhanced on the downstream side of a canyon (Allen, 1995; Klinck, 1995). Onshore flow and upwelling rates are as much as a factor of ten stronger within the canyon than over the nearby continental slopes (Allen, 1995) and the upwelled

water is lifted out of the canyon at the head and along the downstream edge (Figure 5). Little spatial asymmetry occurs in the case of downwelling, at least in the steady state model (Figure 5) (Klinck, 1995). Thus, one might expect to more readily observe dramatic canyon effects on regional water properties in areas and seasons in which upwelling is dominant. Klinck's (1989) model for the flow within a coastal channel suggests that strong density disturbances can occur even for canyons much narrower than the internal Rossby radius.

An example of enhanced upwelling on the downstream side of a canyon was obtained in the field study of Astoria Canyon (Figure 3). Data in Shaffer (1976) are also suggestive of localized upwelling near the head of a canyon off the African coast. Time series of temperature data within Quinault Canyon and on the nearby slope illustrate that the canyon upwelling is stronger during each individual upwelling event (Hickey, 1989). To my knowledge no such explicit examples have been presented for canyons in western boundary systems, on which wind-driven upwelling is less common.

Whether upwelled water actually breaks the surface above or near the canyon is a question of great interest, particularly to biological oceanographers. Localized upwelling of nutrient-rich water into the euphotic zone would provide an explanation for enhanced zooplankton biomass in the vicinity of some canyons. In Juan de Fuca Canyon, upwelled water reaches close enough to the surface to allow erosion by entrainment into the surface mixed layer (Freeland and Denman, 1982). However, the driving mechanism for this upwelling depends in part on the buoyantly driven coastal current associated with the effluent from the Strait of Juan de Fuca; this physical situation is unlikely to occur near most canyons. The majority of the data available as well as the recent model results for stratified situations suggest that upwelled water is likely confined to a bottom boundary layer in most cases. If a canyon cuts across the shelf sufficiently close to the coast to be within the coastal upwelling zone (a Rossby radius), water upwelled from the canyon might be upwelled further by upwelling near the coastal wall. Shaffer (1976) seems convinced that water upwelled from a canyon breaks the sea surface just shoreward of the canyon. However, the evidence as it is presented in his paper is far from conclusive.

Rosenfeld et al. (1994) have recently demonstrated that during at least one coastal upwelling event, the cold surface water observed in Monterey Bay came from water upwelled outside the bay that was advected laterally into the bay. The upwelling plume passed straight over the canyon and was not connected to either the local coastline or the canyon in any way. The prevailing idea prior to this study was that upwelled water within Monterey Bay was due to the presence of Monterey Canyon. This example demonstrates that studies of canyon effects should always be done within a regional context.

Modification of Regional Currents and Water Properties by Submarine Canyons

Regional circulation will attempt to follow the topography as it bends around the canyon at the shelf edge. How successfully it can do so will likely depend on stratification, vertical and horizontal structure of the incident flow, canyon width and the Rossby number of the incident flow. Canyon model studies to date have confirmed that the amount of steering is a function of both stratification and the Rossby number of the incident regional flow (Allen, 1995; Klinck, 1995). Steering of streamlines by canyon topography has been observed over a number of canyons. One example, obtained from hydrographic data off the coast of Spain, is shown in Figure 8 (Maso et al., 1991). The data illustrate that the degree of steering increases with proximity to the bottom. Likewise, over Astoria Canyon, direct current measurements show that whereas the flow 80 meters above bottom is not strongly affected by the canyon, the flow 50 meters above bottom is strongly affected by the topography (Hickey, 1995; and see Figure 3, this paper). A Rossby number dependence has been confirmed observationally by the Astoria data: the higher the Rossby number, the less the flow over the canyon turns to follow canyon isobaths (Hickey, 1995).

The abruptness of the canyon topography, i.e., the angle between the incident flow and the canyon isobaths, would also be expected to have a significant effect on the resulting interaction between the incident flow and the canyon. The greater than 90° bend in local isobaths on the upstream side of Astoria Canyon (see Figure 3) may provide an explanation for the semi-permanent cyclonic circulation pattern observed above that canyon. A similar situation may occur near Carson Canyon (Kinsella et al., 1987). In this case, the strongly bent isobaths are also on the upstream side of the canyon (for downwelling-favorable flow). The flow only 10 m above bottom passes directly across the local isobaths of Carson Canyon, making little attempt to follow the larger scale canyon curvature.

The enhancement of upwelling on the downstream side of canyons must also affect regional flow patterns and mass balances. In particular, during upwelling events, significant quantities of water are pumped out of a canyon. This water is advected downstream and also inshore of the canyon. On the west coast of North America, canyons provide about 15% additional shelf edge for upwelling (assuming that upwelling occurs only on the downstream side of each canyon). If the canyon upwelling rate is only a factor of two greater than non-canyon regions (a very conservative estimate based on model results to date), a total of 30% more water would be upwelled along the shelf break in this region due to the existence of the canyons. Moreover, the greater the upwelling rate within the canyon in comparison with that

outside the canyon, the greater will be the water property anomaly on the shelf in the vicinity of the canyon. Localized fronts must occur within the bottom boundary layer, and these fronts, in turn, would be expected to cause spatial variations in the quasi-geostrophic, baroclinic flow patterns downstream and somewhat inshore of the canyon. The structure of the bottom boundary layer, which is a function of stratification, would also be expected to be affected by a nearby canyon.

Another important feature of submarine canyons is that they can allow much deeper, nutrient-rich water to reach the nearshore zone than would otherwise be possible. If the canyon lies sufficiently close to the coast, the canyon-upwelled water might be further upwelled into the euphotic zone where it would become readily available to the biota.

Critical Research Areas

Considerable progress has been made within the last year in understanding the interaction of the abrupt and realistic topography of coastal canyons with time-dependent, stratified coastal circulation (Allen, 1995; Hickey, 1995; Klinck, 1995). For adequate verification in the field (Astoria Canyon), the effort required a combination of moored and shipboard surveys as well as the fortuitous occurrence of several strongly forced events during those surveys (Hickey, 1995). The models used appropriately steep and abrupt topography, realistic stratification and incident flow conditions, and a canyon that included a headwall on its nearshore end. The results of these studies indicate that during upwelling-favorable incident flow conditions, downwelling of shelf water occurs over the upstream wall of the canyon and upwelling occurs over the canyon axis and over the downstream wall. Upwelling water flows shoreward within the canyon and exits at the head and along its downstream wall. In the upper water column the flow is essentially straight over the canyon. Cyclonic vorticity occurs on the upstream side of the canyon near the rim, and anticyclonic, on the downstream side. The cyclonic vorticity is associated with shelf water which has fallen into the canyon. For realistic incident flows over Astoria Canyon, cyclonic vorticity is observed over about 2/3 of the canyon due to the relatively large inflow velocity and the consequently important nonlinear effects, which tend to sweep spatial patterns downstream. The deeper circulation is cyclonic, a result of layer stretching during upwelling. The data for Astoria Canyon suggest that a Taylor cap-like circulation pattern exists over this particular canyon for Rossby numbers below about 0.25. Closed streamlines have not been observed in model results for the cases examined to date.

The research to date has addressed some straightforward questions, and qualitative agreement between models and observations has been obtained for simple incident flow and simple canyon shapes under strong forcing. Numerous questions remain. For example,

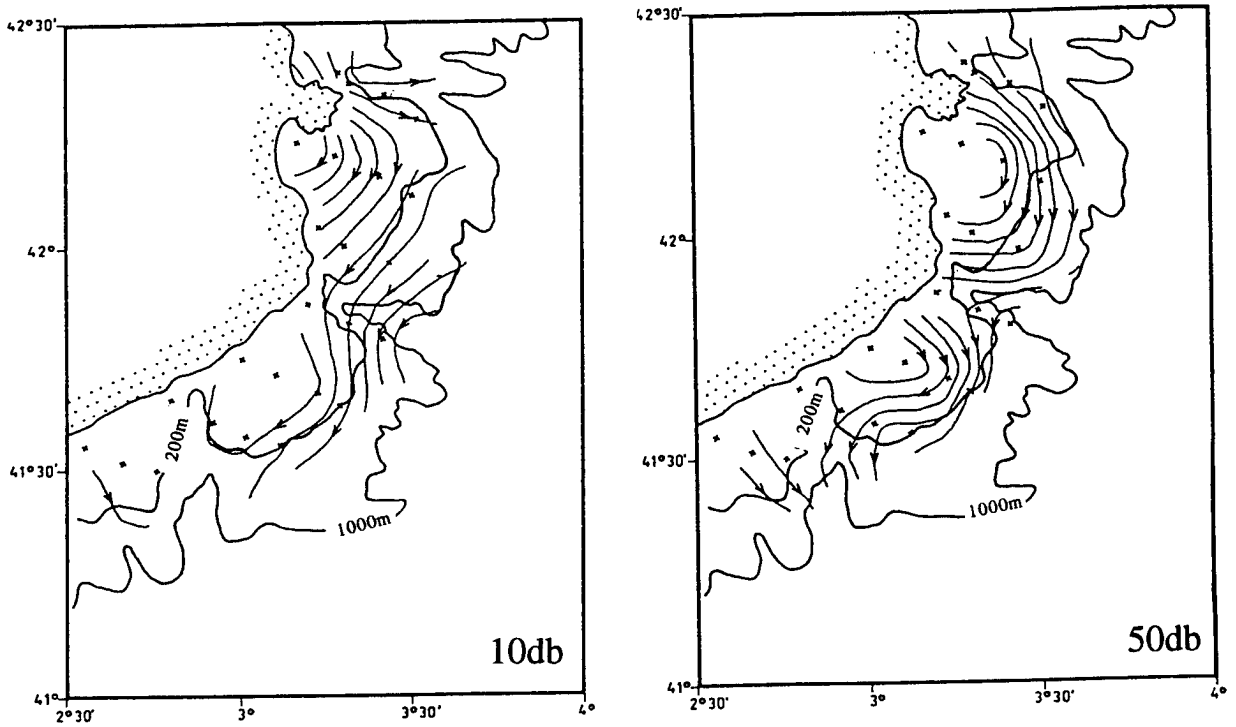


Figure 8. Dynamic topography relative to 100 db in the vicinity of several submarine canyons off the coast of Spain. From Maso et al. (1991).

as the canyon narrows towards its floor, does the flow change from primarily around the canyon walls (quasi-geostrophic) to primarily up and down its axis (quasi-frictional)? What is the role of side wall friction at various depths within the canyon? Model studies suggest that canyons may be energy sinks for barotropic shelf waves. How does a canyon affect wave scattering under stratified conditions?

The extent to which a canyon can trap particles is particularly important to many interdisciplinary problems. Under what conditions does a vortex occur *over* the topography of a canyon? Under what conditions is the circulation *within* the canyon completely closed? How does a two layer flow (e.g., a coastal jet with an undercurrent over the slope) or a stratified flow interact with a steep canyon? The only spatially and temporally comprehensive data set is that for Astoria Canyon. To what extent is Astoria Canyon unique? The more than right angle bend in the shelf break isobaths north of this particular canyon may funnel the incident flow offshore near the apex of the bend. This could lead to a steady cyclonic vortex under all incident conditions as observed. In the real ocean, canyons have many shapes, depending on the geology of their formation. How does the shape of a canyon affect the details of its interaction with the coastal flows? These and other aspects of canyon circulation and canyon-flow interactions are the subject of ongoing research.

Finally, we note that there is strong evidence to suggest that submarine canyons have an important effect on marine ecosystems. The effects include the entire food chain, from phytoplankton to marine mammals. The exact mechanisms for such effects have not been addressed to date. Future efforts in canyon studies would benefit greatly from an interdisciplinary approach.

Acknowledgments

This paper was funded by grant OCE 94-17048 from the National Science Foundation.

References

Allen, J.S., 1976: Continental shelf waves and alongshore variations in bottom topography and coastline, *J. Phys. Oceanogr.*, 6, 864-878.

Allen, S.E., 1995: Topographically generated, subinertial flows within a finite length canyon, *J. Phys. Oceanogr.*, submitted.

Baker, E.T. and B.M. Hickey, 1986: Contemporary sedimentation processes in and around an active West Coast submarine canyon, *Marine Geology*, 71, 15-34.

Baines, P.G., 1983: Tidal motion in submarine canyons—a laboratory experiment, *J. Phys. Oceanogr.*, 13, 310-328.

Bohrer, R., 1995: Asymmetric water mass distributions across a submarine canyon with implications for shelf-slope exchange, in preparation.

Cannon, G.A. and G.S.E. Lagerloef, 1983: Topographic influence on coastal circulation: A review, in H. Gade, A. Edwards and H. Svendsen, (eds.) *Coastal Oceanography*, Plenum Publishing Corporation, pp. 235-252.

Church, T.M., C.N.K. Mooers and A.D. Voorhis, 1984: Exchange processes over a middle Atlantic bight shelfbreak canyon, *Estuarine, Coastal and Shelf Science*, 19, 393-411.

Cushman-Roisin, B. and J.J. O'Brien, 1983: The influence of bottom topography on baroclinic transports, *J. Phys. Oceanogr.*, 13, 1,600-1,611.

Faucher, A. and H. Whitehead, 1992: The bottlenose whales of the Gully: final report for 1988-91 to WWF-Canada (unpublished).

Freeland, H.J. and K.L. Denman, 1982: A topographically controlled upwelling center off southern Vancouver Island, *J. Mar. Res.*, 40(4), 1,069-1,093.

Gardner, W.D., 1989: Periodic resuspension in Baltimore Canyon by focusing of internal waves, *J. Geophys. Res.*, 94(C12), 18,185-18,194.

Garrett, C.J.R. and W.H. Munk, 1975: Space-time scales of internal waves; a progress report, *J. Geophys. Res.*, 80, 291-297.

Grimshaw, R.H.J., P.G. Baines and R.C. Bell, 1985: The reflection and diffraction of internal waves from the junction of a slit and a half-space, with application to submarine canyons, in *Dynamics of Atmospheres and Oceans*, Elsevier Science Publishers B.V., Amsterdam, 9, 85-120.

Hickey, B.M., 1989: Patterns and processes of circulation over the Washington continental shelf and slope, in *Coastal Oceanography of Washington and Oregon*, M. Landry and B. Hickey (eds.), Elsevier Science, Amsterdam, pp 41-116.

Hickey, B.M., 1995: Response to a narrow submarine canyon to strong wind forcing, *J. Phys. Oceanogr.*, submitted.

Hickey, B.M., E. Baker and N.B. Kachel, 1986: Suspended particle movement in and around Quinault Submarine Canyon, *Marine Geology*, 71, 35-83.

Hotchkiss, F.S. and C. Wunsch, 1982: Internal waves in Hudson Canyon with possible geological implications, *Deep-Sea Res.*, 29, 415-422.

Hunkins, K., 1988: Mean and tidal currents in Baltimore Canyon, *J. Geophys. Res.*, 93, 6,917-6,929.

Hurlburt, H.E., 1974: The influence of coastline geometry and bottom topography on the eastern ocean circulation. Ph. D. thesis, Florida State Univ., 103 pp.

Hsueh, Y., 1980: On the theory of deep flow in the Hudson Shelf Valley, *J. Geophys. Res.*, 85, 4,913-4,918.

Kinsella, E.D., A.E. Hay and W.W. Denner, 1987: Wind and topographic effects on the Labrador current at Carson canyon, *J. Geophys. Res.*, 92(C10), 10,853-10,869.

Klinck, J.M., 1988: The influence of a narrow transverse canyon on initially geostrophic flow, *J. Geophys. Res.*, 93, 509-515.

Klinck, J.M., 1989: Geostrophic adjustment over submarine canyons, *J. Geophys. Res.*, 94, 6,133-6,144.

Klinck, J.M., 1995: Circulation near submarine canyons: a modeling study, *J. Geophys. Res.*, submitted.

Lentz, S.J. and J.H. Trowbridge, 1991: The bottom boundary layer over the northern California shelf, *J. Phys. Oceanogr.*, 21(8), 1,186-1,201.

Lueck, R.G. and T.R. Osborn, 1985: Turbulence measurements in a submarine canyon, *Cont. Shelf. Res.*, 4(6), 681-695.

Maso, M., P.E. La Violette and J. Tintore, 1991: Coastal flow modification by submarine canyons along the NE Spanish coast, *Sci. Mar.,* 54(4), 343-348.

Nelson, T.A., P.E. Gadd and T.L. Clarke, 1978: Wind-induced current flow in the upper Hudson Shelf valley, *J. Geophys. Res.,* 83, 6,073-6,082.

Nittrouer, C.A., 1978: The process of detrital sediment accumulation in a continental shelf environment: an examination of the Washington shelf, Ph.D. Thesis, Univ. of Washington, Seattle, Wa. 243 pp.

Noble, M. and B. Butman, 1989: The structure of subtidal currents within and around Lydonia Canyon: Evidence for enhanced cross-shelf fluctuations over the mouth of the canyon, *J. Geophys. Res.,* 94, 8,091-8,110.

Peffley, M.B. and J.J. O'Brien, 1976: A three-dimensional simulation of coastal upwelling off Oregon, *J. Phys. Oceanogr.,* 6, 164-180.

Petruncio, E.T., J.D. Paduan and L.K. Rosenfeld, 1994: Baroclinic tidal currents in Monterey Submarine Canyon, *Trans. Amer. Geophys. Union EOS,* 75(44), Supplement.

Rosenfeld, L.K., F.B. Schwing, N. Garfield and D.N. Tracy, 1994: Bifurcated flow from an upwelling center: a cold water source for Monterey Bay, *Cont. Shelf. Res.,* 14(9), 931-964.

Shaffer, G., 1976: A mesoscale study of coastal upwelling variability off NW Africa, *Meteor Forsch.-Ergebn. A.*, 17, 21-72.

Shepard, F.P., N.F. Marshall, P.A. McLoughlin and G.G. Sullivan, 1979: *Currents in Submarine Canyons and Other Seavalleys,* 173 pp.

Wang, D.P., 1980: Diffraction of continental shelf waves by irregular longshore geometry, *J. Phys. Oceanogr.,* 10(8), 1187-1199.

Wilkin, J.L. and D.C. Chapman, 1990: Scattering of coastal-trapped waves by irregularities in coastline and topography, *J. Phys. Oceanogr.,* 20(3), 396-421.

Shelf Break Momentum Transport by Internal Waves Generated by Along-Slope Currents over Topography

S.A. Thorpe, D. Jiang, and J.M. Keen

Department of Oceanography, The University, Southampton, SO9 5NH, UK

Abstract. The along-slope currents flowing over topography of small, typically < 10 km, scale on the continental slopes produce internal lee waves with a predominant transfer of momentum towards shallower water, that is up the slope towards and across the shelf break and onto the continental shelf, at least when, in summer, stratification permits their propagation. Analytical results show that even when the lee waves at generation have a component of their group velocity directed towards deeper water, reflection at the sloping sea bed may lead to a turning towards shallower water. A numerical model is used to examine internal wave propagation and to quantify the flux of their momentum across the shelf break. The flux is usually dominated by the larger currents, greater stratification and rougher topography near the top of the slope, and, in conditions in which $f/N << 1$, is parameterised by a stress (momentum flux per unit vertical area along the shelf break) per unit length down-slope, τ_*, given by $\tau_* = k\rho_0 VNh^2 \cos^4(\beta + \beta_0)$, where ρ_0 is the mean water density, V is the mean along-slope flow over the slope, N is the buoyancy frequency in the vicinity of the shelf break, f is the Coriolis parameter, and h^2 and β are the mean square amplitude of the topography of wave number, l, such that $Vl/N < 1$, and its mean orientation relative to the upslope direction, respectively. The constant β_0 is $7 \pm 2°$and estimates are for $\beta <$ about 60°. A working value of k of about $(9 \pm 4) \times 10^{-6}$ m^{-2} is suggested, with values near 1.3×10^{-5} m^{-2} when the topography is dominated by wavelengths less than $4\pi V/N$, or 5×10^{-6} m^{-2} when they exceed $20V/N$. This flux represents a transfer of momentum to the shelf currents in a direction contrary to the current over the slope leading to the generation of the internal waves. Time-scales of about 5 days are associated with this transfer on 5° slopes with 10-m-high topography when $N \approx 10^{-2}$ s^{-1}.

1. Introduction

The continental slopes are major topographic features of the surface of the solid Earth, being 4-5 km in height and extending for thousands of kilometres. They have great importance for the oceans. They are sites of upwelling, major fisheries, and generally a maximum (near 1 km depth) in biodiversity. They act as the natural boundaries for the circulation of waters deeper than about 200 m (or more generally, the depth of the shelf-break) and they form the outer boundary of shelf-sea circulations. They are zones of exchange between the shelf seas and the deep ocean of water, particles and solutes, some of anthropogenic origin derived from land. Visual observations show in conditions of summer stratification the shelf break and slopes are often regions of intense internal wave activity (Apel et al., 1975; Baines, 1981; Fedorov and Ginzberg, 1986) and therefore sites at which, if anywhere in the surface ocean, internal wave effects on momentum flux may be significant.

In some areas the tidal streams are directed with large components normal to the shelf break (or across the slope) and generate internal waves and soliton packets as explained, for example, by Maxworthy (1979; see also Hibiya, 1986, 1988; Huthnance, 1989; Lamb, 1994; Gerkema, 1994), but this is not generally the case, and the *mean* currents near the slope at depths greater than that of the shelf break are constrained by stratification and the Earth's rotation to flow approximately along isobaths. Many of the theoretical investigations cited ignore the variation of the continental slope along its length and assume two-dimensionality, whereas inspection of high resolution bathymetric charts of the continental slopes show them to be highly convoluted along their length, being cut by channels, rills, gullies and canyons of a variety of scales; below the shelf break the major variation in small-scale topography is generally in the along-slope direction and so the features lie normal to the mean current direction.

Interaction between the mean along-slope flow and topography generates internal waves and hence a transfer of momentum into the internal wave field (Bretherton, 1969). In the deep ocean the momentum associated with these waves is generally small; they are constrained to lie in a wavenumber band between f/U and N/U, where f is the Coriolis parameter, N is the buoyancy frequency, and U is the current speed, and this band is narrow since N/f is not large. Bell (1975) shows that it is indeed only small, about 300 m horizontal scale, topography, which is effective in generating internal waves in the deep ocean. However, as pointed out by Holloway (1992), N/f is relatively large in the upper ocean and, where topographic variability is large, as near the shelf break, internal wave drag may be important.

This paper describes the transfer of momentum onto a continental shelf by internal waves generated by flow over the slope. It builds on an observation (Thorpe, 1992; see section 2.1 below) that the energy associated with internal

lee waves produced by flow along sloping topography has a bias toward shallow water, being carried by a preferentially positive component of group velocity up the slope and into shallower water, rather than towards deeper water, provided that the characteristics of the water mass allow for internal wave propagation to continue in this direction. This earlier work was based on analytical studies of waves in an infinitely deep ocean and in a fluid with a uniform and steady along-slope flow, V, and uniform buoyancy frequency, N, so that waves of any vertical scale could be generated, propagation was in straight rays, with the effects of surface reflection and subsequent bottom reflections largely ignored. We emphasise that, although concerned primarily with wave *generation* by the along-slope current, the full problem now to be addressed includes the possible subsequent *reflection* of waves from the sea bed, and in principle all the complexity of that much studied problem (see references above). Further progress by analytical methods appears unlikely to be very productive and therefore we have resorted instead to numerical studies (sections 3 and 4) guided by further analysis (section 2), with the overall objective of deriving a parametric description of internal wave drag which might prove useful in numerical models of ocean or shelf-sea circulation.

Such modelling of internal wave momentum transport and breaking in the *atmosphere* is relatively commonplace (see for example, McFarlane, 1987); internal wave drag is now recognised as having a large effect on the circulation (see for example Lilly, 1972; Palmer et al., 1986; Miller et al., 1989; Hoinka and Clark, 1991; Clark and Miller, 1991). In the oceans, the drag contributes to the *lateral* boundary condition which should be applied to models of ocean circulation abutting the continental slopes; we are concerned with both the vertical flux of horizontal momentum *and* in the horizontal flux of horizontal momentum. In this examination of the effects of internal waves we shall only begin to probe the problem of describing the boundary conditions; a full solution demands study both near the boundary itself (where the waves are generated) and in the presently less-well-known regions where waves are dissipated. Our modest objective is to characterise the possible magnitude of the flux rather than to attempt to derive a formulation valid for all slopes, stratification, and flow structures. After all, if the flux is negligible there is little sense in estimating its destination. The parameterisation (see section 4) may require more observations at sea.

The need to correctly describe the lateral boundary conditions on the velocity field in ocean circulation models is discussed by Ierley (1990); he stresses that the choice of conditions is particularly important because of the effect which they may have on the conservation (or otherwise) of potential vorticity.

2. Analytical Results

2.1. The Generation of Internal Lee Waves on a Slope

Internal waves can be generated by the flow over topography on a slope. For simplicity we consider a uniform and steady flow, V, of a fluid with constant buoyancy frequency, N, parallel to the mean isobaths of a uniform slope, which is tilted at angle α to the horizontal and covered by corrugations of wavelength $\lambda = 2\pi/l$ running down the slope at an angle β to the line of maximum slope (Fig. 1), adopting the approach that any topography may be decomposed into Fourier components and a *linear* wave field found by summation. The inclination of an internal wave constant phase surface to the horizontal is given by

$$\theta = \sin^{-1}(\sigma/N), \tag{1}$$

and phase of the waves is stationary if the intrinsic frequency of the waves, σ, satisfies $\sigma/l = Vc_\beta$, so that

$$\theta = \sin^{-1}(\chi c_\beta), \tag{2}$$

where $\chi = Vl/N$ is a Froude number of the flow, such that

$$\left[ps_\alpha^2 + (1-p)c_\beta^{-2}\right]^{1/2} < \chi < c_\beta^{-1}, \tag{3}$$

where $p = 1 - (f/N)^2$ (Thorpe, 1992; here $c_\beta = \cos\beta$ etc.). This may be written $2\pi V/N < \lambda_y < 2\pi V/(N\,[ps_\alpha^2 + (1 - p)\,c_\beta^{-2}]^{1/2})$, where λ_y is the wavelength of the topography measured along the slope in the y-direction. This implies that even though N may be small in deep water, the values of λ_y for which internal waves will be

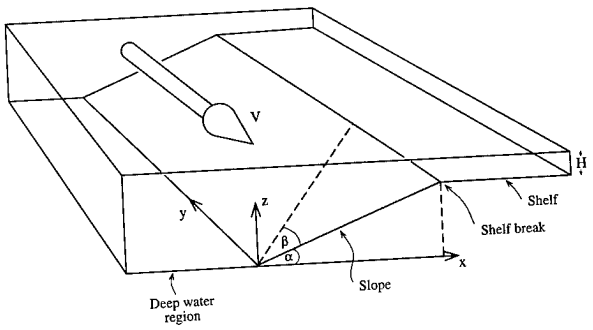


Figure 1. Sketch of the model geometry. The deep water region is generally taken to be 1000 m deep and the shelf 200 m deep. Both are bounded by vertical walls (or by 'spongy layers' to absorb wave energy). Topography is superimposed on the slope (shown 'stippled'). The model is periodic in the along-slope direction. The mean flow is parallel to the line of the shelf break and uniform across the channel formed between the side walls. In section 2 the effect is considered of 'ripples' with crests aligned at angle β as shown.

generated in the ocean are generally limited to scales between about 100 m and 10 km. We find that that waves generated near the upper part of the slope are most effective in the transport of momentum. The Burger number, B = *NH/fL*, where *H* is the water depth, is large there and generally it is justified to take $(f/N)^2 << s_\alpha^2 << 1$ (see also caption to Fig. 2). Then (3) becomes

$$s_a < \chi < c_\beta^{-1}. \qquad (4)$$

(This can be written $s_\alpha c_\beta < V_1 l/N < 1$, where V_1 is the component of V normal to the crest lines of the topography, a more general form of eq. (4) when the direction of V is in any direction parallel to the plane of the slope). Although the wave phase is stationary in the flow, wave energy propagates with a positive component of group velocity towards shallow water when

$$-\left|\cos^{-1}(s_\alpha/\chi)\right| < \beta < \beta_{crit}, \qquad (5)$$

where β_{crit} is the positive root of $c_\beta c_a = \left(1-s_\alpha^2/\chi^2\right)^{1/2}$. There is a preferential trend towards shallow water for moderate values of β; the area of the χ - β plane (Fig. 2) is dominated by propagation towards shallow water. The bias increases as χ decreases from $c_{\beta\text{-}1}$ (when $\beta_{crit} = 0$) to s_α (when $\beta_{crit} = \pi/2$ and all waves generated with stationary phase travel towards shallow water whatever the value of β). It is found by simple geometry that the angle between the projection of the relative wave group velocity vector onto the horizontal plane and a horizontal direction pointing upslope normal to the isobaths is φ given by

$$\cos\phi = \left[s_\alpha c_\alpha - t_\beta \left(t_\theta^2 c_\alpha^2 + t_\theta^2 t_\beta^2 - s_\alpha^2 \right)^{1/2} \right] / \left[t_\theta \left(c_\alpha^2 + t_\beta^2 \right) \right] \qquad (6)$$

(e.g., see Eriksen, 1982; Gilbert, 1990).

2.2. Reflection of Internal Waves at the Sea Surface and Slope; *N* and α Uniform

The ocean, unlike the atmosphere, has an upper boundary, the sea surface. Reflection of waves from a smooth sea surface or from a smooth slope will preserve the wave frequency and along-slope wavenumber and waves will therefore remain stationary in the along-slope flow.

After downward reflection at the sea surface, waves will return to the sea bed. Provided that θ > α, the angle φ will decrease towards zero at each successive reflection of the waves from the slope, even if the internal waves are *generated* with a positive component of their group velocity directed towards deeper water (see Eriksen, 1982, figure 2b). The internal lee waves are therefore *trapped* within the slope-shelf region when θ > α, their group velocity relative to the mean flow progressively turning towards the up-slope direction on each reflection from the bottom. The only waves to escape will be either those generated with a component of group velocity towards deeper water, the areas which are not stippled in Figure 2, or those which, on generation, propagate towards shallow water but have θ > α (those in the area in Fig. 2 with β > 0 and $s_\alpha < \chi < s_\alpha/c_\beta$). The latter reflect towards deeper water on their first reflection from the slope. Of the former there are two classes: those which propagate at an angle below the horizontal, which may not intersect the slope, and those which, after their first reflection from the sea

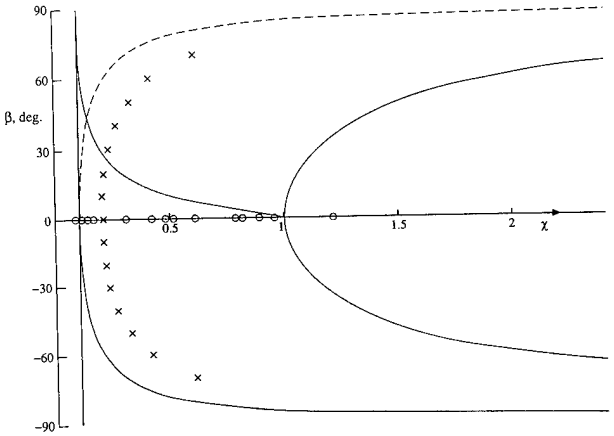


Figure 2. The β - χ plane for $\sin^{-1}\alpha = 0.1$ showing the areas, $s_\alpha < \chi < c^{-1}{}_\beta$, in which stationary phase waves can be formed over sinusoidal topography on a slope. The direction of group propagation of these waves is towards shallow water in the stippled area. This area is bounded by the curve $\beta = \beta_{crit} = \cos^{-1}[(1-s_\alpha^2/\chi^2)^{1/2}/c_\alpha]$ when β > 0 , and by the curve $\chi = s_\alpha/c_\beta$ when β < 0. The value of θ is π/2 (vertically propagating waves) on $\chi = c^{-1}{}_\beta$. $\theta = \tan^{-1}(s_\alpha/t_\beta)$ on the full curve separating the areas of different propagation directions for β > 0. θ = α on the dashed curve where β > 0 and on the curve separating directions for β < 0. Between the latter and $\chi = s_\alpha$ wave propagation is below the horizontal and towards deeper water. On $\chi = s_\alpha$ $\theta = \sin^{-1}(s_\alpha c_\beta)$ and so is less than α. All waves in the sector $s_\alpha / c_\beta < \chi < c^{-1}{}_\beta$ will (after sufficient reflections if β > 0) propagate towards shallower water depths (see 2.2). The effect of non-negligible *f/N* is to increase the lower values of χ to $(s_\alpha^2 + f^2/N^2)^{1/2}$. The lower bound of χ increases with increasing |β|, and the curve separating the regions of wave propagation towards deeper or shallower water in β > 0 has increasing values of χ at large β. The overall effect is to reduce the area of the χ - β plane in which stationary waves are possible. Crosses and circles correspond to the parameter values at which numerical experiments are made (see Figs. 4 and 5).

surface or on a subsequent group velocity towards deeper water, reach the abyssal plain. (Some waves generated sufficiently near the foot of the slope will always "escape" in this way). Over the area in the χ - β plane in which $s_\alpha/c_\beta < \chi < c_\beta^{-1}$ (Fig. 2) all stationary phase waves, including those which are propagating towards deeper water when generated (provided they reflect sufficiently often from the slope and do not reach the abyssal plain), will eventually propagate towards shallower water depths.

If the the sea surface or slope is rough where the reflection occurs, some of the internal wave energy may be scattered (see Baines, 1971 a,b; Thorpe, 1992) or, for surface reflection, the internal waves may even interact resonantly with the surface waves. For simplicity, these latter effects are disregarded here but should be considered when it comes to comparison of theoretical estimates with observations.

2.3 Effects of Non-Uniform N and α

The conclusions of section 2.2 ignore the variations of N and α which occur in the ocean. Waves propagating upwards towards the sea surface from the lower parts of the slope will encounter regions where the density gradient and therefore N increases. Since the intrinsic frequency, σ, is conserved, the angle of the group velocity vector to the horizontal, $\theta = \sin^{-1}(\sigma/N)$, decreases as N increases, and the wave paths will be refracted towards the horizontal. Since generally α increases towards the shelf break, the waves propagating towards shallower water may therefore return to meet the slope (i.e., propagating at an angle, θ, which is smaller than the local slope), and generally be reflected back toward deeper water. Waves propagating towards deeper water at generation may never reach the surface and will therefore not be reflected back to the slope, will continue to radiate into deeper water, and will not be trapped in the shelf region.

In contrast, If N becomes very small at some depth level below that of the shelf break, as for example, it will do when the depth of the winter convectively mixed layer exceeds that of the continental shelf, internal waves will be unable to propagate beyond the level at which $\sigma = N$ and will be reflected down to be trapped in the wedge between the slope and the level at which $\sigma = N$, possibly with enhanced amplitudes and breaking which may serve to contribute to the further deepening of the convective layer if dissipation is not sufficient to limit them. No momentum will then be carried by the waves onto the shelf.

3. Numerical Results

3.1 The Model

We used a semi-spectral hydrostatic primitive equation model developed by Haidvogel and others (see Haidvogel et al., 1991; Chapman and Haidvogel, 1993) to examine stratified uniform flow along a channel with a section consisting of a constant 200-m-depth shelf, slope with angle α generally taken such that $s_\alpha = 0.1$, giving an 8-km length slope, and constant 1 km depth abyssal plain (Fig. 1). The uniform flow runs parallel to the isobaths of the slope and is laterally constrained by parallel vertical boundaries on the shelf and abyssal plain. Periodic conditions were chosen in the along-slope direction. The vertical flow structure is represented through modified Chebyshev polynomials, seven being found adequate when the buoyancy frequency, N, of the fluid is constant in depth, but twenty-one being found necessary to satisfactorily resolve the flow in some runs (Thorpe, 1995) in which N varies with depth. Experiments were made with uniform and oscillatory flows over topography of various kinds on the slope.

Like Chapman and Haidvogel we adopted a free slip boundary condition at the lower and upper (rigid lid) boundary and included only 'horizontal viscosity', usually set to zero. Where necessary, higher viscosity spongy layers were introduced in the vicinity of the lateral boundaries to prevent their affecting the flow over the slope.

3.2 Steady Flow Over 'Bump' Topography

First test runs of the model proved its integrity through its ability to reproduce earlier results of stratified flow around isolated Gaussian topography on a horizontal plane. Figure 3 is an example of the effect of the slope on the perturbation field caused by an along-slope flow with $N = 10^{-3}$ s^{-1} and speed $V = 0.1$ m s^{-1} over an isolated 10 m high Gaussian 'bump' with scale radius 2.1 km at the position marked with a circle. Shown is the along-slope component of the current field at the sea surface 30 hrs after the onset of the flow, when (a) the slope angle is zero and the water depth is 600 m and (b) when the topography is located at 600m water depth, half way up a uniform slope with $s_\alpha = 0.1$ between the 200 m 'shelf' and the 1000-m deep plain. The wave pattern is distorted in the upslope direction. The momentum flux across the 20-km-long shelf break is given by $Fx_1/\rho_0 VN = 1.55\times10^4$ m^3, and this is about six times greater than the momentum flux across the foot of the slope at the same time.

3.2 Steady Flow Over 'Bump' Topography

First test runs of the model proved its integrity through its ability to reproduce earlier results of stratified flow around isolated Gaussian topography on a horizontal plane. Figure 3 is an example of the effect of the slope on the perturbation field caused by an along-slope flow with $N = 10^{-3}$ s^{-1} and speed $V = 0.1$ m s^{-1} over an isolated 10-m-high Gaussian 'bump' with scale radius 2.1 km at the position marked with a circle. Shown is the along-slope component of the current field at the sea surface 30 hrs after the onset of the flow, when (a) the slope angle is zero and the water depth is 600 m and (b) when the topography is located at 600 m water depth, halfway up a uniform slope with $s_\alpha = 0.1$ between the 200 m 'shelf' and the 1000-m-deep plain. The wave pattern is distorted in the upslope direction. The momentum flux across the 20-km-long shelf break is given by $Fx_1/\rho_0 VN = 1.55 \times 10^4$ m^3, and this is about six times greater than the momentum flux across the foot of the slope at the same time.

3.3 Steady Flow Over Sinusoidal Topography

Further tests of the model were made to establish it produced waves over sinusoidal ripples on the slope at times of about 3-12 hr which were consistent with predictions of the analytical model; their inclinations were in accord with the theory.

Several runs were made to explore the properties of the model with 'typical' values and rippled topography of amplitude a. Seven polynomials were usually taken to define the vertical structure and an along-slope grid of 14 points and an upslope direction grid of 101 point was generally used. Values of the momentum flux through a vertical plane at the shelf break, Fx_1, generally increased with time after the flow was switched on, before settling to a value about which fluctuations of 5-10% occurred after a 'spin-up' time estimated to be approximately equal to that required for waves to arrive from the foot of the slope. Eventual numerical instability proved to be unavoidable with zero viscosity, but was usually delayed until the model had run for some 90 hrs. It was commonly preceded by a fall and then a huge and rapid rise in flux.

The 'steady' momentum flux Fx_1 scales with a^2 as expected by linear theory, at least up to values of $al = 0.024$.

Figure 4 shows the variation of the scaled flux at the shelf break, $F_1 = Fx_1/(a^2\rho_0 VNA)$, where ρ_0 is the mean (reference) density and A is the area of the vertical section at the shelf break, for various values of β and with $V = 0.1$ m s^{-1}, $a = 0.5$ m, $\lambda_y = 3$ km and $N = 1\text{x}10^{-3}$ s^{-1} (the corresponding χ and β values are shown by crosses in Figure 2. Values of Fx_1 are factors of (3.4 ± 1.1) greater than those found for $|\beta| \leq 40$ ° when $\nu_H = 1$ m^2 s^{-1}, demonstrating the large damping produced by viscosity when it is included in the numerical model). Slightly higher fluxes are found for $\beta < 0$ than at the corresponding

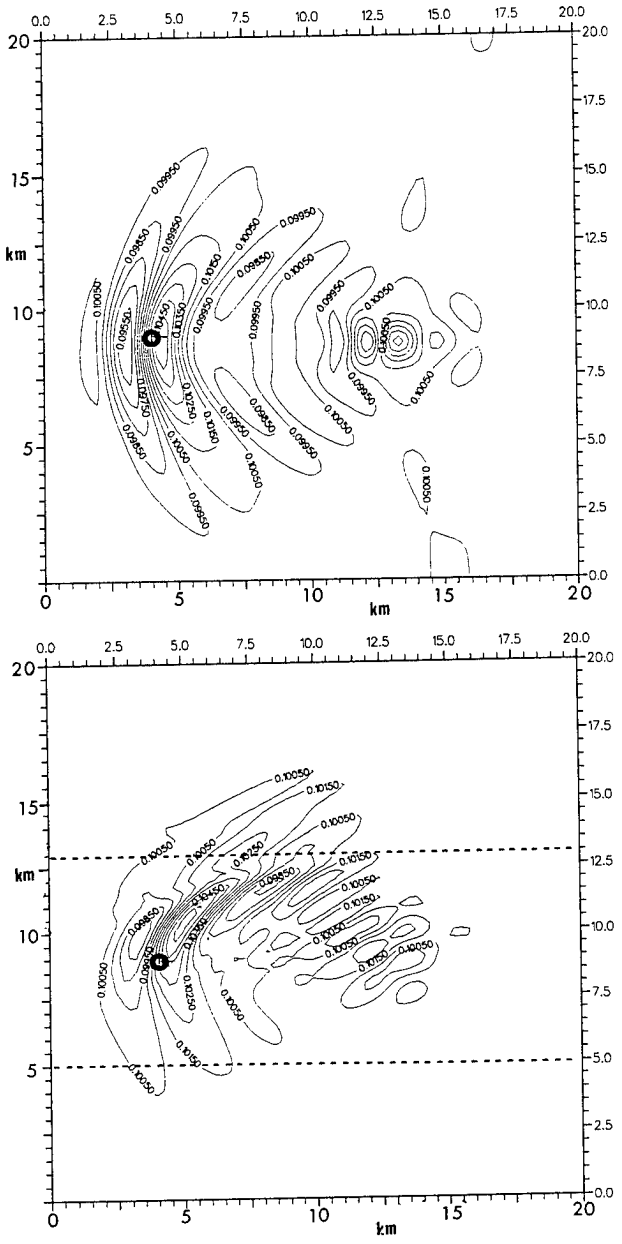


Figure 3. The effect of the slope on the perturbation field caused by an along-slope flow over an isolated 10-m-high Gaussian 'bump' with scale radius 2.1 km at the position marked with a circle. Here $N = 10^{-3}$ s^{-1} and the flow $V = 0.1$ m s^{-1} is to the right. The scales are in km. (a) shows the along-slope component of the current field at the sea surface 30 hr after the onset of the flow, with zero slope angle and 600 m uniform water depth. (b) shows the same current component at the same time when the topography is located at 600 m water depth, but now half way up a uniform slope marked by dashed lines with $s_\alpha = 0.1$ and which lies between the 200 m 'shelf' (at the top) and the 1000-m-deep plain (at the bottom of the figure). Contours are shown at 0.05 cm s^{-1} intervals. The largest current component fluctuation from the mean 10 cm s^{-1} current is 0.45 cm s^{-1}. The effect of the slope is to distort the wave pattern in the upslope direction towards and across the shelf break.

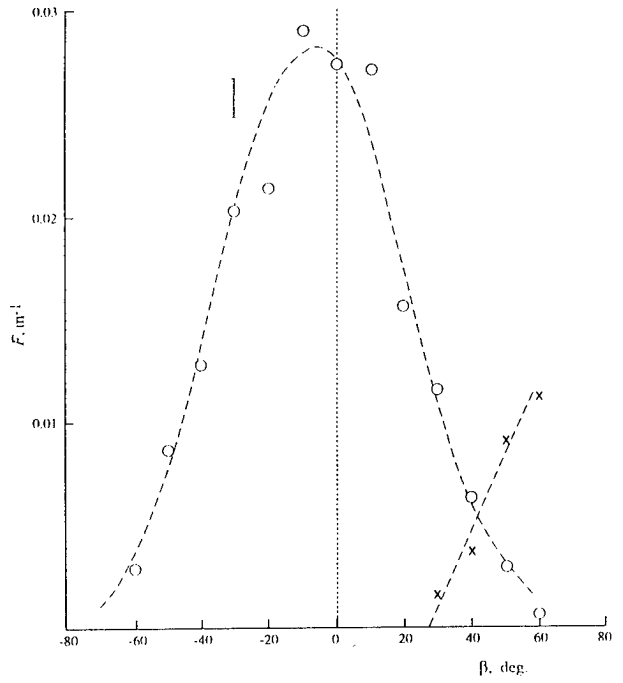


Figure 4. Plot of values of the scaled horizontal flux of horizontal momentum, $F_1 = Fx_1/(a^2\rho_0 VNA)$ (circles) and $F_2 = Fx_2/(a^2\rho_0 VNA)$ (crosses) vs β, derived from the numerical model with values of V = 0.1 m s^{-1}, α = 5.74°, N = 10^{-3} s^{-1}. Larger values of the flux, F_1, are found at negative values of β than at the corresponding positive values. F_2 is significantly greater than zero only when β is greater than about 28° and dominates the flux from the slope when β > 40°. The dashed curve is $F_1 = 0.028\cos^4(\beta + 7.0°)$.

positive values of β, as expected from the analytical results. The dashed curve in Figure 4 is the best fit of $F_1 = F_{10}\cos^q(\beta + \beta_1)$ to the data having $q = 3.9 \pm 0.15$ and $\beta_1 = 7 \pm 2°$. This figure also shows the scaled horizontal momentum flux through a vertical plane at the foot of the slope, F_2. The value of β_{crit} at which the infinite depth analytical model predicts that the direction of the wave flux changes direction from being towards shallower water depths ($\beta < \beta_{crit}$) to being towards deeper water, is 27.9°. F_2 is negligible for $\beta < \beta_{crit}$ (when all wave propagation is towards shallow water) but increases for larger β, becoming equal to F_1 at β = 42° and exceeding F_1 at larger β. F_1, however, does not approach zero as β increases towards β_{crit}, supporting our earlier conclusion that even when the group velocity of the generated waves has a positive component towards deeper water, reflections from the sea bed will lead to momentum transfer towards shallow water.

Figure 5 shows the variation of the scaled flux, F_1, with χ, when β = 0 and with a = 0.5 m and with V taking values from 0.07 to 0.2 m s^{-1}, N values from 0.5 × 10^{-3} s^{-1} to 2 × 10^{-3} s^{-1}, and λ_y values from 0.5 to 6 km. The mean flux is estimated between 48 and 84 hr after the onset of the flow. At values of χ = 0.105 (close to $\chi = s_\alpha$, when waves propagate with θ close to α) and at 0.90 and 0.97 (near $\chi = c_\beta^{-1}$ when θ is close to π/2) the values of F_1 were unsteady and still generally increasing when numerical instability occurred. Very small values of flux are found when χ > 1. The mean values of the scaled flux are about 0.035, with a rise in values occurring near χ = 0.44. At time t such that Nt = 64.8 (18 hr if N = 10^{-3} s^{-1}) F_1 has reached about half the 'steady' value when 0.1 < χ < 0.3, but is already within the uncertainty of the 'steady' values when 0.5 < χ < 0.8. Over the limited range of values tested, the scaling gives consistent results, at least within the uncertainty of the variations of the estimates, and are independent of λ_y except in so far as it affects χ. As expected, the momentum flux into deep water at the foot of the slope was very small, but positive, for all values of χ. When s_α = 0.2, similar values of F_1 are found near χ = 0.3, but values 50% lower than those shown in Figure 5 when χ = 0.48 and 0.62, suggesting that here at least the flux is proportional to the area of slope generating the waves. F_1 must be zero at α = 0, β = 0.

The magnitude of the stress at the shelf break can be compared to that on the sea bed

$$\tau_B = C_D \rho_0 V^2, \qquad (7)$$

where C_D is a drag coefficient, approximately equal to 3×10^{-3} (Heathershaw, 1979). The maximum momentum flux across the shelf break per unit area when β = 0 is 5 × $10^{-2}\rho_0 a^2 VN$, which is equal to τ_B (with V = 0.1 m s^{-1}, N = 1

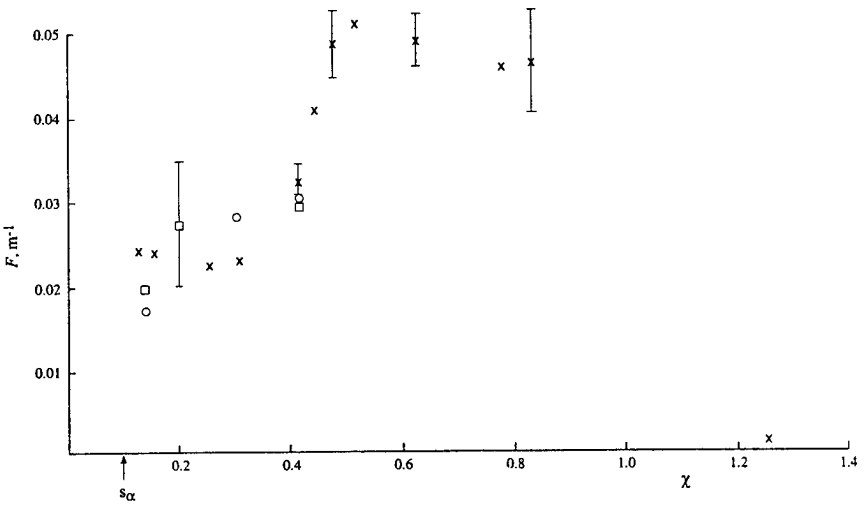


Figure 5. Plot of values of the scaled horizontal flux of horizontal momentum across the shelf break $F_1 = Fx_1/(a^2\rho_0 VNA)$, versus χ at s_α = 0.1 and β = 0. The points represent variation of (crosses) λ (circles) U, and (squares) N, from 'typical' values, λ = 3 km, U = 0.1 m s^{-1}, and N = 1×10^{-3} s^{-1}. Th vertical bars represent the range of variability of the numerical estimates.

$\times 10^{-3}$ s^{-1}) when a = 2.5 m. This is a small value. The *net* stress in the 200-m-deep water at the shelf break is equal to that on the 8-km sloping boundary when a = 15.5 m, which is not untypical of the amplitude of the real topography on continental slopes. Smaller corresponding values of a would be found if N were larger.

Flow over model 'canyons' is found to produce wave patterns propagating onto the 'shelf', with intensification of currents near the canyon head.

3.4 Other Cases

The effect of flow oscillation and stratification is found to modify the area of the slope and the time over which wave generation is possible, and to create an oscillatory flux. Even a relatively small mean flow can result in a rectified momentum flux of mean magnitude similar to those found in steady flows alone. An area of real topography with mean bottom slope close to 5° and with superimposed topography with relative rms amplitude, h, of 9.2 m has also been modelled. Stress values within the range of those in Figure 5 were found.

4. Discussion

4.1 A Working Value for the Flux Across the Shelf Break

As a working scheme for parameterising the drag coupling between the deep water circulation and the shelf water circulation at the shelf break, the model results described above and comparison with the parameterisation of wave drag in the atmosphere (Thorpe, 1995) suggest a stress τ_* at the shelf break produced by waves generated per unit area of the slope given by

$$\tau_* = k\rho_0 VNh^2\cos^4(\beta + \beta_0), \qquad (8)$$

where ρ_0 is the mean water density, V is the mean along-slope flow over the slope, N is the buoyancy frequency in the vicinity of the shelf break, and h and β are the rms amplitude of the topography of scale such that $\chi < 1$, and its mean orientation respectively. The β variation is derived from Figure 4 with $\beta_0 = 7 \pm 2°$and is probably valid only when $\beta < 60°$. The value k determined from Figure 5 is about 9×10^{-6} m^{-2}, with values near 1.3×10^{-5} m^{-2} when the topography is dominated by wavelengths less than $4\pi V/N$ ($\chi > 0.5$), or 5×10^{-6} m^{-2} when they exceed $20V/N$ ($\chi < 0.3$).

4.2 Is the Momentum Flux Significant?

Equation (8) provides an outer boundary condition for the shelf circulation. Where the momentum is surrendered to the shelf-sea circulation will depend upon the processes which lead to the transfer of stress from the waves, such as wave breaking or wave-flow interaction, and corresponding distances over which these are effective. Internal waves near the shelf break frequently appear as soliton packets which, in a shallow thermocline or water depth, evolve from localised, often single crest or trough, tidal disturbances (Gerkema, 1994). In reality, the waves generated in our models may evolve in a similar fashion. The course resolution of the numerical model fails to show this evolution. Sandstrom and Elliott (1984) observed that internal tidal waves and associated wave solitons are dissipated within about 10 km of the shelf break and over periods of about 5×10^4 s, with shear flow instability probably playing a part. In their analysis of other observations of internal waves propagating on the shelf, Sanford and Grant (1987) conclude that dissipation in the benthic boundary layer is unable to account for the dissipation observed; other mechanisms must be important.

We may estimate an eddy diffusion coefficient for momentum at the shelf break, κ, from the equation $\tau/\rho_0 = \kappa\, dU/dx$. If we write $dU/dx = U/\mathrm{Ro}$, where Ro is the internal Rossby radius of deformation of the shelf waters (equal to NH/f) and which we might suppose provides a scale for wave-flow momentum transfer (arguably the scale might increase with H and f^{-1}, and decrease when stratification decays in winter), then with $\tau = \tau_*$, $\kappa = k N^2h^2H/f$, so that the coefficient scales with h^2, the mean square roughness of the topography on the slope. The value of κ falls to zero when N tends to zero, a condition (as in winter) in which no internal waves can propagate onto the shelf. With $N = 10^{-3}$ s^{-1}, $f = 10^{-4}$ s^{-1}, H = 200 m and h = 10 m, $\kappa = (14 \pm 6) \times 10^2$ m^2 s^{-1}, a large value at the scale, 20 km, of the corresponding Ro (less than the 10 km found by Sandstrom and Elliott, 1984).

We may alternatively estimate a time-scale associated with the rate of transport across the shelf break, the ratio of the momentum in the slope current divided by the flux. The momentum per unit along-slope length of the current is its cross-sectional area multiplied by $V\rho_0$ and, using the $s_\alpha = 0.1$ slope from 200 m depth to 1000 m depth, this is $9.6 \times 10^6\, V\rho_0$ (SI units). The corresponding momentum flux is $\tau_* x$ (200 m) × (8 km), and the time scale is $1.2 \times 10^4/kNa^2$, or (4.9 ± 2.1) days if $N = 10^{-2}$ s^{-1}. This is sufficiently small for the flux to be a significant factor in the balance of forces driving and dissipating the flows.

The wave momentum is positive in the direction of wave propagation through the mean flow, and therefore has a positive component in a direction *contrary* to the mean flow which is supported by the pressure acting on the sea bed. The momentum transferred back into the mean flow when waves break, or otherwise interact with the flow field to transfer their momentum to it, will therefore accelerate the fluid in a direction contrary to the mean flow over the slope generating area, retarding the mean current where it is in the slope flow direction or possibly driving a counter current on the shelf. Since the internal waves reaching the shelf have a component of

momentum directed in the on-shelf direction, the source of which is a component of the lift forces experienced by the topography, they may also tend to drive flow onto the shelf, at least until resisted by the production of adverse pressure gradients from the shoreward boundary.

Acknowledgement. Jiang and Keen had funding from NERC Grant GR3/8001 and Keen received funding from the EEC MAST II OMEX programme MAS2 CT93-0069. We are grateful for the support provided.

References

Apel, J.R., H.M. Byrne, J.R. Proni, and R.J. Charnell, 1975: Observations of oceanic internal and surface waves from the Earth Technology Resources Satellite. *J. Geophys. Res.* 80, 865-881.

Baines, P.G., 1971a: The reflection of internal/inertial waves from bumpy surfaces. *J. Fluid Mech.*, 46, 273-291.

Baines, P.G., 1971b: The reflection of internal/inertial waves from bumpy surfaces: Part 2. Split reflection and diffraction. *J. Fluid Mech.*, 49, 113-131.

Baines, P.G., 1981: Satellite observations of internal waves on the Australian north-west shelf. *Aust. J. Mar. Freshwater Res.* 32, 457-463.

Bell, T.H., 1975: Topographically generated internal waves in the open ocean. *J. Geophys. Res.*, 80, 320-327.

Bretherton, F.P., 1969: Momentum flux by gravity waves. *Q. J. R. Meteorol. Soc.*, 95, 213-243.

Chapman, D.C., and D.B. Haidvogel, 1993: Generation of internal lee waves trapped over a tall isolated seamount. *Geophys. Astrophys. Fluid Dyn.*, 69, 33-54.

Clark, T.L., and M.J. Miller, 1991: Pressure drag and momentum fluxes due to the Alps. II: Representation in large-scale atmospheric models. *Q. J. R. Meteorol. Soc.* 117, 527-552.

Eriksen, C.C., 1982: Observations of internal wave reflection off sloping bottoms. *J. Geophys. Res.* 87, 525-538.

Fedorov, K.N., and A.I. Ginzberg, 1986: Visually observed sea surface phenomena. *Oceanology*, 26, 1-7.

Gerkema, T., 1944: Nonlinear dispersive internal tides: generation models for a rotating ocean. PhD dissertation for the Universiteit Utrecht, 149 pp.

Gilbert, D., 1990: Theory and observation of internal wave reflection off sloping topography. PhD dissertation, Department of Oceanography, Dalhousie University, Nova Scotia, Canada, 180 pp.

Haidvogel, D.B., J.L. Wilkin, and R. Young, 1991: A semi-spectral primitive equation ocean circulation model using vertical sigma and orthogonal curvilinear horizontal coordinates. *J. Comp. Phys.*, 94, 151-185.

Heathershaw, A.D., 1979: The turbulent structure of the bottom boundary layer in a tidal current. *Geophys. J. Roy. Astronom. Soc.* 58, 395-430.

Hibiya. T., 1986: Generation mechanism of internal waves by tidal flow over a sill. *J. Geophys. Res.*, 91, 7697-7708.

Hibiya, T., 1988: The generation of internal waves by tidal flow over Stellwagen Bank. *J. Geophys. Res.*, 93, 533-542.

Hoinka, K.P., and T.L. Clark, 1991: Pressure drag and momentum fluxes due to the Alps. II: Comparison between numerical simulations and observations. *Q. J. R. Meteorol. Soc.* 117, 495-525.

Holloway, G., 1992: Representing topographic stress for large-scale ocean models. *J. Phys. Oceanogr.* 22, 1033-1046.

Huthnance, J.M., 1989: Internal tides and waves near the continental shelf edge. *Geophys. Astrophys. Fluid Dyn.*, 48, 81-106.

Ierley, G.R., 1990: Boundary layers in the general ocean circulation. *Ann. Rev. Fluid Mech.*, 22, 111-142.

Lamb, K.G., 1994: Numerical experiments of internal wave generation by strong tidal flow across a finite amplitude bank edge. *J. Geophys. Res.* 99, 843-864.

Lilly, D.K., 1972: Wave momentum flux - a GARP problem. *Bull. Am. Meteorol. Soc.* 53, 17-23.

Maxworthy, T., 1979: A note on the internal solitary waves produced by tidal flow over a three-dimensional topography. *J. Geophys. Res.* 84, 338-346.

McFarlane, N.A., 1987: The effect of orographically excited gravity wave drag on the general circulation of the lower stratosphere and troposphere. *J. Atmos. Sci.*, 44, 1775-1800.

Miller, M.J., T.N. Palmer, R. Swinbank, 1989: Parametrization and influence of subgridscale orography in general circulation and numerical weather prediction models. *Meteorol. Atmos. Phys.* 40, 84-109.

Palmer, T.N., G.J. Shutts, and R. Swinbank, 1986: Alleviation of a systematic westerly bias in general circulation and numerical weather prediction models through an orographic gravity wave drag parametrisation. *Q. J. R. Met. Soc.* 112 , 1001-1039.

Sandstrom, H., and J.A. Elliott, 1984: Internal tide and solitons on the Scotian Shelf; a nutrient pump at work. *J. Geophys. Res.*, 89, C4, 6415-6426.

Sanford, L.P. and W.D. Grant, 1987: Dissipation of internal wave energy in the bottom boundary layer on the continental shelf. *J. Geophys. Res.*, (C2), 1828-1844.

Thorpe, S.A., 1992: The generation of internal waves by flow over the rough topography of a continental slope. *Proc. R. Soc. Lond. A*, 439, 115-130.

Thorpe, S.A., 1995: The cross-slope transport of momentum by internal waves generated by along-slope currents over topography. Submitted to *JPO*.

Flow Separation in the Ocean

Chris Garrett

Department of Physics and Astronomy, University of Victoria, Victoria, British Columbia, Canada

Abstract. Flow separation, which can lead to major modifications of flow patterns and drag, appears in many different guises in the rotating, stratified ocean. Some of these are reviewed, with an emphasis on the role of bottom slope. In particular, this can affect the surfacing of the interface for a coastal current flowing around a bend, and may also enter the criterion for boundary layer separation for low Rossby number flow past a submerged topographic feature.

Introduction

Boundary layer separation is a fluid mechanical process of fundamental importance in a variety of engineering situations. Aerodynamic lift on wings or propellors would be impossible without it, thus ruling out workshops in Hawaii! More typically than for these examples, which involve smooth separation at a sharp trailing edge, boundary layer separation in high Reynolds number flow past a bluff body generally leads to the advection of significant amounts of boundary layer vorticity into the fluid interior, causing a much more turbulent wake and more drag than if the boundary layer remained attached.

Given this potential for separated flow to lead to considerable turbulent stirring and mixing, and for the drag to be very different from that in attached flow, it would thus seem important to investigate the circumstances under which flow separation occurs at topographic features in the ocean. If the flow is homogeneous and at high enough Rossby number for the earth's rotation to be unimportant, then flow past isolated features on the sea floor may be similar to that in familiar engineering configurations, though sometimes complicated by the pre-existence of a bottom boundary layer in the upstream flow (Taylor, 1988). Situations in which the water depth goes to zero, as for shallow water flow past coastal features, are particularly different, in that turbulent bottom friction is more important than lateral friction, giving a criterion for flow separation that is different from the familiar engineering one. This will be reviewed, with particular reference to the instructive study of Signell and Geyer (1991).

The effect of rotation is readily included in the analysis of homogeneous nearshore flows. It also enters into consideration of stratified flow in the ocean and is associated with another type of flow separation: the surfacing, at the shore, of the interface in an inviscid reduced gravity flow around a bend. An analysis of this, involving the competition of Coriolis and centrifugal forces, was conducted by Klinger (1994) for the case of a vertical side wall. This, and the extension to allow for a more realistic bottom slope, will be reviewed, along with a qualitative discussion of viscous boundary layer separation, within the upper layer, even if the interface does not surface. It is also possible to speculate on the secondary cross-stream flows that would be expected in this situation as well as in the previous example of homogeneous flow past a headland.

The flow of a continuously stratified flow past an isolated topographic feature has been discussed in the meteorological literature for high Rossby number, as reviewed by Kaimal and Finnigan (1994). In the ocean the Rossby number may well be small, so that it is necessary to consider the evolution of the bottom Ekman layer as the flow passes the object. This topic, and some surprising possibilities, will be introduced later, but we start with a reminder of the fluid dynamics of boundary layer separation in the flow past a bluff body.

Flow Separation at High Reynolds Number

Kundu (1990) and other fluid dynamics texts describe the basic physics of flow separation in a typical engineering situation. The pressure gradient parallel to a surface is the same at the surface as just outside a boundary layer if this is thin, and, by Bernoulli's theorem, changes sign at the point where the external flow is a maximum (Figure 1). Beyond this point the opposing pressure gradient slows the external flow. It also slows the flow in the boundary layer, but this is already weak and so tends to be reversed, causing separation. This tendency can be offset, however, by the effects of viscosity, since right at the boundary (with x along it and y the normal coordinate)

$$\frac{1}{\rho}\frac{\partial p}{\partial x} = \nu \frac{\partial^2 u}{\partial y^2}, \tag{1}$$

where ν is the viscosity, thus only requiring an inflection point in $u(y)$, and not necessarily flow reversal, in a region with $\partial p/\partial x > 0$. In many practical situations separation does occur fairly soon after the point at which the pressure gradient reverses, but it can be delayed by making the change gradual, or by increasing the effective viscosity by triggering turbulence (e.g. Kundu, 1990).

Shallow Water Flow

Signell and Geyer (1991, henceforth SG) contrast this conventional situation with that of the flow past a head-

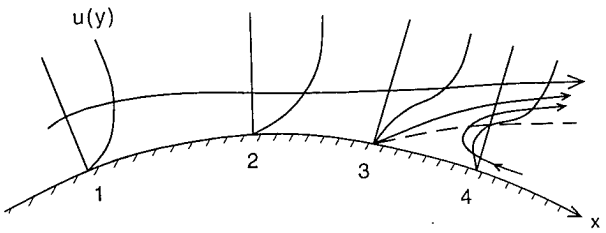


Figure 1. Velocity profiles and streamlines for separating flow past a bluff body. The flow outside the boundary layer increases from 1 to 2 where it is a maximum and the pressure is minimum. Beyond this $\partial^2 u/\partial y^2 > 0$ at the boundary, with reversed flow beyond the point of separation 3. The dashed line has $u = 0$. (Modified from Kundu, 1990).

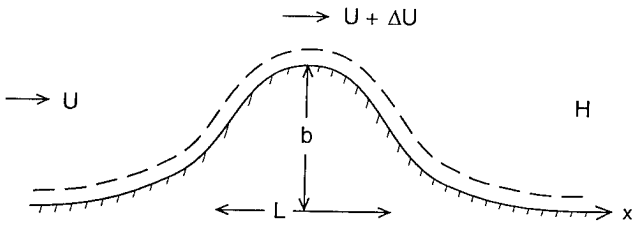


Figure 2. Flow past a coastal feature separated by a narrow sloping region from a sea of constant depth H.

land, in a situation governed by the shallow water equations

$$\frac{\partial \mathbf{u}}{\partial t} + \mathbf{u}\cdot\nabla\mathbf{u} + f\mathbf{k}\times\mathbf{u} = -g\nabla\eta - \frac{C_D\mathbf{u}|\mathbf{u}|}{(h+\eta)} + \nabla\cdot A_H\nabla\mathbf{u} \quad (2)$$

$$\frac{\partial \eta}{\partial t} + \nabla\cdot[(h+\eta)\mathbf{u}] = 0 \quad (3)$$

where $\mathbf{u} = (u, v)$ is the depth averaged horizontal velocity, f the Coriolis parameter, $\mathbf{k}$ a unit vertical vector, g gravity and η the surface elevation in water of depth h at rest. Bottom friction involves a drag coefficient C_D and lateral mixing of momentum is allowed for through a horizontal eddy viscosity A_H. This corresponds to the viscosity of the conventional problem, but the associated term, the last in (2), is small compared to bottom friction near the coast where the water is shallow and A_H must decrease due to limited eddy size.

Close to the coast, then, the alongshore momentum balance is

$$\frac{\partial u}{\partial t} + u\frac{\partial u}{\partial x} = -g\frac{\partial \eta}{\partial x} - \frac{C_D u|u|}{(h+\eta)} \quad (4)$$

where x is the curvilinear longshore coordinate, u the velocity component in that direction and the offshore velocity component is small enough for fv to be negligible. SG make the important point that, from simple scaling of (4), the terms on the left hand side are unimportant right at the shore, so that the balance is between the alongshore pressure gradient and bottom friction, requiring flow reversal as soon as the pressure gradient reverses.

On the other hand, as SG remark and again in contrast to the conventional situation, the influence of friction away from the very nearshore region means that a reversal of the pressure gradient does not occur at the maximum of the alongshore current on a particular streamline, and need not occur at all if the current slows down no more rapidly than would be caused by friction alone.

SG obtain an estimate of the alongshore pressure gradient for the situation in which the water depth is constant outside a narrow region (Figure 2). In this case the external flow is approximately irrotational (in the horizontal), due to the vanishing of the main vorticity generating term involving $C_D\mathbf{u}\times\nabla h$, and so may be estimated and then used in (4) to derive the alongshore pressure gradient which applies also right at the coast if the sloping region is sufficiently narrow.

To avoid a reversal of the pressure gradient for steady flow we require $|u\,\partial u/\partial x| < C_D u^2/H$, where H is the (constant) offshore water depth. SG evaluate u for a headland with the shape of a half ellipse, but in general, for a headland of width L and departure b from a straight coastline, we expect a change $\Delta U \simeq (b/L)U$ in the alongshore flow. Assuming b/L to be small, flow separation is thus avoided if $U\Delta U/L < C_D U^2/H$, or if the headland aspect ratio $b/L \lesssim C_D L/H$. Equivalently, though not expressed in these terms by SG, the radius of curvature, L^2/b, of the coastal feature, must be greater than about H/C_D. This is 10 km if $C_D \simeq 2\times 10^{-3}$ and $H = 20$ m, with flow separation occurring even for steady flow if the radius of curvature is any less.

SG find that separation is even more likely if b/L is not small, or if the flow is time dependent (as is readily apparent from (4)), and use a two-dimensional numerical model to study the evolution of flows in which separation occurs, carrying significant amounts of vorticity into the flow interior and thus producing vigorous eddy activity.

From this, and earlier work referenced by SG, the physics of two-dimensional flow separation in the coastal ocean is reasonably well understood. A limitation of the SG model is perhaps the assumption of constant water depth outside a narrow strip with a slope. Relaxation of this assumption to permit the slope to continue offshore would invalidate the approximation of two-dimensional potential flow outside a boundary layer, but a numerical model could be effective.

The discussion so far describes only the depth averaged flow. As the frictional forces act at the bottom, rather than throughout the water column, three-dimensional secondary flows, across the depth averaged flow, can be expected. This will be discussed briefly later in the paper.

An Upwelling Density Front

The above discussion has shown the importance of coastline curvature for boundary layer separation in frictional homogeneous shallow water flow in the coastal ocean. Another form of separation that has attracted attention recently is that associated with a two-layer inviscid reduced gravity flow past a curved coastline (Figure 3). The current is held near the straight coast upstream by the Coriolis force, but tends to be pushed offshore by the centrifugal force as it rounds a cape. If the curvature is small enough the interface may surface at the coast, so that the buoyant coastal current detaches itself from the coast and flows into the fluid interior as a jet. This phenomenon was observed in laboratory simulations (Whitehead and Miller, 1979; Bormans and Garrett, 1989) of the initial formation of the Alboran Gyre, in the Western Mediterranean, by Atlantic water flowing through the Strait of Gibraltar. Bormans and Garrett (1989) suggested that separation might require the radius of curvature of the coast to be less than the

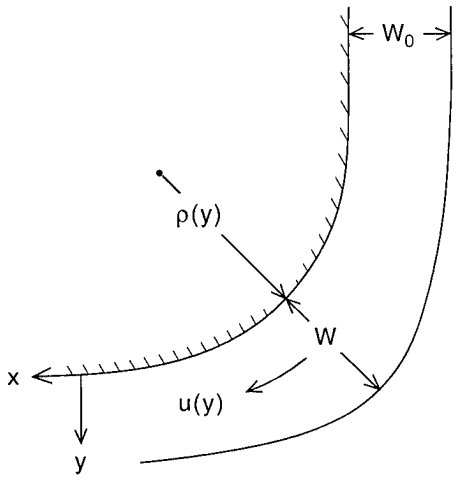


Figure 3. A reduced gravity coastal current flowing past a curved coastline.

inertial radius u/f, where u is the upstream current, and the problem has been addressed theoretically by Klinger (1994). He also considered different configurations in which the coastal current is confined near the coast but the upper layer extends infinitely far offshore. Here I will restrict the discussion to the first case, reviewing Klinger's (1994) analysis for a vertical sidewall and then discussing its extension to allow for a bottom slope.

Vertical Sidewall

Ignoring terms involving derivatives in the downstream, x, direction, the problem involves the cross-stream momentum equation

$$fu + g'\frac{dh}{dy} - \frac{u^2}{\rho + y} = 0 \tag{5}$$

and the potential vorticity conservation equation

$$h^{-1}\left(f - \frac{du}{dy} - \frac{u}{\rho + y}\right) = \text{constant}. \tag{6}$$

Here ρ is the local radius of curvature of the coast (Figure 3), $u(y)$ the current and $h(y)$ the interface depth. The sea surface displacement is very small compared with h and has been neglected in the potential vorticity equation. For simplicity, the potential vorticity has been chosen to be uniform across the stream.

The physics of (5) is that the Coriolis force leads to an increase of h as the coast is approached from offshore, but for small enough ρ this can be offset near the coast by the centrifugal term, causing h to decrease.

Klinger (1994) nondimensionalized the current speed with $(g'h_0)^{1/2}$, where h_0 is the upstream depth of the interface at the sidewall (Figure 4), y and ρ with the associated internal Rossby radius of deformation $(g'h_0)^{1/2}/f$, h with h_0 and the potential vorticity with f/h_0.

The governing equations are then

$$u + \frac{dh}{dy} - \frac{u^2}{\rho + y} = 0 \tag{7}$$

$$1 - \frac{du}{dy} - \frac{u}{\rho + y} = \delta h \tag{8}$$

where δ is the nondimensionalized, constant, potential vorticity. It and the nondimensionalized W_0 are the only two external dimensionless parameters. The problem may be solved for $u(y)$, $h(y)$, and the current width W, for any choice of δ, W_0 and local radius of curvature ρ. In particular, Klinger (1994) evaluated the critical radius $\rho_c(\delta, W_0)$ for which $h(0) = 0$, with the interface surfacing at the coast. He found that, to a good approximation, and almost independent of the value

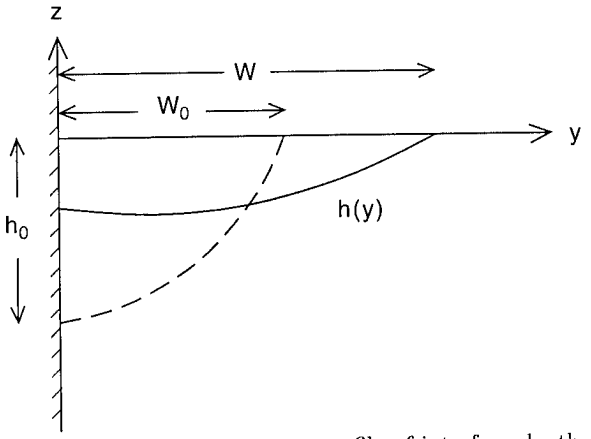


Figure 4. The cross-stream profile of interface depth $h(y)$ upstream (dashed), where the coastline is straight, and past a convex bend. The width of the current changes from W_0 to W.

of the potential vorticity δ, $\rho_c = 0.9W_0^{-1}$. In dimensional terms this becomes $\rho_c = 0.9g'h_0(f^2W_0)^{-1}$, or, using the geostrophic equation upstream, $\rho_c = 0.9\overline{u}/f$, where $\overline{u}$ is the cross-stream average current upstream. This supports the hypothesis of Bormans and Garrett (1989); a typical critical radius, for $\overline{u} = 1$ m s^{-1} and $f = 10^{-4}$ s^{-1}, is 9 km.

Sloping Sidewall

In reality, the sides of the ocean are sloping, not vertical! Jiang (1995) has analyzed the effects of this in the present context by extending Klinger's (1994) study to the configuration of Figure 5. The maximum current depth is still denoted h_0, but W_0 now refers to the upstream width of the current beyond the point where the interface intersects the bottom; the total current width is $s^{-1}h_0 + W_0$, where s is the bottom slope.

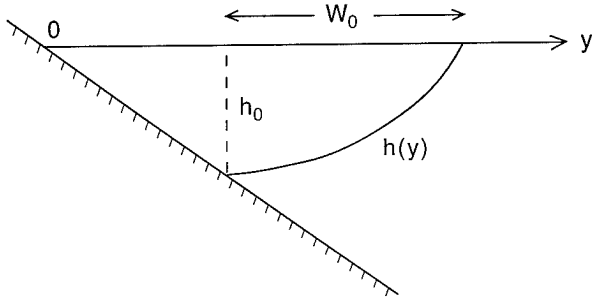


Figure 5. Upstream profile for a linear bottom slope.

The governing equations are still (7) and (8) in the "free" region where an interface exists between the upper layer and the stagnant lower layer. In the "wedge" region, inside the point where the interface intersects the bottom, we may still take (7) as the momentum equation, with $h(y)$ now a proxy for the proportional sea surface elevation, or pressure, but the correct depth to use in the potential vorticity equation is now sy rather than h. Thus the right hand side of (8) becomes δsy rather than δh. Here the bottom slope s has been scaled by $fh_0(g'h_0)^{-1/2}$.

As before, the current width, and interface and velocity profiles as functions of y, may be calculated for a given coastal radius of curvature ρ. In particular, the critical radius of curvature ρ_c at which the interface surfaces may be determined, but it is now a function of the three independent dimensional variables δ, W_0 and s. Figure 6 shows ρ_c as a function of W_0 for various slopes s, all for $\delta = 1.1$, and demonstrates that a nondimensional slope less than about 1 is required for any significant difference from the results for a vertical wall. For a given W_0 (and δ), separation requires a smaller radius of curvature if s is small, although the interpretation is more complicated if ρ_c is plotted versus the total upstream current width $W_0 + s^{-1}$. The curves of ρ_c versus W_0 do not vary greatly with δ.

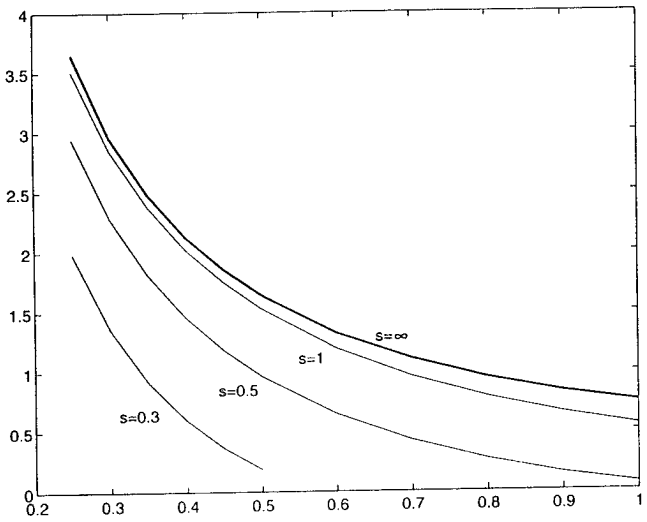


Figure 6. The critical coastal radius of curvature ρ_c, as a function of the upstream current width W_0 for a dimensionless potential vorticity $\delta = 1.1$ and for various values of the scaled slope s.

One interesting change for finite bottom slope is that the current can become narrower, rather than wider, as it rounds a bend of critical radius. This is illustrated in Figure 7, showing $u(y)$ and $h(y)$ upstream and at a bend of critical curvature. For a vertical sidewall ($s = \infty$) the current spreads out; it does so less for $s = 1$ and, for $s = 0.3$, it actually narrows. In order to narrow while still conserving the total volume flux, the current speeds up considerably near the coast. This is a consequence of the need for shear vorticity to offset curvature vorticity, much as in the flow of a river around a bend.

For the case of the Alboran Gyre, which was one motivation for these studies, the non-dimensionalized bottom slope seems to be about 4, sufficiently larger than 1 that Klinger's (1994) theory for a vertical wall is appropriate. Thus the suggestion by Bormans and Garrett (1989), that attached flow might be possible if the surface current speed were to drop below about 0.4 m s^{-1}, is not changed, though it remains imprecise due to the complicated nature of the real topography.

The value of the potential vorticity for the example of Figure 7 has been chosen partly to illustrate the flow for a situation in which the upstream current at the coast is very small, as might occur in response to bottom friction. Bottom friction would, of course, oppose the increase in coastal current so that, even for a minimum radius of curvature greater than ρ_c, streamline separation at the coast might be expected at a point downstream of its point of greatest curvature even though the interface did not surface.

Bottom friction would also lead to depth-dependent cross-stream flow within the wedge region, again as for river flow, except that here the near bottom flow would be expected to be offshore in the upstream region with a straight coastline. Offshore bottom flow would depend, in fact, not on having $u^2(\rho + y)^{-1} > fu$, where u is the

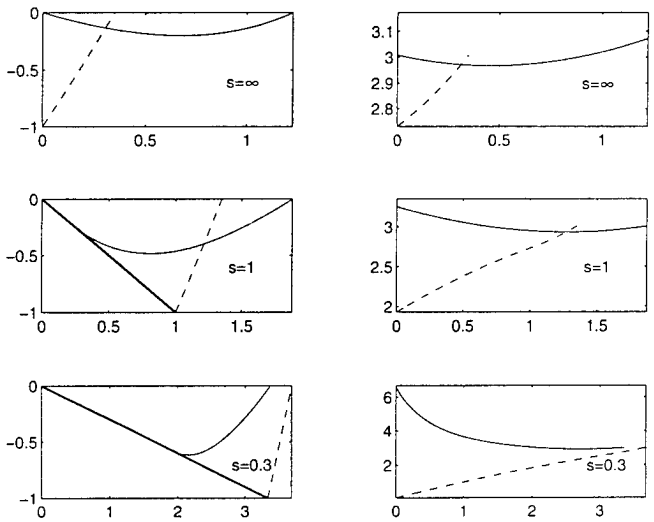


Figure 7. Profiles of interface depth $h(y)$ and current speed $u(y)$ both upstream ($\rho = \infty$) and at the separation point ($\rho = \rho_c$) for $\delta = 0.4$, $W_0 = 0.35$ and three values of bottom slope ($s = \infty, 1, 0.3$).

depth averaged current, but on the u derivative $2u(\rho + y)^{-1} > f$.

All of the discussions in this section have depended on slow downstream variation of the flow, so that x derivatives, and terms involving the velocity component normal to the coast, can be ignored. As pointed out by Klinger (1994), very slow variation of ρ is not possible if the total change in direction is not to exceed, say, 90°. He finds that the ratio of neglected to retained terms is of the order of W/ρ, and so not small for all of the (δ, W_0) parameter space. Further investigation of the problem therefore requires solution of a fuller set of equations.

Stratified Quasigeostrophic Flow Past an Obstacle

Flows past submerged topographic features in the ocean are influenced by bottom slope, stratification and the earth's rotation as well as by bottom friction. Even for homogeneous flow at high Rossby number (so that rotation is unimportant) the simple ideas of boundary layer separation that apply for high Reynolds number flow past objects isolated in three dimensions do not always apply directly because the upstream flow already has the characteristics of a boundary layer (Taylor, 1988). Flow separation then seems not to occur at small bottom slopes, perhaps because, as for the coastal problem of SG, a negative pressure gradient is required just to overcome viscous effects even away from the surface of the feature. Taylor (1988) suggests that separation will occur, however, if the maximum slope is greater than 0.3, at least for two dimensional features. The steepness required for separation appears to be larger for three-dimensional hills, but less so if surface roughness is added (Kaimal and Finnigan, 1994).

If stratification is taken into account, though still ignoring rotation, a wide range of possiblities exists, partly characterized by Froude numbers based on the width and height of the feature (e.g. Kaimal and Finnigan, 1994, and references therein). In particular, the generation of internal gravity lee waves can lead to downslope acceleration in the lee of the obstacle, associated with a negative pressure gradient and thus ruling out separation. In this case, the slowing of the inviscid flow, and hence the possibility of boundary layer separation, occurs upstream, not downstream!

A similar downstream acceleration was found by Richards et al. (1992) to be associated with the non-separation, for sufficiently small Rossby number of rotating, homogeneous, flow past an obstacle. They remark that a predicted positive pressure gradient upstream did not lead to flow separation in their laboratory experiments; perhaps this effect is a function of the Reynolds number.

A general oceanographic situation, involving both stratification and rotation, is thus likely to be very complicated, but it seems clear that a first step is to consider the inviscid flow and then the nature of the bottom boundary layer and the possibility of its direction of flow reversing.

In some situations it may be relevant to invoke the "arrested Ekman layer" concept of MacCready and Rhines (1991, 1993). If the alongslope flow is "upwelling favorable" a bottom Ekman layer will be pushed up the slope, but with a decreasing flux as the buoyancy force becomes more important and eventually balances the pressure gradient which, above the Ekman layer, is in geostrophic balance with the Coriolis force on the alongslope flow. As shown by MacCready and Rhines (1993), this complete arrest of the bottom Ekman layer by buoyancy forces is equivalent to the development of sufficient isopycnal slope for the associated thermal wind to bring the alongslope velocity to zero at the boundary.

If a flow accelerating past a topographic feature were moving slowly enough for the bottom Ekman layer to become arrested, and remain arrested as the flow increased, then the associated thermal wind would reverse the flow near the bottom if the inviscid flow outside the boundary layer decreased downstream. On the other hand, if the water were moving quickly enough that the bottom Ekman layer were only partly arrested, the associated thermal wind might be insufficient to reverse the bottom flow even in a region of deceleration of the inviscid flow.

It thus seems possible that a criterion for the flow not to separate is that the Ekman layer arrest time should be greater than the time for a fluid parcel to flow past the feature. For an upwelling bottom boundary layer, the arrest time is of order $(C_D N/f)^{-1/2} S^{-1} f^{-1}$, where

C_D is the bottom drag coefficient, N the buoyancy frequency outside the boundary layer, f the Coriolis frequency and $S = N^2 \tan^2\theta/f^2$ is the Burger number for a bottom slope making an angle θ with the horizontal (Garrett et al., 1993). If $C_D \simeq 2 \times 10^{-3}$, $N/f = 10$, $S = 1$ and $f = 10^{-4}$ s^{-1}, this arrest time is 7×10^4 s, comparable with the transit time past a 10 km scale object at a speed of 0.14 m s^{-1} (and so with a Rossby number of 0.14, small enough for the quasigeostrophic assumption to be reasonable).

A smaller value of S would give a longer arrest time, and so make non-separated, attached flow more likely, but of course for $S \lesssim 1$ the flow might form a Taylor cone above the base of the object anyway, and so not be attached even in inviscid conditions! Clearly, as stressed earlier, a first step is to solve the inviscid problem, as this may predict separated flow and eddy formation for reasons that have nothing to do with boundary layer behavior.

Returning, however, to the assumption that the inviscid flow is simple and attached, we now contrast the behavior if the basic flow is "downwelling favorable", so that a bottom Ekman layer would be pushed down the slope. In this case the arrest time is increased, due to the thickening of the layer by hydrostatic instability, to a time of order $\frac{1}{2}C_D^{-1}N^{-1}S^{-3/2}$, or 2.5×10^5 s for the same parameter choices as before. We thus appear to have the possibility, for flow past an isolated obstacle, that the flow would separate on one side where the boundary layer upwelled and was quickly arrested, but not on the other, downwelling, side where arrest and separation do not occur! Even if the flow remained attached on both sides, there would be a mismatch in the boundary layer characteristics either side of a downstream stagnation point, with consequences that need exploring.

Further investigation should include laboratory, field and theoretical studies, with the latter including analytical and numerical work and even further discussion of the preliminary nature embarked on here. Some laboratory work has been reported by Zhang and Boyer (1993). They did find attached flow of a stratified rotating flow past a model seamount at very low values of the Rossby number, for which the arrest time is shorter than the transit time, in apparent contradiction of the argument presented above. In these experiments, however, the flow was oscillatory, with a particle displacement considerably less than the seamount scale, and it is not clear what might be expected theoretically.

Zhang and Boyer (1993) found a variety of other flow patterns, some involving eddy shedding, for different values of the Rossby number and oscillation frequency, but it is not obvious, without analysis of the inviscid problem, whether the eddy formation was a consequence of boundary layer separation or an inviscid response to the topography.

Discussion

Flow separation appears in a number of different frictional and inviscid ways in the ocean, and nearly always involves different physics from that associated with boundary layer separation of a high Reynolds number past a bluff body. In some of these oceanographic situations, such as shallow water flow past headlands, the processes are understood, but in others, such as quasigeostrophic flow of a stratified fluid past a topographic feature with sloping sides, studies are only just beginning. Further work is particularly important for this and other problems where the processes responsible for flow separation, or attachment, are unresolved in most models.

Acknowledgments. I thank Xiaojun Jiang for permission to reproduce figures from her M.Sc. thesis, and Keith Ayotte and workshop participants for discussion and for providing references. The support of the Office of Naval Research is also gratefully acknowledged.

References

Bormans, M., and C. Garrett, 1989: A simple criterion for gyre formation by the surface outflow from a strait, with application to the Alboran Sea, *J. Geophys. Res.*, 94, 12,637–12,644.

Garrett, C., MacCready P., and P.B. Rhines, 1993: Boundary mixing and arrested Ekman layers: Rotating stratified flow near a sloping boundary, *Ann. Rev. Fluid Mech.*, 25, 291–323.

Jiang, X., 1995: Flow Separation in the Coastal Ocean, M.Sc. thesis, University of Victoria, British Columbia, 55 pp.

Kaimal, J.C. and J.J. Finnigan, 1994: *Atmospheric Boundary Layer Flows: Their Structure and Measurement,* Oxford University Press, Oxford, 289 pp.

Klinger, B.A., 1994: Inviscid current separation from rounded capes, *J. Phys. Oceanogr.*, 24, 1805–1811.

Kundu, P.K., 1990: *Fluid Mechanics*, Academic Press, San Diego, 638 pp.

MacCready, P., and P.B. Rhines, 1991: Buoyant inhibition of Ekman transport on a slope and its effect on stratified spin-up, *J. Fluid Mech.*, 223, 631–661.

MacCready, P., and P.B. Rhines, 1993: Slippery bottom boundary layers on a slope, *J. Phys. Oceanogr.*, 23, 5–22.

Richards, K.J., D.A. Smeed, E.J. Hopfinger, and G. Chabert d'Hières, 1992: Boundary layer separation of rotating flows past surface-mounted obstacles, *J. Fluid Mech.*, 237, 343–371.

Signell, R.P., and W.R. Geyer, 1991: Transient eddy formation around headlands, *J. Geophys. Res.*, 96, 2561–2575.

Taylor, P.A., 1988: Turbulent wakes in the atmospheric boundary layer. In *Flow and Transport in the Natural Environment: Advances and Applications,* W.L. Steffen and O.T. Edmead, eds., pp. 270–292.

Whitehead, J.A., and A.R. Miller, 1979: Laboratory simulation of a gyre in the Alboran Sea, *J. Geophys. Res.*, 84, 3733–3742.

Zhang, X., and D.L. Boyer, 1993: Laboratory study of rotating, stratified, oscillatory flow over a seamount, *J. Phys. Oceanogr.*, 23, 1122–1141.

An Inertial Model of the General Circulation in an Ocean with Bottom Topography

Janet M. Becker

Department of Ocean Engineering, University of Hawaii, Honolulu, Hawaii

Abstract. The barotropic, wind-driven circulation in a basin bounded at the south by the equator and for which the ocean depth varies smoothly between a constant deep ocean value and zero at the coasts is examined numerically to analyze how inertia and topography affect theoretical models of the general circulaton. As is well known, the inclusion of topography aligns the boundary currents along *f/H* contours. Increasing the wind forcing leads to unsteady inertial circulations that consist of periodic, modulated, and irregular eddy generation.

1. Introduction

The effects of topography on the general ocean circulation have long been recognized as important. The majority of theoretical ocean general circulation models, however, have been confined to flat bottom oceans or have invoked the quasi-geostrophic approximation. One assumption central to the quasi-geostrophic approximation is that variations in the fluid depth are small. As a result, the ocean depth typically is discontinuous at coastlines in these models. While many useful insights about ocean boundary currents have been gained from these theoretical models, open questions remain about how the boundary currents affect the gyre-scale circulation and about model sensitivity to frictional parameterizations (c.f. *Killworth* [1993], *Böning* [1986], *Cummins* [1992]). It may be that the sensitivity of these model circulations is in part due to the singular nature of the topography. We also remark that these models may not readily be extended to incorporate the important effects of finite amplitude topography.

A few theoretical studies have shown that the boundary currents obtained in an ocean with finite amplitude topography differ significantly from those obtained in an ocean with infinitesimal topographic variations (e.g. *Salmon* [1992]). These studies, however, largely have neglected the effects of inertia. In this note, we consider how inertia affects the barotropic circulation in an ocean for which the depth undergoes O(1) variations to vanish smoothly at the coastlines. In section 2, we present the dynamics and review the steady linear circulations and in section 3, we determine how inertia modifies the linear circulation using numerical simulations.

2. Shallow water equations

We consider here the barotropic ocean circulation governed by (in nondimensional form)

$$\mathrm{Ro}\frac{D\mathbf{u}}{Dt} + \boldsymbol{f}\times\mathbf{u} = -\nabla\phi - \varepsilon\mathbf{u} + \frac{\partial\tau}{\partial z} \tag{1}$$

$$\nabla\cdot\mathbf{u} + w_z = 0 \tag{2}$$

and subject to

$$w = 0(z=0), w = -u\cdot\nabla H(z=-H(x,y)), \tag{3}$$

and the condition that the normal component of the transport vanishes on the coastal boundaries. In (1-3), $(uvw)\equiv\mathbf{u},w)$ is the velocity in the (eastward, northward, vertical) direction with coordinates (x,y,z); $\boldsymbol{f} = y\mathbf{k}$ where y is the Coriolis parameter and $\mathbf{k}$ the vertical unit vector; $\phi = p + gz$ where p is the pressure; $\tau = \left(\tau^x,\tau^y,0\right)$ is the stress; $\mathrm{Ro} = U/f_0L$ is the Rossby number and $\varepsilon = \varepsilon_{Ra}/f_0$ is the dimensionless coefficient of Rayleigh friction. Here, we choose to balance the vorticity input by the wind with Rayleigh friction.

The nondimensional variables in (1-3) are scaled conventionally with horizontal/vertical length scales of O(4000 km/4 km), a representative flow speed U of O(0.2 km/day) and $f_0 = \beta L = 10^{-4}\ \mathrm{sec}^{-1}$. We next define the transport stream function

$$\left(-\psi_y,\psi_x\right) = H(u,v) \tag{4}$$

which follows from (2-3) and combine the depth integrated versions of the horizontal components of (1) to form the vorticity equation

$$\mathrm{Ro}\frac{\partial\varsigma}{\partial t} + J\left(\psi,\frac{\mathrm{Ro}\varsigma + y}{H}\right) = -\varepsilon\varsigma + W \tag{5}$$

which is subject to $\psi = 0$ on the coastal boundaries. In (5), $\varsigma\equiv v_x - u_y = \nabla_h\cdot(H^{-1}\nabla_h\psi)$ is the relative vorticity (∇_h is the horizontal gradient operator), $W\equiv\nabla\times$

For a flat bottom ocean with $H(x,y) = 1$, the steady, linear circulation of (5) is described in the classic work of *Stommel* [1948] and consists of an interior wind driven (Sverdrup) flow that is closed by a frictional western boundary current of width ε. For an ocean in which the depth goes to zero smoothly at the coast, the western boundary current system is asymptotically independent of the friction and the flow on the continental slope is determined by *y/H* and by the interior flow (e.g., *Salmon* [1992, 1994]). We also remark that the circulation in a basin bounded at the south by the equator (for which *y/H* lines converge at the equatorial point on the western boundary) differs significantly from that in a basin with a southern coastal boundary (for which closed contours of *y/H* exist) (c.f. *Kawase* [1993]). Here, only the more realistic equatorial case is considered.

The steady, linear (Ro = 0) circulation described by (5) is presented in Figure 1 for a flat bottom ocean and in Figure 2 for an ocean with western and northern continental shelves. The topography, $H(x,y)$, used in all of the experiments (except Figure 1) is presented in Figure 3 (left). In this initial study, the wind stress curl simply is taken as

$$W(x,y) = \begin{cases} -\sin\left(\dfrac{4\pi}{3}\left(y-\dfrac{1}{2}\right)\right) & 1/2 < y \le 2 \\ 0 & 0 \le y \le 1/2 \end{cases} \qquad (6)$$

in all experiments. The coefficient of Rayleigh friction corresponds to a Stommel layer of one grid point. In the absence of topography, the circulation consists of two symmetric, counter-rotating gyres (Figure 1, left) and the vorticity field (Figure 1, right) consists of two isolated, oppositely signed layers concentrated at the western boundary. In contrast, the linear circulation in the basin

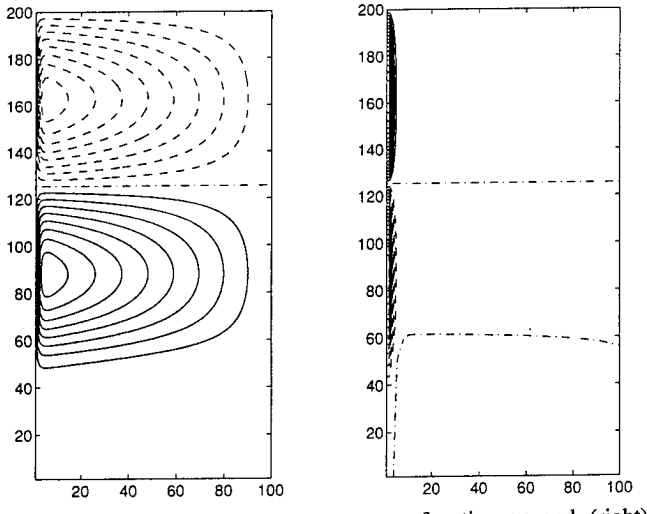


Figure 1. (left) The transport stream function ψ and (right) vorticity ζ that satisfy (5) for Ro = 0, ε = 0.01, $H(x,y) = 1$ and the wind stress curl given by (6). In all figures, the solid/ dashed/dot-dash contours correspond to positive/negative/zero values and the contour interval for ψ/Hζ is 0.1/100.

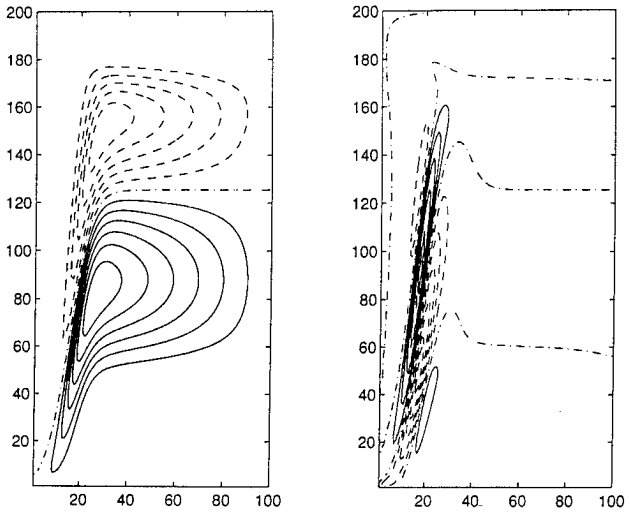


Figure 2. (left) The transport stream function ψ and (right) vorticity (multiplied by the ocean depth, see footnote 1) Hζ for the conditions of Figure 1, but with the $H(x,y)$ of Figure 3.

with topography is asymmetric and may be understood by viewing (5) as an advection-diffusion equation for ψ with advecting velocity $\mathbf{k} \times \nabla(y/H)$ and $-W$ the source (c.f. *Salmon* [1992]). The "streamlines" of this "flow" are presented in Figure 3, right. The difference between the linear topographic and flat bottom circulation is clearly exhibited in the vorticity[1] field. In the flat bottom ocean, the vortex layers are symmetric and isolated, while in the ocean with topography, the layers are asymmetric and aligned along *y/H* contours.

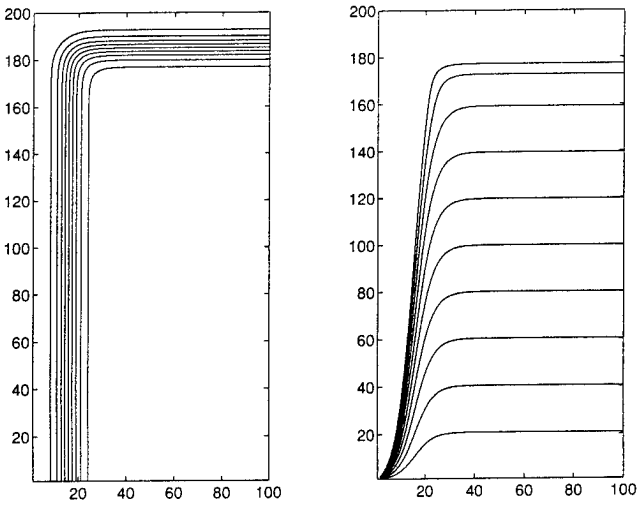


Figure 3. (left) The ocean depth $H(x,y)$ which varies smoothly from zero at the western and northern coasts to unity in the interior. (right) The corresponding contours of *y/H*.

[1] Due to large values of the vorticity in the southwest corner of the basin, contours of Hζ are presented here.

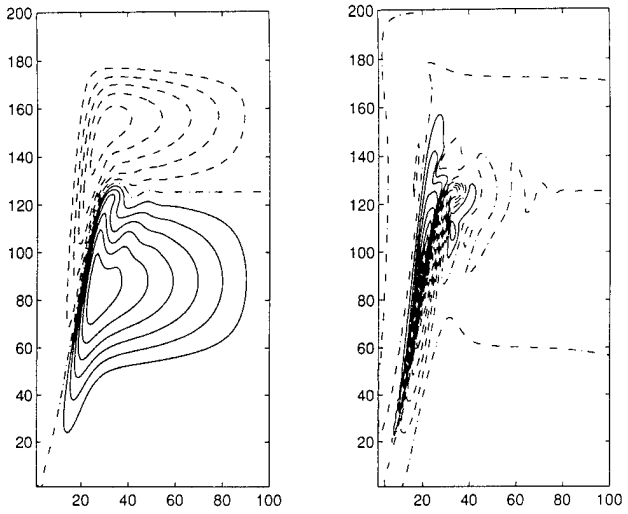


Figure 4. Steady, inertial circulation. (left) ψ and (right) $H\zeta$ for the conditions of Figure 2 but with Ro = 0.0002.

3. Numerical Model

To determine how inertia affects the linear, topographic circulation described above, we solve (5) numerically using a finite-difference method. We time-step (5) to analyze unsteady dynamical processes and to determine the stability of the steady circulations.

Inertial numerical models of the general ocean circulation require a subgrid-scale closure scheme to parameterize the effects of the scales of motion not resolved by the numerical grid. Here, we use an implicit closure scheme to finite difference the advective terms in (5) for which the truncation error corresponds to a biharmonic operator on ζ in the interior, but requires no additional boundary conditions (third-order upwind differencing, *Leonard* [1984]).

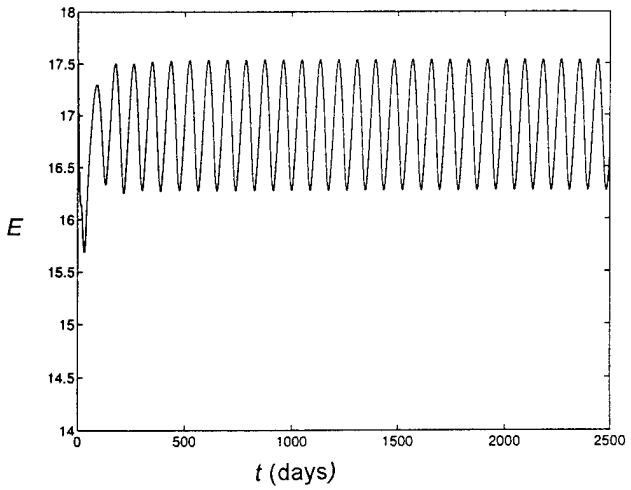


Figure 5. Time-series of the basin integrated total energy E, (7) for the conditions of Figure 2 but with Ro = 0.0005. The period of eddy formation is O(100 days).

The numerical solutions of (5) are presented for a rectangular ocean basin contained in $0 \le x \le 1$, $0 \le y \le 2$. As discussed above, the southern boundary of this model ocean is the equator where the boundary conditions of cross-equatorial symmetry of the dynamics, forcing and topography are applied. The form of the wind stress curl, (6), is chosen for simplicity and to reduce the computing time necessary to obtain steady-state, nonlinear solutions. For all runs shown, the resolution is 100×200 and $\varepsilon = 0.01$ (but see below).

The effects of weak nonlinearity may be understood by considering how advection affects the steady, linear circulation presented in Figures 1 and 2. For the flat bottom ocean, the effects of weak nonlinearity are well known, and, for example, for the subtropical gyre, negative relative vorticity is advected from the south to the north. Then, to dissipate their excess negative relative vorticity, fluid parcels overshoot the latitude where they rejoin the Sverdrup interior. For a two gyre circulation in a flat bottom ocean, inertia results in the isolated, symmetric vortex layers being pulled off the western boundary and aligned along the latitude of zero wind stress curl where vortex interactions then may occur. For an ocean with finite amplitude topography, however, we emphasize that the asymmetric vortex layers are aligned in the *linear* approximation. Then, the introduction of inertia causes the vortex layers to advect each other northeastward (along the axis of alignment), and additionally, to draw the weaker layer around the stronger layer. This behavior is exhibited by the steady inertial solution presented in Figure 4 for which Ro = 0.0002. Advection of vorticity has reduced the southwestward extent of the tails of the gyres and the asymmetry in the strength of the vortex layers has resulted in the bending observed at the northern limit of these layers.

By increasing the magnitude of the wind (Ro = 0.0005), the advection becomes strong enough to wrap around and pinch off an eddy from the weaker (positive) vorticity layer. This eddy formation occurs periodically as may be seen in a time-series of a finite difference approximation of the basin integrated total energy

$$E = \iint \frac{1}{2H} \nabla\psi \cdot \nabla\psi dA \qquad (7)$$

for Ro = 0.0005 (Figure 5). We note that the period of the eddy formation is O(100 days). Figure 6 presents snapshots of this process at quarter period intervals. The pinching off of an eddy occurs near an energy maxima.

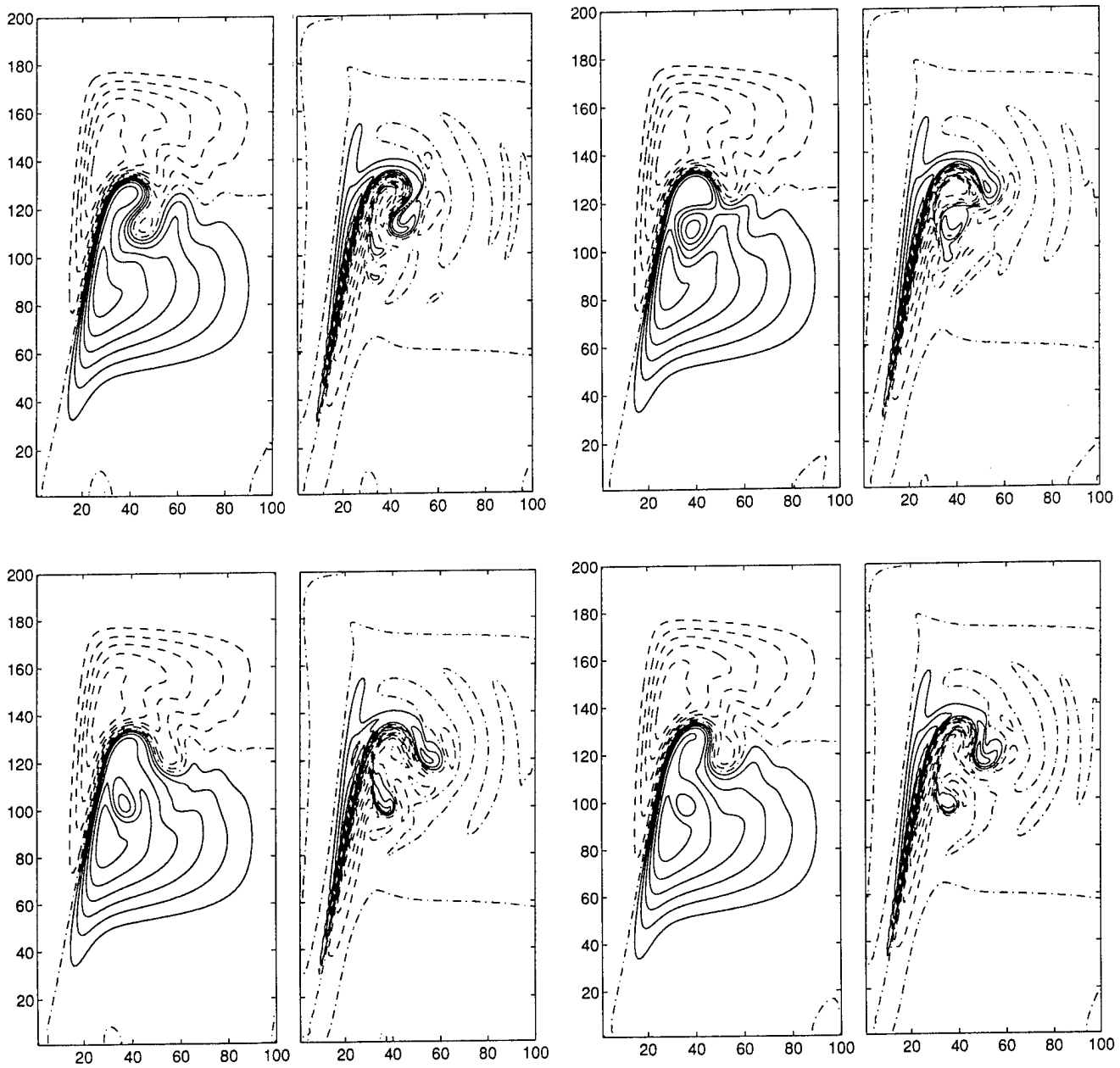


Figure 6. The periodic pinching off of an eddy for the conditions of Figure 5. Snapshots of ψ (left) and $H\varsigma$ (right) at times corresponding to (top left) maximum energy, (top right) approximately one quarter period past the maximum, (bottom left) minimum energy, and (bottom right) approximately one quarter period past the minimum.

A further increase in the wind (Ro = 0.001) results in aperiodic eddy formation.[2] Here, in addition to an eddy of positive vorticity being entrained in the subtropical gyre, an eddy of negative vorticity is entrained subsequently in the subpolar gyre. A time-series of E for Ro = 0.001 (Figure 7) consists of a high frequency carrier signal modulated by a lower frequency envelope. The minima in the low frequency envelope appears to correspond to the two eddies pinching off nearly simultaneously. Snapshots of the circulation exhibiting the formation of the positive and negative vorticity eddies are presented in Figure 8. Increasing the wind further results in more complicated unsteady behavior (not shown).

[2]We emphasize that a spectral analysis of this process has not yet been conducted and will be presented in a future work.

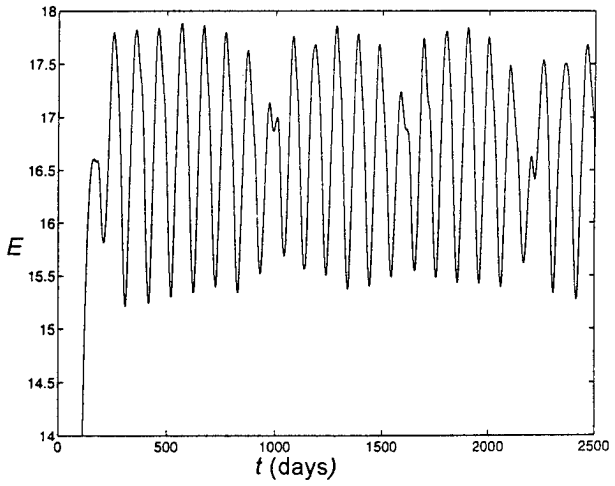


Figure 7. The time-series of E, (7) for the conditions of Figure 2 but with Ro = 0.001.

We remark that the qualitative character of the results presented above appear to be independent of the model resolution in the sense that for coarser or finer resolutions, the sequence of steady circulation, periodic, modulated and irregular unsteady eddy formation still occur, but for different Rossby numbers (i.e., for Ro = 0.001 and 50 × 100 resolution, the eddy formation is periodic while for 200 × 400 resolution, the eddy formation is irregular). A future study will report model sensitivity studies in more detail.

Acknowledgments. I am indebted to Rick Salmon for helpful discussions and for the final numerical model. This work was supported in part by an NSF Mathematical Sciences Postdoctoral Research Fellowship and a URC seed money award from the University of Hawaii. School of Ocean and Earth Science and Technology contribution no. 3915.

References

Böning, C.W., 1986: On the influence of frictional parameterization in wind-driven ocean circulation models,. *Dyn. Atmos. Oceans*, 10, 63-92.

Cummins, P.F., 1992: Inertial gyres in decaying and forced geostrophic turbulence, *J. Mar. Res.*, 50, 545-566.

Kawase, M., 1993: Effects of a Concave Bottom Geometry on the Upwelling-driven Circulation in an Abyssal Ocean Basin, *J. Phys. Oceanogr.*, 23, 400-405.

Killworth, P.D., 1993: On the Role of Dissipation in Inertial Western Boundary Currents, *J. Phys. Oceanogr.*, 23, 539-553.

Leonard, B.P., 1984: Third-order upwinding as a rational basis for computational fluid dynamics, in *Computational Techniques and Applications*: CTAC-83, J. Noye and C. Fletcher, eds. Elsevier North-Holland, 106-120.

Salmon, R., 1992: A two-layer Gulf Stream over a continental slope, *J. Mar. Res.*, 50, 341-365.

Salmon, R., 1994: Generalized two-layer models of ocean circulation, *J. Mar. Res.*, 52, 865-908.

Stommel, H., 1948: The westward intensification of wind-driven ocean currents, *Trans. Am. Geophys. Union*, 29, 202-206.

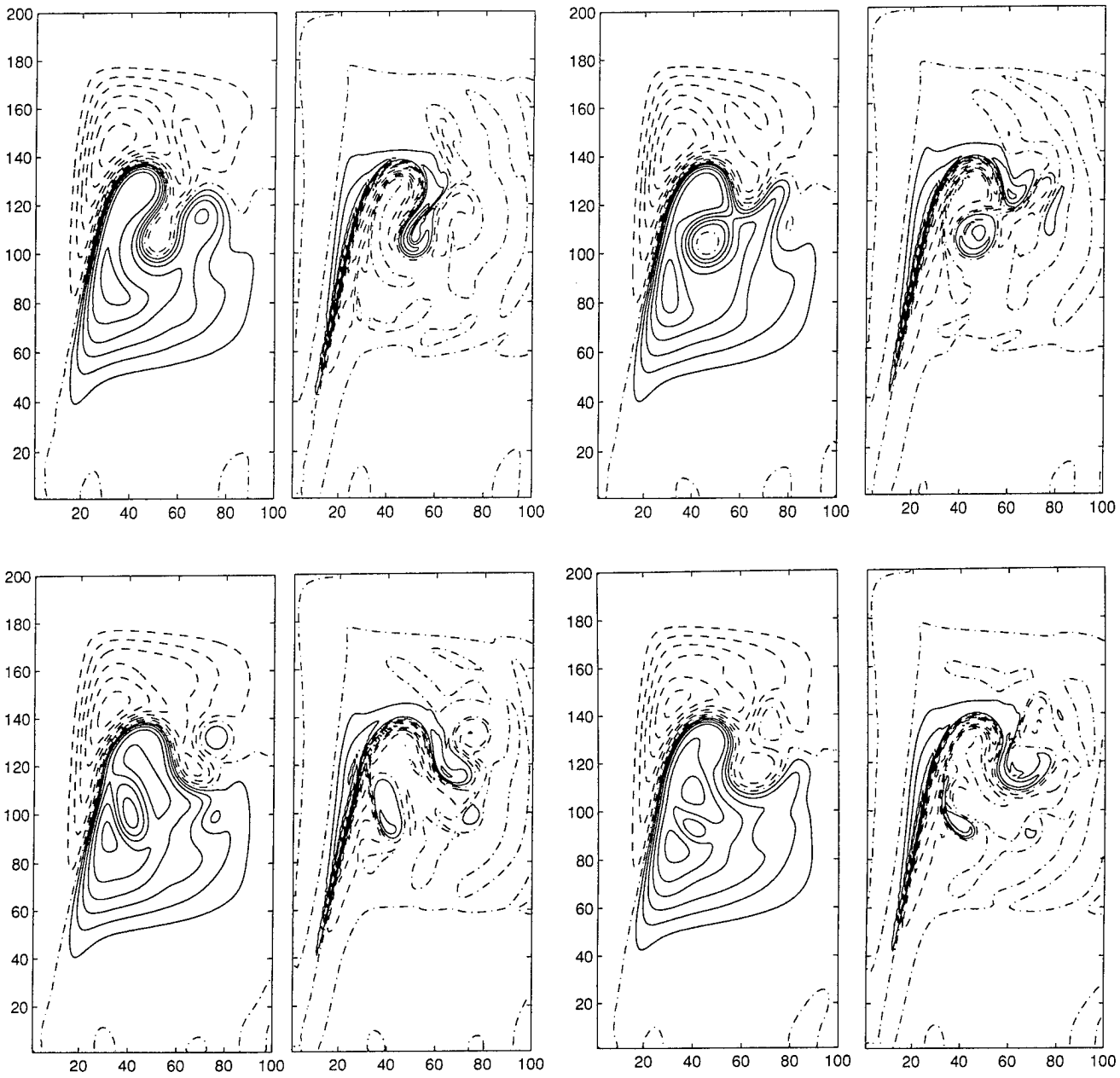


Figure 8. Snapshots of ψ and $H\zeta$ for the conditions of Figure 7 at these times: (upper left) 1184 days (approximately a local maxima of the energy), (upper right) 1201 days, (lower left) 1220 days, and (lower right) 1238 days (approximately a local minima of the energy).

Altimetric Observations of Rossby Wave Variability near Topography

Gary T. Mitchum

Department of Oceanography, University of Hawaii, Honolulu, HI

Abstract. Precise satellite altimetry began with the GEOSAT mission and has reached maturity with the TOPEX/POSEIDON mission. The sea surface height measurements from these instruments are capable of obtaining near-synoptic temporal coverage with a spatial resolution of order 100-300 km and an accuracy of order 4 cm. These sampling characteristics are sufficient to observe Rossby waves at periods longer than a few tens of days and wavelengths longer than a few hundred kilometers. Examples of this type of application are given and directions for future work are discussed.

Introduction

The focus of this paper is on propagating signals, especially Rossby waves, that are associated with topographic features. It is assumed that such propagating signals can have length scales as short as a few hundred kilometers and extend over thousands of kilometers. Similarly, it is assumed that the time scales can be as short as a few tens of days and that the signals can remain coherent over a year or more. Studying such signals from observations presents a formidable challenge, which can probably be met only through the use of remotely sensed variables.

The remote sensing variable of most interest to me is the sea surface height measured by satellite-borne altimeters. This interest stems from the fact that the sea surface height observations, when coupled with the hydrostatic approximation, give an estimation of the surface pressure field of the ocean. Thus, the satellite measurements yield observations of a dynamical variable that can be used more or less directly to diagnose the dynamics of the observed signals. This is in contrast to measurements of sea surface temperature, for example, which can change in response to thermodynamic forcing.

Three altimeters are relevant for the types of studies to be discussed in this paper. GEOSAT, which was flown by the U.S. Navy for geodetic reasons, returned 2 years of repeat cycle data that are particularly appropriate for oceanographic investigations. TOPEX/POSEIDON (T/P) was launched in 1992 as a joint project of the U.S. and France and is unique in that it was designed specifically for the purpose of obtaining high quality measurements of oceanographic variability. ERS-1, launched by the European Space Agency, also carries an altimeter, but these data are not discussed in this paper because at present the failure of the primary tracking system has prevented the determination of precise orbits, which are essential. An overview of results from GEOSAT can be obtained from JGR-Oceans special issues published in March and October of 1990. Also, Mitchum and Kilonsky (1995) have given a review of results from GEOSAT that focuses on the tropical portions of the oceans. T/P results also appear in a special issue of JGR-Oceans published in December 1994.

Mitchum (1994) described an extensive inter-comparison of T/P sea surface heights (SSH) and in situ sea level observations from tide gauges. The basic result (Figure 1) is that for time scales longer than 10 days the two datasets agree to about 4 cm rms and have a correlation of 0.66. The rms differences can be significantly reduced, and the correlations increased, by smoothing the data to monthly means. In that paper a number of potential problems and biases were investigated, and one of these is of particular interest in the present context. Specifically, it was shown that for several sea level stations it was necessary to allow for signals propagating at the local Rossby wave speed (Gill, 1982) in order to obtain reasonable intercomparisons. This correction was necessary because the T/P ground track and the tide gauge location do not exactly coincide.

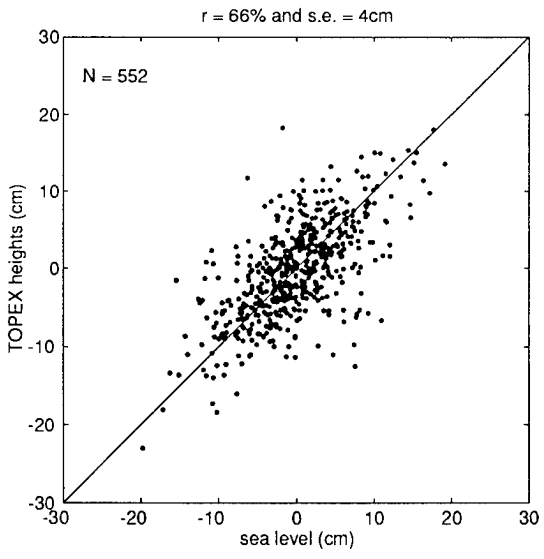


Figure 1. TOPEX sea surface height versus sea level data from tide gauges. Smoothing over 10-day intervals is performed before the data pairs are drawn. The scatter estimate is a robust estimate of the rms difference between the data pairs.

The station at Rarotonga in the South Pacific is a good example (Figure 2). In this case simply ignoring the zonal separation between the ground track and the tide gauge results in a correlation coefficient of -0.06. If, however, the time series are shifted by an amount corresponding to westward propagation at the Rossby wave speed, which was computed a priori rather than fit, the correlation increases to 0.62. Note also that the variance of the differences between the two time series has decreased by 55% as well. Looking at the series in more detail, it is clear that most of this improvement is due to a better match during the event that peaked around day 410, which had a duration of 100 days or so. It is difficult to say without more analysis, though, whether this signal is associated with a Rossby wave, an eddy, or something else.

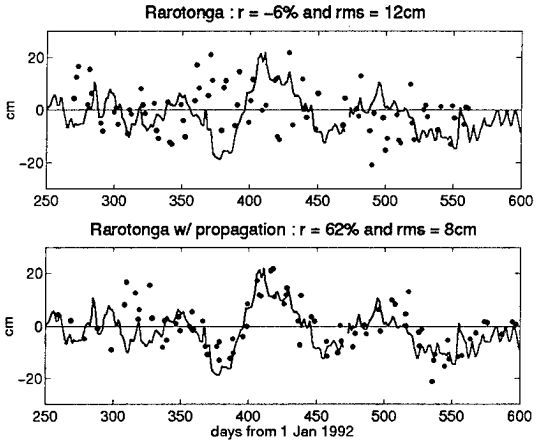


Figure 2. An example of a TOPEX to tide gauge comparison that is improved by allowing for Rossby wave propagation. The solid curve is sea level at Rarotonga and is the same in the upper and lower panels. The circles are the sea surface height values from TOPEX. In the upper panel the values are plotted at the time of observation, while in the lower panel the times are offset by an amount equal to the lag derived from the Rossby wave speed (computed to be 5.9 cm/s to the west) and the distance from the sea level station to the altimeter's ground track.

This paper describes two clear examples of Rossby wave signals observed from altimetric SSH and discusses some future directions for study. The first example is from an analysis of a Rossby wave signal observed at Wake Island in the western Pacific. This study used data from the GEOSAT mission and is described in more detail by Mitchum (1995a). The second example is from the T/P data and discusses a propagating signal found north of the Hawaiian Islands (see also Mitchum, 1995b).

Wake Island 90-day waves

Wake Island is located in western Pacific near 19°N and 166°E. Sea level from the tide gauge there shows an intermittent, but relatively large amplitude, oscillation at a period near 90 days (Figure 3). The data on this figure have been high-pass filtered, and the shaded regions mark time periods where the amplitude of the 90-day signal, as estimated by a complex demodulation, exceeds 8 cm. The years in this figure are aligned such that the leftmost 2 years on each line are ENSO events. It is apparent that the occurrence of the 90-day signals is modulated by ENSO, but the lag of 1-2 years is difficult to explain. In fact, these signals have been noted earlier (K. Wyrtki, personal communication), but the unusual phasing and the lack of other sea level records in the area made it impossible to diagnose the nature of these oscillations.

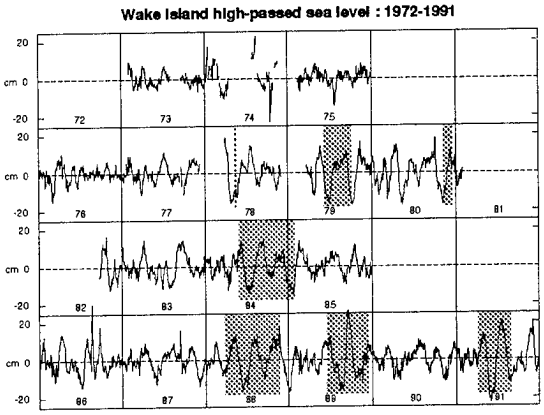


Figure 3. Daily sea level values from Wake Island after high-passing with a convolution-type filter having half-amplitude response at 200 d. Each line of the plot corresponds to the time series from the onset of an ENSO event to the beginning of the next event. Vertical lines are placed at 1 Jan of each year. Sea level units are cm. The shaded areas mark time periods where a complex demodulation analysis indicates that the amplitude of the 90-day oscillation is greater than 8 cm.

The timing of the GEOSAT mission, which produced good repeat cycle data from November 1986 to October 1988, was suitable for an analysis of the 90-day event observed at Wake Island in 1988. As discussed earlier for Rarotonga, it was apparent from simple correlation analyses that the signals were propagating westward at the local Rossby wave speed, and an analysis technique was devised to fit a zonal propagation speed to the GEOSAT space-time series. Briefly (see Mitchum, 1995a, for details), the calculation takes time series along a particular latitude and in an 8° longitude range and stacks them using phase lags computed from the longitude and an assumed propagation speed. The stacked series are then averaged, resulting in a single time series that emphasizes the propagating signals. Finally, the appropriate propagation speed is selected by requiring that the variance of this time series, as compared to a time series averaged without any lags, is

maximum. The results of this calculation for a particular point in space are estimates of the propagation speed, the variance ratio defined above, and a time series that emphasizes the propagating part of the signal.

This calculation was done with the GEOSAT data over much of the Pacific north of the equator, and the estimated zonal speeds were averaged zonally and plotted as a function of latitude (Figure 4). The f^{-2} behavior is consistent with Rossby waves and, since this was not imposed in any way by the fitting procedure, it serves as additional evidence that the propagating 90-day signal was in the form of a group of Rossby waves. One problem with this interpretation, however, is that the period of 90 days corresponds to a frequency that is theoretically too high to occur at this latitude. Based on an estimate of the Rossby radius obtained from several hydrographic profiles in this region (56 km), the mimimum period if the waves are at their turning latitude should be 120 days. It is possible to account for this difference by Doppler-shifting if it is assumed that the mean current is westward at 1-2 cm/s. Whether such a mean current exists is unknown, however, so it is only possible to say that the 90-day waves are close to their turning latitude.

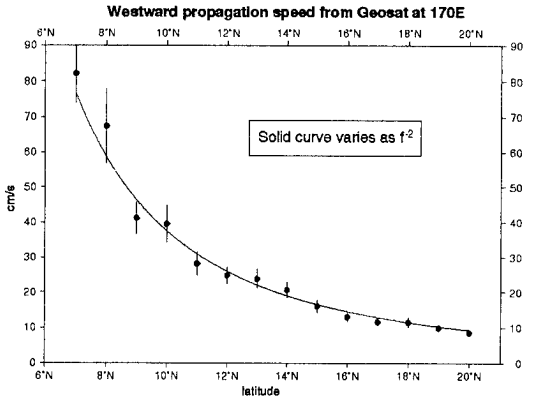


Figure 4. The solid circles represent the zonal average of the propagation speeds found from the procedure described in the text. At each latitude there are approximately 10 independent estimates of the propagation speed. The error bars represent 1 standard deviation about the zonal average. The solid curve shows the meridional variation expected for Rossby waves.

Although the GEOSAT data were very useful in characterizing the 90-day oscillations as Rossby waves in the vicinity of Wake Island, the real advantage of the SSH data is that the complete spatial coverage allows the tracking of the waves backward in time in order to locate the energy source. The fitting procedure used to estimate the wave speeds also returned a SSH dataset that emphasized the propagating signals. These data from the latitude of Wake Island (19°N) are plotted as a function of time and longitude in Figure 5. Similar plots were made at other latitudes (not shown) and these show that the signals observed at Wake Island are restricted to a narrow meridional band. Within this band, of which 19°N is typical, there is clear propagation to Wake Island from approximately 155°W, which corresponds to the longitude of the Big Island of Hawaii. Propagating signals are not significant east of Hawaii.

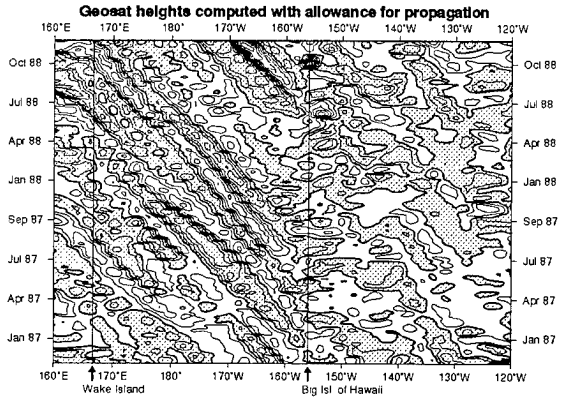


Figure 5. GEOSAT time series (computed with allowance for propagation) were formed between 160°E and 120°W and between 10° and 30°N. This figure shows a time-longitude cut along 19°N. This latitude falls close to both Wake Island and the Big Island of Hawaii. The slanting features in the left portion of the plot are propagating westward at about 7 cm/s. Negative sea surface heights are shaded and the contour interval is 3 cm.

The identification of the Big Island of Hawaii as the energy source for the Wake Island oscillations is also appealing because it helps to account for the phasing of the 90-day waves with ENSO events. The travel time from the Big Island to Wake Island is 1-2 years, which accounts for the observed lag if the energy source is active during the ENSO events themselves. There is thus no need to invoke unusual lags between the ENSO events and the excitation of the 90-day waves. It is still not clear, however, what process is responsible for the initial energy generation.

It is known (Patzert, 1969) that the area around the Big Island is rich with eddies. Different types of eddies are found in the area, however, and several possible generation mechanisms are likely. Regardless of how the eddies are generated, though, a likely scenario to account for the 90-day Rossby waves at Wake Island is that as the eddies propagate away from the topography, they decay into a train of Rossby waves, as described by Flierl (1977). It could be that the eddies are generated in response to flow past the Big Island, but the GEOSAT data are not adequate to examine this possibility. To examine this further, output from a numerical model (Hurlburt et al., 1992) was analyzed in the region of the Big Island. This analysis does in fact show that westward flow anomalies past the island give rise to anticyclonic eddies that separate from the topography and move westward. The model does not, however, decay these

eddies into a Rossby wave train, or reproduce the sea level time series at Wake Island. So, for the present, this scenario remains speculative. Also, since the agreement between model and data was not very good, it was not considered useful to diagnose the eddy generation mechanism in detail. In the paper referred to earlier (Mitchum, 1995a), however, several possibilities are discussed in more detail.

Waves north of the Hawaiian Ridge

The second example of Rossby wave signals from altimetry is from the area north of the Hawaiian islands and comes from the T/P dataset, which is significantly more accurate than the GEOSAT data. This study was motivated by observations from the Hawaiian Ocean Time-series (HOT) site (Karl and Lukas, 1995). Briefly, the HOT program involves the collection of a variety of physical, geochemical, and biological measurements at a single deep water location approximately 100 km north of the Hawaiian Ridge. The target is to make monthly measurements, and the program has been collecting data for over 5 years. A more complete description of the specific results given below can be found in Mitchum (1995b).

During part of the HOT program, time series of dynamic height were estimated from moored inverted echo sounders, which were calibrated against CTD data to give dynamic height differences from 0-1000 db. These measurements revealed a prominent, but intermittent, 130-day signal (Chiswell, 1995), and it should be noted that similar signals have also been observed in GEOSAT and AVHRR measurements (van Woert and Price, 1993). It was natural to ask whether the T/P data could provide a larger scale diagnosis of the nature of these oscillations, and the first question is simply whether the T/P SSH data reproduce these signals at the HOT site. This was addressed by intercomparing the T/P SSH and the dynamic height time series from the HOT site (Figure 6). Although the period of overlap in the two measurements is only about 6 months long, it is clear that the T/P SSH captures the oscillations.

In order to extend these results to a larger spatial area, an extended empirical orthogonal function (EEOF) analysis was carried out. This analysis is designed to capture propagating features, and the 130-day signals were emphasized by high-pass filtering the SSH time series prior to the analysis. The main result from the EEOF analysis is that the 130-day oscillation is very well described by a simple 130-day harmonic with a spatially dependent amplitude and phase functions that slowly vary in time. Since this alternate description is simpler to present and to interpret, the remainder of this discussion will focus on the modulations of the amplitude and phase of this 130-day sinusoid.

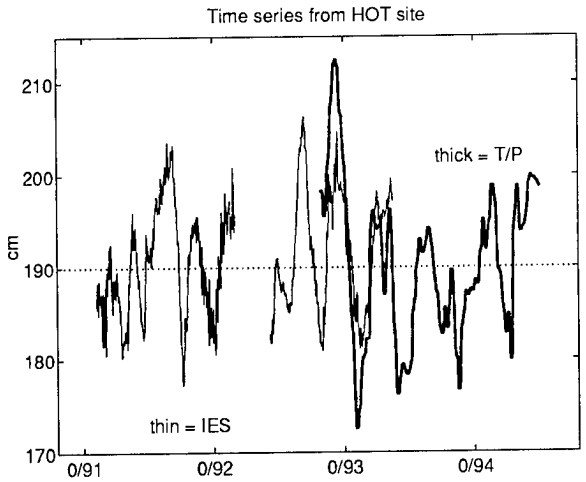


Figure 6. Combined height series from IES data and T/P data. The T/P data are from the crossover point lying immediately northeast of the HOT site. The T/P data are interpolated to a regular grid via an objective interpolation and then joined to the IES height series. The T/P series is lagged by 20 days in order to align the high frequency events. This lag was chosen to give the best fit between the two series, but it is also consistent with the propagation characteristics described in the text. The times are given as Julian day/Year.

The amplitude function is shown in Figure 7. The amplitude of the 130-day signal is initially large near 158°W and just north of the Hawaiian Ridge. The amplitude subsequently evolves away to the north and west, reaching 165°W after 1 year. If this amplitude evolution is interpreted in terms of Rossby wave theory, then this implies that the group velocity is to the northwest. If this is correct, then the phase velocity should be to the southwest.

The phase of the oscillation is represented somewhat differently (Figure 8). In this case it was found that the basic pattern of phase did not change appreciably in time, and so the phase of the mean harmonic at each point in space is shown. Note, however, that the phase is only interpretable when the amplitude is significant, so the phases at any particular location on this figure should only be interpreted as relevant during a temporal subset when the amplitude function (Figure 7) is large at that location. During the earlier times when the signal is near 158°W, the phase propagation is indeed to the southwest in qualitative agreement with theory. Calculation of the actual phase gradient do in fact reproduce the expected phase speed as well.

At the later times, as the area with large amplitudes moves north and west, the phase lines align north-south, indicating westward phase propagation. There is also a suggestion near 165°W that the meridional component of the phase velocity has reversed. This is especially interesting because it could indicate that the Rossby wave packet has reached its turning latitude, and to my

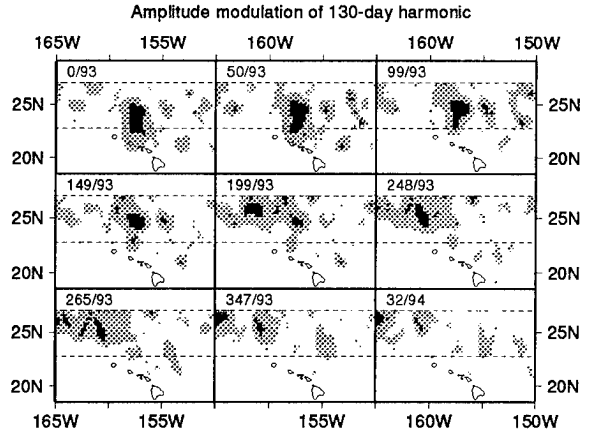


Figure 7. Amplitude of the 130-day harmonic as a function of space and time. The amplitude of a 130-day harmonic is computed along all of the T/P ground tracks north of the ridge and south of 27°N in an overlapping sequence of 200-day intervals. The results are interpolated to a regular spatial grid before drawing the images. Each successive panel in the figure is separated by just under 50 days, and the time associated with each map is given in the upper left hand corner of each panel as Julian day/Year. The light gray shows regions where the amplitude exceeds 5 cm; the dark gray is where it is greater than 10 cm. The broken lines drawn at the latitude of the HOT site and at 27°N are shown to aid the evaluation of meridional propagation.

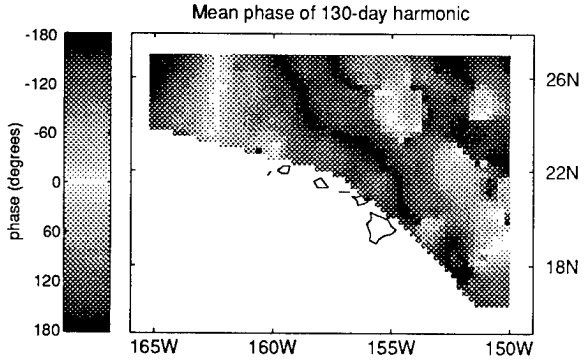


Figure 8. Spatial description of the phase of the 130-day harmonic. To form the phases shown in this figure the sine and cosine coefficients from the harmonic fits in overlapping 200-day intervals are averaged, and the phase is computed from the resulting mean harmonic. This averaging was done only after it was noted that the phase maps from the individual 200-day intervals were similar in pattern in the regions with significant amplitudes. The gray scale is cyclical, with phases of 0° in white and phases of 180° and -180° in black.

knowledge this phenomenon has not been previously observed for Rossby waves. As in the case of the Wake Island wave, the observed period places the wave close to the turning latitude. It is difficult to say at this point whether this interpretation is correct, and this problem will be revisited when longer time series are available.

Work in progress

The use of the altimetric SSH data in the examples given in the previous sections has been motivated by first finding strong oscillatory signals in other in situ time series of sea level or dynamic height. Basically, the better temporal coverage and accuracy of the in situ data makes it easier to identify interesting signals, after which the altimetric data are examined in order to place these point time series in a spatial context. Given the success of the altimetric SSH, especially for T/P, in reproducing the observed signals, it seems reasonable to search for propagating signals using the altimetric SSH alone. At present I am not satisfied with the techniques tried thus far to identify such signals, such as the method described for the Wake Island waves. This method does, however, allow a simple beginning along this new line of investigation, and this calculation was therefore extended to cover the Pacific between 10° and 50° in both hemispheres.

The zonally averaged speed estimates from this calculation, which are analogous to those shown in Figure 5, are shown in Figure 9. The speed estimates match the theory well, indicating that Rossby waves are ubiquitous and relatively easy to identify from the SSH data. It is interesting to note the closer correspondence with theory in the southern hemisphere. If the deviations in the fitted speeds are indeed due to Doppler-shifting, then this may be a consequence of the fact that the subtropical gyre in the southern hemisphere is relatively weak as compared to the northern gyre.

The calculation also results in an estimate of the variance ratio of the propagating signals relative to the stationary ones. When this ratio is large, it indicates that the propagating signals are dominant and that the calculation is sensible. In fact, the speed estimates shown

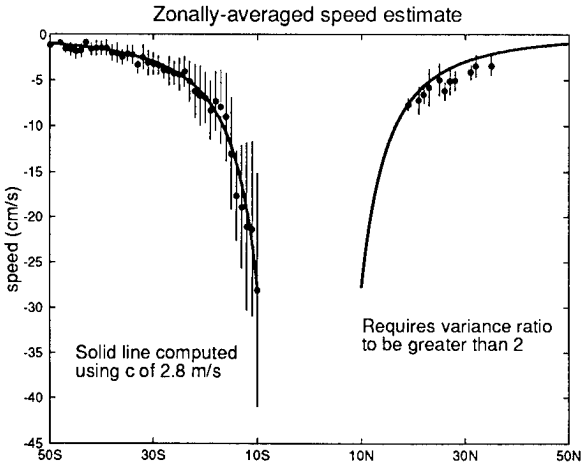


Figure 9. As in Figure 4, but from the larger scale calculation using the T/P sea surface height data.

on Figure 9 only use grid points where the variance ratio exceeds 2. A map of points where this occurs (Figure 10) shows crudely where the propagating signals are largest. Note the tendency for the points to lie in the western half of the basin in both hemispheres, again indicating that the

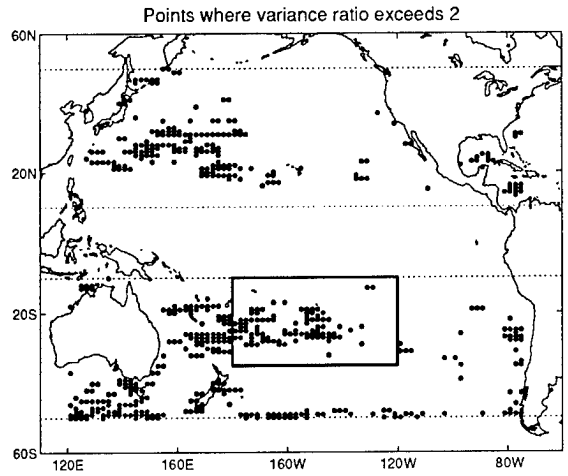


Figure 10. The variance ratio (described in the text) is large when propagating signals dominate the sea surface height time series. Solid circles are placed at grid points where the variance ratio is larger than 2. The spatial grid is 1° latitude by 2° longitude.

calculation is indeed capturing Rossby wave activity. Note also the relatively large number of points in the southern hemisphere. Whether this indicates larger propagating signals, smaller background (stationary) signals, or problems with the analysis is not known at present.

An enlargement of the area in the southern hemisphere bounded by the box is shown in Figure 11. This region was enlarged because it marks a zonal transition from relatively weak propagating signals to strong ones, in analogy to the behavior westward of the Hawaiian Ridge. The analogy appears to be useful, in that the variability

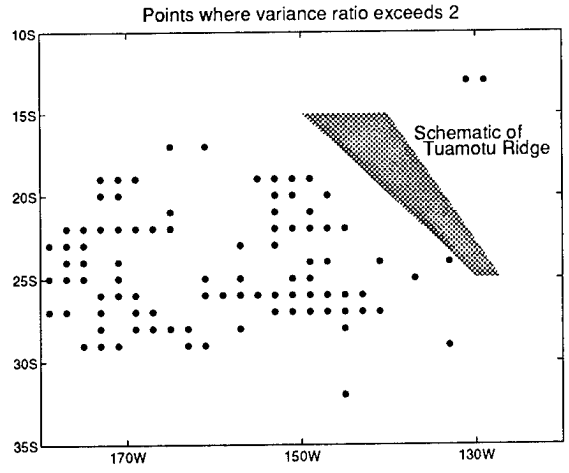


Figure 11. Enlargement of Figure 10 to show the effect of the Tuamotu Ridge.

does occur to the west of a topographic feature, namely the Tuamotu Ridge. Future studies of the wave and eddy signals west of the Hawaiian Ridge will therefore also consider this southern hemisphere analog.

Although the calculation used here to identify propagating signals has worked reasonably well in areas where the propagating signals are relatively large and coherent, it will certainly not work with more subtle signals. Better techniques need to be developed and a number of possibilities are being investigated. Even with this limited tool, however, it is clear that signals propagating at the local Rossby wave speed are common, and often appear to be linked with topographic features.

Finally, recall that both of the prominent signals that I have described appear at frequencies that suggest these waves are found very near their turning latitudes. Although this might be coincidental, it is very intriguing. According to theory, this latitude should trap energy at that period, and verifying this observation in a more general way would be a novel application of the altimetric SSH data.

Acknowledgments. This work was supported by NASA through the Jet Propulsion Laboratory as part of the TOPEX Altimeter Research in Ocean Circulation Mission.

References

Chiswell, S., 1995: Intraseasonal oscillations at Station ALOHA, north of Oahu, Hawaii. *Deep-Sea Res.*, in press.

Flierl, G., 1977: The application of linear quasigeostrophic dynamics to Gulf Stream Rings, *J. Phys. Oceanogr.*, 7, 365-379.

Gill, A., 1982: *Atmosphere-Ocean Dynamics*. Academic Press, Orlando, Florida, 662 pp.

Hurlburt, H., A. Wallcraft, Z. Sirkes, and E. Metzger, 1992: Modeling of the global and Pacific oceans: On the path to eddy-resolving ocean prediction, *Oceanography*, 5, 9-18.

Karl, D. and R. Lukas, 1995: The Hawaii Ocean Time-series (HOT) program: Background, rational and field implementation. *Deep-Sea Res.*, in press.

Mitchum, G., 1994: Comparison of TOPEX sea surface heights and tide gauge sea levels. *J. Geophys. Res.*, 99, 24,541-24,554.

Mitchum, G., 1995a: The source of 90-day oscillations at Wake Island. *J. Geophys. Res.*, 100, 2459-2476.

Mitchum, G., 1995b: On using satellite altimetric heights to provide a spatial context for the Hawaii Ocean Timeseries measurements, *Deep-Sea Res.*, in press.

Mitchum, G., and B. Kilonsky, 1995: Observations of tropical sea level variability from altimeters, To appear in *Oceanographic Application of Remote Sensing*, M. Ikeda and F. Dobson (eds.), CRC Press, Boca Raton, FL.

Patzert, W., 1969: *Eddies in Hawaiian waters*. Technical Report HIG-69-8, Hawaii Institute of Geophysics, University of Hawaii, Honolulu, 51 pp.

van Woert, M. and J. Price, 1993: GEOSAT and Advanced Very High Resolution Radiometer observations of oceanic planetary waves adjacent to the Hawaiian Islands. *J. Geophys. Res.*, 98, 14,619-14,632.

Some Examples of Topographic Influence on the Abyssal Circulation

Nelson G. Hogg

Department of Physical Oceanography, Woods Hole Oceanographic Institution, Woods Hole, Massachusetts

Abstract. Three different geographical regions are discussed where it would appear that topography might play a major, if not dominant, role in the dynamics of the deep circulation. In the Gulf Stream recirculation, although topography does alter the distribution of potential vorticity, especially if considered in a two layer analogue, the eddies resulting from instability of the stream can homogenize the potential vorticity and give rise to intense recirculations. On the other hand the configuration of the western margin topography brings the Deep Western Boundary Current into contact with the Gulf Stream at Cape Hatteras. In attempting to negotiate this intersection and conserve potential vorticity the Deep Western Boundary Current must flow with the stream as it goes into deeper water before being able to escape to the south. Finally, an ambitious international WOCE program known as the Deep Basin Experiment, presently being carried out in the Brazil Basin, is described and some preliminary results shown. For the deeper layers topography isolates the Antarctic Bottom Water except for connecting flows to neighboring basins through a small number of passages.

Introduction

Although the upper ocean general circulation seems, for the most part, to be unaware of the bottom topography except through the constraints of the lateral boundaries the deep circulation is profoundly affected by the extensive undersea ridge systems as well as the configuration of the continental margins. Herein we will describe recent observations of the deep flow in two areas: the region near the Gulf Stream in the North Atlantic and the Brazil Basin of the South Atlantic.

Recirculations and Topography

It has been known for some time that the transport of the Gulf Stream increases by a factor of 5 from the Florida Straits to its maximum near 60°W downstream of Cape Hatteras (e.g., Knauss, 1969; Johns et al., 1995) and that this increased transport (and associated decrease) implies a vigorous recirculation system flanking the stream. It now appears that there are at least two recirculation gyres of opposite circulation sense and roughly equal intensity, one to the north of the stream and the other to the south.

Various explanations exist for this phenomenon ranging from buoyancy forcing (Huang, 1990) to eddy forcing (e.g., Cessi et al., 1987) to purely inertial dynamics (e.g., Marshall and Nurser, 1986; Hogg and Stommel, 1985). Considering the stratification to be modeled in a two layer system with the thermal wind shear of the Gulf Stream causing the lower layer to "outcrop" along its northern edge, Hogg and Stommel (1985) were able to show that the combined effect on the lower layer thickness of the thermocline and bottom depth changes could create a region of closed potential this to be homogenized by eddy stirring and that zonal scales are much longer than meridional, they were able to vorticity contours to the north of the stream. Assuming develop an analytic model which predicted the right order of magnitude of the transport, approximately 30 Sv. Of course, in the presence of dissipation there must be some forcing.

Attempts to model this process numerically have been made and support the notion that the deep part of the recirculation is inertial. Malanotte-Rizzoli et al. (1995) simulate the forcing of the northern gyre through use of a boundary condition along a southern boundary which attempts to mimic the action of Gulf Stream meanders in a barotropic model. Only when the geometry contains closed potential vorticity contours for the ambient field does a vigorous recirculation emerge. In a more realistic barotropic model containing an unstable jet Jayne et al. (1995) find that closed potential vorticity contours arise naturally through the stirring action of the eddies arising from the instability of the jet, even without forcing the issue through distortions of the bottom topography. Hence it would seem that the particular shape of the bottom topography is not essential for forcing recirculations although it can help.

In the Synoptic Ocean Prediction Experiment (SYNOP) several eddy resolving arrays have been deployed across the stream at locations from near Cape Hatteras to just west of the Grand Banks. These data have been used to estimate eddy vorticity fluxes by Hogg (1993) who shows that the deep recirculation is nearly inertial and that the deep potential vorticity is nearly uniform. This flow is maintained against dissipative losses by an eddy "thickness flux" in the manner of Holland and Rhines (1980). The depth averaged flow is not inertial but is driven by lateral eddy vorticity fluxes.

Deep Western Boundary Current—Gulf Stream Crossover

At Cape Hatteras the Gulf Stream from the south intersects the DWBC flowing from the north. Hogg and Stommel (1985), using similar potential vorticity arguments to those for the recirculation, suggested that the DWBC would have to flow with the Gulf Stream into deeper water before being able to completely cross underneath it. It is becoming clearer that the DWBC is a multicomponent system with water derived from different source locations (Pickart, 1992) and evidence now suggests that the simple Hogg and Stommel model is a very crude approximation. Tracer measurements show that the shallower components are most affected by the stream, not surprisingly, and are swept downstream with it. The deepest components appear to make the crossing with only a modest change in depth (Pickart, 1992). This process has been recently modeled with good qualitative accuracy by Spall (1995) with a three layer model.

Brazil Basin

As part of the World Ocean Circulation Experiment an international investigation of processes important to the deep circulation, known as the Deep Basin Experiment (DBE), has been underway in the Brazil Basin. Objectives include quantification of the circulation within the three major water masses, Antarctic Intermediate Water, North Atlantic Deep Water (NADW) and Antarctic Bottom Water (AABW), distinguishing between boundary and interior cross isopycnal processes, and understanding how the passages connecting the Brazil Basin to other deep basins might affect the water flowing through them. The field program has a number of elements including conventional hydrography, tracer measurements and current meter arrays. It also includes releases of a large number of neutrally buoyant floats within each water mass so as to observe directly the circulation and a deliberate tracer release to estimate cross-isopycnal mixing rates.

As the program is underway there is little concrete information available to address these objectives. In order to gain confidence in the neutrally buoyant floats, called RAFOS, which were commercially fabricated for the first time, a number were released for shorter periods than the ultimate design objective of 2.5 years. Trajectories from these early floats are shown in Figure 1. Although these are all less than 400 days in length they indicate a flow which is predominantly zonal with considerable low frequency variability. The zonal aspect is surprising as classical pictures of the flow at this NADW level suggest a meridional flow, southward near the boundary and a northward return flow offshore. It is entirely possible that the more complete set of trajectories available at the end of the DBE will support this by showing a motion with large amplitude zonal sloshing and a slow meridional migration.

The deepest water masses flowing into the Brazil Basin are confined within the basin by the surrounding ridge system through which there are just four important gaps—the Vema and Hunter Channels on the southern boundary, the Romanche-Chain fracture zones at the equator in the Mid-Atlantic Ridge, and an equatorial passage (unnamed) farther west which permits leakage into the western North Atlantic. The transport of water through these passages has been fairly accurately estimated by use of moored current meter arrays in the DBE and it appears that there is an excess of about 4 Sv of AABW entering from the south over that leaving to the north. As the only escape for this water, assuming steady state, is a rise upward across isopcnals this indicates a basin averaged mixing rate of about 5 cm^2/sec, substantially larger than rates measured in the thermocline elsewhere (Hogg et al., 1982).

Where this mixing is occurring is presently unknown but there will be two tracer releases in the deep water within the basin, one in the interior and the other near a

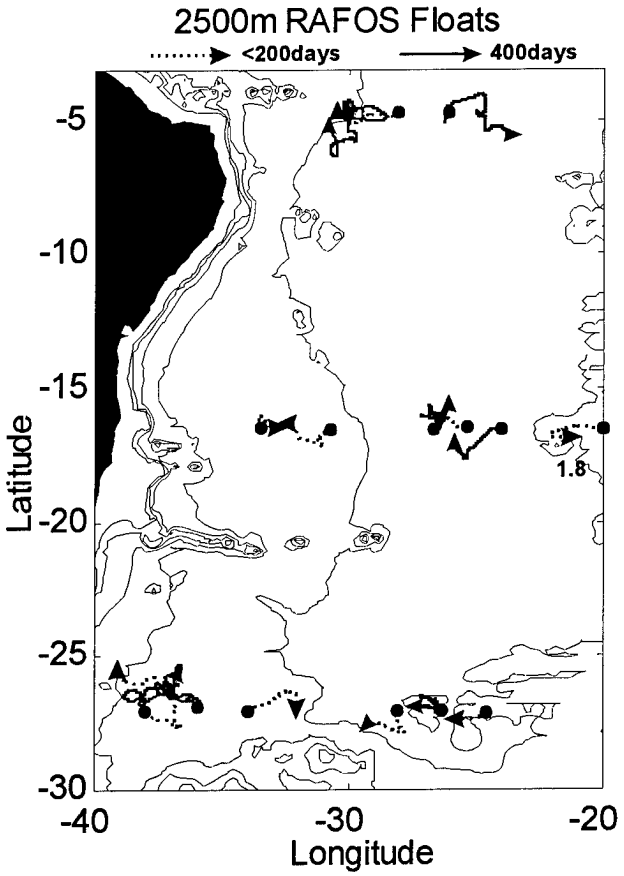


Figure 1. Trajectories of neutrally buoyant floats set near 2500 m depth within the NADW. These vary in length from less than 200 to 400 days.

boundary to help settle this issue. From a moored array in the Vema Channel we calculate cross-channel heat fluxes which would support a cross-isopycnal diffusivity of 50 cm^2/sec if they were not neutralized by a compensating vertical flux. Such a diffusivity, if distributed all along the western boundary would acount for the basin averaged value quoted above.

Summary

We have explored the deep circulation in three regions where the large scale bathymetry might be expected to be important to the lowest order dynamics. In the Northern Recirculation Gyre of the Gulf Stream, several studies have suggested that the geometry formed by the bight between the Grand Banks and Cape Hatteras, combined with the slope of the thermocline, could create regions of closed potential vorticity contours which would be favorable for formation of closed circulations. Numerical experiments suggest that this is not necessary and that the eddy fluxes associated with the instability of the stream can homogenize the potential vorticity and give rise to such recirculation zones. At Cape Hatteras itself, topography is clearly important in determining the manner in which the DWBC negotiates its intersection with the stream. Finally, early results from the Deep Basin Experiment suggesting that the subthermocline flow is primarily zonal are at odds with both published circulation schemes based on hydrography and the classic model of Stommel (1957). This may indicate that cross-isopycnal mixing processes are weak in the interior and this is consistent with crude estimates obtained from moorings in the Vema Channel.

Acknowledgments. This work has been supported by the National Science Foundation (OCE 90-04396 and OCE 90-04864) and the Office of Naval Research (N00014-90-J-1465).

References

Cessi, P., G. Ierley, and W. Young, 1987: A model of the inertial recirculation driven by potential vorticity anomalies, *J. Phys. Oceanogr.*, 17, 1640–1652.

Hoff, N.F., 1993: Toward parameterization of the eddy field near the Gulf Stream, *Deep-Sea Res.*, 40, 2359-2376.

Hogg, N., P. Biscaye, W. Gardner, and W.J. Schmitz, Jr., 1982: On the transport and modification of Antarctic Bottom Water in the Vema Channel *J. Mar. Res.*, 40 (Suppl.), 231–263.

Hogg, N.G., and H. Stommel, 1985: On the relation between the deep circulation and the Gulf Stream, *Deep-Sea Res.*, 32(10A), 1181–1193.

Holland, W.R., and P.B. Rhines, 1980: An example of eddy-induced ocean circulation, *J. Phys. Oceanogr.*, 10, 1010–1031.

Huang, R.X., 1990: Does atmospheric cooling drive the Gulf Stream recirculation? *J. Phys. Oceanogr.*, 20(5), 750–757.

Jayne, S.R., N.G. Hogg, and P. Malanotte-Rizzoli, 1995: Recirculation gyres forced by a beta plane jet, *J. Geophys. Res.*, submitted.

Johns, W.E., T.J. Shay, J.M. Bane, and D.R. Watts, 1995: Gulf Stream structure, transport and recirculation near 68°W, *J. Geophys. Res.*, 100, 817-838.

Knauss, J. A., 1969: A note on the transport of the Gulf Stream, *Deep-Sea Res.* , 16 (Suppl.), 117–123.

Malanotte-Rizzoli, P., N.G. Hogg, and R.E. Young, 1995: Stochastic wave radiation by the Gulf Stream: Numerical experiments *J. Geophys. Res.* , in press.

Marshall, J., and G. Nurser, 1986: Steady, free circulation in a stratified, quasigeostrophic ocean, *J. Phys. Oceanogr.* , 16, 1799–1813.

Pickart, R.S., 1992: Water mass components of the North Atlantic Deep Western Boundary Current, *Deep-Sea Res.*, 39 (9), 1553–1572.

Spall, M. A., 1995: Dynamics of the Gulf Stream/Deep Western Boundary Current Crossover. Part I: Entrainment and recirculation *J. Phys. Oceanogr.*, submitted.

Stommel, H., 1957: The abyssal circulation of the ocean, *Nature*, 180(4589), 733–734.

Critical Control by Topography - Deep Passages, Straits, and Shelf Fronts

J.A. Whitehead
Department of Physical Oceanography, Woods Hole Oceanographic Institution, Woods Hole, Massachusetts

Abstract. Saddle points between neighboring deep ocean basins are the sites of unidirectional flow from one basin to the next, depending on the source of bottom water. Flow in these sites appears to be critically controlled, so the interface between the bottom water and the water above adjusts itself to permit bottom water flow from the basin which contains a source of bottom water into the next. Examples in the Atlantic include flow in the Romanche Fracture Zone, the Vema Channel, the Ceara Abyssal plain, the Anagada-Jungfern passage, and the Discovery gap, but there are many more. Examples are listed for all oceans along with theoretical predictions of volume flux using CTD data archives. These are compared with volume flux estimates using current meters and/or geostrophic estimates for four new cases. Ocean straits also critically control bidirectional flows between basins. Theory of the influence of rotation on such critical flows is reviewed. Predictions of a number of these cases in the ocean are reviewed and compared with ocean estimates of volume flux. Finally, some considerations about fronts on continental shelves are given. A mechanism is shown that uses inertia to produce flux across a geostrophic front that separates two fluids of differing density in a rotating fluid when the front is forced to be narrower than the Rossby radius.

1. Introduction

For over a hundred years, critical control of fluid flowing through constrictions has been understood in a number of compressible, free surface, stratified or rotating fluid situations. One class of these problems combines stratified and rotating constraints to the fluid as it passes over bottom and sidewall constrictions. This class has come to be loosely termed "rotating hydraulics". Problems are typically solved with ocean or atmospheric examples in mind.

This paper reviews a number of ocean-related aspects of this problem. It does not exhaustively review the theoretical studies to date. Rather, the emphasis is on intercomparison of theoretical predictions of volume flux with oceanographic estimates based on direct measurements. The intent is to assess the practical usefulness of the understanding presented here to knowledge of the ocean.

We first review the very simplest concept of critical control of a nonrotating fluid. Consider a simple fluid flow problem as sketched in Figure 1, where water with a free surface in a field of gravity of depth H and velocity U is flowing along a channel and encounters a bump of size b. Assuming friction is negligible, the equations of motion reduce to Bernoulli's equation and conservation of mass,

$$\frac{1}{2}u^2 - g\eta = \frac{1}{2}U^2 \tag{1.1}$$

$$u(H-b-\eta) = UH \tag{1.2}$$

where u is velocity of fluid over the bump and η is downward deflection of the free surface over the bump. These two equations can be combined by eliminating u to produce the following cubic relation between scaled surface deflection $\eta' = \eta/H$, bottom bump $b' = b/H$, and upstream velocity Froude number $F = U/\sqrt{2gH}$.

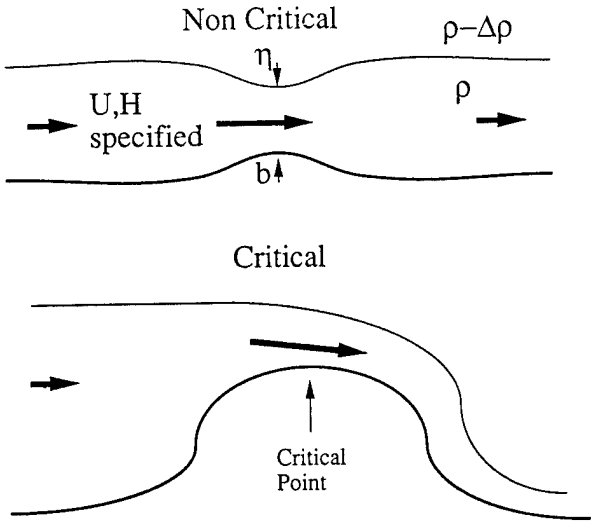


Figure 1. Sketch of an idealized flow of fluid along a channel with upstream velocity U and depth H, and the adjustment to a slowly increasing bottom b. The deflection downward of the interface is η.

$$(1-\eta'-b')^2 = \frac{1}{1+(\eta'/F^2)} \tag{1.3}$$

An easy way to picture these solutions is to investigate the intersection of the left hand parabola with the right hand hyperbola keeping η a freely varying parameter with fixed values of b' and F. Two such cases are shown in Figure 2. The first, represented by theright parabola, has $b' = F = 0.5$. There are three points of intersection: The leftmost point corresponds to the small deviation of b' as drawn in Figure 1. This is the

physically expected solution since it continuously maps to zero deflection as b' approaches zero. The middle point is a very large deviation and corresponds to a flow with local Froude number much greater than one. It cannot be physically realized since momentum flux plus pressure on the two sides of a control volume between upstream and the small bump is unequal. This state is known as a conjugate state. It could be produced by a large bump between upstream and the small bump, since then the large bump would experience pressure that would equalize the force and momentum budget. The right intersection point is physically forbidden since $b'+\eta' > 1$, so the free surface would be below the bottom of the bump.

The left parabola in Figure 2 is shown for $b' = 0.6$; the parabola has simply moved to the left by 0.1 unit of η'. At this value of F, the parabola intersects the hyperbola at only two points. The left point is located where the hyperbola and parabola are tangent. For smaller b', both left and middle points have migrated along the parabola for slowly increasing b' and merged at this point. In addition the local Froude number $F_\ell = 1$ at this point. The right point is still unphysical.

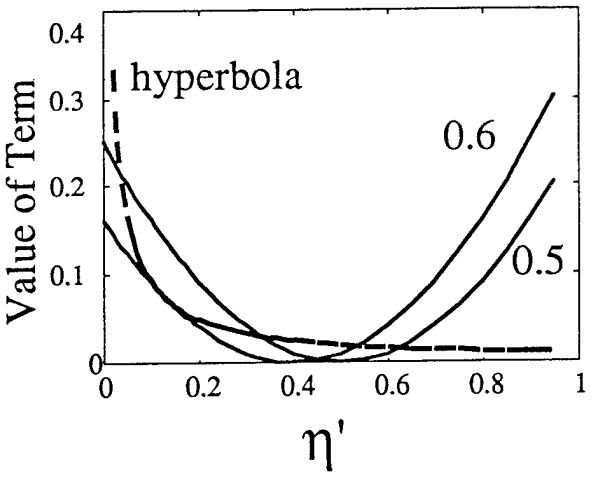


Figure 2. Values of the right and left hand side (a hyperbola and parabola, respectively) of equation 1.3. The hyperbola (dotted line) is drawn for F=0.1. The rightmost parabola corresponds to $b' = 0.5$. The leftmost parabola corresponds to b'=0.6.

For larger values of η' there is no intersection except for the right-hand unphysical one, the two other roots of the quadratic expressed by equation 1.3 are imaginary. Thus if b' is greater than a given value (depending on F), the fluid cannot get over the bump. One of the upstream conditions must be changed. For example, if volume flux is specified, H would need to be bigger. Or, if H is fixed (for instance by a large upstream lake), U may have to change to allow a flow. Often the fluid over the bump adjusts to the critical state. In such cases, the topography determines what is happening upstream.

These situations are found in physical oceanography. Dense water can accumulate in a basin from either surface cooling (in polar latitudes), inflow from an adjacent basin, or surface evaporation. We infer that, as the dense water accumulated, the interface of the dense water rose until it was above sill depth of the deepest passage which connects to another basin. The water above sill depth could then flow out through the passage. When the outflow rate equaled the accumulation rate of dense water, the interface ceased to rise and steady state was achieved. Volume flux of such outflows are useful measurements of interbasin water exchange and hence of fundamental interest in physical oceanography and ocean climate considerations.

We review here some theoretical studies of the critical control problem for rotating fluids with possible ocean applications. Most have been conducted over the past score of years. Geometries include not only a deep passage which we will call a "sill" where one water mass flows between basins, but also surface passageways (straits) where flows in both directions interchange water masses. A particular case in which there are gappy boundaries, so that one strait might support flow in one direction, but return flow is elsewhere, as elucidated by the studies of Nof (Nof and Olson 1983, Agra and Nof 1993, and Nof 1995) will not be reviewed here. Sections 2, 3 and 4 summarize theoretical aspects of sill flows, long strait flows, and very wide strait flows, respectively. Sections 5 and 6 discuss some ocean observations of such flows and some comparison with theory.

2. Sill flow calculations

Figure 3 shows the balance of three forces (Coriolis, inertia, and pressure) that are included in the simplest problems of rotating hydraulic control. Other forces which could be included in more complicated models are acceleration, friction and eddy Reynolds stress. The pressure is conventionally determined using the hydrostatic approximation.

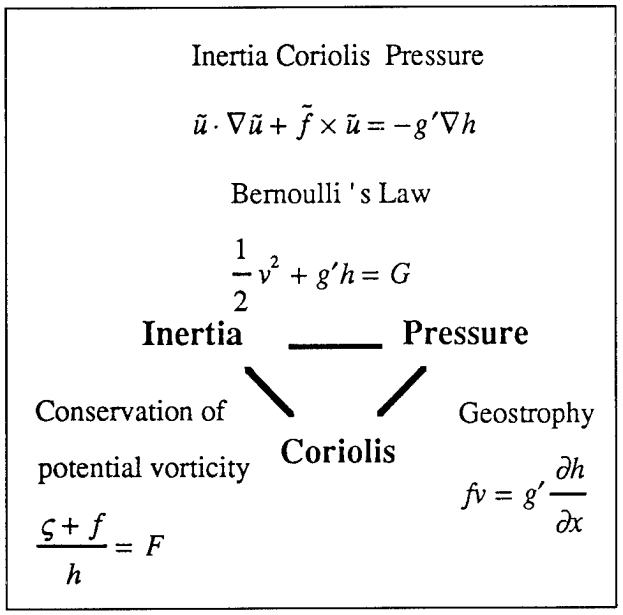


Figure 3. Diagram showing the three forces exerted on a fluid element and how dynamic relations are derived from these three forces.

These three forces are easily transformed into three relations: a geostrophic relation by looking across streamlines, the conservation of potential vorticity by taking the curl of the equation and using continuity, and Bernoulli's law by looking along streamlines. These three relations are redundant, and the cross-streamfunction derivative of the upstream Bernoulli's function must be equal to the upstream potential vorticity. The first, pioneering attempt to calculate critical flow along a channel (Stern 1972) violated this constraint.

Flow in the sill region is determined by using any two of the three above equations. If the geostrophic and potential vorticity equation are used, two constants of integration are introduced, but Bernoulli's equation eliminates one of them. We show for illustration here the simple theory of zero potential vorticity. Fluid of density $\rho+\Delta\rho$ lies in an infinitely deep upstream basin with surface h_u above the lip of a rectangular exit channel. Above is still fluid of density ρ. This problem has very simple algebraic solutions that illustrate the flows in the channel (Whitehead, Leetmaa and Knox, 1974).

The geostrophic equation and zero potential vorticity equation are

$$g'\frac{\partial h}{\partial x}=fv \qquad (2.1)$$

$$\frac{\partial v}{\partial x}=-f \qquad (2.2)$$

which integrate to

$$h=-\frac{f^2x^2}{2g'}+\frac{fv_ox}{g'}+h_o \qquad (2.3)$$

$$v=-fx+v_o \qquad (2.4)$$

where $g'=g\Delta\rho/\rho$, f is the Coriolis parameter, and h_o and v_o are two constants of integration. They represent water depth and velocity at $x=0$. Bernoulli's law exists along each streamline

$$v=\sqrt{2g'(h_u-h)} \qquad (2.5)$$

which can eliminate one constant of integration by making it a function of the other. Note that Bernoulli potential is $g'h_u$ since fluid is stagnant in the upstream basin. In problems with finite values of upstream depth, (i.e. constant upstream potential vorticity [Gill (1977), Pratt and Armi (1987), Whitehead (1989)]), Bernoulli's law may hold along all streamlines, but the Bernoulli potential is not easy to determine. Fortunately, there are some cases where it can be determined for one streamline.

In such cases, the problem is reduced to determining one constant of integration which is found, as we explained for the nonrotating example, by calculating the critical condition. The simplest such condition is that volume flux is maximized through the sill. This results in the following predictions for volume flux for a rectangular opening.

$$Q=\frac{g'h_u^2}{2f} \qquad L>\left(\frac{2g'h_u}{f}\right)^{\frac{1}{2}} \qquad (2.6)$$

otherwise

$$Q=\left(\frac{2}{3}\right)^{\frac{3}{2}}L\sqrt{g'}\left[h_u-\frac{f^2L^2}{8g'}\right]^{\frac{3}{2}} \qquad (2.7)$$

where L is width of the channel. Rydberg (1980) rejected the maximum volume flux argument, which is equivalent to the Froude number of the longest, fastest wave equal to one, in favor of having the local Froude number be one. This makes sense because Froude numbers greater than one would produce Kelvin-Helmholtz instability which would lead in turn to mixing. The resolution of this interesting conflict between local and long wavelength control remains unresolved by either additional theoretical work or direct observation in the laboratory or the ocean.

The first formula (2.6) is familiar to many oceanographers. It could be obtained from a simple geostrophic calculation if one assumes first that the

fluid height on the right-hand side of the sill (looking downstream in the northern hemisphere) equals upstream height h_u and second that the interface intersects the bottom on the left hand side. The critical control calculation justifies the use of h_u in this formula. Not only does it show this value gives maximum flow, but it also connects it to the available upstream potential energy through Bernoulli's equation. The second formula is familiar to hydraulic engineers in the limit of $f = 0$, which was first determined in the last century. As f is increased from 0, it smoothly connects the non-rotating result to equation 2.6.

If potential vorticity is not zero, the functions expressing velocity, height, and volume flux are more complicated, but still readily found by common calculations. However, the connection of Bernoulli potential between upstream and the sill is more challenging. In some cases only one streamline preserves Bernoulli potential from a point upstream to a point on the sill. However, the calculation of maximum flux can be accomplished in many cases. Gill (1977) simply specified the existence of appropriate currents in the upstream basin for constant upstream vorticity and graphically determined the volume flux as a function of dimensionless parameters. No analytic solutions were attained. Whitehead (1989) was able to find analytic solutions to volume flux in general but was unable to determine analytic solutions for the maximum value. Contours of nine values of volume flux from the analytic solution are shown in Figure 4. This figure differs from a comparable figure (Figure 6) in Whitehead 1989. There, negative values of fluid depth were allowed in the computation, so the curves in a region below the volume flux maximum are wrong. This error does not effect the computation of critical flow, however. Thus, the central finding in that paper - that volume flux for this case lies within 22% of the flux for the zero potential vorticity solution - still holds. Thus the feeling held by many in the 1980s, that the zero potential vorticity was essentially incorrect is apparently not born out for issues of volume flux.

Pratt and Armi (1987) investigated the flow patterns in the sill region for more general potential vorticity distributions and found that gyres and countercurrents are possible. Since such cases are characterized by upstream currents, Bernoulli potential varies in the upstream basin so that comparison of volume fluxes with the simple estimates above are not straightforward. Given these complications, volume fluxes were not determined in these cases, but a variety of issues, such as that the control point is at the crest of the sill for a certain class of sill geometries were clarified for more general flows.

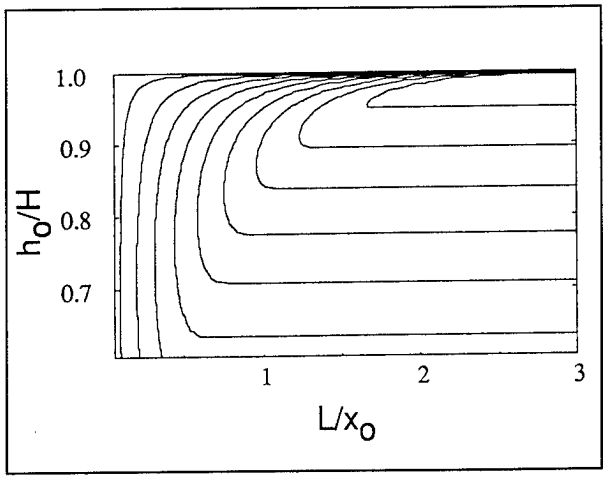


Figure 4. Contours of normalized volume flux $2Qf/g'h_u^2$ as a function of normalized right-hand wall depth and normalized channel width. In the region with horizontal contours, the flow has separated from the left-hand wall.

Both that paper and earlier studies by Borenas and Lundberg (1986), and Gill (1977) focused strongly upon the implications of the definition of control by the geometry of the outlet passage. This is a rich area of study since the nature of control from upstream basins with more general vorticity conditions through openings of more general shape is quite complicated. It is easy to visualize, for example, that some fluid might not possess enough energy to get through an opening while fluid next to it could. In that case, upstream blocking might occur which would be connected not with critical control of the entire current, but current separation. Such a process has the same branch structure used in the above papers, but is distinct from control of the entire current. Other aspects may be connected with particular definitions of critical control. Indeed, Borenas and Lundberg conclude that there is a range of parameters such that parabolic passageways cannot exert control (in the sense they use it). Yet it is difficult for this author to think that the sketch in Figure 1 breaks down because the channel happens to have a parabolic bottom. Other studies (Table 1) have dealt with a variety of other issues. This review will concentrate on volume flux issues, the rest are covered by Pratt and Lundberg (1991).

Most quantitative comparisons indicate that neither n the potential vorticity distribution nor the shape of the sill produce very large changes (order greater than one) in the volume flux. But unquestionably they produce changes of a fractio of order one. Recently, Killworth (1994) has shown that the zero potential sill produce very large changes (order greater than one) in the volume flux. But unquestionably they produce changes

Table 1. A List of Theories

Stern	1972	Trouble with upstream condition
Whitehead, Leetmaa & Knox	1974	Zero potential vorticity, zero currents
Gill	1977	Const. potential vorticity, upstream currents imposed
Rydberg	1980	Local F should = 1
Shen	1982	Zero potential vorticity, more tests
Pratt	1983	Adjustment to obstacle
Pratt	1984	Flow near critical speed
Borenas & Lundberg	1986	Parabolic channel, not controlled?
Pratt & Armi	1987	Nonuniform potential vorticity
Whitehead	1989	Comparison of zero and const. potential vorticity, application
Dalziel	1988, 1990	Zero potential vorticity exchange and control
Pratt & Lundberg	1991	Review of theory
Hunkins & Whitehead	1992	Const. potential vorticity exchange
Killworth	1992	Zero potential vorticity and shapes, application
Killworth & McDonald	1993	Zero potential vorticity and maximum flux
Killworth	1994	Zero potential vorticity is maximum
Johnson & Ohlsen	1994	Frictionally modified exchange
Whitehead & Kimura	1994	Wide exchange flow

of a fraction of order one. Recently, Killworth (1994) has shown that the zero potentialvorticity flow in a rectangular channel has the greatest volume flux of all possible potential vorticity distributions. This is valid for all bottom shapes, and makes the calculation of maximum fluxes easier than before. Earlier, Killworth and McDonald (1993) had found a maximum bound on any flow with non-negative potential vorticity, and showed it was roughly like the zero potential vorticity relation.

3. Strait flow calculations - lock exchange theory

In an ocean context, we will define lock-exchange flow as the flow through straits between basins with two different but uniform densities. In formulating problems, one could picture a gate which, once removed, allows the set-up of a semi-steady exchange of flow and counterflow between the basins. This problem with rotation included was analyzed for zero potential vorticity by Whitehead *et al.* (1974). In that formulation, a somewhat questionable energy conserving formula was used. Although laboratory data agreed with the theoretical prediction, a more complete theory would be useful. Dalziel (1988, 1990) extended the formalism introduced by Gill (1977) and obtained a number of improvements for openings less than one Rossby radius in width. An improvement for wide channels was made by Hunkins and Whitehead as reviewed here. The model (Figure 5) consisted of two basins separated by a channel of depth H. Basin 1 has water of density ρ_1 and basin 2 has water of greater density.

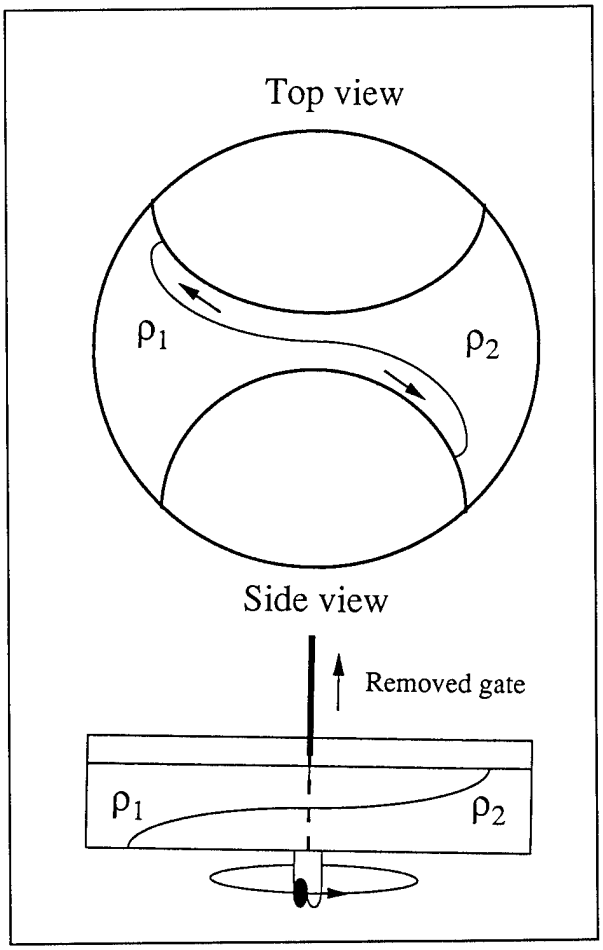


Figure 5. Sketch of a lock-exchange flow through a long straight channel.

The governing equations for the flow in the channel are conservation of depth,

$$h_1(x) + h_2(x) = H \tag{3.1}$$

where h_1 and h_2 are depth of each water in the strait, conservation of potential vorticity

$$\frac{\partial v_1}{\partial x} + f = \frac{f h_1}{H} \tag{3.2}$$

$$\frac{\partial v_2}{\partial x} + f = \frac{f h_2}{H} \tag{3.3}$$

and thermal wind between the two layers

$$f(v_2 - v_1) = g' \frac{\partial h_2}{\partial x} \tag{3.4}$$

One can derive differential equations for h_1, h_2, v_1 and v_2 as follows:

Take $\frac{\partial}{\partial x}$ of (3.4) and use (3.2) and (3.3) to get

$$\frac{\partial^2 h_2}{\partial x^2} - \frac{f^2}{g'}\left(\frac{2}{H}\right) h_2 = -\frac{f^2}{g'} \tag{3.5}$$

We define x as being zero in the middle of the channel. The solution of h_2 is

$$h_2 = \frac{H}{2} + B\cosh\frac{x}{R} + A\sinh\frac{x}{R} \tag{3.6}$$

and from (3.1), the solution of h_1 is

$$h_1 = \frac{H}{2} - B\cosh\frac{x}{R} - A\sinh\frac{x}{R} \tag{3.7}$$

where $R = \sqrt{\frac{g' H}{2f^2}}$, and A and B are constants of integration.

To solve for velocity, use (3.2) and integrate:

$$v_1 = -\frac{f x}{2} - \frac{fRB}{H}\sinh\frac{x}{R} - \frac{fRA}{H}\cosh\frac{x}{R} + C \tag{3.8}$$

or (3.3) and integrate:

$$v_2 = -\frac{f x}{2} + \frac{fRB}{H}\sinh\frac{x}{R} + \frac{fRA}{H}\cosh\frac{x}{R} + D \tag{3.9}$$

where C and D are also constants of integration.

These constants are found as follows: First, equation (3.4) dictates that $C = D$. Second, assume the height profile is antisymmetric about the horizontal centerline of the tank, so that $B = 0$. Because of the symmetry of the profile, the assumption of equal and opposite volume flux through the strait requires that $v_1 - v_2$ at $x = 0$. This requires that $C = 0$, so only the constant A remains to be determined.

Gill (1977) showed that the constant potential vorticity current has a Bernoulli function that is easily determined except for a constant. Since there is no dissipation in the current, the constant is conserved along streamlines. Therefore, the symmetric solution for the current extends throughout the entire region from behind one nose through the passage to behind the other nose.

To solve for the final constant, the time dependent energy equation is used in the form

$$\frac{\rho}{2}\frac{\partial \langle v^2 \rangle}{\partial t} + g\langle w \Delta\rho \rangle = 0 \tag{3.10}$$

where only the deviation of density $\Delta\rho$ from a constant value ρ has been retained. The angled brackets denote a volume integral.

We do not know the detailed flow in the nose region, but we can assume that the nose is fully developed (see Stern 1980, Stern, Whitehead, and Lien Hua 1982, Griffiths and Hopfinger 1983). Hence it will be self-similar between a time t and a time $t + \delta t$. The similarity assumption requires that the volume of the moving nose region be unchanging, in which case we can set $c_i = Q/A_i$ where Q_i is the volume flux of the i^{th} current behind the nose and A_i is the cross sectional area of the current.

Thus the increase in internal kinetic energy in time equals c_i times the areal average of kinetic energy across the current. These are summed for the two on the left and the two on the right to give:

$$\rho\frac{\partial \langle v^2 \rangle}{\partial t} = \frac{\rho}{2}\left(\frac{Q_1}{A_1} + \frac{Q_2}{A_2}\right)\left(\int_{-\lambda/2}^{\lambda/2} v_2^2 h_2 dx + \int_{-\lambda/2}^{\lambda/2} v_1^2 h_2 dx\right) \tag{3.11}$$

Likewise, the increase in potential energy is equal to c_i times the area of the current times the vertical displacement of the center of gravity of each column of width dx. The product of these is integrated across the currents and summed for the two noses to give:

$$g\langle w\Delta\rho \rangle = \frac{Q_2}{A_2}\int_{-\lambda/2}^{\lambda/2} g\,\Delta\rho\frac{h_2^2}{2}dx - \frac{Q_1}{A_1}\int_{-\lambda/2}^{\lambda/2} g\,\Delta\rho\, h_1\left(\frac{h_1}{2} + h_2\right)dx \tag{3.12}$$

Equations (3.11) and (3.12) are set equal, and since $Q_1 = Q_2$, $h_1 = H - h_2$, and $A_1 = A_2$, they simplify to

$$\frac{\lambda^3}{24\,R^3}+\frac{A^2}{H^2}\left(\frac{\lambda}{R}\left(1-\cosh\frac{\lambda}{R}\right)+4\sinh\frac{\lambda}{R}\right) = \frac{\lambda}{R}\left(1+\frac{2A^2}{H^2}\right) \tag{3.13}$$

where

$$A\sinh\frac{\lambda}{2R}=\frac{H}{2}. \tag{3.14}$$

These two equations are satisfied for the values

$$\frac{\lambda}{2R}=2.5940\,, \qquad \frac{A}{H}=0.07514\,. \tag{3.15}$$

Since A was the last remaining unknown, volume flux can now be determined from the integral

$$Q_1=-Q_2=\int_{-\lambda/2}^{\lambda/2}h_1 v_1\,dx$$
$$=fAR\left(\frac{\lambda}{2}\cosh\frac{\lambda}{2R}-2R\sinh\frac{\lambda}{2R}\right).$$
$$=0.156\frac{g'H^2}{f} \tag{3.16}$$

Whitehead, Leetmaa, and Knox (1974) used the above flat bottom energetics with the admittedly incorrect zero potential vorticity velocity profile to predict $Q_1=1/6\frac{g'H^2}{f}$ which is 7% higher. This is consistent with the notion that the zero potential vorticity flux is an upper bound, although this has not yet been shown to be true for the lock-exchange case as Killworth has shown for a sill. This volume flux prediction has been checked by a laboratory experiment by Hunkins and Whitehead (1992). Both the slope and the constant in front agree with the data to better than 10%.

4. Very wide lock-exchange

Fronts are frequently encountered at the edges of long, straight topography. Whitehead and Kimura (1994) explored a mechanism that uses inertia to produce flux across a geostrophic front that separates two fluids of differing density in a rotating fluid. They asked "when the front is forced to be narrower than the Rossby Radius R so the full Rossby adjustment cannot be reached, will fluid continue to flow in a cross-frontal direction and if so at what rate?" The model had flow in a submerged horizontal slot between two very deep basins containing motionless water. The inviscid rotating nonlinear equations for exchange flow were solved for two configurations: The first had Cartesian coordinates and the slot was infinitely wide but of length l in the cross-frontal direction. The second case had cylindrical coordinates.

The model involved a reservoir of still water in the deep ocean separated from a reservoir of still water of different density near the coast by a planar shelf of uniform depth. In order to be sure that the upstream fluids remain motionless even if there is exchange flow between ocean and coastal region, two very deep basins instead of shallow layers containing motionless waters of differing densities were considered. They are separated by a vertical wall except at mid-depth where there is a horizontal slot of depth h, cross-shelf length l and of infinite width (see Figure 6). At some previous time the slot had been opened, the interface between the two fluids slumped from gravity, and fluid started flowing back and forth between the basins (as in the Rossby adjustment problem). A steady exchange flow is reached where low density fluid flows along the top of the slot from basin 1 to basin 2 and a counterflow flows along the bottom of the slot from basin 2 to basin 1. As in most problems, it was assumed that the reservoirs on either side of the slot are large but finite and that fluid is not being added to either basin from the outside. Thus when enough time has elapsed for pressures p_1 and p_2 to adjust, the volume flux from basin 1 to basin 2 becomes the same as the flux from basin 2 to basin 1. We seek to calculate Q, the volume flux per unit slot width for the case of inviscid fluids.

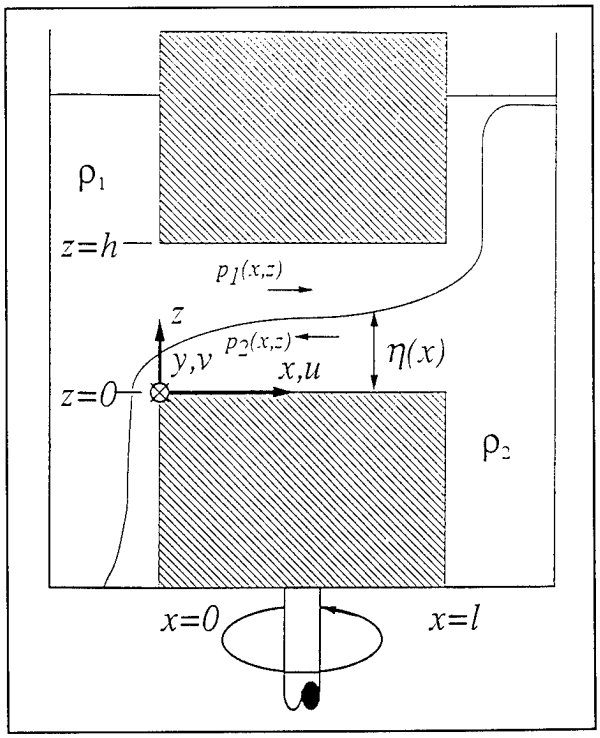


Figure 6. Sketch of a lock-exchange flow through a very wide channel.

In both layers, the steady inviscid Boussinesq rotating shallow water Euler equations were used. The along slot velocity is now called v_n in the direction of y, it obeys

$$\frac{\partial v_n}{\partial x} = -f \tag{4.1}$$

which integrates to

$$v_n = -fx + v_{no} \tag{4.2}$$

The across slot velocity component is u_n, and it obeys Bernoulli's law

$$\frac{1}{2}\left[u_n^2 + v_n^2\right] + \frac{p_n(x,z)}{\rho} = \frac{p_n\left((-1^n)\infty, z\right)}{\rho} \tag{4.3}$$

where it has been assumed that fluid is motionless i.e. $u_n = v_n = 0$ in the reservoirs. Combining equations for both layers, setting volume flux in each layer equal to the magnitude of the other results in the following equation relating volume flux $Q=u_n h_n$ with deviation of the interface δ.

$$\frac{1}{2}Q^2\left[\frac{1}{\left[\frac{h}{2}+\delta\right]^2} - \frac{1}{\left[\frac{h}{2}-\delta\right]^2}\right] - \frac{f^2\left[l^2 - 2xl\right]}{2} + g'\delta = 0 \tag{4.4}$$

To investigate properties of this solution, it is useful to define

$$Q' = \frac{4Q}{\sqrt{g'h^3}},$$

transform to $x' = (2x/l) - 1$ and write equation (4.4) in the form

$$\frac{Q'^2}{4}\left[\frac{1}{\left[1-\varepsilon\right]^2} - \frac{1}{\left[1+\varepsilon\right]^2}\right] = \varepsilon + \alpha^2 x' \tag{4.5}$$

where $\alpha^2 = f^2 l^2 / g'h$ and $\varepsilon(x') = 2\delta/h$. The variable α is the length of the slot divided by the Rossby radius of deformation and is a measure of the strength of rotation. The variable $\varepsilon(x')$ is a freely adjustable parameter corresponding to deviation of the interface from the midplane of the slot.

We ask what values of Q' can exist for each α and ε. We require that there be a continuous range of solutions between the center and the edge at $x' = 1$. The equation there can be rearranged to become

$$Q' = \left[\left[1 - \frac{\alpha^2}{\varepsilon}\right]\left[1 - \varepsilon^2\right]^2\right]^{\frac{1}{2}} \tag{4.6}$$

This is similar in some ways to the equation 1.3 that was given in the introduction. It is easy to see that ε is negative for $Q' > 1$, but Q' is unbounded as negative ε approaches 0. These are supercritical solutions which appear to be unphysical. In addition, for $0 < \varepsilon < 1$, a real solution is not possible for $\alpha > 1$. Also, in general the term $1-\alpha^2/\varepsilon$ is negative for $0<\varepsilon<\alpha^2$ in which case no flux is possible and flux is zero at $\varepsilon = \alpha^2$. For $\varepsilon>\alpha^2$, flux increases rapidly with ε but then it must decrease to zero for $\varepsilon = 1$. In summary, there is a maximum value of flux in the range $\alpha^2<\varepsilon<1$ and either zero or supercritical flow for other values of ε.

The dependence of Q' on ε for 7 values of α^2 is shown in Figure 7. When α^2 approaches zero, flux is maximum for $\varepsilon \cong \alpha^{2/3}$ and takes the value of $Q' = 1$ which is the well known value for the non-rotating exchange problem (Yih (1980) pg. 206).

A two-layer flow in axisymmetric cylindrical geometry can be formulated in a similar manner, but now there are edge conditions for the interface at the inner and outer radius.

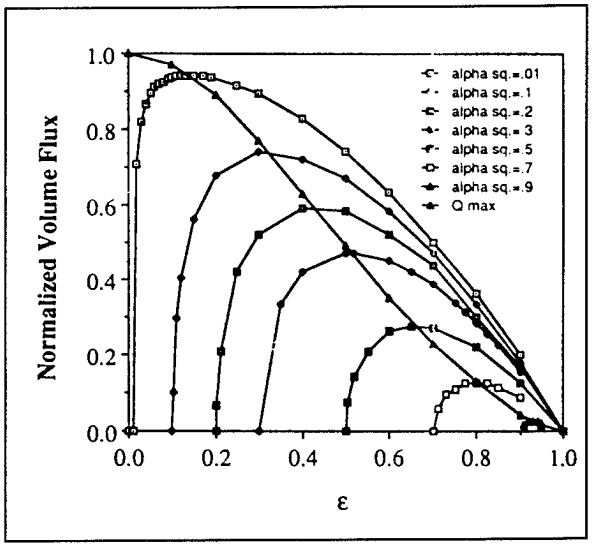


Figure 7. Normalized volume flux Q' as a Figure 7 Normalized volume flux function of scaled interface displacement at the edge of the slot for different rotation rates.

Volume flux F is

$$F = \frac{2\pi r_i \sqrt{g' h^3}}{4}$$

$$\left\{ \frac{\left[\varepsilon_i - \varepsilon_o - \frac{\alpha_r^2}{4\gamma^2}\left[1-\gamma^4\right]\left[1-\gamma^2\right] \right] \gamma^2 \left[1-\varepsilon_i^2\right]^2 \left[1-\varepsilon_o^2\right]^2}{\gamma^2 \varepsilon_i \left[1-\varepsilon_o^2\right]^2 - \varepsilon_o \left[1-\varepsilon_i^2\right]^2} \right\}^{\frac{1}{2}} \quad (4.7)$$

where $\gamma = r_o / r_i$ and $\alpha_r^2 = f^2 r_i^2 / g' h$ are dimensionless variables expressing the effects of the two radii and rotation, respectively. The free parameters denoting the deviation of the interface from midplane are $\varepsilon_i = 2\delta_i / h$ and $\varepsilon_o = 2\delta_o / h$. As in the Cartesian case, flux is scaled by the term outside the brackets which we presume is the solution of the nonrotating problem.

5. Oceanic observations of sill flows

Numerous measurements or estimates of velocity in the vicinity of sills have been made. A number of these are listed in Table 2. This is not an exhaustive list, but a collection of studies with data that either give volume flux measurements or contain measurements from which estimates can be obtained. The location of a number of these are shown in the three maps in Figure 8. The magnitude of volume flux varies from about 10^{-2} Sv. to well over one, depending upon the size of the basin. Most exhibit clear cross-channel tilt, a sign of influence of earth rotation. Indeed, geostrophic estimates have been made of the speeds of many currents.

Four of the examples listed above will be compared with an estimate from the idealized theory from Section 2. To make this comparison, a methodology used earlier (Whitehead 1989) will be used again. Application requires the adoption of a value of $\Delta\rho/\rho$, upstream height over the sill, channel width L and the local Coriolis parameter. With these four parameters, volume flux can be predicted using either equation 2.6 or 2.7 which we repeat here for convenience:

$$Q = \frac{g' h_u^2}{2f} \qquad L > \left(\frac{2g' h_u}{f} \right)^{\frac{1}{2}} \quad (5.1)$$

otherwise

$$Q = \left(\frac{2}{3}\right)^{\frac{3}{2}} L \sqrt{g'} \left[h_u - \frac{f^2 L^2}{8g'} \right]^{\frac{3}{2}} \quad (5.2)$$



Figure 8. Locations of some sills (unidirectional arrows) and straits (bidirectional arrows). a) Atlantic ocean with peripheral seas. b) Pacific ocean. c) Indian ocean. Light grey: <400 m. Dark grey: >5000 m.

Other Sills:

Windward Passage
Amirante Passage
Filchner Depression
[Southern Weddell Sea]
Indonesian Philippine Basin
South Sandwich Island Arc Gap
Ecuador Trench into Panama Basin
Nintyeast Ridge

Table 2. Flux Estimates Through Deep Ocean Sills

Denmark Strait 2.9 Sv., Dickson, Gmitrowicz and Watson (1990), Dickson and Brown (1994).
Charlie Gibbs Fracture Zone 2.4 Sv., Saunders (1994).
Discovery Gap 0.21 Sv., Saunders (1987).
Bornholm Strait 0.02 Sv., Petren and Walin (1975).
Iceland Faeroe Passage, no direct measurements Dickson assigns 1.0 Sv. from indirect considerations
Faeroe Bank Channel 1.5-1.9 Sv., Borenas and Lundberg (1988). They also did both a parabolic and rectangular hydraulic control is the point of zero velocity of current measurements; 1.9 Sv., Saunders (1990).
Windward passage (to Cayman Basin), unknown.
Anegada-Jungfern Passage 0.056 Sv., Stalcup, Metcalf and Johnson (1975). Also contains estimate from WLK theory of 0.04 Sv.
Strait of Sicily eastward flow not estimated directly by Grancini and Michelato (1987), who say the current meter data fully support the hydrographic results which they review as: 0.6 to 0.8 Sv. by Morel (1971), 0.65 Sv. by Molcard (1972), 1.23 Sv. by Garzoli and Maillard (1976), 1.23 Sv. from Geostrophy, 1.21 Sv. by Bethoux (1979) using WLK.
Vema Gap 2.1 to 2.3 Sv. using geostrophy, McCartney et al. (1991). Ceara Abyssal Plain between 0.8 and 2 Sv., Whitehead and Worthington (1982). > 4 Sv. from Geostrophy, McCartney and Curry (1993), Luyten et al. (1993). 2.1 Sv., Hall, McCartney and Whitehead (in prep).
Romanche Fracture Mercier (in prep). Hydraulic estimate 2 Sv., Mercier and Bryden. (1994)
Vema Channel 4 Sv., Hogg, Biscaye, Gardener, and Schmitz, (1982). New number, Hogg et al (in prep).
Samoan Passage 1.0, 5.6 and 4.8 geostrophic estimates Johnson, Rudnick and Taft (1994). 6 Sv., Rudnick (in prep.).
Shag Rocks Passage overflow events detected (Zenk 1981)

To estimate $\Delta\rho/\rho$, we will select at least two density profiles from CTD or bottle data, one upstream and one downstream of the sill. The profiles must extend to the depth of the sill, and the greatest density difference between upstream and downstream will be used. The sill depth is found from bathymetric charts. The depth at which the upstream and downstream profiles diverge will be called the bifurcation depth. The sill depth is subtracted from the "bifurcation depth" to determine h_u. The width of the opening at the bifurcation depth will be used to determine L.

This method was used earlier to predict a volume flux at four oceanic sills: the Denmark Strait, the ridge between Iceland and the Faeroe Islands, the Ceara abyssal plain, and the Vema passage. These fluxes were compared to compared to flow estimates using the current meter data for flow through three of the four passages. The fourth was erroneously compared to geostrophic estimates by Steele et al (1962) downstream of the Iceland-Faeroe ridge which should include overflows from the Faeroe-Scotland ridge as well as the Iceland-Faeroe overflow. The predictions of volume flux were all greater than the direct measurements by factors ranging from 1.6 to 4.1. More recent modern measurements will change those factors; a new version of the table with the latest estimates is found in the first four lines of Table 3. Since the mid-1980s, measurements of volume flux have been made through a number of additional passageways. We repeat the test of this method of predicting flux for four more cases which are discussed in turn.

The first is Discovery gap (Saunders 1987), which connects the Madeira Abyssal Plain which is west of North Africa in the East Atlantic, with the Iberian Abyssal Plain which is west of Portugal and Spain. Water of Antarctic origin (colder than = 2.1 C) flows northward through this gap with a volume flux estimated as 0.2 Sv. Information for our prediction is shown in Figure 9. Data were taken from Saunder's Figure 3 - an along flow section. Upstream conditions were complicated by an unmistakable cross stream tilt that signified a current of unknown origin. From Figure 9b, the bifurcation depth was taken to be 4000 m, the reported sill depth was 4600 m, so $\Delta\rho$ was taken to be 10^{-5}. This produces a Rossby radius R=4 km whereas the gap width is about 80K for the 4000 m contour, so the rapidly rotating formula is used. It predicts volume flows of 0.2 Sv. There is an unusual amount of room for adjustment of this value, and we could easily predict a value smaller than half as big, or more than three times bigger.

The second is the Samoa passage (Figure 10). Data are taken from Geosecs pacific stations 251 and 252 (upstream) and 253 and 257 (downstream). This gives a bifurcation depth of 3950 m. The bathymetric map, traced from the Gebco map shows a width of 240 km at this depth. Since Reid and Lonsdale (1974) report a sill depth of 4770 m, h_u = 820 m and $\Delta\rho/\rho = 3 \times 10^{-5}$. Rossby radius computed from these numbers is R=33 km so the rapid rotating limit should be used. This gives Q=4.6 Sv. Rudnick (pri. comm.) has recently recovered a moored array in this area and reports 6 Sv. This is the first instance where the hydraulics prediction is less than estimate based on current meter measurements.

Table 3. Data and predictions for eight sills, four reviewed and updated from Whitehead (1989) and four new ones

Sill	$\frac{\Delta\rho}{\rho}$	H	f	L	R	Q	Q_{obs}	Ratio	Cit.
	x10^4	(m)	s^{-1}x10^4	(km)	(km)	Sv.	Sv.	Q_o/Q	
Denmark Strait.	3	580	1.3	350	14	3.9	2.9	1.34	Dickson et al., 1990
Iceland Faeroe	5.8	400	1.3	400	17	3.6	1.0	3.6	Dickson et al., 1990
Ceara Ab. Plain	0.5	430	0.1	700	66	4.6	2.1	2.2	Hall Pri Comm
Vema Channel	1	1540	0.7	446	24	16.3	6	2.7	Hogg Pri Comm
Discovery Gap	0.1	600	0.87	80	4	.21	.21	1	Saunders, 1987
Faeroe-Scotland	5	400	2	20	7	9	1.9	1.05	Saunders, 1990
Samoa Passage	0.3	820	0.2	240	33	4.6	6	0.76	Rudnick Pri Comm
Vema Gap	1	950	0.28	9	35	3.1	2.1	1.4	McCartney et al, 1991

The first is Discovery gap (Saunders 1987), which connects the Madeira Abyssal Plain which is west of North Africa in the East Atlantic, with the Iberian Abyssal Plain which is west of Portugal and Spain. Water of Antarctic origin (colder than = 2.1 C) flows northward through this gap with a volume flux estimated as 0.2 Sv. Information for our prediction is shown in Figure 9. Data were taken from Saunder's Figure 3 - an along flow section. Upstream conditions were complicated by an unmistakable cross stream tilt that signified a current of unknown origin. From Figure 9b, the bifurcation depth was taken to be 4000 m, the reported sill depth was 4600 m, so $\Delta\rho$ was taken to be 10^{-5}. This produces a Rossby radius R=4 km whereas the gap width is about 80K for the 4000 m contour, so the rapidly rotating formula is used. It predicts volume flows of 0.2 Sv. There is an unusual amount of room for adjustment of this value, and we could easily predict a value smaller than half as big, or more than three times bigger.

The second is the Samoa passage (Figure 10). Data are taken from Geosecs pacific stations 251 and 252 (upstream) and 253 and 257 (downstream). This gives a bifurcation depth of 3950 m. The bathymetric map, traced from the Gebco map shows a width of 240 km at this depth. Since Reid and Lonsdale (1974) report a sill depth of 4770 m, h_u = 820 m and $\Delta\rho/\rho = 3 \times 10^{-5}$. Rossby radius computed from these numbers is R=33 km so the rapid rotating limit should be used. This gives Q=4.6 Sv. Rudnick (pri. comm.) has recently recovered a moored array in this area and reports 6 Sv. This is the first instance where the hydraulics prediction is less than estimate based on current meter measurements.

The third example is the Vema gap (Figure 11). Historically, the source of the bottom waters of the tropical Eastern Atlantic was considered to be a flow through the Romanch fracture zone that lies almost exactly on the equator. However, the work of Vangriesheim (1980) and Eittreim et al (1983) indicated that the flow through the Vema fracture zone was a major contributor to the water in the eastern North Atlantic. This gap lies at about 11°N in the Mid-Atlantic ridge. Recently, McCartney et al (1991) have measured a flux of 2.1 to 2.3 Sv through the Vema Gap. The data for this example is shown in Figure 11. From it we take h_u = 950 m, d = 10^{-4}, which, along with f = 2.8 x 10^{-5} s^{-1} and g = 9.8 m/s^2, predicts a Rossby radius of 49 km. This is wider than the passage width L = 9 km, so equation 5.2 is used to predict volume flux. With the above numbers, this comes out to be 4.4 Sv. This is a little over twice the geostrophic estimate. Corrections to the hydraulic estimate could be made by accounting for the tapering of the walls of the gap, for the influence of continuous stratification and possibly for friction (Pratt 1986).

The fourth is the Scotland-Faeroe passage (Figure 12), estimated by Saunders (1990) to be 1.9 Sv. This example did not work well using two stations from Geosecs, probably because both stations were in regions where there were surface currents associated with fresh water near the topography. The bifurcation diagram is made using 2880 stations from the NODC data atlas. Stations with the deepest bifurcation have a bifurcation depth of 500. Nearby station pairs that are closer to the shelf have significantly shallower bifurcation depth. The sill depth is reported to be 900 m which gives $\Delta\rho/\rho = 5\times10^{-4}$. This gives R=7 km. Using L=20, the rapid rotation limit is used. The prediction is 2 Sv., whereas Saunders reports 1.9 Sv. Borenas and Lundberg (1988) used a parabolic bottom and selected the 3°C isotherm and also got good agreement with Saunders' measurement.

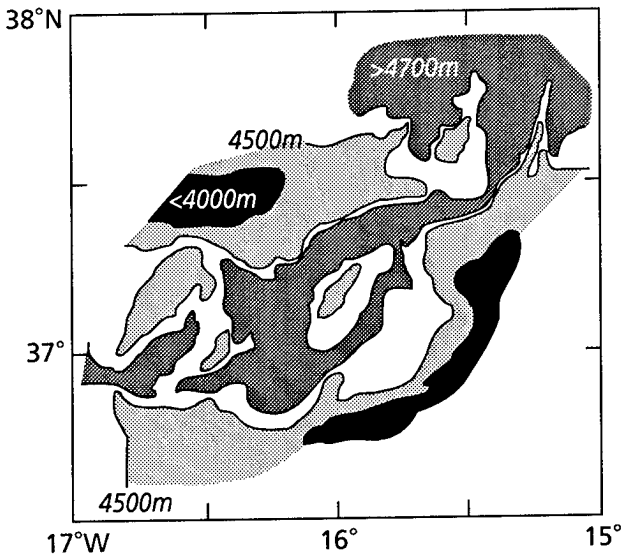


Figure 9a. Map showing the 4000, 4500 and 4700 m contours in the vicinity of Discovery gap

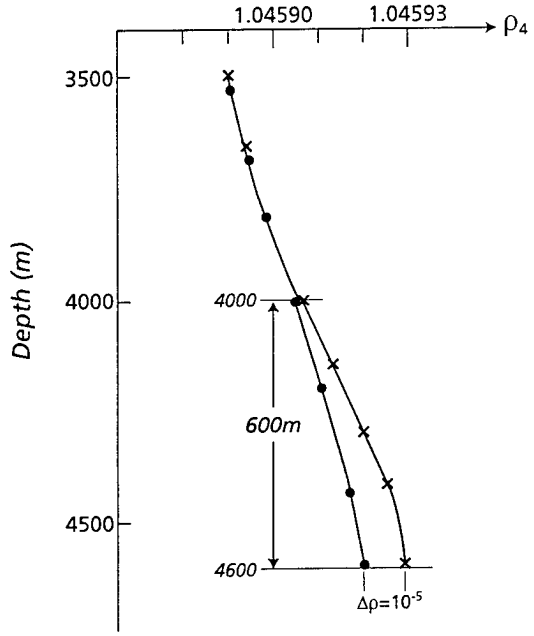


Figure 9b. Density (corrected to surface pressure) versus depth upstream and downstream of Discovery gap.

All the results are shown in Table 3. It is clear that the predictions approach the measured values in most cases. But still the method must be used with caution if additional currents are present. Otherwise the prediction has unrealistically great values of h_u and flux is All the results are shown in Table 3. It is clear that the predictions approach the measured values in most cases. But still the method must be used with caution if additional currents are present. Otherwise the prediction has unrealistically great values of h_u and flux is greatly overpredicted. So far, only one prediction out of eight, the prediction for the Samoa passage, is less than the measurements. (Actually assorted other estimates have been made, but they have not adhered to the

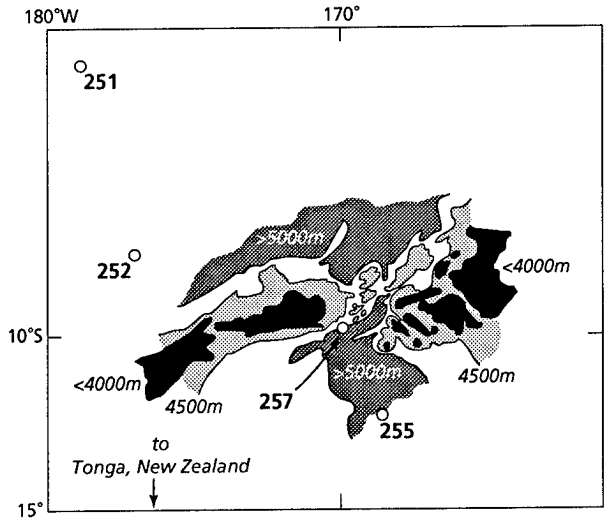


Figure 10a. Map showing the 4000, 4500 and 5000 m bottom contours near the Samoan Passage. Locations of the four GEOSECS stations are also shown.

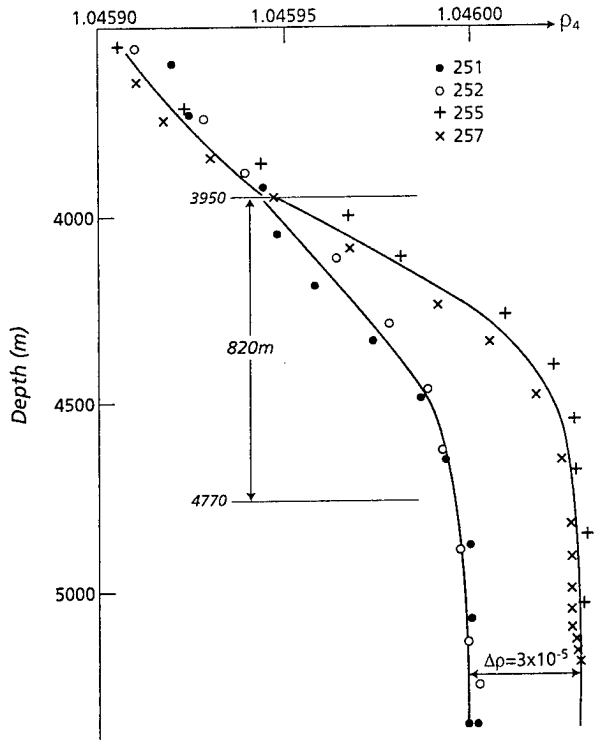


Figure 10b. Density (corrected to 4000 m) versus depth for the four GEOSECS stations upstream and downstream of the Samoan passage.

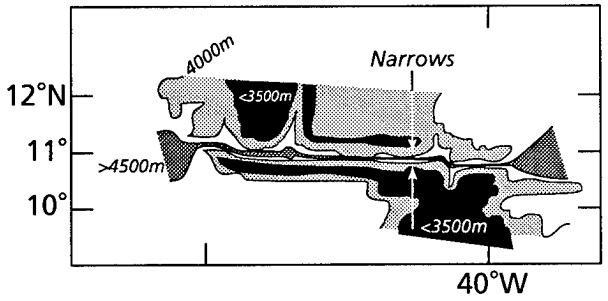


Figure 11a. Map showing the 3500, 4000 and 4500 m contours near Vema gap.

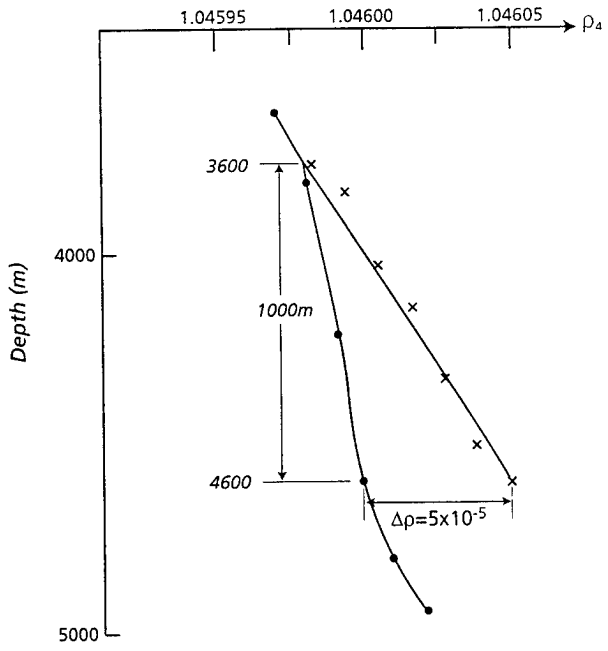


Figure 11b. Density versus depth for selected stations upstream and downstream of Vema gap.

present methodology). Although it would only take a small alteration of the bifurcation diagram to alter the prediction, it is not probable that values over 6 Sv. could be reached, so the Samoan passage may actually be a case where the upper boundedness of the theory doesn't apply. The Samoa passage is very rough and irregular, and possibly the topography produces an effect as though more than one passage wall were present.

6. Oceanic estimates of exchange flows

Lock exchange has now been used in numerous ocean applications; some examples are the Straits of Gibraltar,

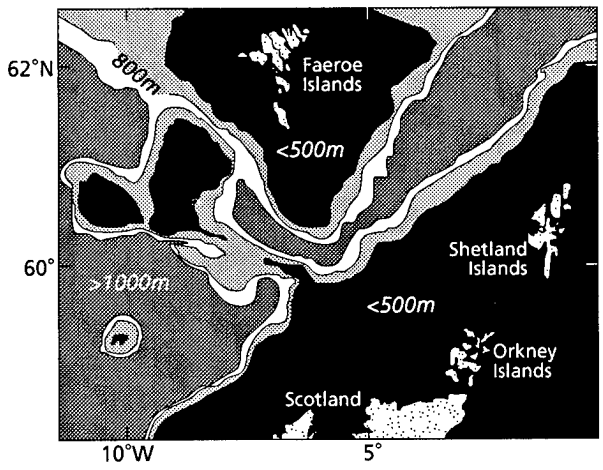


Figure 12a. Map showing the 500, 800 and 1000 m contours near the Iceland-Faeroe passage.

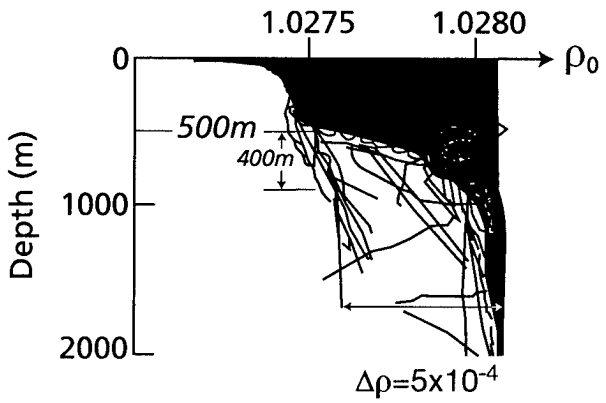


Figure 12b. Density versus depth for 2880 stations upstream and downstream of the Iceland-Faeroe passage.

Spencer Gulf, Chesapeake Bay, Delaware Bay, and Funka Bay. Table 4 contains a list of such straits for which at least partial information of flux through the opening is given. Here we use these formulas for the connecting passage between the Baltic and the North Sea.

Table 4. Strait Flows

Fram Strait	Skagerrak	Strait of Gibraltar
Gulf of Lyons	Adriatic Shelf	Belle Isle
Gaspe' Current	Chesapeake Bay	Gulf of Mexico
Spencer Gulf	Funka Bay	Tsugaru Strait
Vancouver Island	Bass Strait	Bosporus
Tiran Strait	Red Sea	Suez Canal

In the Baltic, Petren and Walin (1975) measured the flow of salty bottom water into the Baltic through the Bornholm Strait during the period of June 1973 to December 1974. They used geostrophic calculations and gel current meters to estimate that the bottom salty water volume flux was somewhere between 11,500 to 17,200 m^3/s. This depended upon the limiting salinity used, which ranged from 8.25 to 9.575 $^o/_{oo}$ and upon the method of averaging. The volume flux estimate was used along with salt conservation considerations of the outflow of surface water with salinity of $8^o/_{oo}$ to estimate how much river inflow would be needed so that the flux of salt is zero. They calculated a fresh water discharge of 9,400 to 12,000 which is reasonably close to the measured mean fresh water supply to the Baltic, which averaged 14,000 m^3/s for the period 1951 - 1970.

Their reason for measuring the flux of deep water through the Bornholm Strait was that such flows are steadier than the flows in the entrance regions. For instance, the Baltic has a narrow, shallow (~ 18m) entrance region, and currents in the region are variable due to variations in surface level. Such variations make measurements difficult unless taken for very long periods of time. We can, however, use a lock-exchange estimate using the considerations in Bye and Whitehead (1975) to predict the salinity difference between the deep and shallow water in the Baltic. This will assume that salinity difference is controlled by exchange flow in the Baltic entrance, in response to the mean fresh water supply of 14,000 m^3/s. In this the balances of volume flux Q and salt flux are

$$Q_i = Q_o + Q_r \tag{6.1}$$

$$S_i Q_i = S_o Q_o \tag{6.2}$$

where subscripts i, o, and r stand for into the Baltic, out of the Baltic and from river inflow, respectively. In this, we assume that Q_r and S_i are fixed by climatological factors and specified, whereas the other quantities can vary. Equations (6.1) and (6.2) can be combined to give

$$Q_o \Delta S = S_i Q_r \tag{6.3}$$

where $\Delta S = S_o - S_i$. A dynamic condition relating the volume flux to the density difference between inflowing and outflowing water in a shallow sill region is:

$$Q_o = \frac{g \Delta \rho H^2}{6 \rho f} = \frac{g \beta \Delta S H^2}{6 \rho f} \tag{6.4}$$

where $\beta = 0.71 \times 10^{-3}\, kg/1/^o/_{oo}$ is the coefficient of density change due to change in salinity, H is depth of the sill, $\rho = 1.01$ is average density of the water and $f = 1.2 \times 10^{-4}\ s^{-1}$ is the Coriolis parameter for 55°N. This formula applies to steady flow in a flat channel of both length and width greater than Rossby radius (to be calculated *post facto*), and it is assumed that both $Q_o \approx Q_i$ and $S_o \approx S_i$. Equations (6.3) and (6.4) are combined to eliminate Q_o and a salinity difference is predicted to be

$$\Delta S = \left(\frac{6 \rho f S_i Q_r}{g \beta H^2} \right)^{\frac{1}{2}} \tag{6.5}$$

Using g = 9.8 m/s, H = 18 m, $S_i = 18^o/_{oo}$, Q_r = 14,000 m^3/s, and the above values for f, β and ρ, the formula predicts salinity difference between outflow and inflow is $8.3^o/_{oo}$.

We next calculate volume flux from (6.4), and it is 25,700 m^3/s, which is close to the value of the outflows estimated by Petren and Walin. Since Q_r is roughly the same magnitude as Q_o, they both are roughly twice the value of the inflow. Therefore, the assumption that $Q_o \approx Q_i$ is relatively poor. If the salinity of the inflowing water with $8^o/_{oo}$ was used, we would predict a salinity difference of about 2/3 as large as the present prediction. In that case, the volume flux, which is linearly proportional to salinity difference, would also be 2/3 of the present value.

Finally the Rossby radius of deformation can be calculated from the formula

$$R_o = \frac{1}{2} \left(\frac{g \beta \Delta S H}{\rho f^2} \right)^{\frac{1}{2}} \tag{6.6}$$

and it is 1.75 km using the above values.

The same technique has been used for a number of other basins. These are listed in Table 5. Again it is clear that predictions approach the measured values in many cases. The test is deliberately crude, but it is applied to a number of examples over a wide range of parameters, so that the suitability of the calculations can be assessed for future, more thorough studies.

Closing Remarks

By employing the very simplest theory and by deliberately using easily obtainable archival data, we indicate that to a crude first approximation, the simple control-flow formulas produce sensible estimates of inter-basin flux. Our comparisons depend on having ocean estimates of flux through the opening. Fortunately, since

Table 5. Flux and density difference estimates for some oceanic strait flows.

Strait	FW Flux	H	f	L	R	$\frac{\Delta\rho}{\rho}$	Q	$\frac{\Delta\rho}{\rho}/_{obs}$	Cit.
	(m^3/s)	(m)	s^{-1} x10^4	(km)	(km)	x10^4	Sv.	x10^4	
Gibraltar		300	1.0	12	20	2	.8	3	Whitehead et al, 1974
Spencer Gulf	-200	40	.8	50	3.2	6.8	0.02	9	Bye & Whitehead, 1975
Chesapeake Bay	2237	10	.9	19	4	50	0.01	65	Whitehead, 1989
Funka Bay	*	80	1.0	21	3.9	*	.03	3	Miyake et al.,1988
Fram	10^4	200	1.4	>200	5.0	7	0.3	7	Hunkins & Whitehead, 1992
Baltic	14,000	18	1.2	100	1.75	6	0.03	9	Present

* This information was not used for this study.

That crude first approximation, the simple control-flow formulas produce sensible estimates of inter-basin flux. Our comparisons depend on having ocean estimates of flux through the opening. Fortunately, since flow through such constrictions is often concentrated, superior oceanographic estimates of flux, velocity and time dependence can be made in such regions. This has attracted a sizable number of oceanographers to make measurements in such regions. Consequently, the number of comparisons has steadily risen from the three or four in the mid-1970s to over 20 now. Thus, the range of parameters over which tests like these have been made is steadily increasing.

Along with the improvement in the ocean data, numerous theoretical advances have been made. Most of them concern assorted effects from variable potential vorticity. These effects include altered upstream flow patterns and control behavior. No significant effects upon volume flux have been reported by the varation of potential vorticity unless such variation produces very large upstream currents. A few studies have been made of the role of friction and time dependence. Two areas needing work, but with little or nothing done to date, are numerical modeling and effects of continuous stratification.

In the ocean, we know almost nothing about the local aspects of such flows. What is the nature of a real upstream flow? How much does local topography influence the currents? Is there significant dynamic influence by nearby currents? Is friction enhanced by the concentrated currents, and if so, where? Is vertical mixing influenced near the control region, as it is known to be downstream of the control point? Is vertical mixing enhanced in certain regions such as on the left hand side where currents are greatest? Is side or bottom friction enhanced there? I hope that the answers to some of these questions will be found by future studies.

References

Agra, C. and D. Nof, 1993: *Deep Sea Research* 40, 2259-82.

Bethoux, J.P., 1979: Budgets of the Mediterranean Sea. Their dependence on the local climate and the characteristics of the Atlantic waters, *Oceanol. Acta.* 2, 3, 157-163.

Borenas, K. and P. Lundberg, 1986: Rotating hydraulics of flow in a parabolic channel, *J.Fluid Mech.* 167, 309-26.

Borenas, K.M. and P. A. Lundberg, 1988: On the Deep-Water Flow Through the Faeroe Bank Channel, *J. Geophys. Res.* 93, 1281-1292.

Bye, J.A.T. and J.A. Whitehead, Jr., 1975: A Theoretical model of the flow in the mouth of Spencer Gulf, South Australia, *Estuarine and Coastal Marine Science* 3, 477-81.

Dalziel, S.B., 1988: Two-layer hydraulics: maximal exchange flows. Ph.D. thesis, University of Cambridge.

Dalziel, S.B., 1990: Rotating two-layer sill flows. *Physical Oceanography of Sea Straits*, NATO-ASI Ser., Ed. L.J. Pratt, Dordrecht, Klewer Press.

Dickson, R.R., E.M. Gmitrowicz and A.J. Watson, 1990: Deep Water Renewal in the Northern Atlantic, *Nature* 344, 848-50.

Dickson, R.M. and J. Brown, 1994: The production of North Atlantic Deep Water: Sources, rates and pathways, *J. Geophys. Res.* 99, 12319-12341.

Ettreim, S.L., P.E. Biscaye and S.S. Jacobs, 1983: Bottom-Water Observations in the Vema Fracture Zone, *J. Geophys. Res.* 88, 2609-2614.

Garzoli, S. and C. Maillard, 1976: Hydrologie et circulation hivarnales dans les canaux de Sicile et de Sardaigne, *Rapp. Int. Lab. Oceanogr. Phys. Museum National d'Histoire Naturelle*, Paris, 21 pp.

Gill, A. E., 1977: The hydraulics of rotating channel flow, *J. Fluid Mech.* 80, 641-71.

Grancini, G.F. and A. Michelato, 1987: Current Structure and variability in the Strait of Sicily and adjacent area, *Annales Geophysicae* 5B, (1) 75-88.

Griffiths, R.W. and E.J. Hopfinger, 1983: Gravity current moving along a lateral boundary in a rotating fluid, *J. Fluid Mech.* 134, 357-399.

Hogg, N., P. Biscaye, W. Gardner and W.J. Schmitz, 1982: On the transport and modification of Antarctic Bottom Water in the Vema Channel, *J. Marine Res.* 40 (suppl.), 231-63.

Hunkins, K. and J.A. Whitehead, 1992: Laboratory simulation of exchange through Fram Strait, *J. Geophys. Res.* 97, 11299-11321.

Johnson, G.C. and D.R. Ohlsen, 1994: Frictionally modified rotating hydraulic channel exchange and ocean outflows, *J. Phys. Oceanogr.* 24, 66-78.

Johnson, G.C. , D.L. Rudnick and B.A. Taft, 1994: Bottom water variability in the Samoa Passage, *J. Marine Res.* 52, 177-96.

Killworth, P.D., 1992: Flow properties in rotating, stratified hydraulics, *J. Phys. Oceanogr.* 22, 997-1017.

Killworth, P.D. and N.R. McDonald, 1993: Maximal reduced-gravity flux in rotating hydraulics, *Geophys. Astrophys. Fluid Dyn.* 70, 31-40.

Killworth, P., 1994: On reduced-gravity flow through sills, *Geophys. Astrophys. Fluid Dyn* 75, 91-106.

Luyten, J.M., M. McCartney, H. Stommel, R. Dickson and E. Gmitrowicz, 1993: *J. Phys. Oceanogr.* 23, 1885-92.

McCartney, M.S., S.L. Bennett and M.E. Woodgate-Jones, 1991: Eastward flow through the Mid-Atlantic Ridge at 11°N and Its Influence on the Abyss of the Eastern Basin, *J. Phys. Oceanogr.* 21, 1089-1120.

McCartney, M.S. and R.A. Curry, 1993: Trans-equatorial flow of Antarctic bottom water into the Western Atlantic Ocean, *J. Phys. Oceanogr.* 23, 1264-76.

Mercier, H. and H. Bryden, 1994: Flows of Antarctic Bottom Water over the Sill for the Romanche Fracture Zone. *International WOCE Newsletter*, 17, 9-10.

Miyake, H., I. Tanaka and T. Murakami, 1988: Outflow of Water from Funka Bay, Hokkaido, during early Spring. *J. Oceanogr. Soc. Japan*, 44, 163-70.

Molcard, R., 1972: Preliminary results of current measurements in the Strait of Sicily in May 1970, *Proc. Saclant Conf.*, 7, 82-95.

Morel, A., 1971: Caracteres hydrologiques des eaux echanges entre le bassin oriental et le bassin occidental de la Mediterranee, *Cah. Oceanogr.* 22, 3, 329-42.

Nof, D. and D. Olson, 1983: On the Flow Through Broad Gaps with Application to the Windward Passage, *J. Phys. Oceanogr.* 13, 1940-56.

Nof, D., 1995: Choked flows and wind-driven interbasin exchange. *J. Mar. Res.* 53, 23-48.

Petren, O. And G. Walin, 1975: Some observations of the deep flow in the Bornholm Strait during the period June 73-December 74.

Pratt, L.J., 1983: On inertial flow over topography. Part 1. Semigeostrophic adjustment to an obstacle, *J. Fluid Mech.* 131, 195-218.

Pratt, L.J., 1984: On inertial flow over topography. Part 2. Rotating channel flow near the critical speed, *J. Fluid Mech.* 145, 95-110.

Pratt, L.J., 1986: Hydraulic control of sill flow with bottom friction, *J. Phys. Oceanogr.* 16, 1970-80.

Pratt, L.J. and L. Armi, 1987: Hydraulic control of flows with nonuniform potential vorticity, *J. Phys. Oceanogr.* 17, 2016-29.

Pratt, L. J. and P.A. Lundberg, 1991: Hydraulics of rotating strait and sill flow, *Annu. Rev. Fluid Mech.* 23, 81-106.

Reid, J.L. and P.F. Lonsdale, 1974: On the flow of water through the Samoan Passage, *J. Phys. Oceanogr.* 4, 58-73.

Rydberg, L., 1980: Rotating hydraulics on deep-water channel flow, *Tellus* 32, 77-89.

Saunders, P.M., 1987: Flow through Discovery Gap, *J. Phys. Oceanogr.* 17, 631-43.

Saunders, P.M., 1990: Cold Outflow from the Faeroe Bank Channel, *J. Phys. Oceanogr.* 20, 29-43.

Saunders, P.M., 1994: The flux of overflow water through the Charlie-Gibbs Fracture Zone, *J. Geophys. Res.* 99, 12343-55.

Shen, C.Y., 1982: The rotating hydraulics of open-channel flow between two basins, *J. Fluid Mech.* 112, 161-88.

Stalcup, M.C., W.G. Metcalf and R.G. Johnson, 1975: *J. Marine Res. Suppl.* 33, 15-35.

Steele, J.H., J.R. Barrett and L.V. Worthington, 1962: Deep currents south of Iceland, *Deep Sea Res.* 9, 465-74.

Stern, M.E., 1972: Hydraulically critical rotating flow, *Phys. Fluids* 15, 2062-65.

Stern, M.E., 1980: Geostrophic fronts, bores, breaking and blocking waves, *J. Fluid Mech.* 99, 687-704.

Stern, M.E., J.A. Whitehead and B.L. Hua, 1982: The intrusion of a density current along a coast of a rotating fluid, *J. Fluid Mech.* 123, 237-265.

Vangriesheim, A., 1980: Antarctic bottom water flow through the Vema fracture zone, *Oceanologica Acta* 3, 199-207.

Whitehead, J.A. , A. Leetmaa and R.A. Knox, 1974: Rotating hydraulics of strait and sill flows, *Geophys. Fluid Dyn.* 6, 101-25.

Whitehead, J.A., Jr. and L.V. Worthington, 1982: The flux and mixing rates of Antarctic Bottom Water within the North Atlantic, *J. Geophys. Res.* 87 (C10), 7903-7924.

Whitehead, J.A., 1989: Internal hydraulic control in rotating fluids - applications to oceans, *Geophys. Astrophys. Fluid Dyn.* 48, 169-192.

Whitehead, J.A. and Ryuji Kimuura, 1994: Rotating Hydraulic Models of Fronts at the Continental Shelf Break and in Circular Eddys, *Geophys. Astrophys. Fluid Dyn.* 76, 1-27.

Yih, C.S., 1980: Stratified Flows, *Academic Press, New York*, 418 pp.

Zenk, W., 1981: Detection of Overflow Events in the Shag Rocks Passage, *Scotia Ridge Science* 213, 1113-14.

A Simple Model of Abyssal Flow

Rick Salmon

Scripps Institution of Oceanography, University of California at San Diego, La Jolla Ca 92093-0225

Abstract. The planetary geostrophic equations (PGE) have special properties that greatly facilitate analytical and numerical solution. In particular, when the potential vorticity is assumed to be an arbitrarily prescribed function of the buoyancy, then the ideal three-dimensional PGE exactly reduce to a pair of coupled equations in two space dimensions. As an example of this method of reduction. I offer a simple model of abyssal flow in the southwestern Pacific.

I, among many others, have advocated the use of ocean models based upon the planetary geostrophic equations (hereafter PGE),

$$\begin{aligned} -fv &= -\frac{1}{r\cos\theta}\frac{\partial p}{\partial \lambda} - \varepsilon u \\ fu &= -\frac{1}{r}\frac{\partial p}{\partial \theta} - \varepsilon v \\ 0 &= -\frac{\partial p}{\partial z} + T \\ \frac{\partial}{\partial \lambda}\left(\frac{u}{r\cos\theta}\right) &+ \frac{1}{\cos\theta}\frac{\partial}{\partial \theta}\left(\cos\theta\frac{v}{r}\right) + \frac{\partial w}{\partial z} = 0 \end{aligned} \tag{1}$$

and

$$\begin{aligned} \frac{\partial T}{\partial t} + \frac{u}{r\cos\theta}\frac{\partial T}{\partial \lambda} + \frac{v}{r}\frac{\partial T}{\partial \theta} + w\frac{\partial T}{\partial z} = \\ \nabla\cdot(\kappa\nabla T) + \frac{\partial}{\partial z}\left(\kappa\frac{\partial T}{\partial z}\right) \end{aligned} \tag{2}$$

Here, θ is the latitude, λ the longitude, z is the vertical distance, r the radius of the Earth, T is the buoyancy (which I will call temperature), and the other symbols have their conventional meanings. Wind- and thermal forcing terms can also be appended.

The defining characteristic of the PGE (1-2) is their complete neglect of inertia, leading to *linear* equations of motion *except* for the advection of temperature in (2). However, this single nonlinearity is enough to make the PGE dynamics both challenging and very rich. Nevertheless, because of their relative simplicity (compared to say, the primitive equations) the PGE have a number of important advantages.

First, numerical solutions of the PGE (with steady forcing) seem always to approach a steady state. This effectively reduces the number of independent variables by one, and it means that if only the final steady state is of interest, it can usually be found using numerical relaxation methods that are much more efficient than time-stepping.

Second, since the PGE omit the advection of momentum, they do not require a diffusive (i.e., Laplacian) friction. In fact, the simpler Rayleigh friction in (1) is sufficient to meet boundary conditions of *no-normal-flow* at rigid boundaries *provided* that the ocean depth vanishes smoothly at the coastline (Salmon, 1986, 1992). (However, if any part of the boundary is vertical, then the vertical momentum equation (1c) must also contain a Rayleigh friction term.) The simpler Rayleigh friction leads to a much simpler boundary- and internal-layer structure and greatly facilitates analytical and numerical solution.

Third, analytical and numerical solutions of the PGE contain internal boundary layers of thickness $\kappa^{1/2}$, corresponding to the ocean's mean thermocline (Salmon 1990, Salmon and Hollerbach 1991) and leading to a picture of the subtropical ocean as two *inhomogeneous* layers in which temperature diffusion is unimportant, separated by a thin region in which T changes rapidly and diffusion is important *no matter how small the value of* κ. This result calls into question the many attempts to explain the structure of the main thermocline on the basis of the ideal (κ=0) equations and to justify such explanation by appeal to the smallness of measured values of κ.

Finally, on account of their simplicity, the ideal PGE admit an exact reduction from three to two space dimensions. This reduction, which leads to equations that generalize the conventional two-layer PGE equations, further facilitates analytical and numerical solution. In this brief report on work in progress, we show how the reduction principle can be used to obtain a simple equation governing the flow of a dense layer of fluid along the ocean bottom. The simplicity of the dynamics offsets the difficulty of incorporating real bathymetry and makes the results easier to understand.

The basic idea of reduction goes back to Welander (1971) and Needler (1971). In the ideal-fluid limit (ε=κ=0), the PGE conserve the temperature and potential vorticity on fluid particles,

$$\frac{DT}{Dt}=0, \quad \frac{D}{Dt}\left(f\frac{\partial T}{\partial z}\right)=0. \tag{3}$$

Therefore, the ansatz,

$$f\frac{\partial T}{\partial z}=G(T), \tag{4}$$

where G( ) is an arbitrary function is *consistent*, in that sense that if (4) holds at some initial time, it then holds at all future times. But (4) integrates immediately to

$$T=F''\left(\frac{z}{f}+S(\lambda,\theta,t)\right), \tag{5}$$

where $F''()$ is another arbitrary function, related to G, and the primes, which denote differentiation, are introduced for later convenience. $S(\lambda,\theta,t)$ is a function of integration, *independent of* z, which must be determined by substituting (5) back into (1-2). The result (still assuming $\varepsilon=\kappa=0$) is

$$r^2 f\frac{\partial S}{\partial t}+\frac{1}{\cos\theta}\frac{\partial(P,S)}{\partial(\lambda,\theta)}+\frac{1}{f\sin\theta}\frac{\partial D}{\partial\lambda}=0, \tag{6}$$

an evolution equation for $S(\lambda,\theta,t)$ in which the vertical coordinate z does not appear.

The S-equation (6) contains two additional dependent variables, $P(\lambda,\theta,t)$ and $D(\lambda,\theta,t)$, which are determined by boundary conditions at the top and bottom of the ocean. If these boundary conditions are taken to be no-normal-flow at the ocean surface and bottom, then D is easily determined, and P (or alternatively ψ, the streamfunction for the vertically integrated horizontal velocity) is determined by a second equation, also containing S. The dynamics then reduce to a pair of coupled equations in $S(\lambda,\theta,t)$ and $\psi(\lambda,\theta,t)$, which together determine the whole flow. Salmon (1994) called these the *generalized two-layer equations* (GTLE), because they reduce to the conventional, two-homogeneous-layer analogue of (1-2) when the arbitrary function $F''()$ in (5) is chosen to be a Heaviside function. However, other choices of $F''()$ were found to be both more realistic and numerically convenient. In particular, the conventional two-layer model is an inconvenient basis for numerical modeling because of the difficulty in following the *outcropping line* at which the meniscus between the layers intersects the ocean surface or bottom. However, if two nearly homogeneous layers are really wanted, then $F''()$ can be chosen to be a function that changes rapidly but *continuously* between temperature values corresponding to the two layers. The outcropping lines are then regions of rapid but continuous temperature change, which need not be explicitly followed.

Of course, full-basin solutions require wind- and thermal forcing, and the PGE can satisfy *coastal* boundary conditions of no net transport across coastlines only if $\varepsilon \neq 0$. Moreover, if the model ocean spans the equator, then the ansatz (5) itself contains a singularity at $f=0$. To avoid this singularity, Salmon (1994) generalized (5) to

$$T=F''\left(\frac{z}{\sqrt{f^2+f_0^2}}+S(\lambda,\theta,t)\right), \tag{7}$$

where f_o is a small constant. With T of the form (7), the linear equations (1) and no-normal-flow boundary conditions can still be completely satisfied; they serve to determine the velocity field (u,v,w) in terms of T. However, substitution of this velocity field and (7) back into (2) no longer yields a z-independent equation. This is because of the modification of (5) to (7) and because forcing, friction, and diffusion anyway destroy the conservation properties (3) on which (5) relies. Salmon (1994) therefore replaced (2) by its vertical average. The resulting equation, which is essentially (6) with forcing and dissipation terms appended, has "three-dimensional accuracy" except at very low latitude, where the f_o term in (7) is significant, and the GTLE have the character of a Galerkin approximation. For many further details, refer to Salmon (1994).

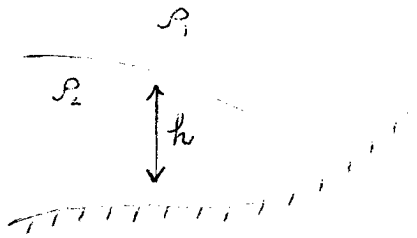


Figure 1. A simple model of the flow of dense water along a bumpy ocean bottom—the so-called one-and-one-half layer model. The water above the moving layer is assumed to be at rest.

In this note, we consider an ansatz of the general form (5) or (7) that leads to dynamics even simpler than the generalized two-layer equation. This new model, which could accurately be described as a *generalized one-and-one-half layer model*, bears the same relation to the simple model of abyssal flow shown in Figure 1, as the GTLE bear to the conventional two-layer model. In Figure 1, the upper fluid layer is assumed to be infinitely deep and at rest, so that (neglecting the inertia, the lower-layer dynamics are governed by

$$-fv=-\frac{g'}{r\cos\theta}\frac{\partial\eta}{\partial\lambda}-\varepsilon u$$

$$+fu=\frac{g'}{r}\frac{\partial\eta}{\partial\theta}-\varepsilon v$$
$$\frac{\partial h}{\partial t}+\frac{\partial}{\partial\lambda}\left(\frac{hu}{r\cos\theta}\right)+\frac{1}{r\cos\theta}\frac{\partial}{\partial\theta}(hv\cos\theta)=0 \quad (8)$$

where h is the thickness of the moving layer, $\eta = h- H$ is the height of the interface between the layers, and g' is the reduced gravity. Eliminating u and v yields a single equation for h,

$$\frac{\partial h}{\partial t}+\frac{g'}{r^2\cos\theta}\frac{\partial\left(h-H,\frac{f}{f^2+\varepsilon^2}h\right)}{\partial(\lambda,\theta)}= \quad (9)$$
$$\varepsilon g'\nabla\cdot\left[\frac{h}{f^2+\varepsilon^2}\nabla(h-H)\right].$$

Now consider the more general case in which the temperature is given by (5), but still approaches a uniform value (conveniently taken to be zero) as $z\to\infty$. This imposes the condition $F''(\infty) = 0$ on the profile function. The quantities P and D are now determined by the requirements that the horizontal velocity (u,v) vanish as $z\to\infty$ and that there be no flow through the ocean bottom at $z = -H$. The ideal ($\varepsilon = 0$) S-equation (6) takes the form of a "bottom-layer" potential vorticity equation,

$$\frac{\partial q}{\partial t}-\frac{F'(q)}{r^2\sin\theta}\frac{\partial q}{\partial\lambda}+\frac{F''(q)}{r^2 f\cos\theta}\frac{\partial(H,q)}{\partial(\lambda,\theta)}=0, \quad (10)$$

where

$$q\equiv S-\frac{H}{f}, \quad (11)$$

and $F'''(q)$ is the potential vorticity fT_z at the ocean bottom. The second term in (10) induces a westward propagation of q at speed determined by q itself; the third term propagates q along isobaths in the sense of clockwise propagation around deeps in the southern hemisphere.

Next, assuming $\varepsilon \neq 0$, adopting (7) instead of (5), and following the procedure summarized after (7), we obtain the frictional generalization of (10), namely

$$\frac{\partial q}{\partial t}-\frac{f^3}{\sqrt{f^2+f_0^2\left(f^2+\varepsilon^2\right)}}\frac{F'(q)}{r^2\sin\theta}\frac{\partial q}{\partial\lambda}+ \quad (12)$$
$$\frac{f}{\left(f^2+\varepsilon^2\right)}\frac{F''(q)}{r^2\cos\theta}\frac{\partial(H,q)}{\partial(\lambda,\theta)}=\textit{diffusion}$$

where the right-hand side stands for relatively simple diffusion terms which will not be written out. In the special case

$$F''(\xi)=\begin{cases}0, & \xi>0\\ -g' & \xi<0\end{cases} \quad (13)$$

in which the profile function is a step function, (12) reduces exactly to (9) with $q= -h/f$ (the layer-depth potential vorticity).

I have used (12) as the basis for a simple numerical model of bottom water flowing northward in the southwestern Pacific. Observations (Mantyla and Reid 1983, Taft et al. 1991) show that the densest abyssal water enters the North Pacific through the Samoa Passage at 10°S, 170°W. I solve (12) on an open computational domain extending from 25°S to 5°S, and from 180° to 160°W, including the Samoa Passage and several apparently less important passages for the northward moving bottom water. Refer to Figure 2. The temperature profile function is a "smooth step,"

$$F''(\xi)=\frac{1}{2}T_0\left[\tanh(\xi/\Delta)-1\right] \quad (14)$$

with constant amplitude T_o and "step-width" Δ chosen to agree roughly with the local Levitus data. The boundary conditions are fixed q (i.e., fixed temperature) on the computational domain. The Rayleigh damping coefficient ε is 0.15 times a representative value of f.

The calculation begins from a state (Figure 2, top) in which the cold bottom water is pressed against the southern computational boundary at 25°S. As time increases, this cold water spreads northward, steered by the bathymetry in the potential vorticity equation (12). After 128 days (Figure 3a), the cold, dense water has filled the Tonga Trench, turning westward (with the axis of the trench around the Samoa Islands. By 558 days (Figure 3b), significant flow is also occurring around the eastern side of the islands. By 1192 days (Figure 3c) cold water is spilling through the Samoa Passage and through a shallower passage in the Robbie Ridge at 175°W. The maximum current speed of 9.8 km day^{-1} in the Samoa Passage agrees well with recent direct measurements of the current (Dan Rudnick personal communication)

Figure 4 shows three temperature sections at 1563 days. The north-south section at mid-domain (Figure 4, bottom) passing through the Samoa Passage shows that the cold water has nearly reached the northern computational boundary. A section along 17°S (Figure 4, middle) shows how the cold water has filled up the abyss south of Samoa. The top section in Figure 4 corresponds to the broken line on Figure 2 (bottom) and crosses the axes of all the important passages into the North Pacific. This top section shows the coldest water flowing northward through the Samoa Passage, but cold water is also flowing northward

through the passes in the Robbie Ridge, and to the east of the Manihiki Plateau.

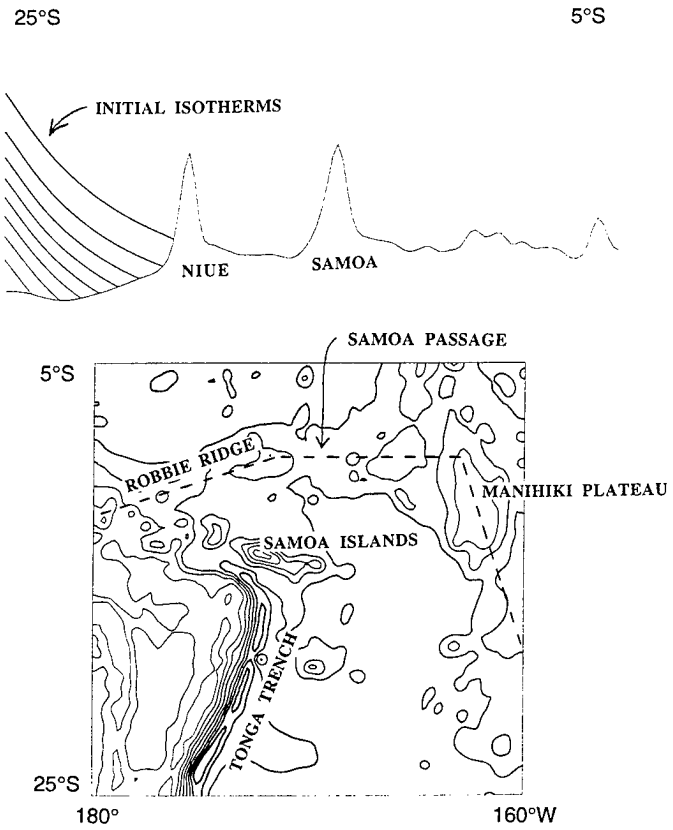


Figure 2. The ocean depth (bottom) and initial temperature (top) in a mid-domain section along 170°W in the preliminary study of the northward spread of bottom water in the southwest Pacific. The computational domain is open, with boundary conditions of prescribed temperature. The model topography is a smoother version of the "etopo-5 topography with a grid spacing of 0.1667 degrees in latitude and longitude.

The initial-value calculation summarized on Figures 2 to 4 is mainly intended to show the feasibility of using reduced-PGE models with realistic bathymetry. I chose the Samoa Passage for its importance as a source of North Pacific abyssal water and because the assumption of a level-of-no-motion far above the bottom is perhaps easier to defend there than in other places. With one-sixth-degree resolution (121 by 121 grids) the calculation required three hours CPU time on a Sparc-120 workstation. Thus even higher spatial resolution and a broader computational domain are quite feasible. I am particularly interested in the influence of spatial resolution (i.e., the very small scales in the bathymetry) on the solutions.

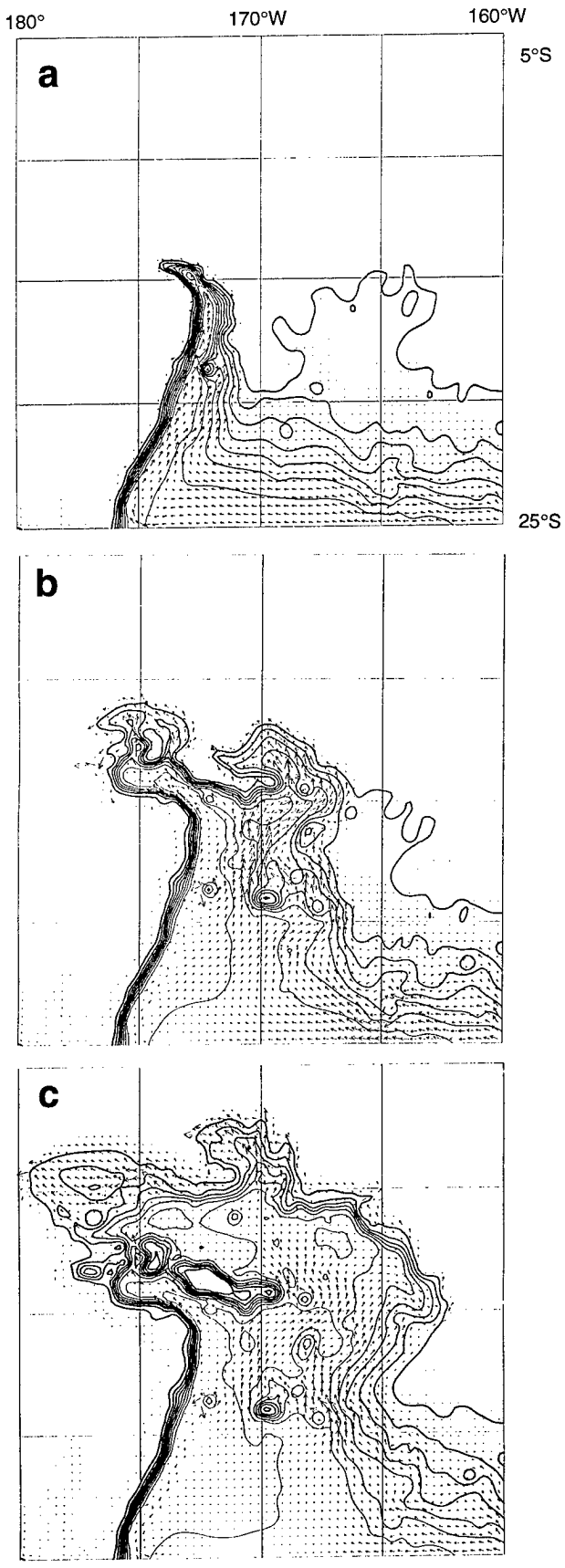


Figure 3. The temperature (contours) and horizontal velocity (arrows) at the ocean bottom at three successive times in the numerical solution of (13) with the bottom topography shown in Figure 2. (a) The flow after 128 days, (b) after 558 days, (c) after 1192 days. →

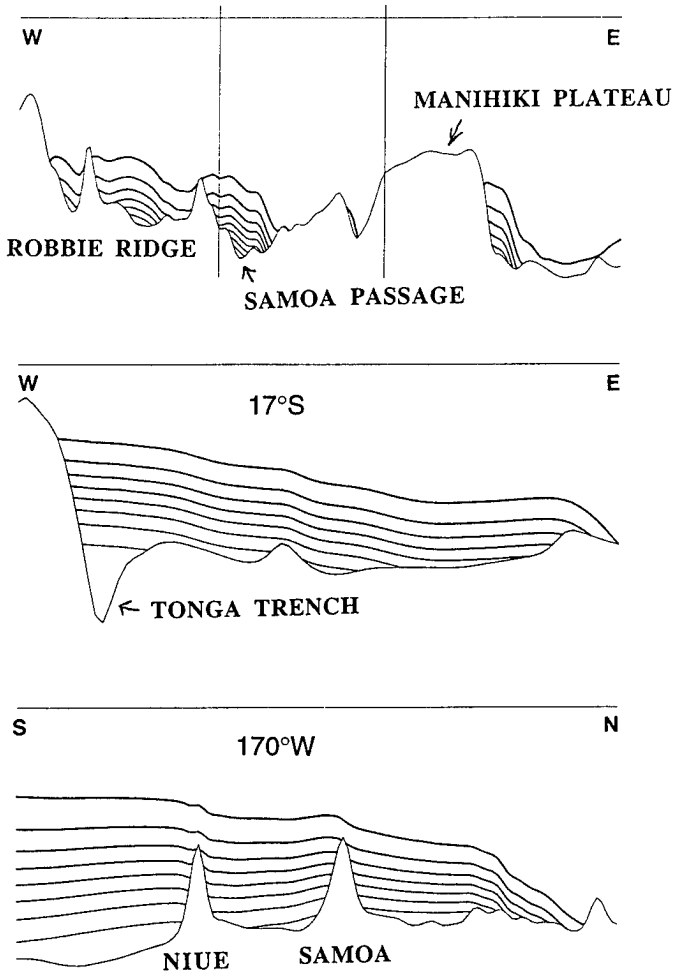


Figure 4. Temperature after 1563 days along 170°W (bottom), 17°S (middle), and (top) along the dashed line shown on Figure 3, which crosses the axes of all the major passages into the North Pacific. The densest water and highest flow speeds occur in the Samoa Passage, but the top section also shows significant deep flow through the pass in the Robbie Ridge, and east of the Manihiki Plateau.

Of course it is a great conceit to imagine that one can explain the observed ocean flow with no inertia whatsoever; with the highly constrained buoyancy (7) required for reduction to two space dimensions; or without separate equations for the temperature and salinity. And I am certainly aware of the widely held opinion that flow through some deep ocean passes is hydraulically (and therefore inertially) controlled. But for me it is very important to start with dynamics, like (12), which is simple enough that its solutions can be physically understood, this simple dynamics will certainly not explain everything that is observed, but what it can explain can at least be understood. However, my general strategy is grounded in the belief that accurate incorporation of realistic bathymetry may actually be more important than much of the "higher order" physics.

Acknowledgment. Work was supported by the National Science Foundation, OCE-92-16412. It is a pleasure to thank Rupert Ford for stimulating discussion and advise.

References

Mantyla, A, and J. Reid, 1983, Abyssal characteristics of the world ocean waters, *Deep-Sea Res.*, 30, 805-833.

Needler, G.T., 1971, Thermocline models with arbitrary barotropic flow, *Deep-Sea Res.*, 18, 895-903.

Salmon, R, 1986, A simplified linear ocean circulation theory, *J. Mar. Res.*, 44, 695-711.

Salmon, R, 1990, The thermocaline as an "internal boundary layer," *J. Mar. Res.* 48, 437-469.

Salmon, R., and R. Hollerbach, 1991, Similarity solutions of the thermocline equations, *J. Mar. Res.*, 49,249-280.

Salmon, R., 1992, A two-layer Gulf Stream over a continental slope, *J. Mar. Res.*, 50, 341-365.

Salmon, R., 1994, Generalized two-layer models of ocean circulation, *J. Mar. Res.*, 52, 865-908.

Taft, B.A., S.P. Hayes, G.E. Friederich, and L.A. Codispoti, 1991, Flow of abyssal water into the Samoa Passage. *Deep-Sea Res.*, 38, suppl. 1, S103-128.

Welander, P., 1971, Some exact solutions to the equations describing an ideal-fluid thermocline. *J. Mar. Res.*, 19, 60-68.

Realistic-Bathymetry, Small-Dissipation Solutions for the North Atlantic/Caribbean

R. Ford
Scripps Institution of Oceanography, University of California at San Diego, La Jolla, California 92093-0225[1]

Abstract

New solutions for non–inertial barotropic flow in the North Atlantic/Caribbean are presented using realistic bathymetry and using a technique that enables relaxation to solution at much smaller values of friction than have previously been presented. The technique consists of exploiting the dynamical significance, in the barotropic case, of contours of h/f, where h is the depth of the ocean and f is the Coriolis parameter. A triangulation of the entire domain based upon points which lie on a small finite number of these contours is constructed. The result is a hybrid advection-diffusion, upwind–finite-element scheme, in which the advective upwinding part is substantially less numerically diffusive than standard advective upwinding methods for finite-element schemes. In particular, in the absence of closed contours of h/f and with no explicit diffusion, the scheme would be exactly hyperbolic, in that the solutions on neighbouring contours of h/f would be independent of each other.

Introduction

In a Boussinesq fluid, density and potential vorticity are both conserved on fluid particles, in the absence of forcing and dissipation. It follows that, if we postulate a functional relationship between density and potential at some initial instant, that functional relationship will hold for all time. In a recent paper, Salmon (1994) has shown how to make use of this fact to derive a class of models suitable for modelling large-scale ocean circulation. The crucial step is to use the "planetary geostrophic" or "thermocline" equations, for which the potential vorticity q is given by

$$q = f\frac{\partial \theta}{\partial z} \tag{1}$$

where f is the Coriolis parameter and θ is the buoyancy. The *ansatz*

$$f\frac{\partial \theta}{\partial z} = F(\theta) \tag{2}$$

may then be integrated to

$$\theta = G\left(\frac{z}{f} + S(x,y,t)\right) \tag{3}$$

To ensure static stability of the ocean, $G(\cdot)$ is taken to be a monotonic function of its argument. The dependent variable S is then related via an invertible function to the surface temperature. If $G(\cdot)$ is chosen to vary rapidly in the neighbourhood of zero, to simulate a thermocline, fS may be then be interpreted as the thermocline depth.

The simplest choice of $G(\cdot)$ is $G \equiv 0$. This corresponds to the case of a homogeneous ocean. The equation to be solved is then

$$J\left(\psi, \frac{f}{h}\right) = \boldsymbol{k}.\nabla \times \left(\frac{\tau}{h}\right) - \nabla.\left(\frac{\epsilon}{h}\nabla\psi\right) \tag{4}$$

where h is the ocean depth, ψ is the transport streamfunction, τ is the wind stress, and ϵ is a Rayleigh friction introduced in the horizontal momentum equation. The equation (4) is an advection-diffusion equation for ψ, in which the advection takes place along lines of constant f/h.

If the domain consists of only open contours of f/h, which connect the eastern and western boundaries of the domain at the equator, the sign of the diffusion is such that boundary layers, in which advection and diffusion balance, may exist at the western boundary but not at the eastern one. However, realistic bathymetry requires that we be able to cope with closed contours of f/h, such as are encountered in the North Atlantic in the neighbourhood of the Azores, and in the Caribbean basins.

The numerical model

A numerical model was designed and constructed to solve (4) in an arbitrary geometry. We re-

[1]Permanent affiliation: Department of Mathematics, Imperial College, 180 Queen's Gate, London, SW7 2BZ, UK

quired that the model should not diffuse ψ across f/h-lines, except at a rate proportional to ϵ – in other words, the discretization of the advective term should introduce no numerical diffusion in the cross-(f/h) direction.

This was achieved by using a hybrid scheme, in which the advective term is discretized using third-order upwinding along f/h lines, and the diffusive term is discretized using a finite element method.

The discretization proceeds as follows:

1. Contour the domain of interest at prescribed values of h/f.
2. Adjust the node distribution along the contours such that the local distance between adjacent nodes on the contour is approximately equal to the local distance between contours.
3. Obtain a Delaunay triangulation of the domain based on the nodes obtained from step 2 (see, for example, Weatherill, 1992, for a description of the algorithm).
4. Obtain the trial functions N_i for each vertex, such that N_i is one at vertex i, 0 at neighbouring vertices, and linearly interpolated between.
5. Solve (4) as follows:

$$\sum_j f_j^2 J\left(\psi, \frac{H}{f}\right)_j \int N_i N_j \quad + \quad \int h^2 \boldsymbol{k}.\nabla \times \left(\frac{\tau}{h}\right) N_i \quad + \quad \sum_{j,k} \psi_j h_k \epsilon \int (2N_i \nabla N_j.\nabla N_k + N_k \nabla N_i.\nabla N_j) = 0 \quad \text{for all i} \qquad (5)$$

where $J(\psi, h/f)_j$ is sum of weighted values of ψ at node j and other nodes on the same h/f contour corresponding to an upwind-difference representation of $J(\psi, h/f)$ at node j.

Equation (5) is solved by simultaneous relaxation. The relaxation method employed consists of sweeping along successive h/f contours. Thus,

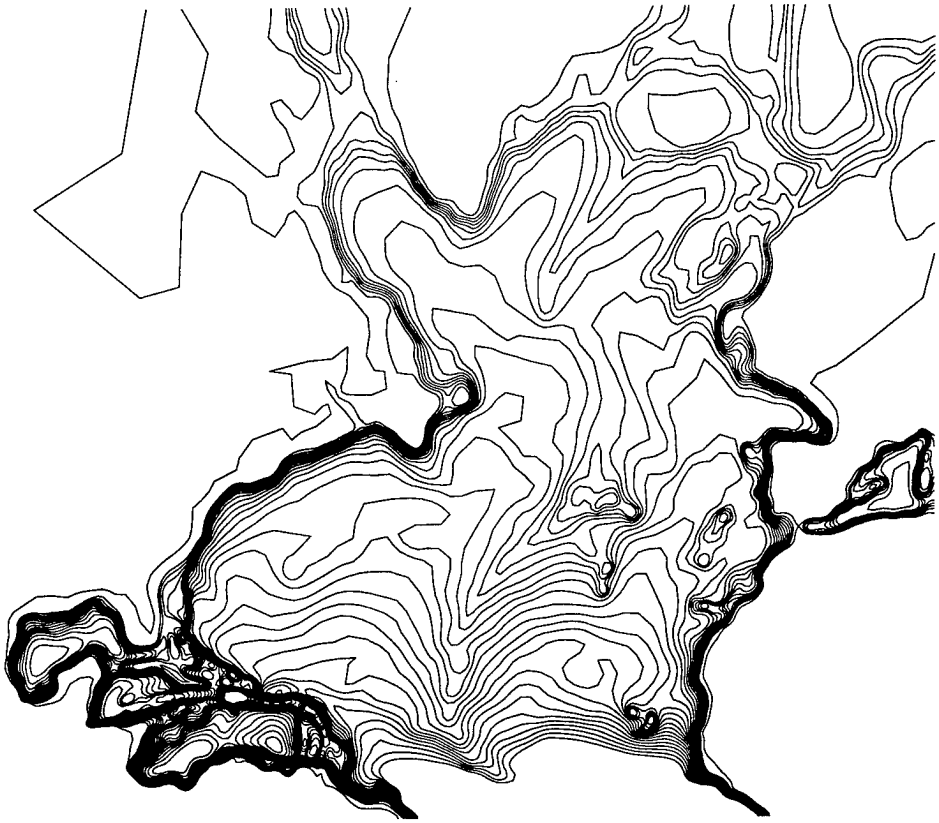


Figure 1. Contours show the f/h contours used in the calculation. There are 30 contour levels, giving 189 contours.

in the limit of small ϵ, a good approximation to ψ is obtained, at least for open contours of h/f, after a single iteration.

Results

The North-Atlantic/Caribbean basin was discretized using contours are 30 levels of h/f. The contours are shown in Figure 1. Using the node–spacing algorithm described above, the Delaunay triangulation shown in Figure 2 was obtained. Taking the forcing from annual-averaged Hellerman & Rosenstein (1983) winds, solutions were obtained at 3 values of ϵ: 0.001, 0.0033 and 0.01.

The solution obtained for $\epsilon = 0.001$ is shown in Figure 3. Two features suggest that this value of ϵ may be too small to be appropriate for the barotropic model.

Firstly, the transport in the sub-tropical gyre is found to be 42 Sverdrups. This is slightly larger than the 30–35 Sverdrups suggested by Schmitz & McCartney (1993). A larger value of friction would be expected to reduce the transport.

Secondly, there is almost no significant sub-polar gyre. This suggests that the influence of f/h contours is too strong, particularly in shallow regions. To appreciate this, consider first the case of a flat-bottomed ocean. In the flat-bottomed case, the value of ψ is obtained by integrating the wind stress curl from east to west. At latitudes where the wind stress curl is positive, which are typically in sub-polar regions, corresponding to a cyclonic subpolar gyre, the cyclonic gyre builds up immediately as one integrates westward along a line of constant latitude. On the other hand, integrating along lines of constant f/h, we see that nearly all the f/h–contours in the region of cyclonic wind stress curl originate in the southeast corner of the domain, and pass through a region of substantial anticyclonic wind stress curl (see Hellerman & Rosenstein, *op. cit.*). Greater diffusion will cause "memory loss" in an otherwise-hyperbolic system, and so a larger value of ϵ could be expected to restore the sub-polar gyre which would be obtained in a flat-bottomed ocean.

There is a third significant difference between the solution shown in Figure 3 and the circulation in the North Atlantic: there is almost no flow between the Atlantic and Caribbean basins. Particularly, the Gulf Stream through the Florida straits

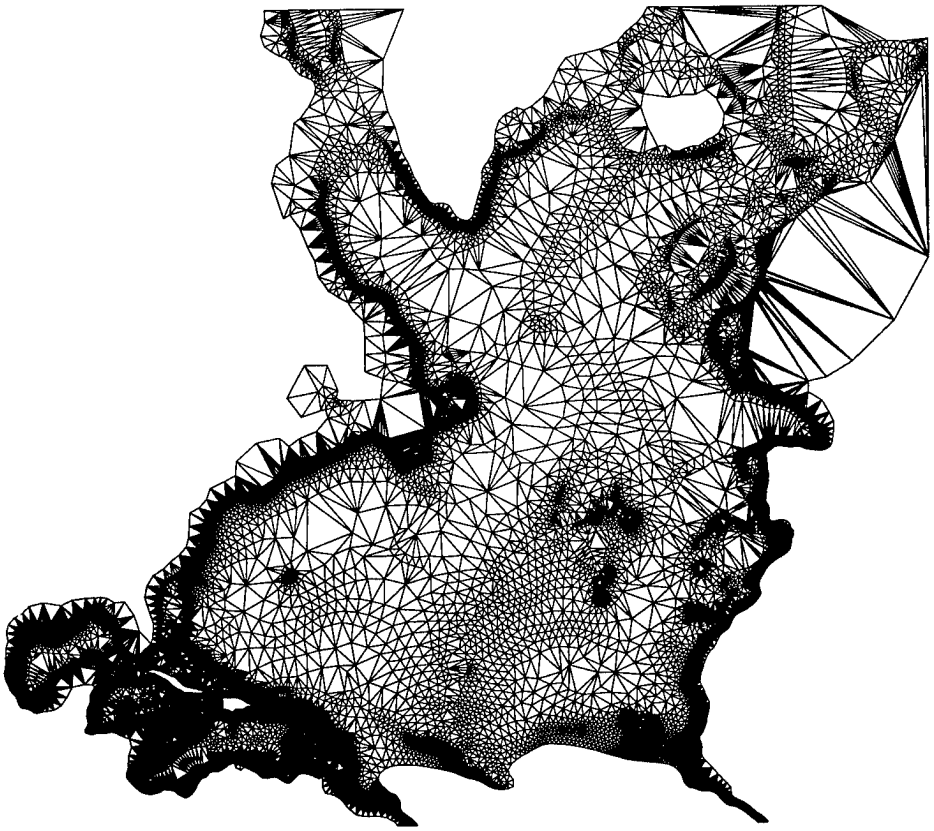


Figure 2. The triangulation based on the contours of f/h shown in figure 1. There are a total of 71582 vertices, 141407 triangles and 212991 edges shown in the figure.

is replaced by a flow of equivalent strength on the seaward side of the Antilles. Although it is possible that this could also be rectified by increasing the value of ϵ, this seems less likely, since a higher value of diffusion is likely to reduce flow though restricted passages.

Figures 4 and 5 show the solutions obtained for $\epsilon = 0.0033$ and $\epsilon = 0.01$ respectively. As predicted, the maximum transport in the sub-tropical gyre decreases from 42 Sverdrups to 35 in the case of $\epsilon = 0.0033$ and 29 in the case $\epsilon = 0.01$. For these values of ϵ the sub-polar gyre remains very weak, and the exchange between the Atlantic and Caribbean basins is seen to decrease as ϵ is increased, as predicted. It appears that even larger values of ϵ are required to restore the sub-polar gyre in the barotropic model. However, since the solution for $\epsilon = 0.01$ already appears quite diffusive when compared with the observed circulation in the North Atlantic, an investigation of this point has not been undertaken.

Discussion

The flow obtained from the barotropic model is clearly not in agreement with observations in every respect. However, the magnitude of the circulation in the subtropical gyre is approximately correct. Preliminary experiments with a baroclinic model (not shown) have demonstrated that baroclinicity can enhance separation of the western boundary current, restoring a sub-polar gyre in the Labrador and Greenland seas.

A further discrepancy between the flow shown in Figures 3–5 and observations is the lack of flow through the Florida Straits. This appears to signify that the effect of topography is exaggerated in a barotropic model. The effect of baroclinicity on the path of the Gulf Stream remains the principal unanswered question in this research, and is currently being addressed.

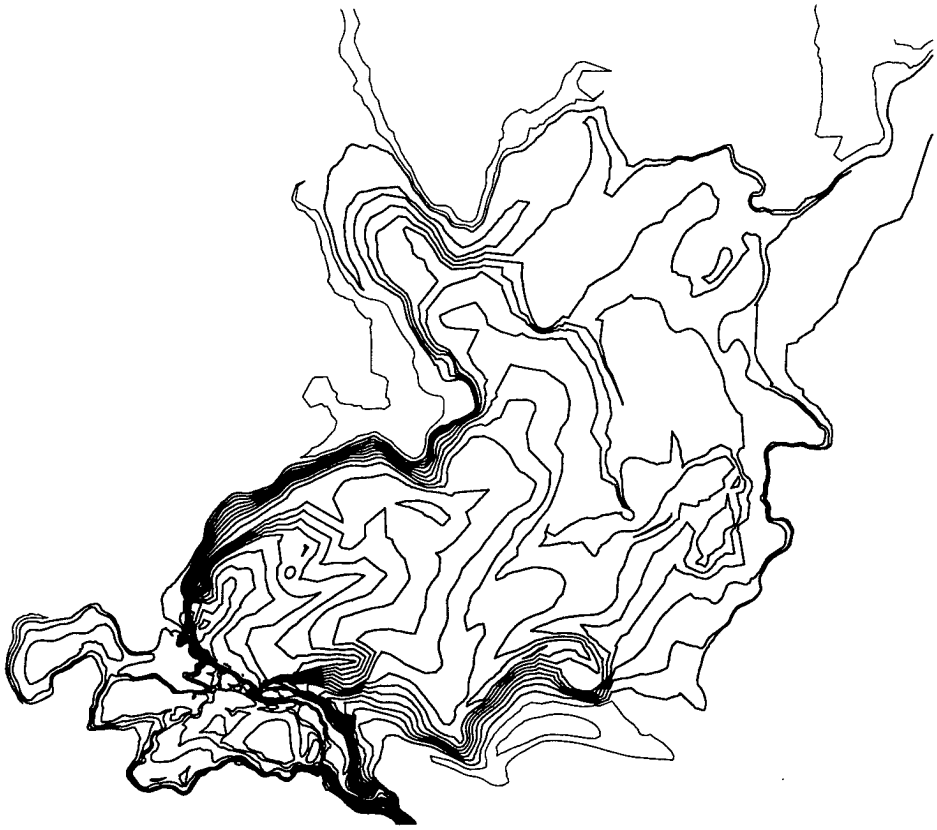


Figure 3. Streamfunction for barotropic relaxation in North Atlantic, forced by Hellerman & Rosenstein (1983) annual-averaged winds, $\epsilon = 0.001$, corresponding to an ϵ-boundary-layer thickness of 6.4km. The darker lines correspond to positive (i.e. anticyclonic) values of ψ, and the lighter lines correspond to negative (i.e. cyclonic) values. The maximum value of ψ, found just off Blake Plateau, corresponds to a subtropical gyre transport of 42 Sverdrups

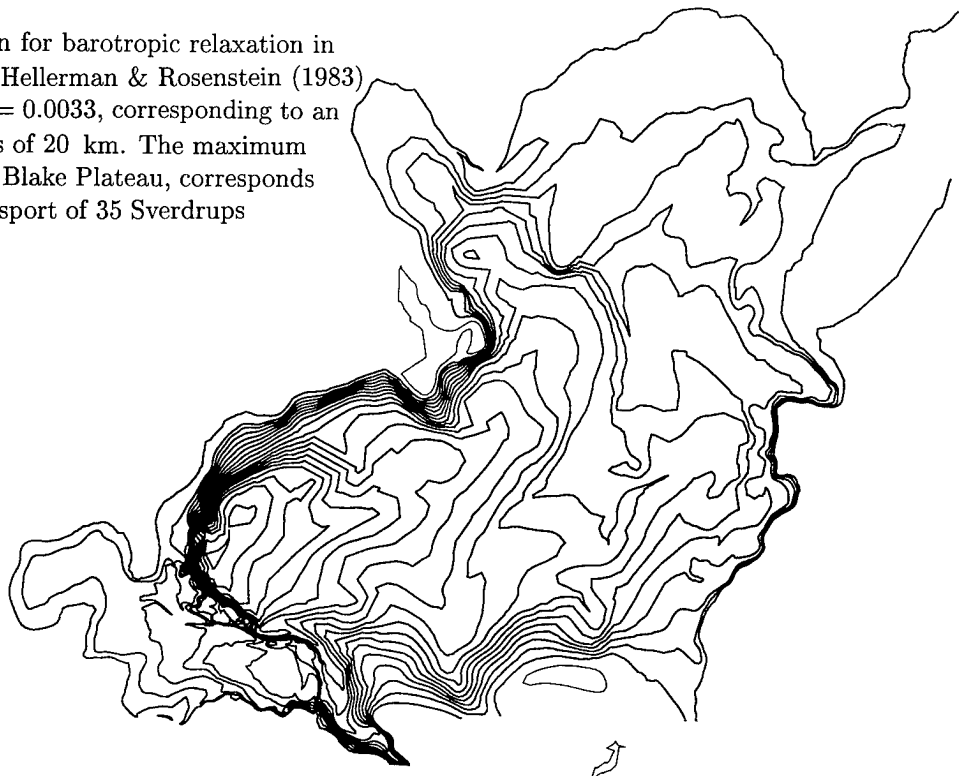


Figure 4. Streamfunction for barotropic relaxation in North Atlantic, forced by Hellerman & Rosenstein (1983) annual-averaged winds, $\epsilon = 0.0033$, corresponding to an ϵ-boundary-layer thickness of 20 km. The maximum value of ψ, found just off Blake Plateau, corresponds to a subtropical gyre transport of 35 Sverdrups

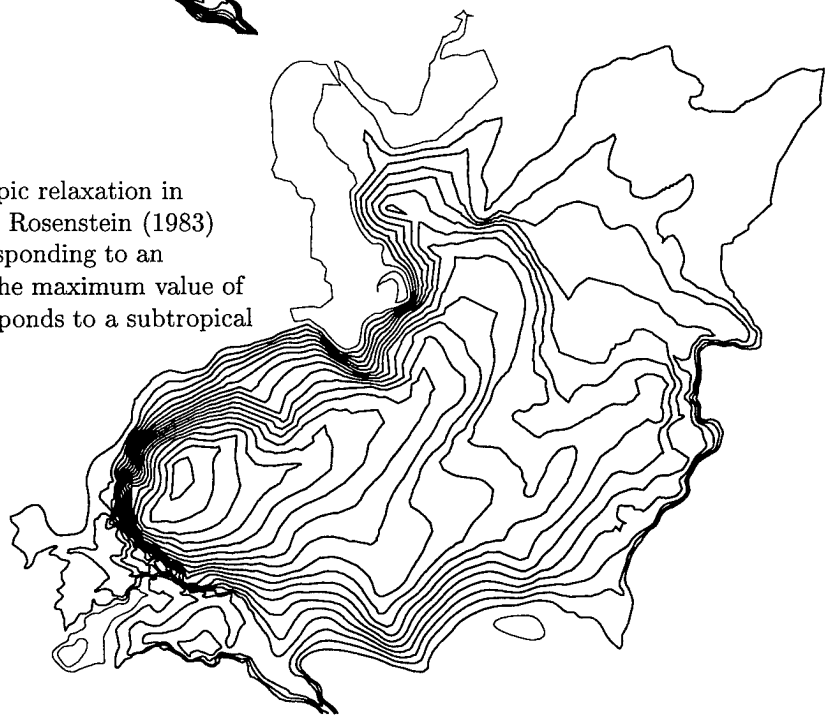


Figure 5. Streamfunction for barotropic relaxation in North Atlantic, forced by Hellerman & Rosenstein (1983) annual-averaged winds, $\epsilon = 0.01$, corresponding to an ϵ-boundary-layer thickness of 64km. The maximum value of ψ, found just off Blake Plateau, corresponds to a subtropical gyre transport of 35 Sverdrups

Acknowledgments

This work is collaborative work with R. Salmon. R. Ford is supported by a UCAR Ocean Modeling post-doctoral research fellowship.

References

Hellerman S. and Rosenstein M., 1983: Normal monthly wind stress over the world ocean with error estimates. *J. Phys. Oceanogr.*, **13**, 1093–1104.

Salmon R., 1994: Generalized two-layer models of ocean circulation. *J. Mar. Res.*, **52**, 865–908.

Schmitz W.J. and McCartney M.S., 1993: On the North Atlantic Circulation. *Rev. Geophys.*, **31**, 29–49.

Weatherill N.P., 1992: Delaunay triangulation in computational fluid dynamics. *Computers Math. Applic.*, **24**, 129-150.

Quasi-Geostrophic Flow over Anisotropic Topography

G.F. Carnevale
Scripps Institution of Oceanography, University of California, San Diego La Jolla, California 92093, USA

R. Purini
Istituto di Fisica dell'Atmosfera, P.le Luigi Sturzo 31, Roma, Italy

P. Orlandi and P. Cavazza
Dipartimento di Meccanica e Aeronautica, Universita di Roma, "La Sapienza", Via Eudossiana 16, 00184 Roma, Italy

Abstract. The orientation of an anisotropic topographic feature in a large-scale flow will affect the vorticity production that results from the topography-flow interaction. This in turn affects the amount of form drag that the ambient flow experiences. For quasi-geostrophic flow over a hill with an elliptical cross section in the horizontal, it is shown that the strength of the form drag depends not only on the magnitude of the angle that the topographic axis makes to the oncoming stream, but also on the sign of that angle. For sufficiently low topography, it is found that a positive angle of attack leads to a stronger form drag than that obtained with the corresponding negative angle. For strong topography, this relation is reversed, with the negative angle then resulting in the stronger form drag.

Introduction

We explore how the local vorticity distribution over topography changes as a function of the orientation of the topography with respect to the ambient large-scale flow. Our original motivation in this line of inquiry stemmed from recent work showing that the Antarctic Circumpolar Current's strength is strongly affected by the underlying topography. The dynamical balance of the Antarctic Circumpolar Current has long been a mystery. Bottom friction and continental borders alone are insufficient to absorb the momentum input from wind forcing. The simulations of McWilliams, Holland and Chow (1978), Wolff and Olbers (1989) and Treguier and McWilliams (1990) have gone a long way toward proving the hypothesis that the input from wind stress is ultimately balanced through form stress involving submerged ridges. The ridges under the Antarctic Circumpolar Current are not oriented meridionally, perpendicular to the mean current, but rather are at oblique angles (e.g., Macquarie Ridge, South East Indian Ridge, Pacific Antarctic Ridge, etc.). Treguier and McWilliams (1990) included randomly generated topographies in their studies, and Wolff, Meier-Reimer, and Olbers (1991) included a realistic representation of the Macquarie Ridge Complex. Another reason for interest in the effects of changing the flow-topography orientation follows from the fact that local flow over topography will depend on this orientation, and this local flow will be important in determining the distribution of temperature, nutrients and, hence, biology over the topography. For example, in the Southern California Bight there are several banks of elliptical shape (e.g., Nidever Bank). When the direction of the large-scale current in this region changes, one expects the current regime over the bank to change (including the distribution of the regions of strongest upwelling). The local flow then determines the distribution of plankton and predators over the bank (Genin 1987). Similar comments could be made about seamounts which have an elongated structure (e.g. Horizon Guyot) (cf. Genin, Noble and Lonsdale 1989).

The general question of large-scale flow over topography in a rotating environment has been subject to very intense investigation due to the many possible applications to both the atmosphere and the oceans. In particular, the flow over bottom irregularities such as seamounts is an important source of eddy variability in the oceans. Also, the interaction of the flow with the topography produces a reaction on the flow called form drag that can, in both atmospheric and oceanic applications, significantly retard or block the oncoming flow. Numerous studies of flow-topography interaction have been performed with analytical, numerical and laboratory methods. For purposes of analysis and intuitive understanding, many of these studies have focused on models using

isolated, circularly-symmetric hills. Excellent historical reviews of that work can be found in Huppert and Bryan (1976), Johnson (1978), Bannon (1980), and Verron and Le Provost (1985). For such simplified models, the question of orientation of the topography with respect to the flow does not come into question. However, those models point out a basic asymmetry of the flow over topography problem, in that vortex tube compression always produces an anticyclone above a hill and this advects the fluid around the hill in the anticyclonic direction. We will see below, that for non-circularly symmetric topographies, the basic asymmetry of the flow interacts with the asymmetry of the topography in a way that produces a dependence on the orientation of the topography for vorticity production and for form drag. Consider, for example, Figure 1. Two configurations are shown (from above) in which a large-scale flow crosses an elliptical topography. The situations look symmetric, but, in fact, the form drag is different in the two cases. This will be explained in detail below.

Of course, there are already many notable works that examine flow-topography interactions with a model of topography more complicated than the circularly symmetric hill. Merkine and Kalnay-Rivas (1976) consider an elliptical topography with two orientations, cross stream and along stream. Pierrehumbert and Malguzzi (1984) consider a dipolar topographic forcing (but with a single orientation). Cook and Held (1992) have investigated flow over an elliptical topography, with a single orientation, in a general circulation model. We should also note that there have been many excellent studies of flow over elongated topography in the form of ridges. In most cases, however, the ridge is of infinite extent and oriented perpendicular to the flow. An exception is the study by Boyer (1971) who considers flow over a ridge of infinite extent at an angle to the large-scale flow. This list of examples does not even begin to mention all of the studies with irregular or random topography or those with actual representations of features on the earth's surface. On the whole, however, there have not been any systematic studies of the effects of orientation of anisotropic topography of finite extent.

For flow in a rotating environment, the simplest model that captures the essential effects of vortex tube compression/stretching is the quasi-geostrophic model. Within the context of that model, in section 2, we set up the basic equations for the problem of determining how the local flow around the topography depends on the orientation of that topography

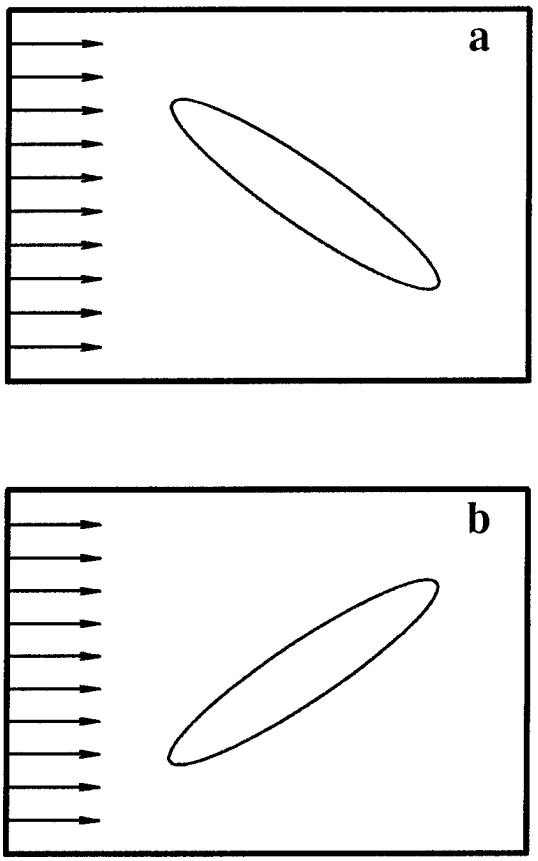


Figure 1. Schematic of large-scale flow over elliptical hills. In which case will the drag be greater, for the (a) positive angle of attack or for the (b) negative angle of attack?

with respect to the large-scale flow. In section 3, we give the results of simulations that show how the vorticity distribution over the topography depends on the orientation of that topography in the current. In section 4, we examine the dependence of the form drag on the topographic orientation, and relate the results to the vorticity distributions described previously in section 3. We develop the perturbation theory for the case of weak topography, and compare the predictions to results from the simulations. Furthermore, we present a simple point-vortex model that helps to explain the transition from the behavior of the form drag as a function of the angle of attack, as observed in the weak topographic regime, to the very different behavior observed in the strong topographic regime. This report is a greatly expanded version of Carnevale, Purini, Orlandi and Cavazza (1995).

The Model

The variation of the flow with topographic orientation is captured, in simplest form, by the quasi-geostrophic model for a single homogeneous layer under a rigid lid. For this model to be appropriate first requires that the rotation rate of the environment is sufficiently high so as to dominate local advective processes. The relative importance of rotation can be measured by the Rossby number, which is defined by

$$\epsilon = \frac{U}{fL}, \tag{1}$$

where L is a typical horizontal scale for the topography, f is the Coriolis parameter, which is twice the rotation rate, Ω, and U is the velocity of the oncoming stream. For ϵ sufficiently small, the flow will be in geostrophic balance, that is, the pressure force, including the centrifugal force, is balanced entirely by the Coriolis force in the momentum equation. Thus we have

$$2\boldsymbol{\Omega} \times \mathbf{u} = -\frac{\nabla p}{\rho}, \tag{2}$$

where $\mathbf{u}$ is the velocity of the flow and ρ is the fluid density, which we will assume is constant, and p is the thermodynamic pressure plus the potential for the centrifugal force. Taking Ω to be in the z-direction, we can write the components of the geostrophic flow as

$$u = -\frac{1}{f\rho}\frac{\partial p}{\partial y} \tag{3}$$

$$v = \frac{1}{f\rho}\frac{\partial p}{\partial x}, \tag{4}$$

in the x and y directions respectively, and the pressure is constant in the z-direction. Further, assuming that the rotation rate does not vary with position, and using incompressibility, it follows that if there is no flow through the upper surface, the flow is entirely two-dimensional (the Taylor-Proudman theorem). The streamfunction for this flow can be taken as proportional to the pressure:

$$\Psi = \frac{p}{f\rho}. \tag{5}$$

Furthermore, we assume that the layer thickness variation is a small fraction of the mean depth. The essence of the quasi-geostrophic model then is the horizontal advection of potential vorticity defined by

$$q = \nabla^2\Psi + h. \tag{6}$$

h is the scaled topography given by $h = f\Delta H/H_0$, $-H_0$ is the average depth, and ΔH is the height of the bottom above the mean bottom level. Thus the quasi-geostrophic evolution equation is given by

$$\frac{\partial q}{\partial t} + J(\Psi, q) = -r\zeta + \nu\nabla^2\zeta, \tag{7}$$

where J is the Jacobian defined as usual by

$$J(A, B) = A_x B_y - A_y B_x. \tag{8}$$

This is the simplest model which captures the effect of vortex tube stretching due to passage over topographic features. Besides the advection, we have also included two viscous effects: a bottom drag due to Ekman pumping, and a horizontal diffusion of relative vorticity. For a systematic derivation of the quasi-geostrophic evolution equation, see Pedlosky (1987).

We need to define a model of a confined asymmetric topography. The studies of Verron and Le Provost (1985) were performed with a Gaussian shaped topography, which in our notation would be

$$h(x, y) = h_0 e^{-(x^2+y^2)/R^2}, \tag{9}$$

with R a constant. As a simple generalization of this form to elongated structures, we take

$$h(x, y) = h_0 e^{-(x'^2/a^2+y'^2/b^2)}, \tag{10}$$

where the coordinates x' and y' are just the old coordinates x and y rotated by the angle of attack of the topography with respect to the oncoming stream, as defined in Figure 2. Specifically

$$x' = x\cos\alpha - y\sin\alpha \tag{11}$$

$$y' = x\sin\alpha + y\cos\alpha, \tag{12}$$

where a and b define the major and minor axes of the contour of topography at the level with value $h(x, y) = e^{-1}$.

This topography is confined in the sense that its height a few lengths R from the origin is negligible for our purposes. This is the topography used for the discussion in the next two sections. It will be convenient to designate specific terms for the two ends of the ellipse representing the topography. Accordingly, the upstream end of the ellipse will be referred to as the nose of the topography, and the downstream end as the tail. Also we will refer to the line of highest points along vertical cross sections parallel to the minor axis as the crest of the topography.

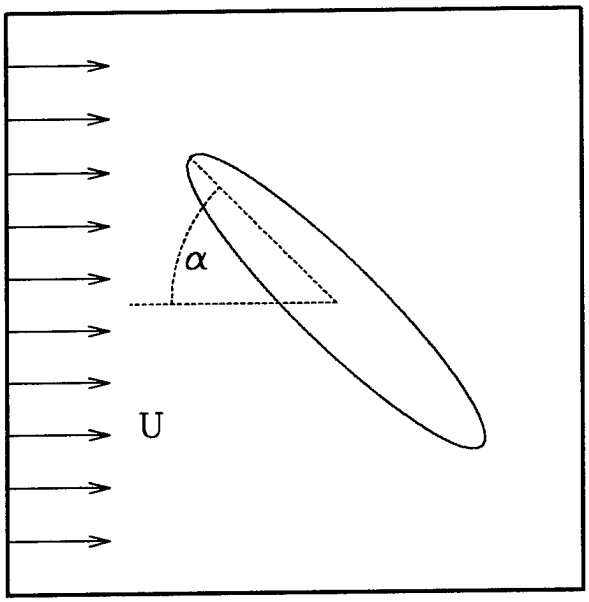


Figure 2. Schematic defining the angle of topographic orientation with respect to the flow. The scaled topographic height, defined in the text, is given by $h(x,y) = h_0 exp(-x'^2/a^2 - y'^2/b^2)$, in coordinates x' and y' that are aligned with the topographic principal axes in a horizontal cross section. The lengths of the major and minor axes of the contour of topography at level $h(x,y) = e^{-1}$ are a and b. The angle of attack, α, is defined as the (counterclockwise) angle from the major axis to the axis of the large scale-flow. A positive angle of attack, $\alpha = 45°$, is illustrated here.

Verron and Le Provost (1985) define a nondimensional parameter that measures the importance of topographic terms relative to the pure advective terms in equation (14). This parameter is given in our notation by

$$\mu = h_0 \frac{L}{U}, \tag{13}$$

where L is a typical horizontal length scale for both the topography and variations in the flow. Verron and Le Provost (1985) consider only the case of circularly symmetric topography in which our parameters a and b are both equal and take the value $\frac{1}{2}L$. For sufficiently small viscosity, Verron and Le Provost identified two distinct flow regimes separated by the critical value $\mu_d = 11$. When $\mu < \mu_d$, i.e. when the topography is 'weak' or the flow is strong, the flow is close to the inviscid solution given by $\zeta = -h$. For $\mu > \mu_d$, trapping of the positive vortex can occur, at least temporarily, forming a dipole, which is unstable in the purely inviscid case. Unless there is substantial viscosity, the positive vortex is eventually shed downstream.

For our case, the definition of μ is somewhat ambiguous since there are now two length scales associated with the topography. In what follows, we have chosen to nondimensionalize all length scales by $L = 2a$ where a is the larger of a and b. Thus the length of the major axis is fixed at $a = 0.5$. We choose to fix the length of the minor axis at $b = 0.1$ as a representative value giving a topography which is far from circular but yet not in the realm of long thin bodies. Furthermore, we nondimensionalize time with the advective time scale, U/L. In all of the simulations with fixed, U, its value is taken to be 1, and so, the value of h_0 in these units is the same as μ.

As for the boundary conditions on the streamfunction Ψ, we consider the case in which the flow is uniform at infinity. Thus we can put $\Psi = \psi - Uy$, where the boundary conditions are that ψ vanishes at infinity. These boundary conditions present some difficulties in deciding on the appropriate numerical simulation scheme. From previous studies, we know that if we impulsively start a large-scale flow over a hill, the zero vorticity flow originally situated over the hill will be pushed off and become a cyclone, which may be completely or partially shed downstream. For our problem, we need to allow such shed vorticity to pass out of our limited computational domain. We have actually performed our simulations with three different codes with different boundary conditions to check that the effects discussed here are independent of the exact specifications of the boundaries. In one case, we have a finite difference code in a rectangular domain. Slip boundary conditions are used on the two walls aligned along the flow direction. The velocity on the inflow side of the channel is specified to be exactly U in the x-direction and zero in the y-direction. The outflow boundary has a radiation condition based on the Orlanski (1976) scheme. In the second case, we replaced equation (7) with the following

$$\frac{\partial q}{\partial t} + J(\psi - Uy, q) = -r\zeta + \nu\nabla^2\zeta, \tag{14}$$

where we have explicitly introduced the decomposition $\Psi = \psi - Uy$. We solve this advection equation spectrally assuming ψ is periodic in both x and y directions. We used the dealiased pseudospectral method as described in Patterson and Orszag (1972). The problem of the shed vorticity is dealt with by adding to this code a physical space filter on the vorticity. Specifically, the local vorticity, ζ, is set equal

to zero every time step at all points beyond a certain radius, which is taken to be larger than L, the representative horizontal scale of the topography. In the third case, simulations were also performed with a doubly-periodic spectral code. Here the shed vorticity re-enters the domain, but when we are considering the long term limit, when all transients have died out, this does not adversely affect the results. All the results reported below were found for all three types of codes and thus appear, at least qualitatively, to be independent of the details of the boundary conditions. This was also checked by doubling the domain size and the filter radius while keeping the resolutions fixed. Thus the phenomena reported below appear local, limited to the region where the confined topography is centered. Also, questions of sensitivity to computational resolution were tested by running all simulations both at resolutions 64×64 and 128×128, with additional key tests at resolution 256×256.

Finally, we must specify the values of the viscous coefficients in the evolution equation (14). When considering stationary flow, the inviscid solution is somewhat uninteresting from the point of view of form drag because, in a manifestation of D'Alembert's paradox, there turns out to be no drag at all in that case, as has been pointed out in Bannon (1980) and elsewhere. In other words, if the perturbation flow is stationary and confined (so that there is no possibility of transferring energy into the flow or to infinity), then there can be no energy input for there is no energy sink (see Batchelor, 1967). Thus we have to decide on what non-zero values to give for the viscous coefficients r and ν. To limit our search of parameter space, we have decided to set $\nu = 0.01$ and $r = 0.2$, taking these values from the parameter range explored by Verron and Le Provost (1985). In test cases we have varied these values by over an order of magnitude in each direction in order to verify that the phenomena reported are not qualitatively sensitive to these values; however, the results presented here, from sequences of simulations in which other parameters are varied, all have kept these viscous coefficients fixed at the values specified above.

Structure of the vorticity field

We consider flow over the elliptical hill with the large-scale flow started impulsively. That is, the flow is initially set at $U = 1$ everywhere. The large-scale component of the flow is maintained at that value thereafter. Initially there is no perturbation field, and since there is no vorticity associated with the large-scale flow, there is initially no vorticity anywhere in the flow. As zero vorticity fluid is advected onto the topography, it must develop negative relative vorticity to compensate for the positive topographic contribution to the conserved potential vorticity, $q = \zeta + h$. Similarly, fluid advected off the hill must develop positive vorticity. Thus the earliest stage of evolution involves the creation of negative vorticity on the upstream side of the hill and positive vorticity on the downstream side. The later stages of evolution and, in particular, the final stationary flow depend on the strength of the topography. Here we shall take two extreme cases, $h_0 = 1$ and $h_0 = 100$, to illustrate the results for 'weak' and 'strong' topography, where the magnitudes are suggested by the circularly symmetric topography case in Verron and Le Provost (1985).

Weak topography

We illustrate the early evolution of the vorticity field over the peak of the topography in the case $h_0 = 1$ for positive and negative angles of attack in Figure 3. In panels (a) and (c), the very earliest stage is shown. The time is $t = 0.1$ after the beginning of the evolution. Here we have zoomed in on the flow over the topography, showing only the central area of size 3×3 of the full 5×5 computational domain. The fluid particles have so far been displaced approximately only a distance 0.1 in the downstream direction. This results in a dipolar vorticity distribution over the topography with roughly elliptical structure for both components. As the large-scale advection continues to have its effect, the core of the trailing positive relative vortex is advected downstream to eventually leave the computational domain, and this leaves primarily a negative vortex over the topography. This is shown in panels (b) and (d) at time $t = 1.4$. By this time there has been advection through distances greater than the topographic axes lengths a and b. The peak amplitude of the fixed relative vortex at that time is -0.84, which is also the final stationary flow value. Thus unlike the inviscid case, the fixed vortex does not match the amplitude of the hill, and so the potential vorticity over the hill will not vanish. In this case, the relative vorticity is also not perfectly elliptical. Instead, it is relatively larger in magnitude on the upstream side than on the downstream side. We can understand this as simply the result of the fact that once the vorticity is created on any fluid particle being advected over the topography, the viscosity continually decreases the magnitude

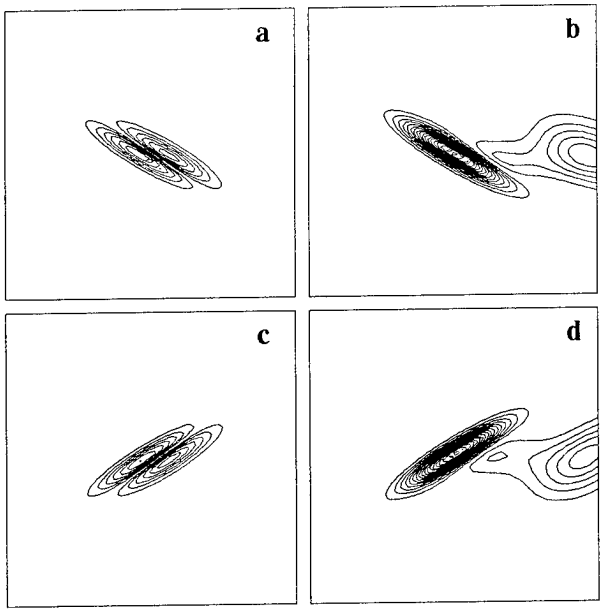


Figure 3. Vorticity contour plots showing the early evolution in the weak topography case, $h_0 = 1$. The large-scale flow comes from the left, and the top/bottom panels represent the vorticity for the case where the angle of attack is $\alpha = +/-30°$. The left panels correspond to time $t = 0.1$, while the right are taken at $t = 1.4$. The thick/thin curves correspond to positive/negative vorticity levels. The contour interval is 0.05. The zero vorticity level is not drawn. Only the central region of size 3×3, of the computational domain of 5×5, is shown.

of that vorticity as the particle moves downstream; hence, the vorticity will be stronger on the upstream side. This asymmetry to the negative relative vortex means that the potential vorticity field, $q = \zeta + h$ (not shown), over the topography will be dipolar with negative potential vorticity on the upstream side and positive on the downstream side, and this is also the case in the final stationary flow.

In the long term, the core of the positive relative vortex is shed downstream, eventually to be completely dissipated by viscous effects. However, a remnant of this vortex is left with a peak situated downstream of the topographic peak. The final stationary vorticity fields for cases representing four angles of attack are shown in Figure 4. The angles represented are $\alpha = -90°$, $-30°$, $0°$ and $+30°$. These results are representative of the full set that we studied spanning the range $\alpha = \pm 90°$ in $5°$ increments. For all of these cases, the local or perturbation flow due to the presence of the topography is weak in the sense that the lines of flow or the contours of total streamfunction (not shown) are all nearly parallel to the large-scale flow direction.

For all angles of attack, there is a peak of positive relative vorticity downstream of the negative vorticity peak. It appears from these plots that the amplitude of both the positive and negative vorticity peaks depends strongly on the angle of attack. A quantitative measure of this dependence for the whole range of attack angles is shown in Figure 5a. We graph the extremal values of relative vorticity as a function of α. The dashed curve corresponds to the absolute value of the negative vorticity peak value, while the solid curve is the value of the positive vorticity peak value. The negative vorticity is strongest at $\alpha = 90°$ (coming up to 95% of the value of the topography maximum) and weakest for $\alpha = 0°$ and *vice versa* for the positive vorticity. To help understand these results, consider the fluid element which comes from upstream, crosses the peak of the topography, and then moves downstream. A fluid element approaching from up-

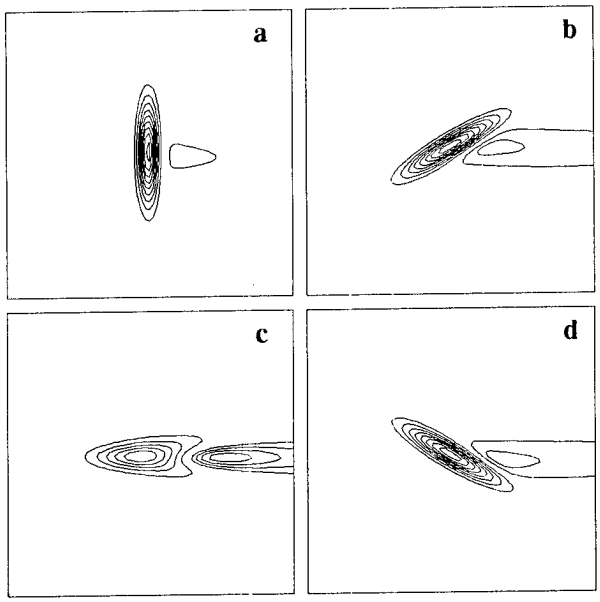


Figure 4. Contour plots of the stationary relative vorticity field for the weak topography case, $h_0 = 1$, for various angles of attack. These panels represent the stationary vorticity field for flow over the elliptical topography for the angles of attack $\alpha = -90°$, $-30°$, $0°$ and $+30°$, ordered from left to right, top to bottom. The thick curves correspond to positive vorticity levels spaced 0.05 units apart, while the thin curves correspond to negative vorticity levels spaced 0.1 units apart. The zero vorticity level is not drawn. Only the central region of size 3×3, of the full computational domain of 5×5, is shown.

stream has zero relative vorticity, and, for each 'step' that it takes going uphill, it acquires exactly enough negative vorticity to balance the positive topographic contribution in the conservation of the potential vorticity. Thus for inviscid flow the stationary potential vorticity is exactly zero everywhere with relative vorticity being exactly anticorrelated with the topography, $\zeta = -h$. With viscosity, however, the relative vorticity generated on the fluid element by the topographic effect also dissipates continuously. Thus, when this fluid element reaches its highest point on the topography, its relative vorticity will be weaker in strength than it would have been inviscidly. Then, as it descends the hill, the positive vorticity generated by the conservation of potential vorticity more than cancels the relative vorticity remaining from its climb with the destructive effects of viscosity acting. Thus, net positive relative vorticity will result on the descent. Of course, the positive relative vorticity on the fluid element will continue to diminish as it moves downstream. Furthermore, we see that the strength of the positive vortex depends strongly on the angle of attack. Of all the cases shown in Figure 4, the ascent to the top of the hill by the fluid element is shortest for $\alpha = 90°$. In that case, there is little time for viscosity to act during the ascent and descent. Hence, the discrepancy between the total vorticity production during those two phases is relatively small. In contrast, in the case with $\alpha = 0°$, the excursion to the top is the longest, and hence the effect of viscous decay on the vorticity is the greatest. Thus the positive relative vortex generated on the descent will the the strongest of any angle of attack.

As we shall see in section 4, it is also of interest to consider the position of the positive relative vortex in relation to the topography. Clearly from Figure 4, the peak of positive vorticity will lie nearly on the x-axis. A secondary advective effect, due to the non-zero strength of the negative vortex, displaces the peak of positive vorticity to a position below the x-axis. The negative vortex over the hill induces positive velocity in the y direction (i.e., $v = \partial\psi/\partial x > 0$) on the upstream side of the topography and negative v on the downstream side. This secondary flow tends to displace the positive vorticity in an arc in the clockwise direction about the center of the topography. In Figure 5b we plot the angle for the position of the peak of the positive vorticity measured from the direction of the nose of the topography. Also on the same graph is a dashed curve showing the line of no displacement. The fact that the observed displacement angles lie on a line that is predominantly above the dashed line is due to the clockwise displacement of the positive vortex.

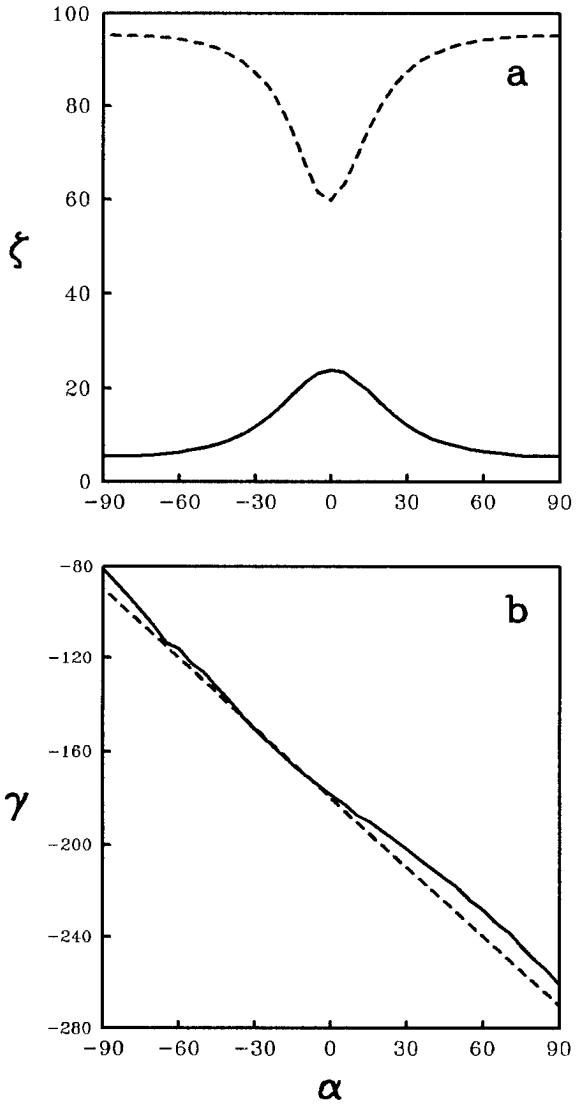


Figure 5. Position and amplitude of relative vorticity extrema in the weak topography case, $h_0 = 1$. (a) The solid curve shows the angular position of the peak of positive relative vorticity. This angle is measured from the direction of attack, that is, from the direction along the long topographic axis facing in the upstream direction. The dashed curve shows the angular position, measured in the same way, of a point on the x-axis (i.e. the curve of no displacement). (b) The solid/dashed curve shows the magnitude of the vorticity at the extremal positive/negative value.

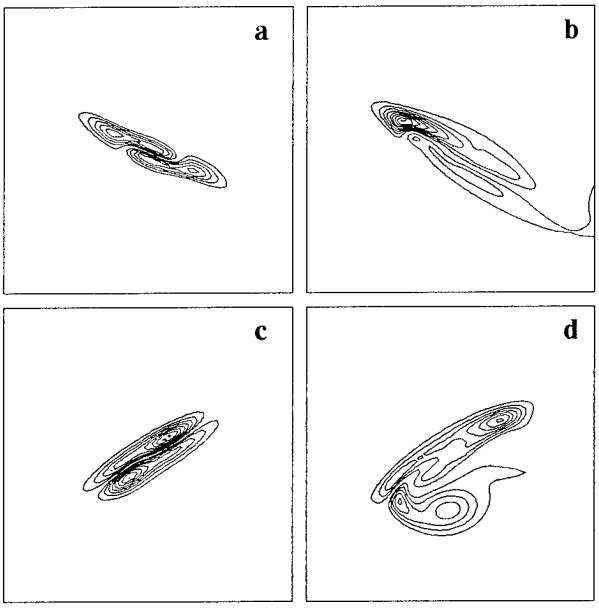


Figure 6. Contour plots showing the early evolution for the relative vorticity field in the strong topography case, $h_0 = 100$. The large-scale flow comes from the left, and the top/bottom panels represent the vorticity for the case where the angle of attack is $\alpha = +/- 30°$. The left panels correspond to time $t = 0.1$, while the right are taken at $t = 1.4$. The thick/thin curves correspond to positive/negative vorticity levels. The contour interval is 4 in panels (a) and (c) and 2 in panels (b) and (d). The zero vorticity level is not drawn. Only the central region of size 3×3, of the full computational domain of 5×5, is shown.

Strong topography

The structure of the vorticity field in the strong topography case contrasts greatly with that in the weak case. At the earliest times, when the large-scale flow is first applied, the structure of the generated vorticity field must be the same as in the weak topography case since the same arguments for its generation apply again. However, that early phase is very short lived because, for sufficiently strong topography, the vorticity generated over the topography can induce flows comparable in speed to the large-scale flow. In Figure 6, we show the early evolution for the example corresponding to $h_0 = 100$, at the same times as shown in figure (3) for the weak topography case. Already at time $t = 0.1$, when the fluid has only been advected a short distance, the induced vortices are strong enough to make their mutual interaction as important as the advection by the large-scale flow. By this time, the early simple structure like that shown in Figure (4), has already been disrupted by the dynamics of the induced vortices. Intuitive arguments are much more difficult in the strong topography case, and less trustworthy, so perhaps it is best just to attempt a description at this point. In the $\alpha = +30°$ case shown in Figure 6, panels (a) and (b), we see that local vortex dynamics has already strongly distorted the symmetric dipolar field. The positive and negative vortices have both developed two centers. Later these interact in a complicated way and the positive vorticity temporarily breaks into several pieces. The strongest positive vorticity center is eventually shed downstream and is just barely visible at the edge of the region shown in panel (b), and the rest of the positive vorticity joins together to form an elongated patch. Also in panel (b) we note that the negative vorticity has become concentrated at the 'forward end' or 'nose' of the topography, while the residual part of the negative vortex has become elongated along the upstream side of the topography. In the $\alpha = -30°$ case shown in Figure 6 panels (c) and (d), the $t = 0.1$ vorticity structure has not departed as severely from

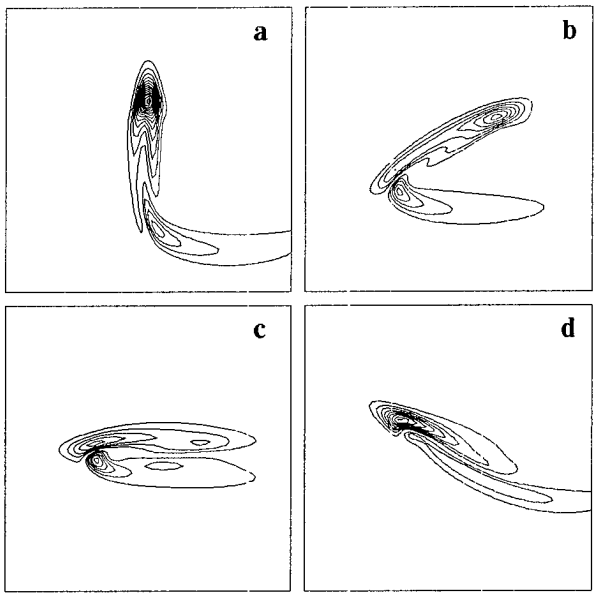


Figure 7. Contour plots of the relative vorticity field for the strong topography case, $h_0 = 100$. These panels represent the stationary vorticity field for flow over the elliptical topography for the angles of attack $\alpha = -90°$, $-30°$, $0°$ and $+30°$, ordered from left to right, top to bottom. The thick/thin curves correspond to positive/negative vorticity levels spaced 2.0 units apart. The zero vorticity level is not drawn. Only the central region of size 3×3, of the full computational domain of 5×5, is shown.

the weak topography case. However, note the tendency for the negative vortex to peak over the 'tail' or downstream end of the topography, while the positive vortex concentrates at the 'nose.' Later, the positive vortex forms a secondary peak of weaker amplitude as seen in panel (d), but this is then shed downstream.

The final stationary configurations for these two attack angles are shown in Figure 7, along with the $\alpha = 0°$ and $\alpha = 90°$ cases. The negative vortex is no longer elliptical. For all the attack angles, the negative vortex is more concentrated at one end of the topography, and the positive vortex is now no longer simply trailing on the x-axis. Even though the negative vortex is now, at its most intense point, only 30% of the peak amplitude of the topography, the topography is so strong that the nonlinear term $J(\psi, \zeta)$ competes with the large-scale advection. The negative vortex here is intense enough to strongly displace the trailing positive vortex from the positive x-axis. For $-90° \leq \alpha < -15°$, the negative vortex is concentrated at the tail of the topography, while the positive vortex is concentrated at the nose, although it also has a broad tail elongated in the downstream direction. As α increases, a secondary negative vorticity peak develops. This is just beginning in panel (b) at $\alpha = -30°$. From $-30° \leq \alpha < 0°$, the negative vorticity has two peaks, the one near the tail, induced primarily by the large-scale advection of fluid, and the second induced by the influence of the positive vortex advecting fluid off the peak and upstream along the crest of the hill. At $\alpha = -15°$, the negative vorticity peak near the nose dominates, comprising, with the primary positive vortex, a dipole at the nose. At $\alpha = 0°$ (panel c), we see a secondary positive vortex has also developed, and by $\alpha = +30°$ that trailing positive vortex peak has higher amplitude than the one at the nose. For moderate positive angles α, the two distributions are broad forming a dipole with positive vorticity on the leading edge of the topography and negative vorticity concentrated on the nose and along the crest. The transitions from the dominance of the original vortices present at $\alpha = -90°$ to the secondary vortices that develop are shown by the graph in Figure 8b. The angle is measured from the direction of the nose, so the transition from 180° to 0°, on the dashed curve, corresponds to the transition from the trailing negative vortex at the tail to the leading vortex induced by the positive vortex. The transition from 0° to −180°, on the solid curve, corresponds to the transition from the leading positive vortex at the nose to the trailing positive vortex.

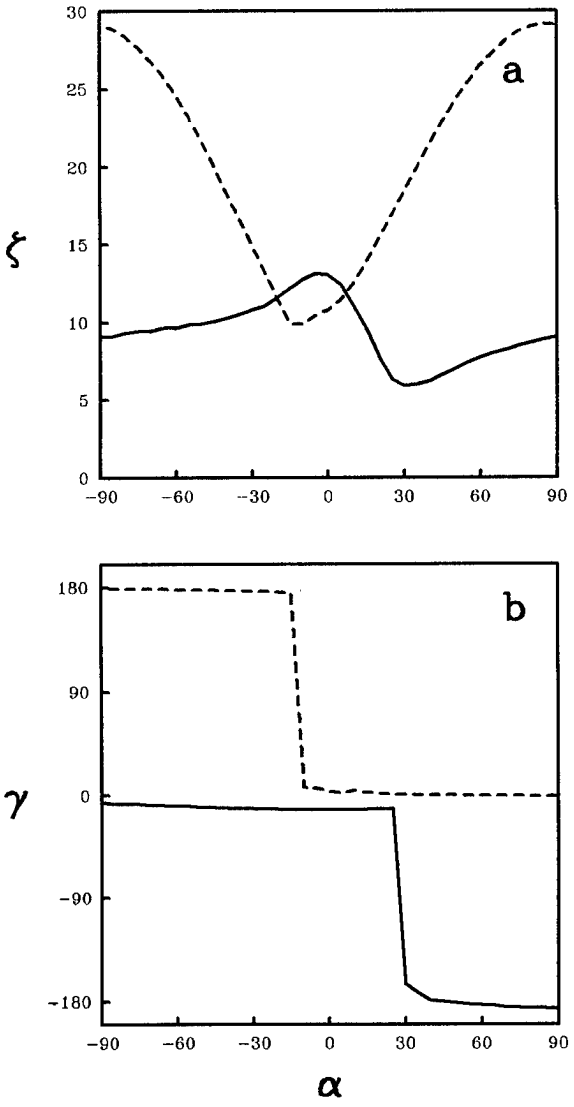


Figure 8. Position and amplitude of relative vorticity extrema in the strong topography case, $h_0 = 100$. (a) The solid/dashed curve shows the angular position of the peak of positive/negative relative vorticity. This angle is measured from the direction of attack, that is, from the direction along the long topographic axis facing in the upstream direction. (b) The solid/dashed curve shows the amplitude of vorticity at the extremal positive/negative value.

In Figure 8a, we show the magnitude of the vorticity extrema for the full range of attack angles. The dependence on attack angle is somewhat more complicated than in the weak topography case (note especially the minimum in the amplitude of the peak positive vorticity at $\alpha = 30°$). Nevertheless, like the

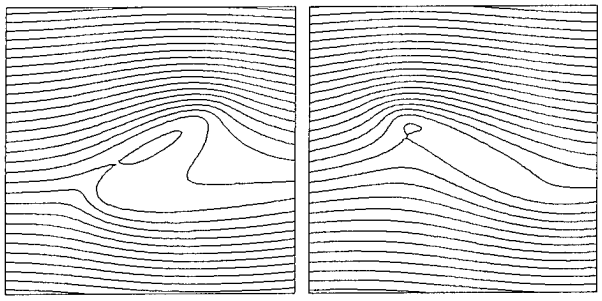


Figure 9. Contour plot of the stationary total streamfunction for the strong topography case, $h_0 = 100$. In panel (a), $\alpha = -30°$, and in panel (b) $\alpha = +30°$. The contour interval is 0.1. Only the central region of size 3×3, of the full computational domain of 5×5, is shown.

weak topography case, the negative vortex is weakest/strongest for small/large angle of attack, and the positive vortex is strongest for small angle of attack. Note that the maximum negative vorticity extremum is only 30% of the peak topographic amplitude as opposed to the 95% that is reached in the weak topography case. Also, looking at the vorticity contour plots, we see that the strong topography case is far from the inviscid solution, $\zeta = -h$.

In Figure 9, we show the total streamfunction for the flow. Here we see that the induced negative vortex is strong enough to reverse the flow locally and produce closed contours. We should mention that such closed contours, or recirculating regions, would not be possible for the stationary flow if the only dissipation acting was Ekman bottom drag. This follows from the fact that on any closed contour the fluid element circulating over and over again on the same path would have no way to replenish its decaying vorticity; however, the presence of Laplacian friction allows these closed contours because there is then diffusion of vorticity across them. As for the border between values of topography for which these closed contours do or do not form, this will depend on the attack angle as well as the strength of the topography.

Remarks on the position of the cyclone in the stationary flow

The discussion above strongly suggests that in the stationary flow there is always a cyclone to be found near the hill, even if this is just a remnant of the original transient cyclone. This is fairly straightforward to prove in the case in which the bottom drag parameter, r, is non-vanishing. The equation for the steady state is, from (14),

$$J(\psi - Uy, \zeta + h) = -r\zeta + \nu\nabla^2\zeta. \qquad (15)$$

If we assume that the that ζ and h vanish sufficiently rapidly as the distance from the center of the hill increases, then on integrating over the whole plane, we obtain

$$r \int\int \zeta dx dy = 0. \qquad (16)$$

Thus the circulation must vanish. Since ζ vanishes at infinity, this means that there must be both positive and negative extrema somewhere on the plane. Unfortunately, this proof tells us nothing about the case in which $r = 0$. Our experience with a few test cases shows that even in that situation there is still a remnant cyclone in the stationary flow as long as ν is nonvanishing.

At an extremum of ζ, its gradient vanishes. Hence, from (15), we have

$$J(\psi - Uy, h)_\pm = -r\zeta_\pm + (\nu\nabla^2\zeta)_\pm. \qquad (17)$$

where all the terms are evaluated at the position, $\mathbf{r}_+$ of the maximum or at $\mathbf{r}_-$, the position of the minimum. At the maximum, we have $\zeta = \zeta_+ > 0$ and $(\nabla^2\zeta)_+ < 0$, and thus $J(\psi - Uy, h)_+ < 0$. This implies that the position of the peak must lie on the topography. Similarly, one can show that the minimum ζ must also lie over the topography. Now with the Gaussian hill, the topography technically covers the plane, but for compact topography, the extrema of vorticity would clearly be restricted to lie in the compact region defined by the hill. In the case of strong flow, in which U dominates ψ, we further have that

$$U \left.\frac{\partial h}{\partial x}\right|_+ < 0 \qquad (18)$$

implying that the cyclone must in that case (weak topography) be on the downstream side of the hill.

Form drag in the stationary flow

Topographic form drag is the net force exerted on the flow by the topography along the direction of the large-scale flow. Consequently, the drag is the negative of the net force acting on the topography in flow direction. To calculate the total force, $\mathcal{F}$, acting on the topography, we integrate the pressure force over the entire surface of the topography: $\mathcal{F} = -\int\int p\mathbf{n}da$, where $\mathbf{n}$ is the outward unit normal vector from the surface of the topography, and da is the element of

area on the surface. Since the surface of the topography is defined by $z = -H_0 + \Delta H(x, y)$, we have the standard results:

$$\mathbf{n} = \frac{(-\partial\Delta H/\partial x, -\partial\Delta H/\partial y, 1)}{\sqrt{1 + (\partial\Delta H/\partial x)^2 + (\partial\Delta H/\partial y)^2}}, \quad (19)$$

and

$$da = \sqrt{1 + (\partial\Delta H/\partial x)^2 + (\partial\Delta H/\partial y)^2}\,dxdy. \quad (20)$$

Thus, the total force, $\mathcal{F}$, in the x-direction is

$$\mathcal{F} \cdot \hat{\mathbf{x}} = \int\int p\frac{\partial\Delta H}{\partial x}dxdy = f\rho\int\int \Psi\frac{\partial\Delta H}{\partial x}dxdy, \quad (21)$$

where we have introduced the definition of the streamfunction in terms of the pressure in the last line. Consider, for example, the case of flow in the positive x direction impinging on a hill. If the pressure is higher on the upstream side of the topography, where $\partial\Delta H/\partial x$ is positive, than on the downstream side, where $\partial\Delta H/\partial x$ is negative, then there is a net force on the topography in the direction of the flow, as we would expect. If we integrate by parts, we can express these results in terms of the pressure gradient or, equivalently, the velocity field. Using the definition of the scaled topography, and integrating by parts, we obtain

$$\mathcal{F} \cdot \hat{\mathbf{x}} = -\rho H_0 \int\int h\frac{\partial\psi}{\partial x}dxdy. \quad (22)$$

Thus we see that an enhanced pressure gradient on one side of the topography relative to the other, yields a net force on the topography.

The drag on the flow is the negative of the force on the topography. The product ρH_0 is just the mean mass per unit area, and it is convenient to factor this out of the definition for drag. Thus we shall define this normalized drag as

$$D = \int\int h\frac{\partial\psi}{\partial x}dxdy \quad (23)$$

(cf. Bannon 1985, Carnevale and Frederiksen 1987).

Considering the drag in the case of stationary flow, we first check that the drag in the inviscid case is zero as discussed above. The solution to the inviscid problem is given by $q = 0$, that is, $\nabla^2\psi = -h$. Substitute $-\nabla^2\psi$ for h directly in the expression for D and integrate by parts. All that remains after the integration is a boundary term at infinity that vanishes. Next, we turn to numerical results for the stationary states with viscosity. As in the case where we considered the structure of the vorticity field, we will see that the behavior of the drag is rather different in the weak and strong topography limits.

Weak topography

To obtain the stationary flows for given topography and large-scale flow velocity, we simulated the evolution, from an initial condition of uniform flow, long enough in time for all transients to die down. In Figure 10, we show the results from a series of such simulations performed with the periodic boundary condition code with spatial filter. In this series, the angle of attack of the topography was varied from $-90°$ to $+90°$ in $5°$ increments. As in the previous section, the weak topography case is represented by using the topographic amplitude $h_0 = 1$. Since the form drag is always negative, opposing the large-scale flow, we consider only its magnitude. In Figure 10a, we plot the form drag in the stationary state as a function of the attack angle. The form drag is greatest when the long axis of the topography is perpendicular (i.e., $\alpha = \pm 90°$) rather than parallel ($\alpha = 0°$) to the flow. As we might have expected from the discussion in the previous section on the vorticity structure, the curve is not symmetric about $\alpha = 0°$. It appears that the form drag is stronger for a positive angle of attack than for a negative angle of the same magnitude. In Figure 10b, we plot the relative variation of that difference, that is, we plot $(|D(\alpha)| - |D(-\alpha)|)/|D(\alpha)|$, where $D(\alpha)$ is the form drag for a given angle of attack. The Figure shows that the difference is greatest when the size of the attack angle is about $20°$, with a 2% variation at that angle. For somewhat higher topographies ($h_0 \approx 20$), the relative variation reaches about 20%, as we shall see below.

For the weak topography case, form drag dependence on attack angle can be predicted from perturbation theory. To examine the effects of weak topography, we begin by rewriting the stationary form of equation (14) as

$$U\frac{\partial\zeta}{\partial x} + r\zeta - \nu\nabla^2\zeta = -U\frac{\partial h}{\partial x} - J(\psi, \zeta + h). \quad (24)$$

We assume the primary balance for weak topography is between the terms on the left, which are linear in the vorticity, and the first forcing term on the right, $-U\partial h/\partial x$. This permits us to treat the quadratically nonlinear Jacobian term as a small perturbation. It also means that at lowest order the streamfunction is linear in the topography, and all succeeding terms are

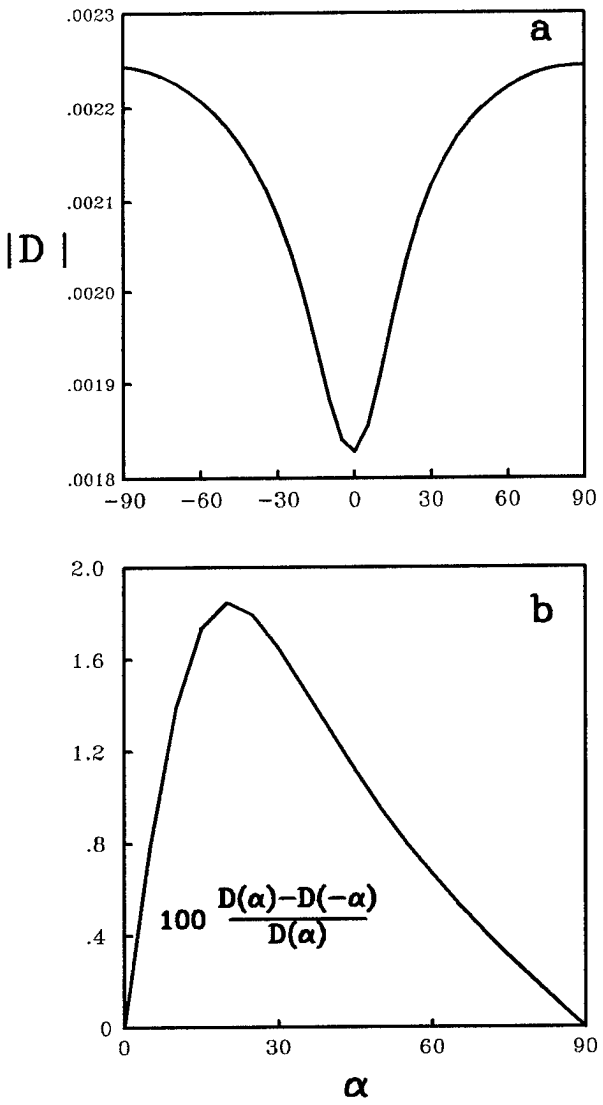


Figure 10. Form drag for the weak topography case, $h_0 = 1$. This data is taken from simulations using the spatially cutoff code. (a) The absolute value of the stationary form drag is plotted as a function of attack angle. (b) The percent of relative variation of the difference between the drag at positive and negative angles of attack is plotted versus attack angle. Specifically, the graph represents $100(D(\alpha) - D(-\alpha))/D(\alpha)$, where $D(\alpha)$ is the form drag for a given angle of attack, α.

of higher integral order. Thus we write

$$\psi = \psi^{(1)} + \psi^{(2)} + \psi^{(3)} + \ldots, \tag{25}$$

$$\zeta = \zeta^{(1)} + \zeta^{(2)} + \zeta^{(3)} + \ldots, \tag{26}$$

where $\zeta^{(n)} = \nabla^2\psi^{(n)} = O(h_0^n)$.

To evaluate the terms in the perturbation series, we first take the continuous Fourier transform in both x and y to obtain

$$g_{\mathbf{k}}^{-1}\zeta_{\mathbf{k}} = -ik_xUh_{\mathbf{k}} - J_{\mathbf{k}}(\psi, \zeta + h). \tag{27}$$

Here the linear Green function $g_{\mathbf{k}}$ is given by

$$g_{\mathbf{k}} = \frac{1}{ik_xU + d_k}, \tag{28}$$

where $d_k = r + \nu k^2$, and $J_{\mathbf{k}}(A, B)$ is the Fourier transform of the Jacobian of fields A and B. An explicit formula for $J_{\mathbf{k}}(A, B)$ in terms of the Fourier transforms of A and B is given in the appendix.

The first and second order solutions can then be written as

$$\zeta_{\mathbf{k}}^{(1)} = -ik_xUg_{\mathbf{k}}h_{\mathbf{k}}, \tag{29}$$

and

$$\zeta_{\mathbf{k}}^{(2)} = -g_{\mathbf{k}}J_{\mathbf{k}}(\psi^{(1)}, \zeta^{(1)} + h). \tag{30}$$

The form drag can now be calculated order by order. Directly from the formula (23) for the form drag and the fact that the streamfunction at lowest order is linear in the topography, we see that the form drag is quadratic in the topography at lowest order. Thus the perturbation series for the form drag will be

$$D = D^{(2)} + D^{(3)} + D^{(4)} + \ldots \tag{31}$$

Using the Fourier transform within the formula for the form drag, we have

$$D = \int\int h\frac{\partial\psi}{\partial x}dxdy = -\int\int \frac{ik_x}{k^2}\zeta_{\mathbf{k}}h_{-\mathbf{k}}\frac{d^2k}{(2\pi)^2}. \tag{32}$$

Then by direct substitution of (29) into (32), we obtain

$$D^{(2)} = -U\int\int \frac{k_x^2}{k^2}g_{\mathbf{k}}|h_{\mathbf{k}}|^2\frac{d^2k}{(2\pi)^2} \tag{33}$$

$$= -U\int\int \frac{k_x^2(-ik_xU + d_k)|h_{\mathbf{k}}|^2}{k^2(U^2k_x^2 + d_k^2)}\frac{d^2k}{(2\pi)^2} \tag{34}$$

Notice that the last expression is decomposed into a real and imaginary part. But the form drag is a real quantity. The vanishing of the imaginary part of the integral can be checked by considering the change of sign $\mathbf{k} \to -\mathbf{k}$ for the dummy integration variables. Since the topography is real we have the Hermiticity constraint, $h_{\mathbf{k}}^* = h_{-\mathbf{k}}$, and so $|h_{\mathbf{k}}|^2$ is unaltered by this sign change. Thus we see that the imaginary part of the integrand changes sign under this sign reversal

and so must vanish on integration over the range from $-\infty$ to $+\infty$ for k_x and k_y. Finally we have

$$D^{(2)} = -U \int\int \frac{k_x^2 d_k |h_{\mathbf{k}}|^2}{k^2(U^2 k_x^2 + d_k^2)} \frac{d^2k}{(2\pi)^2}. \qquad (35)$$

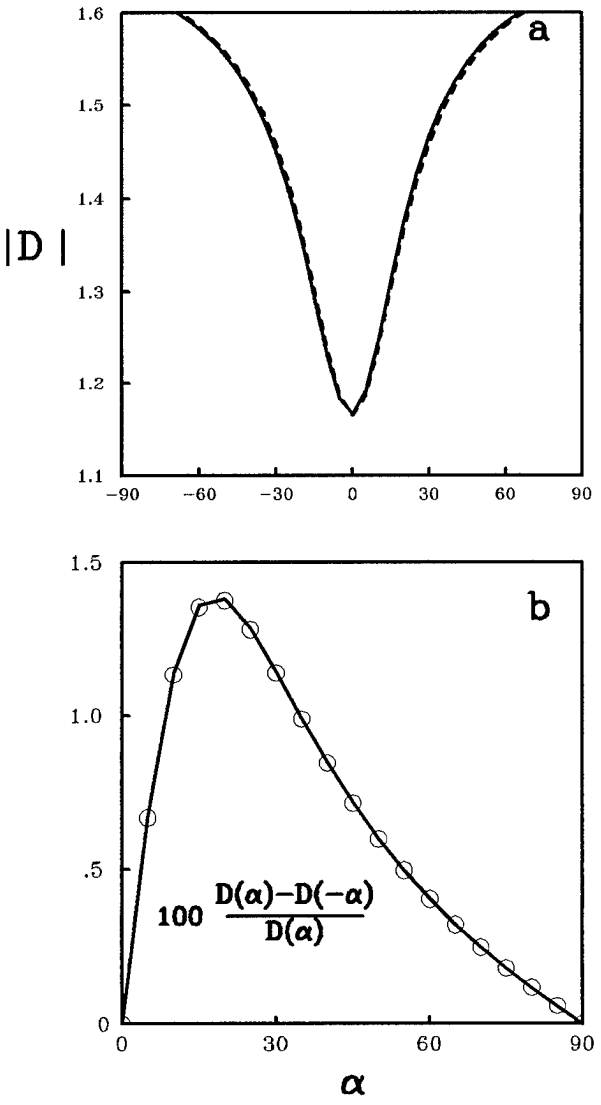


Figure 11. Form drag from weak topography perturbation theory for $h_0 = 1$. (a) The solid curve is the form drag from the fully nonlinear simulation. The dashed curve is the prediction of the lowest order perturbation theory, $D^{(2)}$ (here in units of 10^{-3}). (b) The open circles mark the results for the relative variation of the difference between the drag at positive and negative angles of attack for the fully nonlinear simulations. The solid curve shows the prediction of the perturbation theory truncated at next to lowest order, that is with $D \approx D^{(2)} + D^{(3)}$.

It is difficult to apply this perturbation theory, meant for the infinite domain, directly to the simulations with the channel and radiation boundary conditions or the spatially filtered simulation. However, for simulations with periodic boundary conditions, the result is simply a discretization of the continuous formulas. We used a quasi-geostrophic doubly periodic code to calculate the stationary solutions for the same set of experiments used to make Figure 10. In Figure 11a, we compare the actual result for the dependence on α for the full nonlinear doubly periodic calculation with the lowest order result. Although the quantitative values are somewhat different than for the case with the spatial filter, qualitatively they are alike. In Figure 11a, we see that the lowest order perturbation theory does account for most of the form drag. The small difference is essentially due to the next order term in the theory, but before proceeding to show that, let us first note that the lowest order form drag, $D^{(2)}$ is symmetric in the attack angle. In fact, this will be the case for any topography with a reflection symmetry. Let us include the dependence on the attack angle explicitly. We can define the attack angle either with reference to the angle between the line of symmetry or perpendicular to it. Then we can write $h(x, y; \alpha) = \phi(x', y')$, where x' and y' are just the rotated coordinates defined previously in equations (11) and (12). A reflection symmetry corresponds to the fact that either $\phi(x, y) = \phi(-x, y)$ or $\phi(x, y) = \phi(x, -y)$. We shall write the Fourier transform of $h(x, y; \alpha)$ as $\hat{h}_{\mathbf{k}}(\alpha)$. By using the fact that rotations do not change area, this Fourier transform is found to be

$$h_{\mathbf{k}}(\alpha) = \hat{\phi}(k_x', k_y'), \qquad (36)$$

where $\hat{\phi}(k_x, k_y)$ is the Fourier transform of $\phi(x, y)$, and

$$k_x' = k_x \cos\alpha + k_y \sin\alpha, \qquad (37)$$

$$k_y' = -k_x \sin\alpha + k_y \cos\alpha. \qquad (38)$$

By direct substitution in equation (35), we have

$$D^{(2)}(\alpha) = -U \int\int \frac{k_x^2 d_k |\hat{\phi}(k_x', k_y')|^2}{k^2(U^2 k_x^2 + d_k^2)} \frac{d^2k}{(2\pi)^2} \qquad (39)$$

$$= -U \int\int \frac{k_x^2 d_k}{k^2(U^2 k_x^2 + d_k^2)} \qquad (40)$$

$$\times |\hat{\phi}(k_x \cos\alpha + k_y \sin\alpha, -k_x \sin\alpha + k_y \cos\alpha)|^2 \frac{d^2k}{(2\pi)^2}. \qquad (41)$$

Thus,

$$D^{(2)}(-\alpha) = -U \int\int \frac{k_x^2 d_k}{k^2(U^2k_x^2 + d_k^2)} \tag{42}$$

$$\times\, |\hat{\phi}(k_x \cos\alpha - k_y \sin\alpha, k_x \sin\alpha + k_y \cos\alpha)|^2 \frac{d^2k}{(2\pi)^2}. \tag{43}$$

If $\phi(x,y) = \phi(-x,y)$, which implies $\hat{\phi}(-k_x,k_y) = \hat{\phi}(k_x,k_y)$, then the substitution $k_x \to -k_x$ shows that $D^{(2)}(-\alpha) = D^{(2)}(\alpha)$. If $\phi(x,y) = \phi(x,-y)$, then the same point is demonstrated by the change of variables $k_y \to -k_y$.

These results show that the asymmetry in the form drag, as seen in Figure 10, must come from higher order terms in the perturbation theory. We shall next demonstrate that for $h_0 = 1$ the second term in the perturbation series captures the observed deviation from symmetry very well. That term, $D^{(3)}$, is derived in general form in the appendix. If the topography has the point reflection symmetry $h(x,y) = h(-x,-y)$, as is the case for the elliptical topography, then the expression for $D^{(3)}$ simplifies and we have

$$D^{(3)} = -U^3 \int 2 d_p d_q q^2 k_x^2 p_x q_x b_{\mathbf{k}} b_{\mathbf{p}} b_{\mathbf{q}} \mathcal{D}_{\mathbf{kpq}}, \tag{44}$$

where

$$b_{\mathbf{k}} \equiv \frac{h_{\mathbf{k}}}{k^2(U^2k_x^2 + d_k^2)}, \tag{45}$$

and

$$\mathcal{D}_{\mathbf{kpq}} = \hat{z} \cdot \mathbf{p} \times \mathbf{q} (2\pi)^2 \delta(\mathbf{k}+\mathbf{p}+\mathbf{q}) \frac{d^2k}{(2\pi)^2} \frac{d^2p}{(2\pi)^2} \frac{d^2q}{(2\pi)^2}, \tag{46}$$

as shown in the appendix.

If, in addition to the symmetry of reflection in a point, the topography is also symmetric to reflection through a line, then we can show that $D^{(3)}(\alpha) = -D^{(3)}(-\alpha)$. For example, if the topography is symmetric about the y'-axis, then $h_{k_x,k_y}(\alpha) = \hat{\phi}(k_x',k_y') = \hat{\phi}(-k_x',k_y') = h_{-k_x,k_y}(-\alpha)$. Thus, a change of variables in which all k_x, p_x, q_x change sign in the expression for $D^{(3)}(-\alpha)$ shows that the integrand is simply the negative of that in the expression for $D^{(3)}(\alpha)$ (note that $\hat{z} \cdot \mathbf{p} \times \mathbf{q}$ changes sign). Similarly if $h_{k_x,k_y}(\alpha) = h_{k_x,-k_y}(-\alpha)$, then a change of variables in which all k_y, p_y, q_y change sign, in the expression for $D^{(3)}(-\alpha)$, shows again that the integrand is simply the negative of that in the expression for $D^{(3)}(\alpha)$. By rotation, this result can be further extended to the case for topography with reflection symmetry in any horizontal line. For the periodic boundary condition case, it is again an easy matter to calculate the theoretical drag by discretizing the Fourier representation. In Figure 11b, we show the relative difference between the form drag for positive and negative angles of attack (open circles) calculated from the fully nonlinear simulations with periodic boundary condition. These values are compared to the predictions (solid curve) from the perturbation theory truncated at the $D^{(3)}(\alpha)$ contribution. For this weak topography case, the match is almost perfect. The form drag contribution coming solely from $D^{(3)}(\alpha)$ is shown in Figure 12, and is antisymmetric as anticipated.

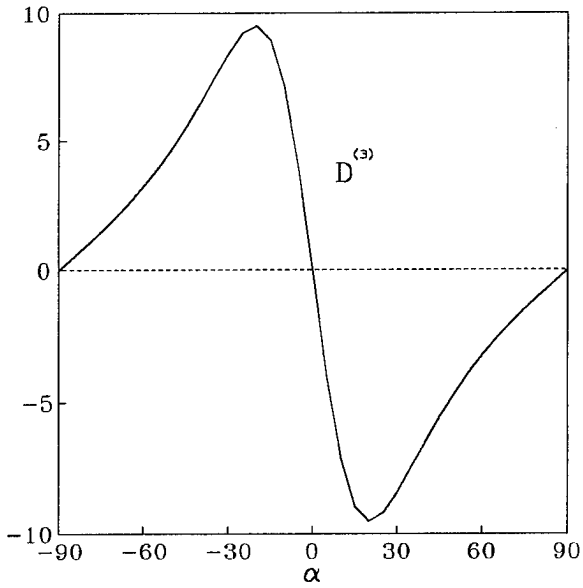


Figure 12. Antisymmetric contribution to the form drag from the next to lowest order in perturbation theory, $D^{(3)}(\alpha)$. The calculation is made for the doubly periodic boundary condition case. This contribution accounts almost entirely for the difference between the dashed and solid curve in Figure 11a. $D^{(3)}(\alpha)$ is measured here in units of 10^{-6}.

Strong topography

As we increase the amplitude, h_0, of the topography, the perturbation theory can be expected to fail. In two series of experiments, in which the angle of attack was fixed at $\pm 30°$ respectively, the topography amplitude was varied from 1 to 150. The absolute values of the stationary form drag for these experiments are plotted in Figure 13a. The solid/dashed curve corresponds to the experiments with attack angle

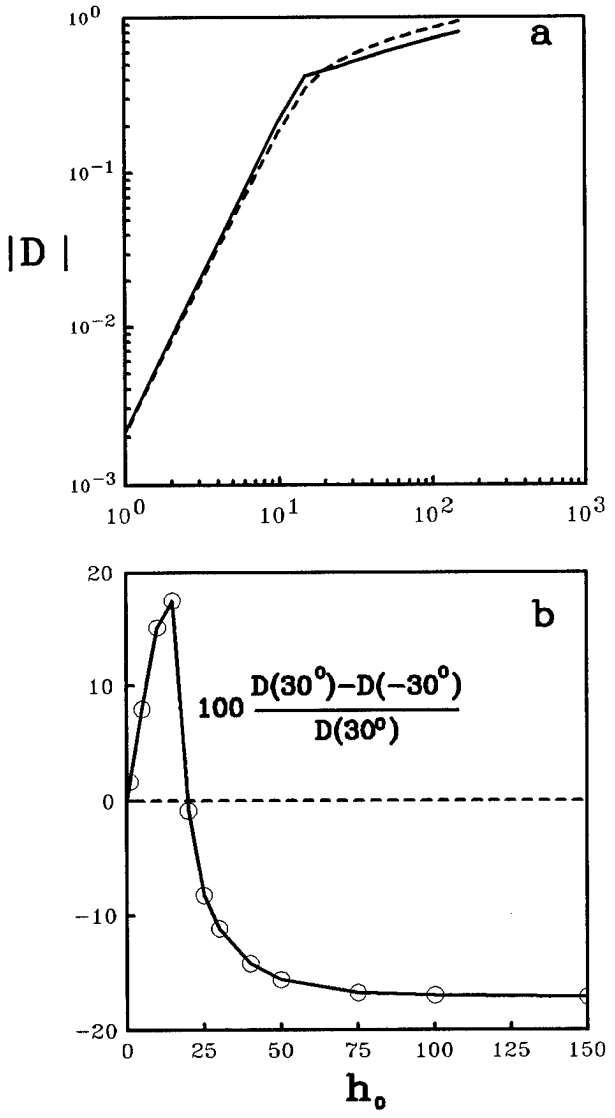


Figure 13. Form drag as a function of topographic height. (a) Two series of experiments are represented, with the angle of attack, α, fixed in each series at $+30°$ and $-30°$ respectively. The solid/dashed curve shows the absolute value of the stationary form drag from the experiments with $\alpha = +/-30°$. Note that at $h \approx= 15$ there is a cross-over between the regime in which the positive angle of attack gives a stronger form drag to the regime with just the reverse relationship. b) The relative difference in form drag strength between the plus and minus $30°$ cases is plotted as a function of topographic strength (the dashed line is simply the zero level).

$+/-30°$. Firstly, we note that for the range of topography roughly from $h_0 = 1$ to $h_0 = 15$, the form drag for both curves is approximately a quadratic function of h_0. This is what one would expect in a weak topography regime where $D^{(2)}$, the lowest order approximation to the form drag, would dominate. Also note that, in this region, the strength of the form drag for the positive angle is stronger than that for the negative angle. Near $h_0 = 15$ there is a transition to a new regime where the scaling with topography no longer follows the quadratic law. In the strong topography regime, the drag seems to increase with topography amplitude roughly as $h_0^{0.3}$. Also in the strong topography regime, the relation between the form drag for positive and negative angles has reversed, with negative angles of attack corresponding to stronger form drag than positive angles. This last point is emphasized in Figure 13b, where the relative difference in form drag strength between the plus and minus $30°$ cases is plotted as a function of topographic strength.

As an example of the functional dependence of the form drag on angle for a case of strong topography, we plot this relation for the case of $h_0 = 100$ in Figure 14a (solid curve). There have been several papers which discuss in part the theory of strong topographic forcing (cf., Pierrehumbert and Malguzzi, 1984); nevertheless, we have not been able to predict the shape of this form drag curve. We note that this curve is somewhat broader about $\alpha = 0°$ than the corresponding curve for $h_0 = 1$ in Figure 10a. As an aid to judging the symmetry and smoothness of the curve, we have also plotted the symmetric dashed curve corresponding to $A \sin^2 \alpha + B \cos^2 \alpha$, where A and B were chosen so that the two curves would have the same extremal values. In Figure 14b, we plot the relative difference in strengths between positive and negative angles of attack. The shape of the curve is similar to that shown in Figure 10b except, of course, for the sign since in this regime the negative angles correspond to stronger form drag. Here we see that the maximum difference is about -18% at around attack angle $|\alpha| = 20°$. This is a great deal stronger that the $h_0 = 1$ case, but similar to the results for $h_0 = 15$ (see Figure 13b), which is still in the regime where the positive attack angle leads to the stronger form drag.

The crossover from the weak to the strong topography regime seems, from Figures 13a and 13b, to occur roughly near $h_0 = 15$. As we noted above, in section 3, when $h_0 = 1$ the total streamfunction is only slightly perturbed from that for uniform flow, but for topographies as strong as $h_0 = 100$, a Taylor column, i.e. a region of recirculating, closed streamlines is evident (cf. Figure 9). It is tempting to try

to attribute the transition of the form drag behavior in the weak and strong limits with the occurrence of the Taylor column. However, the formation of Taylor columns occurs in these simulations for topographic amplitudes above roughly $h_0 = 50$, depending somewhat on the angle of attack, and not at $h_0 = 15$. Of course, in the regime from $h_0 = 15$ to $h_0 = 50$, the streamlines are strongly distorted from the unperturbed case of uniform flow even though closed contours do not form. The behavior of the form drag as a function topographic height, as well as its dependence on attack angle, are better understood in terms of the structure of the stationary vorticity field, as we will now consider further.

Effects of the structure of the vorticity field

In order to try to build some intuitive understanding of these results on the form drag, we shall examine the vorticity field associated with the stationary flow for the weak and strong topography cases. Consider the $\alpha = -90°$ case in Figure 4a along with the formula (23) for the form drag. The negative vortex over the hill induces a positive pressure gradient, $v = \partial\psi/\partial x$, on the upstream side of the topography, and a negative v on the downstream side. If these pressure gradients on each side were equal in strength, then the form drag would vanish as in the inviscid case. The presence of the positive vortex, on the downstream side of the hill, will increase the magnitude of v on that side relative to the upstream side. Thus, on multiplying v by h and integrating, the net effect is a negative form drag. The same analysis applies in the $\alpha = 0°$ case (panel 3c). In both the $\alpha = -90°$ case and the $\alpha = 0°$ case, there is an enhanced gradient of pressure on the downstream side that accounts for the negative net form drag. In the $\alpha = -90°$ case, this enhanced pressure gradient lies along the whole downstream side of the topography, while in the $\alpha = 0°$ case, the region of enhanced pressure gradient is aligned perpendicular to the long topographic axis. The result is that so only a smaller portion of the region of enhanced pressure gradient effectively contributes to the form drag in the $\alpha = 0°$ than in the $\alpha = -90°$ case.

Now we turn to the question of why, in the weak topography case, the drag is stronger for the positive angle of attack than for the negative angle of the same magnitude. In the perturbation theory, we noted that the lowest order form drag does not have this asymmetry, and it is necessary to go to the next order to capture this effect. This higher order effect results from the nonlinear advection produced by the Jacobian, $J(\psi, h + \zeta)$. In the appendix, we show that the interaction, $J(\psi, h)$, does not contribute at the order of $D^{(3)}$ for elliptical topography. Thus it is only

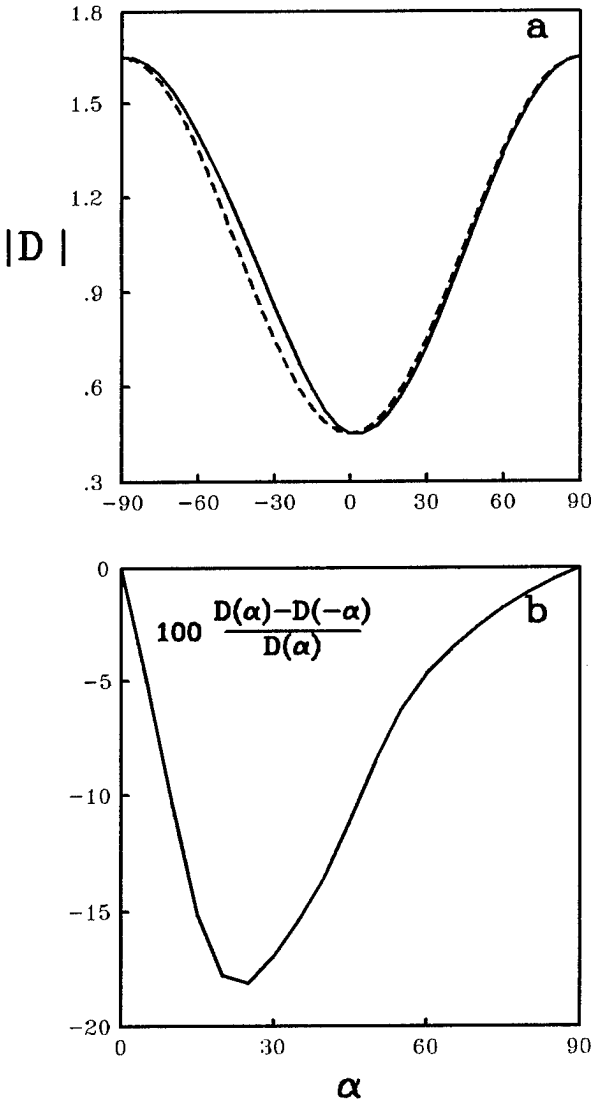


Figure 14. Form drag for the strong topography case, $h_0 = 100$. This data is taken from simulations using the code with spatial cutoff. (a) The absolute value of the stationary form drag is plotted as a function of attack angle. This is compared to the fit to the symmetric curve $A\sin^2(\alpha) + B\cos^2(\alpha)$ with A and B chosen to give a good fit at the extremal values of the data. (b) The relative variation of the difference between the drag at positive and negative angles of attack is plotted versus attack angle. Specifically the graph represents $100(D(\alpha) - D(-\alpha))/D(\alpha)$, where $D(\alpha)$ is the form drag for a given angle of attack, α.

through the vortex-vortex interaction, $J(\psi,\zeta)$, that $D^{(3)}$ contributes to the drag. Physically this term is related to the tendency of negative vorticity over the topography to displace the positive vortex in an arc in the clockwise direction about the center of the topography. In the $\alpha = -30°$ case, in panel 3b, the negative vortex is displaced away from the crest of the topography and away from the region of negative vorticity. This results in a weaker induced pressure gradient compared to what it would have been without this angular displacement. In the $\alpha = +30°$ case, in panel 3d, the negative vortex is displaced toward the crest of the topography and toward the region of negative vorticity. This results in a stronger induced pressure gradient compared to the lowest order case. Thus the form drag is stronger for the positive α case than for the negative α case. If we imagine steadily increasing α from $\alpha = -90$, we see the positive vortex first on the left side (looking upstream) of the crest of the topography, then at $\alpha = 0$ lying right over the crest, and then on the right side for $\alpha > 0$. Thus for $\alpha < 0$, the nonlinear advection displaces the negative vortex away from the topography, while for $\alpha > 0$ the displacement is toward the topography. This accounts for the result that the form drag is stronger for positive angles of attack than negative angles of the same size.

Given the above analysis for the weak topography case, how can we understand the transition to what we have called the strong topography regime in which the form drag is stronger for the negative angle of attack than for the positive angle? As noted above, this effect is not directly related to the formation of Taylor columns. Instead, the answer will be found in the relative positions of the vortices with respect to each other and to the topography. Figure 15 displays data gathered from a series of experiments representing topographies with amplitudes from $h_0 = 1$ to $h_0 = 50$, and to angles of attack $\alpha = \pm 30°$. The positions of the peak of positive relative vorticity (triangles) and negative relative vorticity (dots) are shown over ellipses which represent the topography. First of all, note that for the $h_0 = 1$ case, the negative vortex peak is located almost directly over the center of the topography, and as h_0 increases, it is displaced along the crest, toward the nose of the topography in the $\alpha = +30°$ case, but toward the tail in the $\alpha = -30°$ case. For $h_0 = 1$, the positive peak vorticity is located slightly below the x-axis, directly downstream of the center of the topography. As h_0 increases, the displacement of the positive vorticity peak is rather

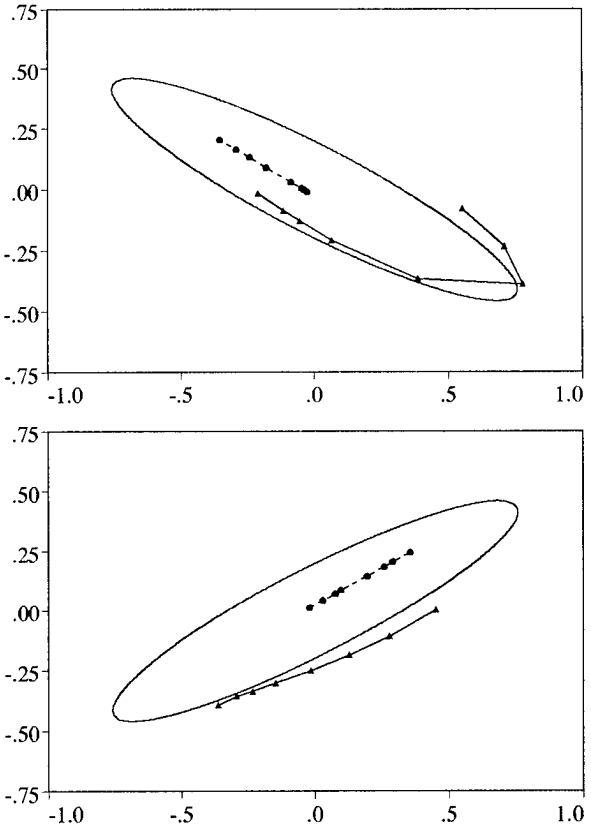


Figure 15. Positions of vorticity extrema for different values of the topographic height, h_0. The flow is in the positive x-direction, and the orientation of the topography is indicated by the ellipses, with $\alpha = +30°$ in panel (a) and $\alpha = -30°$ in panel (b). The position of the positive (negative) vorticity peaks are indicated by the solid triangles (circles). The topographic heights represented are $h_0 = 1$, 10, 15, 20, 25, 30, 40, and 50. In each panel, for $h_0 = 1$, the negative vortex is located approximately over the center of the ellipse, and the positive peak is just slightly below the x-axis, directly downstream of the center of the ellipse.

different for the two topographic orientations. For the $\alpha = -30°$ case, the peak of positive vorticity simply moves further and further toward the nose of the topography but always remaining on the downstream side. For the $\alpha = +30°$ case, the positive vorticity peak is displaced in an arc. Between $h_0 = 10$ and $h_0 = 15$, this peak crosses over the crest of the topography, moving from the downstream to the upstream side. From $h_0 = 15$ to $h_0 = 40$, the peak is displaced more and more toward the nose of the ellipse, remaining always on the upstream side. There then appears to be a discontinuous jump with a large displacement

putting the $h_0 = 50$ position back downstream but still on the upstream side of the ellipse. Actually this discontinuity in the graph is related to the fact that, in the positive α cases, with very strong topography, there are two peaks of positive relative vorticity, as we can see in Figure 7d. Between $h_0 = 40$ and $h_0 = 50$ the trailing positive vorticity peak becomes stronger than the leading one, resulting in the jump in the graph in Figure 15a. The value of h_0 for which this jump occurs is also approximately the value of topography for which Taylor column formation first occurs. However, as we noted before, the transition to what we have called the strong topography regime occurs at the much smaller value of $h_0 \approx 15$. This shows that the relevant effect is that for $h_0 \approx 15$ the positive vortex peak crosses over from the trailing side of the topography to the leading side in the $\alpha = +30°$ case, while no such transition occurs in the $\alpha = -30°$ case.

We have found that a simple point vortex model based on the idea that it is the position of the positive vortex that determines whether we are in the strong or weak topographic regime can capture the transition between these regimes. Consider replacing the actual positive and negative vortices by two point vortices, one of each sign. Note that if the negative vortex was exactly at the center of the topography, then, by symmetry, it can have no contribution to the form drag. For topographic strengths less than $h_0 \approx 15$, the negative vortex is only displaced by a relatively small amount from the center of the topography; hence, as a first approximation, we neglect its contribution to the form drag and consider only the contribution coming from the positive vortex. Let us further assume that the only effect of increasing the strength of the topography is to change the angular position (θ measured from the x-axis) of the positive vortex. Accordingly, in the model, the positive vortex is taken to be a fixed distance r_0 from the center of the topography. Thus, we evaluate the contribution to the form drag from a point vortex placed in the position $(r_0 \cos\theta, r_0 \sin\theta)$ as a function of θ. The streamfunction for a point vortex of strength Γ at this position is given by

$$\psi = \frac{\Gamma}{2\pi} \ln(|\mathbf{r} - \mathbf{r}_0|). \tag{47}$$

The resulting form drag is

$$D = \frac{\Gamma}{2\pi} \int\int \frac{x - x_0}{|\mathbf{r} - \mathbf{r}_0|^2} h dx dy. \tag{48}$$

Performing the integration numerically, and varying only the angle θ, we obtain the plots shown in Figure 16. The solid graph is the drag, normalized by Γh_0, for the topographic orientation $\alpha = +30°$, and the dashed graph is for $\alpha = -30°$. Keeping in mind that for this model the magnitude of the angle θ corresponds to the height of the topography, we note that for small θ the drag is stronger (i.e. more negative) for positive α than for negative α, and vice versa for large $|\theta|$. Thus, this point-vortex model does capture the same behavior, at least qualitatively, that we observed in the simulations. Here we have used $r_0 = 0.4$ in the calculations of the drag. The angle θ at which the model passes from the weak to the strong regime is about $\theta = -30°$, which corresponds to placing the point vortex right over the crest of the topography. However, the cross-over point does depend somewhat on the value chosen for r_0. Furthermore, note that as the angle θ becomes very large, a point will be reached at which the point vortex contributes positively to the form drag, as may be intuitively obvious. But, of course, the total drag must be negative, so it is clear that for very large displacements, θ, the contribution of the negative vortex cannot be neglected. To properly capture all aspects of the dependence of form drag on topographic orientation and height would require a far more elaborate model than

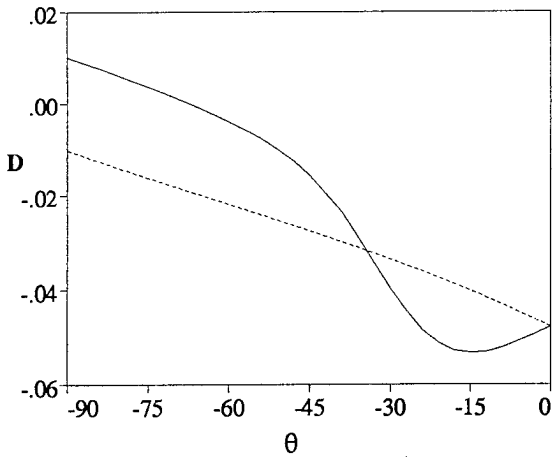


Figure 16. Drag due to a positive point vortex. The solid (dashed) curve shows the value of the drag, D, for the angle of attack $\alpha = +30°$ ($\alpha = -30°$). The drag is given as a function of the angular position, θ, measured from the positive x-axis, of the point vortex. The distance of the point vortex form the center of the topography has been fixed at $r_0 = 0.4$. The drag is normalized by $h_0\Gamma$, where h_0 is the topographic height and Γ is the strength of the point vortex.

our one point model. Nevertheless, this model does capture the essential feature of the form drag's asymmetric dependence on the sign of α in the weak and strong topography regimes.

Conclusion

We have explored how the drag that an elongated hill exerts on a flow, in a rotating fluid, depends on the orientation of that hill with respect to the flow direction. As might be expected intuitively, the drag is strongest when the hill's long axis is perpendicular to the flow direction, and it is least when that axis is parallel to the flow. A somewhat less intuitive result was that the strength of the form drag, even for hills with a horizontal cross section which is symmetric about its long axis, depends not only on the size of the "angle of attack," but also on the sign of that angle. We related this asymmetric dependence on angle to an interaction between the basic asymmetry in the mechanism of vortex tube compression and the breaking of the circular symmetry of the topography. The advection of zero relative vorticity fluid up onto the topography always results in an anticyclone over the topography and this tends to shift the downstream cyclone in an anticyclonic direction, which puts the cyclone either closer to or further from the topography depending on the topographic shape and orientation. Whether a positive angle of orientation results in more or less drag than the corresponding negative angle depends on the height of the hill. We defined a weak and strong (i.e., low and high) topography regime. For weak topography, the drag is stronger for a positive angle of attack than for an angle of the same size but opposite sign. For strong topography, this relationship is reversed, with the negative angle of attack giving the stronger form drag. It is often convenient to associate Taylor column formation with a strong topographic regime. However, in this study, we found that the formation of Taylor columns did not signal the transition from the qualitatively different behaviors of the form drag in the weak and strong regimes. Rather, we found that these regimes were defined by the qualitatively different distributions of vorticity over the topography. The weak topography regime corresponds to the case in which the positive vortex is located on the downstream side of the topography for *both* the positive and negative angle of attack, while, in the strong topography regime, the positive vortex is on the downstream side for the negative angle of attack, and on the upstream side for the positive angle of attack. We also provided a simple point-vortex model which captures these same effects.

In these studies, we have explored a wide range of values of the topographic height. The values of the viscosity were also varied in test cases designed simply to insure that the phenomena reported do exist over a range of over an order of magnitude in each direction for ν and r. There are, of course, many other physical effects that we have not included in the simple model used here, and some of these could modify our results. Perhaps the most interesting effects to consider would be those that would allow the propagation of waves. Recall that, as we noted above, in the absence of viscosity, in our simple model, the inviscid stationary flow suffers no form drag due to the presence of the hill, a manifestation of D'Alembert's paradox. However, the possibility of radiating energy infinitely far away, allows for a finite drag even in the inviscid case (see Batchelor, 1967). Two very natural candidates for such radiation would be Rossby waves and internal gravity waves. Rossby waves will result either from a large-scale bottom slope or a variation of rotation rate with latitude. Internal gravity waves require density stratification.

Acknowledgments

This research has been supported in part by Office of Naval Research grant N00014-93-1-0459 and by National Science Foundation grant OCE 91-21998. R.P. thanks the Progetto Nazionale Ricerche in Antardide (PNRA) and the Physics Committee of the National Research Council (CNR) for providing financial support for this study. The numerical simulations were performed at the San Diego Super Computer Center. We are grateful for helpful discussions with William Young.

References

Bannon, P.R. 1980: Rotating barotropic flow over finite isolated topography. J. Fluid Mech. **101**, 281-306.

Bannon, P.R. 1985: Flow acceleration and mountain drag. *J. Atmos. Sci.* **42**, 2445-2453.

Batchelor, G.K. 1967: *An Introduction to Fluid Dynamics.* Cambridge University Press.

Boyer, D.L. 1971: Rotating flow over long shallow ridges. *Geophys. Fluid Dyn.* **2**, 165-183.

Carnevale G.F. and Frederiksen J.S. 1987: Nonlinear Stability and Statistical Mechanics of Flow over Topography. J. Fluid Mech. **175**, 157-181.

Carnevale G.F., Purini R., Orlandi P., and Cavazza P. 1995: Barotropic quasi-geostrophic f-plane flow over anisotropic topography. *J. Fluid Mech.* **285**, 329-347.

Cook, K.H. and Held, I.M. 1992: The stationary response to large-scale orography in a general circulation model and a linear model. *J. Atmos. Sci.* **49**, 525-539.

Genin, A. 1987: Effects of seamount topography and currents on biological processes, Thesis, University of California, San Diego.

Genin, A., Noble M. and Lonsdale P.F. 1989: Tidal currents and anticyclonic motions on two North Pacific seamounts, Deep-Sea Research **36**, 1803-1815.

Hart, J.E. 1979: Barotropic quasi-geostrophic flow over anisotropic mountains, J. Atmos. Sci. **36**, 1736-1746.

Huppert, H.E. and Bryan, K. 1976: Topographically generated eddies. Deep-Sea Res. **23**, 655-679.

Johnson, E.R. 1978: Trapped vortices in rotating flow. J. Fluid Mech. **86**, 209-224.

Merkine, L. and Kalnay-Rivas, E. 1976: Rotating stratified flow over finite isolated topography. *J. Atmos. Sci.* **33**, 908-922.

McWilliams J.C., Holland W.R., and Chow J. 1978: A description of numerical Antarctic circumpolar currents, Dyn. Atmos. Oceans **2**, 213-291.

Orlanski I. 1976: A simple boundary condition for unbounded hyperbolic flows. J. Comp. Phys. **21**, 251-269.

Patterson, G.S. & Orszag, S.A. 1972: Spectral calculations of isotropic turbulence, efficient removal of aliasing interactions. *Phys. Fluids* **14**, 2538-2541.

Pedlosky, J. 1987: *Geophysical Fluid Dynamics.* New York: Springer-Verlag. 2nd ed.

Pierrehumbert, R.T. and Malguzzi, P. 1984: Forced coherent structures and local multiple equilibria in a barotropic atmosphere. *J. Atmos. Sci.* **41**, 246-257.

Treguier A.M. and McWilliams J.C. 1990: Topographic influence on wind-driven, stratified flow in a β-channel: an idealized model for the Antarctic Circumpolar Current, J. Phys. Ocean., **20**, 321-343.

Verron J. and Le Provost C. 1985: A numerical study of quasi-geostrophic flow over isolated topography, J. Fluid Mech. **154**, 231-252.

Wolff J-O. and Olbers D.J. 1989: The dynamical balance of the Antarctic Circumpolar Current studied with an eddy resolving quasi-geostrophic model, in *Mesoscale/Synoptic Coherent Structures in Geophysical Turbulence*, pp. 181-195 Ed's. J.C.J. Nihoul and B.M. Jamart (Elsevier, Amsterdam).

Wolff J-O., Meier-Reimer E., and Olbers D.J. 1991: Wind-Driven Flow over Topography in a zonal β-plane channel: a quasi-geostrophic model of the Antarctic Circumpolar Current. J. Phys. Ocean. **21**, 236-264.

Appendix: calculation of $D^{(3)}$

The basis for small topography perturbation theory was developed in equations (24)-(35). Since the drag,

$$D = \int h \frac{\partial \psi}{\partial x} dx dy = - \int \frac{ik_x}{k^2} \zeta_{\mathbf{k}} h_{-\mathbf{k}} \frac{d^2k}{(2\pi)^2},$$

explicitly contains the topography to the first power, and since the vorticity,

$$\zeta = \zeta^{(1)} + \zeta^{(2)} + \zeta^{(3)} + \ldots,$$

is at lowest order proportional to the topography, it follows that the lowest order contribution to the form drag, as given in (35), denoted by $D^{(2)}$, is second order in the topography. The next order term $D^{(3)}$ is given by

$$D^{(3)} = - \int \frac{ik_x}{k^2} \zeta^{(2)}_{\mathbf{k}} h_{-\mathbf{k}} \frac{d^2k}{(2\pi)^2}, \qquad \text{(A1)}$$

and since

$$\zeta^{(2)}_{\mathbf{k}} = -g_{\mathbf{k}} J_{\mathbf{k}}(\psi^{(1)}, \zeta^{(1)} + h), \qquad (30)$$

this is the lowest order term to involve the nonlinear self-advection. The Fourier transform of the Jacobian can be represented as

$$J_{\mathbf{k}}(A,B) = \int e^{-i\mathbf{k}\cdot\mathbf{r}} \left(\frac{\partial A}{\partial x}\frac{\partial B}{\partial y} - \frac{\partial A}{\partial y}\frac{\partial B}{\partial x}\right) d^2r \qquad \text{(A2)}$$

$$= - \int e^{i(-\mathbf{k}\cdot\mathbf{r}+\mathbf{p}\cdot\mathbf{r}+\mathbf{q}\cdot\mathbf{r})}(p_x q_y - p_y q_x) \times A_{\mathbf{p}} B_{\mathbf{q}} d^2r \frac{d^2p}{(2\pi)^2}\frac{d^2q}{(2\pi)^2}$$

$$= - \int \hat{\mathbf{z}} \cdot \mathbf{p} \times \mathbf{q} A_{\mathbf{p}} B_{\mathbf{q}} (2\pi)^2 \delta(-\mathbf{k}+\mathbf{p}+\mathbf{q}) \frac{d^2p}{(2\pi)^2}\frac{d^2q}{(2\pi)^2},$$

where $\hat{z} \cdot \mathbf{p} \times \mathbf{q} = (p_x q_y - p_y q_x)$ and $\delta(\cdot)$ is the multi-dimensional Dirac delta function.

Now we can calculate the $D^{(3)}$ term. Begin by changing the sign of the dummy integration variable, $\mathbf{k}$, in (A1), and substituting for $\zeta^{(2)}$ from (30) to obtain

$$D^{(3)} = D^{(3)}_{\psi,h} + D^{(3)}_{\psi,\zeta}$$

$$= - \int \frac{ik_x}{k^2} g_{-\mathbf{k}} J_{-\mathbf{k}}(\psi^{(1)}, \zeta^{(1)} + h) h_{\mathbf{k}} \frac{d^2k}{(2\pi)^2}.$$

Here we consider the two components, $D^{(3)}_{\psi,h}$ and $D_{\psi,\zeta}$, which correspond to vortex-topography and vortex-vortex interactions separately. After introducing the

expression for $J_{\mathbf{k}}$ and the definition (28) for the linear Green's function, we obtain, for the vortex-topography contribution, the result

$$D^{(3)}_{\psi,h} = I_1 = -U \int \frac{k_x p_x}{k^2 p^2} g_{-\mathbf{k}} g_{\mathbf{p}} h_{\mathbf{k}} h_{\mathbf{p}} h_{\mathbf{q}} \mathcal{D}_{\mathbf{kpq}} \tag{A3}$$

$$= -U \int k_x p_x [(k_x p_x U^2 + d_k d_p) + iU(k_x d_p - p_x d_k)] \tag{A4}$$

$$\times b_{\mathbf{k}} b_{\mathbf{p}} h_{\mathbf{q}} \mathcal{D}_{\mathbf{kpq}},$$

where

$$\mathcal{D}_{\mathbf{kpq}} \equiv (\hat{\mathbf{z}} \cdot \mathbf{p} \times \mathbf{q}) \times (2\pi)^2 \delta(\mathbf{k} + \mathbf{p} + \mathbf{q}) \frac{d^2k}{(2\pi)^2} \frac{d^2p}{(2\pi)^2} \frac{d^2q}{(2\pi)^2}, \tag{46}$$

and

$$b_{\mathbf{k}} \equiv \frac{h_{\mathbf{k}}}{k^2(U^2 k_x^2 + d_k^2)}. \tag{45}$$

Note that since the Dirac delta function forces $\mathbf{k} + \mathbf{p} + \mathbf{q} = 0$, it follows that $\mathbf{k} \times \mathbf{p} = -\mathbf{k} \times \mathbf{q} = \mathbf{q} \times \mathbf{k}$, and so $\mathcal{D}_{\mathbf{kpq}}$ is symmetric under cyclic permutation of the wavevectors $\{\mathbf{k}, \mathbf{p}, \mathbf{q}\}$, and it is antisymmetric under their pairwise interchange.

The first term in the integrand of the integral $D^{(3)}_{\psi,h} = I_1$ integrates to zero. To see this, note that this term is antisymmetric under the interchange the dummy variables $\mathbf{k}$ and $\mathbf{p}$. since $\mathcal{D}_{\mathbf{kpq}} = -\mathcal{D}_{\mathbf{pkq}}$ while the rest of the factors are symmetric in these variables. Subsequently, integration over $\mathbf{k}$ and $\mathbf{p}$ eliminates this antisymmetric term, leaving

$$I_1 = -iU^2 \int k_x p_x (k_x d_p - p_x d_k) b_k b_p h_q \mathcal{D}_{\mathbf{kpq}} \tag{A5}$$

In general, I_1 need not vanish; however, it will vanish if the topography has the point reflection symmetry, $h(x, y) = h(-x, -y)$, as is the case for our elliptical topography. The point reflection symmetry implies $h_{\mathbf{k}} = h_{-\mathbf{k}}$. If the topography has this symmetry, then changing the signs of all three wavevectors of integration changes the sign of the integrand (note $\mathcal{D}_{\mathbf{kpq}} = \mathcal{D}_{-\mathbf{k},-\mathbf{p},-\mathbf{q}}$). Thus, the vortex-topography interaction contributes to the form drag, $D^{(3)}$ only if the topography does not have point reflection symmetry.

Next we turn to the vortex-vortex interaction. For this we have

$$D^{(3)}_{\psi,\zeta} = -U \int \frac{k_x p_x}{k^2 p^2} g_{-\mathbf{k}} g_{\mathbf{p}} h_{\mathbf{k}} h_{\mathbf{p}} h_{\mathbf{q}} (-iq_x U g_{\mathbf{q}}) \mathcal{D}_{\mathbf{kpq}} \tag{A6}$$

$$= -U \int k_x p_x [(k_x p_x U^2 + d_k d_p) + iU(k_x d_p - p_x d_k)] \tag{A7}$$

$$\times \left(-\frac{iq_x U(-iq_x + d_q)}{(q_x^2 U^2 + d_q^2)}\right) b_{\mathbf{k}} b_{\mathbf{p}} h_{\mathbf{q}} \mathcal{D}_{\mathbf{kpq}}.$$

Expanding this integral further leads to an integrand containing several terms, but most of these can be shown to vanish by using the symmetry properties of $\mathcal{D}_{\mathbf{kpq}}$. There are five different kinds of terms which appear in the expansion. We will name these I_i for i =2-6, and discuss each separately.

The next integral to consider is

$$I_2 = iU^2 \int q^2 k_x p_x q_x d_k d_p d_q b_k b_p b_q \mathcal{D}_{\mathbf{kpq}}. \tag{A8}$$

This integral vanishes for any topography. To demonstrate this, we first note that the fact that $\mathcal{D}_{\mathbf{kpq}} = -\mathcal{D}_{\mathbf{kqp}}$ allows us to write

$$I_2 = \frac{i}{2} U^2 \int (q^2 - p^2) k_x p_x q_x d_k d_p d_q b_k b_p b_q \mathcal{D}_{\mathbf{kpq}}. \tag{A9}$$

Then, by using the cyclic permutation symmetry of $\mathcal{D}_{\mathbf{kpq}}$, we obtain

$$I_2 = \frac{i}{6} U^2 \int [(q^2 - p^2) + (k^2 - p^2) + (p^2 - q^2)] \times k_x p_x q_x d_k d_p d_q b_k b_p b_q \mathcal{D}_{\mathbf{kpq}}. \tag{A10}$$

This last expression is seen to vanish identically on noting that the terms within the square brackets sum to zero.

The next contribution is the integral

$$I_3 = iU^4 \int q^2 d_q k_x^2 p_x^2 q_x b_k b_p b_q \mathcal{D}_{\mathbf{kpq}}. \tag{A11}$$

This integral also vanishes for all topography as can be seen by interchanging the dummy variable $\mathbf{k}$ and $\mathbf{p}$ and noting that the integrand then reverses sign.

Continuing, we have

$$I_4 = iU^4 \int q^2 (k_x d_p q_x - p_x q_x d_k) k_x p_x q_x b_k b_p b_q \mathcal{D}_{\mathbf{kpq}}. \tag{A12}$$

This expression can be simplified by interchanging $\mathbf{k}$ and $\mathbf{p}$ in the second term in the integrand and then adding the result to the first term. Thus

$$I_4 = 2iU^4 \int q^2 d_p k_x^2 p_x q_x^2 b_k b_p b_q \mathcal{D}_{\mathbf{kpq}}.$$

As in the case of I_1, the resulting integral vanishes if $h_{\mathbf{k}} = h_{-\mathbf{k}}$. This can be seen by noting that the changing the signs of all three wavevectors of integration simply changes the sign of the integrand. Thus I_4 only contributes to the form drag if the topography does not have point reflection symmetry.

The next integral is

$$I_5 = U^5 \int q^2 k_x^2 p_x^2 q_x^2 b_k b_p b_q \mathcal{D}_{\mathbf{kpq}}. \tag{A13}$$

We can see that this integral vanishes for all topography by using the same steps that we used in the case of I_2.

The final integral is

$$I_6 = -U^3 \int q^2 (k_x d_p d_q - p_x d_q d_k - q_x d_k d_p) \times k_x p_x q_x b_k b_p b_q \mathcal{D}_{\mathbf{kpq}}. \tag{A14}$$

The third term in the parentheses will not contribute to the integral since for that term the integrand is antisymmetric under interchange of $\mathbf{k}$ and $\mathbf{p}$. Then by interchanging $\mathbf{k}$ and $\mathbf{p}$ in the second term in the integrand, we obtain

$$I_6 = -2U^3 \int q^2 k_x d_p d_q k_x p_x q_x b_k b_p b_q \mathcal{D}_{\mathbf{kpq}} \tag{A15}$$

Even for topography with point reflection symmetry, this term need not vanish. Hence it is the only third order term that will contribute in the case of our elliptical topography.

To summarize, we have shown that in general $D^{(3)} = I_1 + I_4 + I_6$, but in the case of topography with point reflection symmetry, as is the case of the elliptical topography, both I_1 and I_4 vanish. Also we have shown that for elliptically symmetric topography, there is no contribution to $D^{(3)}$ directly from the vortex-topography interaction, except indirectly through the vortex-vortex interaction.

The Frequency Dependence of Bottom Trapping and its Implications for Gravity Current Interaction with Topography

Susan E. Allen

Department of Oceanography, University of British Columbia, Vancouver, British Columbia, Canada

Abstract. Experiments are discussed which clearly show a lack of coupling between surface gravity currents and dramatic topography. Contrasts are given with other baroclinic flows over topography. The frequency dependence of the vertical structure of topographically induced flow structures is reviewed. This concept can then be used to interpret the differences between the gravity experiments and the other baroclinic flows. Further limits on the types of flows which inhibit coupling between topography and surface layers are given using numerical modeling.

1 Introduction

Surface gravity currents generated by warm or fresh sources of water are common features of coastal regions (Norwegian Coastal Current, Leeuwin Current and the Vancouver Island Coastal Current). The interaction of these strongly nonlinear flows with underlying topography is of interest, particularly when one considers the strong interaction of coastally upwelled water with topography such as the streamers associated with the Mendocino Escarpment shown in Willmott (1984).

Following the study of Gill *et al.*, (1986) which investigated the effect of a step on a baroclinic current, experiments were performed to look at the effect of bottom topography on surface gravity currents and bores in a two layer fluid. The results were intriguing. There was basically no effect unless the surface layer directly interacted with the topography. These results contrasted sharply with the experiments of Gill *et al.*, (1986) and the later experiments of Allen (1988).

The next section will present the gravity current and bore experiments which will be contrasted with a number of baroclinic flows over topography from the literature in the following section. In section 4 linear theory will be invoked for a number of geometries to illustrate the frequency dependence of topographic coupling. Numerical simulations using flow over a canyon are used to put further limits on the flow conditions under which coupling will be inhibited. In the last section, an explanation and discussion linking all the results and explaining the lack of interaction of surface gravity currents and topography is given followed by a few conclusions.

2 Gravity Currents over Topography

2.1 Experimental Apparatus

The experiments were performed in a tank of dimensions 152.0 x 30.5 x 16.5 cm which was mounted on a 1 m diameter horizontal turntable which rotated counter-clockwise. For the first set of experiments a slab of styrofoam was wedged into the bottom of the tank, so that half the tank was 5 cm shallower than the other half. The second set of experiments incorporated a sharp ridge of height 7 cm and width 1.5 cm completely dividing the tank into two sections. The Coriolis parameter, f, was varied from 0.26 to 1.3 s^{-1}. The tank was filled to a height of $H = 6.5$ to 11 cm and salt was added to increase the density to give a reduced gravity (with respect to fresh water) of $g' = 3.3$ to 9 cm s^{-2}. For some experiments, a fresh water layer of depth $h_2 = 1$ to 2 cm was floated on top of the salt water. A dam was inserted into one end of the tank and fresh, dyed water was carefully floated onto the salt water in the manner of Stern *et al.* (1982) and Griffiths and Hopfinger (1983). The depth, h_1, of fresh water behind the dam varied from 2.5 to 6 cm and the length, ℓ, of the fresh water region was varied from 17 to 25 cm. A full list of the experimental parameters is given in Tables 1 and 2.

The experiment was started by removing the dam. The ensuing current was photographed both from above and the side (using a 45 degree mirror). By including a clock in the field of view, measurements of the speed of the current could be made.

2.2 Results

As the dam is pulled the fresh water flows out over the salt water. However, within an inertial period, the flow is turned to the right by the Coriolis force. Where the flow meets the wall, a gravity current is formed which flows down the tank, hugging the right-hand wall. The properties of rotating gravity currents (in the absence of topography) are described by Stern *et al.* (1982) and Griffiths and Hopfinger (1983).

The gravity current travels down the right hand wall until it reaches the topography. Unless the gravity current hits the topography, the current itself is unaffected by the topography. That is, no dyed fluid crosses the tank at the topography and the

Table 1: Experimental Parameters for Gravity Currents over a Step

#	ℓ (cm)	f (s^{-1})	g (cm s^{-1})	h_1 (cm)	h_2 (cm)	H (cm)
1	(15.0 ± 0.5)	(1.06 ± 0.02)	(5.7 ± 0.1)	(5.0 ± 0.3)	0.	(10.0 ± 0.2)
2	(15.0 ± 0.5)	(1.08 ± 0.04)	(5.6 ± 0.1)	(5.0 ± 0.3)	0.	(11.2 ± 0.2)
3	(15.0 ± 0.5)	(1.06 ± 0.02)	(4.9 ± 0.1)	(5.0 ± 0.3)	0.	(11.4 ± 0.1)
4	(17.5 ± 0.5)	(1.03 ± 0.02)	(8.2 ± 0.1)	(5.2 ± 0.3)	0.	(10.0 ± 0.2)
5	(17.5 ± 0.5)	(1.05 ± 0.02)	(7.6 ± 0.1)	(5.0 ± 0.3)	0.	(8.5 ± 0.2)
6	(27.0 ± 0.5)	(1.06 ± 0.02)	(7.0 ± 0.1)	(4.9 ± 0.3)	0.	(8.5 ± 0.2)
7[1]	(20.5 ± 0.3)	(1.05 ± 0.02)	(9.0 ± 0.1)	(2.6 ± 0.4)	0.	(9.3 ± 0.2)
8	(22.5 ± 0.3)	(1.02 ± 0.02)	(6.5 ± 0.1)	(5.0 ± 0.5)	0.	(11.9 ± 0.2)
10	(21.6 ± 0.2)	(1.04 ± 0.02)	(8.1 ± 0.1)	(4.5 ± 0.4)	0.	(9.6 ± 0.1)
11	(22.2 ± 0.2)	(1.02 ± 0.02)	(7.9 ± 0.1)	(4.9 ± 0.3)	(1.0 ± 0.3)	(10.2 ± 0.1)
13	(19.2 ± 0.2)	(0.262 ± 0.001)	(3.5 ± 0.1)	(3.6 ± 0.2)	0.	(10.0 ± 0.2)
14	(24.8 ± 0.2)	(0.266 ± 0.001)	(3.3 ± 0.1)	(3.6 ± 0.2)	0.	(8.0 ± 0.2)
15	(22.0 ± 0.3)	(1.02 ± 0.02)	(6.4 ± 0.1)	(5.1 ± 0.3)	0.	(7.0 ± 0.2)
16	(23.6 ± 0.2)	(1.07 ± 0.02)	(5.7 ± 0.1)	(5.1 ± 0.2)	0.	(6.5 ± 0.1)
17	(17.0 ± 0.1)	(0.359 ± 0.003)	(4.3 ± 0.1)	(4.0 ± 0.2)	(2.0 ± 0.2)	(10.0 ± 0.1)
18	(17.4 ± 0.1)	(0.510 ± 0.002)	(4.0 ± 0.1)	(4.0 ± 0.2)	(1.0 ± 0.2)	(10.1 ± 0.1)
19	(17.1 ± 0.1)	(0.515 ± 0.002)	(4.1 ± 0.1)	(4.4 ± 0.2)	(1.0 ± 0.2)	(10.0 ± 0.1)
20	(17.1 ± 0.1)	(0.532 ± 0.002)	(4.1 ± 0.1)	(4.5 ± 0.2)	(1.5 ± 0.2)	(10.1 ± 0.1)
21	(17.0 ± 0.1)	(1.05 ± 0.01)	(4.1 ± 0.1)	(5.0 ± 0.3)	(2.0 ± 0.2)	(10.0 ± 0.1)
22	(17.2 ± 0.2)	(0.528 ± 0.002)	(4.1 ± 0.1)	(6.0 ± 0.3)	(3.0 ± 0.2)	(10.0 ± 0.1)
23	(17.0 ± 0.1)	(0.517 ± 0.002)	(4.1 ± 0.1)	(3.0 ± 0.3)	0.	(10.0 ± 0.1)
24	(17.2 ± 0.1)	(0.526 ± 0.002)	(4.1 ± 0.1)	(4.0 ± 0.3)	0.	(10.0 ± 0.1)
25	(17.1 ± 0.1)	(0.519 ± 0.002)	(4.2 ± 0.1)	(5.0 ± 0.3)	(2.0 ± 0.2)	(9.9 ± 0.1)
26	(17.1 ± 0.1)	(0.519 ± 0.002)	(4.1 ± 0.1)	(3.9 ± 0.2)	(1.0 ± 0.2)	(10.0 ± 0.1)
27	(17.0 ± 0.1)	(0.521 ± 0.002)	(4.1 ± 0.1)	(5.0 ± 0.2)	(2.0 ± 0.2)	(10.0 ± 0.1)
28	(17.4 ± 0.1)	(0.517 ± 0.002)	(4.1 ± 0.1)	(4.1 ± 0.2)	0.	(10.0 ± 0.1)
29	(17.2 ± 0.1)	(0.535 ± 0.002)	(3.9 ± 0.1)	(5.0 ± 0.2)	(2.0 ± 0.2)	(10.3 ± 0.1)
30	(16.9 ± 0.1)	(0.536 ± 0.002)	(4.2 ± 0.1)	(4.0 ± 0.3)	(1.0 ± 0.2)	(9.8 ± 0.1)
31	(16.8 ± 0.1)	(0.528 ± 0.002)	(3.7 ± 0.1)	(3.3 ± 0.2)	0.	(10.0 ± 0.1)
32	(17.1 ± 0.2)	(1.31 ± 0.01)	(8.3 ± 0.1)	(3.0 ± 0.3)	0.	(10.0 ± 0.1)
33	(17.4 ± 0.1)	(0.519 ± 0.002)	(4.1 ± 0.1)	(3.2 ± 0.2)	0.	(10.0 ± 0.1)

[1] The gravity current started in the shallow water and flowed over the step into deeper water.

Table 2: Experimental Parameters for Gravity Currents over a Ridge

#	ℓ (cm)	f (s^{-1})	g (cm s^{-1})	h_1 (cm)	h_2 (cm)	H (cm)
38	(17.0 ± 0.1)	(0.528 ± 0.002)	(4.0 ± 0.1)	(5.0 ± 0.3)	(2.0 ± 0.2)	(7.3 ± 0.1)
39	(17.1 ± 0.1)	(0.535 ± 0.002)	(6.2 ± 0.1)	(5.0 ± 0.3)	(2.0 ± 0.2)	(7.0 ± 0.1)
42	(17.2 ± 0.1)	(0.526 ± 0.002)	(6.0 ± 0.1)	(5.0 ± 0.2)	(2.0 ± 0.2)	(8.0 ± 0.1)
43	(17.2 ± 0.1)	(0.528 ± 0.002)	(6.0 ± 0.1)	(4.1 ± 0.2)	0.	(8.0 ± 0.1)
44	(17.0 ± 0.1)	(0.532 ± 0.002)	(6.0 ± 0.1)	(4.1 ± 0.2)	0.	(9.0 ± 0.1)
45	(17.3 ± 0.1)	(0.532 ± 0.002)	(6.0 ± 0.1)	(4.0 ± 0.2)	0.	(10.0 ± 0.1)
46	(17.3 ± 0.1)	(0.524 ± 0.002)	(6.0 ± 0.1)	(4.0 ± 0.2)	0.	(11.0 ± 0.1)
47	(17.2 ± 0.1)	(0.530 ± 0.002)	(6.0 ± 0.1)	(5.0 ± 0.2)	(2.0 ± 0.2)	(8.0 ± 0.1)
48	(17.0 ± 0.1)	(0.526 ± 0.002)	(6.1 ± 0.1)	(5.0 ± 0.2)	(2.0 ± 0.2)	(9.0 ± 0.1)
49	(16.8 ± 0.1)	(0.539 ± 0.002)	(6.0 ± 0.1)	(5.0 ± 0.2)	(2.0 ± 0.2)	(10.0 ± 0.1)
50	(17.5 ± 0.1)	(0.535 ± 0.002)	(6.0 ± 0.1)	(4.0 ± 0.2)	0.	(7.5 ± 0.1)

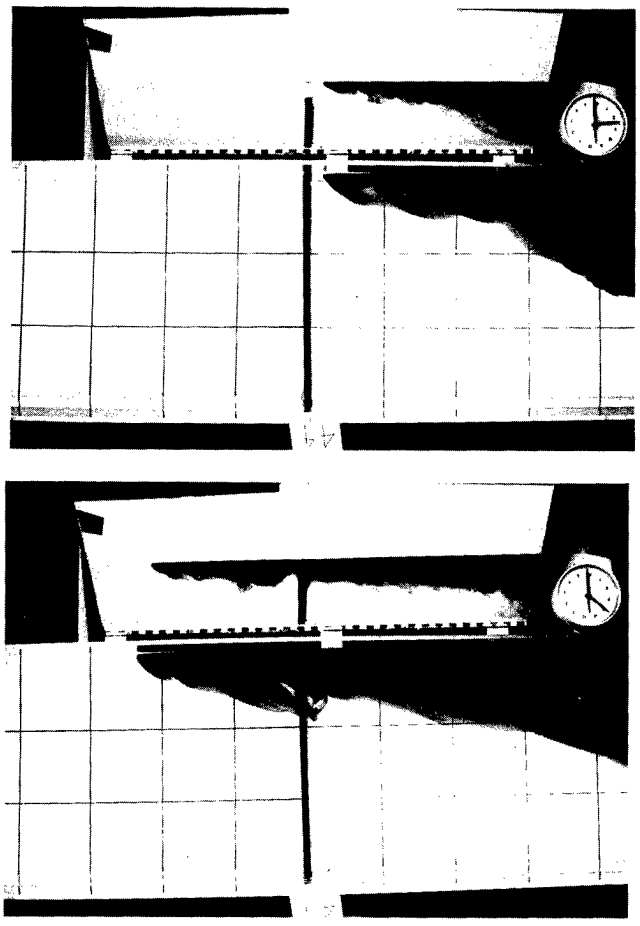


Figure 1: Figure showing a gravity current a) approaching and b) passing over a ridge. The top part of each frame shows a side view whereas the lower part of the frame is from above. The marked squares are 10 cm x 10 cm. Only the centre part of the tank is shown. See Table 2 for parameters; this is experiment 44.

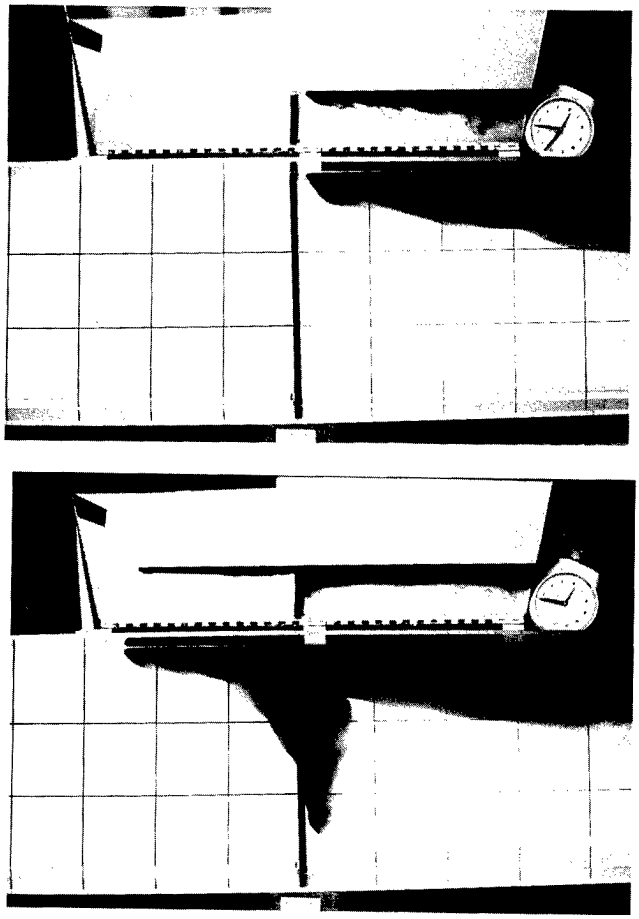


Figure 2: Figure showing a gravity current a) approaching and b) bifurcating over a ridge. See Figure 1 for details of the field of view. See Table 2 for parameters; this is experiment 50.

speed, depth and width of the gravity current remains the same (within measurement limits) as the current crosses the topography. An example, showing the current approaching and passing over a ridge, is given in Figure 1.

In the absence of topography the gravity current generates a return flow in the deep water which is broad (stretches across the tank) and is about 1/5th as strong as the current itself (Allen and Allen, 1995). Thus, the deep water flow must be affected by the topography; it is only the surface gravity current which is unaffected.

Occasionally an eddy formed at the step after the passage of the head. This eddy would tend to move fluid across the tank. However, it was not the only eddy to form and not necessarily the largest.

Deep water movement was observed under the gravity current, towards the barrier region. A deep current forms over the step in the two layer case running across the step away from the approaching bore. A sketch is given in Figure 3. This current is stronger for deeper original surface layers. Generally, this current forms after the current has traversed the step.

If the current actually hit the topography, a secondary current formed which crossed the tank, generally to the left of the topography. Occasionally it would stray over the step and cross at as much as a 45 degree angle. The original current continued with reduced size and speed. An example showing a gravity current hitting the ridge and bifurcating is shown in Figure 2. In a two layer fluid. the cross tank current usually took the form of a series of eddies. In the case of the step and a two layer fluid, an eddy formed where the current hit the jet and cross tank current/eddies formed out of this eddy. Examples for the two layer fluid are shown in Figure 4 and Figure 5.

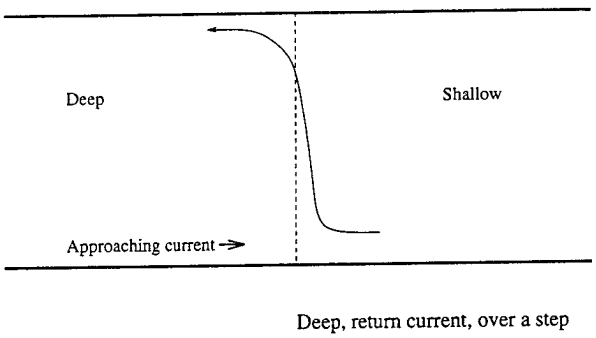


Figure 3: Figure showing, from above, the deep return current seen over a step for a two layer fluid. The direction of the approaching bore is marked.

3 Other Baroclinic Flows over Topography

The lack of effect of a dramatic piece of topography is not common. This section presents three examples where topography strongly affects surface layers not in contact with it.

3.1 Two layer geostrophic flow over a Step or Slope

The experiments described in Gill *et al.*, (1986) and Allen (1988) consider geostrophic flow forced over a step and slope respectively. The step was identical to the one described above. The slope was 4 cm high and 8 cm long. In both cases the flow was forced by placing a barrier *along* the wall, across the topography. In each case distinct cross tank flow at the topography is seen. An example of a numerical solution is shown in Figure 6. Note the flow out along the topography at the bottom on the slope and the flow towards the wall at the bottom. These along-slope flows are in the same sense as those in the lower layer even though the along-wall flows are in opposite directions (Allen, 1988).

3.2 Eddy experiments

Consider a circular tank mounted on a rotating table and initially containing a homogeneous fluid at rest. If a constant flux of buoyant water is introduced away from the tank walls a circular anti-cyclonic eddy will form (Griffiths and Linden, 1981). If this is done over a sloping bottom, the eddy elongates in a direction which keeps the shallow water to the right (in the direction topographic Rossby waves propagate). If the eddy is unstable, it breaks up into a string of eddies and each eddy propagates across the tank, again in the direction which keeps the shallow water on the right (Linden, 1991; Davey and Killworth, 1989). Thus, although the eddy is a surface phenomena, it directly feels the bottom topography.

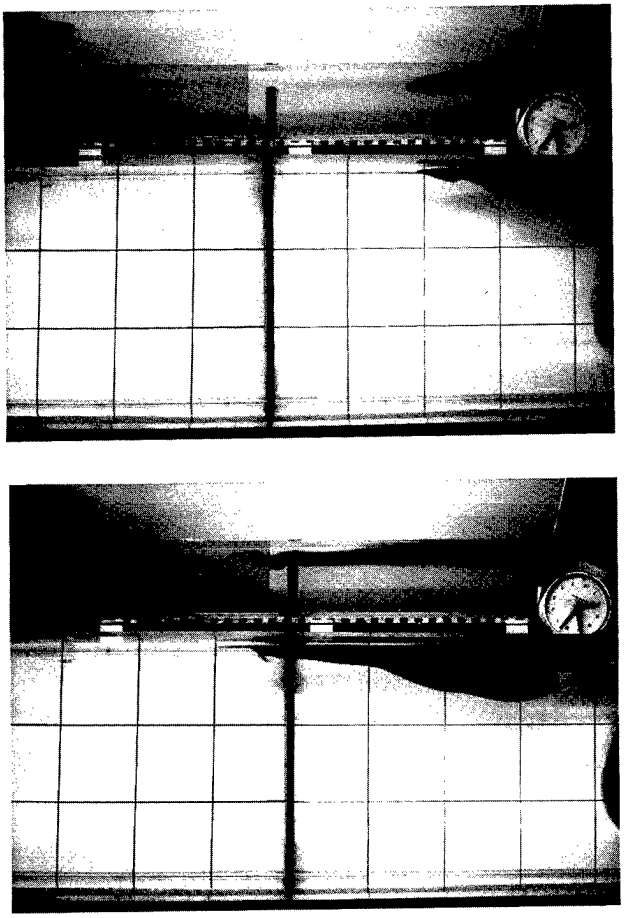


Figure 4: Figure showing a gravity current a) approaching and b) crossing over a ridge. See Figure 1 for details of the field of view. See Table 2 for parameters; this is experiment 42.

Davey and Killworth (1989) give an analytic solution for the similar β-plane problem assuming the lower layer is quiescent. In the laboratory case however, the lower layer must move as that is the only way the upper layer could "feel" the bottom topography (unlike the β effect). If one follows Davey and Killworth's arguments but considers a barotropic solution (ignoring the density difference between the two fluids) one gets the same flow pattern as they derived for the linear baroclinic flow. Under the source itself, the flow is towards the deeper water ("south") whereas "west" of the north half of the source, the flow is towards the source and "west" of the south half of the source, the flow is away from the source. This derived, linear flow pattern is three quarters of an elongated anti-cyclonic vortex stretching out to the west of the source.

3.3 Ridge

Experiments conducted in Grenoble by D. Renouard (Allen *et al.*, 1995) investigated barotropic tidal flow over a long bank or ridge in a two layer fluid. To gener-

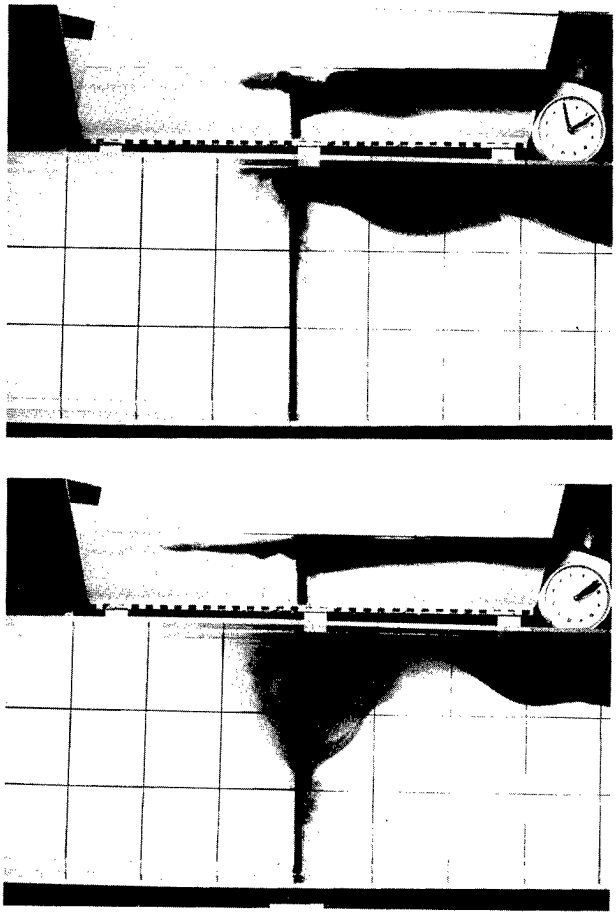


Figure 5: Figure showing a bore a) approaching and b) splitting over a ridge. See Figure 1 for details of the field of view. See Table 2 for parameters; this is experiment 39.

ate the tides, the ridge was oscillated. Measurements were made in the centre of the ridge of the velocity in each layer. The frequency of oscillation of the ridge, ω and the period of rotation $4\pi/f$ were varied. A number of experiments were performed (Germain and Renouard, 1991) but I will discuss only two examples here.

The ridge is 30 cm high and 4 m long. The lower layer is 40 cm deep, the upper layer is 4 cm deep and the reduced gravity between the two layer is 6.5 cm s^{-2}. Thus, the ridge is 3/4 of the depth of the lower layer and the topography can be classified as large. The ridge was oscillated back and forth 30 cm.

For the first, a weakly rotating case, $\omega/f = 0.67$. The lower layer velocity has an amplitude of 5.5 cm/s in the cross-ridge direction and about 1 cm/s in the along ridge direction. The upper layer velocities are 2 cm/s across and about 1 cm/s along the ridge. Contrast these values with a strongly rotating case, $\omega/f = 0.14$. The lower layer velocities are 5 cm/s and 4 cm/s across and along the ridge but the upper layer velocities are almost as strong at 3.5 cm/s across and 3 cm/s along.

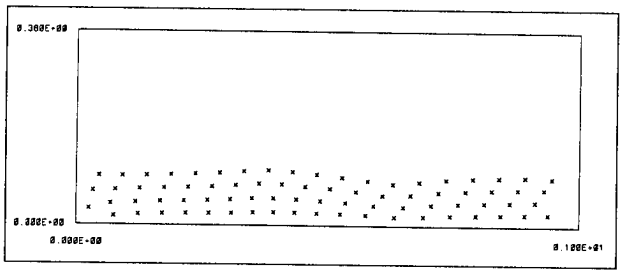


Figure 6: Figure showing movement of tracers in a numerical simulation of the Allen (1988) experiments. The fluid is stratified, with the upper layer deeper near the wall initially. The tracers mark the upper layer inside the barrier. Note the movement out across the tank. Depth of upper layer 14.4 cm, depth of lower layer 7.9 cm, reduced gravity 4.24 cm s^{-2}, barrier 5.1 cm from the wall.

Thus at a high, although still subinertial, frequency there is weak coupling whereas at a much lower frequency the upper layer flows are almost as strong as the lower layer flow.

4 Linear theories of the vertical height of topographic effects

4.1 Steady Flow

In Hogg (1973) steady, low Rossby number stratified flow over a circular cylinder is considered. If the fluid is homogeneous, by the theory of Taylor and Proudman, a Taylor column will form over the cylinder and no streamlines from off the cylinder will penetrate the area over the cylinder. If the fluid is stratified, such behaviour is limited in vertical extent over the body. Hogg's theory gives the height to which a Taylor cone will exist in a stratified fluid, over a circular body, as L^2/R^2 times the height of the body, where L is the radius of the body and R is the internal Rossby radius.

In the flows considered here, the width of the topography is much greater than the width of the background current. Assuming that in this case the appropriate lengthscale is the lengthscale of the current, all flows in sections 2 and 3 have L^2/R^2 of approximately one. Thus, if these flows were steady (they are not) and of low Rossby number (they are not), they all should show topographically influenced flow right to the surface.

4.2 Oscillatory Flow

Rhines (1977) presents a coherent picture of subinertial waves trapped over a sloping bottom (his fast baroclinic waves). These topographic Rossby waves are trapped with a depth $f\lambda/N$ of the bottom for wavelengths of order of or smaller than the internal Rossby radius. The symbols f, λ and N represent the Coriolis frequency, one over the wavenumber, and

the Brunt-Väisälä frequency, respectively. For longer wavelengths the flow is barotropic.

If one considers the topographic waves which travel along a simple linear slope between two flat basins (as would be appropriate for the slope geometry of sections 2 and 3) the dispersion relation has a similar form to that for β-plane Rossby waves. Long waves are non-dispersive; at some intermediate wavenumber the group speed goes to zero and thereafter the frequency decreases with wavenumber. For two layer flow over a slope, those waves having wavelengths of approximately one internal Rossby radius have the highest frequencies (group speed near zero).

Thus higher frequency motions are bottom trapped whereas long wavelength, low frequency motions are felt throughout the water column. Note that Rhines' theory is for low Rossby number and infinitely wide topography.

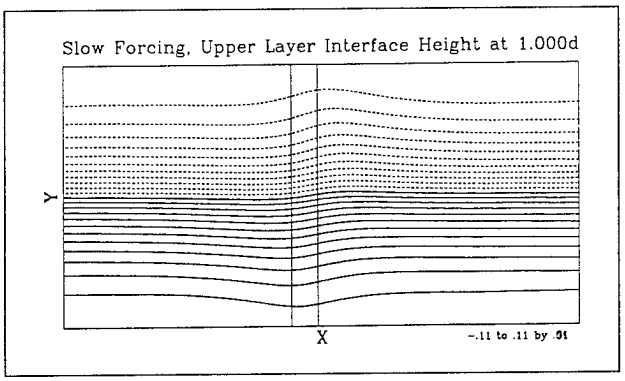


Figure 7: Figure showing a the surface elevation one day after forcing began. The contour levels are in metres. The domain is 240 km by 120 km and the position of the canyon is marked. The surface layer is 50 m deep and the lower layer is 200 m deep in the canyon, 100 m deep over the shelf. The reduced gravity between the two layers is 0.1 m s^{-2}.

5 Discussion

Interpretation of the oscillating ridge experiments, section 3.3, follows directly from Rhines (1977) assuming 1) the nonlinear nature of the flow is not important in determining its vertical scale and 2) forced waves behave similarly to free waves. The fast subinertial frequency excites bottom trapped topographic waves whereas the slower frequency excites long, almost barotropic Rossby waves. For these forced waves, the wavelength is the length of the ridge, N is approximately $(g'/H)^{1/2}$ where H is the depth of the upper layer. This gives trapping within 4 cm of the ridge for the high frequency, low rotation rate flow which would imply little effect in the upper layer as is observed. For the low frequency, high rotation rate flow the wavelength is much greater than Rossby radius and as expected the effect of the ridge is strong in the upper layer.

The eddy experiments are forced slowly. Fluid is added over many inertial periods. Thus the frequency of the forcing is low and it has barotropic as well as baroclinic character (fluid is not removed from the lower layer so the forcing is not purely baroclinic). This type of forcing leads to the generation of low frequency, long wavelength topographic waves. Invoking Rhines' theory, and again assuming the nonlinearity is not important to the vertical structure, these waves should be nearly barotropic. Thus the surface flow is strongly affected by the bottom topography in this case.

The step and slope experiments with the barrier placed along the topography are also forced relatively slowly. Although the dam break is sudden, the initial response is flow parallel to the topographic contours. Only as the flow turns due to the Coriolis force does it "feel" the topography. Thus the frequency scales of the forcing of the topographic waves are fairly low. As is observed, these waves have near barotropic behaviour and the surface flow is affected by the topography.

In the surface gravity current experiments, on the other hand, the current topography interaction is quite quick. The subinertial frequencies generated are close to f and these waves are bottom trapped. Thus currents at the topography are seen in the lower layer but the upper layer is unaffected by the topography.

6 Complications due to wavelength

Numerical and analytic modelling (Allen, 1995) has considered multi-layer flow over a canyon. Here we will consider two layers where the lower layer is in contact with the topography but the upper layer lies above. The flow is forced by assuming that wind forcing generates an Ekman layer which, through Ekman pumping, removes water from the main fluid column over the shelf. The Ekman layer is not modeled and the Ekman pumping is modeled as a sink. Simplifying the problem further, here we neglect the shelf break.

The wind is assumed to start at zero and linearly increase in intensity over one half of an inertial period. Thereafter it decreases linearly in intensity. The surface elevation (which approximates the upper layer streamlines) after one day (about 1.4 inertial periods) is shown in Figure 7. The effect of the canyon is clearly visible with along canyon, down pressure, flow generated within the canyon.

To consider the fast introduction of topography, a case with a flat bottom was forced in the same way as above. After one day, a canyon was suddenly added. The lower layer flow in the canyon was reduced to conserve momentum and match the flux across the canyon walls. The surface elevation is shown in Figure 8 one day after the canyon was introduced (two days after the start of the flow). The surface flow is similar to

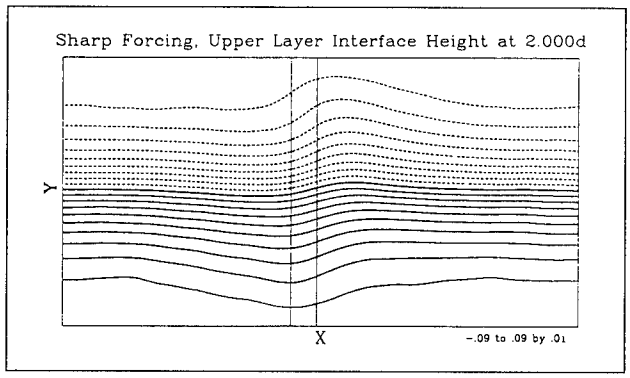


Figure 8: Figure showing the surface elevation one day after a canyon was introduced; see text. Other parameters as in Figure 7.

the gently forced case and is strongly affected by the topography. The pattern is noisier because the sharp introduction of the canyon generates Poincaré waves.

This numerical experiment illustrates that the frequency of the forcing is not the sole mechanism for determining the wavelength and frequency of the topographic waves. At the time the canyon is introduced, the surface and interface elevation change from high to low values along the canyon. Thus the wavelengths of the topographic Rossby waves which travel along the canyon (Chen and Allen, 1995) are of order of the Rossby radius up to half the size of the domain. The long waves are primarily barotropic (assuming Rhines' (1977) theory holds) and so the surface flow is influenced by the topography.

Various numerical complications make it difficult to consider the unrealistic case of flow over a canyon near the wall. Consider again the experiments. The width of the gravity current and the flow set up by the barrier along the wall were similar as the barrier was placed, in some cases, closer than a Rossby radius to the wall. In this case frequency of forcing, not the initial along-topography wavelength, gives an explanation.

7 Conclusions

Linear theory (Hogg, 1973 and Rhines, 1977) gives the basis for determining the vertical scale of topographic influence. Nonlinear effects do not seem to be important. From the type of forcing and the geometry, the frequency and wavelength of the topographic Rossby waves is estimated and compared to the Rossby radius. Provided short wavelength, high frequency waves are generated the flow is confined to $\lambda f/N$ of the bottom. Lower frequency, long waves are expected to follow the Hogg limit of L^2/R^2H.

The above explanation was applied to the laboratory results for gravity currents over steps and slopes, eddies over a slope, oscillatory flow over a ridge, and the numerical results for wind driven flow over a canyon.

References

Allen, M. C. and S. E. Allen, 1995: Beyond $(g'h)^{1/2}$, the speed of rotating gravity currents. In preparation.

Allen, S. E. 1988: *Rossby adjustment over a slope.* PhD thesis, University of Cambridge, 206 pp.

Allen, S. E. 1995: Topographically generated, subinertial flows within a finite length canyon. Submitted to *J. Phys. Oceanogr.*

Allen, S. E., D. P. Renouard, and J.-M. Baey, 1995: Currents and internal waves generated by periodic flow over topography. In preparation.

Chen, X. and S. E. Allen, 1995: Influence of canyons on shelf currents – a theoretical study. Submitted to *J. of Geophys. Res.*

Davey, M. K. and P. D. Killworth, 1989: Flows produced by discrete sources of buoyancy. *J. Phys. Oceanogr.* **19**, 1279–90.

Germain, J.-P. and D. Renouard, 1991: On permanent nonlinear waves in a rotating fluid. *Fluid Dyn. Res.* **7**, 263–278.

Gill, A. E., M. K. Davey, E. R. Johnson, and P. F. Linden, 1986: Rossby adjustment over a step. *J. Marine Res.* **44**, 713–738.

Griffiths, R. W. and E. J. Hopfinger, 1983: Gravity currents moving along a lateral boundary in a rotating fluid. *J. Fluid Mech.* **134**, 357–399.

Griffiths, R. W. and P. F. Linden, 1981: The stability of buoyancy-driven coastal currents. *Dyn. Atmos. Oceans* **5**, 281–306.

Hogg, N. G. 1973: On the stratified Taylor column. *J. Fluid Mech.* **58**, 517–537.

Linden, P. F. 1991: Dynamics of fronts and eddies. In Osborne, A., editor, *Nonlinear topics in ocean physics* Int. School of Physics, "Enrico Fermi". North Holland.

Rhines, P. B. 1977: The dynamics of unsteady currents. In Goldberg, E. D., I. N. McCave, J. J. O'Brien, and J. M. Steele,, editors, *The Sea. Volume 6: Marine Modelling.* John Wiley & Sons.

Stern, M. E., J. A. Whitehead, and B.-L. Hua, 1982: The intrusion of a density current along the coast of a rotating fluid. *J. Fluid Mech.* **123**, 237–265.

Willmott, A. J. 1984: Forced double Kelvin waves in a stratified ocean. *J. Marine Res.* **42**, 319–358.

Internal Waves, Bottom Slopes and Boundary Mixing

G.N. Ivey, P. De Silva and J. Imberger

Department of Environmental Engineering, Centre for Water Research, University of Western Australia, Nedlands, Western Australia, 6009.

Abstract: Laboratory experiments in continuously stratified fluids with internal waves breaking on planar bottom slopes indicate that while mixing is most intense near the local critical frequency ω_c, contributions to mixing are observed over the frequency range where $0.5 < \omega/\omega_c < 2.5$. For the critical case when the turbulence is most energetic, the turbulent benthic layer is not well mixed. The benthic layer varies in thickness over a wave cycle and the laboratory data indicate the mean thickness h is 15% of the wavelength of the incident wave, measured perpendicular to the slope. A simple model relates the mean rate of dissipation of turbulent kinetic energy $\bar{\varepsilon}$ and the diffusivity K within the benthic layer to the properties of the incident wave field, and yields a simple criterion for a buoyancy flux to occur within the benthic layer. Even though this criterion appears to be readily satisfied in the field, available observations do not yield clear evidence of a buoyancy flux. The turbulent activity in the benthic layers on the sloping bottoms therefore must be significant for the chemical and biological productivity, but the consequences for basin scale mixing in either lakes or the oceans are as yet undetermined.

Introduction

The dynamics of the turbulent benthic boundary layers and their role in mixing and transport processes on the basin scale have long been an area of great interest, particularly since Munk (1966) suggested that mixing at the boundaries could be responsible for the basin scale vertical mixing. Much attention has since been focussed on mixing at the boundaries, e.g., in recent review articles by Garrett, MacCready and Rhines (1993) and by Imberger (1994), with application to oceanography and limnology, respectively.

Models of the near boundary flows resulting from turbulence near a sloping bottom have been proposed (e.g., Phillips *et al.* 1986, Garrett 1990, Salmun *et al.* 1991) based on assumptions about the distribution of turbulent diffusivity with height above the bottom. Imberger and Ivey (1993) showed that a number of flow regimes were in fact possible, depending on the relative magnitudes of two ordering parameters: the Grashof number $Gr = (g\Delta\rho h^3/\rho_0 K^2)\cos\beta$ and the aspect ratio $A = h/L << 1$. In their formulation the benthic layer was assumed well-mixed over a depth h, $\Delta\rho$ was the density anomaly between the well-mixed boundary layer and the interior, L the along-slope scale characterising the background density gradient variability, β the bottom slope, and K the eddy diffusivity within the benthic layer, assumed the same for momentum and species. Using a perturbation solution in the small parameter A, they argued that in the flow regime likely to be relevant to lakes when $Gr = O(A^{-3/2})$, the interior vertical eddy diffusivity K_I at the depth of the density gradient extremum was given by

$$K_I = \left(8 \times 10^{-6}\right) \frac{N^4 h^9 \sin^3\beta \cos^2\beta}{K^3 L_B} \qquad (1)$$

where L_B is the horizontal basin dimension and N is the maximum value of the buoyancy frequency in the thermocline.

In order to utilise such models, one therefore needs a knowledge of both the readily determinable geometrical properties of a basin, such as the bottom slope and basin size, but also two properties of the flow field: the benthic layer thickness h and the turbulent diffusivity K. As eq. (1) illustrates, the interior diffusivity K_I is particularly sensitive to the choice of either parameter, a conclusion which holds no matter what flow regime governs the dynamics of the benthic layer on the slope. The specification of the these two flow parameters is the issue we wish to address in the present work, and our focus here is on the mechanisms driving mixing at the boundary and how they influence h and K.

While the near boundary mixing can be driven by a mean flow over the hydraulically rough boundary, the more likely mechanism for driving boundary mixing is due to the interaction of the internal wave field with the sloping bottom - an observation which has motivated a number of laboratory studies (e.g., Ivey and Nokes 1989, Taylor 1993, De Silva *et al.* 1995) and field studies (e.g., Eriksen 1985, Eriksen 1995, Thorpe *et al.* 1990, Van Haren *et al.* 1994).

Laboratory Experiments

There have been three laboratory studies which have investigated breaking internal waves on slopes with a monochromatic incident internal wave: an initial study by Ivey and Nokes (1989,1990) conducted on a 30° bottom slope and over a range of incident frequencies around the critical frequency ω_c (group velocity vector of the reflected wave parallel to the bottom slope); a study by Taylor (1993) on a 20° bottom slope and confined to the critical frequency; and a study by De Silva *et al.*

(1995) on a 20° bottom slope using a very different configuration for generating internal waves and focusing on the frequency range above the critical frequency.

Ivey and Nokes (1989) showed that at the critical frequency a turbulent benthic boundary layer formed along the bottom. The thickness of the benthic layer h varied over the wave cycle, with maximum thickness during the upslope phase of the motion. The turbulence intensity in the layer also appeared to vary, although no direct measurements were made of turbulence properties. Sustained forcing over many wave cycles led to a change in potential energy P of the fluid in the laboratory tank. The average mixing efficiency in the benthic region over a wave cycle defined as $R_f = P/W$, where W was the net energy input into the benthic region, was dependent on wave amplitude but had a maximum value of $R_f = 0.2$, indicating the process can be quite efficient compared to other mixing mechanisms (e.g. Ivey and Imberger 1991). As seen in Figure 1, the mixing efficiency also varies with frequency ω with the maximum near the critical frequency ω_c but still a significant contribution coming from a bandwidth in the range $0.7 < (\omega/\omega_c) < 1.8$. For a typical internal wave spectrum in the ocean or lake, the implication is that even though the mixing efficiency is lower away from the local critical frequency, there can still be a significant contribution to mixing, particularly for the sub-critical frequencies with higher energy levels.

Taylor (1993) extended these experiments to a lower bottom slope of 20° and, by examining the microstructure signals in the boundary layer, confirmed that the turbulence intensity varied in intensity over a wave cycle. The most intense mixing occurred on the upslope phase of the wave cycle - as also observed in the field observations reported by White (1994) and Van Haren *et al.* (1994), for example. Mixing efficiencies were slightly smaller but comparable to those reported by Ivey and Nokes (1989). The direct numerical simulations reported by Slinn and Riley (1994) were the first to examine the case of critical waves on very low slopes down to 3.4°. Their results suggested that for steep slopes (defined to be greater than 20°) the mixing appeared nearly continuous over the wave cycle, while for shallow slopes (defined to be less than 10°) the mixing was more intermittent in nature over a wave cycle. Mixing efficiencies were reported as high as 0.39, but as there are differences in the definition between the numerical calculation and the laboratory experiments, it is difficult to draw definitive conclusions. From measurements of the velocity field, Taylor (1993) observed a strong interaction between the upslope and downslope flow and concluded that the mechanism generating the turbulence was not simply described by either a simple shear flow or a convective type instability, but had elements of both depending on the phase of the wave cycle and position relative to the bottom.

These early experiments had used a flap wavemaker at one end of a long channel which produced a wave with wavelength comparable to the slope length. The flow field was more in the nature of flow in a horizontal duct rather than a discrete wave ray impinging on an infinite planar slope. Recently, De Silva *et al.* (1995) have used a rather different means of generating the internal wave as shown schematically in Figure 2. The configuration has the advantage of producing an internal wave ray with wavelength small compared to the length scale of the slope and minimises the potential geometrical dependence introduced by the presence of the wedge shaped region at the top of the slope, of particular importance to the study of supercritical wave reflection.

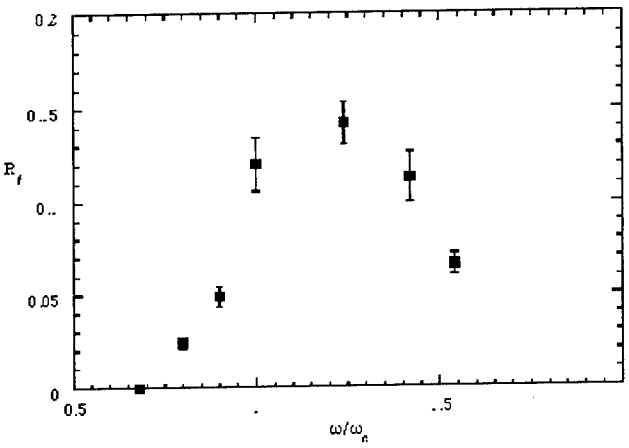


Figure 1. Cycle averaged mixing efficiencies as a function of forcing frequency where the incident wave amplitude is fixed in all cases. Paddle amplitude A = 2.2 cm and β = 30.

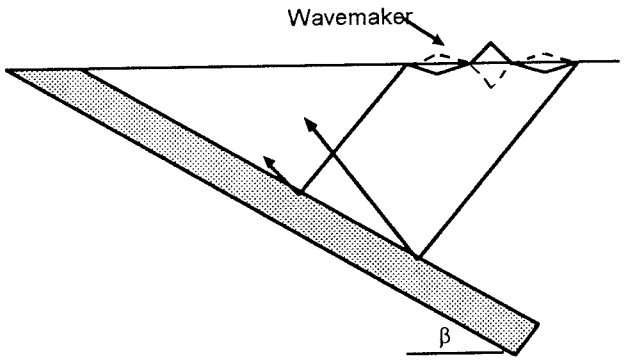
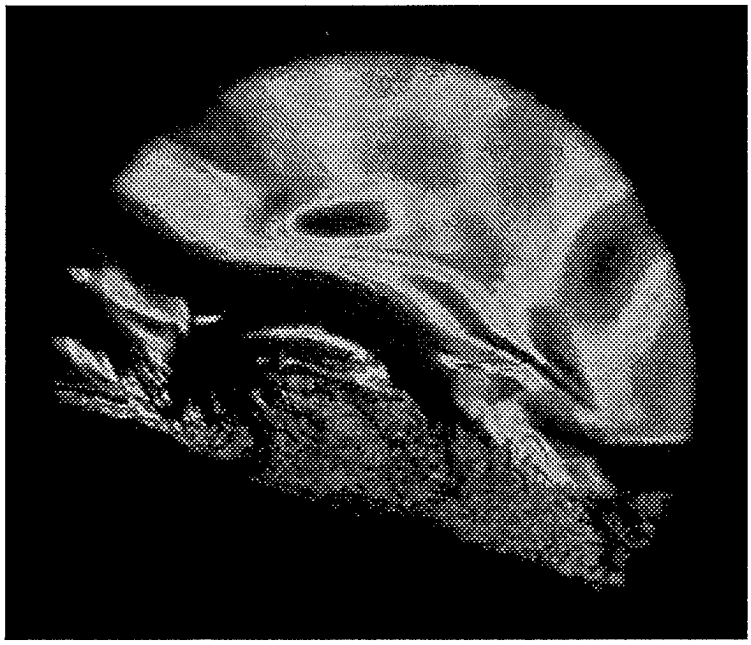
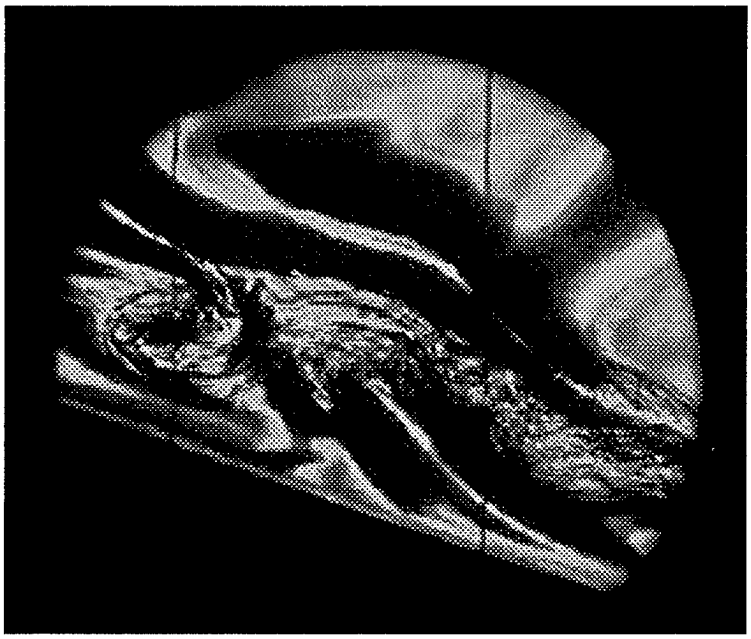


Figure 2. Schematic of horizontal articulated internal wave maker as employed by Teoh *et al.* (1995) and De Silva *et al.* (1995). Wavemaker is arranged so there is zero net displacement at the surface and a confined wave ray, of horizontal scale 1.5 wavelengths, is directed down onto the sloping bottom.



(a)



(b)

Figure 3. Rainbow schlieren images of breaking internal waves taken just after mixing has initiated. In Figure 3a, $\omega/\omega_c = 2.07$ and in Figure 3b $\omega/\omega_c = 2.43$. In both cases the incident wave amplitude is 2 cm.

In Figure 3 we show two rainbow schlieren images of the waves breaking on the slope. The schlieren technique used is described in some detail by Ivey and Nokes (1989), and the optical arrangement used here is identical. In Figure 3a we show the case where ω/ω_c = 2.07 with the incident ray coming in from the top right and reflecting forward toward shallow water on the left, and the image is taken a few cycles after the initiation of paddle motion. Even at this relatively high forcing frequency compared to the critical frequency, a mixing region is observed which has developed at the slope itself and extends along the slope a distance of the width of the incoming ray. Conversely at the higher forcing frequency in Figure 3b where ω/ω_c = 2.43, the mixing region has been established off the slope and there is a laminar region immediately adjacent to the slope. With continual wave forcing, the mixing region grows and extends down to the bottom. Thorpe (1987) has shown that non-linear second and third order resonances can occur between incident and reflected waves, which lead to regions of static instability off the slope, reminiscent of what is shown in Figure 3b. However, the theory predicts this should only occur for bottom slopes $\beta < 10^0$, considerably less than the 20° in figure 3, so the explanation of this observation is not yet clear. Note also that mixing is occurring at a range beyond that shown in Figure 1, implying that if there is enough energy available in the incident wave field at a given frequency, mixing can occur over a surprisingly broad bandwidth.

In Figure 4 we show some typical results of microstructure profiles over the depth. Note that the resolution of measurements made with the conductivity and temperature probes is comparable with that of the schlieren system which is able to resolve spatial scales down to about 0.7 mm (Taylor 1993). From the density profiles which extend to within 5 mm of the bottom, while there is variability during the wave cycle there is no evidence of any persistent well mixed regions close to the bottom. If we take the turbulent benthic region as the height at which overturning scales shown in the second panel disappear, the benthic layer is about 10 cm thick - consistent with the visual observations in Figure 3. Note also that the turbulence intensity does vary over the cycle where even the largest displacement scales are, at most, about 20% of the total thickness of the benthic region.

Mixing in the benthic region

These observations suggest the following simple mixing model. Consider the configuration shown in Figure 2. For an internal wave train in two dimensions, linear theory (e.g. Phillips 1977) indicates the velocity and density perturbations are described by

$$w = \alpha \cos\theta \cos(kx + nz - \omega t)$$

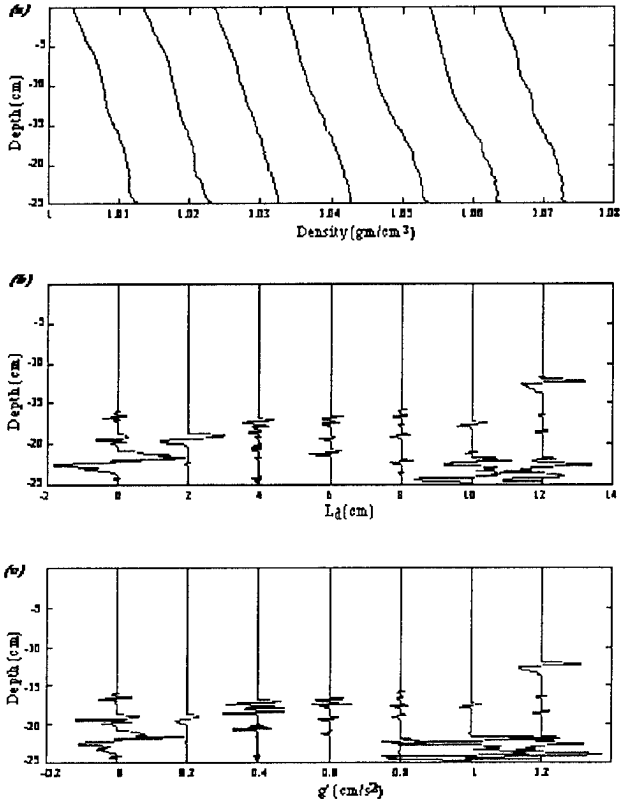


Figure 4. Microstructure profiles through a typical wave cycle once mixing has been initiated. Parameters are N = 0.64 rs^{-1}, ω = 0.45 rs^{-1}, wave amplitude 2.9 cm. Profiles are at intervals of 0.14 ($2\pi/\omega$). In the first panel, all profiles are displaced by 0.01 gm/cm^3 from the first profile. The second panel shows sample displacement scales and the third panel the corresponding buoyancy anomaly g'.

$$u = -\alpha \sin\theta \cos(kx + nz - \omega t) \qquad \text{(2a.b.c)}$$

$$\rho = -\frac{\alpha}{g\omega}\rho_0 N^2 \cos\theta \sin(kx + nz - \omega t)$$

where u and w are the horizontal and vertical velocities (x and z direction, respectively), k and n are the horizontal and vertical wavenumbers, ρ is the density perturbation, α is the maximum particle speed and θ the angle of the group velocity vector to the horizontal. The average over one wave period of the vertical energy flux passing though a horizontal surface with dimensions of one wavelength in the x direction and unit width in the y direction is

$$\dot{E}_i = \frac{\pi}{k}\rho_0 \alpha^2 C \sin\theta \qquad (3)$$

where C is the phase speed.

When the waves are incident on a bottom of slope β, the reflected energy is in general given by $\dot{E}_r = (1-r)\dot{E}_i$, (where the reflection coefficient $r = 0$ for perfect reflection). On the basis of the laboratory observations of Ivey and Nokes (1989), Taylor (1993) and De Silva *et al.* (1995), it seems reasonable to assume that for the case of critical wave reflection, once a turbulent mixing layer is established along the bottom, no energy is reflected at the incident or at any other frequency - due to dispersion in the frequency content resulting from mixing in the turbulent region, for example.

Then for the critical case, the average dissipation over one wave cycle is

$$\bar{\varepsilon} = \frac{\dot{E}_i}{M} = \frac{\dot{E}_i}{\rho_0 h l} \tag{4}$$

where M is the mass of fluid (per unit width) in which the incident wave energy is dissipated, h is the average thickness of the benthic layer and l is the along-slope length over which mixing is occurring.

In Figure 5a we plot the observed values of boundary layer thickness h obtained by Ivey and Nokes (1989) against the Reynolds number based on incident wave properties. It is apparent that above a minimum Reynolds number of about 50, the observed value of boundary thickness h is remarkably constant in the range of (0.10 - 0.15)λ_v, where λ_v is the wavelength of the incident wave measured perpendicular to the slope. In Figure 5b, we plot similar observations from De Silva *et al.* (1995), and while the data set is small it appears $h \approx 0.15\lambda_v$ for supercritical waves as well although there may also be some dependence on wave amplitude. These results are also consistent with the experiments of Taylor (1993) (see his Figure 3, for example), and the field data of Van Haren *et al.* (1994) and White (1994), although smaller than the values found by Slinn and Riley (1994).

If we take the benthic layer thickness as $h = 0.15\lambda_v$ then this can be written as

$$h = 0.15\left(\frac{2\pi}{\sqrt{k^2+n^2}\cos 2\beta}\right) \tag{5}$$

Substituting (5) into (4) and noting from the geometry that $l = \pi / (k \cos \beta)$, we obtain

$$\bar{\varepsilon} = \left(\frac{3\alpha^2 N}{4\pi}\right)\sin 4\beta \cos\beta \tag{6}$$

Using the result from Osborn (1980), the eddy diffusivity for the stratifying species in the benthic boundary layer can thus be written as

$$K = \left(\frac{R_f}{1-R_f}\right)\left(\frac{3\alpha^2}{4\pi N}\right)\sin 4\beta\cos\beta \tag{7}$$

A necessary condition for the turbulence to be sufficiently energetic to sustain a buoyancy flux is $\bar{\varepsilon}/\nu N^2 > 15$(e.g. Ivey and Imberger 1991), where ε is the instantaneous dissipation rate. Cycle averaged values (e.g. Ivey and Nokes 1989, Taylor 1993) are about a factor of two lower than this, so a conservative estimate would say $\bar{\varepsilon}/\nu N^2 > 15$ is a necessary condition for a buoyancy flux.

Ivey and Imberger (1991) also demonstrated that the value of the mixing efficiency R_f depends strongly on the turbulent Froude Number defined as $Fr_T = (L_o/L_c)^{2/3}$, where the Ozmidov scale $L_o = (\varepsilon/N^3)^{1/2}$ and the displacement scale is L_c. If $Fr_T = 1$, then the mixing is highly efficient with $R_f = 0.2$, but for values of Fr_T either above or below $Fr_T = 1$, the value of R_f decreases rapidly. Laboratory observations (De Silva *et al.* 1995) and field observations (see below) indicate that $Fr_T = 1$ only occasionally and it appears to vary greatly from profile to profile.

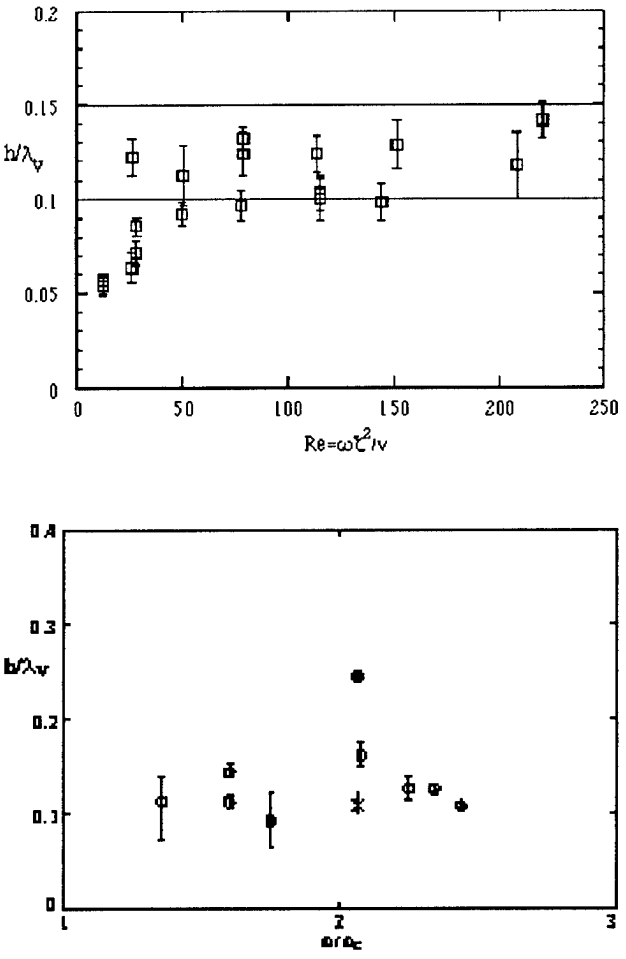


Figure 5. Measurements of boundary layer thickness obtained from schlieren images. (top) panel shows data from Ivey and Nokes (1989) where ζ is wave amplitude. (bottom) panel shows data from experiments by De Silva et al. (1995) in the configuration shown in Figure 2.

It is tempting to generalise the arguments above to the case of non-critical reflection where $0<r<1$, hence (6) becomes

$$\bar{\varepsilon} = r\left(\frac{3\alpha^2 N}{4\pi}\right)\sin 4\beta\cos\beta \qquad (8)$$

Javam *et al.* (1995), for example, have examined the reflection of an internal wave at a critical level, and find the reflection coefficient varies between 0.2 to 1.0, depending on the Reynolds number. Comparable calculations thus need to be made for waves reflecting off the bottom when a turbulent mixing region is present in order to utilize (8).

Field observations

Using data from Lake Biwa, Japan, Imberger (1994) demonstrated that in order to explain the typical internal wave spectral levels and relatively rapid decay of large scale internal waves, generated by aperiodic wind events for example, the benthic boundary regions must be regions of very high dissipation compared to the interior - at least two orders of magnitude larger than typical interior levels of dissipation of order 10^{-9} m^2 s^{-3}. In the ocean, Eriksen (1985) estimated that 8% of the Garrett Munk internal wave energy flux had to be converted to potential energy to yield Munk's (1966) canonical interior vertical diffusivity of 10^{-4} m^2 s^{-1}. More recent calculations (e.g. Gilbert and Garret 1989) and measurements (e.g. Eriksen 1995) imply values an order of magnitude less than this seem more likely. Only recently have observations been made which have attempted to link the internal wave field, near boundary turbulence and the resulting buoyancy flux.

Thorpe *et al.* (1990) and White (1994) describe results from the Hebrides Slope, where the M_2 internal tide is locally critical to the bottom slope, which show clear evidence of enhanced mixing on the upslope phase of motion, and much weaker mixing in the downslope phase, as seen in the laboratory experiments. With a local vertical wavelength of about 1 km, White (1994) shows evidence of mixing up to and including their last instrument at 110 m off the slope - consistent with the laboratory prediction of benthic layer thickness in Figure 5a. Van Haren *et al.* (1994) find benthic layers of height of thickness 10 m when the local vertical wavelength was 120 m. Intriguingly, while their dissipation estimates indicate that $\bar{\varepsilon}/\nu N^2 \approx 400$, they were unable to find any evidence for significant buoyancy fluxes.

Eriksen's (1995) observations from Fieberling Guyot seamount in the North Pacific clearly show significant levels of enhanced activity near the local critical frequency of 0.42 cph where N = 1.02 cph (i.e. $\beta = 24°$). With a vertical wavelength of 3 km, equation (5) predicts turbulent activity up to a level of some 450 m off the bottom, although this is clearly an oversimplification of the issue for such large vertical wavelengths. Such a steep bottom slope would suggest relatively continuous mixing over a wave cycle. Taking $\beta = 24°$, N = 1.02 cph and taking as the incident wave field the background GM spectrum close to the bottom, we obtain (e.g. Eriksen 1995 figure 3a) $\alpha \approx 0.5$ cm s^{-1}, and hence from (6) $\bar{\varepsilon} = 1\times10^{-8}$ m^2 s^{-3}. Toole *et al.* (1994) report direct microstructure measurements near the base of Fieberling Guyot. Their results clearly show an increase in dissipation as the bottom is approached with the deepest estimate, still some 500 m off the bottom, having a value of $\varepsilon = 10^{-9}$ m^2 s^{-3}.

Microstructure measurements in the benthic boundary layer in Lake Kinneret, Israel have been reported by Imberger *et al.* (1995). One of the most striking features of their results shown in Figure 6 is the considerable variation in the turbulent Froude number Fr_T. Many events occur which have Froude numbers very different than one, implying the mixing efficiency R_f is very small and the events have little or no buoyancy flux associated with them. The implication is that even if the dissipation is significant compared to background levels, the buoyancy flux or species diffusivity K, may be negligibly small.

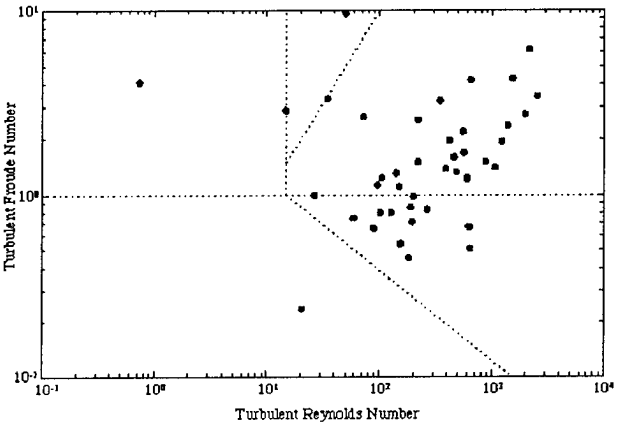


Figure 6. Microstructure measurements in the benthic boundary layer in Lake Kinneret, Israel from Imberger *et al.* (1995). Data plotted on an activity diagram where the Turbulent Froude number $Fr_T = (L_o/L_c)^{2/3}$ and the Turbulent Reynolds number $Re_T = (L_c/L_k)^{4/3}$. The Ozmidov scale $L_o = (\varepsilon/N^3)^{1/2}$ is based on the re-sorted density profile, L_k is the Kolmogorov scale and L_c is the displacement scale.

Conclusions

Recent laboratory experiments give some insight into the dynamics of the turbulent mixing region that can form along a sloping bottom boundary in a continuously stratified fluid where mixing is driven by breaking

internal waves. Using a simple model, it is possible to obtain expresions for the benthic layer thickness h and the turbulent diffusivity K within this benthic region in terms of the properties of the incident wave field. Further laboratory and numerical experiments need to be conducted, particularly for non-critical waves, to test the validity of these expressions. Both in the laboratory and the field, care is needed in distinguishing between the measurements made from instantaneous measurements and values valid over one wave cycle and longer.

While the evidence so far is hardly conclusive, it may transpire that the benthic layer on the sloping bottom is one of enhanced turbulent dissipation but with a negligible turbulent buoyancy flux. This has significant implications for circulation modelling and for the chemistry and biological processes near the boundary in lakes and the ocean (cf. Imberger 1994). Such a scenario does explain one obvious feature of lakes: they stay stratified unless seasonal cooling occurs. Only careful experiments in the future will enable these questions to be answered.

This work is supported by the Australian Research Council. Environmental Dynamics Report ED 807 GI.

References

De Silva, P., G.N. Ivey, and J. Imberger, 1995: Turbulence and mixing due to breaking internal waves on sloping boundaries. in preparation.

Ericksen, C.C., 1985: Implications of ocean bottom reflection for internal wave spectra and mixing. *J. Phys. Oceanogr.*, 15, 1145-1156.

Ericksen, C.C., 1995: Internal wave reflection and mixing at Fieberling Guyot, *J. Geophys. Res.*, submitted.

Garrett, C., 1990: The role of secondary circulation in boundary mixing. *J. Geophys. Res.*, 95, 3181-3188.

Garrett, C., O. Macready, and P. Rhines, 1993: Boundary mixing and arrested Ekman layers: rotating stratified flow near a sloping boundary. *Ann. Rev. Fuid Mech.*, 19, 1716-1729.

Gilbert, D. and C. Garrett, 1989: Implications for ocean mixing of internal wave scattering off irregular topography. *J. Phys. Oceanogr.*, 19, 1716-1729.

Imberger, J. and G.N. Ivey, 1993: Boundary mixing in stratified reservoirs. *J. Fluid Mech.*, 183, 25-44.

Imberger, J., 1994: Transport processes in lakes: a review. in *Limnology Now: a Paradigm of Planetary Problems*. R. Margalef (ed.), Elsevier, 99-193.

Imberger, J., T. Zohary, and C. Thomson, 1995: Boundary mixing in lakes. in preparation.

Ivey, G.N. and R.I. Nokes, 1989: Mixing driven by the breaking of internal waves against sloping boundaries. *J. Fluid Mech.*, 204, 479-500.

Ivey, G.N., and R.I. Nokes, 1990: Mixing driven by the breaking of internal waves against sloping boundaries. In *Proc. Intl. Conf. Physical Modelling of Transport and Dispersion*, M.I.T., Cambridge, Mass., 11A.3-11A.8

Ivey, G.N., and J. Imberger, 1991: On the nature of turbulence in a stratified fluid, Part 1: The efficiency of mixing. *J. Phys. Oceanogr.*, 21, 650-658.

Javam, A., S.W. Armfield, and J. Imberger, 1995: Numerical study of internal wave generation in a stratified fluid. *J. Fluid Mech.*, submitted.

Munk, W. H., 1966: Abyssal recipes. *Deep Sea Res.*, 13: 207-230.

Osborn, T.R., 1980: Estimates of the local rate of vertical diffusion from dissipation measurements. *J. Phys. Oceanogr.*, 10, 83-89.

Phillips, O.M., 1977: The dynamics of the upper ocean. Cambridge.

Phillips, O.M., J.-H. Shyu, and H. Salmun, 1986: An experiment on boundary mixing: mean circulation and transport rates. *J. Fluid Mech.*, 173, 473-499.

Salmun, H., P.D. Killworth, and J.R. Blundell, 1991: A two-dimensional model of boundary mixing. *J. Geophys. Res.*, 96, 18,447-18,474.

Slinn, D.N., and J.J. Riley, 1994: Turbulent mixing in the oceanic boundary layer due to internal wave reflection from sloping terrain. in *Proc. 4th International Symp. Stratified Flows*, Grenoble, France, to appear.

Taylor, J., 1993: Turbulence and mixing in the boundary layer generated by shoaling internal waves. *Dyn. Atmos. Oceans.*, 19, 233-258.

Thorpe, S.A., 1987: On the reflection of a train of finite-amplitude internal waves from a uniform slope. *J. Fluid Mech.*, 178, 279-302.

Thorpe, S.A., P. Hall, and M.White, 1990: The variability of mixing on a continental slope. *Proc. Roy. Soc.*, A439,115-130.

Teoh, S.G., G.N. Ivey, and J. Imberger, 1995: Observations of interactions between two internal wave rays. *J. Fluid Mech.* in preparation.

Toole, J.M., K.L. Polzin, and R.W. Schmitt, 1994: Estimates of diapycnal mixing in the ocean. *Science*, 264, 1120-1123.

Van Haren, H., N. Oakey, and C. Garrett , 1994: Measurements of internal wave band eddy fluxes above a sloping bottom. *J. Mar. Res.*, 52, 909-946.

White, M., 1994: Tidal and subtidal variability in the sloping benthic boundary layer. *J. Geophys. Res.*, 99, 7851-7864.

Rectified Flows over a Finite Length Shelf Break: a Bank and a Canyon Case

J. Verron, D. Renouard

Laboratoire des Ecoulements Géophysiques et Industriels, URA 1509 CNRS, BP 53X, 38041 Grenoble Cedex, France

D. L. Boyer

Environment Fluid Dynamics Program and Department of Mechanical and Aerospace Engineering, Arizona State University, Tempe, AZ 85287-1903

Abstract.

Rectified processes over a submerged elongated bank and over a canyon in an otherwise long shelf break were investigated by means of numerical and laboratory experiments for the bank and by means of numerical experiments only for the canyon.

The physical experiments were conducted in the Grenoble 13 m diameter rotating tank. The background oscillating motion was obtained by periodically varying the platform angular velocity. Fluid motions were visualized and quantified by direct velocity mesurements and particle tracking. The numerical model employed was a tridimensional model developed by *Haidvogel et al.* [1991]. It consists of the traditional primitive equations; i.e., the Navier-Stokes equations for a rotating fluid with the addition of the hydrostatic, Boussinesq and incompressibility approximations.

In the bank case, both the laboratory and numerical experiments show that in the range of dimensionless parameters considered, two distinct flow regimes, based on general properties of the rectified flow patterns observed, can be defined. It is further shown that the flow regime designation depends principally on the magnitude of the temporal Rossby number, Ro_t, defined as the ratio of the flow oscillation to the background rotation frequency. Good qualitative and quantitative agreement is found between the laboratory experiments and the numerical model for such observables as the spatial distribution of rectified flow patterns.

In the canyon case, although the geometry is quite different, strong similarities are observed especially the existence of flow regimes having a strong analogy with the ones identified in the previous case. The temporal Rossby number, Ro_t, is also an essential controlling parameter although the standard Rossby number, Ro, interplays significantly. The most important result however, in this case, is the capability for the canyon to be a downstream source of mean rectified current at distances which are large with regard to the horizontal scale of the canyon .

Introduction

The nonlinear generation of a mean flow by oscillatory or other unsteady currents or turbulence (i.e. rectification), is for the most part studied in relation to the ubiquitous presence of tides. Such rectification processes have been observed in numerous places, for instance along the Georges Bank [*Butman et al.*, 1982; *Tee*, 1985] and along the La Chapelle Bank [*Garreau and Mazé*, 1991]. There are also observations of rectified flows around Bermuda [*Stommel*, 1954], Fieberling Guyot in the North Pacific [*Genin et al.*, 1989; *Eriksen*, 1991], in the Bay of Biscay [*Pingree and Le Cann*, 1990], in the Straits of Dover [*Brylinski and Lagadeuc*, 1990] and the North Sea [*Maas and Van Haren*, 1987]. Rectification may not be only driven by tides but by a complete spectrum of motions as discussed by *Holloway* [1987]. This may include for example, long and short periods of wind forcing [*Haidvogel and Brink*, 1986].

Whatever the direction of the unsteady forcing flow is, the local mean rectified flow is in a direction such that the shallow water is on the right, facing downstream (in the Northern Hemisphere). In the case of a simple slope, the topographically equivalent β-effect will therefore induce a rectified "westward-equivalent" current. The amplitude of this rectified flow can be a significant fraction of the amplitude of the forcing flow. Consequently, rectification can contribute significantly to mean current systems in the vicinity of the shelf break and, by extension, to the structure of the coastal current system itself.

In the context of tides, *Robinson* [1981] described three possible generation mechanisms for a rectified flow: (i) the change in relative vorticity necessary for the conservation of potential vorticity, (ii) the generation of vorticity when there is lateral shear in a flow, even when the depth is uniform, and (iii) the generation of vorticity due to the shear in the depth distributed friction force when there is a depth variation

in a direction normal to the local velocity. The second mechanism appears only if one adopts a quadratic representation of the bottom friction. Note that depth variation alone, may be sufficient to support rectification. *Zimmerman* [1978] derived the applicable vorticity equation depending on the presence of depth variations and Coriolis and viscous effects. It is seen that rectification requires a phase shift between the vorticity field and the background tidal current.

Among the theoretical studies employing these mechanisms for depth independent models are those of *Huthnance* [1973, 1981], *Zimmerman* [1978, 1980], *Tang and Tee* [1987], *Loder* [1980] and *Loder and Wright* [1985]. *Maas and Zimmerman* [1989a, 1989b] have developed a numerical model for oscillatory, stratified flow normal to infinitesimal shelf breaks. Their resulting along- and cross-isobath residual and tidal circulations and isopycnal elevations have a well-defined localized structure in the cross-isobath vertical plane. More recently, *Chen* [1992] considered numerically the tidal rectification of a stratified ocean in the vicinity of two-dimensional model topography, including a model for Georges Bank, and suggests that stratification plays a significant role in the spatial structure of the rectified currents. *Garreau and Mazé* [1991] developed an interpretative model for their observations near La Chapelle bank in which they indicated that the nonlinear dynamics of an inviscid ocean can act as a flow rectification mechanism.

Motivated by field observations in the vicinity of Fieberling Guyot, *Boyer et al.* [1991] studied the oscillatory motion of a homogeneous, rotating fluid in the vicinity of an isolated topographic feature, both in the laboratory and numerically. The experiments clearly showed that a mean anticyclonic vortex is formed above the topographic feature, and that the spatial and temporal Rossby numbers of the background flow are key parameters for determining the typical trajectories. This analysis was extended to stratified oscillating flows [*Boyer and Zhang*, 1990a, 1990b; *Zhang and Boyer*, 1993]. Little interest seems to have been brought so far to rectification effects associated with the presence of canyons although canyons by themselves have been recognized as having possible important dynamical influences for example in the Mediterranean [*Maso et al.*, 1990].

The purpose of the present study is to explore the flow characteristics, including rectified currents, resulting from a homogeneous, zero-mean, oscillatory motion past over a submerged elongated bank next to a vertical wall boundary and over a canyon in an otherwise infinitely long shelf break of constant cross-section. The general emphasis is on obtaining a better understanding of the motion fields produced by the interaction of oscillatory background motions with idealized topography. But more specific interest is with considering how longitudinal variation of the transverse topographic gradients may be a source of rectification. Both numerical and laboratory approaches are used so that intercomparisons can lead to a deeper understanding of the physical processes involved. So far only numerical computations have been used in the canyon case but laboratory investigations are underway.

Case	Ro	Ro_t	X
1	0.041	0.40	0.32
2	0.041	0.60	0.22
3	0.041	0.80	0.16
4	0.041	1.20	0.11
5	0.081	0.60	0.43
6	0.081	0.80	0.32
7	0.081	1.20	0.21
8	0.081	1.59	0.16
9	0.122	0.60	0.64
10	0.122	0.80	0.48
11	0.122	1.20	0.32
12	0.122	1.59	0.24
13	0.127	0.16	2.50
14	0.139	0.22	2.00
15	0.134	0.28	1.50

Table 1. Dimensionless parameters for the various numerical and laboratory experiments performed over the bank.

The layout of the paper is as follows. In Section 2, the physical and numerical model systems are presented. In Section 3 the results obtained with the bank obstacle are discussed. Section 4 relates the results for the rectified flow over the canyon. Finally in Section 5, general conclusions are being presented.

Model System

Physical and model flow

In this work, we consider the interaction of an oscillating, along-shore current with (i) an elongated topographic bank located along a vertical side wall (Figure 1) and (ii) a canyon cutting an infinite length shelf break (Figure 2). The same bank model was used for both the laboratory and numerical experiments.

The bank. A layer of homogeneous fluid is confined by a rectilinear wall. The depth of this layer is H. The system rotates about a vertical axis with an angular velocity Ω (Coriolis parameter $f = 2\Omega$). A bank, whose maximum height is h_0, is placed along the wall. The horizontal direction along the coast is denoted as x, y is the direction normal to the coast, while z is vertically upward. The origin of this cartesian coordinate system is at the free surface along the coast (wall), at the center of the topographic feature. In the mid-transverse section, the height of the bank is defined as:

$$\begin{aligned} h &= h_0 && 0 < y < D/2 \\ h &= h_0 \cdot cos^2\pi(y - D/2)/D && D/2 < y < D \\ h &= 0 && y > D \end{aligned} \quad (1)$$

But relation (1) also describes the profile for a vertical section at all locations along the perimeter of the bank. The characteristic along-shore dimension, L, is defined as the length of the flat plateau along the coast.

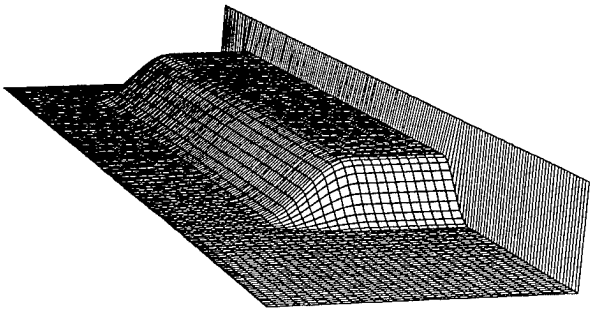


Figure 1. Perspective view of the bank. The forcing flow is parallel to the main bank direction.

The canyon. In this case, we consider a homogeneous fluid which flows over an infinite length shelf break, the height of which is given by

$$\begin{aligned} h &= h_0 & 0 < y < D \\ h &= h_0 \cdot cos^2\pi(y-D)/2D & D < y < 2D \\ h &= 0 & y > 2D \end{aligned}$$

A canyon is present in this shelf break, the horizontal shape of which is also given by a cos^2 profile.

In both situations, an oscillatory current is flowing in the direction parallel to the coast and is defined by

$$U = U_1 \cdot sin(\omega t),$$

where U_1 and ω are the amplitude (uniform in space) and the frequency of the current. The mean forcing velocity during one-half cycle of the flow oscillation

$$\overline{U}_1 = 2/\pi U_1$$

is taken to be the characteristic velocity scale. The width scale of the shelf break, D, is chosen as the characteristic lateral length scale.

It is convenient to characterize the system by the following non-dimensional parameters:

$$\begin{aligned} Ro &= \overline{U}_1/fD, \\ Ro_t &= \omega/f, \\ E_h &= A_h/fD^2, \quad E_v = A_v/fH^2, \\ Fr &= f^2D^2/gH; \end{aligned}$$

i.e. respectively the (spatial) Rossby number, the temporal Rossby number, the horizontal and vertical Ekman numbers and the Froude number. There also geometrical non-dimensional parameters such as the aspect ratios H/D, h_0/D and L/D. A_h and A_v are assumed to be constant eddy viscosity coefficients in the horizontal and vertical dimensions, respectively. In the laboratory, A_h and A_v are taken to be as the kinematic viscosity ν and g is the gravitational acceleration. Note that the Reynolds number can be expressed from the previous numbers as $Re = \overline{U}_1 D/A_h = Ro/E_h$. It is also convenient to define X as the normalized distance travelled by an undisturbed fluid parcel in one-half of a flow cycle

$$X = \pi\overline{U_1}/\omega D = \pi Ro/Ro_t$$

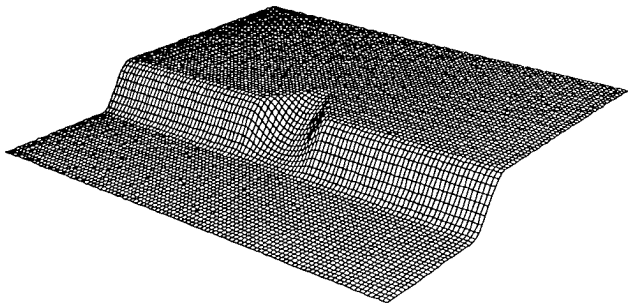


Figure 2. Perspective view of the canyon. The forcing flow is parallel to the main shelf break direction.

The laboratory experiments

The laboratory experiments were carried out on the large rotating table at the Institut de Mécanique de Grenoble. This 14 m diameter rotating platform is equipped with a 13 m diameter, 1.2 m deep cylindrical tank. For the purposes of laboratory convenience, the configurations of Figures 1 and 2 must be adapted to a circular geometry. The obstacle is placed along the wall. Its shape is defined by (1) with $D = 1$ m, $L = 5$ m and $h = 0.3$ m. The tank is filled with fresh water, the total fluid depth of which is $H = 0.35$ m. The background flow is established by oscillating the platform with an angular rotation Ω given by

$$\Omega = \Omega_0 + \Omega_1 \cdot sin(\omega t)$$

with $\Omega_0 = 0.125$ s^{-1} and $\Omega_1 \ll \Omega_0$. Such a system is dynamically equivalent to a current fluctuating over a fixed bottom.

Because $\Omega_1 \ll \Omega_0$ the Coriolis parameter f can be considered as constant and equal to $f = 0.25$ s^{-1}. The inertial period is therefore 25 s and the background rotation period $2\pi/\Omega_0$ is 50 s. Thus we are simulating an oscillatory movement parallel to a coast. The tangential velocity at $r = 6$ m is chosen as the reference velocity, $U_1 = \Omega_1 r$, and then used to define the mean forcing velocity $\overline{U_1}$. The geometrical parameters and the Ekman number are constant in the experiments. The only varied parameters are thus Ro and Ro_t.

In the laboratory, the topographic slope may be exaggerated because H/D is not a similarity parameter. The Froude number, Fr, is such that $Fr \ll 1$ support-

ing the assumption that external gravity waves do not primarily affect the situation under investigation. The Ekman numbers are small and thus viscous effects in the fluid interior, including the shelf slope region, are small away from the lateral boundaries. As discussed by *Pedlosky* [1979], a scale for the relative thickness of the vertical Ekman layer is given by

$$\delta_v/H = E_v^{1/2}$$

Regarding the effect of the side-wall, the same author proposes a scale for the lateral boundary layer thickness (Stewartson layer) as

$$\delta_h/D = E_h^{1/2}/E_v^{1/4}$$

As estimated from the above relations, the side-wall boundary layer is expected to be significantly larger than its bottom counterpart; i.e. $\delta_v \ll \delta_h$. It is clear, however, that in the vicinity of the coastline, the bottom Ekman layer will influence the nature of the flow in that region.

The velocities in the tank were measured at six locations (y = 0.25, 0.5, 0.65, 0.75, 0.85 and 1.1 m) along three radii, at $x = -1.5$, 0 and 1.5 m, at $z = -2.5$ cm below the free surface. Vertical velocity profiles were also determined for three experimental conditions. The velocities were measured by ultra-sonic current meters. In addition, we recorded the trajectories of surface floats and used image processing to obtain an overall view of the characteristic flow patterns. Dye tracers were also used to visualize the fluid movements and check the general behavior recorded by the current meters and the floats.

The numerical model

The numerical model used is the tri-dimensional primitive equation model introduced by *Haidvogel et al.* [1991] written in its channel configuration version. This model is based on the standard Navier-Stokes equations for a rotating fluid in which the hydrostatic, Boussinesq and incompressibility approximations have been made. In addition, the rigid lid approximation is assumed for filtering external gravity waves. This saves substantial amounts of computing time by permitting larger time steps. This approximation is justified by the smallness of the Froude number, Fr, as noted above. Note that while the rigid lid approximation does not allow the free surface to slope, it can nevertheless accommodate pressure gradients, thus simulating a free-surface slope, in particular cross-stream.

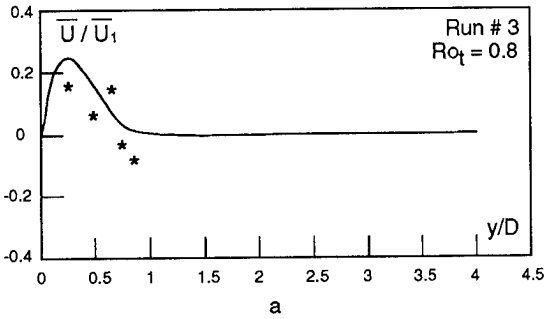
The model system is configured in a channel geometry where L_X and L_Y are respectively the channel length and width. Periodic boundary conditions are applied in the longitudinal direction of the channel. No-slip numerical boundary conditions are applied along the wall next to the bank. For simplicity, a slip condition is assumed on the opposite wall which, in any case, has negligible influence on the flow over the bank. Note that keeping the slip boundary condition on the opposite wall avoids grid refinement in that region and the associated increase in computational cost. In the canyon case, the slip boundary condition was implemented for both channel walls. The possible large downstream extent of the rectified flow induced by the canyon has obliged us to implement a buffer zone at the downstream part of the the channel in order to damp flow perturbations. In the buffer zone, the lateral friction is progressively increased to 10 times the actual fluid viscosity. For this same reason the channel length has also been significantly extended with regard to the bank case.

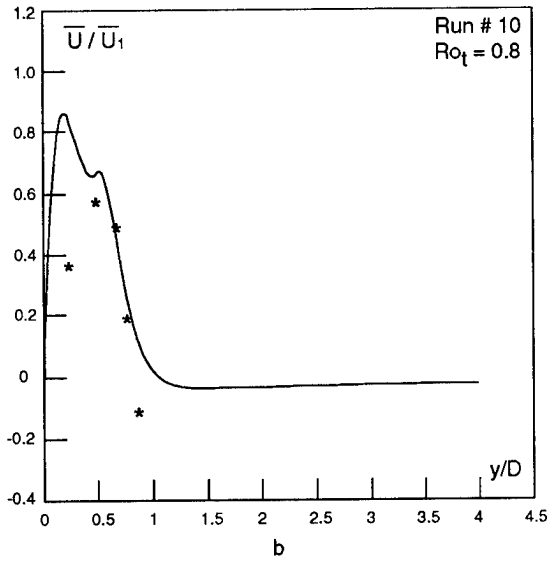
The ability of the *Haidvogel et al.* [1991] model to handle a variable grid was used to refine resolution where needed. It is indeed useful to solve for the nonlinear interactions more precisely in regions where they are expected to be more active. This is the case over the steepest shelf break gradients and along the vertical wall next to the obstacle in the bank case.

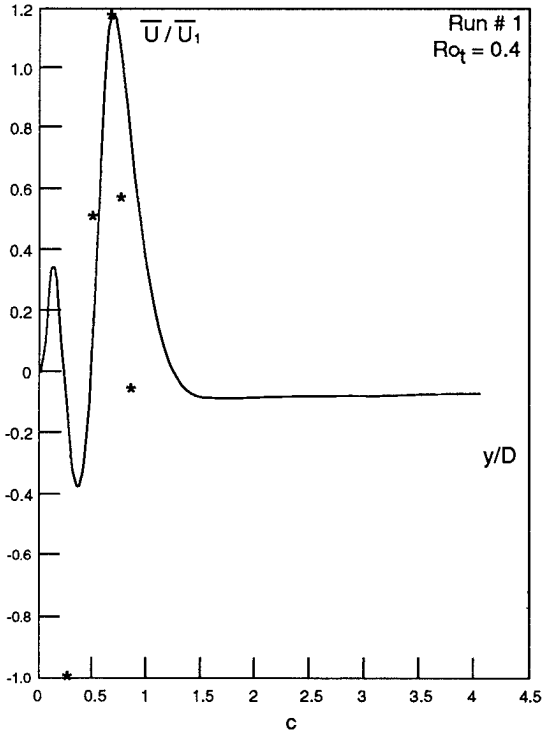
The lateral viscosity coefficient A_h was chosen as $1.3 \times 10^{-4} m^2/s$ leading to a horizontal "numerical" Ekman number of $E_h = A_h/fD^2 = 5.3 \times 10^{-4}$. This choice results from a compromise between having the finest possible grid resolution (and the related smallest possible lateral viscosity required for numerical stability) and conserving computational capabilities. The number above, while significantly larger than the typical Ekman number for the laboratory, is considered as an acceptable order of magnitude for the ocean [*Pedlosky*, 1979]. Since we assume no bottom friction and no vertical friction in the fluid interior, the vertical eddy viscosity coefficient, A_v, is zero.

The numerical model employed a channel domain with limited streamwise and crossstream extent. The channel dimensions were chosen in order that neither the opposite wall nor the channel extremities significantly influenced the flow in the regions of interest.

The parameters used, apart from viscosity, are identical to the ones in the laboratory experiments: $H = 0.35\ m$, $h_0 = 0.30\ m$ and $f = 0.25\ s^{-1}$. The length of the bank is $L = 5\ m$ and the one of the canyon $L = 1\ m$. The width of the bank is such as $D = 1\ m$ and for the canyon $D = 0.5\ m$. For the bank, we choose $L_X = 20\ m$. A width of $L_Y = 4\ m$ was found to be sufficient to ensure that the "deep ocean" side wall did not perturb the flow in the vicinity of the topographic feature. For the canyon, we choose $L_X = 15\ m$ and $L_Y = 4\ m$.







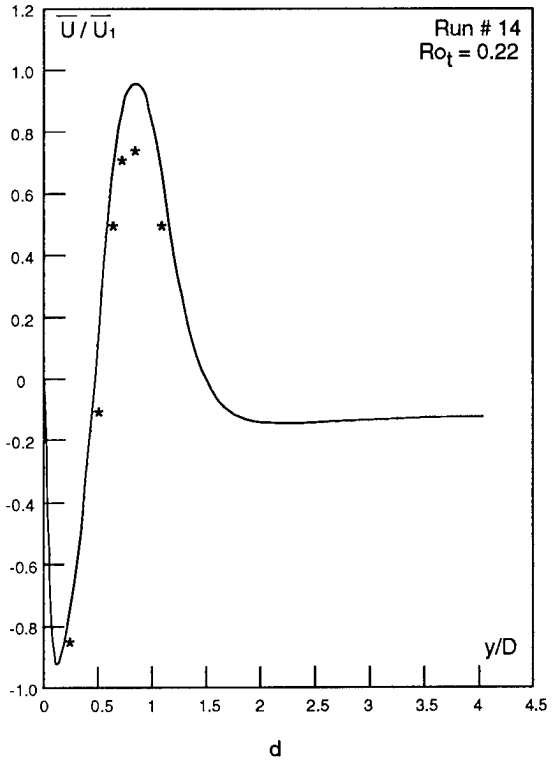


Figure 3. Typical velocity profiles $\overline{U}/\overline{U_1}$ in the mid-section. Runs # 3 (a), # 10 (b), # 1 (c) and # 14 (d). Computed values are shown by a solid line, laboratory measurements are indicated by stars.

The Bank Case

Fifteen experiments were performed, the conditions of which are indicated in Table 1.

In analyzing the results, attention was directed mainly to characterizing the flow based on the general nature of the rectified currents. Comparisons between the laboratory flows and the numerical computations were made for all the 15 experiments.

It was found convenient first to define the various characteristic flows in terms of the mid-section profiles of the streamwise rectified velocity component near the free surface. Figures 3a-d show some examples for Runs # 3, 10, 1 and 14, respectively. These plots present the computed (solid line) and measured (stars) u-components of the normalized residual current $\overline{U}/\overline{U_1}$ along the mid-section ($x = 0$), at $z = 2.5$ cm below the free surface. The scale is identical for all graphs. We note that, for the most part, there is good qualitative agreement between the numerical results and the laboratory experiments. It was observed that the dimensional rectified velocities measured in the laboratory may be very small; in Run # 3 for example, the maximum velocity is 1.6 mms^{-1}. The following typical flow regimes were defined after examining the various profiles:

- A "tips" flow regime. This flow is characterized by (i) a broad rectified flow $\overline{U}/\overline{U_1} < O(1)$ towards positive-x over the shelf and slope region (i.e. $0 < y/D < 1$) and (ii) a weak flow toward negative-x for $y/D > 1$, see Figures 3a, b.
- A "bank" flow regime. This flow is characterized by (i) a rectified current toward negative-x over the plateau, (ii) a current toward positive-x near the slope and over the near deep ocean region and (iii) a weak negative-x flow for $y/D > 1.5$, see Figure 3d.
- A transitional flow regime in which the flow is characterized along $y/D = 0$ by (i) a narrow rectified current toward positive-x along the coast, (ii) a narrow current toward negative-x on the plateau to the left of the shelf break, (iii) a strong flow toward positive-x over the slope region and (iv) a weak negative-x flow for $y/D > 1$, see Figure 3c. Along $y/D = 1.5$, the profile is the same as that along $y/D = 0$ for the bank flow regime, and along $y/D = -1.5$ it is the same as that corresponding to $y/D = 0$ for the tips flow regime.

Figures 4 a-b are typical plots of the model, horizontal, rectified velocity field for the tips and bank flow regimes, respectively. Figure 4a for the tips regime

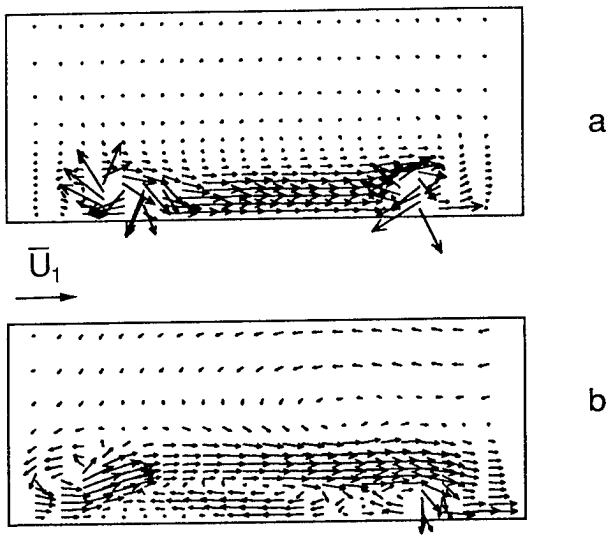


Figure 4. Examples of model horizontal velocity fields in typical tips (Run #6) and bank (Run #13) flow regimes. (The actual computational domain is larger than the ones focused on here).

(Run # 6) shows that the rectified flow for the major portion of the ridge is uni-directional towards positive-x, while strong anticyclonic eddy structures are located over the tips of the topography. In Figure 4b for the bank flow regime (Run # 13), on the other hand, the rectified flow shows a strong anticyclonic cell over the plateau and slope region, with cyclonic and anticyclonic eddy structures above the left and right tips of the topography respectively.

The vertical structure of the flow was assessed in the laboratory by measuring the time-dependent horizontal velocity as a function of depth at selected locations. The principal conclusion is that the rectified flow, within experimental error, is roughly independent of height. This also validates the model approximation of a homogeneous vertical structure.

First and foremost we found that, considering the complexity of the physical system addressed and the simplifications used in the numerical model, there is fairly good agreement between the laboratory and numerical experiments.

The study raises the consideration of the origin of the rectified current. The possible mechanisms for flow rectification are the effect of the bathymetric variation and the frictional effects. It will be recalled that bottom friction was neglected in the numerical model and thus that frictional effects enter the numerics only by lateral friction. The good agreement between the laboratory and numerical experiments suggest that bottom friction is thus proven not to be an essential ingredient of the rectification process observed in the laboratory. Moreover, scaling arguments led us to hypothesize that lateral friction is also not of leading order importance away from the wall. Bathymetric variation alone would thus appear to be the main causal factor for the observed rectified currents. Thus, in a similar way as in *Boyer et al.* [1991], the production of relative vorticity induced by bathymetric change may account for most of the rectified current.

It is of particular interest to look at the maximum values of the rectified current in the different cases with respect to the non-dimensional controlling parameters. Figure 5a shows a plot of the normalized maximum rectified current in the positive-x direction $\overline{U}_{\max}/\overline{U_1}$ as a function of Ro_t^{-1} for both the laboratory and the numerical experiments. Again good agreement is seen between the laboratory and the numerical results, although the latter are often larger. The data in Figure 5a from this limited experimental program strongly suggest that the principal parameter determining the qualitative nature of the resulting flow fields is the temporal Rossby number, Ro_t. Some of the data scatter is due to the fact that the observable $\overline{U}_{\max}/\overline{U_1}$ is also a function of Ro. Interestingly, it appears that the quantity $\overline{U}_{\max}/\overline{U_1}$ is maximum when $Ro_t^{-1} \approx 1.7$, i.e. when the forcing period is approximately twice the inertial period.

Figure 5b presents the same quantity $\overline{U}_{\max}/\overline{U_1}$ as a function of X, the normalized flow excursion during one half of the oscillatory cycle. The data collapse is similar to that of Figure 5a. Because $X \sim Ro/Ro_t$ this reinforces the fact that Ro is playing a limited role and provides additional support for the idea that the

principal governing parameter is Ro_t^{-1}. Figure 5b also reveals that the rectified velocity maximum occurs for $X \approx 0.5$, i.e., when the flow excursion approximates the width of the slope region.

Two different types of behavior can further be identified on Figures 5a and 5b: (i) a range for which the rectified velocity increases approximately linearly with Ro_t^{-1} and X ($0 < Ro_t^{-1} < 2$; $0 < X < 0.5$) and (ii) a range in which the velocity decreases with Ro_t^{-1} and X ($Ro_t^{-1} > 2$; $X > 0.5$). Within the range of parameters being investigated, the maximum velocity reached in the mid-section is about 1.5 $\overline{U_1}$, which is approximately equal to $\pi/2 \cdot \overline{U_1} = U_1$. No rectified flows exceeding U_1 were found in any of the experiments at any location. The maximum amplitude of the rectified flow seems therefore constrained in all cases by $\overline{U} < U_1$, i.e., by the maximum amplitude of the incident forcing flow. Note that this maximum value is reached approximately at the transition point between the tips and bank flow regimes.

Using all these results it was possible to classify the experiments of Table 1 according to the previous general definitions and to draw a flow regime diagram in (Ro_t, Ro) parameter space (Figure 6). The respective run numbers are also indicated with reference to Table 1. This diagram clearly shows the dominance of Ro_t in determining flow regimes.

Figure 7 summarizes the way in which maximum normalized rectified velocity $\overline{U}_{\max}/\overline{U_1}$ in the mid-section $x = 0$, varies in (Ro, Ro_t) parameter space. As in Figure 5a, it shows that the rectified flow amplitude has a maximum for $Ro_t \approx 0.5$, i.e., when the forcing flow oscillation is twice the inertial period.

A number of remarks may usefully be made about the so-called tips and bank flow regimes. As stated earlier, for the largest values of Ro_t, we observe the tips flow regime in which the rectified flow in the mid-bank portion is very weak. This is consistent with previous studies showing that rectification does not occur in the along-shore direction for an along-shore oscillatory current along a coastline of uniform cross-section. In the absence of other mechanisms, such as non-linear bottom friction, an infinite length obstacle like this will not give rise to any rectification [*Haidvogel and Brink*, 1986]. This result was checked numerically in the present case by extending the obstacle length L to infinity. This can also be seen simply as a consequence of simple analytical considerations (see e.g. *Verron et al.*, 1994), which suggest no rectification from an oscillatory flow parallel to the bank slope.

The basic rectification processes over the bank could therefore be interpreted as follows. The longitudinal variations of the transverse bathymetric gradients where they exist (tips) initiate local rectification ($U.\nabla H \neq 0$) and, where they are absent (mid-bank slope) local rectification is also lacking ($U.\nabla H = 0$). Thus, when the flow excursion is at the scale of the tips ($X \sim D$),

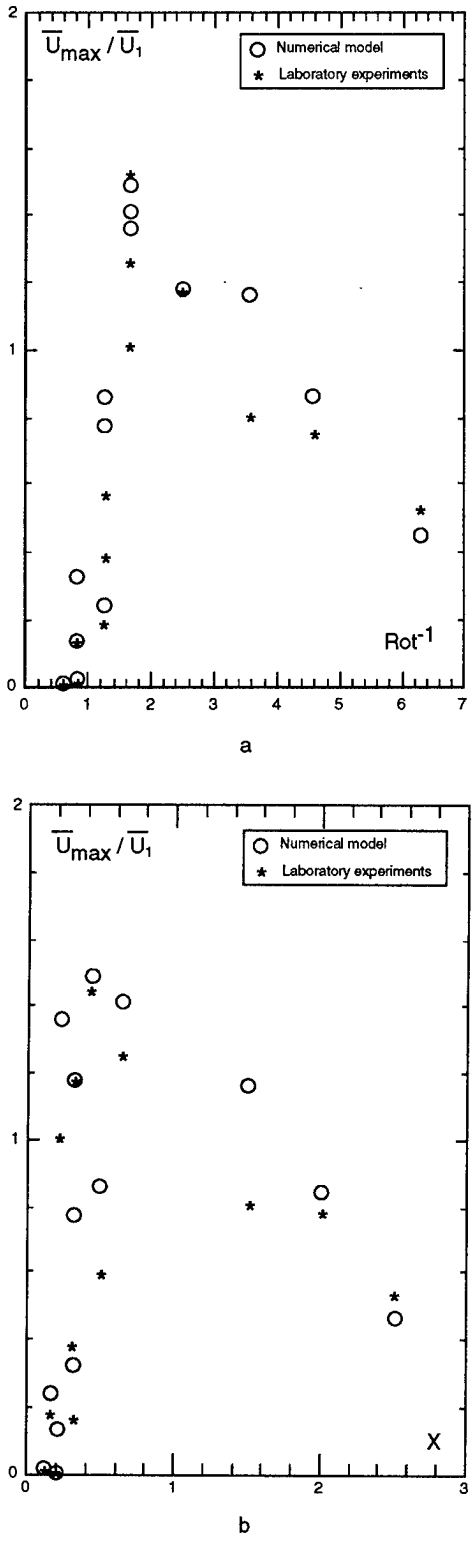


Figure 5. Maximum rectified velocity in the mid-section as a function of Ro_t^{-1} (a) and X (b).

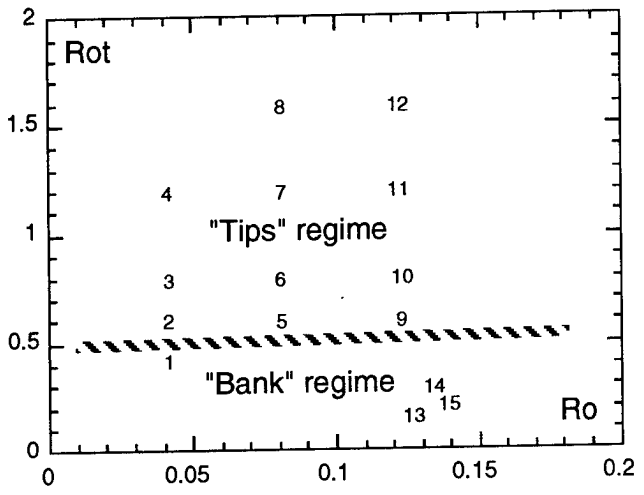


Figure 6. Flow regime diagram in the (Ro, Ro_t) parameter space.

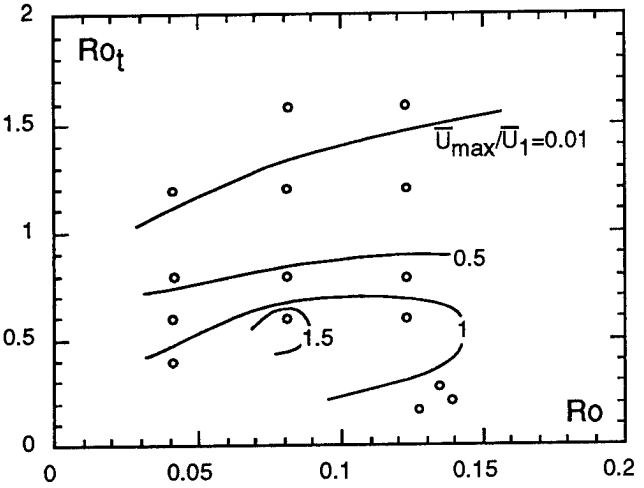


Figure 7. Maximum rectified velocity in the mid-section in the (Ro, Ro_t) parameter space.

rectification stays confined to the tips and remains weak at mid-bank. For such cases, the tips flow regime is observed. When the flow excursion is at the scale of the characteristic streamwise length of the bank ($X \sim L$), the rectifying effects of the tips are sufficient for the whole bank to be taken over. The bank flow regime is then observed. In a word, one could say that longshore rectified currents are present only because the bank has tips.

This study indicates the importance of along-shore variations in the shelf break geometry. It suggests that off-shore canyons and ridges will strongly affect the rectification patterns resulting from along-shore oscillatory currents and motivates the second part of this investigation over a simplified canyon feature.

The Canyon Case

We have investigated 16 situations corresponding to the sets of controlling parameters indicated in Table 2.

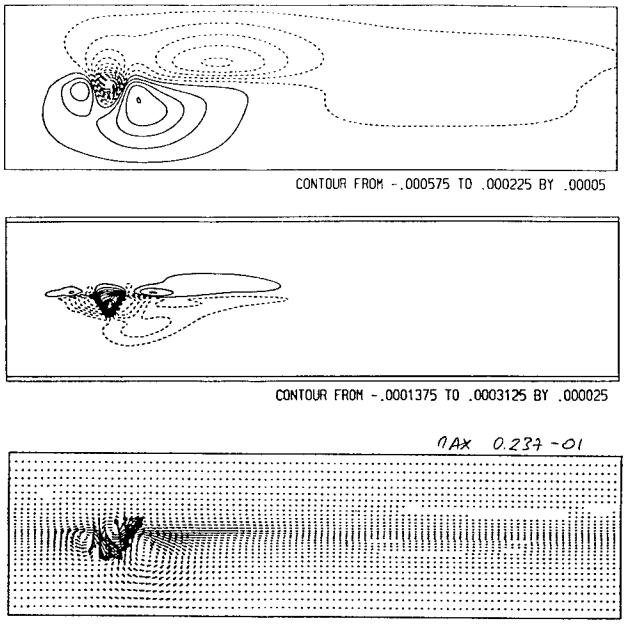
Figures 8a and 8b show typical situations observed in the study. For each figure, the mean streamfunction and vorticity patterns are shown as well as the mean velocity vectors pattern. A general description of the flow pattern can be made looking at the velocity vectors and is globally valid for all cases: a rectified flow is generated along the longitudinal direction of the shelf break. This

Case	Ro	Ro_t	X
1	0.05	0.25	0.628
2	0.10	0.25	1.257
3	0.15	0.25	1.885
4	0.20	0.25	2.513
5	0.05	0.50	0.314
6	0.10	0.50	0.628
7	0.15	0.50	0.942
8	0.20	0.50	1.257
9	0.05	0.75	0.209
10	0.10	0.75	0.419
11	0.15	0.75	0.628
12	0.20	0.75	0.838
13	0.05	1.00	0.157
14	0.10	1.00	0.314
15	0.15	1.00	0.471
16	0.20	1.00	0.628

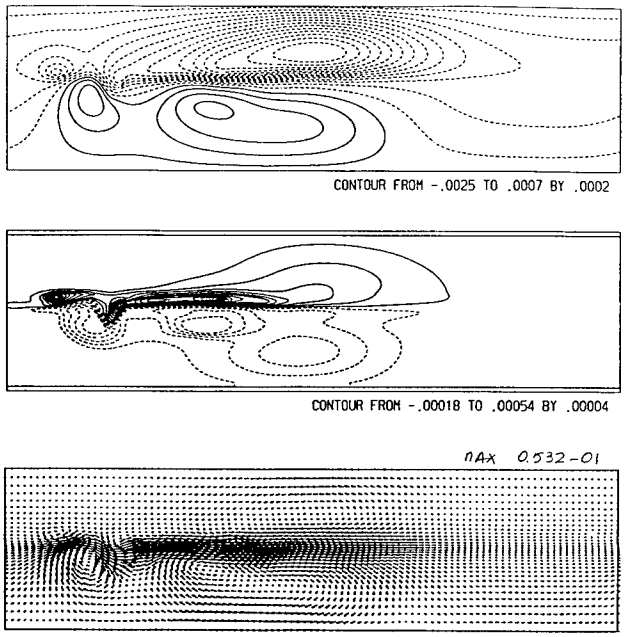
Table 2. Dimensionless parameters for the various numerical experiments over the canyon.

rectified flow has a mean direction meandering over the canyon area, first towards the abysses, then towards the shelf, then back to the abysses, to finally stay more or less rectilinear, parallel to the shelf break and mostly confined at the upper part of the break. The current meandering over the canyon is more or less in spatial phase with the canyon structure. The intensity of the rectified flow is strongly dependent on the flow parameters. The mean flow meandering pattern corresponds to a succession of alternating eddies, positive, negative and positive, over the canyon region. The intensities of these eddies and their precise positions with regard to the canyon are a function of the flow parameters.

The most noticeable dynamical feature in many situations is the existence of a downstream mean current along the shelf break which can radiate in some cases far from the canyon area. Figure 9 presents one example of the section of the rectified current velocity one meter downstream the middle of the canyon. The velocity profile in all cases is very much centered at the top part of the shelf break, i.e. at the location where the topographic height is decreasing. This profile is rather sharp. An horizontal width scale based on the e-folding factor would be something like the canyon scale D. It



(a)



(b)

Figure 8. Examples of mean rectified streamfunction, vorticity and velocity fields over the canyon for Run # 16 (a) and Run # 3 (b).

is also noted that a small transverse asymmetry in the velocity profile is observed with the increase of Ro_t.

It is possible in particular to analyse the variation of the rectified current maximum velocity induced over the canyon (sections performed right in the middle of the canyon) and one meter downstream. The results are shown in Figures 10a and 10b, respectively, as a function of Ro_t^{-1}. The data scatter with regard to Ro_t

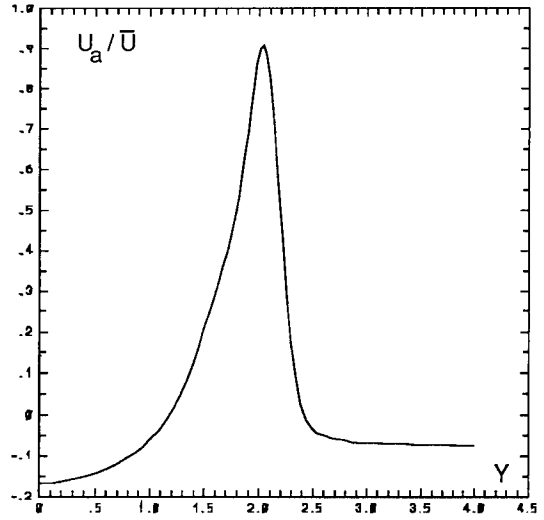


Figure 9. Example of mean rectified velocity transversal profile at a distance of one m downstream of the middle of the canyon for Run # 3.

is relatively large which would show that Ro_t is not as clearly the leading parameter for the rectified flow amplitude as in the bank problem. Things must however be said cautiously. Indeed, data scatter is most important in the case of the mid-canyon rectified flow rather than in the case of the downstream rectified flow. The mean flow pattern within the canyon is rather complex and the averaging procedure may have residuals due to insufficient convergence. Conversely, the flow pattern downstream has a more stable configuration and may be of greater interest. The downstream maximum flow amplitude is more satisfactorily described in terms of the parameter Ro_t although some noticeable impact of Ro is visible.

With regard to the control parameter R_0, Figure 11 shows that the velocity maximum amplitude for the downstream flow reveals two main things: (i) there are clearly two main regimes of rectified flow intensities, a "slow" downstream rectified flow for the largest values of Ro_t ($Ro_t = 0.75$ and 1.00) and a "fast" downstream rectified flow for the smallest values of Ro_t ($Ro_t = 0.25$ and 0.50), (ii) for the "slow" regimes, the velocity amplitude increases with Ro while, for the "fast" regimes, the velocity amplitude roughly decreases with Ro. Note that, similar to the bank case, the rectified flow intensity can be as large as the forcing. By looking at all of the data obtained, it is tempting to say that, similar to the bank problem, there are two rectified flow regimes over the canyon:

- a "local" regime in which the rectified flow is roughly confined to the canyon area without really affecting neighbouring regions (analogous to the "tips" regime),

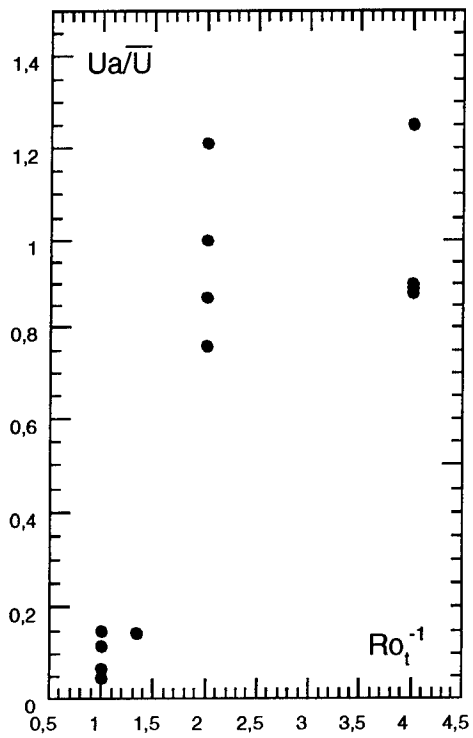


Figure 10. Maximum rectified velocity as a function of the temporal Rossby number Ro_t at a distance of oneone m downstream of the middle of the canyon (a) and at mid-canyon (b).

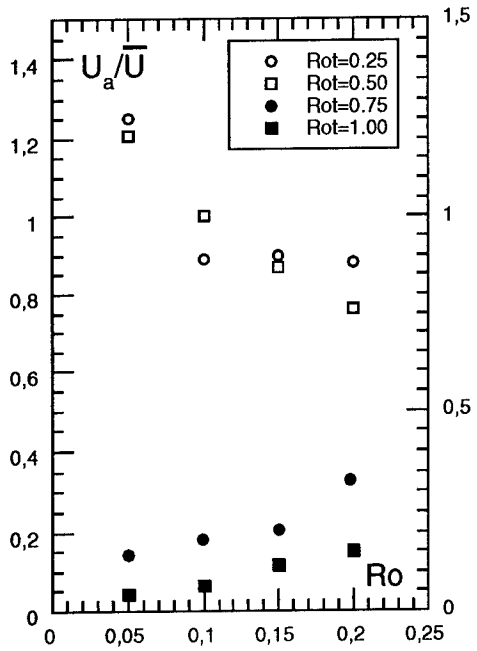


Figure 11. Maximum rectified velocity as a function of the Rossby number R_0 at a distance of one one m downstream of the middle of the canyon.

- a "non-local" regime in which the rectified flow due to the canyon extends away from the originating area (analogous to the "bank" regime).

This non-local regime is clearly of much interest since it would indicate that a canyon of limited geographical extent may have influence at large distances. Figure 12 focusses more information on this point by plotting the approximate length of penetration of the rectified flow pattern (non-dimensionalized by D) in the controlling parameter space. This penetration length, L_P, is measured from the middle axis of the canyon and is estimated approximately from the mean streamfunction/vorticity pictures for all cases. The larger Ro_t (and smaller Ro) correspond to the smallest values of L_P/D, i.e. to the "local" regime. One must be cautious when considering the largest L_P/D since the "buffer zone" employed in the model for treating the open boundary condition problem as already mentioned, may spuriously damp the downstream penetration at large distances.

Conclusions

Firstly, the interaction between an along-shore oscillatory current and an elongated bank placed along a vertical wall was investigated by means of laboratory and numerical experiments. The main conclusions focus on the intense rectified currents which are observed

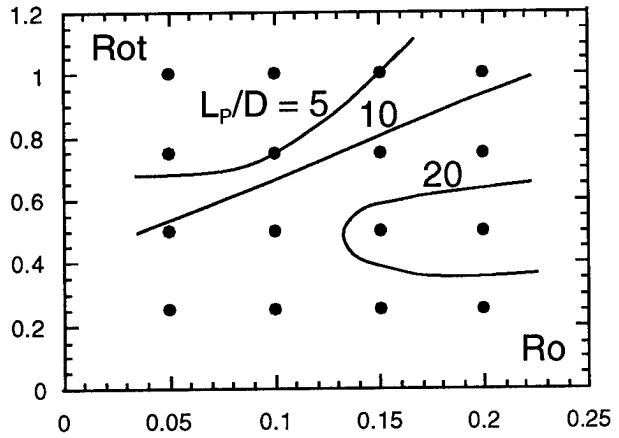


Figure 12. Approximate length of penetration for the rectified mean current over the canyon in the (Ro, Ro_t) parameter space.

over the bank and along the coast. These rectified currents are mainly controlled by the topographic influences of the tips; i.e. by the most significant longitudinal variations of the transverse topographic gradients. The study has demonstrated the crucial role of the temporal Rossby number in determining the general nature of the characteristic flow patterns. For large Ro_t, one observes the tips regime in which the rectified flow over the mid-bank is unidirectional, but relatively weak. For small Ro_t, one obtains a relatively strong anticyclonic rectified flow pattern over the entire topographic feature, i.e., the flow near the mid-bank has the coastline on the right over the shelf break, but reverses in direction near the coast.

Secondly, the interactions between an along-shore oscillatory current and a canyon in an otherwise long shelf break of constant cross section was investigated by numerical simulations. The main conclusion focuses on the possible large, downstream (i.e. with the shallow fluid on the right), range of action that the canyon may have in terms of rectification. The horizontal scale associated with the rectified mean current penetration may for example be typically of one order of magnitude larger than the horizontal scale of the canyon itself. This may have important physical consequences as it shows that through the process of rectification, a simple canyon topographical irregularity may have large distance effects. Two flow regimes were observed which have strong similarities with the "tips" and "bank" regimes. The controlling parameter is mainly Ro_t as it was also in the case of the bank. But the influence of Ro is, however, more clearly sensitive here. As in the bank case, the intensity of the rectified current may be of the order of the amplitude of the forcing current. A tidal forcing velocity may for example generate a mean rectified current of the same velocity amplitude.

The complex role of bottom boundary layers has not been investigated (and lateral boundary for the bank situation) and is therefore not well-understood at this time. The good agreement between the laboratory experiments and the numerical model in the first part of the present study, however, suggests that the present model is dominated by topographic effects and thus captures most of the physics involved in the rectification process. The present study has also neglected stratification effects which should be considered to be important in most oceanic applications. Although the present models are crude representations of real flows, it is suggested that the basic mechanisms leading to flow rectification are representative of physical mechanisms at work in nature.

Acknowledgments. This work was supported by the Centre National de la Recherche Scientifique (CNRS-INSU). The calculations were made possible by the numerical facilities of the Centre de Calcul Vectoriel pour la Recherche in Palaiseau. The support of the Ocean Sciences Division of the U.S. National Science Fundation is also acknowleged.

References

Boyer, D.L. and Zhang, X., 1990a: The interaction of time-dependent rotating and stratified flow with isolated topography, *Dyn. Atmos. Oceans*, 14, 543-575.

Boyer, D.L. and Zhang, X., 1990b: Motion of oscillatory currents past isolated topography *J. Phys. Oceanog.*, 20, 1425-1448.

Boyer D.L., G. Chabert d'Hières, H. Didelle, J. Verron, R.R. Chen and L. Tao, 1991: Laboratory simulations of tidal rectification over seamounts: homogeneous model. *J. Phys. Oceanogr.*, (21) 10, 15559-1579.

Brylinski, J.M. and Lagadeuc, YL, 1990, The inshore/offshore waters interface off the French coast in Dover Strait: a frontal area, *C.R. Acad. Sci. Paris*, t. 311, Serie II, 535-540

Butman B., R.C. Beardsley, B. Magnell, D. Frye, J.A. Vermesch, R. Schlitz, R. Limeburner, W.R. Wright and M.A. Noble, 1982: Recent observations of the mean circulation on Georges bank. *J. Phys. Oceanogr.*, 12, 569-591.

Chen, C., 1992, Variability of current in Great South Channel and over Georges Bank: observations and modelling, Ph.D. Dissertation, Massachusetts Institute of Technology and Woods Hole Oceanographic Institution, 283 pages

Ericksen, C. 1991, Observations of amplified flows atop a large seamount, *J. Geophys. Res.*, 96 (C8), 15.227-15.236

Garreau P. and R. Mazé, 1992: Tidal rectification and mass transport over a shelf break: a barotropic frictionless model. *J. Phys. Oceanogr.*, 22 (7), 719-731.

Genin, A., Noble, M. and Lonsdale, P.F., 1989, Tidal currents and anticyclonic motions on two North Pacific seamounts, *Deep-Sea Res.*, 36, 1803-1816

Haidvogel D. B. and K. H. Brink, 1986: Mean currents driven by topographic drag over the continental shelf and slope., *J. Phys. Oceanogr.*, 16, 2159-2171.

Haidvogel D. B., J. Wilkin and R. Young, 1991. A semi-spectral primitive equation ocean circulation model using vertical sigma and orthogonal curvilinear horizontal coordinates. *J. Comp. Phys.*, 94, 151-185.

Holloway G., 1987: Systematic forcing of large scale geophysical flows by eddy-topography interaction. *J. Fluid Mechanics*, 184, 463-476.

Huthnance, J.M., 1973, Tidal current asymmetries over the Norfolk Sandbanks, *Estuarine and Coastal Marine Science*, 1, 89-99

Huthnance, J.M., 1981, On mass transports generated by tides and long waves, *J. Fluid Mech.*, 102, 367-387

Loder, J.W., 1980, Topographic rectification of tidal currents on the sides of Georges Bank, *J. Phys. Ocean.*, 10, 1399-1416

Loder, J.W. and Wright, D.G., 1985, Tidal rectification and frontal circulation on the sides od Georges Bank, *J. Mar. Res.*, 43, 581-604

Maas, L.R.M. and van Haren, J.J.M., 1987, Observations on the vertical structures of tidal and inertial currents in the North Sea, *J. Mar. Res.*, 45, 293-318

Maas, L.R.M. and Zimmerman, J.T.F., 1989a, Tide-topography interactions in a stratified shelf sea: I- Basic equations for quasi-nonlinear internal tides, *Geophys. Astrophys. Fluid Dyn.*, 45, 1-35

Maas, L.R.M. and Zimmerman, J.T.F., 1989b, Tide-topography interactions in a stratified shelf sea: II- Bottom trapped internal tides and baroclinic residual currents, *Geophys. Astrophys. Fluid Dyn.*, 45, 37-69

Maso M., P. E. La Violette and J. Tintore, 1990: Coastal flows modificiation by submarine canyons along the NE Spanish coast. *Sci. Mar.*, 54 (4), 343-348.

Pedlosky J., 1979: Geophysical fluid dynamics. Springer-Verlag. New York Heidelberg Berlin.

Pingree, R.D. and Le Cann, B., 1990, Structure, strength and seasonality of the slope currents in the vicinity of the Bay of Biscay region, *J. Mar. Biol. Ass. U. K.*, 70, 857-885

Robinson I.S., 1981: Tidal vorticity and residual circulation. *Deep Sea Research*, 28 A, 3, 195-212.

Stommel, H., 1954, Serial observations of drift currents in the Central North Atlantic Ocean, *Tellus*, 6, 204-214

Tang, Y. and K.T. Tee, 1987, Effects of mean current interaction on the tidally induced residual current, *J. Phys. Oceanog.*, 17, 215-230

Tee, K.T., 1985, Depth-dependent studies of tidally induced residual currents on the sides of Georges Bank, *J. Phys. Oceanog.*, 15, 1818-1846

Verron J., D. Renouard, D. L. Boyer, G. Chabert d'Hières, T. Nguyen and H. Didelle, 1995: Rectified flows over an elongated topographic feature along a vertical wall. To appear in the *J. Phys. Oceanog.*

Wright, D.G. and Loder, J.W., 1985, A depth dependent study of the topographic rectification of tidal currents, *Geophys. Astrophys. Fluid Dyn.*, 31, 169- 220

Zhang, X. and Boyer, D.L., 1993, Laboratory study of rotating, stratified, oscillatory flow over a seamount, *J. Phys. Oceanog.*, 23, 1122-1141

Zimmerman J.T.F., 1978: Topographic generation of residual circulation by oscillatory (tidal) currents. *Geophys. Astrophys. Fluid Dynamics*, 11, 35-47.

Zimmerman, J.T.F., 1980, Vorticity transfer by tidal currents over an irregular topography, *J. Mar. Res.*, 38, 601-630

Wind-Driven Residual Currents over a Coastal Canyon

D.B. Haidvogel

Institute of Marine and Coastal Sciences, Rutgers University, P.O. Box 231, New Brunswick, NJ 08903-0231, USA

A. Beckmann

Alfred Wegener Institute for Polar and Marine Research, Am Handelshafen 12, D-27570 Bremerhaven, F.R.Germany

Abstract. Systematic form stress forces can drive mean currents of observable magnitude in the coastal ocean; however, the resulting mean momentum balances are non-linear and solutions, even to simplified form stress problems, must be obtained numerically. Here we ask: what time-mean circulation patterns are produced by an oscillatory wind stress in a coastal ocean featuring a steep coastal canyon intersecting an otherwise smoothly varying continental shelf/slope? Five coastal models of differing algorithmic design are asked to provide answers to this question. If the coastal ocean is homogeneous, the five models give qualitatively similar results—i.e., residual circulation in the sense of intrinsic shelf wave propagation; however, the results are in quantitative disagreement by almost an order of magnitude. If the coastal ocean is stratified, the models are also in qualitative disagreement. Two factors which appear related to these disparities are model vertical coordinate and subgridscale parameterization.

Introduction

Both simplified numerical process studies and statistical mechanical considerations suggest that topographic form stress may contribute significantly to the maintenance of the observed time-mean circulations on and near continental shelves (Haidvogel and Brink, 1986; Holloway et al., 1989). Here we explore the effects of form stress in a topographically irregular coastal channel driven by a time-varying, along-channel wind stress. The topographic irregularity is provided by a steep, cross-shelf canyon, superimposed on a smooth continental shelf/slope profile.

Because non-linearity is important, solutions to the form stress problem are sought numerically using several readily available coastal models. The models include at least one drawn from each vertical coordinate model class (z, sigma, isopycnal). Both low- and high-order numerical algorithms are represented among those tested. The models include the well-known Geophysical Fluid Dynamics Laboratory Modular Ocean Model (GFDLM; Bryan, 1969; Cox, 1984), the Miami Isopycnic Coordinate Ocean Model (MICOM; Bleck et al., 1992), the Princeton Ocean Model (POM; Blumberg and Mellor, 1987), the Spectral Element Model of Iskandarani and colleagues (SEM; Iskandarani et al., 1995), and the SPEM model (Haidvogel et al., 1991; Hedstrom, 1994).

A schematic diagram of the experimental configuration is shown in Figure 1. The geometry is annular, that is, a coastal channel periodic in the x direction, bounded by two (inshore and offshore) walls. The channel dimensions are L_x = 128 × L_y = 96 km. The topography is a continental shelf increasing in depth with cross channel distance intersected by an isolated and idealized canyon:

$$h(x,y) = H_{min} + \frac{1}{2}(H_{max} - H_{min}) \cdot (1 + \tanh(y - Y_c / L_s))$$

with

$$Y_c = Y_0 - L_c \sin^{24}(\pi x / L_x)$$

and H_{min} = 20 m, H_{max} = 4000 m, Y_0 = 32 km, L_s = 10 km, and L_c = 16 km. The resulting topography is both tall (20 m to 4000 m) and steep (maximum slope 30%).

The circulation in the coastal channel is driven by an along-shore wind stress, applied as a body force acting uniformly over the water column:

$$\tau^x = \tau_o \cdot \frac{1}{2}(1 - \tanh((y - \frac{1}{2}L_y)/L_w))$$

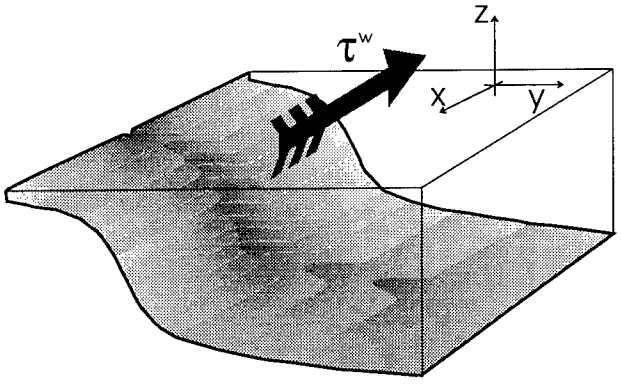


Figure 1. Schematic diagram of the coastal canyon.

with a periodically varying amplitude of

$$\tau_o = 10^{-4} \sin(2\pi t / T_w) \quad \text{Pa kg}^{-1}\text{m}^3$$

with L_w = 10 km and T_w =10 days. Common to all experiments are the constant rate of rotation $f = 1 \cdot 10^{-4}$ m s^{-1}, the gravitational constant $g = 9.81$ m s^{-2}, and a linear bottom stress coefficient $r_B = 3\ 10^{-4}$ m s^{-1}. (Bottom stress is also taken to act uniformly with depth.) Initialized from rest, all runs are carried out to day 120; the last 30 days ($90 < t \leq 120$ days) are averaged to give time-mean fields. Integrations of longer duration (out to day 500) produce slight changes in the time-mean currents; however, the changes are small compared to the differences among individual sets of model results.

Results

The time-mean momentum balance in this fluid system is expected to be intrinsically non-linear (Haidvogel and Brink, 1986). This, together with the deterministic, yet nonetheless complicated, topographic profile, precludes a simple analytic solution. Despite the absence of a known analytical solution, however, we can intercompare the model solutions and assess model-to-model differences. Three bulk measures of model output are discussed here: the maximum pointwise residual (time-mean) current speed at the surface (maximum of $\overline{|\vec{v}(z=0)|}^t$), the maximum residual along-channel averaged current (maximum of $\bar{u}^{xt}$), and the net residual transport through the channel (across-channel integral of $\overline{hu}^{xt}$. These bulk measures are reported for each model in Table 1.

Since the problem as posed is homogeneous, and forced and damped in a depth-independent manner, the flow is expected to remain depth-independent. In principle, therefore, only a single degree of freedom is necessary to represent the vertical structure. Of the models appearing in Table 1, all but one can accommodate the geometry of the coastal channel with a single (or at most a small number of) vertical degrees of freedom. Both the isopycnal and terrain-following models (MICOM, POM, SEM and SPEM) have this capability. The remaining model (GFDLM), being z-coordinate, must represent the irregular topography as a number of steps. Table 1 shows GFDLM results for a total of 10, 20, and 40 levels.

All models require a finite value of lateral viscosity in order to produce smooth, stable results. To insure maximum intercomparability, three of the models (MICOM, SEM and SPEM) have been run with identical sub-gridscale closures (harmonic viscous operators with a constant lateral viscosity coefficient of 5 m^2/s). (Lower values of viscosity produce noisy results in all models.) The GFDLM results were also obtained using a harmonic closure; however, a higher value of viscosity (15 m^2/s) was required for stability. The POM model employed a Smagorinsky formulation (adjustable constant = 0.2). Accompanying these finite values of lateral viscosity, the models are required to impose a lateral boundary condition on horizontal velocity. Since free-slip (no lateral stress) boundary conditions are troublesome to implement on the B-grid GFDLM code, a mixture of free- and no-slip experiments were carried out.

The time step values used in the models (Table 1) roughly reflect the CFL constraints on each. The free sea surface models, with their explicit treatment of surface gravity waves, require quite short time steps, while the two rigid lid models can be run with time step increases of two orders of magnitude.

Table 1. Model intercomparison for the homogeneous form stress experiment.

Model	vertical deg. of freedom	lateral viscosity [m^2/s]	time step [s]	lateral boundary condition	max. $\overline{\lvert\vec{v}(z=0)\rvert}^t$ [cm/s]	max. $\bar{u}^{xt}$ [cm/s]	net transp. [Sv]	comments
GFDLM	40	15	432	no slip	6.7	1.7	0.060	
	20	15	432	no slip	6.9	1.9	0.096	
	10	15	432	no slip	6.0	1.4	0.068	
MICOM	1	5	2	free slip	14.6	3.4	0.231	
	1	5	2	no slip	20.3	1.4	0.142	
POM	5	---	30	free slip	4.6	2.0	0.050	0.2 SM
SEM	1	5	1	free slip	14.6	4.1	0.309	
	1	5	1	no slip	8.7	2.5	0.404	
	1		$\frac{1}{2}$	free slip	16.9	4.2	0.305	$\frac{1}{2}\Delta x$
	1	1	$\frac{1}{2}$	free slip	19.0	4.3	0.231	$\frac{1}{2}$
SPEM	2	5	864	free slip	12.0	3.8	0.250	
	2	5	864	no slip	10.7	3.20	0.240	

Reassuringly, all five models produce residual circulations with the expected overall character—that is, time-mean currents in the sense of intrinsic shelf wave propagation. (We will refer to this direction as "prograde.") Figure 2 shows the resulting curves of $\bar{u}^{xt}$ as a function of cross-shelf distance for five simulations taken from Table 1. All models produce a band of strong prograde residual flow at approximately 10 km offshore. Two of the models (GFDLM and POM) have weak mean retrograde flow further offshore. Residual current vectors (Fig. 3) are largely similar across model classes; slight differences occur in the extent of the recirculation upstream of the canyon (e.g., compare POM and MICOM) and the smoothness of the mean vectors. Note that even with elevated levels of lateral smoothing, GFDLM produces the least smooth of the time-mean currents.

Despite varying degrees of qualitative agreement, the model results differ quantitatively by significant amounts. Maximum pointwise time-mean current speeds vary by a factor of four, and residual transports by a factor of six. The *weakest* currents and lowest overall transports are

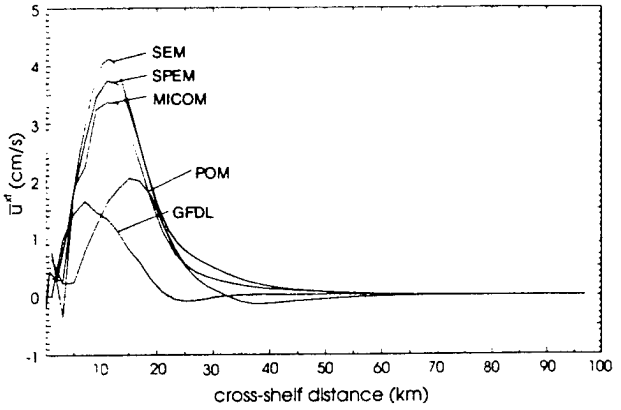


Figure 2. Time- and along-shore mean current $\bar{u}^{xt}$ as a function of cross-shelf distance.

returned by the GFDLM and POM codes. This is likely related in part to the use of a higher value of lateral viscosity in GFDLM and to the Smagorinsky formulation in POM. (Both of these codes produce offshore retrograde flow, which also reduces transport.) Among the free-slip experiments, the *strongest* pointwise residual currents and along-shore transports are found in SEM. Given its high-order formulation, it is tempting to attribute the enhanced strength of the SEM circulation to reduced implicit algorithmic smoothing. Increased horizontal resolution does not result in large changes in any of these model diagnostics, suggesting adequate resolution of all but the inner viscous layer along the coastal wall. Note that the z-coordinate model achieves its highest residual currents with an intermediate number of vertical levels (N=20); increased vertical resolution actually reduces the time-mean circulation. This may indicate incomplete convergence, even with 40 vertical levels.

As might be expected, the introduction of stratification increases model/model differences. Figure 4 (time-mean velocity vectors at a depth of 100 m) shows the outcome of adding a representative vertical stratification to four of the model runs. (Vertical resolution is also increased in each.) This stratified experiment uses a single state variable (density), expressed as a constant (Boussinesq) density (ρ_o) and the initial resting distribution

$$\rho_z = 28.0 - 3.4880 \cdot e^{z/H_\rho} \cdot \left(1.0 - \frac{2}{3}\tanh(z/H_\rho)\right) \sigma\text{-units}$$

with

$$H_\rho = 800$$

and

$$\rho_o = 1000\ \sigma\text{-units}.$$

This choice results in a first baroclinic Rossby radius of deformation of 40 km in deepest part of the fluid.

In addition, a vertical viscosity profile is prescribed as

$$\kappa_{uv}(z) = 10 \cdot 10^{-4} + 95 \cdot 10^{-4} \cdot e^{z/H_v} + 95 \cdot 10^{-4} \cdot e^{-z+h(x,y)/H_v}\ \mathrm{m^2 s^{-1}}$$

with $H_v = 50$ m.

The corresponding vertical viscosity is maximum at the top and bottom, and decays into the interior with an e-folding scale of H_v. Finally, in the stratified experiment, surface and bottom stresses are incorporated as boundary conditions at the surface and bottom, respectively.

With stratification, the maximum speed in GFDLM is 2.5 cm/s; there is a broad prograde flow centered at the location of maximum topographic slope, with some intensification at the upstream flank of the canyon. A large anticyclonic feature dominates at the downstream flank of the canyon. The flow is much weaker than in the other models, in part because of the relatively large diffusivity needed for stability. In MICOM, the maximum velocity is 6.3 cm/s; the main prograde current is only weakly influenced by the presence of the canyon. The additional circulation inside the canyon is driven by upwelling motion at the upstream flank and a boundary flow parallel to the depth contours at the downstream side. In contrast to the other models, POM produces a retrograde offshore mean flow, spatially separated from the prograde boundary circulation by a zone of weaker currents. Inside the canyon, the flow is enhanced and cyclonic with a maximum velocity of 7.2 cm/s. Lastly, in SPEM there is an intense boundary current following the depth contours in the canyon area (maximum current 11.7 cm/s), and a prograde off-shore flow that is deflected towards the canyon. At the downstream flank of the canyon,

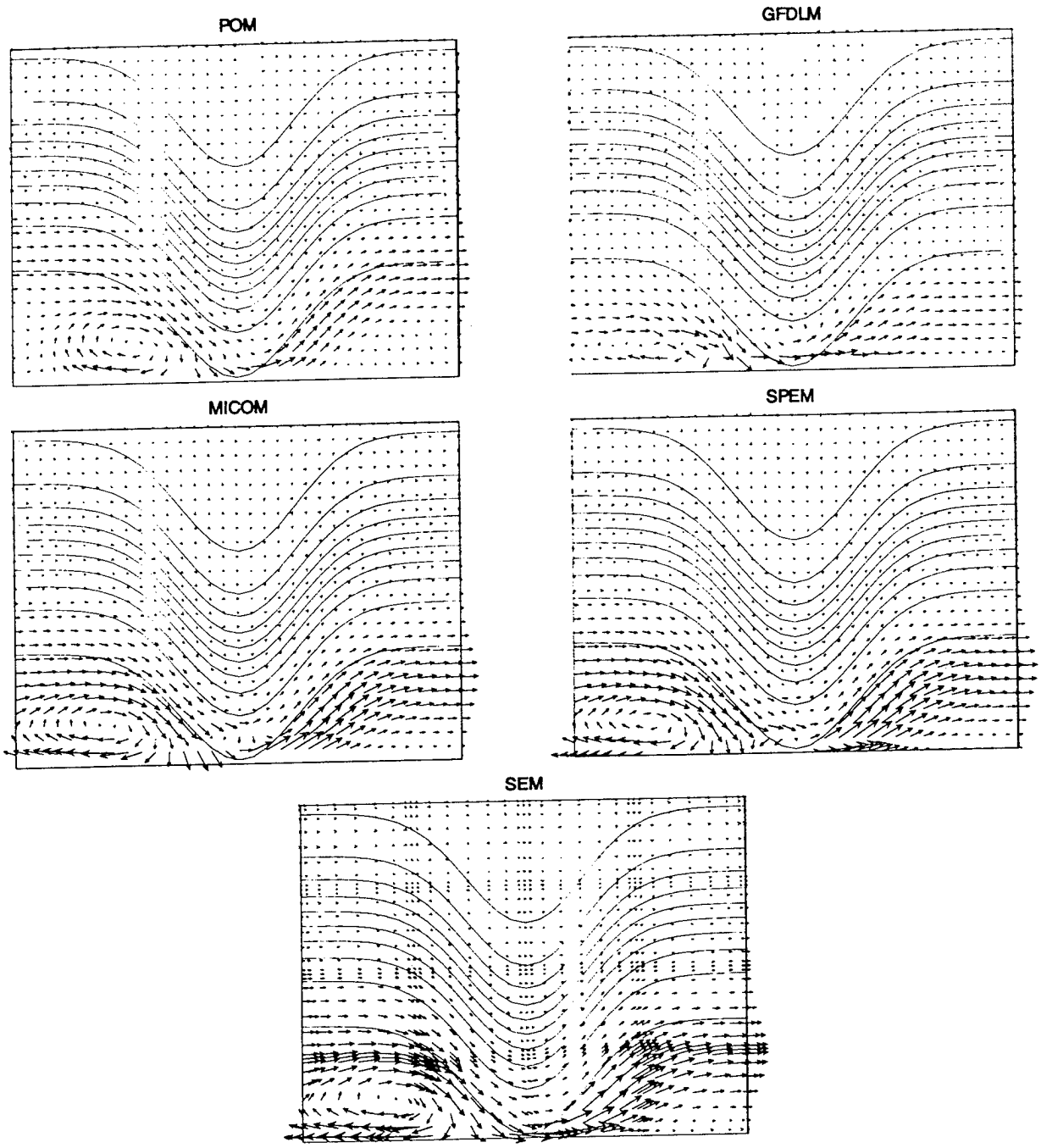


Figure 3. Time-mean surface current vectors for the homogeneous experiment. Maximum vector length is 15 cm s^{-1}. Underlying isobaths are shown (200 m to 3800 m at an interval of 400 m). For clarity, only half of the computational domain is shown in each of the horizontal directions.

pronounced boundary current separation occurs. Undoubtedly, these rather substantial differences reflect a complex interplay between the algorithmic and subgridscale parameterization choices made in each of these models. A more thorough discussion of these intercomparisons is given in Haidvogel and Beckmann (1995).

Interpretation and Discussion

With this single, simple set of intercomparisons, it is of course not possible to unambiguously sort out the respective roles of the many algorithmic differences among the five models employed here. Despite evidence for the impact of higher-order differences in the homogeneous experiment (e.g., SEM gives the strongest

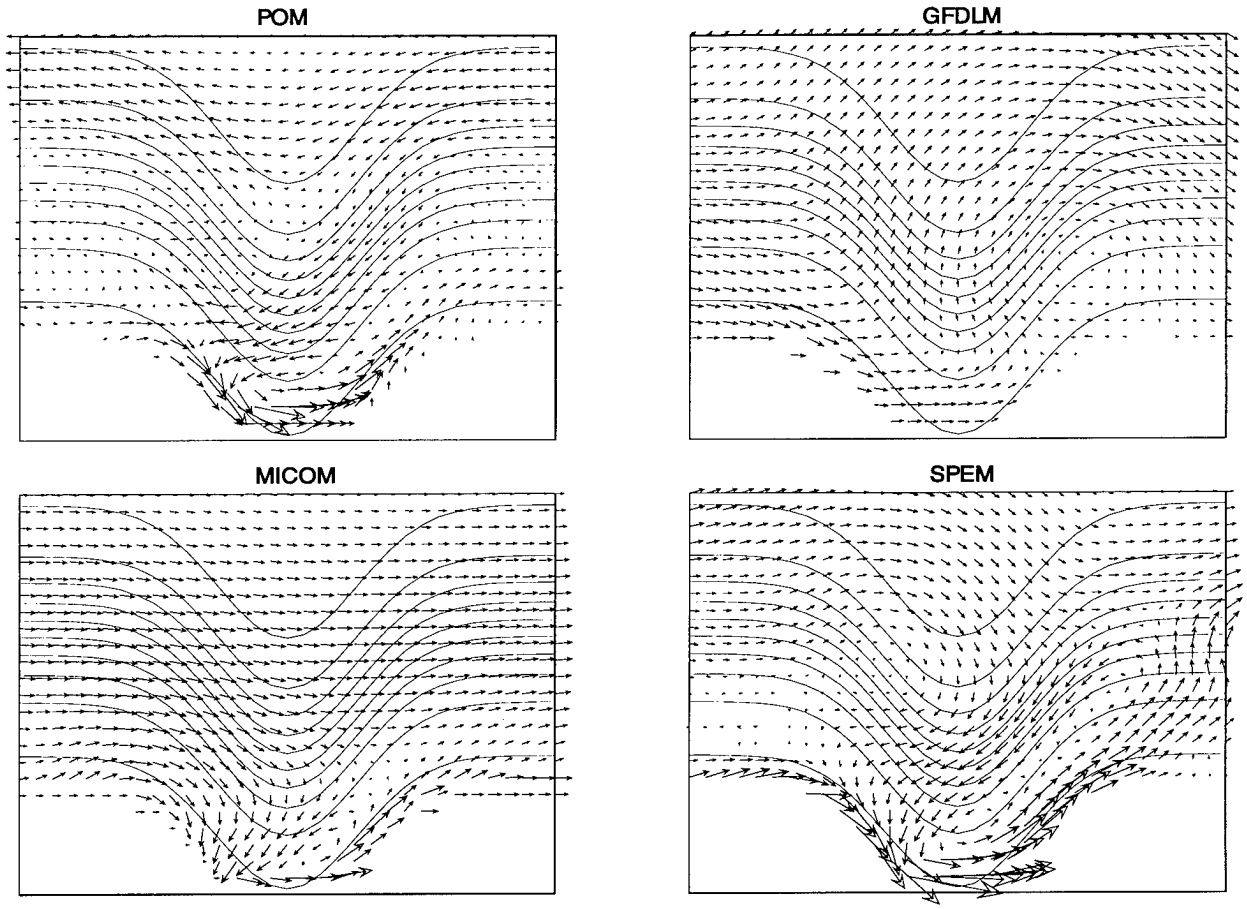


Figure 4. Time-mean current vectors at a depth of 100 m for the stratified problem. Maximum vector length is 12 cm s^{-1} for all models *except* for GFDLM, where 2 cm s^{-1} has been used. Underlying isobaths are shown (200 m to 3800 m at an interval of 400 m). For clarity, only half of the computational domain is shown in each of the horizontal directions.

residual flows), it seems to us that the primary factors involved in determining model differences on these problems are vertical coordinate and subgridscale parameterization.

These two factors are sometimes linked. For example, the requirement for elevated levels of explicit smoothing in the GFDLM code is arguably related to the noise generated in these tests by the stepwise topography. Nonetheless, the precise form of the subgridscale operator is also related to our model results. The POM and SPEM models are rather similar in their algorithmic attributes, except for their use of different subgridscale closures. Even so, they produce rather different pictures of the time-mean flow, particularly in the stratified limit.

The moral of the intercomparison, if any, is that simple numerical test problems such as these may have as much to tell us about our coastal ocean models as they have to say about the coastal ocean.

Acknowledgments

We thank Eric Chassignet, Enrique Curchitser, Mohamed Iskandarani and George Mellor for carrying out some of the intercomparison experiments.

References

Bleck, R., C. Rooth, D. Hu and L. Smith, 1992: Salinity-driven thermocline transients in a wind- and thermohaline-forced isopycnic coordinate model of the North Atlantic, *J. Phys. Oceanogr.* 22 , 1486–1505.

Blumberg, A.F., and G.L. Mellor, 1987: A Description of a three-dimensional coastal ocean circulation model, in Mooers, C. (ed.), Three-dimensional coastal ocean models, *Coastal and Estuarine Sciences*, 4, 1–16.

Bryan, K., 1969: A numerical method for the study of the circulation of the world ocean, *J. Comp. Phys.*, 4 , 347–376.

Cox, M.D., 1984: A primitive equation three-dimensional model of the ocean. Tech. Rep. 1. GFDL Ocean Group, Princeton University, 250 pp.

Haidvogel, D.B., and A. Beckmann, 1995: Numerical modeling of the coastal ocean, *The Sea*, submitted.

Haidvogel, D.B., and K.H. Brink, 1986: Mean currents driven by topographic drag over the continental shelf and slope. *J. Phys. Oceanogr.*, 16, 2159–2171.

Haidvogel, D.B., J.L. Wilkin and R.E. Young, 1991b: A semi-spectral primitive equation ocean circulation model using vertical sigma and orthogonal curvilinear horizontal coordinates, *J. Comp. Phys.*, 94, 151–185.

Hedstrom, K.S., 1994: User's manual for a semi-spectral primitive equation ocean circulation model. Version 3.9, Institute of Marine and Coastal Sciences, Rutgers University, 131 pp.

Holloway, G., K. Brink and D.B. Haidvogel, 1989: Topographic stress in coastal circulation dynamics, in Neshyba, S., et al. (eds.), *Poleward Flows along Eastern Ocean Boundaries*. Coastal and Estuarine Studies, 34, Springer-Verlag, New York, 374 pp.

Iskandarani, M., D.B. Haidvogel and J.P. Boyd, 1995:A staggered spectral element model with applications to the oceanic shallow water equations, *Int. J. Num. Meth. Fluids*, 20, 393–414.

Interaction of Turbulent Barotropic Shallow-Water Flow With Topography

Alexander. F. Shchepetkin [1]

Center for Ocean-Atmospheric Prediction Studies [2],
Florida State University, 020 Love Bldg., Tallahassee, FL 32306-3041

Abstract. It was recognized recently that the interaction of the mesoscale eddy field with bottom topography of the the ocean does not only lead to the dissipation of large scale ocean currents, but may appear as a driving force that strongly affects the large scale circulation. A high resolution numerical model is employed to investigate the evolution of the turbulent eddy flow over topography. Our attention is focused on the extreme case, when the change of layer depth is comparable to its maximum value. Under these conditions the flow is primarily controlled by the vorticity dynamics, particularly by the stretching of vorticity lines and the tendency to conserve potential vorticity. Because the cross-isobatic motion of fluid particles causes changes of the relative vorticity comparable to the local Coriolis parameter, the flow is no longer in the geostrophic regime. The particular goal is to explore the mechanisms of large-scale rectified flow emerging from an initial random eddy field. Several numerical experiments with the barotropic shallow water model were performed with low dissipation and with idealized geometry and topography were performed.

Introduction

Rhines and Young (1982a,b) presented a quasi-geostrophic (QG) theory of the wind-driven circulation in the presence of bottom topography. This theory combines the ideas of topographic forcing of the fluid motion and of homogenization of the potential vorticity field by mesoscale eddy interaction. The topographic forcing results in the tendency that water parcels move along the contours of *constant planetary potential vorticity*, i.e., f/H lines, where f is the *local* Coriolis parameter and H is the depth. Earlier numerical experiments by Rhines (1975) investigate the development of geostrophic turbulence in a periodic domain in the presence of β-effect and topography. It was found that the planetary β-effect partially inhibits the eddy merger process, restricting the maximum scale to which the coherent structures may grow to (Rhines' rule)

$$k_{\min} = \sqrt{\frac{\beta}{\sqrt{< u^2 >}}}\,, \qquad (1)$$

where $k_{\min}$ is the minimum wavenumber associated with the streamfunction or the potential vorticity (PV) field, while $\sqrt{< u^2 >}$ is the mean square velocity of the random field.

A theoretical study by Carnevale and Frederiksen (1986) applies Arnold's criterion to the nonlinear stability properties of QG flows over topography. It was shown that minimum enstrophy states have potential vorticity proportional to the streamfunction and are nonlinearly stable.

In the spirit of the quasigeostrophic theory, the effects of bottom topography were always treated as modification to the β-effect, e.g., Salmon *et al.*, 1976. This theory makes a qualitative distinction between regions where lines $f/H = const$ intersect the boundaries of the domain and regions of closed f/H contours. In the latter case the geostrophic flow is topographically trapped and the potential vorticity tends to homogenize (Rhines and Young 1982b). A similar effect was observed by Thompson (1993) in a numerical experiment with a QG eddy-resolving three-layer model, which shows the emerging of abyssal cyclonic circulation in the region where f/H contours

[1] Author affiliation and corresponding address effective from May 1, 1995: Institute of Geophysics and Planetary Physics, University of California at Los Angeles, 405 Hilgard Avenue, Los Angeles, CA 90024-1567

[2] Formerly known as Mesoscale Air-Sea Interaction Group (MASIG)

are closed.

On the other hand, coarse resolution numerical models used in climatological studies cannot simulate the effect of the self-organization of the random eddy-field into large scale motion over topography. Holloway proposed to parametrize this subgrid scale effect by relaxing the velocity field to some *nonrest* final state, $\mathbf{u}_*$, i.e. the conventional dissipation in the right hand side of the momentum equations is replaced by terms like

$$\frac{\mathbf{u}-\mathbf{u}_*}{\tau} \quad \text{or} \quad A\Delta(\mathbf{u}-\mathbf{u}_*)\,, \tag{2}$$

where τ is a relaxation time and $\mathbf{u}_*$ is some function of the bottom slope (Holloway 1986, Eby and Holloway 1994, Cummins and Holloway 1994, Holloway and Eby 1994, Alvarez *et al.* 1994).

Several questions remain open.

- The QG theory always assumes that the disturbances of the bottom topography are small in comparison with the characteristic depth. In reality, however, the depth changes continuously from the deep ocean to coastal regions, where it is nearly zero. Consequently, the f/H contours are *always closed.*
- As it was pointed out above, there is the expectation that mesoscale eddy mixing drives the flow to the statistically equilibrium state predicted by the minimum enstrophy principle, but the particular dynamical mechanism of this process and its characteristic time scale remain unexplored.
- It is also not clear how close real flows are to the equilibrium state and to what extent the existent models can simulate this effect directly or must rely on parametrizing it.

In the present study we attempt to simulate the eddy-topography interaction in the simplest case, in the absence of wind forcing and with idealized geometry and topography. Most of the previous theoretical studies are made within the QG framework, while their results were applied to primitive equation models. We chose the barotropic shallow-water equations over finite amplitude bottom topography as the prototype system. This model is free of the restrictions typical for QG models.

Barotropic Shallow-Water Equations With Bottom Topography

Consider the barotropic one-layer shallow water equations with bottom topography, in Cartesian coordinates:

$$\begin{aligned}
\frac{\partial U}{\partial t}+\frac{\partial P_{xx}}{\partial x}+\frac{\partial P_{xy}}{\partial y}-fV &= -H\frac{\partial p}{\partial x}\\
\frac{\partial V}{\partial t}+\frac{\partial P_{xy}}{\partial x}+\frac{\partial P_{yy}}{\partial y}+fU &= -H\frac{\partial p}{\partial y}\\
\frac{\partial R}{\partial t}+\frac{\partial U}{\partial x}+\frac{\partial V}{\partial y} &= 0
\end{aligned} \tag{3}$$

where upper case $U=\rho H u$, $V=\rho H v$ are the mass fluxes in x and y directions; lower case u and v are the velocities; H is the layer thickness; ρ is the density of the fluid; $R=\rho H$ is vertically integrated *mass content*, or the two-dimensional density; $p=\rho g(H-D)$ is the pressure field obtained from the hydrostatic equation, g is the acceleration of gravity, and D is the layer thickness at rest. P_{xx}, P_{xy} and P_{yy} are the components of the *tensor of the momentum flux*, and they are defined as follows:

$$\begin{aligned}
P_{xx} &= Uu-AR(\frac{\partial u}{\partial x}-\frac{\partial v}{\partial y})\\
P_{yy} &= Vv+AR(\frac{\partial u}{\partial x}-\frac{\partial v}{\partial y})\\
P_{xy}=P_{yx} &= \frac{1}{2}(Uv+uV)-\\
&\quad -AR(\frac{\partial v}{\partial x}+\frac{\partial u}{\partial y})
\end{aligned} \tag{4}$$

where A is the horizontal friction coefficient. This definition of the momentum flux tensor is somewhat nonstandard because the pressure term has been excluded. This is done for convenience because the pressure term will always be considered separately in the numerical discussion. The expression for the nonlinear term in the bottom line of eqns (4) looks redundant, because obviously $Uv=uV=Ruv$. However, as we will see soon, this equality will no longer be valid in the discrete case, if a staggered grid is used to discretize eqns (3).

An Arakawa $C-$grid is used to discretize eqns (3). In our elementary stencil $V_{j,k}$ is located half a grid interval to the *south* from $H_{j,k}$, and $U_{j,k}$ is located half a grid interval to the *east* of the $H_{j,k}$ point.

$$\begin{array}{ccccc}
 & & V_{j,k+1} & & V_{j+1,k+1}\\
 & & \downarrow & & \\
U_{j-1,k}\rightarrow & H_{j,k} & \leftrightarrow U_{j,k}\leftarrow & H_{j+1,k} & \\
 & & \updownarrow & & \\
 & & V_{j,k} & & V_{j+1,k}\\
 & & \uparrow & & \\
U_{j-1,k-1} & H_{j,k-1} & U_{j,k-1} & &
\end{array} \tag{5}$$

The grid intervals Δx and Δy are the distances between *alike* points, for instance, $U_{j,k}$ and $U_{j+1,k}$.

The numerical model we use to solve eqns (3) is designed to minimize dissipation. It incorporates a fully implicit Crank-Nicholson time step with spatial discretization of the momentum equations in the flux form, similar to Lilly's (1965) scheme for the nonlinear terms. A backward Euler time step is used for the dissipation terms.

Three features of the computational scheme are worth emphasizing:

• Following Weiyan (1992), Schär and Smith (1993) we have applied the phenomenology of the two-dimensional compressible fluids to the shallow water hydrodynamics. Both the nonlinear and the dissipation terms in the momentum equations have the form of a divergence of a *symmetric* tensor. The discrete scheme we use *retains* this property. On the C-grid, the diagonal elements P_{xx} and P_{yy} are defined at H-points, while the off-diagonal element P_{xy} is defined at vorticity points. After all of the elements of the stress tensor are computed, the second order centered finite difference approximation of the momentum equations is straightforward.

It should be mentioned that the original Lilly scheme for the nonlinear terms conserves the mean kinetic energy *exactly*. This property is based on a delicate balance of the truncation errors of the approximation of different terms and it restricts the choice of the possible discrete scheme for the nonlinear terms. In particular, in the x-momentum equation P_{xy} is approximated as $\bar{V}^x\bar{u}^y$, while in y-momentum it is represented by $\bar{U}^y\bar{v}^x$. Though both of these two expressions approximate the same term with the second order of accuracy, they are *exactly* equivalent only if the layer thickness is uniform. In this case the scheme is equivalent to the discrete Arakawa Jacobian of the third kind, which conserves the mean vorticity *exactly* (Lilly 1965). The symmetric scheme we develop here produces more accurate conservation of the potential vorticity for the case of nonuniform layer thickness, but it does not have the property of formal *exact* conservation of Kinetic energy. Consequences of this choice will be discussed later.

• As an alternative to midpoint averaging (Lilly 1965), an *asymmetric* three-point formula is used to interpolate the velocities and mass fluxes into H and vorticity points when computing the nonlinear terms of P_{xx}, P_{yy} and P_{xy} respectively. The additional points are always taken from the *upstream* direction, so the following expressions are used to approximate U and V at H points (u and v similar):

$$\begin{aligned}
&\bar{U}^u \equiv U_{j-\frac{1}{2},k} = \\
&= \begin{cases} \alpha U_{j,k} + \beta U_{j-1,k} + \gamma U_{j-2,k}, & \text{if } \bar{U}^x > 0 \\ \alpha U_{j-1,k} + \beta U_{j,k} + \gamma U_{j+1,k}, & \text{if } \bar{U}^x < 0 \end{cases} \\
&\bar{V}^v \equiv V_{j,k+\frac{1}{2}} = \\
&= \begin{cases} \alpha V_{j,k+1} + \beta V_{j,k} + \gamma V_{j,k-1}, & \text{if } \bar{V}^y > 0 \\ \alpha V_{j,k} + \beta V_{j,k+1} + \gamma V_{j,k+2}, & \text{if } \bar{V}^y < 0, \end{cases}
\end{aligned} \tag{6}$$

and, at vorticity points,

$$\begin{aligned}
&\bar{U}^v \equiv U_{j,k-\frac{1}{2}} = \\
&= \begin{cases} \alpha U_{j,k} + \beta U_{j,k-1} + \gamma U_{j,k-2}, & \text{if } \bar{V}^x > 0 \\ \alpha U_{j,k-1} + \beta U_{j,k} + \gamma U_{j,k+1}, & \text{if } \bar{V}^x < 0 \end{cases} \\
&\bar{V}^u \equiv V_{j+\frac{1}{2},k} = \\
&= \begin{cases} \alpha V_{j+1,k} + \beta V_{j,k} + \gamma V_{j-1,k}, & \text{if } \bar{U}^y > 0 \\ \alpha V_{j,k} + \beta V_{j+1,k} + \gamma V_{j+2,k}, & \text{if } \bar{U}^y < 0. \end{cases}
\end{aligned} \tag{7}$$

To maintain second order of accuracy, coefficients α, β, γ in (6) and (7) must satisfy

$$\alpha + \beta + \gamma = 1, \qquad \alpha - \beta = 3\gamma \ ,$$

and, therefore, there is only one free parameter among α, β, γ. Let

$$\alpha = \frac{1}{2} + \gamma, \qquad \beta = \frac{1}{2} - 2\gamma \ ,$$

and γ is the adjustable parameter.

Analysis of the truncation error shows that, for example,

$$\begin{aligned}
\delta(P_{xx}) = \frac{\partial P_{xx}}{\partial x} + \text{sign}(U)(\Delta x)^2 \times \\
\times \Big\{ (\frac{1}{6} + \gamma) \Big[u \frac{\partial^3 U}{\partial x^3} + U \frac{\partial^3 u}{\partial x^3} \Big] + \\
+ (\frac{1}{4} + \gamma) \Big[\frac{\partial u}{\partial x} \frac{\partial^2 U}{\partial^2 x} + \frac{\partial U}{\partial x} \frac{\partial^2 u}{\partial^2 x} \Big] \Big\} + \\
+ \mathcal{O}((\Delta x)^3)
\end{aligned} \tag{8}$$

where $\delta(...)$ is the usual centered difference operator. The first term in curly brackets may be interpreted as numerical dispersion in the nonlinear terms, while the second term corresponds to the numerical dissipation in the nonlinear terms. No choice of the upstream parameter γ can eliminate both terms in curly brackets; however, we see that introduction of the upstream scheme may drastically reduce the truncation error in comparison with the original Lilly scheme with $\gamma = 0$. In the present study we set $\gamma = -1/8$, which corresponds to the third order of accuracy approximation

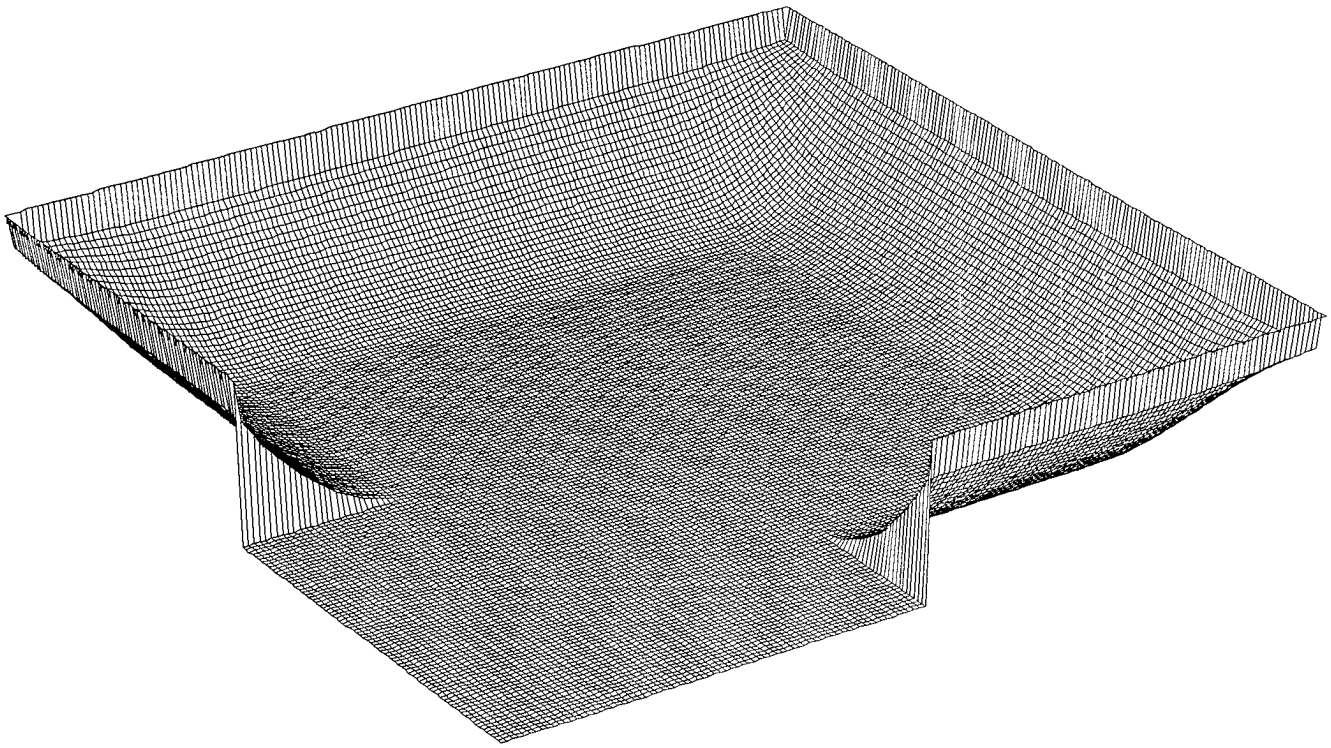


Figure 1. Perspective view of the bottom topography for all four cases. The quarter of the domain closest to the viewer has been lowered down to the deepest value for illustrative purpose. The actual topography is symmetric and has continental slopes along all four sides. The shape of the slope can be easily seen on the cross sections. The minimum depth near the sides is 20% of the deepest value in the middle.

for the nonlinear part of the stress tensor. Though not the best from the point of view of (8), this choice virtually eliminates aliasing errors caused by the subsequent use of spatial averaging and finite differencing of the averaged values. Consequently, the asymmetric scheme does not generate spurious enstrophy cascades to small scales and, therefore, requires a relatively small explicit dissipation to keep the numerical stability.

• *The method of artificial compressibility* is employed to implement the fully implicit time step (Turkel 1987, Gresho and Sani 1987, Soh and Goodrich 1988, Weiyan 1992, Alcubierre and Schutz 1994, Marx 1994). This approach is based on introducing an internal *pseudo*-time and special relaxation procedure between *physical* time steps to obtain the solution. The iterative procedure starts from a second order explicit predictor in *physical* time to obtain the initial approximation for the new time step fields. After that several *ADI*-type split-implicit substeps in *pseudo*-time are applied to obtain the pressure field at the new time step and correct the solution. The time step is unconditionally stable with respect to fast surface gravity waves, can formally be applied to the incompressible limit $g = \infty$, and allows an implicit representation of the nonlinear and dissipation terms. In comparison with the more common three time level semi-implicit version of Kwizak and Robert (1971), the new approach leads to four times smaller truncation errors in the time differencing of both nonlinear and pressure terms. The computations presented here are performed on a 301×301 grid. The nonlinear terms are recomputed 3 times per every *physical*-time step, and $8 \approx \log_2 300$ *ADI* iterations are required to correct the pressure field every time after the nonlinear part is recomputed.

The Topographic Engine Experiment

Because our purpose is to investigate the possibility of conversion of energy from random flow into large scale *rectified* motion, i.e., in thermodynamical terms, from *heat* into *mechanical* energy, we refer to this part of the study as the *topographic engine* experiment. In the present section we discuss several experiments with free decaying shallow-water turbu-

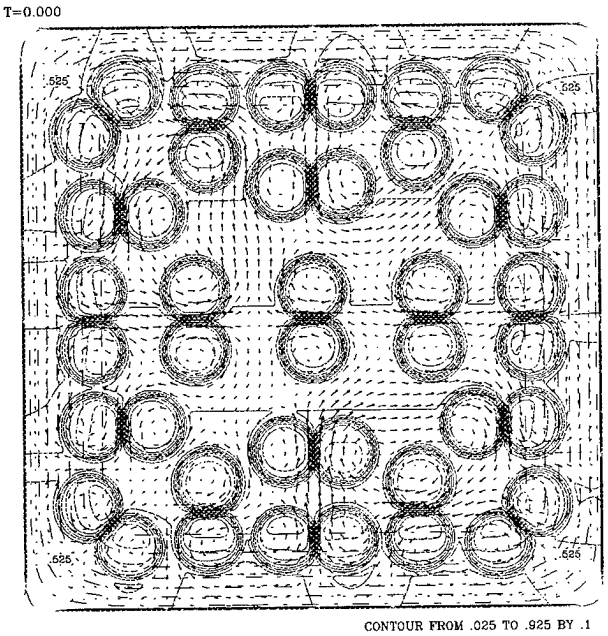


Figure 2. The initial state. The potential vorticity field is shown in contours, while arrows represent velocities. Only every sixth vector is plotted. Note that the initial flow is composed of dipoles and has no specific symmetry. Also, there is no net circulation around the box.

lence in the presence of bottom topography. All of the cases presented here have the same domain geometry and bottom topography shown in Figure 1. The bottom is flat in the middle of the basin and rises near the sides, which simulate the continental slopes. No-slip boundary conditions are imposed on the sides of the rectangular domain.

To specify the initial state, we prescribe the potential vorticity field (f-plane case, see below) or relative vorticity field (β-plane cases), solve the elliptic problem to obtain the streamfunction, and, finally, the mass fluxes of the initial state, which is always assumed to be nondivergent. The (potential) vorticity field of the initial state is always composed of randomly oriented dipoles, so that there is no net circulation around the box (Fig. 2). There is no forcing in any of our experiments.

All computations are performed for nondimensional variables where we set different values of the nondimensional Coriolis parameters and keep all other nondimensional parameters unchanged. To get some impression about the correspondence of our experiments to the dimensional world, the four experimental setups may be identified as follows:

- The first case, hereafter referred as the **f-plane case**, corresponds to a domain of 500×500 km at 45^0N. The Coriolis parameter $f = 10^{-4}\text{sec}^{-1}$ is assumed to be uniform. With velocity scale $V = 1$ m/sec and the advection time scale $T = L/V = 5 \times 10^5$ sec ≈ 6 days, the non-dimensional Coriolis frequency is

$$\mathcal{F} = \frac{fL}{V} = 50$$

Grid resolution is 301×301 for the all cases presented here.

- **Weak β-case**

$$\mathcal{F}(y) = \mathcal{F}_0 + \beta\frac{y}{L} = 50 + 50\Big(\frac{y}{L} - \frac{1}{2}\Big)$$

- **Moderate β-case**

$$\mathcal{F}(y) = \mathcal{F}_0 + \beta\frac{y}{L} = 150 + 150\Big(\frac{y}{L} - \frac{1}{2}\Big)$$

- **Strong β-case** The domain size is 3000×3000 km (from 20 N to 50 N). A velocity scale of $V = 0.5$ m/sec gives

$$\mathcal{F}(y) = 400 + 400\Big(\frac{y}{L} - \frac{1}{2}\Big)$$

The advection time scale $6 \times 10^{+6}$ sec $= 70$ days

The results of the computations are presented in Fig. 3 – Fig. 6. (See also captions for additional discussion.)

The f-plane experiment: To compare the upstream scheme with the original centered difference Lilly scheme, we run the f-plane case twice, using both schemes. All of the conditions are the same, except for the viscous coefficient A. The Reynolds number (based on the domain size) is 10^{+4} for the centered difference case, which is nearly on the edge of the numerical stability for this numerical scheme. Note that the Reynolds number is $3 \times 10^{+5}$ (which is 30 times larger) for all other experiments, when the upstream scheme is used to discretize the nonlinear part of the momentum flux tensor. We did not find any tendency to produce grid size scale oscillations when the upstream version is used. Despite the larger dissipation, the centered difference solution (not shown here) is much noisier, dissipates kinetic energy faster and does not result in a monotonic decay of potential enstrophy. However, the physical behaviour of the flow is similar for both cases. The experiments show that the turbulent flow tends to organize itself

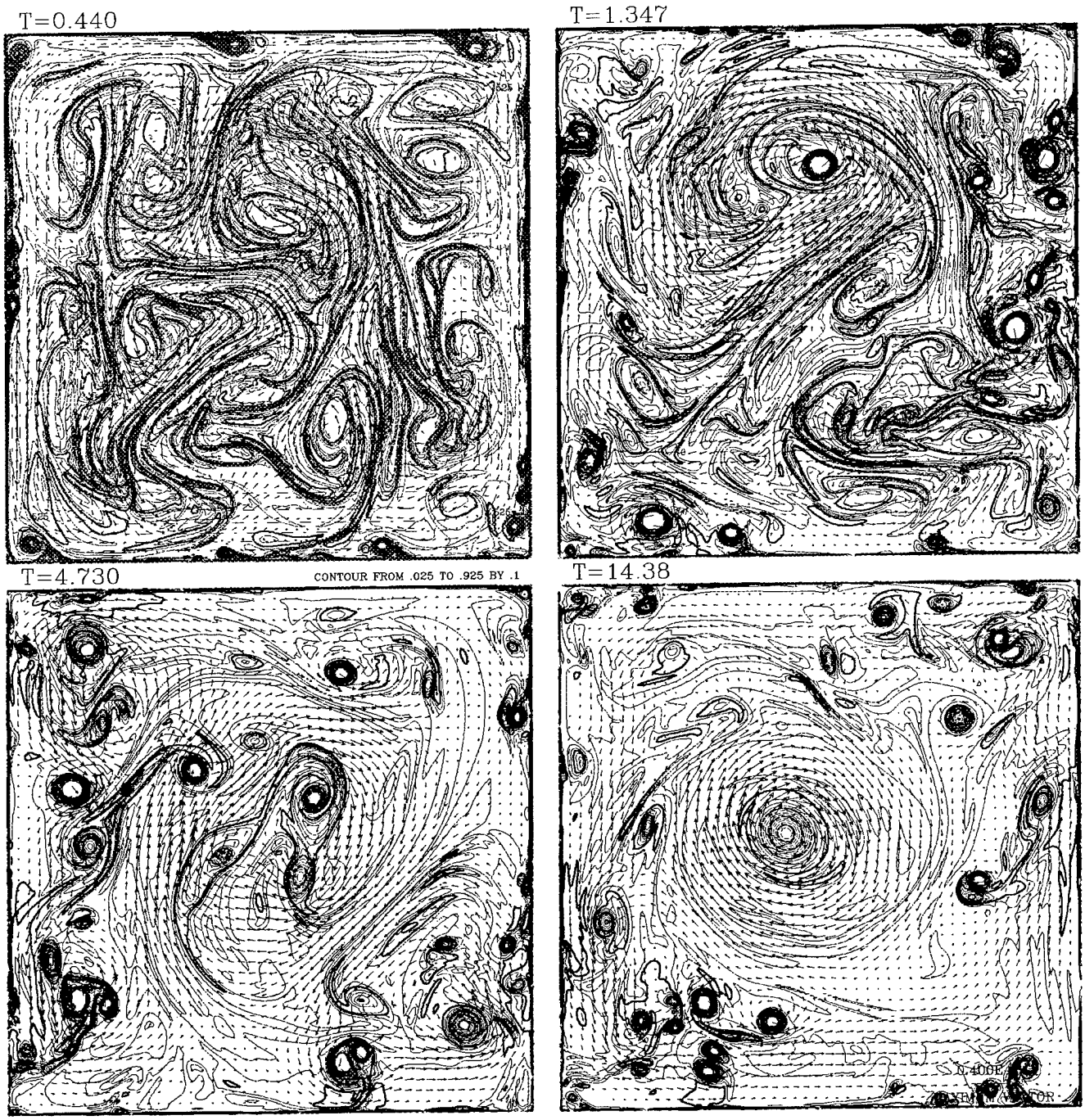


Figure 3. Temporal evolution of the potential vorticity field from the initial state shown on Fig. 2 for the case of an f-plane. Time is scaled by the advection time scale. The upper left panel shows the potential vorticity and velocity field shortly after the beginning. All the original dipolar structures are rapidly destroyed. At the same time, there is formation of new compact eddies near the walls. These eddies may have amplitudes of relative vorticity anomaly larger than the original field. The anticyclonic vorticity tends to concentrate in the middle of the basin, while cyclones are more likely to stay in the shallower regions near the sides. Note the formation of the cyclonic circulation around the box near the boundaries (lower right panel).

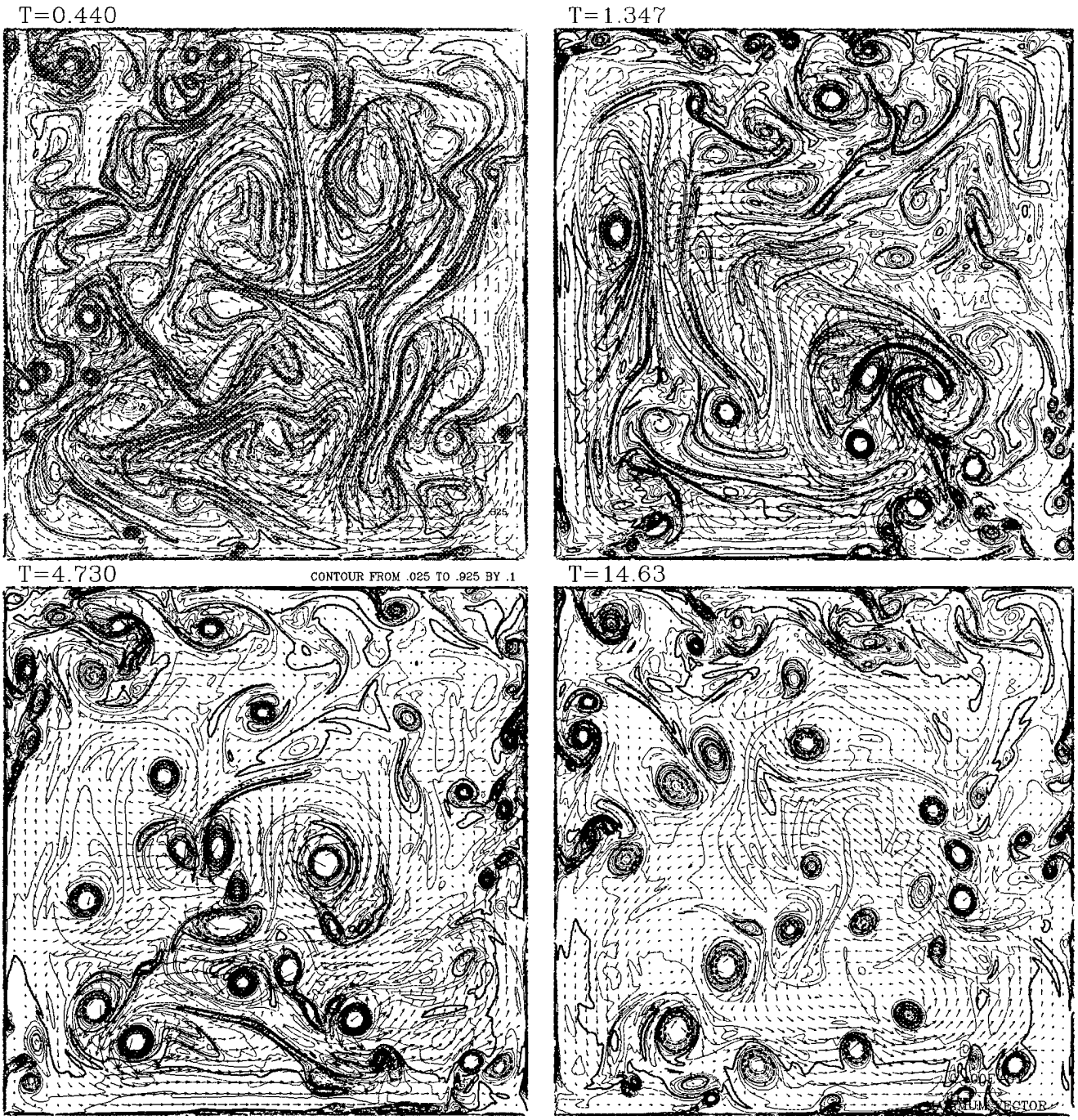


Figure 4. Case of weak planetary β-effect. In this regime the β-effect is not strong enough to either restrict fluid motion in the meridional direction, or to cause decay of mesoscale eddies via radiation of Rossby waves. However, it restricts the size to which the coherent structures may grow. Notice the presence of many small intense eddies in the middle of the domain instead of a large scale merged core, as seen in Fig. 3. There is also evidence of the development of a rectified cyclonic circulation around the domain (bottom right panel).

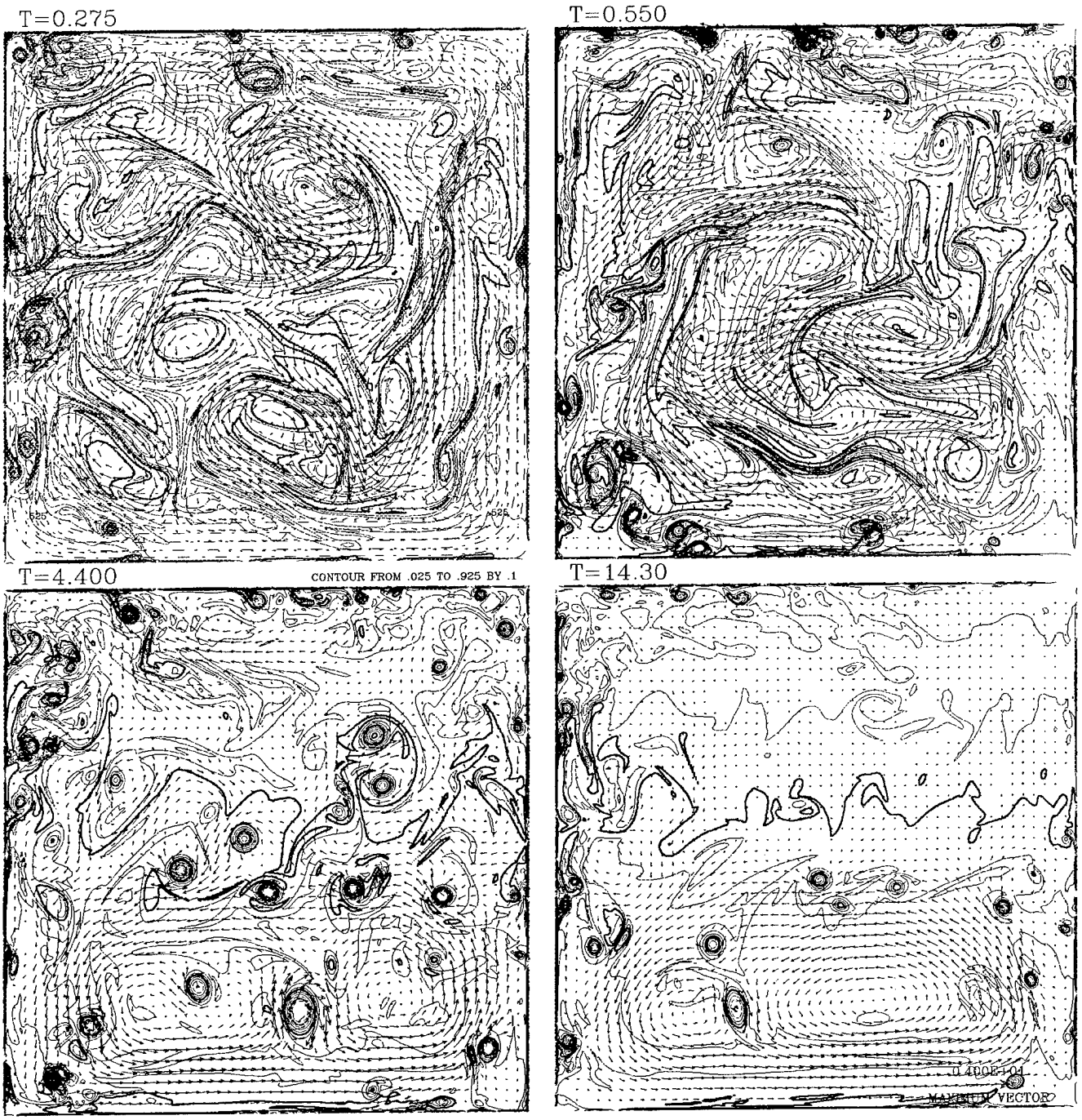


Figure 5. Case of intermediate planetary β-effect. The β-effect is now stronger and decay of mesoscale features due to radiation of Rossby waves becomes more evident. Time is scaled by the advection time scale. Note that these four snapshots are taken at times different from those of the two previous cases. This flow has north–south as well as east–west asymmetry, which were practically absent in the previous two experiments. Rectified circulation intensifies near the southern part of the domain and it detaches from the eastern coast. The separation point becomes also the place where anticyclonic eddies leave the coast and are advected into the interior of the basin, where they eventually will be destroyed by the β-effect. The cyclonic eddies remain topographically arrested and tend to propagate along the eastern coast to the north. Note the appearance of an east-west alignment of eddies as well as a restriction of the fluid motion in the meridional direction.

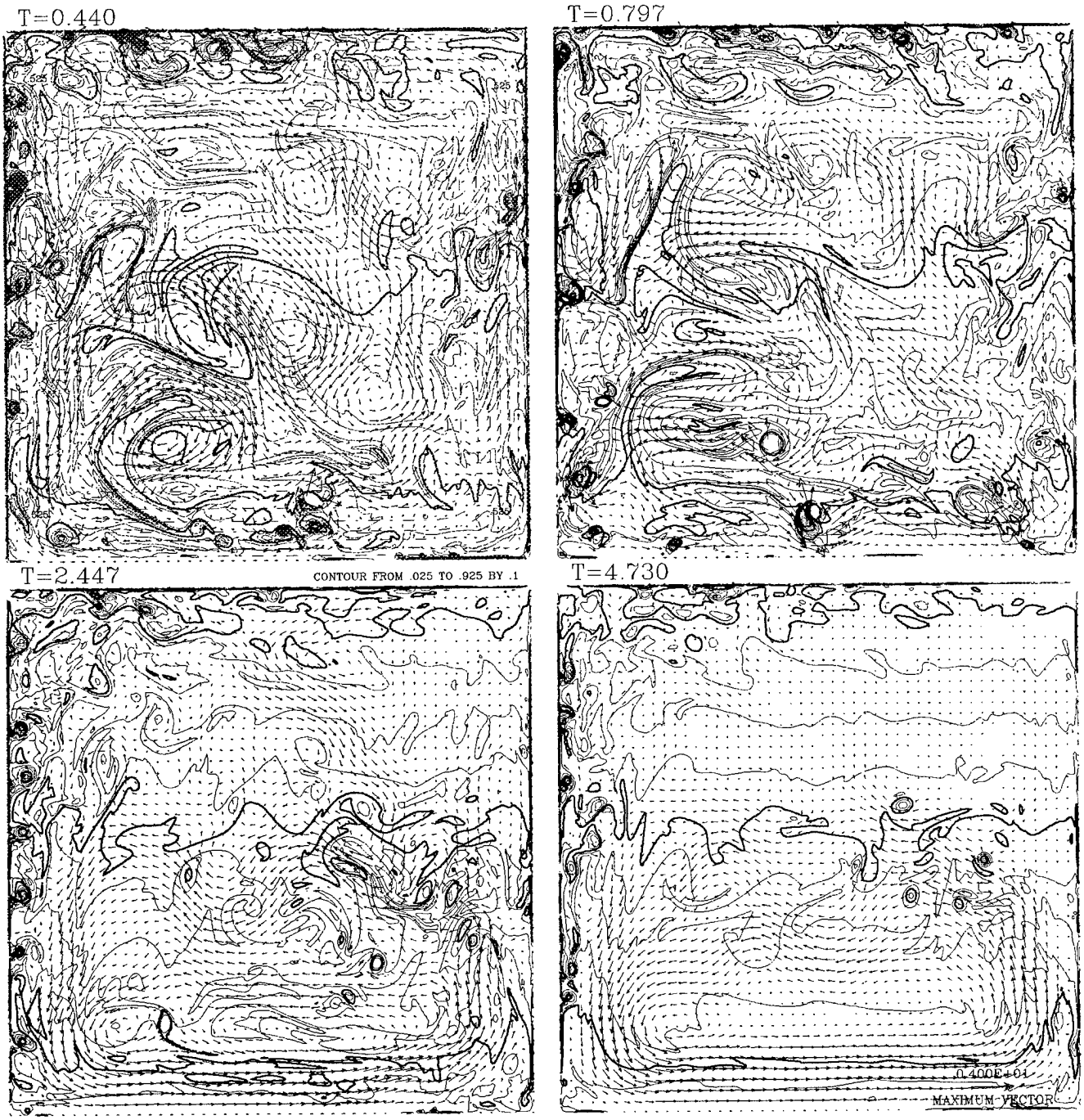


Figure 6. Case of strong planetary β-effect. In this case the meridional change of the Coriolis parameter dominates the relative vorticity anomalies associated with the initial random eddy field. Consequently, the original structures were immediately destroyed. Both the east–west and the north–south asymmetries are more pronounced than in the previous case. There is formation of both cyclonic and anticyclonic eddies near the western coast, but both the planetary β-effect and bottom topography prevent them from being injected into the interior of the basin. Note formation of the intense jet along the southern boundary and recirculation gyre. As in the previous case, we see injection of small scale eddies at the flow separation point on the eastern coast.

into a current along the perimeter of the basin in the counter-clockwise direction, while the negative vorticity tends to concentrate in the middle of the domain (Fig. 3). In classical numerical simulations of free-decaying two-dimensional turbulence there is no process opposite to the vortex merger and, therefore, no small scale structures can be created from large scale structures. In our case, in contrast, there is generation of small scale structures on the no-slip boundaries. Injection of fresh, intense and compact new eddies into the interior of the domain enhances mixing of the low-vorticity anomalies of old vortices. Consequently we observe a relatively uniform potential vorticity background field with several small scale intense coherent structures embedded in it. In this situation, regardless of the details of the initial state, the spatial spectrum of the turbulent flow rapidly reaches some equilibrium state, which persist during a relatively long period of time (bottom left panel of Fig. 3).

Due to the presence of continental slopes and Coriolis effect, the anti-cyclonic eddies are more likely to be driven into the interior of the domain, while anti-cyclones tend to stay near the walls. This can be explained by potential vorticity conservation and the energetics of the flow: moving a cyclonic vortex core from a shallow to a deep region causes its spin up:

$$PV = \frac{f+\omega}{H} = \text{const}, \qquad f > 0, \quad \omega > 0$$

$$\left.\begin{array}{l} f \rightarrow \text{conserved} \\ H \rightarrow \text{increases} \end{array}\right\} \Rightarrow \quad \omega \rightarrow \text{increases}$$

The kinetic energy associated with an eddy is

$$KE \sim Vol \cdot \omega^2 r^2 \sim Vol^2 \frac{\omega^2}{H} \sim \omega \cdot \frac{\omega}{H} ,$$

where $Vol \sim r^2 H$ is the characteristic volume of the vortex core, while r is its radius. Obviously Vol is conserved and both ω and the ratio ω/H increase due to the conservation of potential vorticity. Consequently, the kinetic energy has to increase when a cyclonic core is driven from the shallow to deeper regions. Thus, an external flow *must* produce some work on order to move the core.

Similar considerations may be made for the anti-cyclonic vortices, where ω and f are of different signs. It turns out that there is no energetic barrier for the anti-cyclones to leave the coast. For example, *zero* potential vorticity eddies, $\omega = -f$, are not sensitive to the vortex stretching at all, while they may even release some amount of kinetic energy when H is increasing. On the other hand, assuming some dissipation in the system, one can see that the process of redistribution of the vorticity field becomes *irreversible* in the sense that once an anti-cyclonic eddy leaves the coastal region, it cannot come it back, unless it is pushed by the background flow.

Weak β-effect case. The most noticeable difference from the previous case is the behavior of the turbulent flow in the interior. To some extent, the β-effect inhibits the merging process inside the domain and restricts the size to which the eddies can grow (Rhines rule). There is no evident decay of single eddies due to radiation of Rossby waves. There is some evidence of the meridional restriction of the motion and east-west as well as north south asymmetry of the flow.

Intermediate β-effect case. The differences from the previous case are these: there is evident decay of eddies due to radiation of Rossby waves. The motion tends to be meridionally restricted. The organized flow around the box is intensified in the southern part of the basin, while the northern part exhibits predominantly wave type motion rather than turbulent eddy flow.

Strong planetary β-effect. Rapid decay of initial eddies is due to radiation of Rossby waves. There is an evident formation of the organized flow with the strong jet along the southern boundary.

For the all four cases the decay of the mean kinetic energy is shown in Figure 7, while Figure 8 shows time evolution of the mean potential enstrophy. The kinetic energy is normalized by its initial value, so all curves on Figure 7 start from $KE = 1$ and monotonously decay. The lowest curve corresponds to the dissipative centered difference scheme. It is presented here only to demonstrate difference between the two numerical schemes. For physical considerations it should be ignored. From the other four curves one can conclude that presence of β-effect generally enhances dissipation. This result may require additional investigations, because for the case of unbounded freely decaying geostrophic turbulence (doubly periodic domain) there is an opposite tendency: radiation of Rossby waves in a periodic domain does not dissipate energy, while the eddy mixing process (which causes eddy merging and filamentation – the main dissipative mechanism) tends to be suppressed (Rhines and Young 1982b). The difference may be explained by the presence of no-slip boundaries.

Before interpreting Figure 8, it should be explained

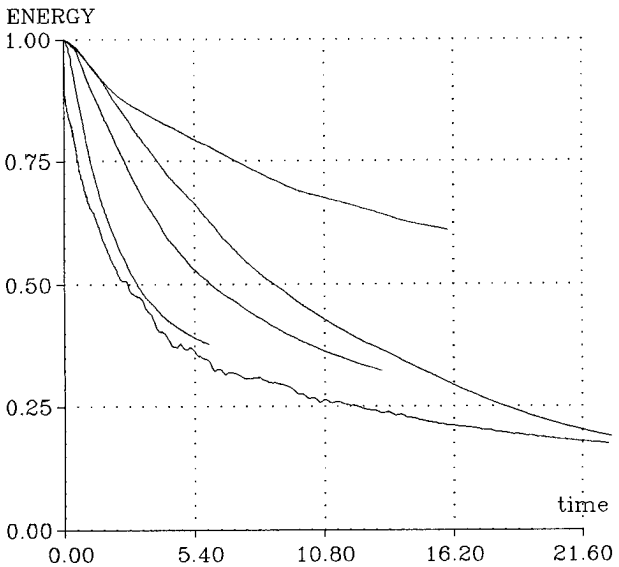


Figure 7. Time decay of the kinetic energy (KE) integral for all four different experiments. The KE is normalized by its initial value. The five curves, starting from the highest, correspond to the f-plane upstream case (terminates at $t = 16.20$); weak planetary β-effect case (goes beyond $t = 21.60$); intermediate β (terminates at $t = 13.5$); strong β (terminates at $t = 5.8$); f-plane case when centered scheme was used (goes beyond $t = 21.60$).

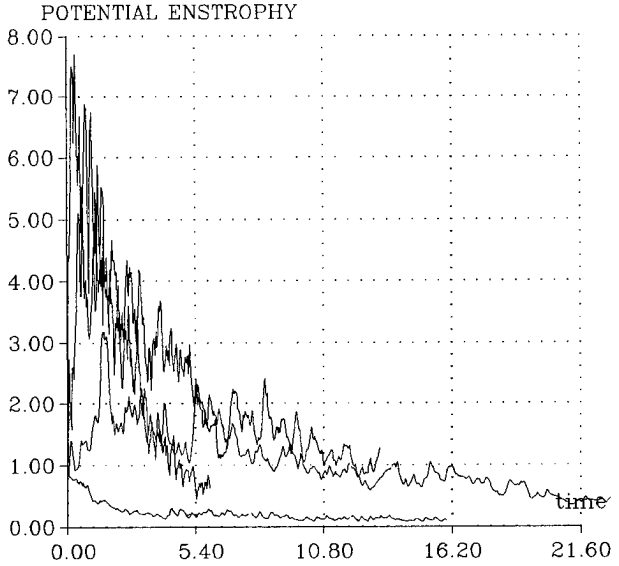


Figure 8. Potential enstrophy integral as the function of time for all four cases. The four curves (f-plane centered difference case is not shown) may be identified by the length of the curve, similar to the previous figure.

that the mean enstrophy is defined as

$$< q >= \left\langle H \cdot \frac{1}{2} PV^2 \right\rangle = \left\langle \frac{(f+\omega)^2}{2H} \right\rangle , \qquad (9)$$

where $\langle ... \rangle$ denotes the integration over the domain. For a given initial state we may define the initial value of the potential enstrophy $q_0 = q(t = 0)$, and the mean potential enstrophy of the rest state

$$q_{\text{rest}} = \left\langle \frac{f^2}{2H_{\text{rest}}} \right\rangle . \qquad (10)$$

Fugure 8 shows the function

$$q^* = \frac{q(t) - q_{\text{rest}}}{q_0 - q_{\text{rest}}} . \qquad (11)$$

Obviously, this function is the normalized mean potential enstrophy. In the case of a closed system, when no potential enstrophy can be generated on the boundary or brought in through the boundary, this quantity must be conserved if there is no internal dissipation. It monotonously decays from 1 to 0 if dissipation is present.

In the case when vorticity (and, consequently, enstrophy) may be created on the boundary, the behaviour of this integral is not so evident. It is interesting to note that in the f-plane case it decays practically monotonously. All β-plane cases may be characterized by an initial burst and a subsequent decay. We suggest that the initial state is very far from the dynamical equilibrium in the β-plane cases, so, shortly after the beginning, the flow tends to readjust itself to bring all fluid parcels to their equilibrium latitudes. This process takes place mostly in the interior of the domain and causes generation of strong shear near the boundaries, which results in the generation of small scale turbulence, which becomes the major contribution to the enstrophy integral. After this readjustment enstrophy decays.

Final Remarks

For the conclusion, we summarize several observations:

- Due to the presence of the no-slip boundaries there is generation of the small scale features which oppose the merging of sign-like eddies in the interior of the basin.
- In the presence of topography on an f-plane, the turbulent flow tends to organize a rim current around the domain and concentrate negative vorticity in the

middle.

• Coupling of bottom topography and Coriolis effect causes *cyclone-anticyclone asymmetry*, even in the case when the Rossby number is small.

• Migration of the eddies along the wall can be explained by *image effect*, topographic β-effect, planetary β-effect and interaction with the viscous boundary layer. Anti-cyclonic eddies are more likely to be ejected into the interior of the domain, while cyclones tend to be coastally trapped. This effect can be explained in terms of conservation of the potential vorticity and energetic consideration.

• A weak planetary β-effect partially inhibits the merger process inside the domain. Rhines (1975) rule may also be applied to the case of ageostrophic dynamics.

• In the presence of topography, both weak and strong planetary β-effects make the anti-cyclonic eddies more likely to separate from the coast than in the case of an f-plane.

• The planetary β-effect causes asymmetry of the rectified flow with intensification of southern boundary currents, which results in configuration of the flow similar to Fofonoff's southern mode inertial boundary current.

• There is an east-west asymmetry in the boundary current behavior (Figs. 5 – 6).

• There is a topographic instability of northward flowing eastern boundary current and cyclone-anticyclone separation near the eastern coast.

From these numerical experiments we see that the *rectification* process is associated with several physical phenomena, such as vortex stretching and turbulent mixing, which are affected by the topography itself as well as by planetary vorticity gradients and lateral friction, which also allows generation of vorticity on the boundaries. This study shows that, in principle, ocean models are capable to simulate this behavior directly, however, at a high computational cost. Parametrization of this effect is desirable, but not obvious. In particular, this effect has *nonlinear* and *nonlocal* nature, so that the statistical equilibrium velocity at some particular point depends on the *global* field, rather than on the local bottom slope and Coriolis parameter. One can expect this keeping in mind the inherent elliptic properties of the barotropic flows. Parametrizations based on variational principles seem to be more attractive.

One should recall that in numerical simulation of the geophysical flows there is a tendency to generate finer and finer scales when the grid size and the lateral viscous coefficient decrease, rather than going to a computational regime when the fields become smooth on the grid scale. This classical mathematical convergence is practically never achieved. This motivates the design of numerical schemes which produce well behaved solutions in all scales up to the grid size. In many cases, special properties, such as non-generation of spurious cascades of enstrophy in small scales as well as properties of monotonicity (i.e. non-generation of spurious minima and maxima), may be more valuable than the formal order of the mathematical convergence. Because there are many desirable properties and no one computational design can reproduce all of them, a compromise should be made. The scheme used in the present study is an example of such a compromise: despite the formal loss of the conservation of kinetic energy in the nonlinear terms, the better cascade properties allow the use of a smaller explicit dissipation. As a result, the model has better *overall* energy conservation than the model which uses the centered scheme.

Acknowledgments. COAPS receives its base support from the Secretary of NAVY Research Grant N00014-85-J-1240 from the Office of Naval Research. This research was also supported by the Advanced Research Projects Agency (ARPA) grant SC25046. Special thanks to Prof. J. J. O'Brien for his support and advise. The author is grateful to Dr. Wesley Jones, Dr. Detlev Müller, Dr. Steven Meyers, Dr. George Sutyrin and Dr. Eduard Zuur for the numerous discussions at several stages of this work. Computations were performed on Florida State University CRAY Y-MP. Special appreciation to Nancy Kellett for her support and patience.

References

Alcubierre, M. and B. F. Schutz, 1994, Time-Symmetric ADI and Causal Reconnection: Stable Numerical Techniques for Hyperbolic Systems on Moving Grids, *J. Comput. Phys.*, **112**, 44-77.

Alvarez, A., J. Tintore, G. Holloway, M. Eby and J. M. Beckers, 1994, Effect of topographic stress on the circulation in the western Mediterranean, *J. Geophys. Res.*, **99**, 16053-16064.

Carnevale, G. F. and J. S. Frederiksen, 1986, Nonlinear stability and statistical mechanics of flow over topography, *J. Fluid Mech.*, **175**, 157-181.

Cummins, P. and G. Holloway, 1994, A note on eddy-topographic stress representation, *J. Phys. Ocean.*, **24**, 700-706.

Eby, M. and G. Holloway, 1994, Sensitivity of a large scale ocean model to a parameterization of topographic stress,*J. Phys. Ocean.*, **24**, 2577-2588.

Gresno, P. M. and R. L. Sani, 1987, On the pressure boundary conditions for the incompressible Navier-Stokes equations, *Int. J. of Num. Meth. in Fluids*, **7**, 1111-1145.

Holloway, G., 1986, Eddies, waves, circulation and mixing: statistical geofluid mechanics, *Ann. Rev. Fluid Mech.*, **18**, 91-147.

Holloway, G., 1992, Representing topographic stress for large scale ocean models, *J. Phys. Ocean.*, **22**, 1033-1046.

Holloway, G. and M. Eby, 1994, Exercising a Hybrid Statistical Mechanics - Ocean circulation model, research activities in atmospheric and oceanic modelling, 19, G. J. Boer, ed., WMO, Geneva

Kwizak, M., A. J. Robert, 1971, A semi-implicit scheme for grid point atmospheric models of the primitive equations, *Mon. Weather Rev.*, **99**, 32-36.

Lilly, D. K., 1965, On the computational stability of the time-dependent non-linear geophysical fluid dynamics problem, *Mon. Weather Rev.*, **93**, 11-26.

Marx, Y.P., 1994, Time integration schemes for the unsteady incompressible navier-stokes equations, *J. Comput. Phys.*, **112**, No 1.

Rhines, P. B. 1975, Waves and turbulence on a beta-plane, *J. Fluid Mech.*, **69**, 417-443

Rhines, P. B. and W. R. Young, 1982a, A theory of the wind-driven circulation. I: Midocean gyres, *J. Marine Res.*, **10(3)**, 559-596.

Rhines, P. B. and W. R. Young, 1982b, Homogenization of potential vorticity homogenization planetary gyres, *J. Fluid Mech.*, **122**, 347-368

Salmon, R., G. Holloway and M. C. Hendershott, 1976, The equivilibrium statistical mechanics of simple quasigeostrophic models, *J. Fluid Mech.*, **75**, 691-703.

Soh, W. Y. and J. W. Goodrich, 1988, Unsteady solutions of incompressible Navier-Stokes equations, *J. Comput. Phys.*, **79**, 113-134.

Schär, C. and R. Smith, 1993, Shallow water flow past isolated topography. Part I: Vortex production and wake, *J. Atmosph. Sci.*, **50**, 1373-1401.

Thompson, L-A, 1993, The effect of continental rises on the wind-driven ocean in an eddy resolving model, *Proceedings of* XIX*th Conference on Atmospheric and Oceanic Waves and Stability*, San-Antonio, Texas, 1992.

Turkel, Eli, 1987, Preconditioned methods for solving the incompressible and low speed compressible equations, *J. Comput. Phys.*, **72**, 277-298.

Weiyan, T., *Shallow Water Hydrodynamics*, Elsevier Science Publishers, Hong Kong, 1992

Topographic Stress Parameterization in a Primitive Equation Ocean Model: Impact on Mid-latitude Jet Separation

Andreas J. Roubicek, Eric P. Chassignet, and Annalisa Griffa

University of Miami, RSMAS/MPO, 4600 Rickenbacker Causeway, Miami, FL 33149

Abstract. In a recent paper, Griffa *et al.* (1995) showed that, despite the fact that it was developed for quasi-geostrophic motions, statistical mechanics theory is able to capture the main aspects of the inertial equilibrium states that are outside the range of validity of quasi-geostrophy. These results encourage the development of subgrid scale parameterizations for oceanic general circulation models based on statistical mechanics predictions. In this paper, the effect of this type of parameterizations on one particular aspect of the oceanic wind-driven circulation, the separation of a western boundary current from the coast and its dependence on bottom topography, is investigated. The maximum entropy state predicted by statistical mechanics is characterized by a southward flow in the western part of the North Atlantic basin, opposite to the wind-driven northward boundary current. It is then natural to expect that, when parameterized in a numerical model, this tendency should have a significant impact on the current separation latitude by moving it to the south. This may be of importance as most coarse resolution numerical simulations of the North Atlantic circulation exhibit an overshooting Gulf Stream.

1. Introduction

The inertial characteristics of the oceanic circulation in a closed basin have been extensively discussed in the literature. In particular, the purely inertial limit (i.e., the limit of no forcing and no dissipation) for quasi-geostrophic flows has been studied using the theory of statistical mechanics. This theory predicts the existence of inertial equilibrium states corresponding to the maximum entropy of the system, characterized by mean flows with a linear relationship between streamfunction and potential vorticity (Salmon *et al.*, 1976). These flows are often indicated as "Fofonoff flows" because in the case of a one layer, flat bottom, β-plane basin, they correspond to the well known two-gyre solutions of the steady quasi-geostrophic equation first studied by Fofonoff (1954). In the presence of topography, the Fofonoff flows are modified and are given by solutions locked to the topography (Carnevale and Frederiksen, 1987).

The predictions of the theory of statistical mechanics, and in particular the emergence of mean Fofonoff flows, have been tested in a number of numerical studies using the quasi-geostrophic equation. The results show good agreement with the theory (e.g., Wang and Vallis, 1994; Cummins and Holloway, 1994). The question as to whether or not the inertial tendency toward the Fofonoff flows persists outside the range of validity of quasi-geostrophy was addressed numerically by Griffa *et al.* (1995). This question is not a simple one to address theoretically, as generalizations of statistical mechanics theories are difficult to achieve. They have been attempted only for some specific cases (e.g., Salmon, 1982; Errico, 1984). As suggested by Holloway (1992), the validity of the statistical mechanics theory outside quasi-geostrophy can have important and practical consequences. If the tendency toward a maximum entropy Fofonoff flow survives within the range of validity of the primitive equations, and if it is characteristic of the nonlinearity, it can then be used as a basis for a new and more accurate parameterization of the actions of subgrid scale nonlinear effects in low resolution ocean general circulation models (OGCMs). The parameterization proposed by Holloway (1992) replaces the traditional eddy viscosity that tends to drive the flow toward a state of rest with a term that would drive the barotropic part of the solution toward a Fofonoff flow (Alvarez *et al.*, 1994; Eby and Holloway, 1994; Fyfe and Marinone, 1995; Holloway *et al.*, 1995).

In Griffa *et al.* (1995), inertial solutions obtained with a primitive equation numerical model were interpreted using the statistical mechanics results developed in the framework of quasi-geostrophic theory. The experiments were "initial release" experiments, where an initial random field of eddies is allowed to evolve freely and the emergence of equilibrium solutions is observed. The process of equilibration of the solutions was studied in detail, and the final states were compared with the Fofonoff solutions predicted by the statistical mechanics theory. The experiments suggest that, despite the fact that the theory was developed for quasi-geostrophic motions, statistical mechanics theory is able to capture the main aspects of the inertial equilibrium states that are outside the range of validity of quasi-geostrophy.

These results therefore support the hypothesis of Holloway (1992) and encourage the development of subgrid scale parameterizations for OGCMs based on the statistical mechanics predictions (Eby and Holloway, 1994). In this paper, we study the effect of this type of parameterizations on one particular aspect of the oceanic wind-driven circulation, the separation of a western boundary current from the coast and its dependence on bottom topography. As shown by Eby and Holloway (1994), the maximum entropy state predicted by statistical mechanics is characterized by a southward flow in the western part of the North Atlantic basin, opposite to the

wind-driven northward boundary current. It is then natural to expect that, when parameterized in a numerical model, the maximum entropy tendency should have a significant impact on the current separation latitude by moving it to the south. This may be of importance as most coarse-resolution numerical simulations of the North Atlantic circulation exhibit an overshooting Gulf Stream.

The layout of the paper is the following. In section 2, the impact of topography on mid-latitude jet separation is briefly reviewed. The numerical model characteristics are introduced in section 3. In section 4, the basic numerical experiments are described and discussed in relation to Holloway (1992). Implementation of the subgrid scale parameterization and its impact on the solution is presented in section 5. Finally, the results are summarized and discussed in the concluding section.

2. Background

Bottom topography has for a long time been recognized as an important factor in the determination of the path of western boundary currents (Greenspan, 1963; Warren, 1963). One of the earliest numerical studies of the influence of bottom topography on the ocean circulation was that of Holland (1967), in a homogeneous, β-plane numerical ocean model with steady wind stress curl. He showed that topography plays a dominant role in the separation of the western boundary current from the coast and concluded that the presence of a western continental slope tends to induce an earlier separation of the jet as the jet follows lines of constant potential vorticity.

Holland (1973) then considered the joint effect of baroclinicity and relief (JEBAR) and showed numerically that the transport of the anticyclonic subtropical gyre was enhanced with respect to the Sverdrup transport when both effects were considered. Holland (1973) noted that a horizontal velocity as small as 0.1 cm s^{-1} perpendicular to a continental slope with gradient 10^{-3} is able to produce topographic torques comparable to those of the average wind stress curl, suggesting that in the real ocean the topographic terms may be more important than the wind itself in determining the magnitude of the western boundary transport.

The effect of continental rises on the wind-driven circulation in a quasi-geostrophic framework was recently further investigated by Thompson (1995), who developed a modification to the theory of Rhines and Young (1982) and carried out three-layer eddy-resolving quasi-geostrophic numerical simulations. The effect of large scale topography has been addressed in the findings of Treguier and McWilliams (1990) that topography of largest scale has the most important effect on the momentum balance of the flow, while small scale topography has an indirect influence and does not contribute as greatly to the stress. Overall, large scale bottom topography has a significant impact on the oceanic flow, acting upon it mainly by means of effects on the potential vorticity field. Together with baroclinicity, it can account for much of the observed intensity and flow pattern of western boundary currents. The effects of topography are felt throughout the water column, but are most notorious in the deep ocean, where closed potential vorticity contours can "trap" the flow and drive it more efficiently.

3. The Numerical Model

The numerical model used in this study is the adiabatic version of MICOM (Miami Isopycnic Coordinate Ocean Model) (see Bleck and Chassignet, 1994, for details). It may be viewed as a stack of shallow water models, each consisting of a momentum and a continuity equation:

$$\frac{d\mathbf{v}}{dt} + f\mathbf{k}\times\mathbf{v} = -g\nabla\eta + \mathbf{F}$$
$$\frac{\partial h}{\partial t} + \nabla(h\mathbf{v}) = 0 \qquad (1)$$

where $\mathbf{v}$ is the horizontal velocity field and $\mathbf{F}$ is an eddy viscosity operator that simulates the action of small scale processes. Other variables retain their conventional meanings. Horizontal velocities and vorticity are defined as layer properties.

The operator $\mathbf{F}$ is expressed as

$$\mathbf{F} = A\frac{1}{h}\nabla(h\nabla\mathbf{v}) \qquad (2)$$

where A is the eddy viscosity coefficient. As shown by Gent (1992), the operator (2) has the important physical property of being energetically consistent, in the sense that it induces energy dissipation during the flow evolution. The operator $\mathbf{F}^*=A\nabla^2\mathbf{v}$, on the other hand, can actually generate energy in the context of the shallow water equations (1) as illustrated by Gent (1992).

The model is configured for this study in a square ocean basin 2580 km on a side, with constant mesh size in the horizontal and three layers in the vertical. The model is driven by a zonally symmetric wind stress

$$\vec{\tau} = \left[-\tau_m \cos\left(\frac{2\pi y}{L_o}\right), 0\right] \qquad (3)$$

where

$$\tau_m = 1\times10^{-4}\ \mathrm{m^2 s^{-2}}.$$

Such forcing results in a Sverdrup circulation which consists of two gyres, subtropical and subpolar. The wind stress is specified as a body force acting only on the layer directly beneath the surface (Chassignet and Gent, 1991; Chassignet and Bleck, 1993). The eddy viscosity A is proportional to the grid spacing and is characterized by a constant diffusive velocity $u_d = A/\nabla x$ equal to 2 cm s^{-1}. The lateral boundary conditions employed on the four side-walls are free slip, i.e., zero vorticity. The bottom topography consists of four shelves (100 km wide) and four slopes (200 km wide of gradient α).

4. The Wind-Driven Experiments

Three weak slope ($\alpha = 2.5\times10^{-3}$) experiments (W1, W2, and W3) were performed with a mesh size of 20, 40, and 80 kilometers, respectively. A second set (S1, S2, and S3) was performed for a stronger slope ($\alpha = 1.25\times10^{-2}$). All the numerical experiments were integrated for 25 model years (1 model year is equal to 360 days) and the presented fields were averaged over the last 5 years. The 80-km experiments are considered the coarse mesh experiments and do not resolve the mesoscale eddies that are present in the fine mesh experiments (20-km grid).

The 5-year time-averaged layer streamfunctions for the weak slope experiments (W1, W2, and W3) are displayed in Figures 1, 2, and 3, respectively. In W1, the mid-latitude jet is highly nonlinear, with large meanders. Mesoscale eddies are formed through baroclinic instabilities and the bottom layer is set in motion. The resulting circulation in the bottom layer is cyclonic and locked to the f/H contours (Figure 4a). It is quite intense (about 31 Sverdrups) with a marked signature in the barotropic streamfunction. As the resolution is decreased from W1 to W3, the eddy activity diminishes and the eddy-driven flow in the bottom layer becomes weaker (Figures 2d and 3d). The jet separation latitude is south of the zero wind stress curl line (ZWCL) in both W1 and W2, but exactly at the ZWCL in W3. The two possible factors responsible for a southward separation of the western boundary current are (1) topography and (2) the fact that the wind is prescribed as a body force over the

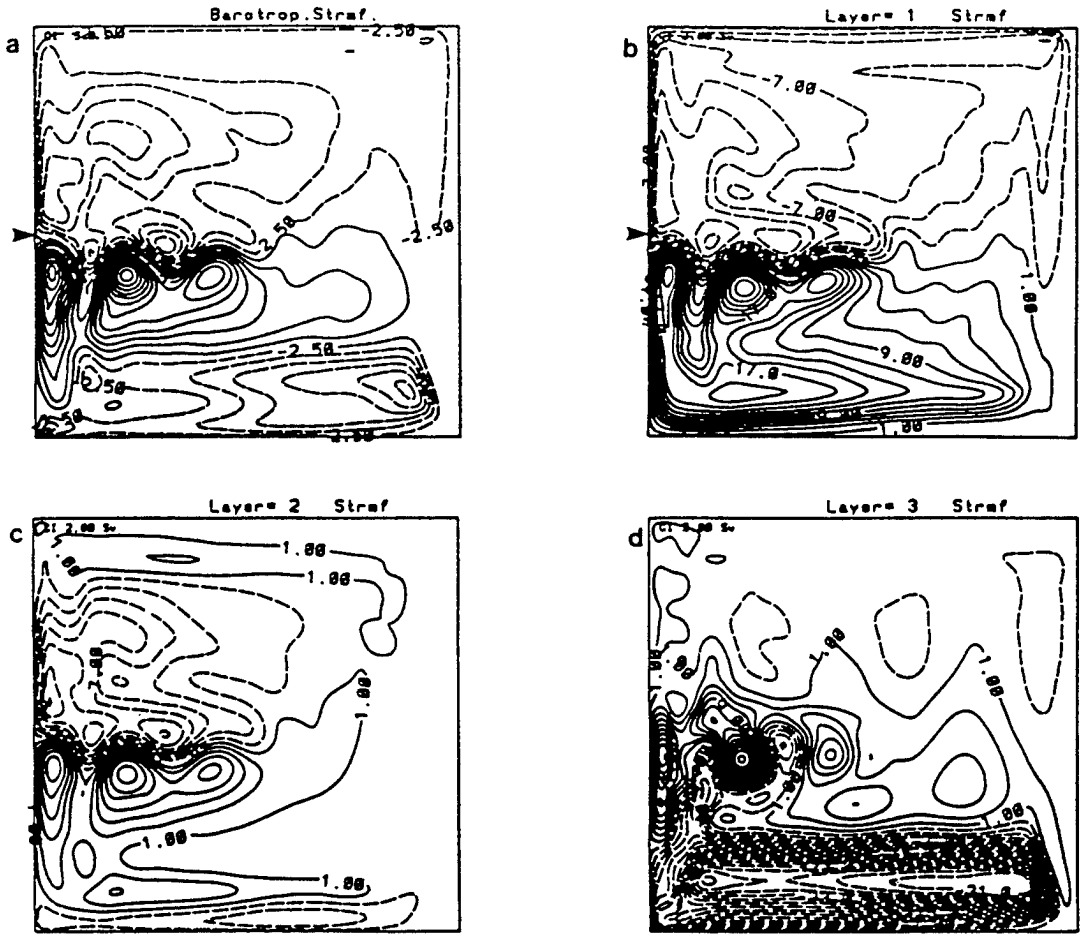


Figure 1. 5-year time average layer streamfunctions (in Sverdrups) for the weak slope experiment W1 (grid spacing 20 km). The arrow represents the ZWCL.

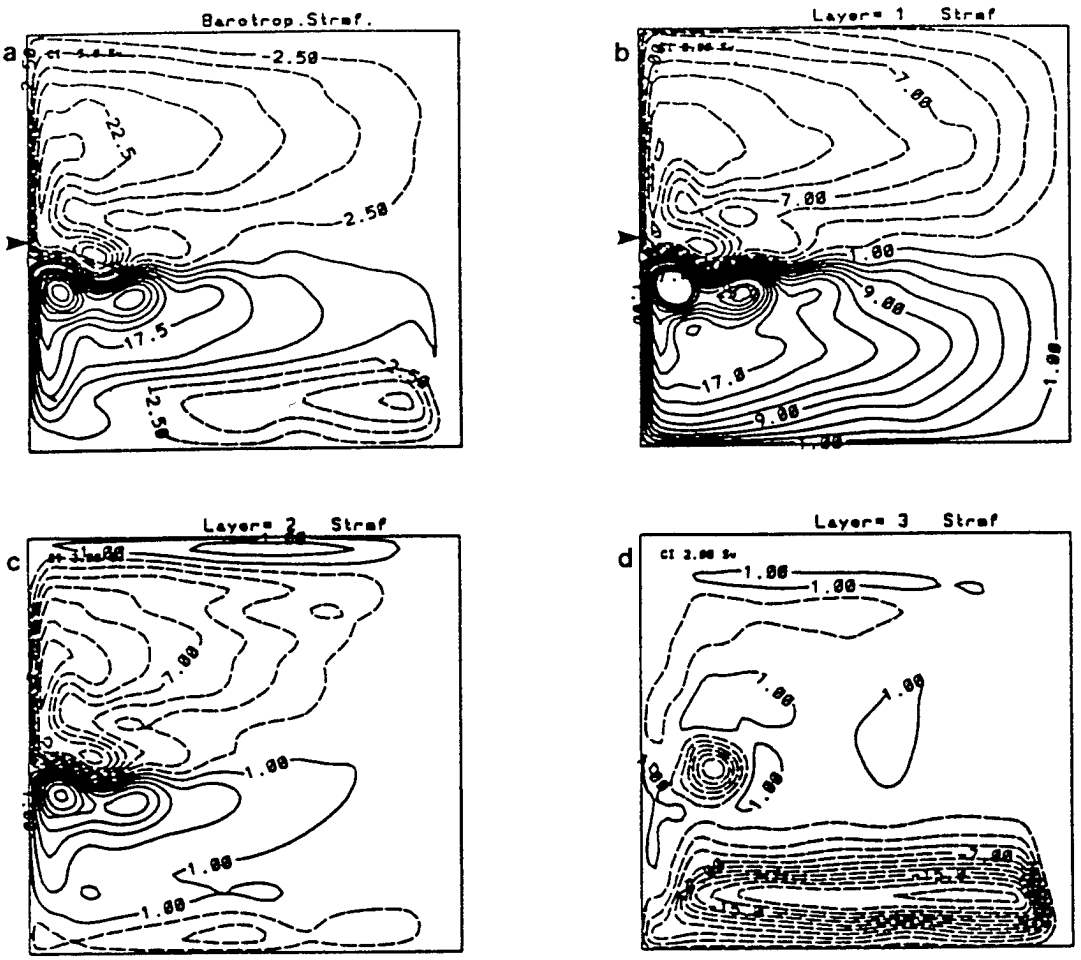


Figure 2. As in Figure 1, for experiment W2 (grid spacing 40 km).

uppermost layer (Chassignet and Gent, 1991; Chassignet and Bleck, 1993). To assess the effect of topography, a control experiment was performed with a flat bottom and high resolution (20 km). For this configuration, the separation is located at the ZWCL (Figure 5) implying that the southern separation in W1 and W2 can be attributed solely to the topography.

A reduction in the bottom layer flow intensity is also observed in the strong slope experiments (S1, S2 and S3) (Figures 6, 7, and 8) with a decrease in resolution, except that the bottom layer cyclonic circulation now encompasses most of the basin, following the f/H contours (Figure 4b).

Topography is seen to play a strong role in determination of the separation latitude, as all of the strong slope experiments show a separation point located farther south than that seen in their weak slope counterparts.

5. Implementation of the Neptune Effect and its Impact on Mid-Latitude Jet Separation

5.1 The Neptune Effect and its Implementation

The so-called "Neptune" effect (Holloway, 1992) is a subgrid scale parameterization that seeks to represent the effect of eddies interacting with topography, an interaction that is capable of exerting large stress upon the mean circulation. This parameterization is achieved by relaxing the velocities toward a maximum entropy solution that depends upon the shape of the topography. The theory (Salmon *et al.*, 1976) was developed using statistical mechanics in the context of quasi-geostrophy. It does not take into account the effects of external forcing or of dissipation.

As suggested by Eby and Holloway (1994), motions on scales larger than the first Rossby radius of deformation

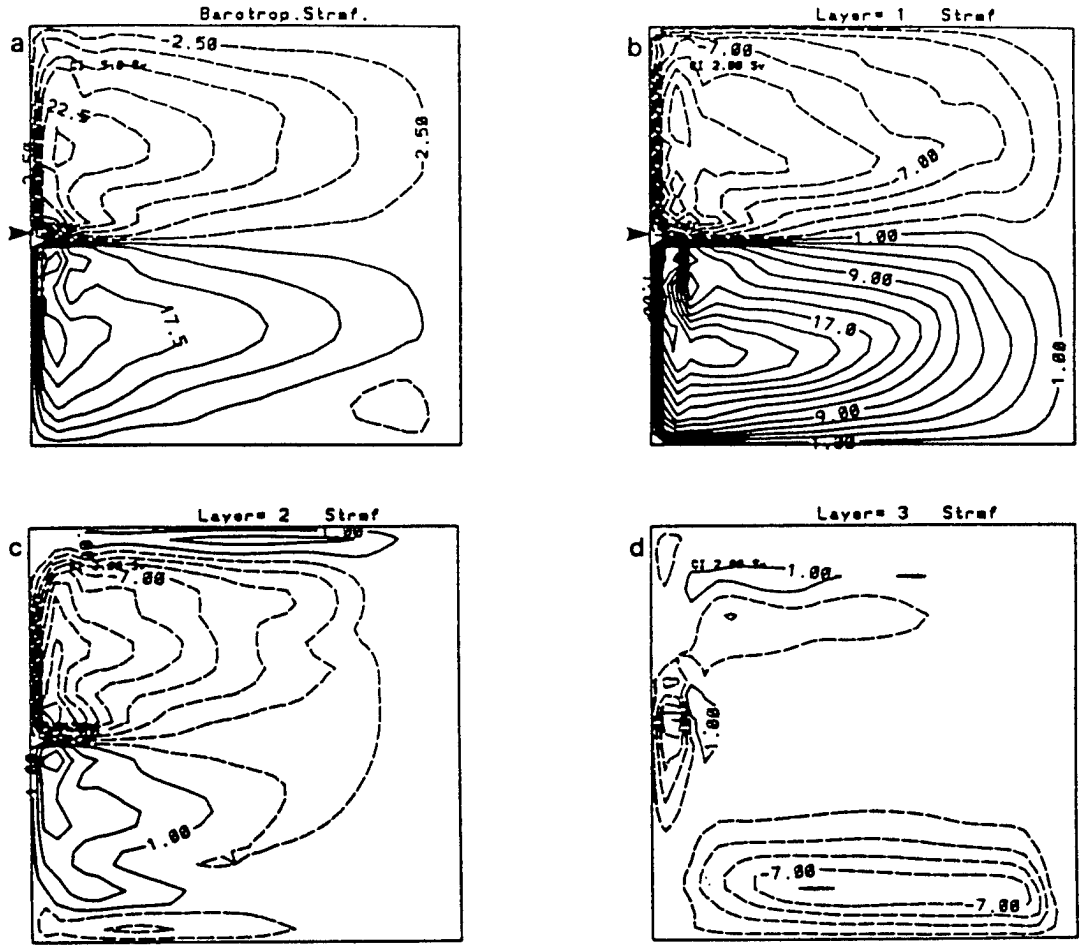


Figure 3. As in Figure 1, for experiment W3 (grid spacing 80 km).

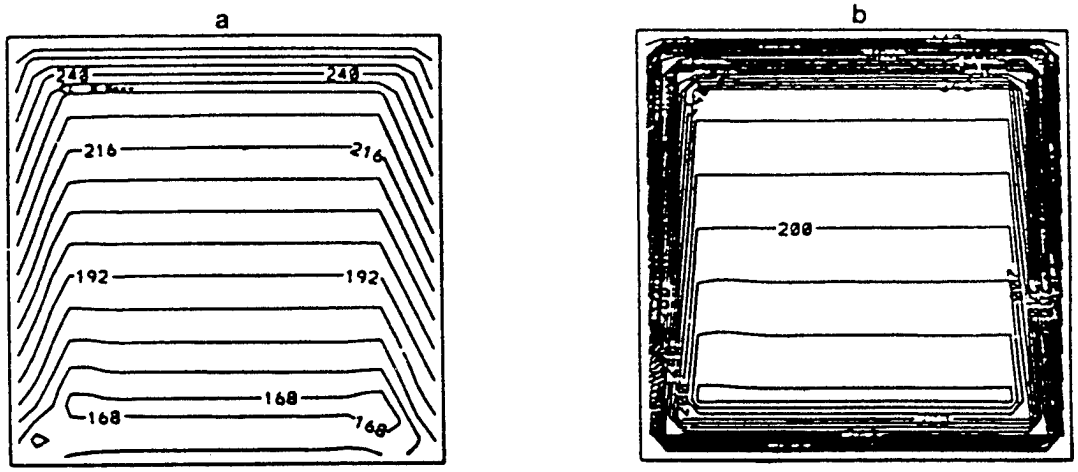


Figure 4. *f/H* contours for (a) the weak slope experiments (α=2.5 × 10^{-3}) and (b) the strong slope experiments (α =1.25 × 10^{-2})

are expected to be barotropic, and, according to the maximum entropy principle of statistical mechanics, their equilibrium states should satisfy

$$\left(\alpha_1/\alpha_2 - \nabla^2\right)\langle\psi\rangle = \langle q\rangle \tag{4}$$

where $\langle\psi\rangle$ is the time-averaged streamfunction, α_1/α_2 is a ratio of Lagrange multipliers, and $\langle q\rangle$ is the time-averaged depth integrated potential vorticity. For a coarse resolution model, Holloway (1992) simplified (3) by assuming that variations in topography are larger than variations of f and that the model grid is larger than $L = \left(\alpha_1/\alpha_2\right)^{1/2}$. He then expressed the maximum entropy equilibrium solution as

$$\psi^* = -f L^2 H \tag{5}$$

where H is the total depth. For more details, the reader is referred to Holloway (1992).

One may question the applicability of such a theory to forced solutions. A number of experiments have been performed with forcing and dissipation to study the relevance of the inertial equilibrium states to forced solutions. In these experiments, Fofonoff flows, despite the presence of forcing, appear to be representative of the

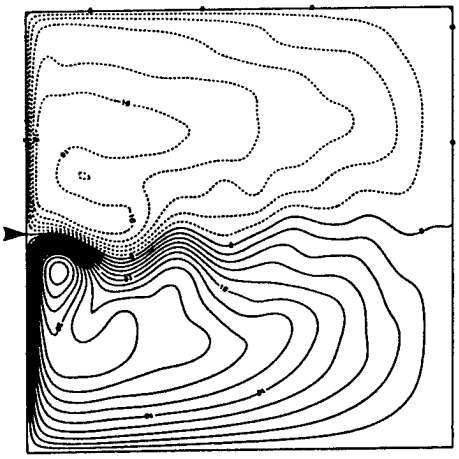


Figure 5. 5-year time average upper-layer streamfunction (in Sverdrups) for the flat-bottom experiment.

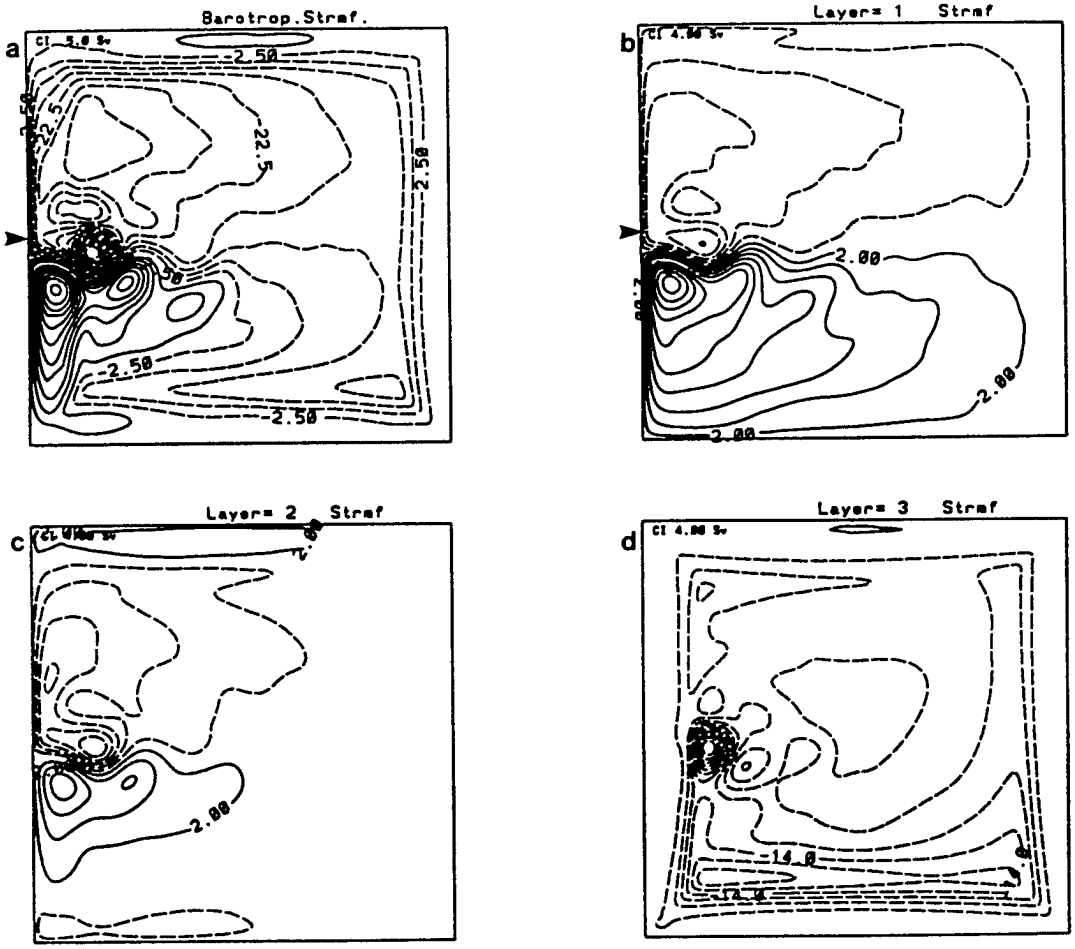


Figure 6. 5-year time average layer streamfunctions (in Sverdrups) for the strong slope experiment S1 (grid spacing 20 km).

tendency of the nonlinearity, and the actual shape of the forced solutions depends upon the competition between this tendency and the effects of the forcing (e.g., Griffa and Salmon, 1989; Cummins, 1992, Griffa and Castellari, 1991). These experiments were performed with a quasi-geostrophic model. Recently, Griffa et al. (1995) also showed that, despite the fact that the theory was developed for quasi-geostrophic motions, statistical mechanics theory is able to capture the main aspects of the inertial equilibrium states which are outside the range of validity of quasi-geostrophy.

Introduction of dissipation in a series of one-layer "initial release" experiments similar to the ones discussed in Griffa *et al.* (1995) does modify the $\langle\psi\rangle$-$\langle q\rangle$ scatter plot from a linear relationship to one with a small curvature and a smaller ratio of the Lagrange multipliers α_1/α_2 (Roubicek, 1995). In the high resolution wind-driven experiments (W1 and S1) introduced in the previous section, only the bottom layer can be considered as a random collection of eddies generated by fluctutions in the uppermost layer. While the forcing is continuous, these eddies tend to organize themselves as Fofonoff flows as illustrated by Figures 2d and 7d. The corresponding $\langle\psi\rangle$-$\langle q\rangle$ scatter plot (not shown) is in qualitative agreement with the dissipative "initial release" experiments, especially for the strong slope experiment S1 (Roubicek, 1995).

These results illustrate the possible relevance of statistical mechanics theory to wind-driven dissipative solutions. For practical applications, L is difficult to determine (Eby and Holloway, 1994) and can be obtained from the $\langle\psi\rangle$-$\langle q\rangle$ scatter plot only for idealized cases. In the remainder of this paper, L was chosen as a constant 15 km based on "initial release" experiments of Rossby number equivalent to the wind-driven experiments (Roubicek, 1995). The simplified maximum entropy solutions ψ^* (Equation 5) corresponding to the sloping topography is displayed in Figure 9. The subgrid scale parameterization proposed by Holloway (1992) relaxes the barotropic velocity field in the absence of forcing toward $\mathbf{v}^*$:

$$u^* = -\frac{1}{H}\frac{\partial\psi}{\partial y}; v^* = \frac{1}{H}\frac{\partial\psi}{\partial x} \tag{6}$$

by modifying the operator $\mathbf{F}$ as $\mathbf{F} = A\frac{1}{h}\nabla(h\nabla(\mathbf{v}-\mathbf{v}^*))$.

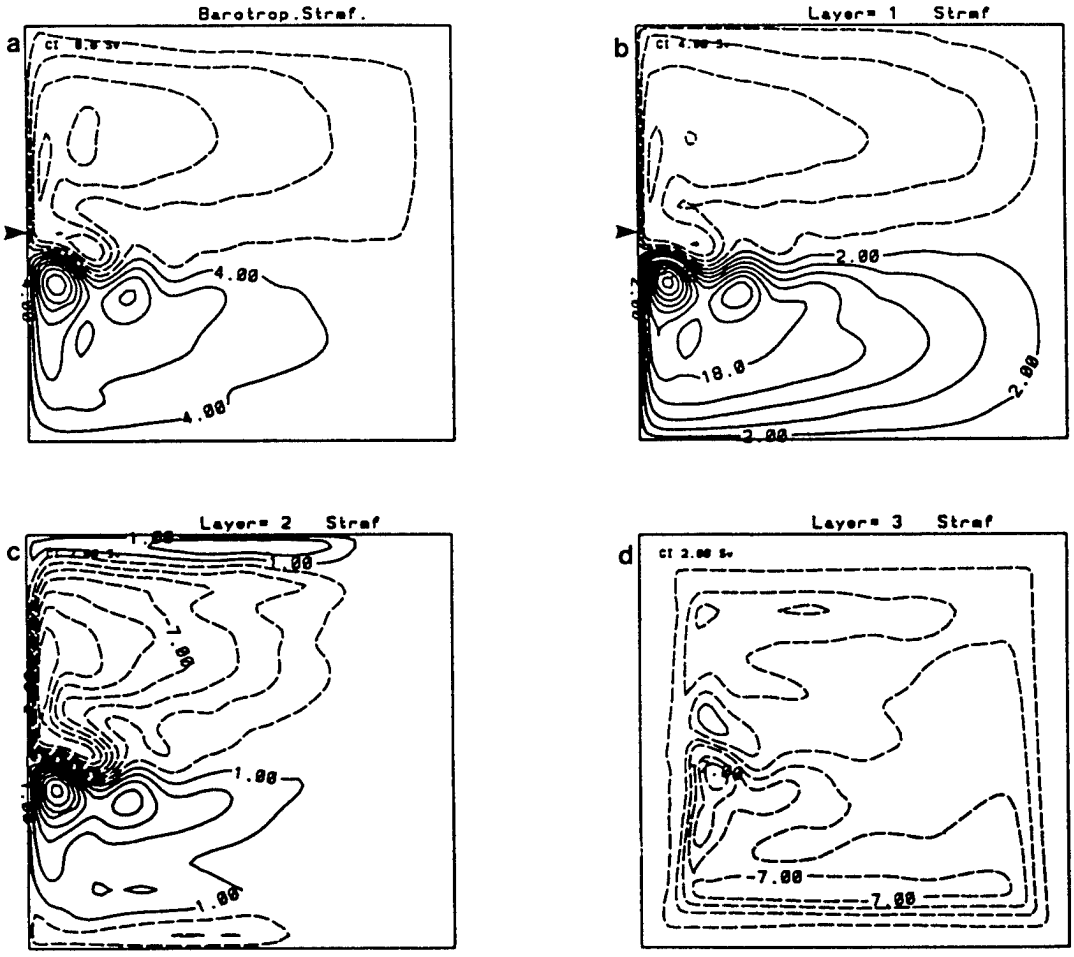


Figure 7. As in Figure 6, for experiment S2 (grid spacing 40 km).

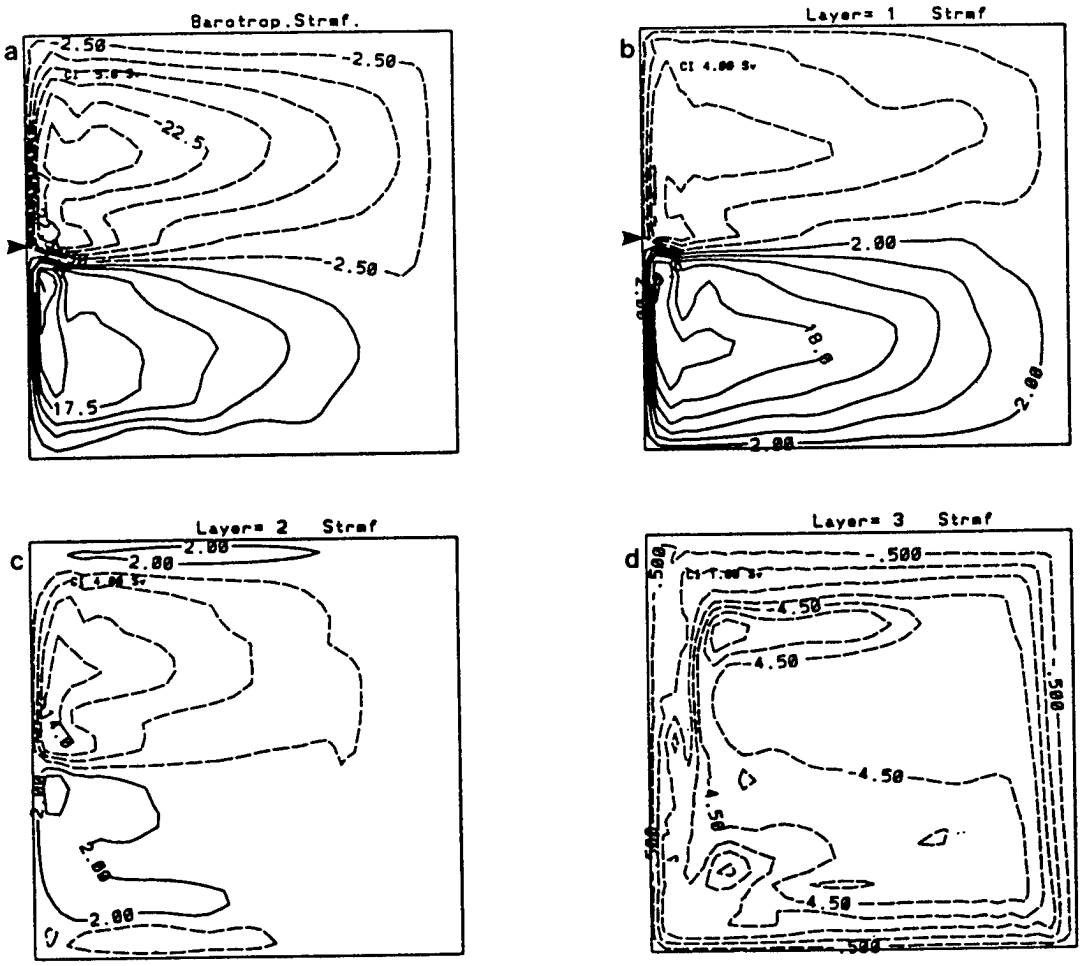


Figure 8. As in Figure 6, for experiment S3 (grid spacing 80 km).

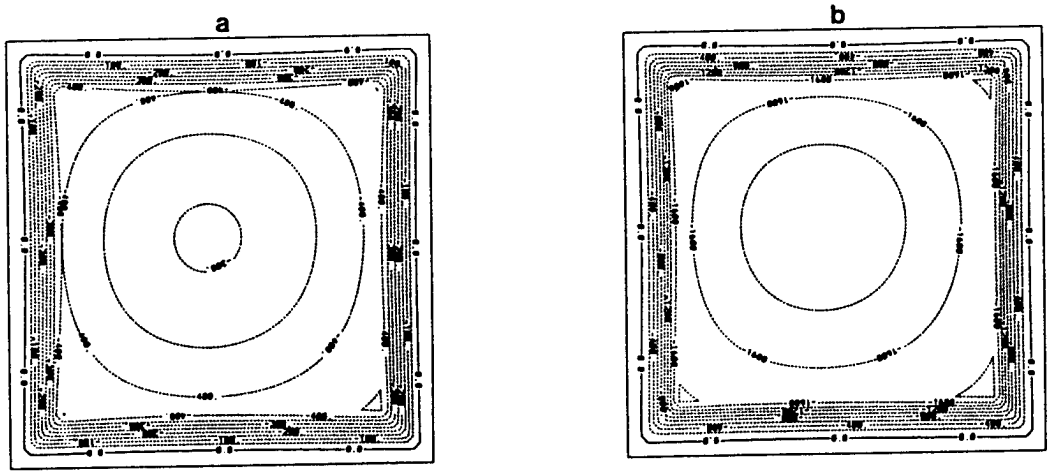


Figure 9. Transport streamfunction ψ^* (in Sverdrups) (a) for the weak slope experiment and (b) for the strong slope experiment.

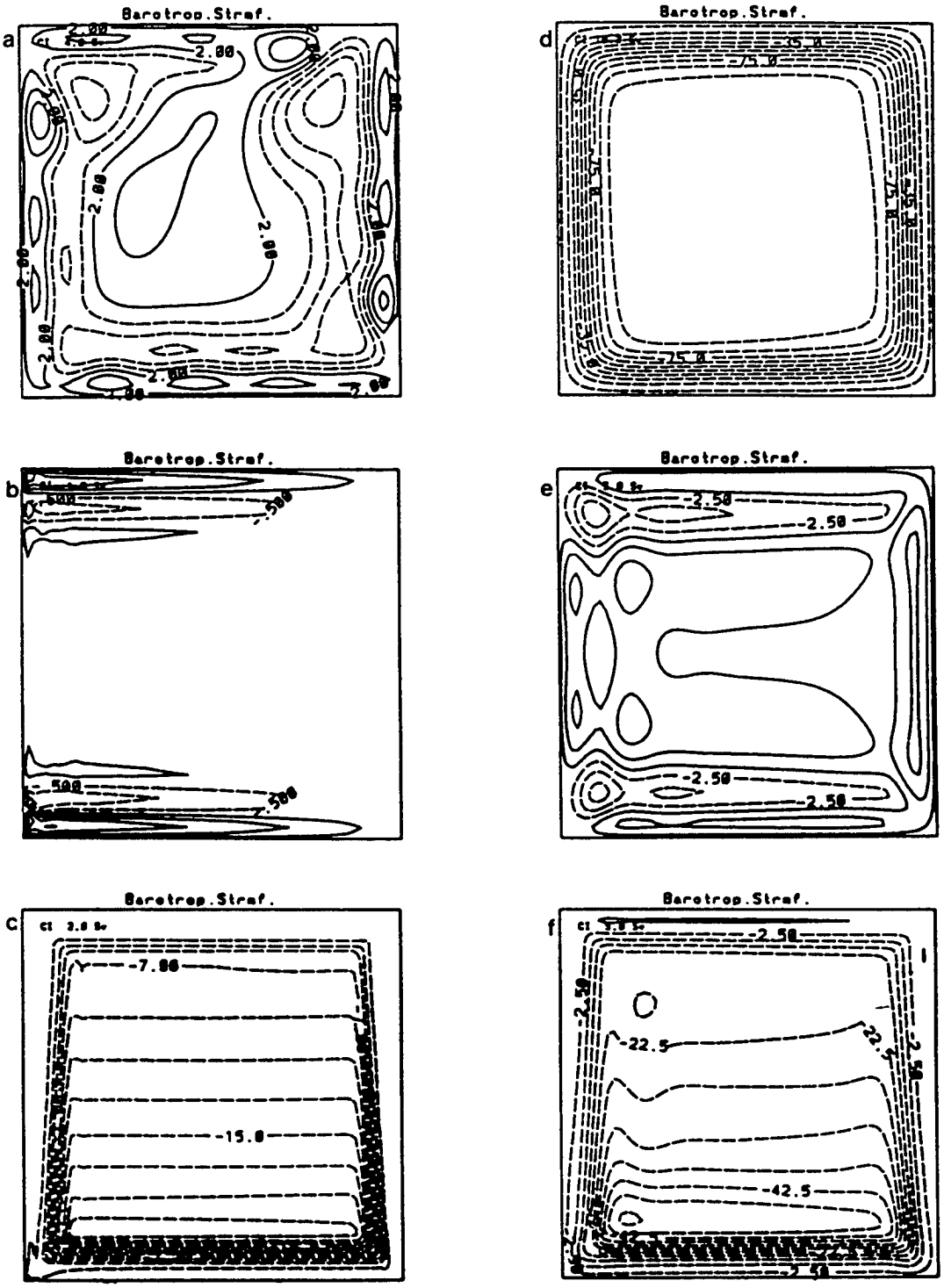


Figure 10. End-state barotropic streamfunctions (in Sverdrups) with the subgrid scale parameterization alone for the weak slope experiments, as described in the text.

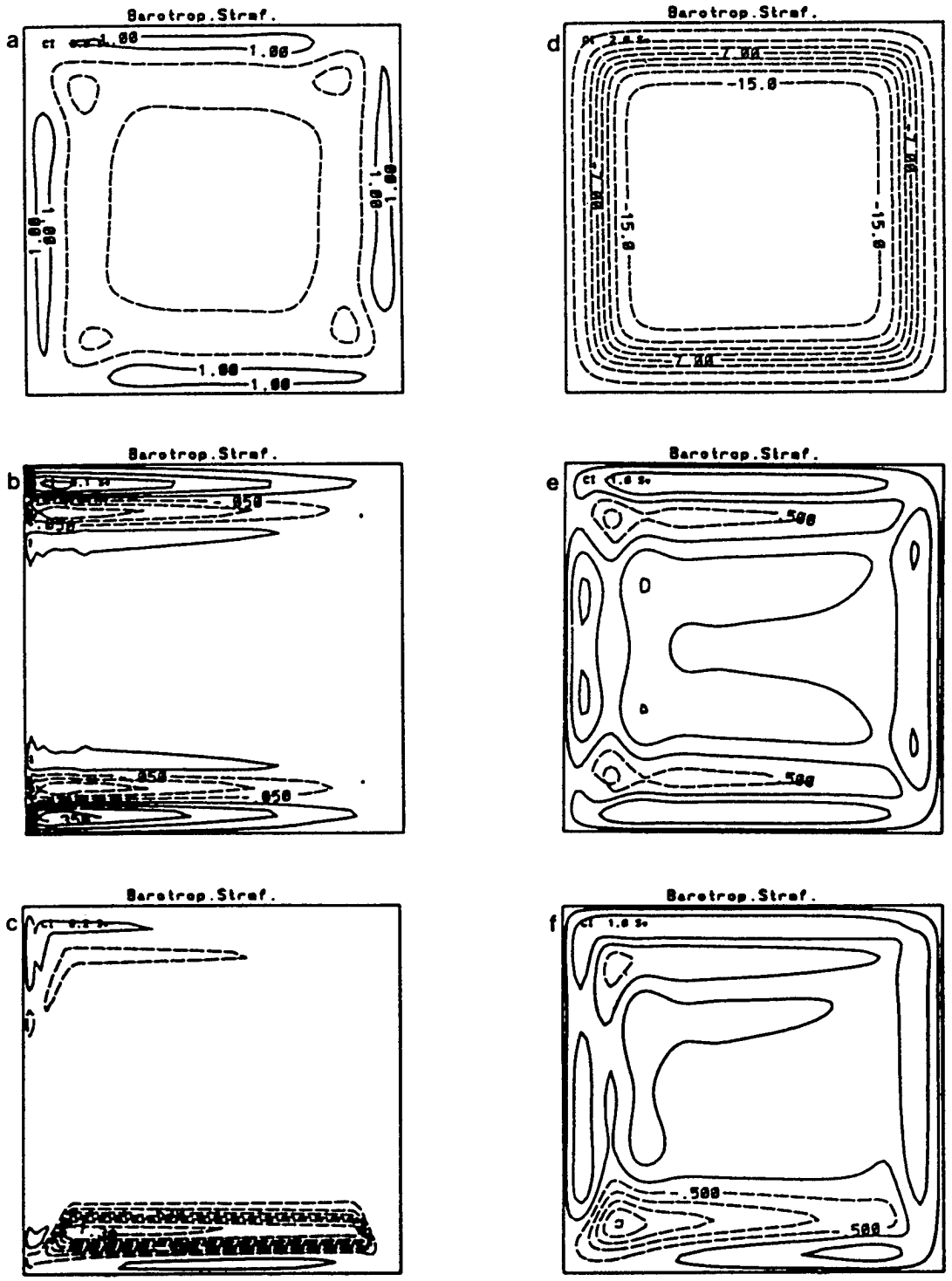


Figure 11. As in Figure 10, for the strong slope experiments.

The effectiveness of this relaxation is dependent upon the magnitude of the eddy viscosity coefficient A .

It is of interest to first investigate this relaxation mechanism in the absence of wind forcing, since both the β-effect and topography play a significant role in the adjustment, whereas only the topography effects are captured by the parameterization. Figures 10 and 11 show the end state barotropic streamfunctions resulting from the integration of (1) with zero forcing and with the sub-grid scale parameterization, for the experiments with weak and strong topography respectively. The adjustment is relatively fast, but the final kinetic energy level varies greatly as a function of the eddy viscosity coefficient (Roubicek, 1995). The left panels in Figures 10 and 11 are for experiments with $A = 80$ m^{2}s^{-1}, and the right panels for experiments with $A = 8000$ m^{2}s^{-1}. From top to bottom, the figures correspond to experiments that were run on an f-plane with no topography, on a β-plane without topography, and on a β-plane with topography.

On the f-plane, the flow for the low viscosity experiments (Figures 10a, 11a) does not have a strong organized cyclonic circulation when compared to the high viscosity cases (Figures 10d, 11d) and to the maximum entropy fields (Figure 9). On the β-plane, this flow is modified into zonal bands of cyclonic and anticyclonic cells (Figures 10b,e and 11b,e). Topography, when present, strongly traps the flows to a cyclonic circulation dictated by the f/H contours (Figures 10c,f and 11c,f). While the subgrid scale parameterization appears to be relatively effective in these experiments, especially for strong topography, the combination of the β-effect and topography can lead to a resulting field different from the maximum entropy solution.

5.2 Impact on Mid-Latitude Jet Separation

The subgrid scale parameterization was applied to the coarse resolution wind-driven experiments of section 4. The 5-year time-averaged streamfunctions for both the weak and the strong slope experiments (W4 and S4, respectively) are displayed in Figures 12 and 13.

When compared to the experiments without the parameterization, the differences are small for the weak slope case (W4). The parameterization has little impact on the circulation of the uppermost layer and the jet separation latitude remains at the ZWCL. The only visible signature is in the bottom layer where the topographically

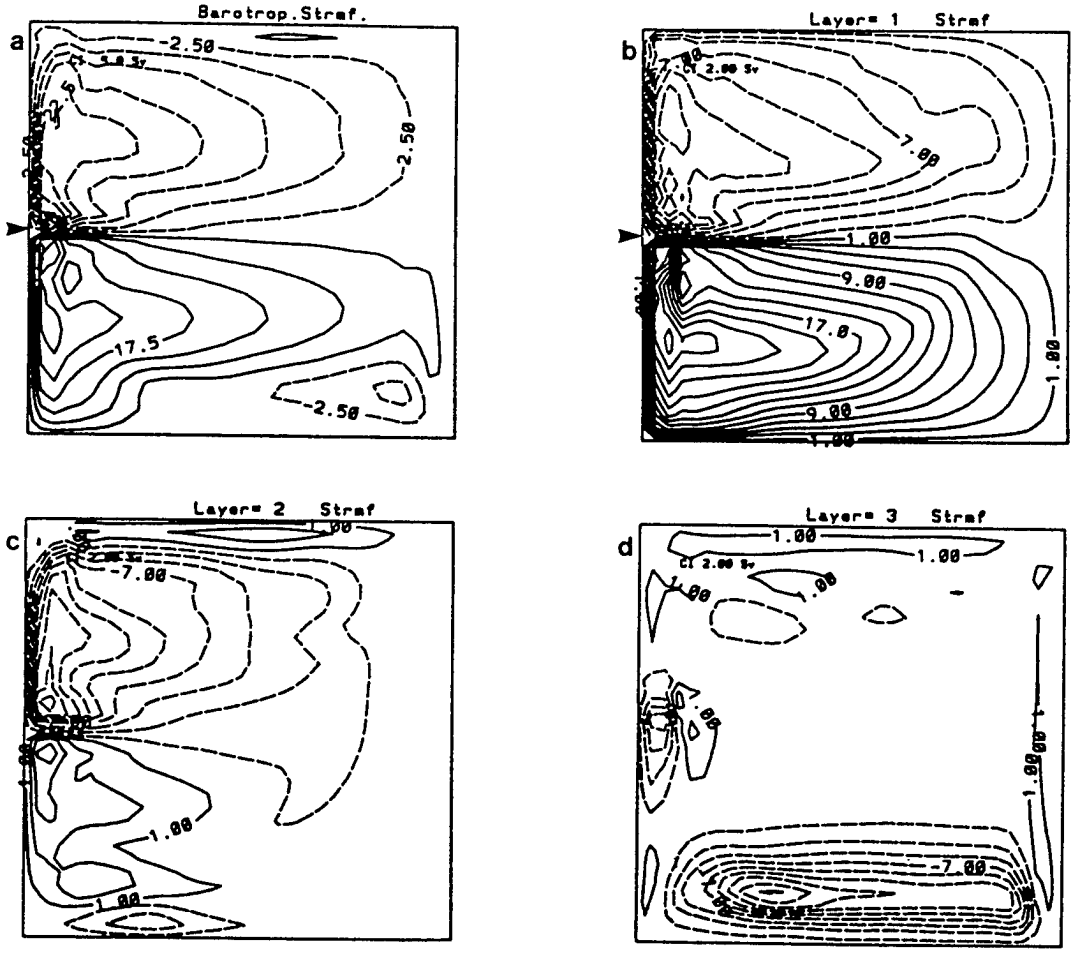


Figure 12. 5-year time average streamfunctions (in Sverdrups) for the weak slope experiment W4.

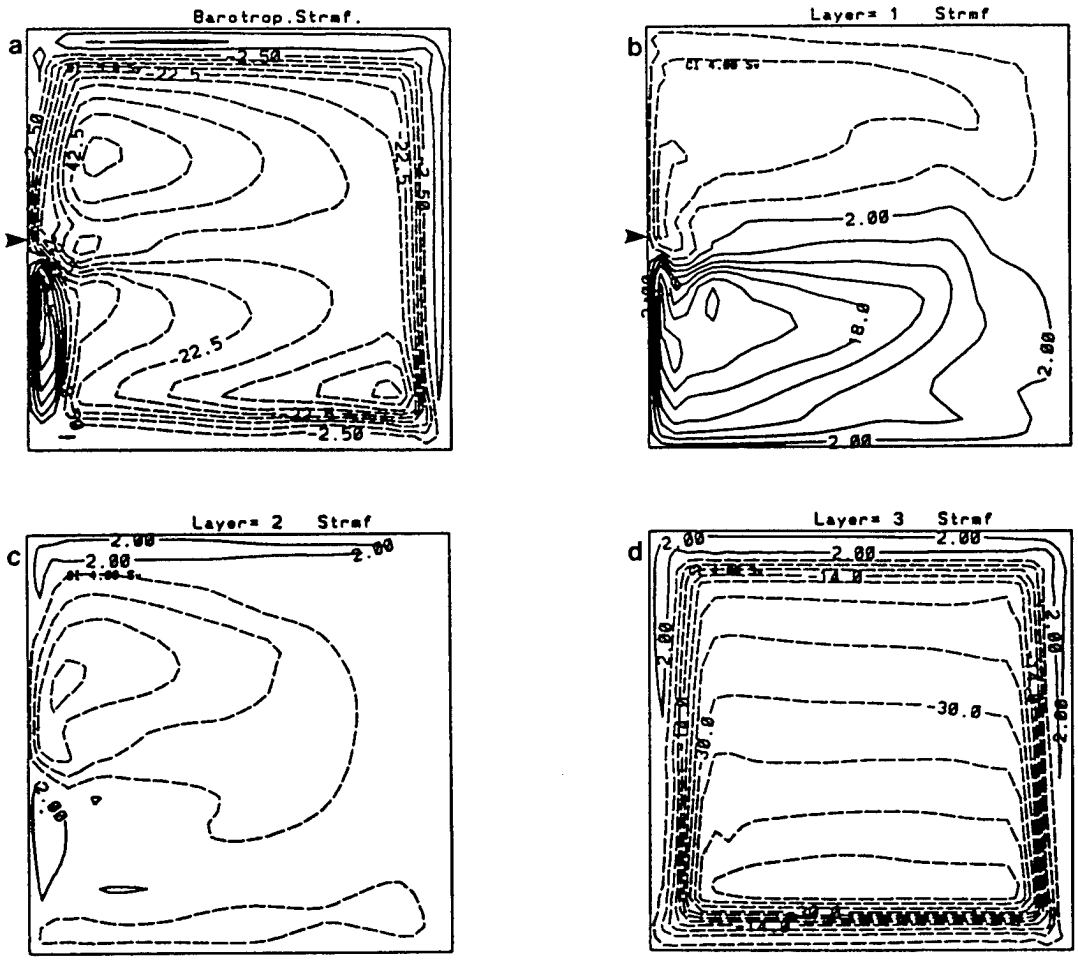


Figure 13. 5-year time average streamfunctions (in Sverdrups) for the strong slope experiment S4.

trapped cyclonic circulation is increased by about 10 Sverdrups (Figure 12d). The effect is more vigorous in the strong slope case (S4) where the signature of the parameterization is present in all layers (Figure 13).

In S4, several features characteristic of the high resolution experiment S1, not observed in the coarser resolution experiment S3, are now present. The mid-latitude jet separates from the coast at a point further to the south and penetrates the interior in a less zonal fashion than in S3. In the bottom layer, the circulation is intense, considerably stronger than in S1, and dominates the barotropic flow.

6. Summary and Concluding Remarks

Implementation of the "Neptune" parameterization in idealized wind-driven experiments with topography led to mixed results. On one hand, in cases with weak topography, the signature of the parameterization is very small and has very little impact on the upper layer circulation and the jet separation latitude. On the other hand, strong topography leads to a stronger parameterized maximum entropy flow and its signature is visible in all layers. The mid-latitude jet indeed separates at a more southern latitude, but the strong cyclonic circulation induced by the parameterization is predominant in the barotropic circulation and much more intense than in the fine resolution case. While it is apparent that such a parameterization is desirable in coarse-resolution experiments, its implementation is not straight forward. The experiments presented in this paper indicate that the value chosen for L may be a function of the chosen topography as one may wish for stronger (weaker) parameterization for weak (strong) topography. As stated by Eby and Holloway (1994), oustanding issues still include the physical basis for the estimation of L and the appropriateness of the operator **F**.

7. Acknowledgments

The authors wish to thank G. Holloway for lively and constructive discussions. This work is part of a Master of Science thesis performed at the University of Miami and was supported by the Office of Naval Research under

Contract N00014-91-JI346 and by the National Science Foundation through Grants OCE-91-02604 and OCE-94-06663.

References

Alvarez, A., J. Tintore, G. Holloway, M. Eby and J.M. Beckers, 1994: Effect of topographic stress on the circulation in the western Mediterranean. *J. Geophys. Res.*, 99, 16,053-16,064.

Bleck, R., and E. P. Chassignet, 1994: Simulating the oceanic circulation with isopycnic, coordinate models. The Oceans: Physical-Chemical Dynamics and Human Impact. S. K. Majumdar, E. W. Miller, G. S. Forbes, R. F. Schmalz and A. A. Panah, Eds., The Pennsylvania Academy of Science, 17-39.

Carnevale, G.F. and J.D. Frederiksen, 1987: Nonlinear stability and statistical mechanics of flow over topography. *J. Fluid Mech.*, 175, 157-181.

Chassignet, E. P., and P. R. Gent, 1991: The influence of boundary conditions on mid-latitude jet separation in ocean numerical models. *J. Phys. Oceanogr.*, 21, 1290-1299.

Chassignet, E. P., and R. Bleck, 1993: The influence of layer outcropping on the separation of boundary currents. Part I: The wind-driven experiments. *J. Phys. Oceanogr.*, 23, 1485-1507.

Cummins, P.F., 1992. Inertial gyres in decaying and forced geostrophic turbulence, *J. Mar. Res.*, 50, 545-566.

Cummins, P.F. and G. Holloway, 1994: On eddy-topographic stress representation. *J. Phys. Oceanogr.*, 24(3), 700-706.

Eby, M. and G. Holloway, 1995: Sensitivity of a large scale ocean model to a parameterization of topographic stress. *J. Phys. Oceanogr.*, (in press).

Errico, R.M., 1984: The statistical equilibrium solution of a primitive-equation model. *Tellus*, 36(A), 42-51.

Fofonoff, N.P., 1954: Steady flow in a frictionless homogeneous ocean. *J. Mar. Res.*, 13, 254-262.

Fyfe, J. and G. Marinone, 1995: On the role of unresolved eddies in a model of the residual currents in the Central Strait of Gerogia, B.C. *Atmos.-Ocean*, (to appear).

Gent, P.R., 1992: The energetically consistent shallow-water equations. *J. Atmos. Sci.*, 50(9), 1323-1325.

Greenspan, H., 1963: A note concerning topography and inertial currents. *J. Mar. Res.*, 21, 147-154.

Griffa, A. and R. Salmon, 1989: Wind-driven ocean circulation and equilibrium statistical mechanics. *J. Mar. Res.*, 47, 457-492.

Griffa, A., E.P. Chassignet, V. Coles and D.B. Olson, 1995: Inertial gyres solutions from a primitive equation ocean model. *J. Mar. Res.*, (submitted).

Griffa, A. and S. Castellari, 1991: Nonlinear general circulation of an ocean model driven by wind with a stochastic component. *J. Mar. Res.*, 49, 53-73.

Holland, W. R., 1967: On the wind-driven circulation in an ocean with bottom topography. *Tellus* XIX, 4, 582-599.

Holland, W. R., 1973: Baroclinic and topographic influences on the transport in western boundary currents. *Geophys. Fluid Dyn.*, 4, 187-210.

Holloway, G., 1992: Representing topographic stress for large scale ocean models. *J. Phys. Oceanogr.*, 22, 1033-1046.

Holloway, G., T. Sou and M. Eby, 1995: Dynamics of circulation of the Japan Sea. *J. Mar. Res.*, (to appear).

Rhines, P.B. and W.R. Young, 1982: A theory of the wind-driven circulation. I: Midocean gyres. *J. Mar. Res.*, 40, 559-596.

Roubicek, A., 1995: Influence of sloping topography on mid-latitude jet separation: A numerical study. Master thesis,R.S.M.A.S, University of Miami.

Salmon, R., 1982: Geostrophic turbulence, *in Topics in Ocean Physics*, A.R. Osborne and P.M. Rizzoli, eds., North-Holland, Amsterdam.

Salmon, R., G. Holloway and M.C. Hendershott, 1976: The equilibrium statistical mechanics of simple quasi-geostrophic models. *J. Fluid Mech.*,75, 691-703.

Thompson, L., 1995: The effect of continental rises on the wind-driven ocean circulation. *J. Phys. Oceanogr.*, (submitted.

Treguier, A.M. and J.C. McWilliams, 1990: Topographic influences on wind-driven stratified flow in a β-plane channel: an idealized model for the Antarctic Circumpolar Current. *J. Phys. Oceanogr.*, 20, 321-343.

Wang, J., and G.K. Vallis, 1994: Emergence of Fofonoff states in inviscid and viscous ocean circulation models. *J. Mar. Res.*, 52, 83-127.

Warren, B.A., 1963: Topographic influences on the path of the Gulf Stream. *Tellus*, 15, 167-183.

Measuring the Skill of an Ocean Model under Eddy-Topographic Effects, Based on a Global Inventory of Long-Term Current Meters

Greg Holloway and Tessa Sou

Institute of Ocean Sciences, Sidney B.C. V8L4B2 Canada

Abstract. From a global inventory of current meters, each of more than 100 days duration, we calculate skills of a global ocean model with and without a parameterization of eddy-topography interaction ("Neptune"). Skills are measured by the kinetic energy of the difference between modeled and observed flow and by error in direction. We assess confidence in the results by repeated tests in which half of the observations are rejected. Without Neptune, the model achieves small but significantly nonzero skills. Inclusion of Neptune improves skills by an increment roughly twice as large as the basic skills without Neptune.

Measuring Model Skill

Advances in computing power have increasingly allowed large scale ocean models to execute with more realistic detail of topography. However, mechanics of eddy-topography interaction may yet require much finer resolution before they can be treated explicitly. An alternative to parameterize eddy effects is an active research topic (Roubicek, Chassignet, and Griffa, this volume). When developing parameterizations for practical application, one seeks "skill measures" based upon observations against which one may refine uncertain model aspects. One tries to identify those ocean attributes which are well observed and which exhibit sensitivity to model components one seeks to refine.

Recently Alvarez et al. (1994), Eby and Holloway (1994, hereafter EH), Fyfe and Marinone (1995) and Holloway et al. (1995) have implemented a representation "Neptune effect") of eddy-topography forcing. These studies considered the western Mediterranean, global ocean, Georgia Strait, and Japan Sea domains, respectively, reporting apparent improvement in fidelity of modeled circulations. Other than modest parameter exploration in the Japan Sea study, little has been done to systematically adjust uncertain Neptune parameters against directly observed flows. Rather, the various authors have only cited examples of currents that may be "better" with Neptune. We seek more quantitative measure of such putative "improvement", perhaps providing a basis for subsequent optimization.

Oceans have been measured in many ways. Distributions of temperature (T), salinity (S), oxygen, and nutrients species are archived. Surveys of transient tracers are reported. Drift bottles, ship drift, current meters, and surface and subsurface floats provide information on currents. Satellite altimetry, electromagnetics, and acoustic methods provide further information.

We considered datasets that provide global coverage, with an aim to measure performance of a global model such as EH rather than a more region-specific study. We first appraised the EH model against T and S from the Levitus (1982) atlas. This proved frustratingly inconclusive. While the EH output exhibited large departures from Levitus, those discrepancies were insensitive to inclusion of Neptune. Errors in temperature and salinity are more dependent upon other factors such as uncertain surface forcing and model misrepresentation of mixing, stirring, and convection. We turned to datasets that directly address circulation features. (Although circulation and tracer distributions are coupled, inference of one from the other is unclear. A model which might get T and S "right" may still have circulation quite wrong, as seen in uncertainty of inverse models, while conversely "right" circulation can produce quite wrong T and S by misrepresentation of mixing, forcing, etc.)

Altimetric products offer an approach to global circulation, at least on larger scales. However, as models tend to produce similar large scale gyres under Sverdrup dynamics (to within eddy-driven recirculation and artifacts of grid-scale smoothing), altimetry may not be decisive with respect to topographic effects upon mean flow We expect some of the swiftest narrow flows to overly steep topographic slopes where geoid uncertainty will contaminate altimetric estimation of mean flow. Other approaches based upon transient tracers or drifters offer promise which we've not yet pursued. We turn to long-term current meter records.

From published results as well as privately contributed archives, we've assembled more than 2000 records based on minimum duration of 100 days. Unhappily, the global distribution is quite nonuniform. Moreover, one may anticipate that any current meter, even if its duration is sufficient to sample some long-term "mean" (itself an ambiguous idea), may be quite unrepresentative of flow resolved on a model with grid spacing of 200 km (as EH). Equally long-term records obtained only some few kilometers apart may differ markedly depending upon specifics of local topography. Our hope is that, if there is not a systematic bias in the unrepresentativeness of each current meter, then large numbers of records should provide useful skill measure.

Definitions of Skill

At each current meter we obtain mean flow $\mathbf{d}_i = (u,v)_i$, where "mean" means time-average over the duration of the i-th record. We also note the total variance σ^2_i of departures from $\mathbf{d}_i$. (In many cases variances of the u- and v-components, and the uv-correlation, or principal axes of a variance ellipse, are available. However, to provide uniformity over as large a global dataset as possible, we use only σ^2_i.)

In the case of EH, the GFDL model "MOM 1.1") was run in global domain on a grid 1.875° longitude by 1.856° latitude by 31 levels. Two runs were made, integrated for 800 years each under climatological mean wind (Hellerman and Rosenstein, 1983) with surface relaxation of T and S to Levitus (1982). One run ("AsUsual") was done in a conventional manner; the other run ("Neptune") centered the lateral viscosity operator about a non-zero flow field $\mathbf{U}^*$, thus $A_m\nabla^2(\mathbf{u}-\mathbf{U}^*)$, where $\mathbf{U}^*$ is obtained from a transport streamfunction $\psi^* = -fL^2H$, where f is Coriolis parameter, H is water depth and L is length parameter given by EH as a weak function of latitude. The velocity fields from EH runs were then interpolated to current meter locations to obtain model velocity mi. Difficulties arose due to coarseness of grid and the "staircase" topography of the GFDL model. Current meters which might be near steep topography were sometimes seen by the model as interior to "earth". Ad hoc rules "rescued" as many current meters as possible, for example by applying the bottom-most model velocity to be located at the current meter when such current meters occurred "not too far" below the model ocean bottom.

We wish to measure the skill of $\{\mathbf{m}_i\}$ against $\{\mathbf{d}_i\}$. A natural choice is to measure energy of the difference $\mathbf{m}$-$\mathbf{d}$, thus an error kinetic energy $eKE = 0.5(\mathbf{m}-\mathbf{d})\bullet\mathbf{V}^{-1}\bullet(\mathbf{m}-\mathbf{d})$ where $\mathbf{V}$ is a diagonal matrix of elements σ^2_i normalized to trace $\mathbf{V} = 1$. Ideally $\mathbf{V}$ would be a matrix of standard error of estimates $\mathbf{d}_i$ of some "true mean" $< \mathbf{d}_i >$. To make this calculation we would need to estimate numbers of degrees of freedom in the current meter records. In some cases, investigators produced such information; but in many cases it is not available. For uniformity while retaining the largest dataset, we've kept only σ^2_i.

As reference for eKE, we compare the weighted KE of the data ($dKE = 0.5\mathbf{d}\bullet\mathbf{V}^{-1}\bullet\mathbf{d}$). Then it is convenient to form a ratio which we call "skillE" ("E" is for "energy"):

$$\text{skillE} = (\text{dKE} - \text{eKE}) / (\text{dKE} + \text{eKE})$$

such that an error-free model (eKE = 0) yields skillE = 1 whereas a model with huge eKE >> dKE yields skillE approaching -1. Within the range -1 <skillE <1 it is also important to note the skill of a completely skill-less model, one whose flows $\mathbf{m}$ are randomly unrelated to $\mathbf{d}$. With the weighted kinetic energy of the model (evaluated at the current meter locations) given by $mKE = 0.5\mathbf{m}\bullet\mathbf{V}^{-1}\bullet\mathbf{m}$, the value of skillE for the skill-less model is called "skillF" ("F" is for "floor"):

$$\text{skillF} = - \text{mKE} / (2\text{dKE} + \text{mKE})$$

so that the achieved energetic skill of the model is the difference skillE - skillF.

We've examined another measure of skill based only on unit vectors $\mathbf{d}_i = \mathbf{d}_i / |\mathbf{d}_i|$ and $\mathbf{m} = \mathbf{m} / |\mathbf{m}|$ by forming the weighted inner product "skillD" ("D" is for "direction"):

$$\text{skillD} = \mathbf{d}\bullet\mathbf{V}^{-1}\bullet\mathbf{m}$$

so that skillD simply asks if the model knows which way the water goes, regardless of speed. SkillD also falls within bounds -1 <skillD <1

Results

As we gather current meter records from various regions, we ask how stable will be the results for skills E, F and D, given the plausible unrepresentativeness of current meters relative to a coarse resolution model. We found that after we had several hundred records in the database, results became more stable with respect to adding further records. With more than 1000 records, similar results were obtained and were like those found in the present paper using nearly 2000 records as given below:

	E	F	E - F	D
AsUsual	0.003	-0.065	0.068 (0.034)	0.103 (.080)
Neptune	0.093	-0.100	0.193 (0.037)	0.288 (.065)
U* only	0.087	-0.080	0.167	0.289

None of the skills are very large. Although this reflects in part model infidelity, both from unfaithful internal dynamics as well as imperfect applied forcing, the small values of skill also reflect the difference between pointwise current meter records and a model representation on vastly coarser scale (even if such a model were "perfect" on its resolved scales).

Results in the first two rows are from EH, without and with Neptune parameterization. To assess stability of the results, we performed ten trials in which individual current meter records were rejected with probability 0.5. Roughly half the data were randomly discarded for each because we cannot know which current meters are influencing skill. The standard deviations of skills E-F and D from these ten independent trials are shown in parentheses.

Although skills are small, some results emerge. All of the E-F and D are positive, which may be encouraging for the numerical modeling enterprise in general! Moreover, the skills are positive by more than one standard deviation across the ten trials that randomly reject half the data. Of concern here is that the *increment* in skill from "AsUsual" to Neptune is roughly *twice* as great as the basic skill of "AsUsual". This increment is substantially larger than the standard deviation across the ten trials.

One sees clear suggestion that eddy-topographic forcing is a major part of ocean dynamics, hitherto omitted in non-eddy-resolving models and possibly quite corrupted by marginally eddy-resolving "eddy-admitting") models. The specific parameterization employed by EH appears to contribute skill. One could imagine repeating the skill calculations above to "tune" the EH parameterization; however, the computational cost to do so is large and may not be warranted given the presently uncertain basis on which the EH parameterization was proposed.

A third line in the table adds a chilling footnote. Our idea with Neptune parameterization is that internal eddy tendencies compete with externally imposed forcing (wind, thermal, freshwater, ...) We suppose that combining the two tendencies by means of parameterization should yield superior results, as the table indeed indicates. Now we "turn the table" by retaining only the parameterized internal tendencies while omitting all external forces. [One may object that without external forcing there wouldn't be eddies hence shouldn't be any such parameterization. However, first, we only mean to pose an "interesting" remark and, second, we omit only mean forcing. Or one could bandy words about stochastic forcing by unresolved monster goldfish.] Without mean external forcing, Neptune simply brings the flow to $\mathbf{u} = \mathbf{U}^*$. Following conventional wisdom that wind and sun and such cause ocean currents, we should expect to see skill markedly reduced when we remove (in the mean) the wind and sun and such. Surprisingly and perhaps distressingly, the table does not support this. Skills E - F and D under U* only are insignificantly different from Neptune (which includes conventional forcing). While the global inventory of current meters shows statistical mechanics at work, after taking this into account the inventory of current meters cannot tell "which way the wind blows". [We haven't taken a next step to blow the mean wind backwards and see if it really doesn't matter.]

There is another footnote. While we have drawn upon statistical mechanics to improve the modeling of mean flow, there is an intimate connection between equilibrium statistical mechanics and nonlinear stability as discussed by Carnevale and Frederiksen (1987), leading us to suggest that flows nearer to $\mathbf{U}^*$ should be more stable hence more steady.

Do current meter records support this? From the inventory, we formed two bins: simply "with" or "against" $\mathbf{U}^*$ (as sign $\mathbf{d} \cdot \mathbf{U}^*$). We found (for the number of current meters then available) there were 677 "against" and 1156 "with" $\mathbf{U}^*$, consistently with skillD. Averaged over each bin, we formed the kinetic energy of fluctuations (eddy KE, "EKE") and the kinetic energy of mean flows "MKE"). Ratios EKE/MKE were 1.78 "with" and 3.03 "against". These are ratios of average quantities. We also considered the ratio EKE_i/MKE_i at each current meter, averaging these ratios over each bin. The results are wilder (less stable) numbers: 35.1 "with" and 99.1 "against". We see evidence that when external forcing admits flows closer to statistical mechanical equilibrium, these tend to exhibit less variability.

Aconclusion

It is too early to draw conclusion about such a "new" idea as the role of entropy gradients forcing ocean flows. The important and rather exciting observation is that it seems possible to make substantial advances in the skill of ocean models (or theory) by recognizing internal eddy tendencies as playing a role far greater than in usual eddy viscosity. We consider a probability distribution of possible oceans, gradients of distribution entropy appearing as forces acting upon realized moments of the distribution. Approximating such forces in practice has consisted of estimating the entropy gradient by (linear) departure from an approximate state of higher entropy (a maximum under idealized quasi-geostrophic (QG) dynamics). In particular we anticipate that eddy-topographic effects ("Neptune") should drive flows toward a non-zero mean state rather than "as usual" state of rest. A poorly determined eddy "fudge factor" appears as the L^2 in the definition of $\mathbf{U}^*$. We surely guess that this prescription is not "right"; only it may be less wrong than "as usual".

Comparing effects of including Neptune tendency with observations from a global inventory of current meters, one may be encouraged by a striking increment in skill. Measured either by kinetic energy of the difference between model flow and observed flow, or simply by agreement in direction, the increment in skill is nearly twice as large as the basic skill "as usual". A caution is needed: These results, based upon model integrations of EH, test skill against a particular configuration of the GFDL ocean model, with coarse resolution and sundry internal parameters under particular conditions of external forcing. Such model outcomes are distressingly sensitive to "fiddles" with internal parameters and external forcing, with "details" of topography, and with respect to underlying model formulation (for example in layers rather than levels). The danger of appearances of right answers for wrong reasons is ever a concern. What we can see is the possibility for substantial progress, both at theoretical understanding and at practical model skill. This motivates fresh attention to such basics as statistical mechanics in QG dynamics and to extensions such as explored by Roubicek et al. While further efforts are made at fundamentals, we may also learn from try-and-see practical application, ranging from global integrations through marginal sea studies (Alvarez et al., 1994; Holloway et al., 1995) to estuarine scales (Fyfe and Marinone, 1995).

Acknowledgment. GH has been supported in part by the National Science Foundation (OCE 93-11550) and TS by the Office of Naval Research (N00014-92-J-1775).

References

Alvarez, A., J. Tintore, G. Holloway, M. Eby and J. M Beckers, 1994, Effect of topographic stress on the circulation in the western Mediterranean, *J. Geophys. Res.*, 99, 16053-64.

Carnevale, G. F. and J. S. Frederiksen, 1987, Nonlinear stability and statistical mechanics of flow over topography, *J. Fluid Mech.*, 175, 157-181.

Eby, M. and G. Holloway, 1994, Sensitivity of a large scale ocean model to a parameterization of topographic stress, *J. Phys. Oceanogr.*, 24, 2577-2588.

Fyfe, J. and G. Marinone, On the role of unresolved eddies in a model of the residual currents in the central Strait of Georgia, B.C., *Atmos-Ocean*, to appear

Hellerman, S. and M. Rosenstein, 1983, Normal monthly wind stress over the World Ocean with error estimates, *J. Phys. Oceanogr.*, 13, 1093-1104.

Holloway, G., 1992, Representing topographic stress for large scale ocean models, *J. Phys. Oceanogr.*, 22, 1033-46.

Holloway, G., T. Sou, and M. Eby, Dynamics of circulation of the Japan Sea, J. Mar. Res., to appear.

Levitus, S., 1982, *Climatological Atlas of the World Ocean*, NOAA Prof. Paper 13, Washington, DC.

The Interaction of Waves, Currents and Nearshore Bathymetry

R.A. Holman

College of Oceanic and Atmospheric Sciences, Oregon State University, 104 Ocean Admin Building, Corvallis, OR 97331-5503

Abstract. The nearshore is, by definition, a region where topography has an O(1) influence on fluid processes. These processes range from the evolution of ocean waves as they peak and break over the shrinking depths of the shoaling bathymetry, to the transfer of energy to other motions spanning a wide range of frequencies from mean flows through infragravity motions forced by modulations of incident wave heights, up to surface-injected turbulence associated with plunging breakers. On simple (monotonic) beach profiles, these processes are fascinating and wide ranging. The introduction of complexity in the bathymetry through the addition of one or more offshore sand bars adds new processes that had not been expected and that are not simple extrapolations of monotonic beach dynamics.

The primary difference between nearshore processes and other regions discussed in this 'Aha Huliko'a workshop is that the bottom boundary is not fixed, but responds itself to the overlying fluid motions. Depth changes can be O(1) on time scales as short as a day. Thus understanding the behavior of the nearshore requires understanding of not just the two components (fluid forcing and bathymetric response) in isolation, but of the behavior that is associated with the interaction between these two components. In analogy to other cases, this feedback introduces the possibility that the nearshore acts a nonlinear system with the potential for unusual and even chaotic behavior. Observations are now confirming this possibility. Success will take a combination of exploratory modeling and a strong but simple field program for the collection of long data sets of system behavior.

The Nearshore Problem

The nearshore is defined by its sloping bottom bathymetry, extending from offshore depths that are greater than an incident wavelength (hence effectively infinite) to zero depths at the shoreline. Over this region a shoaling wave field, propagating from the deep ocean toward the beach, will undergo a profound evolution (Figure 1). The sight of waves steepening, then pitching over into a turbulent breaker is familiar to all. From a spectral point of view, this transformation drives energy from intermediate, ocean frequencies of order 0.1 Hz to both the higher frequencies of peaky wave forms and turbulence as well as to lower frequencies and even mean flows. Thus, the issue of "flow-topography interactions" is a continual presence in the study of nearshore processes; there are no nearshore processes without the sloping topography of the beach. Thus, for the purposes of this conference the topic of the influence of topography on flow was narrowed to focus on the differences in fluid dynamical processes associated with "complex" topography, particularly the presence of a sand bar or other non-monotonic feature in the beach profile.

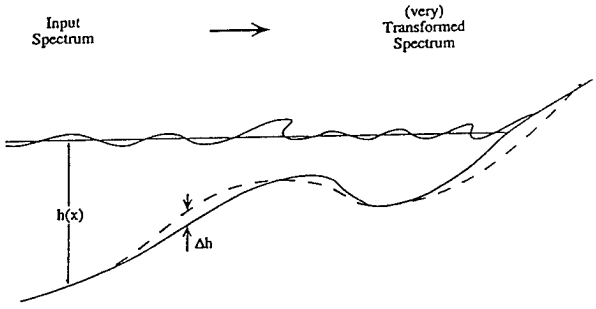


Figure 1. The basic problem in nearshore processes is to understand the shoaling of an incident wave spectrum over a shallowing bathymetry, $h(x)$. Depending on the nature of the bathmetry, transformations of the fluid field are usually strong, spreading energy across the spectrum. Moreover, these motions will cause a slow, cumulative change in the bottom profile that can easily become significant on the time scale of one day. Feedback between these two components can be substantial. Variability in the longshore dimension (not shown) is generally significant.

However, this approach of examining the fluid processes associated with wave propagation over a fixed but non-simple topography is just one half of the problem. In fact, the beach topography, the bottom boundary condition for the fluid motions, is itself made up of unconsolidated sand that will slowly respond to the overlying fluid motions (Figure 1). While the sediment mobility has no substantial impact on instantaneous fluid processes, sediment transport is cumulative, with the time scale of appreciable bathymetric change being about three orders of magnitude longer than that of fluid motions at the corresponding length scale. If the fluid processes are temporarily considered fixed, then models can be formulated for the tendency of the bottom to change form, for example with the generation of a new sand bar form.

If studies of the nearshore system are motivated by development of a predictive capability, then the interaction aspects of the system cannot be ignored. Fluid processes depend crucially upon bottom topography while bottom topography depends on overlying fluid motions. This feedback is the basis of nonlinear dynamical behavior of the entire nearshore system. To tackle the problem, we must be willing (and able) to explore the nature of the entire nonlinear nearshore system.

This paper will provide a flavor of the progress being made and the problems encountered in the contemporary studies of nearshore processes. In the next section, examples of the interesting physics associated with fluid dynamics over non-monotonic bathymetry will be described. Next, the simple, linear models, traditionally invoked to explain the generation of non-simple bathymetry, will be summarized along with their failures. Then the complications that are expected when feedback of the interaction is allowed will be discussed. Finally, some future research directions will be noted.

The Influence on Complex Topography on Nearshore Flow

All nearshore flows are distinguished by the importance of sloping bathymetry. Numerous review articles have been written (e.g., [*Holman*, in press]) describing progress in the understanding of fluid processes over shoaling bathymetry that is considered fixed (this is the situation for the typical field experiment, where nearshore topography is regularly measured and, for modeling purposes, is considered constant between surveys). The range of interesting physics is large, but one noted example has been the generation of infragravity energy (periods of order 60 s), apparently forced by modulation of the incident wave amplitude. While the frequency and longshore wavenumber characteristics of this forcing appear quite broad-banded, the nearshore response appears well tuned (Figure 2), consisting of resonances of topographically trapped edge waves [*Oltman-Shay et al.*, 1989].

In the past decade, earlier studies on monotonic beach profiles have been extended to more complex, barred beaches through field experiments at Duck, NC, and other sites. In many ways, the influence of the increased complexity has not been substantial, merely leading to kinematic changes to the wave form but no new physics [*Howd et al.*, 1992]. However, for low sloping beaches where the bar appears dynamically to be distant from the shoreline, incident band energy can be refractively trapped to the bar, independent of the shoreline fluid field [*Bryan and Bowen*, in review]. The consequences of these bar-trapped edge wave resonances to the behavior of the overall system remain to be determined.

A perhaps more startling consequence of complex topography was found with the discovery of shear waves in the nearshore at far infragravity frequencies (of order 200 s) [*Bowen and Holman*, 1989; *Oltman-Shay et al.*, 1989]. Shear waves are vorticity waves that arise from the instability of mean longshore currents. They are rigid lid phenomena, with longshore propagation rates slightly slower the peak mean longshore current velocity, at least an order of magnitude slower than the slowest gravity wave of similar frequency (Figure 3).

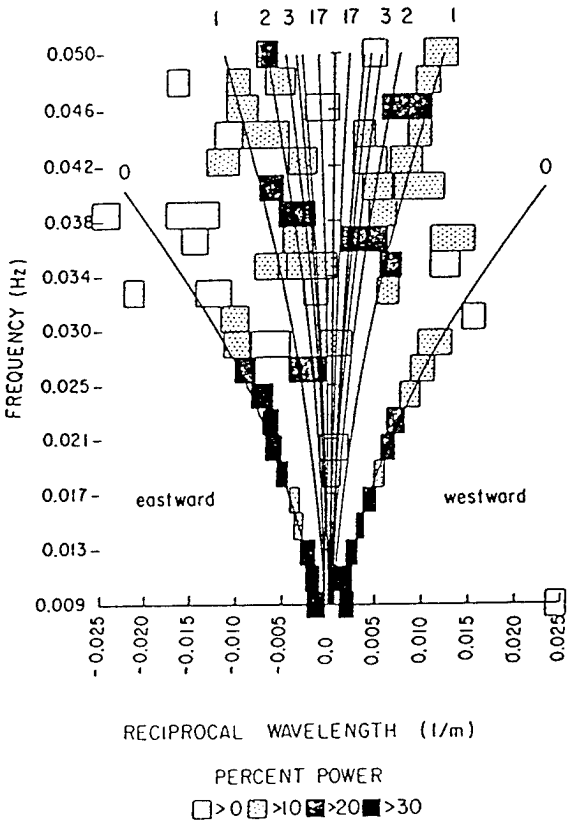


Figure 2. The distribution of wave energy with frequency (vertical axis) and longshore wavenumber (horizontal axis) for a representative day at Santa Barbara, CA, a beach with a monotonic profile. The channel shown is the longshore component of velocity. Through the infragravity band (shown here), the distribution of energy in wavenumber is certainly not broad, instead concentrating strongly at wavenumbers predicted for low mode edge waves (curved lines). From [*Oltman-Shay and Guza*, 1987].

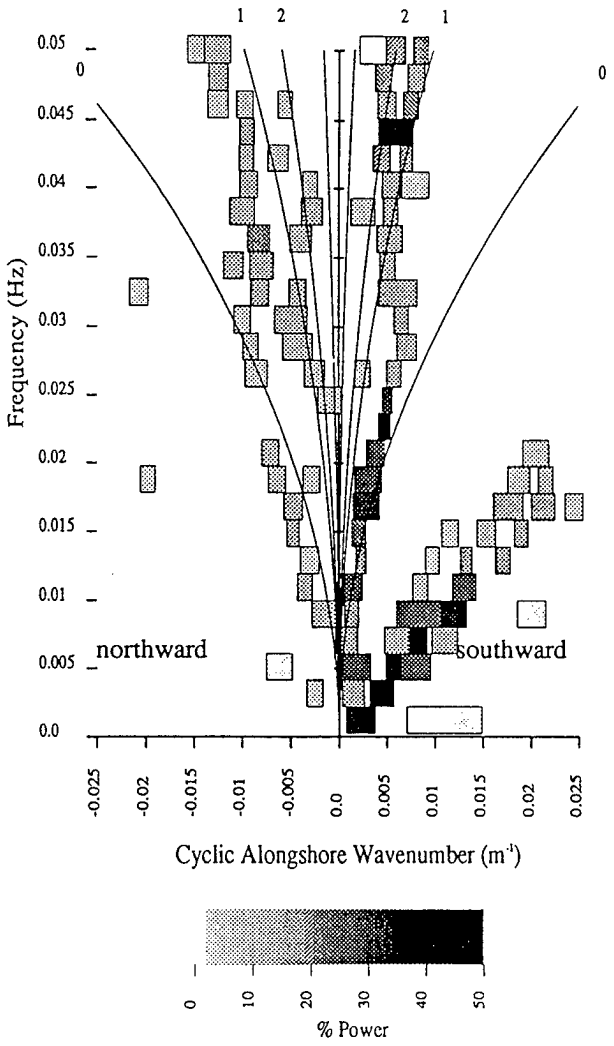


Figure 3. Frequency-wavenumber spectrum of longshore velocity for Duck, NC, a beach with a distinct offshore sand bar. Similar to Figure 2, there is a concentration of energy into narrow bands, associated with edge waves (an offset between theoretical mode lines and the data was later corrected by accounting for Doppler shifting due to the mean longshore current). In contrast to Figure 2, these is also a clear ridge of energy indicating motions progressing to the south at celerities that were substantially too slow to be associated with any gravity wave (the indicated mode 0 dispersion lines are the slowest known gravity wave motions). This ridge represents shear wave energy, driven by an instability of the mean longshore current. From [*Oltman-Shay, et al.*, 1989].

In principle, longshore currents will be unstable on both monotonic and complex beach profiles. However, the strength of the instability depends on the seaward shear of the longshore current jet. On barred beaches, a large shear is forced by wave breaking on the seaward face of the sand bar and the instability is strong. On monotonic beaches, wave breaking is spread over a wide region and the seaward shear is weak; the strength of the instability is weak, barely exceeding frictional dissipation.

Thus, a systematic difference exists in the dynamics of longshore currents between barred and monotonic beaches. The strong shear waves generated over a sand bar have an associated cross-shore Reynolds flux of momentum that serves to diffuse the mean longshore current jet (in fact, there is reason to believe that observed cross-shore profiles of mean longshore current may represent a balance between a jet-like tendency due to strong breaking fixed to the bar crest and a broader form due to the cross-shore mixing of this jet by the shear wave instability whose strength varies with the shear of the jet). Note that the dynamics of this cross-shore mixing would be quite different on a monotonic beach where shear waves play no significant role. Thus, proper modeling of nearshore mixing is fundamentally different on complex versus monotonic beach profiles.

The Influence of Flow on Nearshore Bathymetry

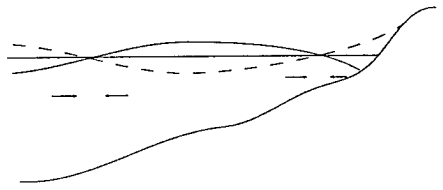
Traditional models for the generation of complexity in nearshore bathymetry have been linear in the sense that a template for sediment transport convergence has been provided by some characteristic of the nearshore flow field. Two popular candidates for producing the template were (a) some change in flow associated with the onset of wave breaking (the break point model), and (b) the nodal patterns of standing wave motions (Figure 4). For the latter, scale analysis showed that standing wave motions of sufficiently large scale to explain natural sand bars were typically of infragravity wave periods. Hence much of the interest in understanding the dynamics of these low frequency waves.

Several problems exist with these simple models. First, the prediction of sediment accumulation according to a particular pattern (for example a sand bar at some cross-shore location) implies that the fluid processes have associated with themselves a single cross-shore scale (or at least a single, simple pattern). Neither models easily fits this criteria. *Holland* [in review] showed that natural infragravity band motions are very broad-banded, with no evidence that spectral peaks are statistically different from that expected for white noise. Thus, there would be no preferred cross-shore scale. For the break point model, natural wave fields have been shown to have wave heights that are Rayleigh distributed such that the location of the onset of breaking will be broadly distributed on monotonic beaches [*Thornton and Guza*, 1983]. While the onset of breaking is concentrated near the bar crest on beaches with a pre-existing sand bar, this is just the response of the fluid to a pre-existing topography, not the reverse.

The latter point illustrates the second problem with "linear" models of sand bar generation; they are limited to

- Establishment of a "template" of sediment convergence by:

a) nodes of standing infragravity waves



b) breakpoint of incident waves

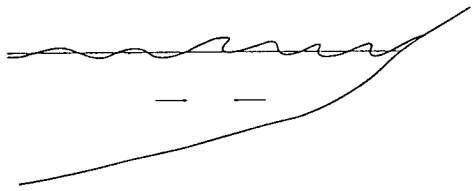


Figure 4. "Linear" models of sand bar generation rely on the slow convergence of sediment toward a pattern (template) that is a function of the fluid field only. Two models associate the template with (a) the nodes of standing wave motions of a particular infragravity frequency, and (b) the location of the onset of incident wave breaking.

small amplitude bathymetric response (the fluid processes are considered fixed and not dependent on slow changes in the bathymetry). In fact, fluid motions are notoriously dependent on the details of the bottom boundary condition. The pattern of wave breaking will vary strongly even for the addition of a small perturbation on a previous simple bathymetry. Similarly, edge waves and other infragravity motions deform kinematically in response to changes in the bathymetry. Thus, linear models for the tendency of a beach profile to change under these fluid influences are limited to now-casting, with predictive capability severely limited by the rapid feedback of small bathymetric changes back into the overlying fluid motions.

The Complete Interaction Problem

The field of nearshore processes is different from other disciplines with respect the to the topic of this 'Aha Huliko'a workshop of fluid topography interactions. Like other discussed GFD problems of the workshop, there is also a substantial and interesting influence of complex topography on nearshore fluid processes. However, unlike other fields, there is also an accompanying response of the topography to the fluids. This response can be on the same order as the local depth in time scales as short as one day.

Thus, the nearshore should be considered as a system with two, fully interacting components. This feedback is one of the primary characteristics of a nonlinear dynamical system. From analogy with other such systems, we realize that these basic nonlinearities can introduce substantial complexity in the system and that our (linear) intuition may not be sufficient even to anticipate the basic phenomenology of the nearshore.

Ample evidence exists that the nearshore system has much more complex behavior than we had previously suspected. For example, long term monitoring in the Netherlands has shown that the ubiquitous multiple offshore bar system there is offshore-progressive, with a period of roughly 4 years on the southern half of the mainland coast, 15 years on the northern half, and a different period on the northern barrier islands (Figure 5) [*Ruessink and Kroon*, 1994; *Wijnberg and Wolf*, 1994]. Such a behavior is not intuitive and has not been a constraint on previous modeling.

Direct observations of the morphology of natural sand bars (the horizontal map pattern of bar crest position) confirm the feared complexity that occurs on natural beaches. For example, at Oregon State University, time exposure imaging of incident wave dissipation patterns has been exploited to study natural morphologies for the past decade [e.g., *Lippmann and Holman*, 1989]. These observations have shown that the simple sand bar morphologies (linear and even crescentic forms) are in the minority and that the most common bar configuration is one that is visually irregular in the longshore [*Lippmann and Holman*, 1990] (e.g., Figure 6).

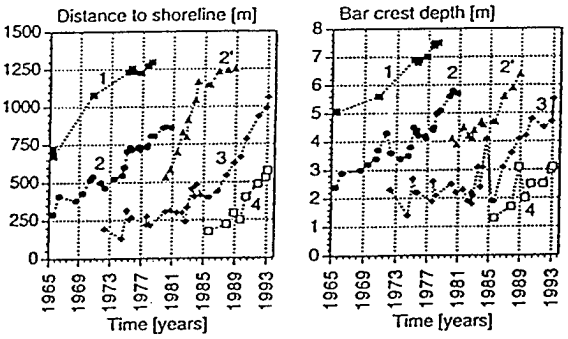


Figure 5. Time variability of the position (a) and depth (b) of the bar crest of a natural bar system on one of the barrier islands on the North Sea Coast of the Netherlands. Bars apparently are formed close to the shore, then propagate steadily offshore to disappear when the bar crest depth reaches about 6 m. Offshore progression was a surprising observation that was only apparent after viewing long time series. From [*Ruessink and Kroon*, 1994].



Figure 6. Example video time exposure taken from Agate Beach, OR, on July 27, 1993. White bands show regions of preferred wave breaking (in taking a ten-minute time exposure, individual wave crests are no longer visible, only their time average dissipation pattern). Dark bands correspond to channels of deeper water, while white bands occur over submerged sand bars (or at the shoreline). The complexity of the bar system in this image is apparent. Substantial variability occurs over short time scales.

The Future - How to Proceed

In analogy to simple nonlinear dynamical systems, we choose to proceed with two approaches. The first is to investigate grossly simplified equations of the system (coupled equations for both the fluid motions over a bathymetry and the bathymetric response to those motions) to study the basic nature of the nonlinearities and to attempt to understand the basic phenomenology inherent in the systems. The emphasis on simplified equations rests on the assumption that the basic behavior (for example, the existence of sand bars and of longshore variability in the bar system) lies with the nonlinearities of the basic equations and is robust to details of the formulation (for example, the details of the wave bottom boundary layer and of sediment transport mechanics).

The second approach is to collect long time series of "system behavior" in order to search empirically for a phase plane in which the behavior is simply understood. This approach is easier to state than to do, with several sources of complication arising. While the use of time exposure techniques (Figure 6) provides a simple, cheap and effective tool for this task (the time series at Duck, NC, the oldest of our stations, now extends to almost one decade), and while the white bands of preferred breaking have been shown to provide a good proxy for crest position of underlying sand bars, there remain complications in interpretation of these data. Primary among these is the need to develop simple metrics of system state (bathymetry is a fully two dimensional field; we need to reduce dimensionality to at most one dimension, but preferably to a few scalar descriptors that can be easily visualized and compared to models). We cannot begin to search for simplifying phase plane representations until the metrics are identified (and the most useful metrics are those that will provide a simplifying phase plane representation!). The situation is further complicated by the need for appropriate non-dimensionalization so that beaches lying in different regions of dimensional parameters space (e.g., different climatological wave height or period) and with visually different behavior can be understood in some universal sense.

Conclusions

The nearshore is, by definition, a region where fluid-topography interactions define the active processes. On simple (monotonic) beach profiles, these processes are fascinating and wide ranging. The introduction of complexity in the bathymetry through the addition of one or more offshore sand bars adds new processes that had not been expected and that are not simple extrapolations of monotonic beach dynamics.

The real distinguishing feature of the nearshore is that the bottom boundary for the flow, the underlying sediment, is movable and depth changes can be O(1) on time scales as short as a day. This feedback of the flow back into the topography makes the nearshore system a nonlinear system with the potential for unusual and even chaotic behavior. Observations are now confirming this possibility. Success will take a combination of exploratory modeling and a strong but simple field program for the collection of long data sets of system behavior.

Acknowledgments. The author would like to acknowledge the long term support of several funding agencies including the U.S. Geological Survey, Coastal Geology program under cooperative agreement 1434-93-A-1124, and particularly the Office of Naval Research (Coastal Dynamics program, grant N00014-90J1118), a supporter since I began this business. Thanks to Peter Muller and Phyllis Haines for the kind invitation to the workshop and their patience waiting for this manuscript and, of course, to Marcia Turnbull for help in all those little, and big, things. Thanks to Megan Burt and best of luck in the next year.

References

Bowen, A.J., and R.A. Holman, Shear instabilities of the mean longshore current, 1. Theory, *J. Geophys. Res.*, *94*(C12), 18,023-18,030, 1989.

Bryan, K.R., and A. J. Bowen, Edge wave trapping and amplification on barred beaches, *J. Geophys. Res.*, in review.

Holland, K.T., C. Valentine, and R.A. Holman, Wavenumber-frequency structure of infragravity swash motions, *J. Geophys. Res.*, in review.

Holman, R.A., Nearshore processes, U.S. National Report to the IUGG (1991-1994), in press.

Lippmann, T.C., and R.A. Holman, Quantification of sand bar morphology: A video technique based on wave dissipation, *J. Geophys. Res.*, *94*(C1), 995-1011, 1989.

Lippmann, T.C., and R.A. Holman, The spatial and temporal variability of sand bar morphology, *J. Geophys. Res.*, *95*(C7), 11,575-11,590, 1990.

Oltman-Shay, J., S. Elgar, and P. Howd, Observations of infragravity-frequency long waves, II, Comparisons with a 2-D wave group generation model, *EOS Trans. AGU, 70*, 1333, 1989.

Oltman-Shay, J., and R.T. Guza, Infragravity edge wave observations on two California beaches, *J. Phys. Oceanogr.*, *17*(5), 644-663, 1987.

Oltman-Shay, J., P.A. Howd, and W.A. Birkemeier, Shear instabilities of the mean longshore current, 2. Field data, *J. Geophys. Res.*, *94*(C12), 18,031-18,042, 1989.

Ruessink, B.G., and A. Kroon, The behavior of a multiple bar system in the nearshore zone of Terschelling, the Netherlands, 1965-1993, *Mar. Geol.*, *121*, 187-197, 1994.

Thornton, E. B., and R.T. Guza, Transformation of wave height distribution, *J. Geophys. Res.*, *88*(C10), 5925-5938, 1983.

Wijnberg, K.M., and F.C J. Wolf, Three-dimensional bar behaviour, in *Proceedings Coastal Dynamics '94*, Edited by A.S.-Arcilla, M. J.F. Stive and N.C. Kraus, pp. 59–73, ASCE, Barcelona, 1994.

Topographic Effects in the Ocean

P. Müller

School of Ocean and Earth Science and Technology University of Hawaii, Honolulu, Hawaii, U.S.A.

G. Holloway

Institute of Ocean Sciences, Sidney B.C., Canada

The effects of seafloor topography on ocean circulations are more complicated and more influential than previously supposed. Recent advances, driven by intensive observational efforts and by increasingly powerful numerical simulations, show the crucial role that topography plays in abyssal circulations, mixing, ocean-shelf exchanges, and the rectification of time-dependent flows. Progress on these and related topics was reviewed at the eighth 'Aha Huliko'a Hawaiian Winter Workshop which was held January 17-20, 1995, at the University of Hawaii in Honolulu and drew together observers, numerical and laboratory modelers, and theorists.

Abyssal Circulations

Topographic influences are most felt by the deep abyssal circulations. Continental margins and ridges confine the flow to basins connected by narrow channels. These abyssal circulations are currently being mapped by ambitious observational programs; among them are the Synoptic Ocean Prediction (SYNOP) program in the Gulf Stream region between Cape Hatteras and the Grand Banks and the Deep Basin Experiment in the Brazil Basin. Both regions show complex flow structures governed by basin topography with in- and outflow through passages (N. Hogg). Flow through these passages might be critically controlled, as seen in laboratory experiments. A comparison of estimates assuming critical control with volume fluxes through the Romanche Fracture Zone, the Vema Channel, the Discovery Gap, and other passages (based on CTD data) shows general good agreement (J. Whitehead).

Numerical simulations of deep abyssal circulations employ various types of models. The flow of dense water from the southern Adriatic Sea into the eastern Mediterranean Basin was simulated by D. Haidvogel using an inverted 1½ layer reduced gravity model with prescribed inflow and uniform upwelling. R. Salmon employed a model based on an abridgement of the planetary geostrophic equations and applied it to the deep flow approaching the Samoan Passage. Numerical models often have to assume unrealistically large friction coefficients; R. Ford solved the linear wind-driven planetary geostrophic equations in realistic bathymetry with a triangular finite element net based on points that lie on a set of geostrophic contours and obtained solutions at much smaller values of friction than have previously been obtained. The aggregate force that topography exerts on mean flows is called "form stress" or "topographic stress". In a barotropic quasigeostrophic model, slightly elongated ridges with axes inclined to a uniform incident flow lead, surprisingly, to different stress regimes when the inclination angle is reversed (G. Carnevale).

Seamounts

An especially intensive observational program was conducted at Fieberling Guyot in the eastern North Pacific to study the flow at and around an isolated seamount. The observations show an anticyclonic vortex cap on top of the seamount produced by tidal rectification, internal wave spectra with peaks at the critical reflection frequency, and trapped diurnal (K1) oscillations that must be interpreted as vertically propagating vortex-trapped or evanescent waves rather than as strictly standing seamount-trapped waves (C. Eriksen, E. Kunze). The wave fields around the seamount are associated with regions of low Richardson numbers, density inversions, and enhanced turbulent mixing. Topographically trapped waves are also observed in other places, e.g., riding along portions of ridges and along rectilinear valleys, and exhibit energy levels well above "background" (D. Luther).

Critically reflected internal waves and topographically trapped waves are an energy source for enhanced turbulent mixing at seamounts and other topographic features. An open problem is how this "boundary mixing" affects the stratification in the ocean interior and whether or not it can account for the large effective diffusivities of several 10^{-4} m^2 s^{-1}, required by mass and heat balances in abyssal basins, and bigger than those found by direct microstructure turbulence measurements in the upper ocean. The observations at Fieberling Guyot suggest that internal waves do not provide enough energy for such a large effective diffusivity, but Fieberling Guyot may not be representative. Another open question is whether or not secondary flows can efficiently move mixed water away from the boundary or can restratify the mixed water.

The large data base obtained at Fieberling Guyot provides essential bounds for numerical simulation. Using a sigma-coordinate model, A. Beckmann investigated the strength and spatial structure of the

rectified flow at the flanks and on the top of a steep isolated seamount. While many aspects of the simulation agree well with the observations at Fieberling Guyot, there are also discrepancies, especially in the time-dependent flow.

The phenomena of wave trapping at topography is of principal interest to theorists and often investigated with methods borrowed from theoretical physics. The circumstances under which trapping occurs at an isolated seamount are fairly well explored. M. Hendershott considered the extension to a random array of seamounts and identified circumstances for which geostrophic flow perturbations remain localized or propagate through the seamount array. The wave equation for long monochromatic surface gravity waves can be transformed to a Schrödinger equation, which facilitates the analysis of the possible wave modes. Trapping of a different kind occurs when a monochromatic internal gravity wave is introduced into a channel. Upon successive reflections the wave becomes focussed to a limiting trajectory (L. Maas).

Ocean-Shelf Exchanges

The coastal ocean meets the deep ocean at the continental shelf edge. The constraint that steep bathymetry poses on ocean-shelf exchanges can be broken by a number of processes: internal tides and waves; upwelling, fronts, and filaments; downwelling and cascading; along-slope currents, instability, and meanders; eddies; tides, surges, and coastally trapped waves. A preliminary assessment of this daunting list was made by J. Huthnance, according to their scales and context. Some of the processes have already been studied in some detail. An intensive observing program at Astoria Canyon showed details of the interaction of a time-dependent along-shelf current with the canyon and points to a special role that canyons may play in ocean-shelf exchanges (B. Hickey). Internal Lee waves generated by along-slope flows over small-scale topography show an asymmetry in the propagation characteristics that lead to a transport of mean-flow momentum onto the shelf (S. Thorpe).

Flow separation is important in numerous areas of engineering fluid mechanics. It is also apparent in many nearshore flows and has significant implications for nearshore dispersion. The physics depends on bottom slope, friction, stratification, and rotation. Most of this parameter space has not, however, been explored (C. Garrett). Using the wind-forced barotropic shallow-water vorticity equation, J. Becker examined the dynamics and energetics of western boundary current detachment above a continental margin. Flow separation may also play a role in the deep ocean and constitutes a mechanism by which mixed fluid layers can detach from the boundary and contribute to interior mixing. Flow separation might also be the cause of a wave-like signal observed in sea level records in the Western Pacific. Using GEOSAT altimetric heights, G. Mitchum has tracked this signal all the way back to South Point on the Big Island of Hawaii.

Laboratory Studies

Theoretical studies and numerical experiments are complemented by laboratory studies. S. Allen studied flows that encounter various sorts of obstacles and delineated the linear effects governed by propagation of topographic Rossby waves from nonlinear effects and the influence of stratification on both. G. Ivey studied in detail the turbulent mixing induced by the critical reflection of internal waves at a slope, and S. Thorpe showed how the presence of a sloping boundary affects the transition to turbulence in a stratified shear flow and leads to "twisted" billows. J. Verron performed experiments in the 13-m diameter rotating tank in Grenoble to study rectification in a coastal geometry with an offshore bank. The laboratory results agree qualitatively with simulations from a homogeneous primitive equation numerical model, showing two distinct flow regimes depending on the ratio of the flow oscillation to the background rotation frequency. Overall, these laboratory studies provide detailed and specific insights into topographic effects that might be at work in the ocean.

Rectification Process

The interaction of eddies, waves, or oscillating flows with topography generates mean flows. This rectification process was the topic of the 1989 workshop "Topographic Stress in the Oceans" (Holloway and Müller, 1990, Eos 71, 12). Since then considerable progress has been made, mostly the result of increasingly powerful simulations. When considering the rectification process, a distinction needs to be made between the direct forcing by independently driven eddy processes and the reorganization of the mean flow caused by instabilities (as in the Gulf Stream recirculation). High-resolution experiments with a barotropic shallow water model show that an initial field of random eddies in a basin surrounded by continental margin topography produces a vigorous rectified flow (A. Shchepetkin). Experiments in a similar setting with a three-layer fluid of coarser resolution were performed by E. Chassignet to investigate how well the topographic stress exerted by unresolved eddies can be represented in a coarser resolution model, following statistical mechanical tendencies. Coarse resolution models with parameterized eddy-topography interaction showed improved fidelity when compared with data from a global inventory of long-term current meter observations (G. Holloway).

In a coastal configuration, D. Haidvogel compared five differently formulated numerical models. While rectification of an imposed oscillatory flow occurred in each of the models, specific results differed substantially among the models.

The Surf Zone, Where Topography and Flow Interact

In many circumstances, the topography is given and the flow responds. But there are circumstances when the topography yields. This was impressively documented in a time-lapsed video by R. Holman. It showed the sandbank patterns shifting under the influence of the pounding surf at an Oregon beach over a two year period. Here, flows and topography truly interact with nonlinear feedback loops that are not fully understood yet.

Conclusions

The influence of topography on ocean circulations is greater than previously supposed. Though confident characterization of the dynamic processes is still problematic ambitious observing programs and powerful numerical simulations have caused some striking advances in recent years:

- One of the last frontiers in oceanography, the circulation in deep basins, is being mapped and its dynamics explored by various types of numerical models and ideas from hydraulic control.
- Processes, like internal wave reflection and topographically trapped wave modes, are now recognized to lead to vigorous mixing near slopes. The larger scale consequences of this boundary mixing are being explored.
- While the importance of understanding ocean-shelf exchange processes is increasingly recognized, this remains a daunting subject for laboratory studies, numerical simulations, and comprehensive field experiments.
- The parameterization of topographic stress (rectification), while not yet a fully resolved issue, has seen marked progress since the 1989 meeting as a result of novel approaches based on statistical mechanical tendencies and increasingly powerful numerical simulations.

Acknowledgments

We thank the participants of the workshop for their contributions to this report and for their permission to quote unpublished material. Copies of the proceedings are available from Peter Müller, Department of Oceanography, University of Hawaii, 1000 Pope Road, MSB 307, Honolulu, HI 96822. The eighth 'Aha Huliko'a Hawaiian Winter Workshop was supported by Department of Navy grant N00014-94-1-0600 issued by the Office of Naval Research. The U.S. government has a royalty-free license throughout the world in copyrightable material contained herein.

UNCLASSIFIED
SECURITY CLASSIFICATION OF THIS PAGE

REPORT DOCUMENTATION PAGE

1a. REPORT SECURITY CLASSIFICATION Unclassified	1b. RESTRICTIVE MARKINGS
2a. SECURITY CLASSIFICATION AUTHORITY	3. DISTRIBUTION / AVAILABILITY OF REPORT Approved for public release; distribution unlimited
2b. DECLASSIFICATION / DOWNGRADING SCHEDULE	
4. PERFORMING ORGANIZATION REPORT NUMBER(S)	5. MONITORING ORGANIZATION REPORT NUMBER(S)
6a. NAME OF PERFORMING ORGANIZATION School of Ocean and Earth Science and Technology 6b. OFFICE SYMBOL (If applicable)	7a. NAME OF MONITORING ORGANIZATION Office of Naval Research
6c. ADDRESS (City, State, and ZIP Code) Department of Oceanography, Univ. of Hawaii 1000 Pope Road Honolulu, HI 96822	7b. ADDRESS (City, State, and ZIP Code) Department of the Navy 800 No. Quincy Street Arlington, VA 22217
8a. NAME OF FUNDING / SPONSORING ORGANIZATION 8b. OFFICE SYMBOL (If applicable)	9. PROCUREMENT INSTRUMENT IDENTIFICATION NUMBER N00014-94-1-0600
8c. ADDRESS (City, State, and ZIP Code)	10. SOURCE OF FUNDING NUMBERS PROGRAM ELEMENT NO. / PROJECT NO. 3222973-01 / TASK NO. / WORK UNIT ACCESSION NO.

11. TITLE (Include Security Classification)

Topographic Effects in the Ocean

12. PERSONAL AUTHOR(S)
Muller, Peter and Henderson, Diane (eds.)

13a. TYPE OF REPORT	13b. TIME COVERED	14. DATE OF REPORT (Year, Month, Day)	15. PAGE COUNT
Workshop proceedings	FROM 12/1/94 TO 1/30/95	September 1995	280

16. SUPPLEMENTARY NOTATION

Proceedings, 'Aha Huliko'a, Hawaiian Winter Workshop, January 1995, Honolulu, Hawaii

17. COSATI CODES		
FIELD	GROUP	SUB-GROUP

18. SUBJECT TERMS (Continue on reverse if necessary and identify by block number)
abyssal circulations; seamounts, topographic waves, ocean-shelf exchanges, topographic stress, mixing, rectification

19. ABSTRACT (Continue on reverse if necessary and identify by block number)

These proceedings contain the lectures given at the eighth 'Aha Huliko'a Hawaiian Winter Workshop on "Flow-Topography Interactions" and a meeting report. The lectures and the meeting report cover the major effects that sea-floor topography causes on ocean circulation.

20. DISTRIBUTION / AVAILABILITY OF ABSTRACT	21. ABSTRACT SECURITY CLASSIFICATION
☒ UNCLASSIFIED/UNLIMITED ☐ SAME AS RPT. ☐ DTIC USERS	Unclassified
22a. NAME OF RESPONSIBLE INDIVIDUAL	22b. TELEPHONE (Include Area Code) / 22c. OFFICE SYMBOL

DD FORM 1473, 84 MAR 83 APR edition may be used until exhausted. All other editions are obsolete.

SECURITY CLASSIFICATION OF THIS PAGE
UNCLASSIFIED